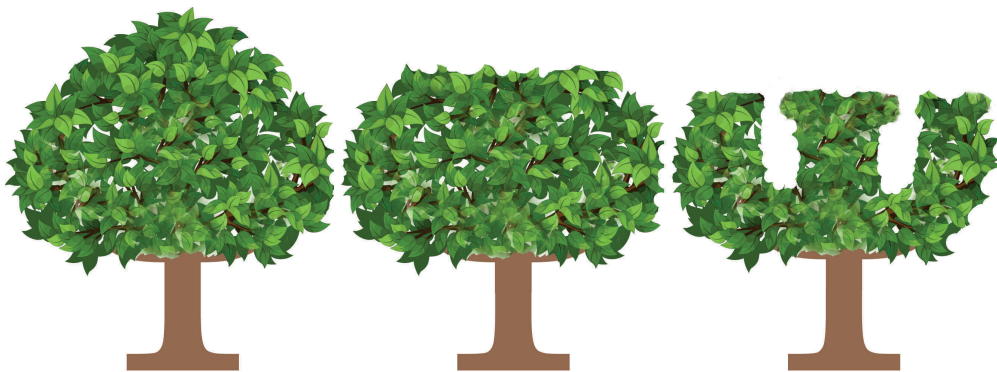
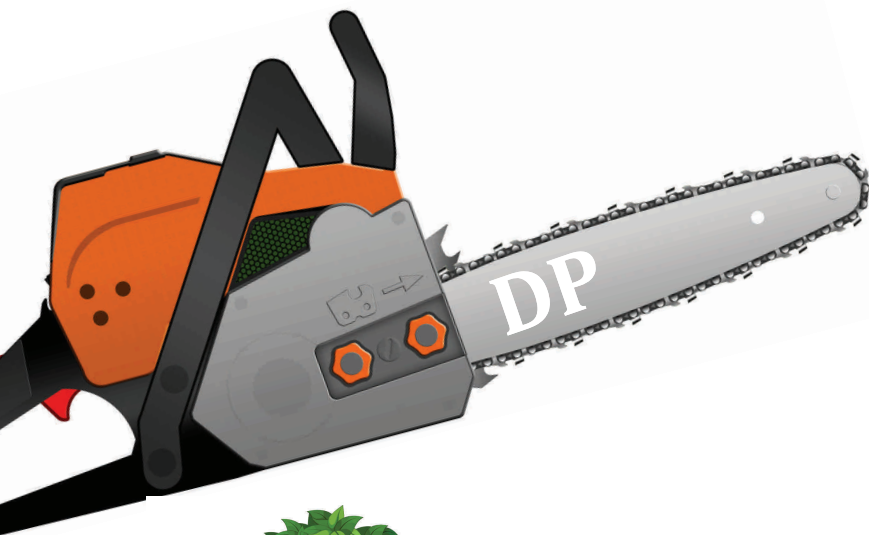
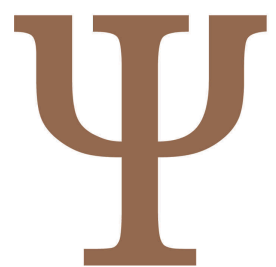


Efficient Approaches to Multidimensional Quantum Dynamics

Dynamical Pruning in Phase, Position
and Configuration Space



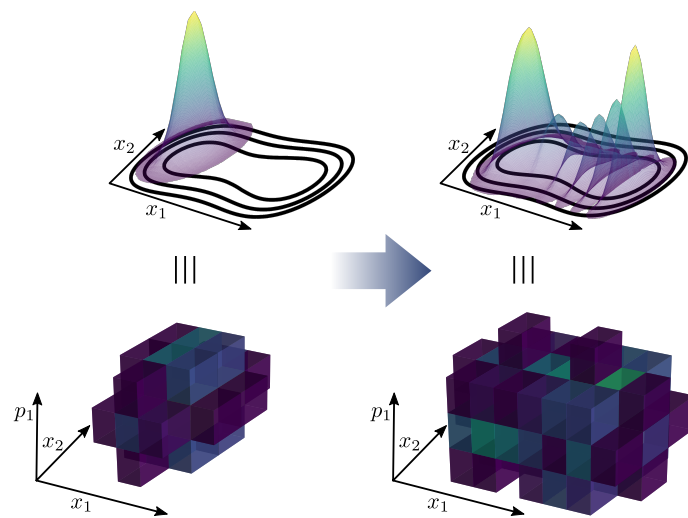
**Henrik R.
Larsson**



Dissertation for the degree Doctor rerum naturalium
at Christiana Albertina University of Kiel

Efficient Approaches to Multidimensional Quantum Dynamics

Dynamical Pruning in Phase, Position and Configuration Space



Dissertation

in partial fulfillment of the requirements
for the degree

Doctor rerum naturalium

of the Faculty of Mathematics and Natural Sciences
at Christiana Albertina University of Kiel

submitted by

Henrik R. Larsson

Kiel, March 2018

Henrik R. Larsson

Efficient Approaches to Multidimensional Quantum Dynamics

Dynamical Pruning in Phase, Position and Configuration Space

Dissertation, March 2018

First referee:	Prof. Dr. Bernd Hartke, Kiel University, Germany
Second referee:	Prof. Dr. David J. Tannor, Weizmann Institute of Science, Rehovot, Israel
Third referee:	Prof. Dr. Hans-Dieter Meyer, Heidelberg University, Germany
Date of the disputation:	May 18, 2018
Approved for publication:	May 18, 2018

Abstract

Quantum dynamical calculations of larger molecular systems are difficult to perform because of an exponential scaling of the (direct-product) basis size with dimensionality. A similar difficulty is observed for electronic ionization dynamics in strong laser fields where the continuum needs to be described. In this thesis, methods are developed that reduce the scaling and speed up the computation by dynamically selecting the most contributing functions from a direct-product basis during the propagation. This is called dynamical pruning (DP).

The DP approach is applied to coordinate-space localized discrete variable representation (DVR) bases, phase-space localized bases (projected von Neumann with biorthogonal exchange (PvB) and projected Weylet (pW)) and, within the multi-configuration time-dependent Hartree (MCTDH) method, to single-particle functions (SPFs). Standard direct-product bases give a favorably computational scaling of the action of the Hamiltonian onto a wavefunction. A new and efficient algorithm is developed that enables the same scaling for pruned orthogonal bases. It is shown that nonorthogonal pruned bases like PvB give an inferior scaling. Possible approximations to re-obtain favorable scaling for PvB are discussed but turn out to be not accurate enough. Instead, the orthogonal but phase-space localized pW basis is developed. It is tested and compared with DVR for real-world applications and for up to six-dimensional systems. Although typically fewer basis functions are required when using pW, DVR is faster and easier to use because the potential operator representation is diagonal. This leads to a lower prefactor of the scaling and, in contrast to phase-space bases and MCTDH, there is no need for a specific sum of products (SoP) form of the potential. Compared to conventional simulations, DP simulations perform up to 25 times faster in runtime while retaining accuracy.

Additionally, DP is combined with MCTDH by pruning either the primitive basis or the SPFs. Pruning the primitive basis enables the usage of higher-dimensional mode combination and reduces the requirements regarding SoP forms of the Hamiltonian. Pruning the SPF basis typically reduces the runtime more drastically than pruning the primitive basis. Both methods can be combined. DP-MCTDH with mode combination is benchmarked for dynamics of a 24-dimensional vibronic coupling model of pyrazine. There, nine-dimensional SPF spaces are pruned. Compared to conventional MCTDH dynamics, DP-MCTDH is up to 50 times faster in runtime without jeopardizing accuracy. This makes it competitive with state-of-the-art but more complex multilayer MCTDH.

The newly developed methods are implemented in a new, modern and full-fledged quantum dynamics package. Its implementation is briefly discussed.

Further, **DP-DVR** is applied to resonance calculations and decay dynamics simulations of the deuterated formyl radical DCO. Its accidental Fermi resonance of the vibrational modes leads to strong coupling of zero-order states, making the dynamics more complicated. Decay dynamics of selected resonances are analyzed and older results from a polyadic model Hamiltonian are confirmed. Computed kinetic energy release spectra show good agreement with experimental spectra obtained from velocity-map imaging.

DP-DVR is also tested for electronic ionization dynamics. Accurate photoelectron momentum distributions (**PMDs**) for the hydrogen atom are computed and the runtime is compared with other, more established methods. There, not only a **DVR** basis but also Legendre polynomials are pruned. The resulting runtime of **DP-DVR** is average but can be improved by further optimizations to this particular problem and by the inclusion of surface flux methods. In contrast, **DP-DVR** performs much better for double ionization dynamics of a one-dimensional helium model; there it outperforms conventional methods. In order to control the ejection of the two electrons into opposite directions *via* the form of the external field, extensive quantum control optimizations are performed. Several optimization algorithms are compared. With derivative-free optimization routines and local control algorithms, fields that lead to the desired behavior of the electrons are found. A common mechanism can be identified where the field first displaces the wavepacket such that both electrons are ejected into the *same* direction while they are close to each other. When the field vanishes, the repulsion of the electrons and the attraction by the nucleus lead to the desired movement of the electrons into *opposite* directions.

As a final application, the statically pruned time-dependent generalized active space configuration interaction (**TD-GAS-CI**) method is employed in order to study extreme ultraviolet (**XUV**) initiated high harmonic generation (**HHG**) in helium. The intensity of the harmonics can be controlled by changing the temporal delay between an **XUV** pulse and an infrared pulse. Accurate simulations show good agreement with experimental data.

Kurzzusammenfassung

Quantendynamische Simulationen größerer molekularer Systeme sind aufgrund der exponentiellen Skalierung konventioneller Direkter-Produktbasen mit der Dimensionalität nur sehr schwer durchzuführen. Ähnliches gilt für Elektronenionisationsdynamik in starken Laserfeldern, bei denen auch das Kontinuum beschrieben werden muss. In dieser Arbeit werden Methoden entwickelt, welche die Skalierung reduzieren und Computersimulationen beschleunigen. Dies wird erzielt durch eine dynamische Auswahl der am meisten beitragenden Funktionen aus einer Direkten-Produktbasis. Die Methode wird dynamische Beschneidung (DP) genannt.

DP wird auf koordinatenraumlokalisierte Funktionen der Diskreten Variablendarstellung (DVR), phasenraumlokalisierte Basen, sog. projizierte Von-Neumann-Basen (PvB) und projizierte Welyets (pW), sowie, innerhalb der multikonfigurationellen zeitabhängigen Hartree-Methode (MCTDH), auf sog. „Einteilchenfunktionen“ (SPFs) angewandt. Konventionelle Direkte-Produktbasen ergeben eine günstige Skalierung der Anwendung des Hamiltonoperators auf die Wellenfunktion bezüglich der benötigten Rechenressourcen. Eine ebensolche Skalierung wird durch eine neue Entwicklung eines Algorithmus für beschnittene, orthogonale Basisfunktionen erzielt. Nichtorthogonale Funktionen wie PvB ermöglichen diese Skalierung für beschnittene Basen nicht. Näherungen, welche die günstige Skalierung wiedereinführen, werden diskutiert, sind derzeit aber nicht genau genug. Anstelle dessen wird die orthogonale und phasenraumlokalisierte pW-Basis entwickelt. Diese wird zusammen mit beschnittenen DVR-Basen für bis zu sechsdimensionale, reale Systeme getestet und verglichen. Auch wenn pW typischerweise weniger Basisfunktionen benötigt, ist die DVR-Methodik schneller und einfacher zu benutzen, da die Potentialoperatordarstellung diagonal ist. Dies resultiert in einem reduzierten Vorfaktor in der Skalierung. Zudem wird keine Summe-von-Produkten-Form (SoP) benötigt, wie es bei pW und MCTDH der Fall ist. Im Vergleich zu konventionellen Simulationen ergeben DP-Simulationen eine um bis zu 25 Mal kürzere Laufzeit, ohne dass Genauigkeit eingebüßt wird.

Des Weiteren wird DP mit dem MCTDH-Verfahren verbunden. Dabei wird die sog. primitive Basis und/oder die SPF-Basis beschnitten. Eine Beschneidung der primitiven Basis ermöglicht die Verwendung von höherdimensionalerer Modenkombination und reduziert damit die Anforderungen an eine SoP-Darstellung des Hamiltonoperators. Allerdings reduziert die Beschneidung der

SPF-Basis die Programmlaufzeit typischerweise drastischer. Beide Beschneidungen können aber kombiniert werden. Die resultierende DP-MCTDH-Methode wird für 24-dimensionale Dynamik eines vibronischen Kopplungsmodells von Pyrazin mittels Modenkombination getestet. Dazu werden neundimensionale SPF-Räume beschnitten. Verglichen mit Standard-MCTDH-Dynamik ist DP-MCTDH um bis zu 50 Mal schneller, ohne dabei größere Genauigkeitsverluste aufzuweisen. Damit ist DP-MCTDH ähnlich schnell wie das kompliziertere, hochmoderne Mehrschicht-MCTDH-Verfahren (multilayer MCTDH).

Die neu entwickelten Methoden sind in einem neuen, modernen und flexiblen Quantendynamikprogrammpaket implementiert. Dies wird kurz diskutiert.

Als Anwendung von DP-DVR werden die Berechnung von Resonanzen im deuterierten Formylradikal DCO und die Simulation der Zerfallsdynamik dieser Resonanzen betrachtet. Aufgrund einer zufälligen Fermiresonanz der Vibrationen ergibt sich eine starke Kopplung der Zustände nullter Ordnung, was in eine komplizierte Zerfallsdynamik mündet. Diese wird für ausgewählte Resonanzzustände analysiert und damit ältere Resultate eines Polyadenmodells bestätigt. Berechnete Energiespektren des Deuteriums ergeben eine gute Übereinstimmung mit Daten aus Geschwindigkeitskartographiemessungen.

Zusätzlich wird die Anwendung von DP-DVR auf Elektronenionisationsdynamik getestet. Genaue photoelektronische Impulsverteilungen für das Wasserstoffatom werden berechnet und die Laufzeit von DP-DVR wird mit denen von anderen, etablierten Methoden verglichen. Zusätzlich zur DVR wird hier auch eine Legendrebasis beschnitten. Im Laufzeitvergleich schneidet DP durchschnittlich ab. Die Methodik kann aber durch weitere, für das System zugeschnittene Optimierungen und durch die Kombination mit Flusstechniken verbessert werden. Dahingegen ist die Laufzeit bei der Zweifachionisationsdynamik eines eindimensionalen Heliummodells deutlich besser als die von konventionellen Methoden. Um die Austrittsrichtung der Elektronen im Helium durch eine geeignete Wahl eines externen Feldes zu kontrollieren, werden umfassende Quantenkontrolloptimierungen durchgeführt und mehrere Optimierungsalgorithmen verglichen. Das Ziel ist, dass die Elektronen in entgegengesetzte Richtungen austreten. Sowohl ableitungsfreie als auch lokale Kontrollalgorithmen ergeben Felder, welche zur erwünschten Austrittsrichtung führen. Ein für diese Felder gemeinsamer Mechanismus wird aufgezeigt. In diesem wird das Wellenpaket erst so versetzt, dass beide Elektronen in *dieselbe* Richtung austreten. Sobald das Feld verschwindet, ergeben die elektronische Abstoßung und die Anziehung durch den Atomkern die gewünschte Bewegung hin zu einem Austritt in *entgegengesetzte* Richtungen.

Zuletzt wird die statisch beschnittene, zeitabhängige Konfigurationswechselwirkungsmethode mit verallgemeinertem aktiven Konfigurationsraum (time-dependent generalized active space configuration interaction (TD-GAS-CI)) verwendet, um die durch extrem ultraviolettes (XUV) Licht initiierte Bildung von höheren Harmonischen (HHG) in Helium zu studieren. Die Intensität der auftretenden Harmonischen kann durch Änderung des zeitlichen Abstands zwischen einem XUV- und einem Infrarot-Puls kontrolliert werden. Genaue Simulationen liefern eine gute Übereinstimmung mit experimentellen Daten.

Contents

List of Figures	xv
List of Tables	xvii
List of Listings	xix
List of Acronyms	xxi
List of Publications	xxv
Motivation	1
I Developing the Dynamical Pruning Approach	9
I.1 Phase Space and Coordinate Space Methods	11
I.1.1 Publication: Review of the Methods	15
I.1.1.1 Own Contributions	15
I.1.1.2 Bibliographic Data	15
I.1.1.3 Article	16
I.1.1.4 Complementary Information	48
I.1.2 Publication: Projected von Neumann Bases	53
I.1.2.1 Own Contributions	53
I.1.2.2 Bibliographic Data	53
I.1.2.3 Article	54
I.1.2.4 Complementary Information	67
I.1.3 Publication: Projected Weylets and Discrete Variable Representations	68
I.1.3.1 Own Contributions	68
I.1.3.2 Bibliographic Data	68

I.1.3.3	Article	69
I.1.3.4	Supplementary Information	82
I.1.3.5	Complementary Information	87
I.2	Configurational Space Methods	89
I.2.1	Publication: Dynamically Pruned Multi-Conf. Time-Dependent Hartree	92
I.2.1.1	Own Contributions	92
I.2.1.2	Bibliographic Data	92
I.2.1.3	Article	93
I.2.1.4	Complementary Information	105
I.2.1.5	Implementation of the Equations for the Single-Particle Functions	108
I.3	The LAGOM package	111
I.3.1	Capabilities of the Package	112
I.3.2	Requirements of the Package	114
I.3.3	Already Available Packages	114
I.3.4	Choice of Programming Languages	115
I.3.4.1	Python	116
I.3.4.2	C++	116
I.3.4.3	Other Languages	117
I.3.5	Elements and their Implementation of Quantum Dynamics Methods	117
I.3.5.1	Conventional Discrete Variable Representation Dynamics	117
I.3.5.2	Conventional Multi-Conf. Time-Dependent Hartree Dynamics	118
I.3.5.3	Dynamically Pruned Dynamics	119
I.3.6	Used Programming Concepts	119
I.3.6.1	Combining Various Programming Languages	119
I.3.6.2	Functional Programming	119
I.3.6.3	Generic Programming	120
I.3.6.4	Object Orientation	121
I.3.6.5	Design Patterns	124
I.3.6.6	Data Structures	126
I.3.7	Overall Structure of the Package	127
I.3.8	Input Example	127
II	Applying Pruning Methods	131
II.1	Resonance Decay Dynamics of the Deuterated Formyl Radical	133
II.1.1	Publication	134
II.1.1.1	Own Contributions	134
II.1.1.2	Bibliographic Data	134

II.1.1.3	Article	135
II.1.1.4	Supplementary Information	150
II.2	Photoelectron Momentum Distributions of Atomic Hydrogen	165
II.2.1	External Fields	165
II.2.2	Electron Dynamics and Strong Field Physics	167
II.2.2.1	Ponderomotive Potential	167
II.2.2.2	Keldysh Parameter	168
II.2.2.3	Tunnel Ionization	168
II.2.2.4	High Harmonic Generation	170
II.2.3	Computation of Photoelectron Momentum Distributions	171
II.2.3.1	How to Obtain Scattering States	171
II.2.3.2	Surface Flux Methods	172
II.2.3.3	Window Operator Method	172
II.2.4	Publication: Benchmark of Time-Dependent Schrödinger Equation Solvers	173
II.2.4.1	Own Contributions	174
II.2.4.2	Bibliographic Data	174
II.2.4.3	Problem Definition	174
II.2.4.4	Outgoing Scattering States	175
II.2.4.5	Setup	176
II.2.4.6	Results	177
II.2.4.7	Conclusions and Outlook	180
II.3	Control of Double Ionization Dynamics of Helium	181
II.3.1	Quantum Optimal Control Theory	182
II.3.1.1	General Formulation	183
II.3.1.2	Time Discretization	185
II.3.1.3	Krotov Method	187
II.3.1.4	Variants and Extensions	188
II.3.1.5	Alternatives	188
II.3.2	Local Quantum Control Theory	189
II.3.3	Many-Particle Systems	190
II.3.4	The One-Dimensional Helium Model	192
II.3.4.1	Model	192
II.3.4.2	Coordinate System	192
II.3.4.3	Control Targets and Control Strategies	194
II.3.5	Results and Discussion	199
II.3.5.1	Optimal Control	200
II.3.5.2	Local Control	212
II.3.6	Conclusions and Outlook	216

II.4 High Harmonic Generation of Helium Initiated by Extreme Ultraviolet Radiation	217
II.4.1 The Time-Dep. Generalized Active Space Conf. Interaction Approach	218
II.4.1.1 Choice of Orbitals	218
II.4.1.2 Determining the Pruned Configuration Space	219
II.4.1.3 Comparison to Multi-Configuration Time-Dependent Hartree-Fock	222
II.4.1.4 Comparison to Dynamical Pruning	223
II.4.2 Publication: Extreme Ultraviolet-Initiated High Harmonic Generation	225
II.4.2.1 Own Contributions	225
II.4.2.2 Bibliographic Data	225
II.4.2.3 Article	226
II.4.2.4 Supplementary Information	235
II.4.2.5 Complementary Information	253
III Conclusions	255
III.1 Résumé	257
III.2 Prospects	261
III.2.1 Full Configuration Interaction	261
III.2.1.1 On-The-Fly Potential Calculation	263
III.2.2 Multi-Configuration Time-Dependent Hartree	264
III.2.3 Electron Dynamics	266
III.2.4 Molecular Dynamics	266
IV Appendix	267
Bibliography	i
Declaration	xxi
Academic Curriculum Vitae	xxiii
Acknowledgments	xxvii

List of Figures

0	Depiction of what the DP-Scheme has been applied to.	7
I.1.1	Wavepacket reaction dynamics for a collinear model of $D_2 + F$	12
I.1.2	Cartoon of the DP scheme.	13
I.1.3	Error of using vN with numerical integration.	49
I.1.4	Error of using vN with different DVRs.	51
I.1.5	Comparison of SG-, vN -functions and Weylets in coordinate space.	52
I.2.1	Cartoon-like comparison of grid methods against optimal direct-product bases. . .	90
I.2.2	Comparison of spectra from (ML-)MCTDH and DP-MCTDH.	105
I.2.3	Sparsity analysis of the wavefunction coefficient tensor.	108
I.3.1	State class hierarchy.	122
II.2.1	Example of strong-field ionization.	169
II.2.2	Cartoon of the HHG generation process.	170
II.2.3	Computed photoelectron momentum distributions (PMDs).	178
II.2.4	Accuracy of the PMDs versus wave amplitude threshold.	178
II.3.1	Depiction of the rotated coordinate system for 1D helium.	193
II.3.2	Potential of the helium model.	194
II.3.3	Regions of the helium atom in the continuum.	195
II.3.4	One of the used target states in optimal control.	197
II.3.5	Behavior of a Krotov optimization.	202
II.3.6	Wavefunction for an optimized field.	202
II.3.7	Field for different Krotov iterations.	203
II.3.8	Optimized pulses and final wavefunctions.	206
II.3.9	Coordinate and phase-space analysis of a propagation with pulse (c).	208
II.3.10	Coordinate and phase-space analysis of a displaced wavepacket.	209
II.3.11	Mechanism of the ionization dynamics with optimized pulse.	210

II.3.12 Coordinate and phase-space analysis of a propagation with pulse (b).	211
II.3.13 Optimized pulses and final wavefunctions for local control.	213
II.3.14 Coordinate and phase-space analysis of the local control propagation.	215
II.4.1 Example of a partially rotated basis.	219
II.4.2 Example of electronic configurations.	220
II.4.3 Example of a generalized active space division.	222
II.4.4 Comparison of HHG spectra for various GAS.	253
II.4.5 Comparison of delay-scans for various GAS.	254

List of Tables

I.1.1	Error of the standard harmonic oscillator for variants of vN	50
II.2.1	Runtimes for computing the photoelectron momentum distributions.	179
II.3.1	Optimized pulse parameters.	205

List of Listings

I.3.1 Update of active basis set using lists.	126
I.3.2 Update of active basis set using hash tables.	126
I.3.3 Example input of the program.	128
I.3.4 Operator file for the example input.	130

List of Acronyms

API	Application Programming Interface	117
BLAS	Basic Linear Algebra Subprograms	116
CAP	Complex Absorbing Potential	172
CAS	Complete Active Space	221
CAS-CI	Complete Active Space Configuration Interaction	221
CAS-SCF	Complete Active Space Self-Consistent Field	223
CC	Coupled Cluster	4
CDVR	Correlation Discrete Variable Representation	115
CI	Configuration Interaction	191
CIS	Configuration Interaction Singles	253
CISD	Configuration Interaction Singles Doubles	220
CMF	Constant Mean Field	113
CPU	Central Processing Unit	112
DFT	Density Functional Theory	263
DOI	Digital Object Identifier	15
DP	Dynamical Pruning	5
DP-DVR	Dynamically Pruned Discrete Variable Representation	133
DP-MCTDH	Dynamically Pruned Multi-Configuration Time-Dependent Hartree	91
DVR	Discrete Variable Representation	13
EOM	Equation Of Motion	91
FBR	Finite Basis Representation	176
FCI	Full Configuration Interaction	4
FE-DVR	Finite Element Discrete Variable Representation	113

FFT	Fast Fourier Transform	262
FGH	Fourier Grid Hamiltonian	48
FPGA	Field-Programmable Gate Array	112
GAS	Generalized Active Space	217
GAS-CI	Generalized Active Space Configuration Interaction	221
GPGPU	General-Purpose Graphics Processing Unit	112
GTO	Gaussian-Type Orbital	4
HF	Hartree-Fock	218
HHG	High Harmonic Generation	5
IR	InfraRed	170
LAPACK	Linear Algebra PACKage	118
LASER	Light Amplification by Stimulated Emission of Radiation	166
MCTDH	Multi-Configuration Time-Dependent Hartree	3
MCTDHF	Multi-Configuration Time-Dependent Hartree-Fock	218
ML-MCTDH	MultiLayer Multi-Configuration Time-Dependent Hartree	3
ODE	Ordinary Differential Equation	113
ORMAS	Occupation-Restricted Multiple Active Space	221
PES	Potential Energy Surface	2
PMD	Photoelectron Momentum Distribution	113
PvB	Projected von Neumann with Biorthogonal exchange	13
PvN	Projected von Neumann	48
pW	projected Weylet	13
RAS	Restricted Active Space	221
SAE	Single Active Electron	253
SCF	Self-Consistent Field	221
SE	Schrödinger Equation	2
SG	momentum-Symmetrized Gaussian	49
SIL	Short Iterative Lanczos	113
SoP	Sum of Products	109
SPF	Single-Particle Function	91
SVD	Singular Value Decomposition	91

TD	Time-Dependent	
TD-FCI	Time-Dependent Full Configuration Interaction	5
TD-GAS-CI	Time-Dependent Generalized Active Space Configuration Interaction	217
TDSE	Time-Dependent Schrödinger Equation	2
TISE	Time-Independent Schrödinger Equation	2
VCI	Vibrational Configuration Interaction	116
vMCG	variational Multi-Configuration Gaussian	115
VMF	Variable Mean Field	113
vN	von Neumann	48
WAT	Wave Amplitude Threshold	120
XUV	eXtreme UltraViolet	166

List of Publications

(In order of appearance.)

1	Phase Space vs. Coordinate Space Methods	15
2	Quantum Dynamics in Phase Space using Projected von Neumann Bases	53
3	Efficient Mol. Quantum Dynamics in Coord. and Phase Space using Pruned Bases	68
4	Dynamical Pruning of the MCTDH (DP-MCTDH) Method	92
5	Resonance dynamics of DCO	134
6	Benchmark of time-dependent Schrödinger equation solvers	174
7	XUV-initiated HHG	225

Motivation

“ *The deepest part of theoretical chemistry must end up in quantum mechanics*

— **Richard P. Feynman**

With the early works in metallurgy and cooking, chemistry has a history going back thousands of years. Despite this history of millennia, it has been for a very long time a completely phenomenological science. The establishment of a better understanding of chemistry began roughly with the work of LAVOISIER and others in the 18th century. At that time, LAVOISIER, the “father of modern chemistry”, published his groundbreaking work on combustion and stoichiometry.^[1,2] This led to the publishing of the first (German) book on “theoretical chemistry” by SCHERER.^[3,4] Nevertheless, more than ten years after the work of LAVOISIER (but before SCHERER tried to circularize LAVOISIER’s work in Germany), the famous philosopher KANT wrote in 1786 that the principles of chemistry are merely empirical and thus “the whole does not in strictness deserve the name of science; chemistry indeed should be rather termed systematic art than science”.^[5,6] Even almost 50 years later, the philosopher of science COMTE wrote a withering assessment about the combination of mathematical concepts with chemistry:^[7]

Every attempt to refer chemical questions to mathematical doctrines must be considered, now and always, profoundly irrational, as being contrary to the nature of the phenomena. [. . .] if the employment of mathematical analysis should ever become so preponderant in chemistry (an aberration which is happily almost impossible) it would occasion vast and rapid retrogradation, by substituting vague conceptions for positive ideas, and an easy algebraic verbiage for a laborious investigation of facts.

However, at the same time, the “father of the computer” BABBAGE already predicted a glorified future on the predictability of chemistry.^{[8]1}

¹I am grateful to B. Hartke for pointing me to the work of Comte and Babbage.

Hence the whole of chemistry [...] would become a branch of mathematical analysis, which, like astronomy, taking its constants from observation, would enable us to predict the character of any new compound, and possibly indicate the source from which its formation might be anticipated.

Luckily, BABBAGE was right and COMTE not. During the 19th century, especially physical chemistry grew and allowed, for example, to quantify thermodynamic processes.^[2,4] Still, the major breakthrough was only achieved with the rise of quantum mechanics in the beginning of the 20th century.^[4,9-14] It turned out that quantum mechanics (and sometimes also special relativity) was the theory needed to allow for precise predictions of the properties of molecules and their reactions. The time-dependent Schrödinger equation (TDSE) and time-independent Schrödinger equation (TISE) developed by SCHRÖDINGER allowed for the description of physical systems in terms of a wavefunction or wavepacket that is subject to a partial differential equation.^[15-21]

The Schrödinger equations (SEs) can be used for molecular systems as well. Indeed, the foundations of employing quantum mechanics to chemistry were laid at that time. In 1927, BORN AND OPPENHEIMER^[22] separated the nuclear from the electronic problem leading to the approximation named after them.² At the same time, the bonding of the simplest molecule, H₂, was described and explained by quantum calculations performed by HEITLER AND LONDON. Already in 1931, EYRING AND POLANYI developed the first potential energy surface (PES) for the reaction H₂ + H.^[24] Six years later and about 100 years after the two comments on the combination of chemistry with mathematical principles by BABBAGE and COMTE, the first textbook on *Quantum Chemistry* was written by HELLMANN.^[25,26] This text book covers many standard examples of quantum chemistry like the Morse potential and its eigenstates, higher-dimensional PESs, avoided crossings in adiabatic potential energy curves and scattering calculations for an Eckart potential.³

The “only” remaining problem was to make computations of larger molecular systems solely based on quantum mechanical principles feasible. Indeed, in 1929, DIRAC wrote the following famous words that almost every theoretical chemist knows by heart:^[27]

The underlying physical laws necessary for the mathematical theory of a large part of physics and the whole of chemistry are thus completely known, and the difficulty is only that the exact application of these laws leads to equations much too complicated to be soluble. It therefore becomes desirable that approximate practical methods of applying quantum mechanics should be developed, which can lead to an explanation of the main features of complex atomic systems without too much computation.

Thirty years later in the editorial of the inaugural issue of the *International Journal of Quantum Chemistry*, LÖWDIN clearly described the nature and the tasks of quantum chemistry.^[28] He wrote that “a great deal of attention must [...] be devoted to numerical computations, to numerical analysis, and to the use of large-scale computers”.

²See Ref. [14] for further reading.

³All these examples are still taught in today’s lectures on quantum chemistry.

Since these years, theoretical chemistry has proceeded a lot. In addition to the exponential progress in computer power,^[29] a similarly incredible progress happened in the development of algorithms, suitable approximations and implementations, especially in electronic structure theory.^[30] Nowadays, highly accurate electronic structure computations of even proteins consisting of more than 600 atoms are possible with black-box computer programs.^[31-33] The computation of the electronic structure of a typical molecule to a reasonable accuracy is now a routine procedure both in academic and industrial research.⁴

However, the electronic structure is a *static* property for a fixed arrangement of the nuclei in a molecule. The arrangement changes during a chemical reaction and the reaction is thus only properly described by taking nuclear motion into account. In many applications, a classical treatment of nuclear motion is sufficient.^[34] Nevertheless, the classical description neglects effects such as tunneling,^[35-39] zero-point energy,^[40] resonances^[41,42] or interference phenomena^[14,43,44] and can only approximately and non-rigorously describe nonadiabatic effects.^[45,46] These effects are definitely not only of academic interest. For example, next to thermodynamic and kinetic control, the chemical reactivity can nowadays also be controlled by tunneling.^[39,47] The importance of the *time-dependent* description of nuclear motion was already emphasized by electronic structure theorist (!) LÖWDIN in the aforementioned editorial:^[28]

All phenomena in physics and chemistry are of course time-dependent, and the “stationary states” correspond in reality to idealized physical situations of a particular type which lead to time-independent eigenvalue problems. A large part of quantum chemistry has so far been devoted to these eigenvalue problems and the fact that many of the fundamental problems in physics and chemistry are strongly characterized by their time-dependence, as, for example, radiation theory and chemical kinetics, has perhaps been somewhat neglected.

Despite the progress in electronic structure theory, the accurate treatment of nuclear motion is still a great challenge. Although with state-of-the-art methods like multi-configuration time-dependent Hartree (MCTDH) and multilayer multi-configuration time-dependent Hartree (ML-MCTDH),^[48-53] quantum dynamical calculations of model systems with up to thousands of degrees of freedom are possible,^[49,51,54,55] full-dimensional state-to-state reactive scattering and reaction-rate dynamics can only be achieved for up to 12-dimensional vibrational systems like $\text{CH}_4 + \text{X}$.^[36,42,56] These state-of-the-art calculations can take up to one year of computing time.^[57] With that, full-dimensional quantum simulations of systems with more than six atoms or even routine simulations for systems with more than nine degrees of freedom — except for model systems — seem to be out of reach without further method development. Indeed, in a recent essay, GRIMME AND SCHREINER stated the “routine treatment for many nuclear degrees of freedom and entropy” as one of “six grand challenges for the next 25 years”.^[58]

⁴This statement is true for bound-state properties. An efficient treatment of the continuum and of time-dependent properties for electronic systems is still a challenge; see also Chapters II.2, II.3 and II.4.

Why is the treatment of quantum nuclear dynamics so difficult compared to the treatment of the electronic structure? There are four main reasons: 1) Ground state calculations of the electronic structure versus computations of wavefunctions with contributions from many excited eigenstates, 2) more highly correlated wavefunctions in nuclear dynamics, 3) the requirements of more flexible and general basis functions and 4) the need for getting the PES which often includes many-body terms. The four reasons are discussed in the following.

First, in electronic structure theory, the interest lies in the ground state and sometimes also the first excited states. Already the computation of excited states is more difficult and has less black-box character than getting the ground state. In nuclear dynamics, the wavepacket is composed of *many* eigenstates, including continuum states. This makes the computation much more difficult. Of course, once properties that are related to the continuum need to be described for electronic systems, one encounters the same challenges; see Chapters II.2, II.3 and II.4.

Second, the correlation of an electronic quantum state is often well-behaved. So-called dynamic correlation can be handled efficiently and accurately by methods like coupled cluster (CC).^[30] Compared to the simplest approach, full configuration interaction (FCI), which obeys an exponential scaling law with respect to computing and memory requirements, CC only scales polynomially and — in the long-distance limit — close to linearly.^[31,59] FCI simply includes all possible configurations (Slater determinants for Fermions, Permanents for Bosons or Hartree products for distinguishable particles^[60]) created from a one-particle basis. Methods like CC take advantage of the fact that only one configuration dominates for the description of the state of interest. However, the wavefunctions of some molecules have so-called static correlation where many configurations equally contribute to the state. This is still a challenge in electronic structure theory as no black-box methods are available and the methods for handling static correlation are much more costly. In nuclear dynamics, static correlation is the normal case. Simply consider a reaction: During the reaction, both configurations that describe the educts and configurations that describe the transition states and products are important and need to be treated on an equal footing.

Third, the Hamiltonian for describing the electronic structure is relatively simple and does not change so much for different molecules — the potential is just described by Coulomb interaction between the electrons and between the electrons and the nuclei. This allows for the employment of highly-optimized one-particle basis functions — Gaussian-type orbitals (GTOs) — that are very efficient.^[30] In contrast, the nuclear Hamiltonian often contains a complicated kinetic energy operator^[61] and an even more complicated PES.^[62] The PES changes substantially from molecule to molecule. As such, using optimized basis functions is more difficult, especially for problems where the continuum needs to be described as well.

Fourth, for getting the PES scientists actually first have to solve *many* electronic structure problems for different nuclear arrangements and then fit or interpolate the computed energies to obtain an analytic form of the potential. Already this step contains an exponential scaling of computational resources with dimensionality. Further, the PES includes many-body interactions

and is only approximately decomposable into few-body interactions. In contrast, the Coulomb interaction is “only” of two-body type.⁵ Many-body interactions render the porting of methods from electronic structure theory to vibrational applications difficult.^[48,63]

This explains why high-dimensional systems are still challenging and why black-box methods are much more difficult to develop in nuclear quantum dynamics than in electronic structure theory. The main difficulty with conventional quantum treatments of nuclear motion is still the exponential scaling of computing and memory requirements with dimensionality. This is in stark contrast to electronic structure theory. Both in time-dependent full configuration interaction (TD-FCI) and MCTDH, the wavefunction is expanded in a direct product of lower-dimensional basis functions (the aforementioned Hartree products/configurations). This direct-product *ansatz* is not economic, even if the underlying basis functions are time-dependent and optimized at each time step as in MCTDH. Due to the static correlation character of typical nuclear wavefunctions, polynomially scaling vibrational analogs^[63] of CC have only limited applicability to molecular reaction dynamics. The ML-MCTDH *ansatz* allows for a more sophisticated tensorial approximation of the high-dimensional wavefunction. It actually overcomes the exponential scaling^[50] but it is still difficult to apply.^[64-66]

It turns out that both in a TD-FCI and MCTDH treatment, many configurations are negligible at a particular time step. It is thus useful to consider a dynamic selection of the most important configurations during simulation time. This approach, dubbed dynamical pruning (DP), is pursued in this thesis. DP can be combined both with TD-FCI and MCTDH. DP is not system-specific and as such more universal and simpler to use than approaches tightly bound to a specific setting like L-shaped grids in scattering dynamics.^[67] Actually, the idea of using selected configurations in an adaptive way has already been tried in electronic structure theory for static problems many years ago^[68-70] and currently enjoys renewed attention.^[71,72] Besides that DP allows for a drastic reduction of computational resources, it *might* also lead to procedures that compute the required parts of the PES on-the-fly, avoiding the challenging fitting problem and an exponential scaling already at the stage of setting up the PES. This, however, has not been pursued in this thesis.⁶ An overview of what has been done with DP in this thesis is shown in Fig. 0. The development of DP is described in Part I of this thesis.

In his editorial, Löwdin emphasized also the interplay between experiment and theory and described it as the “most difficult part of science”.^[28] Although this thesis is mostly focused on the advancement of the DP method (and thus it is focused on an easier part of science), some applications have been pursued. This is described in Part II. Among others, it includes the analysis of intramolecular vibrational energy redistributions of resonances in DCO in Chapter II.1 and the computation of high harmonic generation (HHG) spectra in Chapter II.4, both in close connection to experimental results.

⁵Two three-dimensional particles interact *via* the Coulomb potential. For a D -dimensional vibrational system, there are, in general, up to D -body terms, of which at least the two- and three-body terms are very important, for some systems even higher-order terms.

⁶An efficient on-the-fly PES generation comes with its own challenges and more efficient techniques for computing global PES may be more appropriate to tackle the problem of PES generation.^[73-77] This is further discussed in Section III.2.1.1.

Even though I have mentioned scientific giants like SCHRÖDINGER, DIRAC and LÖWDIN, it should be clear that this thesis only contributes a *tiny* part to the collective effort of advancing theoretical chemistry and physics. In particular, the development of DP did not grow out of nowhere. In the group of my supervisors, HARTKE and TANNOR, STEFFEN^[78] worked on it as a diploma student, SIELK,^[79] SHIMSHOVITZ^[80] and ABTA^[81] worked on pruning methods as PhD students and TAKEMOTO,^[82] ASSÉMAT^[83-85] and MACHNES^[83-85] worked on them as postdoctoral scientists. Contributions from other scientists to pruning are described in detail in [Part I](#).

In this thesis, the DP *ansatz* could be substantially improved. For the first time, it could be shown that DP is faster than conventional methods (TD-FCI and MCTDH). For some situations, speed-ups of up to 50 could be obtained, see [Part I](#). Method development and a thorough benchmark was the focus of this thesis. The benchmark studies were done for systems that are nowadays easily accessible (up to nine-dimensional spaces have been pruned and up to 24-dimensional model systems have been studied) and where the PES is readily available. Although in this thesis I did not show that my contributions enabled the computation of bigger systems that cannot be handled by conventional methods, treatment of more challenging systems than those studied here should become feasible with DP. This is left for future work; see [Chapter III.2](#) for a discussion. I thus think that the developed methods make computations of higher-dimensional systems easier, both in terms of user input and resource requirements. It is my hope that my contributions will be useful for succeeding in the task of making quantum dynamical simulations more routine.

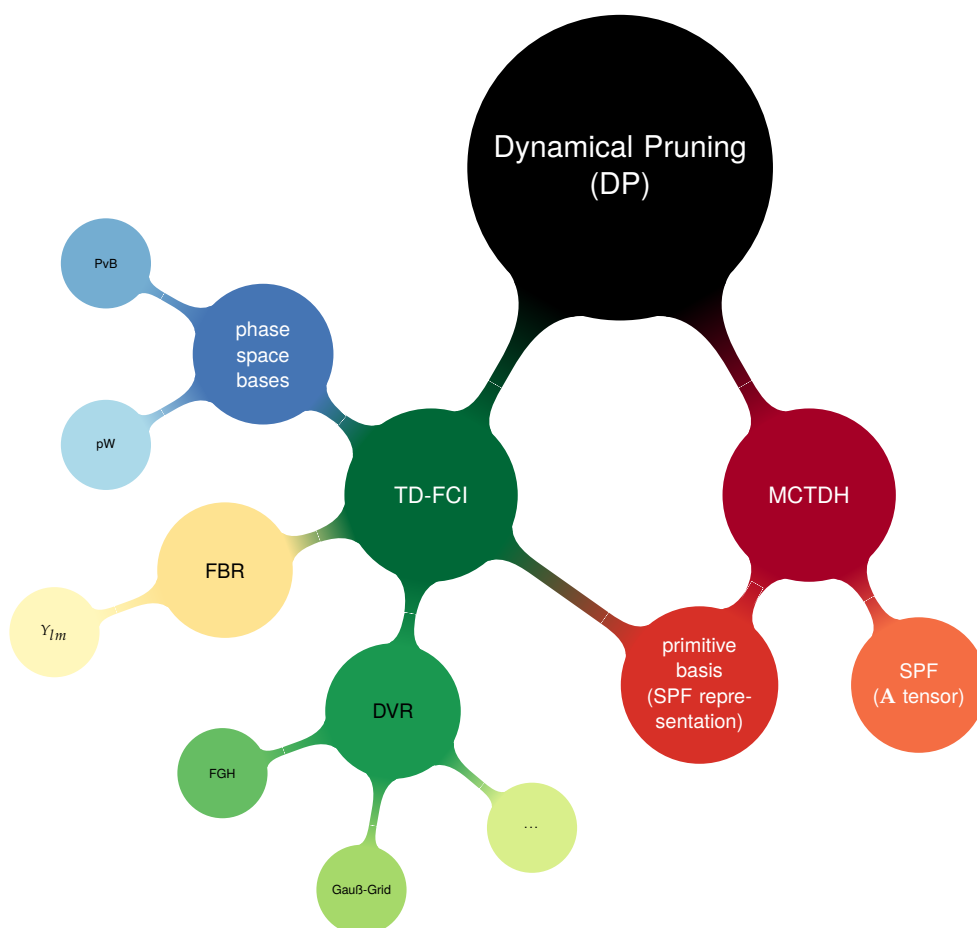


Figure 0.: Depiction to what the dynamical pruning (DP) approach has been applied in this thesis. The time-dependent full configuration interaction (TD-FCI) part is described in [Chapter I.1](#) and the multi-configuration time-dependent Hartree (MCTDH) part in [Chapter I.2](#).

Part I

Developing the Dynamical Pruning Approach

Phase Space and Coordinate Space Methods

” *When one has a particular problem to work out in quantum mechanics, one can minimize the labor by using a representation in which the representatives of the more important abstract quantities occurring in that problem are as simple as possible.*

— Paul A. M. Dirac

A typical wavepacket propagation of a chemical reaction is shown in [Fig. I.1.1](#). The plots shown there clearly illustrate that, although quantum mechanics is non-local, the wavepacket remains quite compact (up to a numerical threshold) in coordinate (and phase) space even for asymptotic propagation times. The only exception is the typically one-dimensional reaction coordinate. A significant portion of the wavepacket will never enter the regions with high potential values because — in a semiclassical interpretation — they are not energetically accessible. Obviously, a simple direct-product (rectangular) grid that covers *all* regions in coordinate (and phase) space is wasteful. This led to the introduction of L-shaped grids.^[67] The ratio of energetically accessible versus non-accessible regions increases with dimensionality and, for higher dimensions, the direct-product grid becomes more and more wasteful.^[86] Of course the regions the wavepacket occupies in coordinate space may change for other systems and for different coordinates describing angles etc. Then, L-shaped grids are not applicable. It is thus useful to employ basis functions or grids localized in a suitable space (coordinate, momentum, phase etc.) and to adapt the required regions where the wavefunction has nonnegligible amplitudes dynamically during propagation time. This leads to the dynamical pruning (DP) approach.

Technically, DP means that a static direct-product-type grid of basis functions localized in a particular space is employed and that at each point in time only those basis functions are selected from this grid that have nonvanishing contributions to the description of the wavefunction. This

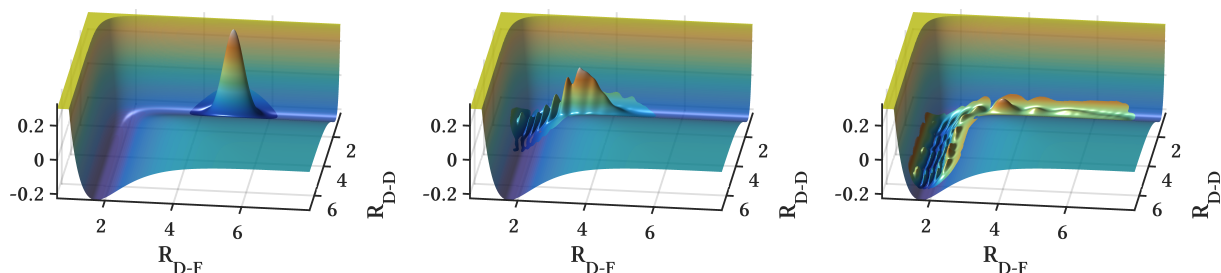


Figure I.1.1.: Wavepacket reaction dynamics for a collinear model of $D_2 + F$. The plots show $|\Psi(R_{D-F}, R_{D-D})|^2$ on top of the potential where R_{X-Y} is the interatomic distance between atoms X and Y. The quantities are given in atomic units. In the three plots, propagation time is increased from left to right. The setup was taken from examples of the wavepacket program from Ref. [87]; see also Section I.3.3. The particular parameters of this simulation are irrelevant in this context but can be found in the program package.

leads to a non-direct-product space although it is based on a direct-product-type basis. Since the wavefunction moves in time, nearest neighbors of contributing basis functions are dynamically added to, and basis functions that cease to contribute are dynamically removed from, the subset of used basis functions. With that, the representation of the wavefunction remains compact during all propagation times. A cartoon of this procedure is depicted in Fig. I.1.2.

Although the TDSE is a complicated high-dimensional partial differential equation, the movement of the wavepacket is smooth in typical physical situations. Given a low enough threshold when to add nearest neighbors, the DP scheme can describe even processes like tunneling, barrier penetration, bifurcation or interference phenomena;^[89] see also Chapter II.1, II.2 and Chapter II.3 for challenging applications in dissociation and ionization dynamics.

While this thesis is not the first work that shows that DP is useful for solving the TDSE,^[78,82,83,89-93] it is actually the first work that provides an *efficient* implementation and that rigorously shows that DP is *faster* (in terms of computing time) and requires less memory than conventional wavepacket dynamics but is as *accurate* as the latter.¹ Further, this is the first work that successfully (meaning faster runtime than conventional methods) applied DP to up to six dimensions and in the context of MCTDH even up to nine dimensions (Chapter I.2). Since these studies were mainly of benchmark type, comparisons to conventional computations without pruning were made for the same systems, and for this reason, system size had to be limited. However, as these comparisons show, the accuracy of DP can be controlled by the user, to practically sufficient levels, while substantial savings still occur. Hence, without such comparisons to conventional computations, treatments of higher-dimensional systems (more than nine dimensions) should be feasible.

The success of the DP approach required the development of efficient algorithms and considerable insight into the structure of high-dimensional quantum dynamics. It turned out that

¹Impressive work for applying pruning to the TISE is mentioned in the following publications. For the TISE, pruning is simpler because the basis does not need to be updated dynamically and semiclassical criteria can be used to select the required basis functions.

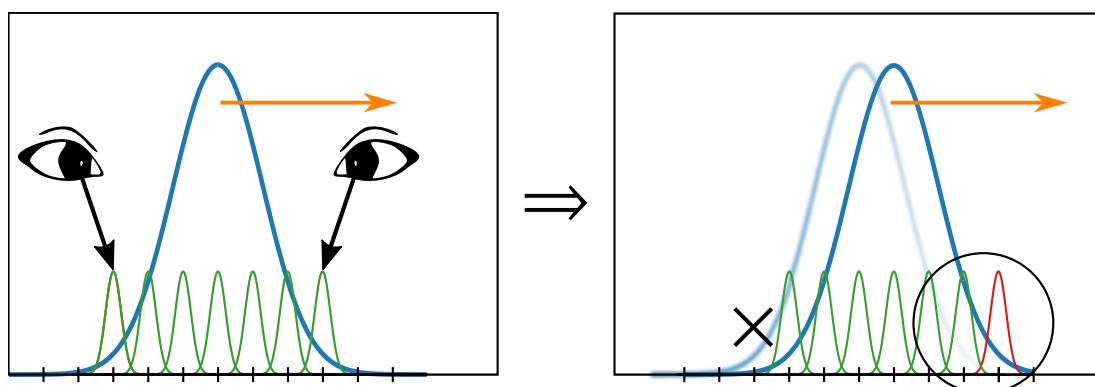


Figure I.1.2.: Cartoon of the DP scheme for a coordinate-space localized basis in one dimension. The wavefunction is described by the blue curve and the movement of the function by an orange arrow. The basis functions are shown in green. Basis function expansion coefficients are not shown explicitly but are roughly given by the amplitude of the wavepacket at each basis function center. The eyes on the left panel (earlier time) denote the checking/update where the coefficient of each basis function is compared with a predefined threshold. If the absolute value of the coefficient is larger than the threshold, nearest neighbors are added. Otherwise, the corresponding basis function is removed. On the right panel, the wavefunction is shown at a later time with that of the previous time (left panel) overlaid (blurred blue curve). The newly added basis function is shown in red and the removed basis function denoted by a cross. Instead of showing the wavefunction in coordinate representation, the wavefunction and basis could also be showed here in momentum representation for momentum-space-localized bases. Adapted from Ref. [88].

interpreting the coefficient vector of the wavefunction representation as a tensor and the action of an operator on this wavefunction as a tensor transformation led to a much better understanding. Further, careful considerations regarding the scaling of the number of operations with respect to basis size in each step of the DP algorithm were inevitable.

These analyses revealed that nonorthogonal phase-space bases (projected von Neumann with biorthogonal exchange (PvB) for example) have many drawbacks in high dimensions, although they give the sparsest representation of the wavepacket (compared to other coordinate/phase-space bases). Consequently, orthogonal phase-space bases were investigated and the projected Weylet (pW) basis was developed and benchmarked against coordinate-space bases. It turned out that coordinate-space bases in form of discrete variable representations (DVRs) lead to faster DP simulations and are simpler to use. This is because of their well-known property that the representation of the potential operator is diagonal which reduces the prefactor of the overall scaling of the method, although typically more basis functions are required, compared to phase-space bases.

These findings and the mathematical details are presented in the following Sections. They are presented not in a chronological order. Instead, the thesis starts with presenting a review of the methods in [Section I.1.1](#). This review gives the best presentation of the methodology and of the mathematical details. Further mathematical details and comparisons of nonorthogonal phase-space projectors and bases are presented in [Section I.1.2](#). They are compared with orthogonal phase-space bases and coordinate bases in [Section I.1.3](#). This last Section presents the three most important contributions to the DP method, namely 1) a favorably scaling algorithm for the action of an operator onto a state in some basis representation, 2) an efficient algorithm for updating the set of used basis functions with the help of hash tables and 3) the introduction of the pW method and real-life comparisons to pruned DVR bases.

Here, no general introduction to molecular quantum dynamics is given, besides [Section I.1.1](#). For introductory texts, it is referred to Refs. [14, 94-99]. More advanced topics are explained and discussed in [Part II](#). Throughout this thesis, all quantities are given in reduced quantities expressed by atomic units, that is \hbar , e , m_e , $4\pi\epsilon_0$ and $a \times c$ are “set to 1” unless explicitly stated otherwise; see Ref. [100] for a discussion of this convention.

I.1.1. Publication: Review of the Methods

I.1.1.1. Own Contributions

- Contributions to Sections I.
- Minor Contributions to Section II.
- Major contributions to Section III A; idea of using a different grid for the projection.
- Contributions to Section III B 3: Identification of $\tilde{\mathbf{P}}$ as a non-orthogonal projector and the relation to inversion of \mathbf{R} *via* singular value decomposition. The connection to the fundamental theorem of linear algebra is due to D. J. Tannor.
- Major contributions to Section III D.
- Writing of Section IV.
- Developing of the matrix/vector view introduced in Section IV B 1 b/IV B 2 b.
- The initial idea of approximating $\tilde{\mathbf{Z}}^{-1}$ in the way shown in Section IV C 4 is due to D. J. Tannor. It has been formalized, rederived in the matrix/vector language from Section IV B 2 b and tested by me.
- Setup and execution of numerical simulations leading to Figures 7–9.
- Writing of Section V.
- Editing of the whole article.

I.1.1.2. Bibliographic Data

Title Phase Space vs. Coordinate Space Methods: Prognosis for Large Quantum Calculations

Authors David J. Tannor, Shai Machnes, Elie Assémat and Henrik R. Larsson

Book Title Advances in Chemical Physics

Volume 163

Chapter 10

Pages 273-323

Year 2018

Digital Object Identifier (DOI) [10.1002/9781119374978.ch10](https://doi.org/10.1002/9781119374978.ch10)

Note Reproduced with permission from Advances in Chemical Physics, Volume 163, First Edition. Edited by K. Birgitta Whaley. Copyright 2018 John Wiley & Sons, Inc. Published 2018 by John Wiley & Sons, Inc.

I.1.1.3. Article

Phase Space vs. Coordinate Space Methods: Prognosis for Large Quantum Calculations

David Tannor

Dept. of Chemical Physics, Weizmann Institute of Science, 76100 Rehovot, Israel

Shai Machnes and Elie Assémat

*Dept. of Chemical Physics, Weizmann Institute of Science, 76100 Rehovot, Israel and
Theoretical Physics, Saarland University, D-66123 Saarbrücken, Germany*

Henrik R. Larsson

*Institut für Physikalische Chemie, Christian-Albrechts-Universität zu Kiel,
Olshausenstraße 40, D-24098 Kiel, Germany and
Dept. of Chemical Physics, Weizmann Institute of Science, 76100 Rehovot, Israel
(Dated: February 3, 2018)*

CONTENTS

I. Introduction	2
II. Pedagogical Aspects of the Discrete Variable Representation	4
A. Spectral Representation and Orthogonal Collocation	4
B. The Pseudospectral Basis	5
1. Definition	5
2. Completeness and Orthogonality	6
C. The Fourier Method	6
1. Continuous k Basis	6
2. Discrete k Basis	7
III. The von Neumann Basis	8
A. The Projected von Neumann Basis (PvN)	8
B. The Biorthogonal von Neumann Basis (PvB)	10
C. Pruning the von Neumann Basis	10
1. Preliminaries	10
2. The Reduced Hilbert Space $\tilde{\mathcal{H}}$	11
3. Orthogonal vs. Nonorthogonal Projection	12
4. Physical Insight into the Distorted Gaussians \tilde{g}	14
a. Ket Perspective on \tilde{g}	15
b. Bra Perspective on \tilde{g}	15
D. The Form of the Time-Dependent Schrödinger Equation	17
1. Reduced Space with Orthogonal Projection	18
2. Reduced Space with Nonorthogonal Projection	18
IV. Multidimensional Considerations	19
A. Introduction	19
B. Efficient Tensor Transformation	20
1. Full Direct Product Basis	20
a. Tensor (Summation) View	20
b. Vector (Matrix Product) View	21
2. Pruned Direct Product Basis	21
a. Tensor (Summation) View	21
b. Vector (Matrix Product) View	22
c. Implementation	22
C. Incompatibility of Nonorthogonal Bases and Multidimensional Decomposition	23
1. Nonorthogonality Means Non-Decomposable Inverse Overlap Matrix $\tilde{\mathbf{Z}}^{-1}$	23

	2
2. Nonorthogonality Prevents Efficiently Scaling Matrix-Vector-Product	23
D. Orthogonalization	23
1. Weylets	23
2. Projected Weylets (pW)	24
3. Pruned DVR	25
4. Approximations to $\tilde{\mathbf{Z}}^{-1}$ in PvB	26
V. Applications	27
A. Two-Dimensional Double Well	28
B. Six-Dimensional Pyrazine	28
VI. Conclusions	30
Acknowledgments	30
References	30

I. INTRODUCTION

The fundamental equation of non-relativistic quantum mechanics is the Schrödinger equation. As noted by Dirac, if this equation could be solved for all the electrons and nuclei in atoms and molecules, all of chemistry would be a solved problem [1]:

The underlying physical laws necessary for the mathematical theory of a large part of physics and the whole of chemistry are thus completely known, and the difficulty is only that the exact application of these laws leads to equations much too complicated to be soluble.

Dirac went on to formulate the main problem that remains, namely the development of efficient methods to solve this equation for systems so big that they are actually of interest for chemists:

It therefore becomes desirable that approximate practical methods of applying quantum mechanics should be developed, which can lead to an explanation of the main features of complex atomic systems without too much computation.

Indeed, a major part of theoretical chemistry deals with developing approximate techniques that are computationally tractable but still have predictive power. An early milestone in this development was the introduction of the Born-Oppenheimer approximation, where the electronic-nuclear problem is separated into two distinct problems, solving the electronic Schrodinger equation for fixed nuclear geometries and solving the nuclear Schrodinger equation in the presence of the adiabatic electronic potentials [2]. This division of the computational problem has led to two separate communities: one that solves the time-independent Schrodinger equation (TISE) for the electrons and one that solves the Schrödinger equation for the nuclear dynamics. These communities by and large use different methods and have limited interaction with each other. Within both the electronic and nuclear communities there are subsets of researchers interested in the time-dependent dynamics of the electrons and nuclei respectively, and who therefore solve the time-dependent Schrodinger equation (TDSE). Solving the TDSE involves its own special set of tools. Despite the limited interaction among these different communities, all run into a computational bottleneck originating from the same source: the exponential scaling of the basis set size with the number of degrees of freedom. This so-called exponential wall was well-articulated by Walter Kohn in his Nobel prize lecture [3] in the context of the solving the TISE for electrons. In fact, the exponential wall in the TISE for multielectron systems was a key motivating factor for the development of Density Functional Theory (DFT), in which the calculation of the n_{el} -electronic wavefunction is circumvented by expressing many of the key chemical quantities of interest in terms of the 3-dimensional electron density. Despite the spectacular successes of DFT, there are many reasons that one should still be interested in the quantum mechanical wavefunction. These reasons include: a) calculation of excited states, where DFT is much more difficult and less accurate; b) time-dependent processes: time-dependent DFT is still of limited applicability; c) multielectron ionization; e. g. TDDFT cannot distinguish between one-electron and two-electron ionization. Moreover, the exponential wall argument is an oversimplification, as Kohn himself must surely have realized. The exponential wall argument is based on the assumption that the Hilbert space spanned by the basis takes a tensor product form. In fact, virtually all electronic structure methods prune this tensor product structure, so a strictly exponential wall is not really encountered. CCSD(T), the “gold standard” in single-reference quantum chemistry, exhibits a scaling of N^7 with respect to the basis size. At the extreme limit of pruning, one has the linear scaling methods in wavefunction-based

electronic structure methods [4], based on the observation that despite the long range Coulomb forces of electrons, the effective interaction of the components within a large molecule generally fall off very quickly, typically within a few chemical monomer units. This enabled CCSD(T) calculations on entire proteins with more than 600 atoms and more than 6000 basis functions [5].

Despite the progress in developing linear scaling methods for electronic calculations, corresponding linear scaling methods for nuclear dynamics have not been forthcoming. This is probably because the correlation between the different motions of the nuclei is much stronger than in the electronic case. Moreover, the potential energy surface for nuclear motion, although generally smoother than the Coulomb potential felt by the electrons, is much more heterogeneous and therefore straightforward transfer of methods from electronic to nuclear calculations is not effective.

There is however a different strategy for solving the Schrodinger equation in which similar methods can be used for both the electronic and nuclear dynamics. Specifically, we are referring to methods in which the TISE or TDSE is solved on a set of grid points [6–9]. Grid methods are very convenient when large amplitude motion is involved, e. g. ionization for electrons or photodissociation and reactive scattering for nuclear motion. If one represents the many-particle wavefunction on a multidimensional grid of points, again one encounters the exponential wall: the overall number of grid points grows as n^D where n is the mean number of grid points per dimension. However, not all grid points in this tensor product Hilbert space are necessary; at the simplest level, one can safely discard points that are located in regions of coordinate space where the energy of the potential is significantly higher than any processes of interest in the calculation. However, there are more sophisticated methods for contracting the grid representation. In particular, the projected von Neumann (PvB) and projected Weylet (pW) methods described in this review exploit linear combinations of grid points that generate phase-space-localized functions. The latter can be pruned very efficiently using classical mechanics as a zeroth order guide for the pruning. Moreover, in the classical limit only one basis function is needed per converged eigenstate! The contraction of the grid representation is one of the central themes of this article. We have applied the contracted grid methods described in this review to both electron (TISE and TDSE) and nuclear (TISE and TDSE) dynamics, although we present applications here only for the latter.

It should be noted that despite the very compact representation of the wavefunction in phase space, there are a variety of factors that impair the effectiveness of the representation relative to coordinate-space grid representations (DVR or FGH). In particular, the potential energy matrix in the phase space representation is non-diagonal, thereby increasing storage and CPU operations significantly; moreover, the phase space representation is generally non-orthogonal, requiring the calculation of the inverse of a multidimensional overlap matrix. Several more years will be needed to reach definitive conclusions on whether the CPU requirements of phase space methods can be made competitive with optimized coordinate space methods.

Several years ago, in this same journal, we published a review of our work on the projected von Neumann (PvB) method [10]. Since that time there have been a number of key developments both in our group and in others: 1) We have applied the PvB method to triatomics, and demonstrated that it can be used in non-Cartesian coordinates [11]; 2) After understanding that the bottleneck to the multidimensional scaling of PvB is the number of basis functions on the boundary of the classically allowed phase space, we developed techniques to contract these boundary functions [12]; 3) We discovered a number of formal properties of the nonorthogonal phase space bases that provide geometrical insight into the projection onto a subspace [13]. The discussion of the formal properties is reviewed and extended here. 4) Brown and Carrington (BC), by introducing a new approximation, were able to combine the advantages of phase-space-localized basis functions with iterative eigensolvers [14–17]. In subsequent work, we identified and formalized the nature of the approximation in BC’s method and benchmarked its accuracy [13]. A full discussion is given in this review below. 5) We discovered the incompatibility of the phase-space basis, which is nonorthogonal, with sequential operations dimension by dimension, unless one introduces larger intermediate vectors. The inability to perform matrix-vector operations one dimension at a time results in an unfavorable scaling compared with orthogonal bases, for example coordinate-space based DVR [18]. 6) We developed a new method called projected Weylets (pW), that applies to the Weylets of Poirier and Salam [19–21] the same methods we used for projecting the von Neumann lattice [18]. The pW basis is orthogonal and an efficiently scaling matrix-vector product can be used. 7) We and Carrington and coworkers developed efficient algorithms for performing the sequential matrix-vector product for arbitrarily pruned bases [17, 18, 22]. 8) Halverson and Poirier developed and applied a massively-parallel solver for phase-space-localized momentum-symmetrized Gaussian functions [23–25]. 9) We have compared phase space and coordinate space methods on several challenging systems, including double ionization of 1D helium (2D electron dynamics) [26] and 6D pyrazine (nuclear dynamics) [18].

The present review, coming so closely after the last review, should be viewed as an intermediate progress report. As mentioned above, several more years will probably be needed to reach definitive conclusions on whether phase-space methods can be made competitive with optimized coordinate-space methods. Nevertheless, the timing of the special issue in memory of John Light, a dear friend and teacher as well as a theoretical chemist with far reaching impact, overrode the optimal timing for writing a review.

The outline of the review is as follows. Section II provides a simple pedagogical presentation of the Discrete Variable Representation (DVR). Although this presentation appears in Ref. 27 it has not been published in the open scientific literature before. Section III reviews the von Neumann basis of phase space Gaussians. This section includes a variety of interesting formal properties of non-orthogonal bases that are an extension of the DVR presentation in Section II and provide insight into the method. Section IV presents an analysis of multidimensional considerations, including details of a highly efficient tensor formulation for performing pruned multidimensional DVR calculations for sparse but unstructured grids. Section V contains illustrative applications and Section VI concludes.

II. PEDAGOGICAL ASPECTS OF THE DISCRETE VARIABLE REPRESENTATION

A. Spectral Representation and Orthogonal Collocation

Consider an orthonormal basis $\{\phi_n\}_{n=1}^N$ where

$$\int \phi_m^*(x)\phi_n(x)dx = \delta_{mn}. \quad (1)$$

Suppose that the basis functions $\phi_n(x)$ obey a set of discrete orthogonality relations at the collocation points $\{x_j\}_{j=1}^N$:

$$\sum_{j=1}^N \phi_m^*(x_j)\phi_n(x_j)\Delta_j = \delta_{mn}, \quad m, n = 1, \dots, N. \quad (2)$$

Equation (2) represents a set of orthogonality relations that are analogous to those of Eq. (1), with the integral replaced by a sum over values at the points, x_j , and dx replaced by a generally j -dependent weight factor Δ_j . Despite the flexibility in choosing the points $\{x_j\}$ and the weights $\{\Delta_j\}$, Eq. (2) is non-trivial to satisfy: the same points and weights must simultaneously satisfy all the orthogonality relations for $m, n = 1, \dots, N$.

For Gaussian quadrature points x_j , the weights Δ_j equal $W_j/\omega(x_j)$, with W_j as the quadrature weight of the DVR point x_j and $\omega(x_j)$ the weight function of the underlying DVR polynomial [7, 27]. They can be interpreted as generalized Christoffel numbers [28].

Equation (2) defines an orthogonal collocation scheme. Orthogonal collocation schemes can be recast in a simple and powerful way. We begin by defining

$$\Phi_n(x_j) \equiv \sqrt{\Delta_j}\phi_n(x_j). \quad (3)$$

With this definition Eq. (2) can be written as

$$\sum_{j=1}^N \Phi_m^*(x_j)\Phi_n(x_j) = \delta_{mn}, \quad m, n = 1, \dots, N. \quad (4)$$

Defining $\Phi_n(x_j) \equiv \Phi_{jn}$ we may rewrite Eq. (4) in matrix notation as

$$\Phi^\dagger \Phi = \mathbf{1}. \quad (5)$$

Equation (5) indicates that the transformation matrix Φ is unitary. The unitarity of the transformation implies a second relation:

$$\Phi \Phi^\dagger = \mathbf{1}, \quad (6)$$

or in component form

$$\sum_{n=1}^N \Phi_n(x_i)\Phi_n^*(x_j) = \delta_{ij}, \quad i, j = 1, \dots, N. \quad (7)$$

Despite the apparent similarity between Eq. (7) and Eq. (4), the physical significance is completely different. Equation (7) is effectively an orthogonality relation for the different grid points, the analog of the relation

$$\langle x' | x \rangle = \sum_{n=1}^{\infty} \langle x' | \phi_n \rangle \langle \phi_n | x \rangle = \delta(x - x') \quad (8)$$

on the infinite Hilbert space. Below, we will refer to relations of the type Eq. (5) as basis orthogonality relations and relations of the type Eq. (6) as grid orthogonality relations. The difference between basis and grid orthogonality relations is shown graphically in Figure 1. The grid orthogonality relation, Eq. (7), is the starting point for our discussion of the pseudospectral basis in the next section.

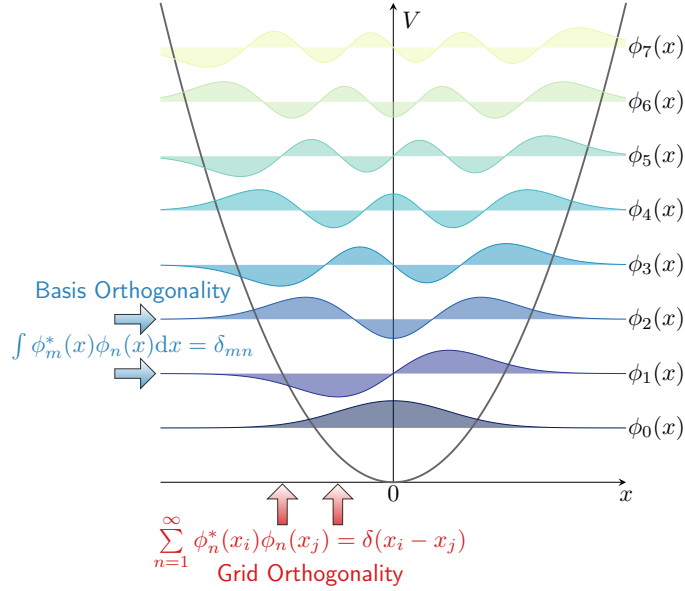


Figure 1. Graphical illustration of the difference between basis orthogonality relations and grid orthogonality relations for the harmonic oscillator wavefunctions.

B. The Pseudospectral Basis

1. Definition

If we replace $\Phi_n(x_i)$ by $\phi_n(x)$ in only the first factor in Eq. (7) we obtain

$$\sum_{n=1}^N \phi_n(x) \Phi_n^*(x_j) \equiv \theta_j(x), \quad (9)$$

where we have defined the pseudospectral basis functions, $\{\theta_j(x)\}$. Because the left-hand side (LHS) of Eq. (9) is in some sense close to the LHS of Eq. (7), we expect the functions $\{\theta_j(x)\}$ to be close to δ -functions. In fact, the functions $\theta_j(x)$ are localized, each one around a different value of x_j . Moreover, they satisfy the modified Kronecker δ -function property

$$\theta_j(x_i) = \Delta_j^{-1/2} \delta_{ij}, \quad (10)$$

as follows immediately from Eq. (9) together with Eq. (3) and Eq. (7). An example of the functions $\theta_j(x)$ may be seen below in Figure 2.

Equation (9) can be written in matrix-vector notation as

$$\Phi^\dagger \phi(x) = \theta(x). \quad (11)$$

Because the basis $\{\theta_j(x)\}$ and the original basis $\{\phi_n(x)\}$ are related by a unitary transformation Φ^\dagger , they span the same subspace of the Hilbert space. Thus, every unitary (or in the case of real basis functions, orthogonal) collocation relation of the form Eq. (4) implies the existence of a set of localized basis functions that span the same space as the original orthogonal functions; the form of the localized basis is determined completely by the points and weights that enter into Eq. (4), and the primary basis of orthogonal functions $\{\phi_n\}$. The localized functions $\theta_j(x)$ are called cardinal functions in the mathematics literature.

2. Completeness and Orthogonality

The localized basis functions $\{\theta_j(x)\}$ have properties of completeness and orthogonality entirely analogous to those of the original basis, $\{\phi_n(x)\}$. To show this, we first invert Eq. (9) by multiplying by $\phi_m^*(x)$ and integrating over the domain. This gives:

$$\Phi_n^*(x_j) = \langle \phi_n | \theta_j \rangle. \quad (12)$$

The grid orthogonality relation Eq. (7) then becomes:

$$\sum_{n=1}^N \Phi_n(x_i) \Phi_n^*(x_j) = \delta_{ij} = \sum_{n=1}^N \langle \theta_i | \phi_n \rangle \langle \phi_n | \theta_j \rangle = \langle \theta_i | \theta_j \rangle. \quad (13)$$

Similarly, the basis orthogonality relation, Eq. (4) becomes

$$\sum_{j=1}^N \Phi_m^*(x_j) \Phi_n(x_j) = \delta_{mn} = \sum_{j=1}^N \langle \phi_m | \theta_j \rangle \langle \theta_j | \phi_n \rangle. \quad (14)$$

Equation (13) is a statement of the orthonormality of the different θ basis functions. This orthogonality may be understood qualitatively, given that each θ function is peaked around a different value of x_i and vanishes at all other values x_j , but the precise orthogonality includes the cancellation of the oscillatory portions of the θ functions away from the peak as well. Equation (14) is a completeness (or closure) relationship with respect to summation over all the grid points x_j . The property of completeness says in essence that representation in terms of the localized θ functions span the exact same subspace as that spanned by the original basis of orthogonal functions. Both the completeness and orthogonality of the θ functions follow immediately from the fact that the transformation matrix with elements $\Phi_n(x_i)$ is unitary (or orthogonal). Thus, the formal statement of the closure relation is

$$P_N = \sum_{n=1}^N |\phi_n\rangle \langle \phi_n| = \sum_{j=1}^N |\theta_j\rangle \langle \theta_j|, \quad (15)$$

where P_N projects onto the N -dimensional Hilbert space $\text{span}(\{\phi_n\}_{n=1}^N)$.

C. The Fourier Method

The Fourier method [6, 29–33] is a special case of a pseudospectral method on a grid of evenly spaced points. In the Fourier method, the orthogonal basis functions are of the general form

$$\phi_k(x) \propto e^{ikx}. \quad (16)$$

and we will assume that there are no components of $|k|$ beyond K , i.e. the basis is "band-limited". We consider two possibilities: if the range of the coordinate space is infinite, then the basis is continuous in k ; if the coordinate space is finite or periodic, only discrete values of k are allowed.

1. Continuous k Basis

We will consider the continuous k case first. If the coordinate range is infinite, then the (k -normalized) basis functions of the form Eq. (16) are

$$\phi_k(x) = \frac{e^{ikx}}{\sqrt{2\pi}}, \quad -K \leq k \leq K, \quad -\infty < x < \infty. \quad (17)$$

The orthogonal collocation matrix is chosen to make the basis orthogonality relation exact:

$$\int_{-\infty}^{\infty} \phi_{k'}^*(x) \phi_k(x) dx = \int_{-\infty}^{\infty} \frac{e^{i(k-k')x}}{2\pi} dx = \delta(k-k') = \sum_{j=-\infty}^{\infty} \phi_{k'}^*(x_j) \phi_k(x_j) \Delta x = \sum_{j=-\infty}^{\infty} \Phi_{k'}^*(x_j) \Phi_k(x_j). \quad (18)$$

Taking $\Delta x = \frac{2\pi}{2K}$, $x_j = j\Delta x = \frac{j\pi}{K}$, the basis orthogonality relation is solved for

$$\Phi_k(x_j) = \frac{e^{ikx_j}}{\sqrt{2K}}. \quad (19)$$

The corresponding grid orthogonality relation takes the form

$$\int_{-K}^K \Phi_k(x_i)\Phi_k^*(x_j)dk = \int_{-K}^K \frac{e^{ik(x_i-x_j)}}{2K}dk = \delta_{ij}. \quad (20)$$

The pseudospectral interpretation of the Fourier method with continuous k is obtained by substituting Eqs. (17) and (19) into Eq. (9):

$$\int_{-K}^K \phi_k(x)\Phi_k^*(x_j)dk = \theta_j(x) = \int_{-K}^K \frac{e^{ikx} e^{-ikx_j}}{\sqrt{2\pi} \sqrt{2K}} dk = \frac{\sin[K(x-x_j)]}{\sqrt{\pi K}(x-x_j)} = \sqrt{\frac{K}{\pi}} \text{sinc}[K(x-x_j)]. \quad (21)$$

Each sinc function is centered on a different grid point, the space between grid points being $\Delta x = \frac{\pi}{K}$. Moreover, the width of each sinc function (position of the first zero) is $\frac{\pi}{K}$.

The behavior of the scaled sinc function is depicted in Figure 2. Note that the scaled sinc functions have properties that correspond to those of pseudospectral basis functions in general: they are $\Delta_j^{-1/2}$ at their own grid point, vanish at all other grid points, are orthogonal to each other, and form a complete, orthogonal set in a subspace of $L^2(-\infty, \infty)$

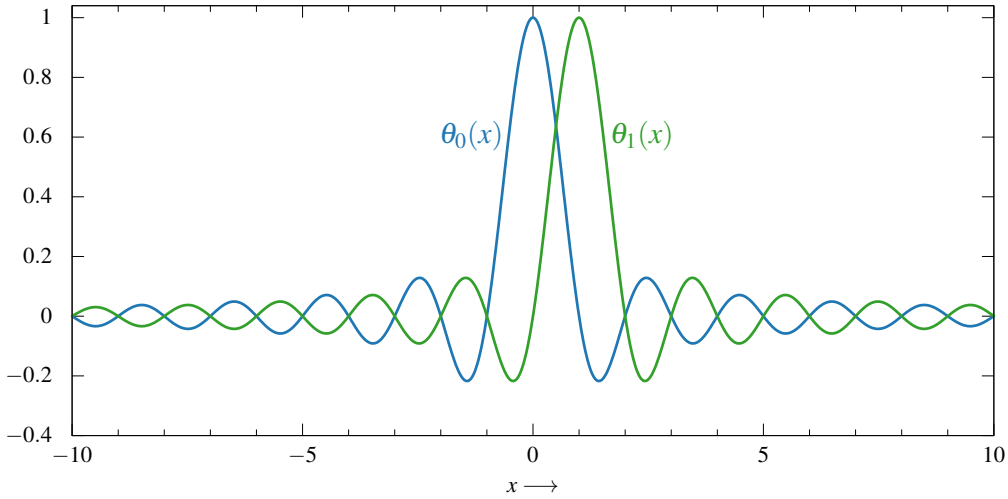


Figure 2. Depiction of the pseudospectral basis functions, $\theta_j(x) = \sqrt{\frac{K}{\pi}} \text{sinc}[K(x-x_j)]$ in the second variant of the Fourier method (see Eq. (21)), for $K = \pi$. These functions display the characteristic properties of all pseudospectral bases: the basis functions are orthonormal and each basis function vanishes at all grid points except the one where it is centered.

that consists of band-limited functions (functions whose Fourier transforms vanish outside the interval $[-K, K]$). The basis of sinc functions is sometimes called the Hardy basis.

2. Discrete k Basis

If one assumes that the Hilbert space spans only a finite range of coordinate space, $0 \leq x \leq L$, the Hilbert space is said to have "finite support". The normalized basis functions of the form Eq. (16) are then determined by the condition

$$\int_0^L \phi_k^*(x)\phi_{k'}(x)dx = \delta_{kk'} = \frac{1}{L} \int_0^L e^{-ikx} e^{ik'x} dx. \quad (22)$$

Note that Eq. (22) can be satisfied only for discrete values of k , satisfying $k - k' = \frac{n2\pi}{L}$ or $\Delta k = \frac{2\pi}{L}$, where Δk is the difference in k between two neighboring basis functions. Defining $k = \kappa\Delta k$ and using the bandlimit condition, $-K \leq k \leq K$, the normalized basis functions are given by:

$$\phi_\kappa(x) = \frac{e^{i2\pi\kappa x/L}}{\sqrt{L}}, \quad 0 \leq x \leq L, \quad -\frac{N}{2} + 1 \leq \kappa \leq \frac{N}{2}. \quad (23)$$

Taking $\Delta x = \frac{L}{N}$, the basis orthogonality relation is solved for

$$\Phi_\kappa(x_j) = \frac{e^{i2\pi\kappa j/N}}{\sqrt{N}}. \quad (24)$$

The discrete pseudospectral functions are obtained by substituting Eqs. (23) and (24) into Eq. (9):

$$\sum_{\kappa=-(N/2-1)}^{N/2} \phi_\kappa(x) \Phi_\kappa^*(x_j) = \theta_j(x) = \sum_{\kappa=-(N/2-1)}^{N/2} \frac{e^{i2\pi\kappa x/L}}{\sqrt{L}} \frac{e^{-i2\pi\kappa x_j/L}}{\sqrt{N}} \quad (25)$$

$$= \frac{\exp(i\frac{A}{2}) \sin(\frac{NA}{2})}{\sqrt{LN} \sin(\frac{A}{2})} = \frac{\exp(i\frac{A}{2})}{\sqrt{LN}} D_N(A), \quad (26)$$

where $D_N(A) = \frac{\sin(\frac{NA}{2})}{\sin(\frac{A}{2})}$ is the Dirichlet function and $A \equiv \frac{2\pi(x-x_n)}{L}$ [34, supp. material 1]. To appreciate the properties of the Dirichlet functions, note that the discreteness of the representation in k implies periodicity in the x representation; specifically, it implies periodic boundary conditions in x with period $L = \frac{\pi}{\Delta k}$. Thus, the pseudospectral basis functions corresponding to Eq. (23) are periodic trains of sinc functions. These pseudospectral functions are the underlying basis in the so-called Fourier Grid Hamiltonian (FGH) method.

III. THE VON NEUMANN BASIS

The von Neumann (vN) basis set [35–41] is a subset of the “coherent states” of the form:

$$\mathcal{G}_{nl}(x) = \left(\frac{2\alpha}{\pi}\right)^{\frac{1}{4}} \exp\left(-\alpha(x-x_n)^2 + i\frac{pl}{\hbar}(x-x_n)\right) \quad (27)$$

where n and l are integers. Each basis function is a Gaussian centered at $(x_n, p_l) = (na + x_0, \frac{\hbar}{a} + p_0)$ in phase space, where x_0 and p_0 are arbitrary shifts. The parameter $\alpha = \frac{\sigma_p}{2\hbar\sigma_x}$ controls the full width at half maximum of each Gaussian in x and p space. Taking $\Delta x = a$, $\Delta p = \hbar/a$ as the spacing between neighboring Gaussians in x and p space respectively, we note that $\Delta x \Delta p = \hbar$ so we have exactly one basis function per unit cell in phase space. As shown in Ref. 42–44 this implies completeness in the Hilbert space [45].

The “complete” vN basis, where n and l run over all integers, spans the infinite Hilbert space. In any numerical calculation, however, n and l take on a finite number of values, producing N Gaussian basis functions $\{\mathcal{G}_n(x)\}$, $n = 1, \dots, N$, where for notational simplicity we henceforth label the Gaussians by only a single index, n . Since the size of one vN unit cell is \hbar , the area of the truncated vN lattice is given by $S^{\text{vN}} = Nh$.

A. The Projected von Neumann Basis (PvN)

By combining the Gaussian and the Fourier basis functions we can generate a “Gaussian-like” basis set that completely spans the truncated space [34]. We use the basis sets $\{\mathcal{G}_n(x)\}$ and $\{\theta_i(x)\}$ to construct a new basis set, $\{g_n(x)\}$:

$$g_n(x) = \sum_{i=1}^N \theta_i(x) \mathcal{G}_n(x_i) \quad (28)$$

for $n = 1, \dots, N$. x_i are the Fourier grid points.

The new basis set is in some sense, the Gaussian functions with periodic boundary conditions and band-limited, henceforth the periodic von Neumann or PvN basis. We can write Eq. (28) in matrix notation as $\mathbf{G} = \mathbf{\Theta}\mathcal{G}$ where

$\mathcal{G}_{in} = g_n(x_i)$ (note that Θ and \mathbf{G} each have a continuous variable). By taking the width parameter $\alpha = \frac{\Delta p}{2\hbar\Delta x}$ we guarantee that the PvN functions have no linear dependence and that the matrix \mathcal{Z} is invertible, that is $\mathbf{G}\mathcal{Z}^{-1} = \Theta$. The invertibility of \mathcal{Z} implies that the $\{g_n\}$ and the $\{\theta_i\}$ bases span the same space. A pictorial description of the transformation of the coordinate-space-localized Fourier functions to the phase-space-localized PvN functions is depicted in Figure 3.

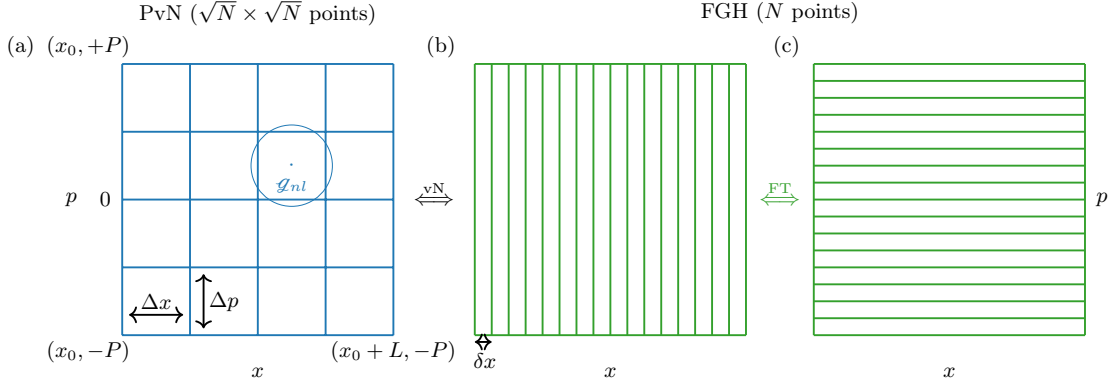


Figure 3. (a) $N = 16$ coordinate grid points and $N = 16$ von Neumann unit cells cover the same area in phase space, $S = Nh$. Shown also is a typical von Neumann function. Note that its boundary conditions are not appropriate for the rectangular area in phase space. (b) Coverage of the same phase space by a discrete coordinate basis. (c) Coverage of the same phase space by a discrete momentum basis [46].

Note that Eq. (28) permits a wide variety of generalizations. First, the $\{\theta_i(x)\}$ functions are not required to be Dirichlet functions — any set of functions can be used, although cardinal functions might be the most convenient ones to use. Eq. (28) then takes the form of

$$|g_n\rangle = \sum_{i=1}^N |\theta_i\rangle \langle \theta_i | \mathcal{G}_n \rangle = \sum_{i=1}^N |\theta_i\rangle \sqrt{\Delta_i} \langle x_i | \mathcal{G}_n \rangle, \quad (29)$$

where $\Delta_j = W_j/\omega(x_j)$ for cardinal functions, see Eq. (2). Due to the projection onto the DVR space in Eq. (29), PvN might also be called projected von Neumann. We have tested Eq. (28) with Gauss-Legendre $\theta_i(x)$ functions in the angle and Dirichlet functions in the radial coordinate(s) to calculate the vibrational levels of LiCN in 2-d and of HCN in 3-d [11]; see also [14–16].

In certain situations, it makes sense to combine the von Neumann lattice with DVR functions other than sinc/Fourier Grid DVRs: 1) if a rectangular grid associated with a sinc DVR would result in a prohibitively large unpruned basis; 2) if nonorthogonal coordinates are used that satisfy specific boundary conditions. However, caution must be exercised: naïve use of Eq. (29) with non-equidistant points leads to numerical stability problems [15] (increased condition number of the overlap matrix $\mathbf{G}^\dagger \mathbf{G}$, see Eq. (30)) [47]. We have found that stability can be recovered by using a hybrid approach, in which the DVR functions in Eq. (29) are retained but the sampling points are equidistant (x_i^{equi}). Technically, this corresponds to a nonorthogonal projection $\sum_{i=1}^N |\theta_i\rangle \langle x_i^{\text{equi}} |$ of the vN functions. The error using this hybrid approach is comparable to PvB combined with sinc DVR/FGH. We have tested this for a Gauss-Lobatto and for a Gauss-Hermite DVR and we found that the error can be reduced to less than 10^{-12} . In contrast, non-equidistant sampling points lead to an error that *increases* for larger basis set sizes (see Fig. 1(b) in Ref. [14], where errors up to 10^{-5} are reported for a Gauss-Hermite DVR).

Another generalization of Eq. (28) is that functions $\{\mathcal{G}_n\}$ on the right hand side of the equation could be any phase space localized functions, not necessarily Gaussians, see subsection IV D 2 for an example [18]. Alternatively, they could be Gaussians but with unequal spacing and widths [48]. Mathematically, the only requirement to obtain equivalence with the FGH method is that the N functions be linearly independent; however in practice, we have found that for numerical stability the functions should correspond to a complete tiling of the FGH phase space using N tiles, each of area h [48].

B. The Biorthogonal von Neumann Basis (PvB)

The von Neumann basis is nonorthogonal. Before proceeding to a discussion of tailored subspaces of the von Neumann Hilbert space, we provide a brief review of some properties of nonorthogonal bases. For a nonorthogonal basis, the orthogonality relation $\langle \phi_m | \phi_n \rangle = \delta_{mn}$ is replaced by the overlap integral $\langle g_m | g_n \rangle = S_{mn}$ and the completeness relation for orthogonal bases $\sum_{n=1}^{\infty} |\phi_n\rangle\langle\phi_n| = 1$ is replaced by the relation $\sum_{m,n=1}^N |g_m\rangle\langle g_n| (S^{-1})_{mn} = 1$. In what follows we will use matrix notation; the reader can easily translate these results back to Dirac notation. Dirac and/or wavefunction notation will be used from time to time to stress the physical interpretation. This section builds on the presentation in Ref. 34.

In the notation of Section II A, the basis orthogonality relation (5), $\Phi^\dagger \Phi = \mathbf{1}$, is replaced by

$$\mathbf{G}^\dagger \mathbf{G} = \mathbf{S} \quad (30)$$

and the grid orthogonality relation (6), $\Phi \Phi^\dagger = \mathbf{1}$, by

$$\mathbf{G} \mathbf{S}^{-1} \mathbf{G}^\dagger = \mathbf{1}. \quad (31)$$

The basis orthogonality condition can be recovered by introducing a set of “biorthogonal” functions $\{b_i\}$ defined by the relation:

$$\mathbf{B}^\dagger \mathbf{G} = \mathbf{G}^\dagger \mathbf{B} = \mathbf{1}. \quad (32)$$

The grid orthogonality relation can be written in a mixed representation of the original and the biorthogonal basis in two ways:

$$\mathbf{B} \mathbf{G}^\dagger = \mathbf{G} \mathbf{B}^\dagger = \mathbf{1}. \quad (33)$$

Comparing Eq. (33) with Eq. (31) we obtain an explicit relation for the $\{b_n\}$:

$$\mathbf{B} = \mathbf{G} \mathbf{S}^{-1}, \quad \mathbf{G} = \mathbf{B} \mathbf{S}. \quad (34)$$

We can reexpress the basis and grid orthogonality relations in terms of \mathbf{B} :

$$\mathbf{B}^\dagger \mathbf{B} = \mathbf{Z}, \quad \mathbf{B} \mathbf{Z}^{-1} \mathbf{B}^\dagger = \mathbf{1}. \quad (35)$$

Note that $\mathbf{Z} = \mathbf{S}^{-1}$, which follows from substituting Eq. (34) into Eq. (35).

The equations (30), (31) and (35) suggest that there is a duality between the $\{b_n\}$ and the $\{g_n\}$. However, it should be noted that while the $\{g_n\}$ functions are localized in phase space, the $\{b_n\}$ functions are not only delocalized but have very jagged features [10]. This asymmetry between the $\{g_n\}$ functions and the $\{b_n\}$ functions will play a crucial role in the next section.

C. Pruning the von Neumann Basis

1. Preliminaries

Combining our conclusions from the previous sections we find that an arbitrary wavefunction can be expanded in three different ways:

$$|\psi\rangle = \sum_{n=1}^N |\theta_n\rangle \langle \theta_n | \psi \rangle = \sum_{n=1}^N |g_n\rangle \langle g_n | \psi \rangle = \sum_{n=1}^N |b_n\rangle \langle g_n | \psi \rangle. \quad (36)$$

On the full Hilbert space $\mathcal{H} = \text{span}(\{\theta_n\}_{n=1}^N)$, all three of these representations are equivalent; however, they may differ dramatically once one begins to eliminate basis functions. Consider first the representation in terms of the $\{\theta_i\}$: a) This basis is localized in coordinate space, but completely delocalized in momentum space, thus the basis may be wasteful in spanning regions where $\hat{\psi}(p)$ (momentum-space-representation) is negligible; b) The $\{\theta_i\}$ are more compact in coordinate space than the $\{g_n\}$, allowing more control over the coordinate space spanned than one has in the latter; c) In multidimensions, one may account for coordinate-coordinate correlation in pruning basis functions, but not account for position-momentum correlation. This is discussed in detail in section IV.

The second representation is in terms of the g_n basis:

$$|\psi\rangle = \sum_{n=1}^N |g_n\rangle \langle b_n|\psi\rangle. \quad (37)$$

Note that although the basis functions $\{g_n\}$ are localized, the coefficients $\langle b_n|\psi\rangle$ that determine the representation are not sparse — they are determined by the pathologically delocalized $\{b_n\}$. In fact, the representation corresponding to the g_n basis counterintuitively leads to a much denser representation than that corresponding to the θ_i basis.

The third representation is in terms of the b_n basis:

$$|\psi\rangle = \sum_{n=1}^N |b_n\rangle \langle g_n|\psi\rangle. \quad (38)$$

Now, although the basis functions $\{b_n\}$ are delocalized, the coefficients $\langle g_n|\psi\rangle$ are sparse — they are determined by the overlap of $|\psi\rangle$ with the phase space localized $\{g_n\}$ [13].

2. The Reduced Hilbert Space $\tilde{\mathcal{H}}$

The pruning of any basis set defines a subspace $\tilde{\mathcal{H}}$ of the original Hilbert space, \mathcal{H} . For nonorthogonal bases, the reduced subspace entails some mathematical features that are not familiar from subspaces defined in terms of orthogonal bases. Moreover, there are interesting geometrical features of this reduced space. We will therefore devote some attention to these issues now. Much of the remainder of this section III is a somewhat restructured version of Ref. 13.

In the previous section we argued that the biorthogonal basis, $\{b_n\}$, rather than the original basis, $\{g_n\}$, provides a compact representation of the phase space localized Hilbert space. We define the reduced basis set $\{\tilde{b}_n\}$ to be the subset of the $\{b_n\}$ with $n = 1, \dots, \tilde{N}$ and the reduced space, $\tilde{\mathcal{H}}$, to be the span of $\{\tilde{b}_n\}$:

$$\tilde{\mathcal{H}} = \text{span}(\{\tilde{b}_n\}_{n=1}^{\tilde{N}}) \quad (39)$$

From this point on, the set of functions $\{\tilde{b}_n\}$ spanning the reduced space become the fundamental quantities. The projection operator \tilde{P} for projection onto $\tilde{\mathcal{H}}$ is given by

$$\tilde{P} = \sum_{m=1}^{\tilde{N}} |\tilde{g}_m\rangle \langle \tilde{b}_m| = \sum_{m=1}^{\tilde{N}} |\tilde{b}_m\rangle \langle \tilde{g}_m| \quad (40)$$

where the $\{\tilde{g}_m\}_{m=1}^{\tilde{N}}$ are a new set of functions — the functions that are biorthogonal to the $\{\tilde{b}_m\}_{m=1}^{\tilde{N}} = \{b_m\}_{m=1}^{\tilde{N}}$ on the space $\tilde{\mathcal{H}}$.

A central role will be played by the overlap matrix of the $\{\tilde{b}_n\}_{n=1}^{\tilde{N}}$ functions on the reduced subspace, $\langle \tilde{b}_m|\tilde{b}_n\rangle = \tilde{Z}_{mn}$, or in matrix notation,

$$\tilde{\mathbf{B}}^\dagger \tilde{\mathbf{B}} = \tilde{\mathbf{Z}}. \quad (41)$$

The $\tilde{\mathbf{B}}$ matrix has dimensions $N \times \tilde{N}$, with columns given by \tilde{b}_n vectors in the θ representation. The projection operator onto the reduced space takes the form

$$\tilde{\mathbf{B}} \tilde{\mathbf{Z}}^{-1} \tilde{\mathbf{B}}^\dagger = \tilde{\mathbf{P}}, \quad (42)$$

where $\tilde{\mathbf{P}}$ has dimensions $N \times N = (N \times \tilde{N})(\tilde{N} \times \tilde{N})(\tilde{N} \times N)$. One may now define a set of biorthogonal functions $\{\tilde{g}_n\}$ on the reduced space that satisfy

$$\tilde{\mathbf{G}}^\dagger \tilde{\mathbf{B}} = \tilde{\mathbf{B}}^\dagger \tilde{\mathbf{G}} = \tilde{\mathbf{I}}, \quad (43)$$

where the columns of $\tilde{\mathbf{G}}$ are the \tilde{g}_n vectors in the θ representation and $\tilde{\mathbf{I}}$ is the $\tilde{N} \times \tilde{N}$ unit matrix. The projection on the reduced subspace can be written in a mixed representation of the $\{\tilde{b}_n\}$ and the $\{\tilde{g}_n\}$ in two ways:

$$\tilde{\mathbf{G}} \tilde{\mathbf{B}}^\dagger = \tilde{\mathbf{B}} \tilde{\mathbf{G}}^\dagger = \tilde{\mathbf{P}}. \quad (44)$$

Comparing with Eq. (42) shows that

$$\tilde{\mathbf{G}} = \tilde{\mathbf{B}}\tilde{\mathbf{Z}}^{-1}, \quad \tilde{\mathbf{B}} = \tilde{\mathbf{G}}\tilde{\mathbf{Z}}. \quad (45)$$

Defining

$$\tilde{\mathbf{G}}^\dagger \tilde{\mathbf{G}} = \tilde{\mathbf{S}} \quad (46)$$

we have

$$\tilde{\mathbf{G}}\tilde{\mathbf{S}}^{-1}\tilde{\mathbf{G}}^\dagger = \tilde{\mathbf{P}}. \quad (47)$$

Substituting Eq. (45) into Eq. (47) and comparing with Eq. (42) we find that

$$\tilde{\mathbf{S}} \equiv \tilde{\mathbf{Z}}^{-1}. \quad (48)$$

Note that the projectors are $N \times N$ matrices in DVR representation.

Schematically, the reduced $\tilde{\mathbf{S}}$ matrix is constructed from the \mathbf{S} matrix by the following circuitous path,

$$\begin{array}{ccc} \mathbf{S}^{-1} = \mathbf{Z} = \mathbf{B}^\dagger \mathbf{B} & \xrightarrow{\text{truncation}} & \tilde{\mathbf{Z}} = \mathbf{R}^\dagger \mathbf{Z} \mathbf{R} = \tilde{\mathbf{B}}^\dagger \tilde{\mathbf{B}} \\ \uparrow \text{inversion} & & \downarrow \text{inversion back} \\ \mathbf{S} = \mathbf{G}^\dagger \mathbf{G} & & \tilde{\mathbf{Z}}^{-1} = (\mathbf{R}^\dagger \mathbf{Z} \mathbf{R})^{-1} = (\tilde{\mathbf{B}}^\dagger \tilde{\mathbf{B}})^{-1} = \tilde{\mathbf{G}}^\dagger \tilde{\mathbf{G}} = \tilde{\mathbf{S}}. \end{array} \quad (49)$$

One starts with the unmodified $\mathbf{S}_{N \times N}$, inverts to get $\mathbf{Z}_{N \times N}$, truncates to get $\tilde{\mathbf{Z}}_{\tilde{N} \times \tilde{N}}$, and then inverts back to get $\tilde{\mathbf{Z}}^{-1} = \tilde{\mathbf{S}}_{\tilde{N} \times \tilde{N}}$. \mathbf{R}^\dagger is defined as

$$\mathbf{R}_{\tilde{N} \times N}^\dagger \equiv \begin{pmatrix} 1 & \dots & 0 & 0 & \dots & 0 \\ \vdots & \ddots & \vdots & \vdots & \ddots & \vdots \\ 0 & \dots & 1 & 0 & \dots & 0 \end{pmatrix} \quad (50)$$

and truncates the basis to the reduced subspace.

The chain of relationships suggest that although \mathbf{G} is simpler than \mathbf{B} , $\tilde{\mathbf{G}}$ is more complicated than $\tilde{\mathbf{B}}$. Specifically, in the multi-dimensional case the columns of the $\tilde{\mathbf{G}}$ matrix do not decompose into products of their one-dimensional counterparts, while the columns of the $\tilde{\mathbf{B}}$ matrix *do* decompose into 1D components. The reduced $\tilde{\mathbf{Z}} = \tilde{\mathbf{B}}^\dagger \tilde{\mathbf{B}}$ matrix is a square matrix that is a projection (a subset of rows and columns) of the unreduced \mathbf{Z} matrix, but the reduced $\tilde{\mathbf{S}} = \tilde{\mathbf{G}}^\dagger \tilde{\mathbf{G}}$ matrix is not a projection of the full \mathbf{S} , due to the inversion in Eq. (49). Nondecomposability of the multi-dimensional $\tilde{\mathbf{S}}$ and $\tilde{\mathbf{G}}$ matrices has significant impact on the computational resources required to compute the reduced Hamiltonian and its action on a wavefunction. The issue is discussed at length in section IV C.

3. Orthogonal vs. Nonorthogonal Projection

In the previous section we defined the $\{\tilde{g}_n\}_{n=1}^{\tilde{N}}$ that span the same Hilbert space $\tilde{\mathcal{H}}$ as is spanned by the $\{\tilde{b}_n\}_{n=1}^{\tilde{N}} \equiv \{b_n\}_{n=1}^{\tilde{N}}$. The projector

$$\tilde{P} = \sum_{m=1}^{\tilde{N}} |\tilde{b}_m\rangle \langle \tilde{g}_m| \quad (51)$$

is an orthogonal projector, but it is not the only possible way of projecting onto $\tilde{\mathcal{H}}$. A second way to project is using

$$\tilde{P} = \sum_{m=1}^{\tilde{N}} |\tilde{b}_m\rangle \langle g_m|, \quad (52)$$

which is a non-orthogonal projector. In this section we clarify the difference between orthogonal vs. nonorthogonal projection onto $\tilde{\mathcal{H}}$.

We begin by defining two new reduced spaces. The first, $\tilde{\mathcal{H}}$ is defined by the span of the reduced basis set $\{\tilde{g}_n\}$, the subset of the $\{g_n\}$ with $n > \tilde{N}$ (here and henceforth, we define $n > \tilde{N}$ to mean $n = \tilde{N} + 1, \dots, N$):

$$\tilde{\mathcal{H}} = \text{span}(\{|\tilde{g}_n\rangle\}_{n=\tilde{N}+1}^N). \quad (53)$$

$\tilde{\mathcal{H}}$ is orthogonal to $\tilde{\mathcal{H}}$ since $\langle g_m | b_n \rangle = \delta_{mn}$ for $m, n = 1, \dots, N$ and hence $\langle \tilde{g}_m | \tilde{b}_n \rangle = 0$ for $m > \tilde{N}, n \leq \tilde{N}$. Since $\dim(\tilde{\mathcal{H}}) = \tilde{N}$ and $\dim(\tilde{\mathcal{H}}) = N - \tilde{N}$ together with the fact that the spaces are orthogonal we conclude that $\tilde{\mathcal{H}} \oplus \tilde{\mathcal{H}} = \mathcal{H}$.

The second reduced space, $\check{\mathcal{H}}$, is defined by the span of the subset of the $\{b_n\}$ with $n > \tilde{N}$:

$$\check{\mathcal{H}} = \text{span}(\{|\check{b}_n\rangle\}_{n=\tilde{N}+1}^N) \quad (54)$$

Note that, $\tilde{\mathcal{H}} \oplus \check{\mathcal{H}} = \mathcal{H}$. However, $\check{\mathcal{H}}$ is not orthogonal to $\tilde{\mathcal{H}}$ since the members of the set $\{b_n\}_{n=\tilde{N}+1}^N$ are not orthogonal to the $\{b_n\}_{n=1}^{\tilde{N}}$.

We now consider the space of functions annihilated by each of the projectors $\tilde{P} = \sum_{n=1}^{\tilde{N}} |\tilde{b}_n\rangle\langle \tilde{g}_n|$ and $\check{P} = \sum_{n=1}^{\tilde{N}} |\check{b}_n\rangle\langle g_n|$. The former annihilates functions in the space $\tilde{\mathcal{H}}$; since this space is perpendicular to the space spanned by the kets of the projector, $\tilde{\mathcal{H}}$, it defines an orthogonal projection. The latter projector annihilates functions in the space $\check{\mathcal{H}}$. However, $\check{\mathcal{H}}$ is not orthogonal to the space spanned by the kets of the projector (again $\tilde{\mathcal{H}}$). Thus the projection is nonorthogonal.

In the terminology of linear algebra, the space of functions spanned by the kets of the projector is called the column space or the image and the space of functions annihilated by the projector is called the nullspace or the kernel. The space of functions spanned by the bras of the projector is called the row space and the space of functions annihilated by the projector acting to the left is called the left nullspace.

We now round out our discussion by introducing one last subspace of the Hilbert space. So far, we have defined three reduced spaces: $\tilde{\mathcal{H}}$, $\check{\mathcal{H}}$ and $\check{\mathcal{H}}$. We may define a fourth reduced space

$$\check{\mathcal{H}} = \text{span}(\{|\check{g}_n\rangle\}_{n=1}^{\tilde{N}}). \quad (55)$$

Note that $\check{\mathcal{H}} \oplus \check{\mathcal{H}} = \mathcal{H}$. Moreover, $\check{\mathcal{H}}$ is orthogonal to $\check{\mathcal{H}}$ since the set $\{g_n\}_{n=1}^{\tilde{N}}$ are all orthogonal to the $\{b_n\}_{n=1}^{\tilde{N}}$ and hence $\langle g_m | b_n \rangle = 0$ for $m \leq \tilde{N}, n > \tilde{N}$.

Given the four reduced spaces, $\tilde{\mathcal{H}}$, $\check{\mathcal{H}}$, $\check{\mathcal{H}}$ and $\check{\mathcal{H}}$, we can make the connection with some fundamental results of linear algebra. In particular, we can verify the so-called fundamental theorem of linear algebra [49, p. 95, p. 138], which states that (i) the nullspace is the orthogonal complement of the row space and (ii) the left nullspace is the orthogonal complement of the column space. This theorem applies to orthogonal as well as nonorthogonal projectors. We now verify it for \tilde{P} and \check{P} . For \tilde{P} : (i) the nullspace of \tilde{P} ($\tilde{\mathcal{H}}$) is orthogonal to its row space ($\tilde{\mathcal{H}}$); (ii) the left nullspace of \tilde{P} ($\tilde{\mathcal{H}}$) is orthogonal to its column space ($\tilde{\mathcal{H}}$). For \check{P} : (i) the nullspace of \check{P} ($\check{\mathcal{H}}$) is orthogonal to its row space ($\check{\mathcal{H}}$); (ii) the left nullspace of \check{P} ($\check{\mathcal{H}}$) is orthogonal to its column space ($\check{\mathcal{H}}$).

For orthogonal projectors row and column space are identical and nullspace and left nullspace are identical. As a result, we have the added features that (i) the nullspace is orthogonal to the column space and (ii) the left nullspace is orthogonal to the row space. Inspection of the previous paragraph shows that these properties are obeyed for \tilde{P} ($\tilde{\mathcal{H}}$ is orthogonal to $\tilde{\mathcal{H}}$) but not for \check{P} ($\check{\mathcal{H}}$ is not orthogonal to $\check{\mathcal{H}}$ and $\check{\mathcal{H}}$ is not orthogonal to $\check{\mathcal{H}}$).

We close with a few additional properties of the projections operators we have been discussing. If P is a projector, $1 - P$ is also a projector since $(1 - P)^2 = 1 - 2P + P^2 = 1 - P$. Moreover $(1 - P)P = P - P^2 = 0$, i.e. applying a projector and then its complement gives zero. These properties hold for any projector, orthogonal or nonorthogonal. Defining $\bar{P} \equiv (1 - \tilde{P})$, we note that the nullspace of \bar{P} ($\check{\mathcal{H}}$) is the column space of \tilde{P} ($\tilde{\mathcal{H}}$) while the left nullspace of \bar{P} ($\check{\mathcal{H}}$) is the row space of \tilde{P} ($\tilde{\mathcal{H}}$). This result makes intuitive sense for orthogonal projectors, but interestingly it applies also to the nonorthogonal projector \check{P} : Defining $\check{\bar{P}} \equiv 1 - \check{P}$, the nullspace of $\check{\bar{P}}$ ($\check{\mathcal{H}}$) is the column space of \check{P} ($\check{\mathcal{H}}$) while the left nullspace of $\check{\bar{P}}$ ($\check{\mathcal{H}}$) is the row space of \check{P} ($\check{\mathcal{H}}$).

Orthogonal projection is a necessary and sufficient condition for projection onto orthogonal subspaces. Nonorthogonal projection is a necessary and sufficient condition for projection onto nonorthogonal subspaces. Consider the two different partitionings of unity: $1 = \tilde{P} + \bar{P}$ and $1 = \check{P} + \check{\bar{P}}$. The former projects onto two orthogonal subspaces: mathematically,

$$\tilde{P}\psi = \tilde{\psi} \in \tilde{\mathcal{H}}, \quad \bar{P}\psi = \bar{\psi} \in \check{\mathcal{H}}, \quad \text{and } \langle \tilde{\psi} | \bar{\psi} \rangle = 0. \quad (56)$$

On the other hand, the latter partitioning does not project onto orthogonal subspaces:

$$\tilde{P}\psi = \check{\psi} \in \tilde{\mathcal{H}}, \quad \check{P}\psi \in \check{\mathcal{H}}, \quad \text{and } \langle \check{\psi} | \check{\psi} \rangle \neq 0. \quad (57)$$

Thus we see that orthogonal projectors, \tilde{P} and \check{P} , project onto orthogonal spaces while the nonorthogonal projectors, \tilde{P} and \check{P} project onto nonorthogonal spaces. It is easy to show these properties by explicit substitutions of the form of the projectors.

Orthogonal projection with \tilde{P} implies that $\|\psi - \tilde{\psi}\|$ is minimized [50]. This is not the case for the nonorthogonal projection with \check{P} : $\|\psi - \check{\psi}\|$ is larger than $\|\psi - \tilde{\psi}\|$. Therefore, $\tilde{\psi}$ is a better approximation to ψ than $\check{\psi}$. Furthermore, note that \tilde{P} is nonhermitian whereas \check{P} is hermitian.

In matrix notation, the form of the projectors are

$$\tilde{P} = \tilde{\mathbf{B}}\tilde{\mathbf{G}}^\dagger, \quad \text{and} \quad \check{P} = \check{\mathbf{B}}\check{\mathbf{R}}^\dagger\check{\mathbf{G}}^\dagger \equiv \tilde{\mathbf{B}}\check{\mathbf{G}}^\dagger. \quad (58)$$

We note that the difference between \tilde{P} and \check{P} is just the difference between $\tilde{\mathbf{G}}^\dagger$ and $\check{\mathbf{G}}^\dagger$. Additional insight can be obtained by rewriting them in alternative forms:

$$\check{\mathbf{G}}^\dagger = \mathbf{R}^\dagger\mathbf{G}^\dagger = \mathbf{R}^\dagger\mathbf{Z}^{-1}\mathbf{B}^\dagger \quad (59)$$

while

$$\tilde{\mathbf{G}}^\dagger = \tilde{\mathbf{Z}}^{-1}\mathbf{R}^\dagger\mathbf{B}^\dagger = [\mathbf{R}^\dagger\mathbf{Z}\mathbf{R}]^{-1}\mathbf{R}^\dagger\mathbf{B}^\dagger. \quad (60)$$

\mathbf{R} is not invertible because it is a rectangular $N \times \tilde{N}$ matrix of rank \tilde{N} (see Eq. (50)). However, we can invert \mathbf{R} in a singular-value-decomposition sense by ignoring diagonal entries of zero. Then, $\mathbf{R}^{-1} \approx \mathbf{R}^\dagger$ and Eq. (60) takes the form

$$\tilde{\mathbf{G}}^\dagger = \mathbf{R}^{-1}\mathbf{Z}^{-1}[\mathbf{R}^\dagger]^{-1}\mathbf{R}^\dagger\mathbf{B}^\dagger \approx \mathbf{R}^\dagger\mathbf{Z}^{-1}\mathbf{B}^\dagger = \check{\mathbf{G}}^\dagger \quad (61)$$

We thus can express the nonorthogonal projection as an approximation to the orthogonal projection where the noninvertible \mathbf{R} is approximately inverted in a singular-value-decomposition sense.

Note that the multidimensional $\tilde{\mathbf{G}}$ is decomposable into one-dimensional matrices whereas $\check{\mathbf{G}}$ is not. The ability to decompose matrices significantly reduces the computational resources but at the expense of reduced accuracy. We return to this issue in section IV C.

The most important definitions and relations are summarized in Table I.

Table I. Summary of the most important definitions and relations of the biorthogonal bases in the reduced subspaces.

Projector	Hilbert Space	Linear Algebra Name	Spanned by	Dimension	Relations
1	\mathcal{H}		$\{ \theta_m\rangle\} = \{ g_m\rangle\} = \{ b_m\rangle\}, m \leq N$	N	
\tilde{P}	$\tilde{\mathcal{H}}$	column space “=” rowspace	$\{ \tilde{b}_m\rangle\} = \{ \tilde{g}_m\rangle\},$	$m \leq \tilde{N}$	$\tilde{\mathcal{H}} = \tilde{\mathcal{H}} \oplus \tilde{\mathcal{H}}$
	$\check{\mathcal{H}}$	nullspace “–” left nullspace	$\{ \check{b}_m\rangle\} = \{ \check{g}_m\rangle\},$	$m > \tilde{N}$	$N - \tilde{N}$ $\tilde{P} = \tilde{P}^\dagger, \tilde{P}\tilde{P} = 0$
\check{P}	$\tilde{\mathcal{H}}$	column space	$\{ \tilde{b}_m\rangle\},$	$m \leq \tilde{N}$	$\tilde{\mathcal{H}} = \tilde{\mathcal{H}} \oplus \tilde{\mathcal{H}}$
	$\check{\mathcal{H}}$	row space	$\{ \check{g}_m\rangle\},$	$m \leq \tilde{N}$	$\check{P} \neq \check{P}^\dagger$
	$\tilde{\mathcal{H}}$	nullspace	$\{ \tilde{b}_m\rangle\},$	$m > \tilde{N}$	$\tilde{P}\tilde{P} = 0$
	$\check{\mathcal{H}}$	left nullspace	$\{ \check{g}_m\rangle\},$	$m > \tilde{N}$	$\tilde{P}\check{P}^\dagger \neq 0$

4. Physical Insight into the Distorted Gaussians \tilde{g}

We will now provide some physical insight into the difference between \tilde{g} and g . We present two perspectives, one corresponding to \tilde{g} being the ket (the basis) and the other corresponding to \tilde{g} being the bra (the representation).

a. Ket Perspective on \tilde{g}

Consider applying the projector \tilde{P} to a single projected Gaussian $|\psi\rangle = |g_n\rangle$, $n \leq \tilde{N}$. Expressing \tilde{P} as $1 - \bar{P} = 1 - \sum_{n=\tilde{N}+1}^N |\tilde{b}_n\rangle\langle\tilde{g}_n|$ we obtain

$$\tilde{P}|g_n\rangle = (1 - \bar{P})|g_n\rangle = |g_n\rangle - \sum_{m=\tilde{N}+1}^N |\tilde{b}_m\rangle\langle\tilde{g}_m|g_n\rangle = |\tilde{g}_n\rangle, \quad (62)$$

where $\tilde{P}|g_n\rangle = |\tilde{g}_n\rangle$ follows from the first equation in Eq. (40). Equation (62) expresses the $|\tilde{g}_n\rangle$ in terms of the original $|g_n\rangle$ and a correction, where the coefficients in the correction are determined by the overlaps of $\{|g_m\rangle\}$ in the complementary space with $|g_n\rangle$ in the subspace. If $|g_n\rangle$ is close to the boundary of the phase space, $\langle g_m|g_n\rangle$ will be non-negligible and $|\tilde{g}_n\rangle$ will be very different from $|g_n\rangle$. However, if $|g_n\rangle$ is in the interior of the phase space, far from the boundary, $\langle g_m|g_n\rangle$ will be negligible and $|\tilde{g}_n\rangle$ will be virtually identical to $|g_n\rangle$. This remarkable property is illustrated numerically in Fig. 4. The fact that the distortion occurs closer to the phase-space boundary seems to bear a close relationship to the property of the states produced by applying to phase-space-localized basis functions the quantum projector defined in Ref. 51; see Fig. 5.

A very different result is obtained if \tilde{P} is applied to $|g_n\rangle$, $n > \tilde{N}$. Using \tilde{P} from Eq. 40:

$$\tilde{P}|g_n\rangle = \sum_{m=1}^{\tilde{N}} |\tilde{g}_m\rangle\langle\tilde{b}_m|g_n\rangle = 0, \quad (63)$$

since $\{\tilde{b}_m\}_{m=1}^{\tilde{N}} \in \tilde{\mathcal{H}}$ while $\{g_n\}_{n=\tilde{N}+1}^N \in \tilde{\mathcal{H}}$.

Applying the projection operator to a general sum of projected Gaussians $|\psi\rangle = \sum_{n=1}^N a_n|g_n\rangle$ with $a_n = \langle b_n|\psi\rangle$ we obtain:

$$\tilde{P}|\psi\rangle = \tilde{P}\sum_{n=1}^N a_n|g_n\rangle = \sum_{n=1}^{\tilde{N}} a_n|\tilde{g}_n\rangle. \quad (64)$$

Thus, provided that $n \leq \tilde{N}$, \tilde{P} alters the basis functions from $|g_n\rangle$ to $|\tilde{g}_n\rangle$ but leaves the coefficients unchanged. However, if $n > \tilde{N}$, \tilde{P} annihilates $|g_n\rangle$, see section III C 3.

 b. Bra Perspective on \tilde{g}

Consider an initial state $|\psi\rangle$ that spans the *full* Hilbert space \mathcal{H} . We may express $|\psi\rangle$ in terms of the complete basis $\{b_n\}_{n=1}^N$ as

$$|\psi\rangle = \sum_{n=1}^N |b_n\rangle\langle g_n|\psi\rangle = \sum_{n=1}^N c_n|b_n\rangle. \quad (65)$$

Note that the coefficients $c_n = \langle g_n|\psi\rangle$ of the expansion are determined by the overlap of the original, undistorted Gaussians $\{g_n\}_{n=1}^N$ with ψ , since the undistorted Gaussians are biorthogonal to the $\{b_n\}_{n=1}^N$ on the full space.

Consider the action of $\tilde{P} = \sum_{n=1}^{\tilde{N}} |\tilde{b}_n\rangle\langle\tilde{g}_n|$ on this state $|\psi\rangle$:

$$\tilde{P}|\psi\rangle = \sum_{m=1}^{\tilde{N}} \sum_{n=1}^N c_n |\tilde{b}_m\rangle\langle\tilde{g}_m|b_n\rangle. \quad (66)$$

Note that $\langle\tilde{g}_m|\tilde{b}_n\rangle = \langle\tilde{g}_m|b_n\rangle = \delta_{mn}$ for $n, m \leq \tilde{N}$, but that $\langle\tilde{g}_m|b_n\rangle \neq 0$ for $m \leq \tilde{N}$, $n > \tilde{N}$. Due to the nonorthogonality, there are contributions to $\tilde{P}|\psi\rangle$ coming from all the $\{b_n\}_{n=1}^N$, not just for $n \leq \tilde{N}$. We may therefore write

$$\tilde{P}|\psi\rangle = \sum_{m=1}^{\tilde{N}} d_m |\tilde{b}_m\rangle, \quad (67)$$

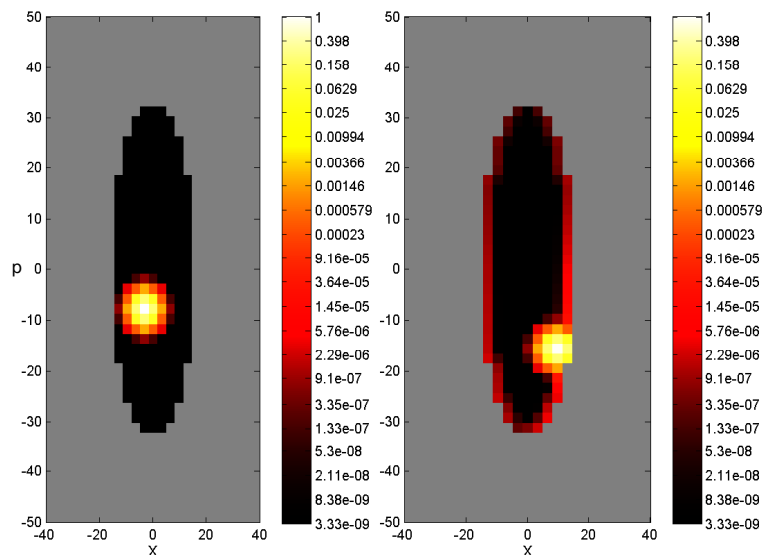


Figure 4. Depiction of the modified Gaussians \tilde{g} associated with the reduced basis. The phase space spanned by the reduced basis is the non-gray area in both plots. On the left, the modified Gaussian \tilde{g}_n , is in the interior of the phase space; is almost identical to the original Gaussian g_n . On the right, we see a heavily deformed Gaussian, \tilde{g}'_n , whose center is close to the reduced subspace boundary; it is significantly different from the original Gaussian g'_n to which it corresponds. The states are plotted as heat maps, where the value of each cell of the von Neumann lattice is the absolute value of the overlap of the state plotted (here the modified Gaussians), with the Gaussian centered at that cell of the lattice, $|\langle g_{x_j, p_j} | \tilde{g} \rangle|$. Reprinted with permission from Ref. 13. Copyright 2016 American Chemical Society.

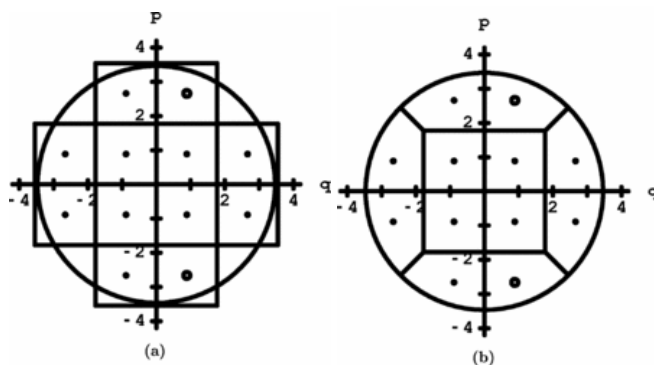


Figure 5. (a) Comparison of the classically allowed phase space for the harmonic oscillator at energy E (circular boundary) vs. the phase space spanned by a (momentum symmetrized) Gaussian basis, showed schematically as the union of black squares. Note that the Gaussian basis protrudes from the classical phase space in some regions and leaves part of the classical phase space uncovered. (b) The same (momentum symmetrized) Gaussians modified by the quantum projector corresponding to $P(E) = \delta(E - H)$. Notice how the quantum projector distorts the Gaussians near the classical phase space boundary to conform to the shape of the boundary while leaving the Gaussians in the interior unchanged. Reprinted figure with permission from Ref. 51. Copyright 2006 by the American Physical Society.

where

$$d_m = \sum_{n=1}^N c_n \langle \tilde{g}_m | b_n \rangle = c_m + \sum_{n=\tilde{N}+1}^N c_n \langle \tilde{g}_m | b_n \rangle. \quad (68)$$

Equation (67) shows that the basis $\{|b_m\rangle\}$ is truncated at \tilde{N} but otherwise unaffected by the projection; however, according to Eq. (68) the coefficients $c_m = \langle g_m | \psi \rangle$ in Eq. (65) now contain additional contribution from the $\{|b_n\rangle\}$ outside the space $\tilde{\mathcal{H}}$. This additional contribution is characteristic of an orthogonal projection in a nonorthogonal basis. If this contribution were neglected it would amount to a *nonorthogonal projection* $\check{P} = \sum_{n=1}^{\tilde{N}} |\tilde{b}_n\rangle\langle g_n|$, see section III C 3. In matrix notation,

$$\mathbf{d} = \tilde{\mathbf{G}}^\dagger \mathbf{B} \mathbf{c}, \quad (69)$$

while if $\check{\mathbf{G}}$ rather than $\tilde{\mathbf{G}}$ is used, one has

$$\check{\mathbf{d}} = \check{\mathbf{G}} \mathbf{B} \mathbf{c} = \mathbf{R}^\dagger \mathbf{G}^\dagger \mathbf{B} \mathbf{c} = \mathbf{R}^\dagger \mathbf{c}. \quad (70)$$

The matrix product $\tilde{\mathbf{G}}^\dagger \mathbf{B}$ is depicted in Fig. 6 (a) while the matrix product $\mathbf{R}^\dagger \mathbf{G}^\dagger \mathbf{B} = \mathbf{R}^\dagger$ is depicted in Fig. 6 (b).

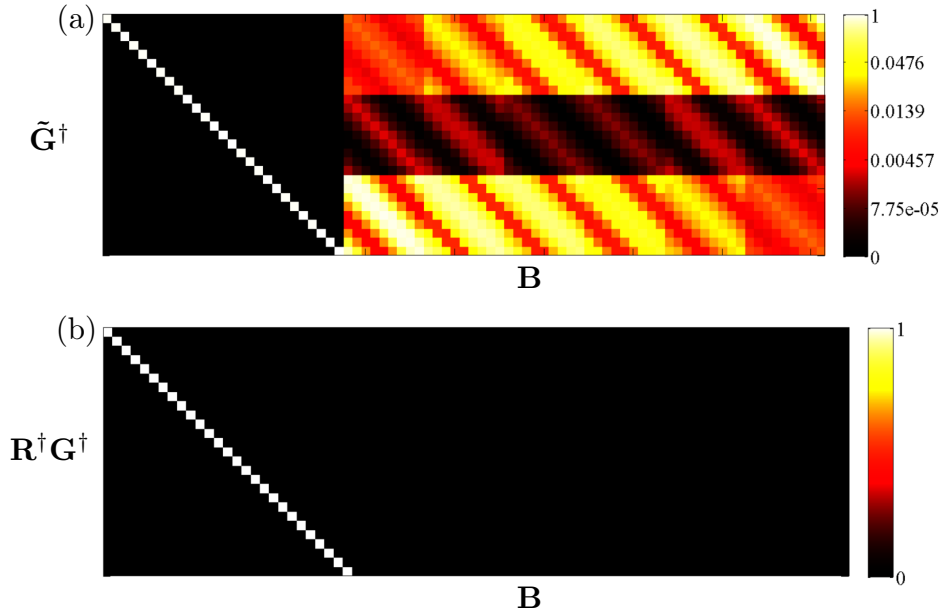


Figure 6. (a) The matrix product $\tilde{\mathbf{G}}^\dagger \mathbf{B}$ that appears in the orthogonal projector onto the $\tilde{\mathcal{H}}$ subspace (Eq. (69)). Note that elements of \mathbf{B} outside of the $\tilde{\mathcal{H}}$ subspace contribute. This structure is characteristic of orthogonal projection in a nonorthogonal basis. (b) The matrix product $\mathbf{R}^\dagger \mathbf{G}^\dagger \mathbf{B}$ that appears in the nonorthogonal projector onto the $\tilde{\mathcal{H}}$ subspace (Eq. (70)). Counterintuitively, the simpler diagonal structure of this object is the signature of a nonorthogonal projection. Reprinted with permission from Ref. 13. Copyright 2016 American Chemical Society.

D. The Form of the Time-Dependent Schrödinger Equation

We now consider the form of the time-dependent Schrödinger equation (TDSE),

$$i\hbar \frac{\partial |\psi\rangle}{\partial t} = H |\psi\rangle. \quad (71)$$

In the $|\theta\rangle$ representation this takes the form

$$i\hbar \frac{\partial \langle \theta_i | \psi \rangle}{\partial t} = \sum_{j=1}^N \langle \theta_i | H | \theta_j \rangle \langle \theta_j | \psi \rangle, \quad (72)$$

or in matrix form

$$i\hbar \frac{d\mathbf{a}}{dt} = \mathbf{H}\mathbf{a}, \quad (73)$$

where $a_i = \langle \theta_i | \psi \rangle$ and $H_{ij} = \langle \theta_i | H | \theta_j \rangle$. The Hamiltonian consists of kinetic and potential terms, $\mathbf{H} = \mathbf{T} + \mathbf{V}$. In the Discrete Variable Representation $\mathbf{T} = \mathbf{\Phi}^\dagger \frac{\hbar^2 \mathbf{k}^2}{2m} \mathbf{\Phi}$ while \mathbf{V} has matrix elements $V_{ij} = \langle \theta_i | V | \theta_j \rangle \approx V(x_i) \delta_{ij}$.

Multiplying Eq. (73) from the left by \mathbf{G}^\dagger and inserting $\mathbf{B}\mathbf{G}^\dagger = \mathbf{1}$ between \mathbf{H} and \mathbf{a} , we obtain

$$i\hbar \frac{d\mathbf{G}^\dagger \mathbf{a}}{dt} = \mathbf{G}^\dagger \mathbf{H} \mathbf{B} \cdot \mathbf{G}^\dagger \mathbf{a} = \mathbf{Z}^{-1} \mathbf{B}^\dagger \mathbf{H} \mathbf{B} \cdot \mathbf{G}^\dagger \mathbf{a}, \quad (74)$$

where in the second equality we have used Eq. (34). Eq. (74) is the TDSE in the $\langle g |$ representation, i.e. the $|b\rangle$ basis.

1. Reduced Space with Orthogonal Projection

We now consider the TDSE on the reduced Hilbert space $\tilde{\mathcal{H}}$. Analogously to our discussion of the full Hilbert space, we will consider the Schrödinger equation expressed in the $|\tilde{b}_n\rangle$ basis. Assuming an orthogonal projection, i.e. representation in terms of $\langle \tilde{g}_n |$, the TDSE takes the following possible forms:

$$i\hbar \frac{d\tilde{\mathbf{G}}^\dagger \mathbf{a}}{dt} = \tilde{\mathbf{G}}^\dagger \tilde{\mathbf{H}} \tilde{\mathbf{B}} \cdot \tilde{\mathbf{G}}^\dagger \mathbf{a}, \quad (75)$$

$$= \tilde{\mathbf{G}}^\dagger \tilde{\mathbf{H}} \tilde{\mathbf{G}} \tilde{\mathbf{Z}} \cdot \tilde{\mathbf{G}}^\dagger \mathbf{a}, \quad (76)$$

$$= \tilde{\mathbf{Z}}^{-1} \tilde{\mathbf{B}}^\dagger \tilde{\mathbf{H}} \tilde{\mathbf{B}} \cdot \tilde{\mathbf{G}}^\dagger \mathbf{a}. \quad (77)$$

Each of these forms has an advantage and a disadvantage. The first form avoids the $\tilde{\mathbf{Z}}$ to the right of H (as opposed to Eq. (76)) but the Hamiltonian must be calculated in the nonlocalized $|\tilde{b}\rangle$ representation (of columns). Its representation is now nonhermitian. Further, note that if the pruned subspace changes during the simulation, $\{|\tilde{g}_i\rangle\}$ changes and the Hamiltonian needs to be recomputed. The second form (76) has the advantage that H is evaluated in a localized basis of the $|\tilde{g}\rangle$ (although note that these are not as localized as the original $|g\rangle$). However, this form requires an application of nonsparse $\tilde{\mathbf{Z}}$ to the right of the Hamiltonian and again, if the pruned subspace changes during the simulation, the Hamiltonian needs to be recomputed. The last form (77) introduces an application of $\tilde{\mathbf{Z}}^{-1}$ to the left of H . Like $\tilde{\mathbf{G}}$, this matrix needs to be recomputed as the subspace changes but its size is $\tilde{N} \times \tilde{N}$ instead of $N \times \tilde{N}$.

The reader should recall that $\tilde{\mathbf{Z}} = \mathbf{R}^\dagger \mathbf{Z} \mathbf{R} = \mathbf{R}^\dagger \mathbf{B}^\dagger \mathbf{B} \mathbf{R}$ maintains the (pruned) direct product form of the basis in multidimensions while $\tilde{\mathbf{Z}}^{-1} = [\mathbf{R}^\dagger \mathbf{Z} \mathbf{R}]^{-1}$ loses this form, see also section IV C.

2. Reduced Space with Nonorthogonal Projection

The TDSE can also be written in terms of the nonorthogonal projection introduced in section III C 3:

$$i\hbar \frac{d\check{\mathbf{G}}^\dagger \mathbf{a}}{dt} = \check{\mathbf{G}}^\dagger \tilde{\mathbf{H}} \tilde{\mathbf{B}} \cdot \check{\mathbf{G}}^\dagger \mathbf{a} = \mathbf{R}^\dagger \mathbf{G}^\dagger \tilde{\mathbf{H}} \tilde{\mathbf{B}} \cdot \check{\mathbf{G}}^\dagger \mathbf{a}. \quad (78)$$

Comparing Eq. (78) with Eq. (75) shows that $\tilde{\mathbf{G}}^\dagger$ has been replaced with $\check{\mathbf{G}}^\dagger = \mathbf{R}^\dagger \mathbf{G}^\dagger$, characteristic of a nonorthogonal projection. As discussed in section III C 3, the multidimensional form of Eq. (78) is decomposable, significantly reducing the computational cost, at the expense of reduced accuracy.

Now, we present some physical considerations about using this form of the TDSE. In section III C 4, we have shown that $|\tilde{g}_n\rangle$ will be virtually identical to $|g_n\rangle$ if it is located in the interior of the reduced phase space. Only the $|\tilde{g}_n\rangle$ that are located at the boundary of the pruned region change drastically, compared to $|g_n\rangle$. It is therefore tempting to replace all $\{|\tilde{g}_n\rangle\}_{n=1}^{\tilde{N}}$ by $\{|g_n\rangle\}_{n=1}^{\tilde{N}}$. With this replacement, Eq. (75) takes the *approximate* form of Eq. (78).

We stress that Eq. (78) is an approximation to the PvB method. 25 years ago, Genossar and Porat have already shown that the use of $\{|\tilde{g}_n\rangle\}$ gives the optimal representation to a state in a minimal norm sense [50], see section III C 3. Therefore, the use of $\{|g_n\rangle\}$ *always* gives lower accuracy than the use of $\{|\tilde{g}_n\rangle\}$. Nevertheless, the approximate form has appealing properties which will become clear in sections IV C 1 and IV D 4. Since only the $|\tilde{g}_n\rangle$ at the boundary differ substantially from $|g_n\rangle$, one can have a good description in the interior of the phase space within this

approximation by using larger subspaces. Therefore, it is useful especially in the context of the time-independent Schrödinger equations where this error is more controllable [13, 16], although a proper error estimation is still missing. For the time-dependent Schrödinger equation, the wavepacket moves and the boundary needs to change in time. The description of the boundaries of the wavefunction therefore is much more important than for eigenstates. Further, the shape of the reduced phase space is often more curvy than for describing eigenstates. Thus, we found no usefulness of this approximation in solving the time-dependent Schrödinger equation [13]; see section V and Figure 10 for a comparison of the different methods.

Note that despite the nonorthogonal projection in Eq. (78), the biorthogonal basis $|b\rangle$ cannot be avoided despite appearances to the contrary [17]; it is inherent to the dual space structure of quantum mechanics [52].

IV. MULTIDIMENSIONAL CONSIDERATIONS

One of the main challenges in quantum molecular dynamics is the treatment of multidimensional systems. The easiest *ansatz* for creating a multidimensional basis is to use a direct or Kronecker product basis and it will be used in the following sections. However, even a direct product basis requires special care in the numerical implementation to obtain the optimal scaling. For a pruned direct product basis, this is even more subtle.

After an introductory section, we will detail different ways to understand efficient tensor transformations needed for the matrix-vector product in quantum dynamical simulations, both for unpruned and for pruned bases of direct product type. We then point out the incompatibility of nonorthogonal bases like PvB with this efficient transformation. Afterwards, we discuss orthogonal bases that still exhibit forms of phase-space localization and discuss the usefulness of pruned coordinate-space-localized basis functions. This section is based heavily on Ref. 18. We end this section with possible avenues to make PvB compatible with the efficient scaling of matrix-vector products.

A. Introduction

We expand our D -dimensional wave function in a linear combination of all possible combinations of one-dimensional, time-independent basis functions $\{|\chi_{i_\kappa}^{(\kappa)}\rangle\}_{i_\kappa=1}^{N_\kappa}$ [27, 53, 54]:

$$|\Psi(t)\rangle = \sum_{i_1=1}^{N_1} \sum_{i_2=1}^{N_2} \cdots \sum_{i_D=1}^{N_D} a_{i_1 i_2 \dots i_D}(t) \bigotimes_{\kappa=1}^D |\chi_{i_\kappa}^{(\kappa)}\rangle, \quad (79)$$

where the basis $\{|\chi_{i_\kappa}^{(\kappa)}\rangle\}_{i_\kappa=1}^{N_\kappa}$ can be of any type (spectral basis, DVR, PvB etc.). All information is now stored in the coefficient tensor \mathbf{a} of size

$$\prod_{\kappa=1}^D N_\kappa = \bar{N}^D, \quad (80)$$

where \bar{N} is the geometric mean of the set $\{N_i\}_{i=1}^D$. Introducing the multiindex $I \equiv i_1 i_2 \dots i_D$, the tensor \mathbf{a} can be viewed as a vector of size \bar{N}^D . The tensor and the vector view are advantageous in different cases and both views will be used in the following. Inserting this *ansatz* into the time-dependent Schrödinger equation,

$$i\hbar \frac{\partial}{\partial t} |\Psi(t)\rangle = H |\Psi(t)\rangle, \quad (81)$$

gives

$$i\hbar \mathbf{S} \frac{d}{dt} \mathbf{a}(t) = \mathbf{H} \mathbf{a}(t), \quad (82)$$

$$H_{IJ} = \bigotimes_{\kappa=1}^D \bigotimes_{\tau=1}^D \langle \chi_{i_\kappa}^{(\kappa)} | H | \chi_{j_\tau}^{(\tau)} \rangle, \quad (83)$$

$$\mathbf{S} = \bigotimes_{\kappa=1}^D \mathbf{s}^{(\kappa)}, \quad s_{i_\kappa j_\kappa}^{(\kappa)} = \langle \chi_{i_\kappa}^{(\kappa)} | \chi_{j_\kappa}^{(\kappa)} \rangle, \quad (84)$$

In typical solvers for the ordinary differential equation (82), matrix-vector products or tensor transformations of the type $\mathbf{S}^{-1}\mathbf{H}\mathbf{a}$ are required [27] and we have to find a way to do the computation quickly.

In a DVR, the inverse overlap matrix, \mathbf{S}^{-1} , is identical to the unit matrix and the matrix representation of the potential of the Hamiltonian is diagonal. The matrix-vector-product of the potential times the coefficient vector hence scales linearly as \bar{N}^D . The remaining term, the kinetic energy operator, T , often has a special structure consisting of a sum of direct products (SoP) of one-dimensional operators,

$$T = \sum_{l=1}^g \bigotimes_{\kappa=1}^D t^{(\kappa,l)}, \quad (85)$$

which gives, in matrix representation,

$$\mathbf{T} = \sum_{l=1}^g \bigotimes_{\kappa=1}^D \mathbf{t}^{(\kappa,l)}. \quad (86)$$

The following subsection will deal with efficient algorithms for this structure.

For other bases like PvB, the potential-term also needs to have a SoP structure to make the matrix-vector product efficient. This can be done by algorithms like potfit [54, 55] or by employing neural networks [56, 57].

B. Efficient Tensor Transformation

In the following, we review an efficient algorithm for the tensor transformation which is crucial for any multidimensional basis of direct product form. The concept for a simple direct product basis is relatively straightforward but some challenges appear for pruned bases of direct product type.

1. Full Direct Product Basis

There are several ways to understand the efficient tensor transformation. We will show two of them: First, in terms of tensors and summations of each tensor entry and second, in terms of matrix-vector and Kronecker products.

a. Tensor (Summation) View

For the sake of simplicity, we use as an example a three-dimensional problem where the Hamiltonian has only one product term, $H = h^{(1)}h^{(2)}h^{(3)}$. The tensor transformation then looks like

$$(\mathbf{H}\mathbf{a})_{pqr} = a'_{pqr} = \sum_{i=1}^{N_1} \sum_{j=1}^{N_2} \sum_{k=1}^{N_3} h_{pi}^{(1)} h_{qj}^{(2)} h_{rk}^{(3)} a_{ijk}. \quad (87)$$

The computation of one single term scales as \bar{N}^3 . Since \mathbf{a}' has \bar{N}^3 values, the transformation would scale as \bar{N}^6 or, in general, as \bar{N}^{2D} . However, this summation can be done sequentially, thereby drastically reducing the scaling [53, 58–60]:

$$a'_{pqr} = \underbrace{\sum_{i=1}^{N_1} h_{pi}^{(1)} \underbrace{\sum_{j=1}^{N_2} h_{qj}^{(2)} \sum_{k=1}^{N_3} h_{rk}^{(3)} a_{ijk}}_{\check{a}_{ijr}}}_{\check{\check{a}}_{iqr}} \quad (88)$$

One first computes the intermediate partially transformed tensor $\check{\mathbf{a}}$ and stores it. Afterwards, the intermediate tensor $\check{\check{\mathbf{a}}}$ is computed and $\check{\mathbf{a}}$ used for its computation. Finally, the fully transformed tensor \mathbf{a}' is computed. In each tensor transformation, only one summation is done such that the computation of one full intermediate tensor scales as \bar{N}^{3+1} , or, in general \bar{N}^{D+1} . Compared to the direct summation, the saving is thus proportional to \bar{N}^{D-1} . Because \bar{N} is often

of the order of 10 or 100, this saving is tremendous and highly desired, already for $D = 2$. A pseudocode exploiting highly optimized matrix-matrix-product routines is given in Ref. 18.

This sequential summation is also well-known in electronic structure theory where it is used, for example, for integral transformations [61, 62].

b. Vector (Matrix Product) View

Another way to look at the sequential tensor transformation is in terms of matrices, consisting of Kronecker products, and their multiplications with the vectorized coefficient tensor. This gives further insight, especially for a pruned basis (subsection IV B 2). For our 3D example, the Hamiltonian matrix can be written as

$$\mathbf{H} = \mathbf{h}^{(1)} \otimes \mathbf{h}^{(2)} \otimes \mathbf{h}^{(3)}. \quad (89)$$

We can now factorize this expression by introducing diagonal matrices [63]:

$$\mathbf{H} = \underbrace{(\mathbf{h}^{(1)} \otimes \mathbf{1}^{(2)} \otimes \mathbf{1}^{(3)})}_{\mathbf{H}^{(1)}} \cdot \underbrace{(\mathbf{1}^{(1)} \otimes \mathbf{h}^{(2)} \otimes \mathbf{1}^{(3)})}_{\mathbf{H}^{(2)}} \cdot \underbrace{(\mathbf{1}^{(1)} \otimes \mathbf{1}^{(2)} \otimes \mathbf{h}^{(3)})}_{\mathbf{H}^{(3)}}. \quad (90)$$

The sequential transformation is nothing other than applying the decomposed terms $\mathbf{H}^{(\kappa)}$ sequentially to \mathbf{a} :

$$\check{\mathbf{a}} = \mathbf{H}^{(3)} \cdot \mathbf{a}, \quad (91)$$

$$\check{\check{\mathbf{a}}} = \mathbf{H}^{(2)} \cdot \check{\mathbf{a}}, \quad (92)$$

$$\mathbf{a}' = \mathbf{H}\mathbf{a} = \mathbf{H}^{(1)} \cdot \check{\check{\mathbf{a}}}. \quad (93)$$

The matrices $\mathbf{H}^{(\kappa)}$ are just permuted (by a perfect shuffle) block-diagonal matrices [64], and hence very sparse. This sparsity accounts for the simple form of the tensor transformation shown in Eq. (88).

2. Pruned Direct Product Basis

In the following, we consider an arbitrarily pruned basis, meaning that the coefficient tensor is sparse but there is no structure of the pruned Hilbert space to simplify the algorithms for the tensor transformation. However, we emphasize that, although the Hilbert space has no direct product structure, the underlying basis is still of direct product type and many features are thus inherited from the unpruned direct product Hilbert space. For a long time, it was thought that it was not possible to have an efficient scaling of the matrix-vector product for an arbitrarily pruned basis [65], but recently, efficient algorithms have been developed [17, 18, 22]. For all pruning types, there is an approximation involved which can be formally defined in terms of projection operators. We analyze this below.

a. Tensor (Summation) View

For our three-dimensional example, the indices ijk of the used basis functions are specified using the sets \mathcal{J} for the first, $\mathcal{J}(i)$ for the second and $\mathcal{K}(i, j)$ for the third index. For each basis index $i \in \mathcal{J}$ used there is one specific set $\mathcal{J}(i)$, and for each set of indices $i \in \mathcal{J}$ and $j \in \mathcal{J}(i)$, there is one specific set $\mathcal{K}(i, j)$. In an analogy, this corresponds to a three-dimensional integration of an arbitrarily shaped area, $\int_{x_1}^{x_2} \int_{y_1(x)}^{y_2(x)} \int_{z_1(x,y)}^{z_2(x,y)} dx dy dz$. For a pruned basis, the index range in Eq. (88) needs to be changed using the sets specified above:

$$a'_{pqr} = \sum_{i \in \mathcal{J}} h_{pi}^{(1)} \sum_{j \in \mathcal{J}(i)} h_{qj}^{(2)} \underbrace{\sum_{k \in \mathcal{K}(i,j)} h_{rk}^{(3)} a_{ijk}}_{\check{\check{a}}_{ijr}}. \quad (94)$$

By looking at the equations for the partially transformed tensors, one sees that a problem arises. To give an example, consider the last transformation

$$a'_{pqr} = \sum_{i \in \mathcal{J}} h_{pi}^{(1)} \check{\check{a}}_{ijr}, \quad (95)$$

where the range (output \mathbf{a}') is given by

$$p \in \mathcal{J}, q \in \mathcal{F}(p), r \in \mathcal{K}(p, q), \quad (96)$$

but the domain (input $\check{\mathbf{a}}$) is

$$i \in \mathcal{J}, q \in \mathcal{F}(i), r \in \mathcal{K}(i, q). \quad (97)$$

On the right hand side, indices igr are needed that are *not* necessarily elements of the employed subsets [18]: It is not necessarily fulfilled that $q \in \mathcal{F}(i)$ and that $r \in \mathcal{F}(i, q)$. The same holds for the computation of $\check{\mathbf{a}}$ from $\check{\mathbf{a}}$. To give an example: Consider the set of pruned indices $\{012, 133\}$. For a'_{133} , Eq. (95) takes then the form of $a'_{133} = h_{10}^{(1)} \check{a}_{033} + h_{11}^{(1)} \check{a}_{133}$, where \check{a}_{033} , needed for the first term, is not included in the initial index set.

Hence, we either have to use intermediate tensors of size larger than the pruned basis size or we have to neglect the values of the intermediate tensors whose indices are not elements of the index sets.

b. Vector (Matrix Product) View

The difficulty with the sequential transformation in a pruned basis becomes more clear if we use matrix notation and use \mathbf{R} from Eq. (50) to project into the pruned space. Then, the *nonsequential* matrix-vector product takes the form of

$$\mathbf{R}^\dagger \mathbf{H} \mathbf{R} \tilde{\mathbf{a}} = [\mathbf{R}^\dagger \mathbf{H}^{(1)} \mathbf{H}^{(2)} \mathbf{H}^{(3)} \mathbf{R}] \tilde{\mathbf{a}}, \quad (98)$$

where $\tilde{\mathbf{a}}$ is already pruned and viewed as a vector. Employing the *sequential* matrix-vector product with intermediate vectors of the same size as the input and output vectors, we obtain

$$\mathbf{R}^\dagger \mathbf{H} \mathbf{R} \tilde{\mathbf{a}} = \underbrace{[\mathbf{R}^\dagger \mathbf{H}^{(1)} \mathbf{R}] [\mathbf{R}^\dagger \mathbf{H}^{(2)} \mathbf{R}] [\mathbf{R}^\dagger \mathbf{H}^{(3)} \mathbf{R}]}_{\tilde{\mathbf{a}}} \tilde{\mathbf{a}} \quad (99)$$

The additional error in this way of employing a sequential transformation comes from the additional intermediate projections \mathbf{R} , because

$$\mathbf{R}^\dagger \mathbf{H}^{(1)} \mathbf{H}^{(2)} \mathbf{H}^{(3)} \mathbf{R} \neq [\mathbf{R}^\dagger \mathbf{H}^{(1)} \mathbf{R}] [\mathbf{R}^\dagger \mathbf{H}^{(2)} \mathbf{R}] [\mathbf{R}^\dagger \mathbf{H}^{(3)} \mathbf{R}]. \quad (100)$$

The introduction of additional projections is similar to the so called product approximation that distinguish the HEG (Harris, Engerholm, Gwinn) method from a Variational Basis Representation (VBR) [22, 27, 53]. Further, the additional projections to the pruned subspace lead to a nonhermitian matrix because $[\mathbf{R}^\dagger \mathbf{H}^{(\kappa)} \mathbf{R}]$ do not commute with each other whereas $\mathbf{H}^{(\kappa)}$ do commute [22]. Using a symmetrized product $1/2\{[\mathbf{R}^\dagger \mathbf{H}^{(1)} \mathbf{R}] [\mathbf{R}^\dagger \mathbf{H}^{(2)} \mathbf{R}] [\mathbf{R}^\dagger \mathbf{H}^{(3)} \mathbf{R}] + [\mathbf{R}^\dagger \mathbf{H}^{(3)} \mathbf{R}] [\mathbf{R}^\dagger \mathbf{H}^{(2)} \mathbf{R}] [\mathbf{R}^\dagger \mathbf{H}^{(1)} \mathbf{R}]\}$ restores hermiticity [22] but may not substantially cure the error introduced by the approximation.

c. Implementation

The strategy to using larger intermediate tensors for the tensor transformation has been employed in many applications for structured pruning [65–68]. For a completely arbitrary pruning, the size of the intermediate tensors would be too large and the numerical implementation too complicated. Therefore, we must neglect values of the intermediate tensors. For an orthogonal basis, this is normally justified but it turns out that this can be a severe approximation for nonorthogonal bases, see section IV C 2.

We have presented and benchmarked an implementation in Ref. 18. There, the tensors are permuted such that the dimension over which the sequential summation is performed is represented contiguously in memory. The cost of the permutation is negligible. A similar idea has been employed in Ref. 22. An algorithm, which uses a more complicated recursive mapping strategy and which leads to noncontiguous memory access, has been developed in Ref. 17. Details of the numerical implementation of either of the two algorithms is out of scope of this review. The implementations are much more complicated than for the full direct product basis.

The approximation introduced by the projections is negligible if the intermediate tensors have approximately the same sparsity pattern as the initial tensor. This is typically fulfilled if a DVR is used as the underlying basis.

C. Incompatibility of Nonorthogonal Bases and Multidimensional Decomposition

Unfortunately, the use of a phase space localized basis entails several disadvantages. Instead of a D -dimensional space, a $2D$ -dimensional space needs to be analyzed for the pruning. Many algorithms for analyzing data in multidimensional spaces, like finding nearest neighbors, have unfavorable scaling relationships; doubling the dimension can mean a significant increase in effort if no care is taken in the algorithms used for pruning [18, 69].

Moreover, for phase-space-localized bases, a SoP form is required for a straightforward matrix representation of the Hamiltonian and for a well-scaled matrix-vector product. Unfortunately, the number of required product terms to sum over can be more than 10^3 for complicated potentials [18, 26]. Exploitation of fast transformations for potentials without SoP form using quadrature is ongoing research [70].

1. Nonorthogonality Means Non-Decomposable Inverse Overlap Matrix $\tilde{\mathbf{Z}}^{-1}$

The overlap matrix, \mathbf{Z} (in $|b\rangle$ representation), is decomposable into a product form, see Eq. (84). For a pruned basis, the structure of \mathbf{Z} is inherited. However, the structure of the inverse, $\tilde{\mathbf{Z}}^{-1} = [\mathbf{R}^\dagger \mathbf{Z} \mathbf{R}]^{-1}$ is not of product form because $[\mathbf{R}^\dagger \mathbf{Z} \mathbf{R}]^{-1} \neq \mathbf{R} \mathbf{Z}^{-1} \mathbf{R}^\dagger$ [13, 16, 18]. The nondecomposability leads to a $\tilde{N}^{\sim 2D}$ scaling both in storage and computing time. Possible ways to circumvent this are discussed in subsection IV D 4.

2. Nonorthogonality Prevents Efficiently Scaling Matrix-Vector-Product

In section IV B 2, we have discussed a $\tilde{N}^{\sim D+1}$ scaling matrix-vector product for a pruned basis and a Hamiltonian with SoP structure. Thereby, we have assumed that the intermediate tensors of the sequential transformation have the same sparsity pattern as the initial vector. However, in general, this is not the case for nonorthogonal bases such as PvB. The needed matrix-vector product involves the inverse overlap matrix: $\tilde{\mathbf{Z}}^{-1} \tilde{\mathbf{H}} \tilde{\mathbf{a}}$, where $\tilde{\mathbf{H}} = \tilde{\mathbf{B}}^\dagger \mathbf{H} \tilde{\mathbf{B}}$ (see section III D 1 for the one-dimensional analogue and Eq. (41) for the definition of the one-dimensional matrix $\tilde{\mathbf{Z}}$ in the $|b\rangle$ representation). Applying $\tilde{\mathbf{H}}$ to $\tilde{\mathbf{a}}$ transforms the latter from a sparse PvB to a nonsparse PvN representation:

$$\tilde{a}'_I = \sum_J \langle \tilde{b}_I | H | \tilde{b}_J \rangle \underbrace{\langle \tilde{g}_J | \Psi \rangle}_{\tilde{a}_J} = \langle \tilde{b}_I | H | \Psi \rangle. \quad (101)$$

Application of $\tilde{\mathbf{Z}}^{-1}$ is therefore required to transform $\tilde{\mathbf{a}}'$ back to the PvB representation. Therefore, the intermediate tensors in a sequential summation are not sparse and the favorable scaling $\tilde{N}^{\sim D+1}$ cannot be reached without introducing intermediate tensors as large as the unpruned basis, i. e., a $\tilde{N}^{\sim D+1}$ scaling instead of $\tilde{N}^{\sim D+1}$.

If $\tilde{\mathbf{Z}}^{-1}$ had a product structure, we could do $\tilde{\mathbf{Z}}^{-1} \tilde{\mathbf{H}}$ in one step, gaining sparse intermediate tensors and therefore the favorable scaling. This is possible with the nonorthogonal projector from section III C 3 which, however, lacks accuracy for quantum dynamical simulations; see the discussion in section III D 2. An improvement is discussed in section IV D 4.

D. Orthogonalization

The unfavorable scaling of the matrix-vector product in phase-space-localized bases is inherently related to nonorthogonality. Unfortunately, orthogonalization entails a sacrifice of phase-space-localization of functions placed on a regular lattice; see the theorem of Balian and Low [71–73].

1. Weylets

Instead of trying to orthogonalize a phase-space-localized basis, Wilson [74] and Daubechies *et al.* [75] orthogonalized momentum-symmetrized basis functions, so called ‘‘Weyl-Heisenberg’’ wavelets or ‘‘Weylets’’. Poirier refined this basis and found a simpler orthogonalization procedure [19–21]. The nonorthogonal basis behind the Weylets are real-valued

momentum-symmetrized Gaussians, localized in x_n and $\pm p_l$:

$$\langle x | \mathcal{G}_{nl}^S \rangle = \left(\frac{8\alpha}{\pi} \right)^{\frac{1}{4}} \exp[-\alpha(x - x_n)^2] \sin \left[p_l \left(x - x_n - \sqrt{\frac{\pi}{8\alpha}} \right) \right]. \quad (102)$$

These functions are then orthogonalized using Löwdin's symmetric orthogonalization (multiplication with $\mathbf{S}^{-1/2}$) [76]. Löwdin orthogonalization ensures that the orthogonalized functions resemble the initial functions as closely as possible. For more details, we refer to Ref. 20, 21.

2. Projected Weylets (pW)

Weylets have been used successfully in solving (ro-)vibrational problems [21, 77]. However, we have found that Weylets are less accurate than a FGH method if both bases span the same phase space (i.e., a rectangular area in phase space is used and the Weylet basis is not pruned within this area) [18]. Moreover, compared to PvB, the transformation of a SoP operator requires more computation and the implementation is trickier if high accuracy is required. Therefore, we combined the advantages of PvB and Weylets to define so called "projected Weylets", pW. For that, we first project the momentum-symmetrized Gaussians onto a DVR basis (compare with Eq. (29)):

$$|g_n^S\rangle = \sum_j |\theta_j\rangle \langle \theta_j | \mathcal{G}_n^S \rangle = \sum_j |\theta_j\rangle \sqrt{\Delta_j} \langle x_j | \mathcal{G}_n^S \rangle, \quad (103)$$

$$\mathbf{G}_{jn}^S = \sqrt{\Delta_j} \langle x_j | \mathcal{G}_n^S \rangle. \quad (104)$$

The projected Weylets are then obtain by Löwdin orthogonalization of \mathbf{G}^S . The procedure is thus very similar to PvB. The only difference is the exchange of the von Neumann functions with momentum-symmetrized Gaussians and Löwdin orthogonalization instead of biorthogonalization.

We now compare pW and Weylets, PvB and FGH. Figure 7 shows the performance of these bases for the simple harmonic oscillator. Clearly, pruning of phase-space localized basis functions is very effective in terms of required basis functions. The Weylets and pW curves lie on top of each other because they have the same phase-space-tiling. However, due to inaccuracies of $\mathbf{S}^{-1/2}$ for the Weylets, the asymptotic error of the latter is larger. This could be repaired by increasing the accuracy of $\mathbf{S}^{-1/2}$, see Ref. 20 for details. However, the transformation of the integrals is more involved for Weylets and can become a bottleneck, see supporting information in Ref. 18.

Figure 7 also shows that PvB provides a more compact representation than the Weylet-type bases. This can be understood from the representation of the wavefunction. PvB is defined as

$$|b_n\rangle = \sum_{m=1}^N |g_m\rangle [S^{-1}]_{mn}, \quad (105)$$

and the basis function coefficients are

$$a_m^{\text{PvB}} = \langle g_m | \Psi \rangle. \quad (106)$$

For Weylets and pW, we have the relations

$$|w_n\rangle = \sum_{m=1}^N |g_m^S\rangle [S^{-1/2}]_{mn}, \quad (107)$$

$$a_m^{\text{pW}} = \langle w_m | \Psi \rangle. \quad (108)$$

The expansion coefficients in pW representation contains exponentially decaying elements of $\mathbf{S}^{-1/2}$ whereas the coefficients in PvB representation involve only one single Gaussian. Hence, the decrease in error in Figure 7 is exponential for pW and Weylets but Gaussian for PvB. Substituting $\mathbf{S}^{-1/2}$ by \mathbf{S}^{-1} in Eq. (107) would preserve Gaussian decay but reintroduce nonorthogonality. The latter is crucial as discussed in sections IV C 1 and IV C 2.

To give an example of the phase-space representation of states, Figure 8 shows the two states

$$f_1(x) = \exp[-(x - a)^2 + ibx] \exp(c)/\pi, \quad (109)$$

$$f_2(x) = \{\exp[-(x - a)^2 + ibx] + \exp[-(x - a)^2 - ibx]\} \exp(c)/\sqrt{4\pi} \quad (110)$$

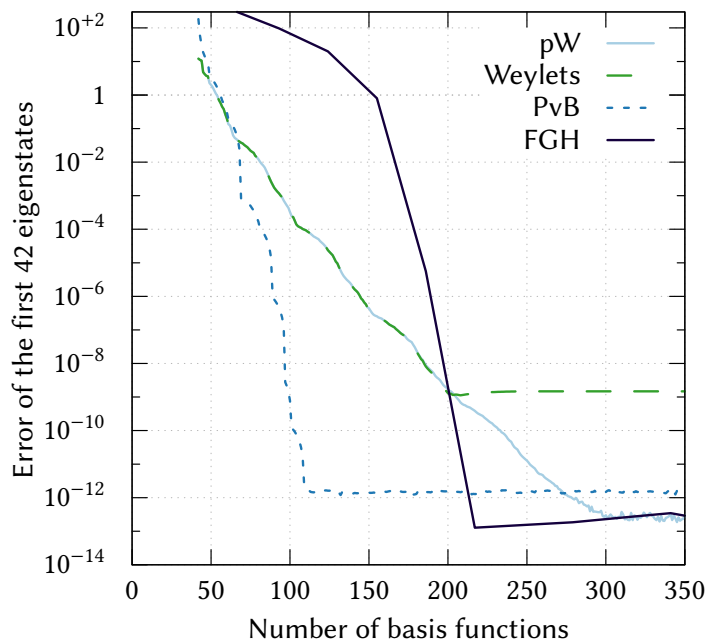


Figure 7. Comparison of pruned pW, Weylets, PvB and FGH for the simple harmonic oscillator. The number of phase-space-basis functions is determined by phase-space pruning based on classical arguments. The FGH basis covers a square area in phase space that is enlarged as the number of basis functions is increased. The error is defined by the L_2 norm of the difference between the vector of the exact and the numerical energies [18].

with $a = 28.83$, $b = 14$, and $c = 49$ in PvB, pW and in a biorthogonal projected symmetrized Gaussian (bpSG) representation. The latter is similar in form to Eq. (105) but with symmetrized Gaussians instead of von Neumann functions. f_1 is asymmetric whereas f_2 is symmetric in phase space. As expected from the arguments in the previous paragraph, the figure reveals Gaussian decay of the coefficients in phase space for PvB and bpSG but exponential decay for pW.

For pW and bpSG, roughly the same number of coefficients are needed to represent either f_1 or f_2 , whereas in PvB only half as many coefficients are needed for representing f_1 compared to f_2 . Hence, momentum-asymmetric states are described by pW and bpSG no more efficiently than momentum-symmetric states. These results hold even without the projection onto a DVR space.

3. Pruned DVR

A straightforward alternative to phase-space-localized basis functions are coordinate-space-localized basis functions like Gaussians, grid-based methods or DVR functions [18, 78–82]. This strategy has been proven to be successful for time-independent problems [32, 83, 84]. Orthogonalization and DVR-like properties (diagonality of representations of functions of x) are easily obtained with coordinate-space-localized basis functions making them simple to use.

One might argue that localization in coordinate space is not enough. During a typical simulation, one begins with a well-localized wavepacket that, during time, spreads over large areas in coordinate space. However, this is true only for some modes where the actual reaction occurs; even in these modes the whole coordinate space is generally not occupied. In spectator modes, the wavepacket remains compact. Thus, pruning in coordinate space is meaningful, especially for higher dimensional problems where the representation in terms of a full direct-product basis becomes extremely wasteful. Further, we note that DVR-like basis functions are inherently more localized in coordinate space than phase-space-localized functions. If the range of momentum does not change significantly with time, localization in coordinate space might be more important. We have found this to be true especially for model potentials. We will

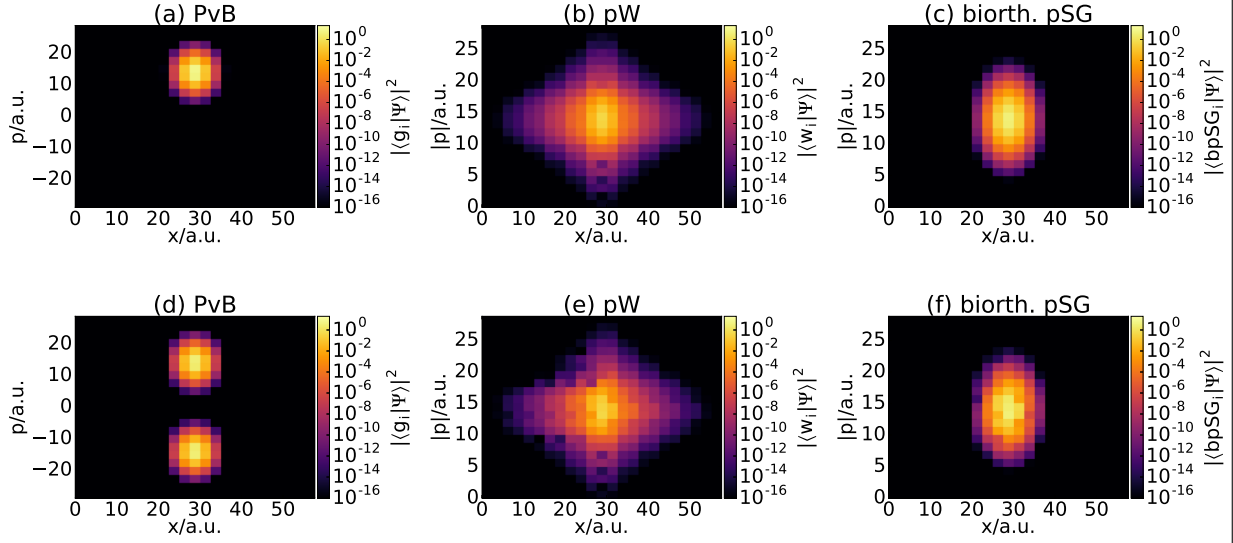


Figure 8. Representation of f_1 , Eq. (109), (panels (a)-(c)) and f_2 , Eq. (110), (panels (d)-(f)) in PvB (panels (a) and (d)), pW (panels (b) and (e)) and biorthogonal projected symmetrized Gaussians (panels (c) and (f)) in phase space [18]. Note the different ordinates for the representations.

give some examples in section V.

4. Approximations to $\tilde{\mathbf{Z}}^{-1}$ in PvB

Since $\tilde{\mathbf{Z}}^{-1}$ is nondecomposable (see subsection IV C 1), storage and computation of matrix-vector products scale as \tilde{N}^{2D} . This becomes the bottleneck of the computation. The matrix inversion formerly scales as \tilde{N}^{3D} , although there exists efficient formulas for updating the matrix if rows and columns have been removed or added [85]. Note that care has to be taken to avoid accumulation of rounding errors if update formulas are used.

The storage can be avoided by solving linear system of equations $\tilde{\mathbf{Z}}\tilde{\mathbf{a}}' = \tilde{\mathbf{a}}'$ using iterative algorithms such as conjugate gradient. This avoids storing a huge matrix, but many matrix-vector products of type $\tilde{\mathbf{Z}}\tilde{\mathbf{a}}'$ are required to reach a sufficient accuracy. The \tilde{N}^{2D} scaling for the matrix-vector product remains, see subsection IV C 2. However, a very efficient preconditioner has recently been found, see below.

If $\tilde{\mathbf{Z}}^{-1}$ were decomposable, the matrix-vector-product $\tilde{\mathbf{Z}}^{-1}\tilde{\mathbf{H}}\tilde{\mathbf{a}}$ could be done in one step by combining decomposed inverse overlap matrix $[\mathbf{z}^{(\kappa)}]^{-1}$ with the terms of the Hamiltonian, $\mathbf{h}^{(\kappa)}$. Is it possible to obtain meaningful approximations to it in an easy way? For our three-dimensional example, using the matrix notation introduced in subsection IV B 2, the correct inverse in the pruned subspace can be written as

$$\tilde{\mathbf{Z}}^{-1} = [\mathbf{R}^\dagger \mathbf{Z} \mathbf{R}]^{-1} = [\mathbf{R}^\dagger \mathbf{z}^{(1)} \otimes \mathbf{z}^{(2)} \otimes \mathbf{z}^{(3)} \mathbf{R}]^{-1}. \quad (111)$$

We can use the same approximation as used for the nonorthogonal projector and invert \mathbf{R} in a singular-value-decomposition sense, meaning that $\mathbf{R}^{-1} \approx \mathbf{R}^\dagger$, see section III C 3:

$$\check{\mathbf{Z}}^{-1} = \mathbf{R}^\dagger \mathbf{Z}^{-1} \mathbf{R} = \mathbf{R}^\dagger [[\mathbf{z}^{(1)}]^{-1} \otimes [\mathbf{z}^{(2)}]^{-1} \otimes [\mathbf{z}^{(3)}]^{-1}] \mathbf{R}. \quad (112)$$

However, this is not a good approximation, see Figure 9 below. We can find a different and better approximation by making use of our notation used in Eq. (90):

$$\mathbf{Z} = \underbrace{(\mathbf{z}^{(1)} \otimes \mathbf{1}^{(2)} \otimes \mathbf{1}^{(3)})}_{\mathbf{z}^{(1)}} \cdot \underbrace{(\mathbf{1}^{(1)} \otimes \mathbf{z}^{(2)} \otimes \mathbf{1}^{(3)})}_{\mathbf{z}^{(2)}} \cdot \underbrace{(\mathbf{1}^{(1)} \otimes \mathbf{1}^{(2)} \otimes \mathbf{z}^{(3)})}_{\mathbf{z}^{(3)}}, \quad (113)$$

$$\Rightarrow \tilde{\mathbf{Z}} = \mathbf{R}^\dagger \mathbf{Z} \mathbf{R} \approx \check{\mathbf{Z}} \equiv \mathbf{R}^\dagger \mathbf{z}^{(1)} \mathbf{R} \cdot \mathbf{R}^\dagger \mathbf{z}^{(2)} \mathbf{R} \cdot \mathbf{R}^\dagger \mathbf{z}^{(3)} \mathbf{R}, \quad (114)$$

$$[\mathbf{R}^\dagger \mathbf{Z} \mathbf{R}]^{-1} \approx \check{\mathbf{Z}}^{-1} \equiv [\mathbf{R}^\dagger \mathbf{z}^{(1)} \mathbf{R}]^{-1} \cdot [\mathbf{R}^\dagger \mathbf{z}^{(2)} \mathbf{R}]^{-1} \cdot [\mathbf{R}^\dagger \mathbf{z}^{(3)} \mathbf{R}]^{-1}. \quad (115)$$

Here, \mathbf{R}^{-1} is not approximated by \mathbf{R}^\dagger . $\mathbf{Z}^{(\kappa)}$ are permuted block-diagonal matrices (see subsection IV B 2) and $\mathbf{R}^\dagger \mathbf{Z}^{(\kappa)} \mathbf{R}$ are still permuted block-diagonal but the blocks have different sizes depending on how many basis functions are used for a particular index combination. Therefore, it is relatively easy to store and invert those matrices. Imagining $\tilde{\mathbf{a}}$ as a cube (three-dimensional tensor), the product $\tilde{\mathbf{Z}}^{-1} \tilde{\mathbf{a}}$ corresponds to applying the transformation sequentially for each dimension and for each slice of $\tilde{\mathbf{a}}$. Therefore, this approximation misses the correlation between the dimensions; moreover, it is nonhermitian. Nevertheless, it is a much better approximation than Eq. (112). Moreover, $\check{\mathbf{Z}}^{-1}$ corresponds *exactly* to $\tilde{\mathbf{Z}}^{-1}$ for one-dimensional systems.

Figure 9 compares $\tilde{\mathbf{Z}}^{-1}$ and its approximations for a two-dimensional problem. Clearly, $\check{\mathbf{Z}}^{-1}$ is a much better approximation than $\tilde{\mathbf{Z}}^{-1}$. Unfortunately, we found no significant increase in accuracy using $\check{\mathbf{Z}}^{-1}$ in dynamics simulations. We tried to refine the values of $\tilde{\mathbf{Z}}^{-1}$ without significant success. In general, it is hard to estimate and reduce the error for various kinds of approximations to $\tilde{\mathbf{Z}}^{-1}$. Nevertheless, this approximation still can serve as a good and very fast preconditioner for use in solving linear systems of equations with direct methods. The number of required iterations is decreased by almost one order of magnitude if this preconditioner is used.

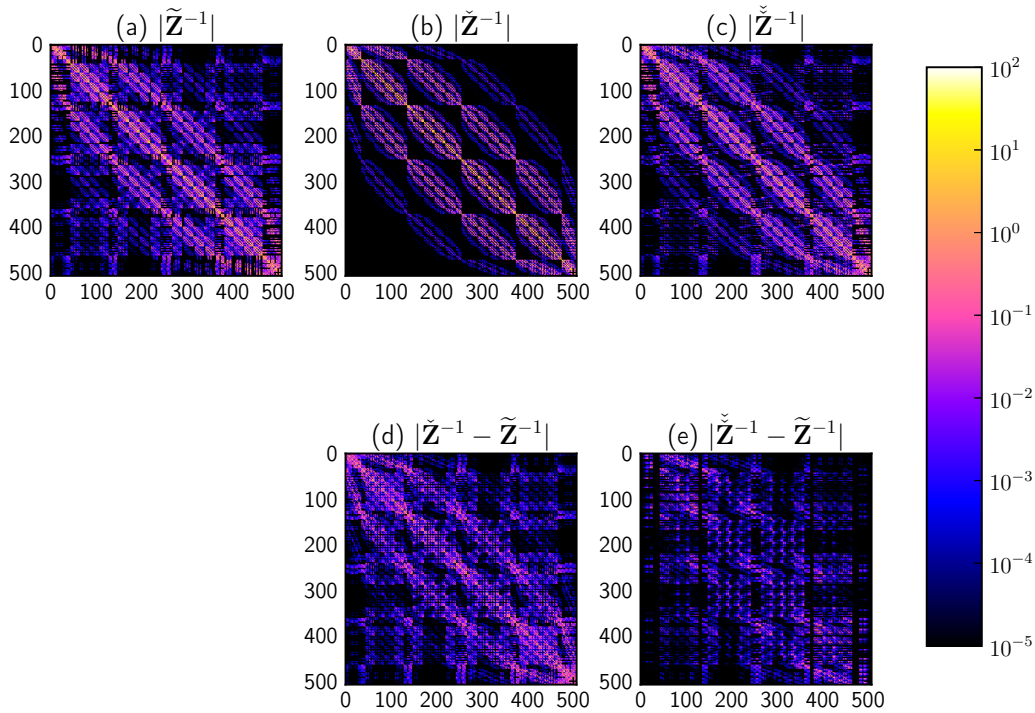


Figure 9. Comparison of the absolute value of the inverse of $\tilde{\mathbf{Z}}$ (panel (a)) and its approximations (panels (b) and (c)). The difference between the correct and the approximate inverse is shown in panels (d) and (e). The pruned basis represents states for a two-dimensional coupled harmonic oscillator.

V. APPLICATIONS

We now turn to some illustrative applications. Pruned phase-space methods have been successfully used for computing eigenenergies of (ro-)vibrational systems. For triatomics, PvB has been used together with the orthogonal [11] and with the nonorthogonal [16] projector. Weylets have been employed for the computation of the rovibrational spectrum, including all bound energy levels, of the neon dimer [77]. A study on the scaling of the method with dimension for

the harmonic oscillator has been given in Ref. 21. Momentum-symmetrized Gaussians have been used by Halverson and Poirier for large-scale, massively parallel vibrational computations of diphosphorous oxide, methyleneimine [23], acetonitrile [24] and even benzene [25] with thirty vibrational modes and for one million quantum states. Recently, the calculations for diphosphorous oxide and methyleneimine have been repeated by Brown and Carrington and the accuracy carefully tested without large-scale calculations using an iterative eigensolver for the lowest energy levels [17]. Depending on the region of interest in the spectrum, it was found that a carefully pruned harmonic oscillator basis can be more efficient than momentum-symmetrized Gaussians [17, 25].

In the following, we will focus on the applications in the context of solving the TDSE. In general, an application to the TDSE is more challenging, because the wavepacket moves in time and the pruned basis has to be adjusted according to this movement. The error involved in the approximation should be stable during the whole propagation. For all the examples below, we define a dynamical pruning scheme in terms of a wave amplitude threshold, ϖ . After some time steps, we observe the square of $\tilde{\mathbf{a}}$. If the value of one coefficient is larger than ϖ , we add nearest neighbors in phase space or coordinate space to the set of used basis functions. If they are newly added, their coefficient value is set to zero. If the value of one coefficient is smaller than ϖ and the same holds for its neighbors, we remove the corresponding basis function from the set. For a discussion about how many nearest neighbors to add and how the implementation is done to avoid an unfavorable scaling of this update procedure, we refer to Ref. 18.

A. Two-Dimensional Double Well

We start by investigating pruned dynamics in a two-dimensional double well. For details about the parameters, we refer to Ref. 13, 18. We compare the orthogonal and nonorthogonal projections of PvB, pW and a pruned DVR, namely FGH. Figure 10 (a) shows the accuracy and timings. Using nonorthogonal projection fails to provide proper accuracy for a reasonably small basis size. It needs 75% of the totally available basis functions to achieve machine accuracy.

PvB with the orthogonal projection gives the sparsest representation and on average only 40% of the basis size is needed to reproduce the autocorrelation to machine accuracy. Due to the inclusion of $\mathbf{S}^{-1/2}$ in the wave function coefficients, pW needs more basis functions than PvB to reach the same accuracy (see the discussion in section IV D 2). This reduced efficiency does not come from momentum symmetrization because pW can, compared to momentum-symmetrized states, describe states of arbitrary shape in phase space (see Figure 8). Surprisingly, FGH outperforms pW in this example for higher accuracies (below 10^{-6}). This comes from the functions being more localized in coordinate space [18].

Much more crucial than the required basis size is the required computing time, see Figure 10 (b). Because of the $\tilde{N}^{\sim 2D}$ scaling, PvB needs orders of magnitude more computing time than even exact DVR dynamics. pW and FGH have a more favorable $\tilde{N}^{\sim D+1}$ scaling and can beat the exact DVR dynamics for certain (pW) or for all (FGH) accuracy ranges. For some infidelity ranges where FGH needs more basis functions than pW, it is actually faster than the latter. This comes from the diagonality of the representation of the potential in FGH, which reduces the prefactor in the $\tilde{N}^{\sim D+1}$ scaling. Only at the low-infidelity end is pW faster.

B. Six-Dimensional Pyrazine

Nonadiabatic dynamics in pyrazine is a well-tested benchmark system [86, 87]. We use a six-dimensional vibronic-coupling model [86] to benchmark pW and FGH [18]. This system is high-dimensional but the wavepacket behaves more smoothly than in the double well example. Figure 11 compares the autocorrelation and timings for different basis sizes against the exact one. On average, only 0.8% of the total number of available basis functions are needed for FGH to accurately reproduce the spectrum, showing that fewer basis functions are needed if the dimensionality is increased. The computing time can be reduced by the pruning from 100 to 6 hours. FGH gives better results than pW because no high momenta are covered during the dynamics and therefore not many basis functions are needed in each mode. It is then more appropriate to use a pruned DVR. However, our pruning scheme disfavors pW and it might be useful to combine pW and pruned DVR, using pW in reactive modes and a DVR in spectator modes. See Ref. 18 for a thorough discussion.

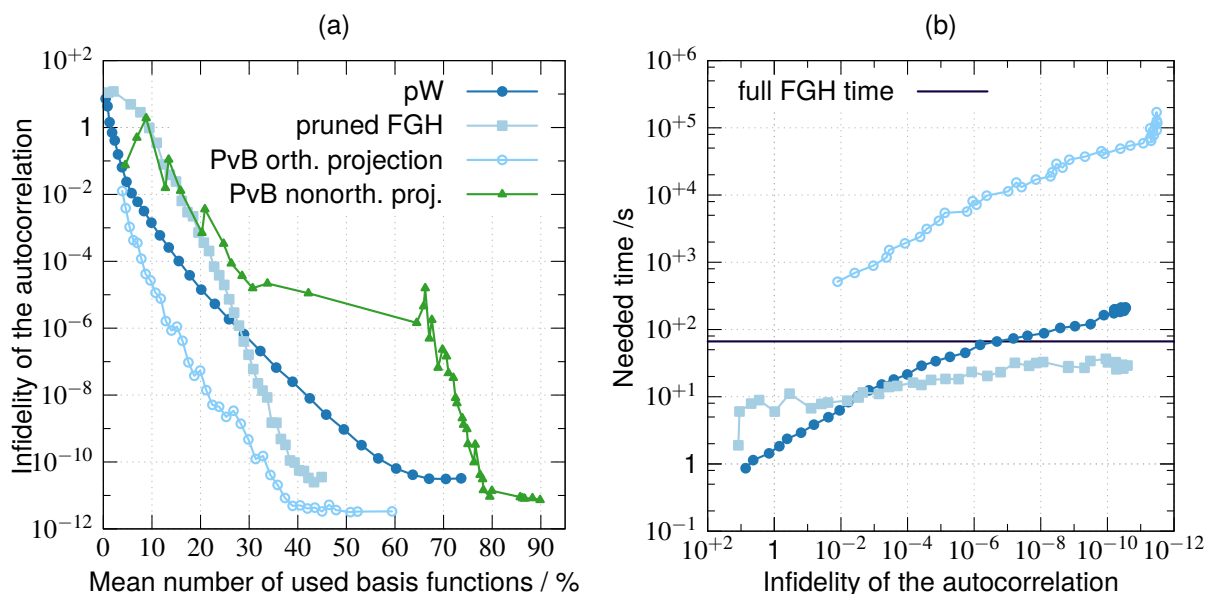


Figure 10. (a): Accuracy of the dynamics for the 2D double well as a function of the percentage ratio of reduced and unreduced basis sizes [13, 18]. The more basis functions are used, the larger the wave amplitude threshold. The full basis size is 13365. The accuracy is determined by the infidelity of the autocorrelation and shown for projected Weylets (pW, filled circles), pruned FGH (squares), PvB with the orthogonal projector (rings) and PvB with the nonorthogonal projector (triangles). (b): Computing time against accuracy. The black horizontal line denotes the computing time of the unpruned FGH method. Due to the inferior behavior in panel a) and the lack of an optimized implementation, values for PvB with the nonorthogonal projection are not shown.

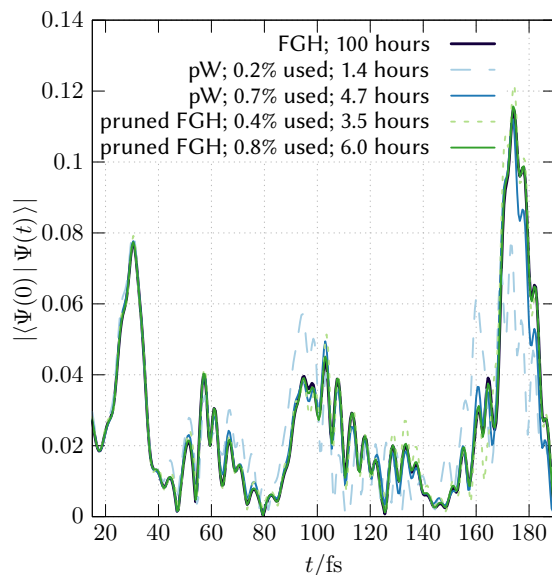


Figure 11. Absolute value of the autocorrelation for pW and FGH dynamics compared to the exact dynamics (black line) for the six dimensional model of pyrazine. The full basis size is $\sim 322 \times 10^6$. The given times are the runtimes. Reprinted from Ref. 18, with the permission of AIP Publishing.

VI. CONCLUSIONS

We have focussed in this review on the comparison, both theoretically and computationally, of phase space methods with coordinate space DVRs. The current state of affairs is that, while phase space methods generally provide a more compact representation of the dynamical state, the nonorthogonality of the phase space basis requires an operation with the inverse overlap matrix, which is incompatible with favorable scaling in multidimensions. One can avoid the operation with the inverse overlap matrix by orthogonalizing the phase space functions, at the price of reducing the localization of the basis functions and therefore the compactness of the representation.

There is an additional down side to phase space bases relative to coordinate space bases. In coordinate space, specifically in a DVR, the potential matrix is diagonal. Thus, there is virtually no cost for the construction of the potential matrix, and the operation of the potential on the state vector scales as N , as for a vector-vector multiplication, as opposed to N^2 , as for a matrix-vector multiplication.

Despite these advantages of the coordinate representation, several ideas that are currently being tested could potentially make the phase space method competitive with respect to CPU time. The use of the Fast Gabor Transform [88, 89], in principle, allows the potential matrix in the von Neumann basis to be constructed in a time of approximately $N \log(N)$. If an efficient way can be found to decompose the overlap matrix in the reduced space, along the lines of our discussion in Section IV D 4, one could potentially have the advantages of a maximally compact representation with favorable multidimensional scaling. The phase space approach is also more natural than the coordinate space approach for combining with classical methods for some of the degrees of freedom, as well as for obtaining a classical mechanical interpretation of the underlying dynamics. The efficiency of phase space vs. coordinate space methods will almost certainly depend on the particular system studied and the strength of coupling between degrees of freedom.

Methodologically, we have found that different notations have different advantages in different contexts. Generally speaking, wavefunction notation is the most direct way of obtaining physical insights into phase space localization. Dirac notation is very convenient for deriving new, equivalent representations spanning the same space, while matrix notation is the most compact and most convenient for numerical work. Similarly, in multidimensions, tensor notation offers a convenient formulation for the numerical implementation whereas vector notation gives physical insights.

Work in progress includes incorporating both the phase space and the coordinate space methods into Multi-Configuration Time-Dependent Hartree (MCTDH) calculations, where individual modes or several coupled modes are treated with full correlation, and then the combined modes are treated using the MCTDH strategy [54, 90].

ACKNOWLEDGMENTS

We thank Asaf Shimshovitz, Norio Takemoto and Rafael Abta for their ongoing contributions to research on this subject. We thank Professor Jeremy Schiff for helpful discussions. We acknowledge stimulating discussions with Professor Tucker Carrington and Professor Bill Poirier. H. R. L. acknowledges Professor Bernd Hartke for his continuous support and helpful discussions. He acknowledges support by the Fonds der Chemischen Industrie, Studienstiftung des deutschen Volkes, and the Deutscher Akademischer Austauschdienst. D. J. T. acknowledges support from the Israel Science Foundation (1094/16) and the German-Israeli Foundation for Scientific Research and Development (GIF).

-
- [1] P. A. M. Dirac, Proc. R. Soc. A **123**, 714 (1929).
 - [2] The adiabatic separation of electronic and nuclear motion as presented in modern texts is actually due to Born and Huang. See the historical review in Ref. 27, p. 387.
 - [3] W. Kohn, "Electronic structure of matter – wave functions and density functionals," (1999), Nobel Lecture.
 - [4] R. Zalesny, M. G. Papadopoulos, P. G. Mezey, and J. Leszczynski, eds., *Linear-Scaling Techniques in Computational Chemistry and Physics*, 2011th ed. (Springer, 2011).
 - [5] C. Riplinger, B. Sandhoefer, A. Hansen, and F. Neese, J. Chem. Phys. **139**, 134101 (2013).
 - [6] R. Kosloff, "Numerical Grid Methods and Their Application to Schrödinger's Equation," (Nato Science Series C, 1993) Chap. The Fourier Method, pp. 175–194.
 - [7] J. C. Light, "Discrete Variable Representations in Quantum Dynamics," in *Time-Dependent Quantum Molecular Dynamics*, edited by J. Broeckhove and L. Lathouwers (Springer, 1992) pp. 185–199.
 - [8] R. A. Friesner, Annu. Rv. Phys. Chem. **42**, 341 (1991).
 - [9] L. Frediani and D. Sundholm, Phys. Chem. Chem. Phys. **17**, 31357 (2015).

- [10] D. J. Tannor, N. Takemoto, and A. Shimshovitz, "Phase Space Approach to Solving the Schrödinger Equation: Thinking Inside the Box," in *Advances in Chemical Physics* (John Wiley & Sons, Inc., 2014) pp. 1–34.
- [11] A. Shimshovitz, Z. Bačić, and D. J. Tannor, *J. Chem. Phys.* **141**, 234106 (2014).
- [12] A. Shimshovitz, *Phase Space Approach to Solving the Schrödinger Equation*, Ph.D. thesis, Weizmann Institute of Science (2015).
- [13] S. Machnes, E. Assémat, H. R. Larsson, and D. J. Tannor, *J. Phys. Chem. A* **120**, 3296 (2016).
- [14] J. Brown and T. Carrington, *Phys. Rev. Lett.* **114**, 058901 (2015).
- [15] A. Shimshovitz and D. J. Tannor, "Reply to Comment by Brown and Carrington on "Phase-Space Approach to Solving the Time-Independent Schrödinger Equation"," (2015), arXiv:1510.04715.
- [16] J. Brown and T. Carrington, *J. Chem. Phys.* **143**, 044104 (2015).
- [17] J. Brown and T. Carrington Jr., *J. Chem. Phys.* **144**, 244115 (2016).
- [18] H. R. Larsson, B. Hartke, and D. J. Tannor, *J. Chem. Phys.* **145**, 204108 (2016).
- [19] B. Poirier, *J. Theor. Comp. Chem.* **02**, 65 (2003).
- [20] B. Poirier and A. Salam, *J. Chem. Phys.* **121**, 1690 (2004).
- [21] B. Poirier and A. Salam, *J. Chem. Phys.* **121**, 1704 (2004).
- [22] J. Cooper and T. Carrington, *J. Chem. Phys.* **130**, 214110 (2009).
- [23] T. Halverson and B. Poirier, *J. Chem. Phys.* **140**, 204112 (2014).
- [24] T. Halverson and B. Poirier, *Chem. Phys. Lett.* **624**, 37 (2015).
- [25] T. Halverson and B. Poirier, *J. Phys. Chem. A* **119**, 12417–12433 (2015).
- [26] E. Assémat, S. Machnes, and D. Tannor, "Double ionization of Helium from a phase space perspective," (2015), arXiv:1502.05165.
- [27] D. J. Tannor, *Introduction to Quantum Mechanics: A Time-Dependent Perspective*, 1st ed. (University Science Books, 2007).
- [28] D. Baye and P. H. Heenen, *J. Phys. A: Math. Gen.* **19**, 2041 (1986).
- [29] D. Kosloff and R. Kosloff, *J. Comp. Phys.* **52**, 35 (1983).
- [30] R. Kosloff, *J. Chem. Phys.* **92**, 2087 (1988).
- [31] M. Feit, J. F. Jr., and A. Steiger, *J. Comp. Phys.* **47**, 412 (1982).
- [32] D. T. Colbert and W. H. Miller, *J. Chem. Phys.* **96**, 1982 (1992).
- [33] C. C. Marston and G. G. Balint-Kurti, *J. Chem. Phys.* **91**, 3571 (1989).
- [34] A. Shimshovitz and D. J. Tannor, *Phys. Rev. Lett.* **109** (2012).
- [35] J. von Neumann, *Math. Annal.* **104**, 570 (1931).
- [36] J. von Neumann, *Mathematische Grundlagen der Quantenmechanik*, 2nd ed. (Springer, 1996).
- [37] H. Weyl, *Z. Phys.* **46**, 1 (1927).
- [38] W. Heisenberg, *Zeitschr. f. Phys.* **43**, 172 (1927).
- [39] D. Gabor, *J. Inst. Elect. Eng.* **93**, 429 (1946).
- [40] M. J. Davis and E. J. Heller, *J. Chem. Phys.* **71**, 3383 (1979).
- [41] I. Daubechies, *IEEE Trans. Inf. Theory* **36**, 961 (1990).
- [42] A. Perelomov, *Theor. Math. Phys.* **6**, 156 (1971).
- [43] V. Bargmann, P. Butera, L. Girardello, and J. R. Klauder, *Rep. Math. Phys.* **2**, 221 (1971).
- [44] H. Bacry, A. Grossmann, and J. Zak, *Phys. Rev. B* **12**, 1118 (1975).
- [45] Actually, the basis is overcomplete by one; see Ref. 42.
- [46] E. J. Heller, *J. Chem. Phys.* **67**, 3339 (1977).
- [47] The condition number is low if a Gauss-Legendre grid is combined with a transformation of the angular coordinates, $\theta_i = \arccos(x_i)$. The transformation makes the grid almost equidistant.
- [48] A. Shimshovitz and D. J. Tannor, *J. Chem. Phys.* **137**, 101103 (2012).
- [49] G. Strang, *Linear Algebra and Its Applications*, 3rd ed. (Harcourt Brace Jovanovich, 1988).
- [50] T. Genossar and M. Porat, *IEEE Trans. Syst., Man, Cybern., Syst.* **22**, 449 (1992).
- [51] R. Lombardini and B. Poirier, *Phys. Rev. E* **74**, 036705 (2006).
- [52] J. J. Sakurai, *Modern Quantum Mechanics*, 2nd ed. (Pearson Education, 2013).
- [53] J. C. Light and T. Carrington, "Discrete-Variable Representations and their Utilization," in *Advances in Chemical Physics* (John Wiley & Sons, Inc., 2007) pp. 263–310.
- [54] M. H. Beck, A. Jäckle, G. A. Worth, and H.-D. Meyer, *Phys. Rep.* **324**, 1 (2000).
- [55] A. Jäckle and H. Meyer, *J. Chem. Phys.* **104**, 7974 (1996).
- [56] S. Manzhos and T. Carrington, *J. Chem. Phys.* **125**, 194105 (2006).
- [57] W. Koch and D. H. Zhang, *J. Chem. Phys.* **141**, 021101 (2014).
- [58] R. A. Friesner, R. E. Wyatt, C. Hempel, and B. Criner, *J. Comp. Phys.* **64**, 220 (1986).
- [59] U. Manthe and H. Köppel, *J. Chem. Phys.* **93**, 345 (1990).
- [60] M. J. Bramley and T. Carrington, *J. Chem. Phys.* **99**, 8519 (1993).
- [61] R. K. Nesbet, *Rev. Mod. Phys.* **35**, 552 (1963).
- [62] C. Bender, *J. Comp. Phys.* **9**, 547 (1972).
- [63] P. A. Regalia and M. K. Sanjit, *SIAM Review* **31**, 586 (1989).
- [64] C. F. Loan, *J. Comp. Appl. Math.* **123**, 85 (2000).
- [65] X.-G. Wang and T. Carrington Jr., *J. Phys. Chem. A* **105**, 2575 (2001).
- [66] G. A. Worth, *J. Chem. Phys.* **112**, 8322 (2000).

- [67] G. Avila and T. Carrington, *J. Chem. Phys.* **131**, 174103 (2009).
- [68] R. Wodraszka and T. Carrington, *J. Chem. Phys.* **145**, 044110 (2016).
- [69] R. Sedgewick and K. Wayne, *Algorithms*, 4th ed. (Addison-Wesley Professional, 2011).
- [70] N. Takemoto and D. J. Tannor, unpublished (2017).
- [71] R. Balian, *C. R. Acad. Sci. Paris* **292**, 1357 (1981).
- [72] F. Low, "A passion for physics: Essays in honor of Geoffrey Chew," (World Scientific, 1985) Chap. Complete sets of wave packets, pp. 17–22.
- [73] G. Battle, *Lett. Math. Phys.* **15**, 175–177 (1988).
- [74] K. G. Wilson, "Generalized wannier functions," Cornell University preprint (1987).
- [75] I. Daubechies, S. Jaffard, and J.-L. Journé, *SIAM J. Math. Anal.* **22**, 554 (1991).
- [76] P. Löwdin, *J. Chem. Phys.* **18**, 365 (1950).
- [77] R. Lombardini and B. Poirier, *J. Chem. Phys.* **124**, 144107 (2006).
- [78] L. R. Pettey and R. E. Wyatt, *Chem. Phys. Lett.* **424**, 443 (2006).
- [79] L. R. Pettey and R. E. Wyatt, *Int. J. Quantum Chem.* **107**, 1566 (2007).
- [80] D. A. McCormack, *J. Chem. Phys.* **124**, 204101 (2006).
- [81] B. Hartke, *Phys. Chem. Chem. Phys.* **8**, 3627 (2006).
- [82] J. Sielk, H. F. von Horsten, F. Krüger, R. Schneider, and B. Hartke, *Phys. Chem. Chem. Phys.* **11**, 463–475 (2009).
- [83] Z. Bačić and J. C. Light, *J. Chem. Phys.* **85**, 4594 (1986).
- [84] Z. Bačić and J. C. Light, *J. Chem. Phys.* **86**, 3065 (1987).
- [85] S. Machnes, E. Assémat, and D. Tannor, "Quantum Dynamics in Phase space using the Biorthogonal von Neumann bases: Algorithmic Considerations," (2016), arXiv:1603.03963.
- [86] G. A. Worth, H.-D. Meyer, and L. S. Cederbaum, *J. Chem. Phys.* **109**, 3518 (1998).
- [87] A. Raab, G. A. Worth, H.-D. Meyer, and L. S. Cederbaum, *J. Chem. Phys.* **110**, 936 (1999).
- [88] R. S. Orr, *IEEE Trans Sig. Process.* **41**, 122 (1993).
- [89] L. Wang, C.-T. Chen, and W.-C. Lin, *IEEE Trans Sig. Process.* **3**, 87 (1994).
- [90] H. R. Larsson and D. J. Tannor, *J. Chem. Phys.* **147**, 044103 (2017).

I.1.1.4. Complementary Information

I.1.1.4.1. Importance of the Projection

In Section III A of the publication (page 23 in this thesis²), it is shown how the projected von Neumann (PvN) functions are formed from the original von Neumann (vN) functions. They have been developed because the original vN basis shows poor convergence.^[101] One way to explain this poor convergence is that the vN functions protrude from the employed phase-space lattice.^[101,102] The projection onto a space, for example spanned by a DVR basis, defines functions in the restricted phase space of the DVR basis. This makes the vN basis band-limited with finite support.^[102]

Numerical Integration However, the projection is just one way of obtaining accurate results in terms of accuracy of the eigenvalues. The vN functions can also simply be evaluated such that the resulting expressions only span the phase-space region of interest. One way to achieve this is to evaluate the matrix elements of all required operators numerically by simple Newton-Cotes quadrature:³

$$\int_{-\infty}^{\infty} dx \mathcal{G}_m^*(x) [\hat{O} \mathcal{G}_n](x) \approx \Delta x \sum_{i=1}^{N_g} \mathcal{G}_m^*(x_i) [\hat{O} \mathcal{G}_n](x_i), \quad \Delta x = x_2 - x_1, \quad m, n \in [1, N]. \quad (\text{I.1.1})$$

If the grid points x_i and as such also the grid spacing Δx are defined as in the Fourier grid hamiltonian (FGH) method, a similar accuracy can be achieved. This is shown in Fig. I.1.3. The error of the vN method is minimal if exactly the same number of grid points N_g as the number of basis functions N is used, like it is the case for PvN. If just one more integration point is used, higher momentum components than the maximal “allowed” momentum defined by the setup of the vN lattice are described. This suddenly *increases* the error towards the value obtained from analytic integration of the matrix elements.⁴ The fact that numerical integration gives improved accuracy has been stressed in Ref. [103].

Working with the Basis Defined on the Infinite Lattice What changes if the basis $\{|\mathcal{G}_m\rangle\}$ is evaluated solely within the restricted phase-space area? It is the basis $\{|\mathcal{E}_m\rangle\}$ which is biorthogonal to $\{|\mathcal{G}_m\rangle\}$. This is similar to what is described in Section III C of the publication: The biorthogonal basis is defined by

$$|\mathcal{E}_n\rangle = \sum_{m=1}^N |\mathcal{G}_m\rangle [\mathbf{S}^{-1}]_{mn}, \quad S_{mn} = \langle \mathcal{G}_m | \mathcal{G}_n \rangle. \quad (\text{I.1.2})$$

²All page references denote pages of this thesis and not of the included publications.

³See also the discussion in Section II B 1 of Publication 3 (Section I.1.3).

⁴The integration range in the numerical integration is finite such that the numerical limit does not exactly correspond to the analytic result where it is integrated from $-\infty$ to ∞ ; compare with Eq. (I.1.1).

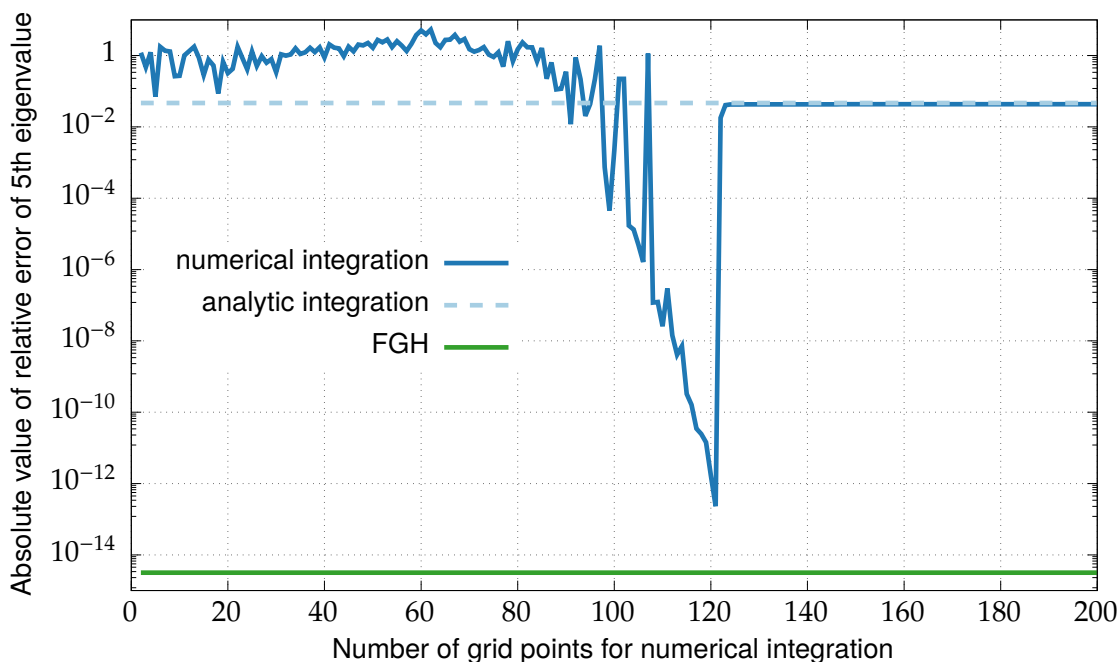


Figure I.1.3.: Absolute value of the relative error of the 5th eigenvalue of the standard harmonic oscillator ($\hat{H} = \hat{p}^2/2 + \hat{x}^2/2$) for the \mathbf{vN} basis using numerical integration of the matrix elements *versus* number of integration points N_g (dark blue curve); see Eq. (I.1.1). In total, $N = 121$ basis functions are used within the range $x \in [-20, 20]$. The numerical integration is performed within the same range. The results from an analytic integration (pale dashed blue curve) and from the FGH method (green curve) are also shown. The FGH method is defined on the same interval and with the same basis size N . The curve for the numerical integration has a minimum at $N_g = N = 121$.

If either numerical integration or sampling by a DVR grid is used, the overlap matrix elements S_{mn} change and thus the biorthogonal basis.

Another approach to restore accuracy of quantum calculations with \mathbf{PvN} is to use the biorthogonal basis defined on the full, infinite lattice and use it on a truncated lattice with finite basis size. Indeed, this is the way Weylets are defined: Essentially, POIRIER evaluated the overlap matrix and its inverse square root on a very large lattice and used it for subsequent calculations on smaller lattices.^[104-106] In contrast, the \mathbf{pW} basis developed in this thesis (Section IV D in the publication; page 39) are formed directly on the smaller lattice *but* the momentum-symmetrized Gaussian (SG) functions are first projected onto the DVR space such that all matrix elements are evaluated using DVR quadrature.

POIRIER's procedure can also be applied to the \mathbf{vN} basis. There, the eigenvalue problem of the TISE takes the form of

$$\mathbf{H}\mathbf{U} = \mathbf{S}\mathbf{U}\text{diag}(\vec{E}), \quad (\text{I.1.3})$$

$$\Leftrightarrow \mathbf{S}^{-1}\mathbf{H}\mathbf{U} = \mathbf{U}\text{diag}(\vec{E}), \quad (\text{I.1.4})$$

$$[\mathbf{S}^{-1}\mathbf{H}]_{mn} = \langle \ell_m | \hat{H} | g_n \rangle. \quad (\text{I.1.5})$$

\mathbf{S}^{-1} can be formed on a much larger lattice and the values of \mathbf{S}^{-1} can be used for the smaller lattice, where the eigenvalue problem is solved in a subsequent computation. Exemplary results are shown in Tab. I.1.1. If the grid length and maximal momentum is increased by a factor of 11 for the computation of \mathbf{S}^{-1} , the accuracy is increased by up to four orders of magnitude.⁵ Actually, the analytic form of the biorthogonal functions on the infinite lattice is known^[107,108] such that one could, in principle, compute the matrix elements $\langle \ell_m | \hat{H} | g_n \rangle$ directly. However, their form is quite complicated and a practical implementation would be difficult.^[109]

Table I.1.1.: Error of the standard harmonic oscillator for variants of \mathbf{vN} . The first column shows the exact energy/eigenvalue of the corresponding eigenvector. The other columns (except for the last one) show the relative error of the eigenvalues computed with the \mathbf{vN} basis for different setups. In each of these columns, \mathbf{S}^{-1} is computed on a phase-space lattice that is increased by a factor shown in the first row. The elements of \mathbf{S}^{-1} are then used in subsequent calculations where the lattice is not increased, compare with Eq. (I.1.4) and (I.1.5) and the text. A factor of 1 (no increase) corresponds to $N = N_x N_k = 11 \cdot 11 = 121$ basis functions and $x \in [-20, 20]$ (as in Fig. I.1.3). A factor of 25 corresponds to $(25 \cdot N_x)(25 \cdot N_k) = 75625$ functions and $x \in [-20 \cdot 25, 20 \cdot 25] \equiv [-500, 500]$ but *only* for computing \mathbf{S}^{-1} . The Hamiltonian is then still diagonalized on the lattice with 121 basis functions. The last column shows the relative error of the eigenvalues computed with the FGH method on the same lattice (no increase).

Energy	factor 1	factor 11	factor 25	FGH
0.5	5×10^{-3}	9×10^{-7}	3×10^{-8}	-1×10^{-14}
1.5	2×10^{-1}	1×10^{-2}	3×10^{-3}	9×10^{-15}
2.5	2×10^{-3}	3×10^{-7}	1×10^{-8}	5×10^{-15}
3.5	3×10^{-1}	1×10^{-2}	2×10^{-3}	3×10^{-15}
4.5	5×10^{-2}	9×10^{-6}	3×10^{-7}	2×10^{-16}
5.5	9×10^{-2}	2×10^{-3}	3×10^{-4}	2×10^{-15}
6.5	3×10^{-3}	6×10^{-7}	2×10^{-8}	-4×10^{-16}
7.5	3×10^{-2}	8×10^{-4}	2×10^{-4}	3×10^{-15}
8.5	1×10^{-2}	3×10^{-6}	1×10^{-7}	-6×10^{-16}
9.5	6×10^{-2}	2×10^{-3}	4×10^{-4}	1×10^{-15}

In any case, the accuracy of the \mathbf{PvN} and FGH methods is still better and they are easier to use. Hence, \mathbf{PvN} should be preferred over other variants of \mathbf{vN} . This analysis just gives more insight. Although further work is needed, it already shows that it is in general sufficient to either define variants of \mathbf{vN} functions such that they are band-limited and of finite support or to work with functions properly defined on the whole lattice. In other words, the basis and its biorthogonal counterpart should span exactly the phase-space area of interest.

⁵Surprisingly, the accuracy is not monotonically decreasing with decreasing eigenvalue. Every other eigenvalue has a substantially lower accuracy. An explanation remains to be found.

I.1.1.4.2. Projecting to other Discrete Variable Representations

In Section III A of the publication (page 24), it is also mentioned that different DVRs with non-equidistant grid-points can be combined with $\nu\mathbf{N}$ by using equidistant grid points for the sampling of the $\nu\mathbf{N}$ functions. This combines two bases (DVR and $\nu\mathbf{N}$) that have different phase-space areas. The numerical results for using different DVRs are shown in Fig. I.1.4. There, the underlying DVR is either of FGH, sinc, sine, Gauß-Lobatto or Gauß-Hermite type. Besides numerical noise, *all* bases give very similar results. This is in stark contrast to the results of BROWN AND CARRINGTON^[Fig. 1 (b), 110] where the error is in general much larger for Gauß-Legendre and Gauß-Hermite DVRs and even increases when more basis functions are employed.⁶

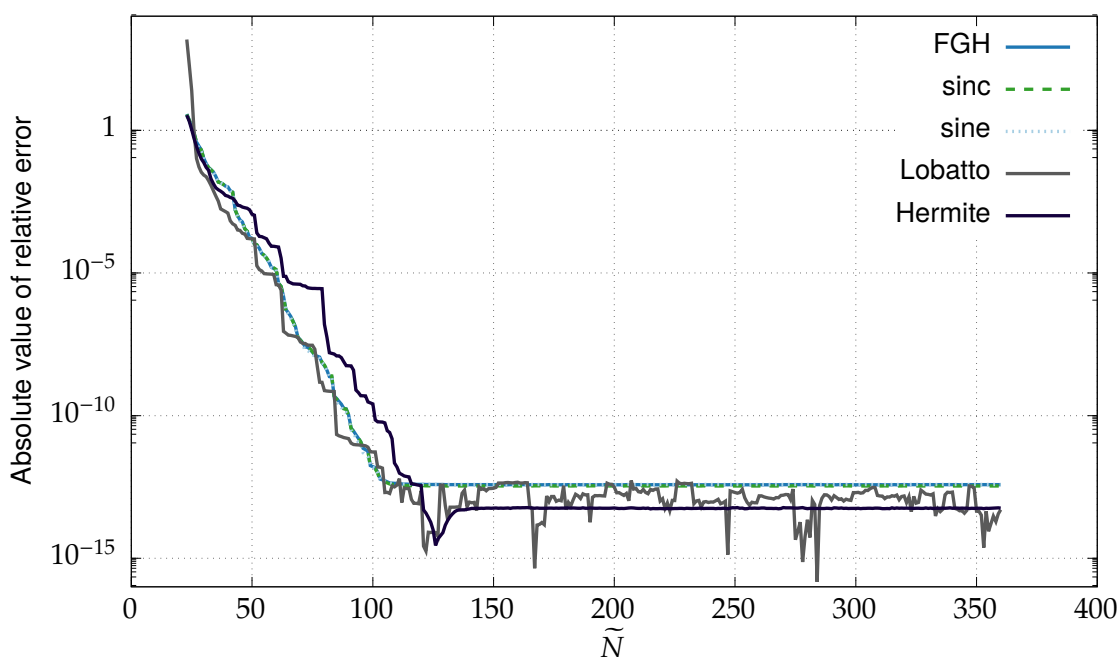


Figure I.1.4.: Absolute value of the relative error of the 23rd eigenvalue of the Morse oscillator from Ref. [102] ($V(x) = D[1 - \exp(-\beta x)]^2$ with $\beta = 0.5$, $D = 12$ and a mass of $m = 6$) versus pruned basis size \tilde{N} for $\mathbf{P}\nu\mathbf{B}$. Different bases are used as the underlying DVR [FGH (blue curve), sinc (dashed green curve), sine (dotted pale blue curve), Gauß-Lobatto (gray curve) or Gauß-Hermite (black curve)]. For all DVRs, the sampling points used for $\mathbf{P}\nu\mathbf{B}$ are the sinc-DVR grid points. The results for the FGH, sinc and sine DVR are on top of each other. The $\mathbf{P}\nu\mathbf{B}$ basis is pruned according to a semiclassical criterion.^[102,105] The full basis is of size $N = N_x N_k = 19 \cdot 19 = 361$ and spans the range $x \in [-2.4, 28]$.

I have also tried to position the $\nu\mathbf{N}$ functions in such a way that the phase-space areas of the $\nu\mathbf{N}$ basis match that of the DVRs but this turned out to be very unstable (that is, large condition numbers of the overlap matrix are obtained). In general, it is not possible to match the phase-space area of a DVR that utilizes non-equidistant grids with a $\nu\mathbf{N}$ lattice.

⁶The erroneous comment in Ref. [110] that there is no need to introduce the $\mathbf{P}\nu\mathbf{B}$ basis is discussed in Publication 1 (Section I.1.1) and in Ref. [111] in detail.

I.1.1.4.3. Locality of Weylets

In Figure 8 of the publication (page 41), two states in the representations of PvB , pW and the biorthogonal variant of the projected SG are shown. It is noted in Section IV D 2 (page 39) that Weylets have exponential decay in phase space and as such are not as localized as PvB or SG , that decay Gaussian-like. This behavior can already be seen in coordinate space and is shown in Fig. I.1.5, where a vN function, a SG and a Weylet function are compared.

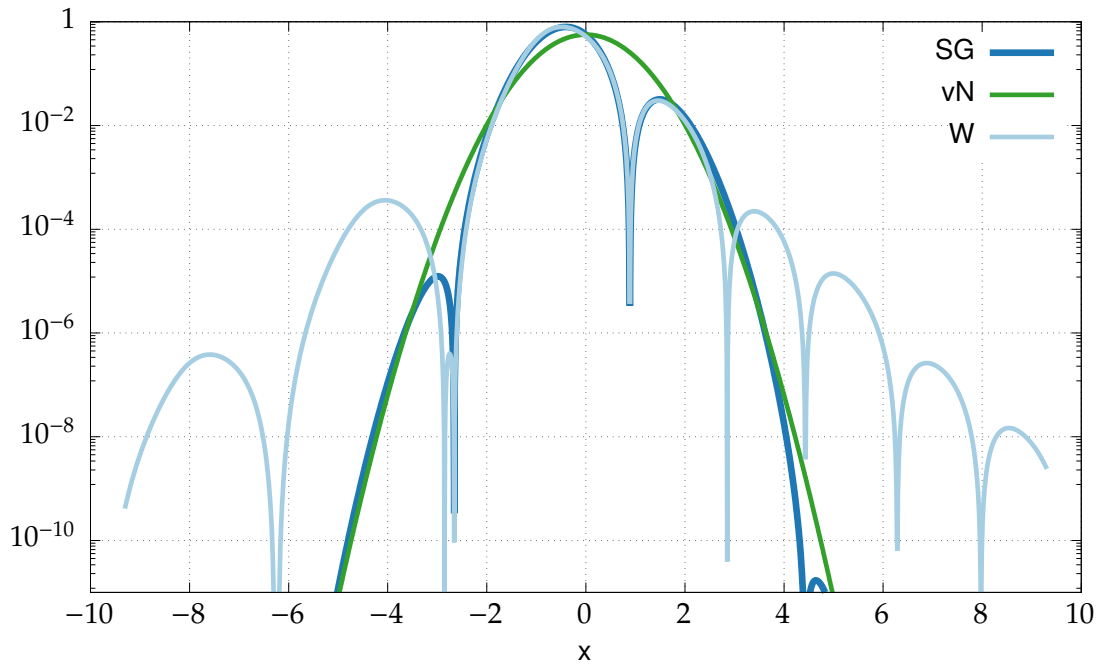


Figure I.1.5.: Plot of a SG (blue curve), a vN function (green curve) and a Weylet (blue curve) with the same phase-space locations. The α value of the vN/SG function [see Eqn. (27) and (102) in Publication 1 (Section I.1.1) (pages 23 and 39)] is 0.5. Note the logarithmic scale of the ordinate.

In Ref. [112], WHITE presents wavelet transformations that increase the locality of an orthogonalized Gaussian basis in coordinate space. It might be possible to do the same for Weylets. Since Weylets are not localized in complete phase space (at positive and negative momenta), the Balian-Low theorem is not valid and it might be possible to localize them further. Unfortunately, initial attempts to do so in the spirit of Ref. [112] were unsuccessful.

Another strategy is pursued in Ref. [113] where the vN functions are Fourier transformed and orthogonalized *via* Löwdin's method. Although the decay of the obtained functions looks slightly worse compared to the decay of Weylets, impressive sparsities of wavefunction representations are obtained.

I.1.2. Publication: Projected von Neumann Bases

I.1.2.1. Own Contributions

- Setup and execution of numerical simulations for Section V.
- Writing of Section V.
- Contributions to the discussion on the usefulness of \check{P} .

I.1.2.2. Bibliographic Data

Title Quantum Dynamics in Phase Space using Projected von Neumann Bases

Authors Shai Machnes, Elie Assémat, Henrik R. Larsson and David J. Tannor

Journal The Journal of Physical Chemistry A

Volume 120

Issue 19; Ronnie Kosloff Festschrift

Pages 3296-3308

Year 2016

DOI [10.1021/acs.jpca.5b12370](https://doi.org/10.1021/acs.jpca.5b12370)

Note Reprinted with permission from (J. Phys. Chem. A, 2016, 120 (19), pp 3296–3308). Copyright (2016) American Chemical Society.

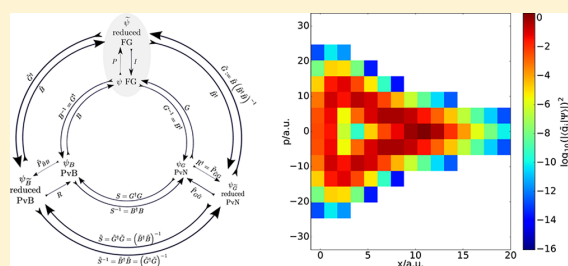
Preprint <https://arxiv.org/abs/1603.03962>

I.1.2.3. Article

Quantum Dynamics in Phase Space using Projected von Neumann Bases

Shai Machnes,^{*,†} Elie Assémat,[†] Henrik R. Larsson,[‡] and David J. Tannor[†][†]Department of Chemical Physics, Weizmann Institute of Science, 76100 Rehovot, Israel[‡]Institut für Physikalische Chemie, Christian-Albrechts-Universität zu Kiel, Olshausenstraße 40, D-24098 Kiel, Germany

ABSTRACT: We describe the mathematical underpinnings of the biorthogonal von Neumann method for quantum mechanical simulations (PvB). In particular, we present a detailed discussion of the important issue of nonorthogonal projection onto subspaces of biorthogonal bases, and how this differs from orthogonal projection. We present various representations of the Schrödinger equation in the reduced basis and discuss their relative merits. We conclude with illustrative examples and a discussion of the outlook and challenges ahead for the PvB representation.



1. INTRODUCTION

The quantum dynamics of many physical systems involve multiparticle continua. Examples range from ionization and high harmonic generation in multielectron atoms to molecular processes such as photodissociation and chemical reactions of polyatomics. The large Hilbert space of these systems makes full simulations extremely challenging. It is therefore of great interest to find a compact representation for quantum dynamics in the continuum where accuracy can be easily controlled.

An attractive option is to represent states as phase space objects, so that only those areas of phase space that are actually occupied are needed for the calculation. The most commonly used phase space representation, the Wigner representation, has proven to be expensive computationally, although there has been some recent progress.¹ An alternative is the Husimi representation, although this too is awkward for direct numerical calculations.²

A third option for a phase space representation is the von Neumann lattice.^{3,4} This representation consists of a discrete lattice of phase space Gaussians, one per each cell of area h^D , where h is Planck's constant and D is the number of degrees of freedom. Initial work using this representation found it to be poorly convergent.⁵ Approximately 10 years ago, Poirier and co-workers^{6,7} found a way to converge the method and have applied it recently to several challenging applications.^{8,9} Independently, a few years later, our group discovered a different way to converge the von Neumann lattice, based on modifying the Gaussians to be periodic and band-limited.^{10–12} We named the method *Periodic von Neumann* (PvN). The PvN basis is guaranteed to have exactly the same accuracy as a discrete Fourier representation,^{13–16} while having the flexibility of a Gaussian basis set.

Since the PvN basis is nonorthogonal, a key aspect of the mathematical formulation involves the concept of biorthogonal bases. We define the Biorthogonal von Neumann (BvN) basis as

the basis biorthogonal to PvN. Since a crucial part of our method is to exchange the roles of the PvN and BvN bases we refer to the method more generally as Periodic von Neumann with Biorthogonal exchange or PvB. In this work we further develop the mathematical underpinnings of the PvB method. In particular, we derive new relations for the reduced Hilbert space associated with nonorthogonal bases when projecting down from the full Hilbert space. Furthermore, we analyze the possible forms of the Schrödinger equation in the reduced basis. These developments become crucial when applying the methodology to more challenging systems, such as the helium atom in strong fields.¹⁷

The paper is organized as follows. In Section 2 we present a brief review of the PvB approach as applied to the full Hilbert space. We begin by clarifying the underlying Hilbert space spanned by the Fourier grid method. We then define the von Neumann basis onto the Hilbert space spanned by the Fourier grid we generate the Periodic von Neumann (PvN) basis (Section 2.2). Since the PvN basis is nonorthogonal we can define the basis that is biorthogonal (Section 2.3). In Section 2.4 we show that the role of the PvN basis and the biorthogonal basis must be exchanged to obtain a sparse representation. We conclude Section 2 with a discussion of the possible forms of the Schrödinger equation in the PvB representation. Having established the formalism on the full Hilbert space, we turn to the representation on a reduced space. Section 3 introduces the reduced PvB method, allowing one to represent only those regions of phase space actually occupied by the current state. We then define the biorthogonal bases for the reduced subspace

Special Issue: Ronnie Kosloff Festschrift

Received: December 17, 2015

Revised: March 14, 2016

Published: March 15, 2016

(Section 3.2) and analyze the projection into the reduced subspace (Section 3.3), highlighting the differences between orthogonal and nonorthogonal projections. In Section 4 we derive the various forms of the Schrödinger equation in the reduced representations and discuss approximations and performance considerations. Section 5 gives some illustrative examples, and Section 6 gives an outlook and some ideas for future work. A detailed treatment of the algorithmic aspects of an efficient and scalable implementation of the PvB representation is given in ref 32.

2. A REVIEW OF PERIODIC VON NEUMANN WITH BIORTHOGONAL EXCHANGE

The PvB representation, developed in refs 10–12, projects the von Neumann lattice of Gaussians (Section 2.2) onto the subspace spanned by the Fourier grid (Section 2.1). As the projected Gaussians form a nonorthogonal basis, we define the basis biorthogonal to the projected Gaussians (Section 2.3). Together these building blocks define the PvB representation (Section 2.4). We then present several alternative but equivalent formulations of the Schrödinger equation in the PvB representation (Section 2.5).

2.1. The Fourier Grid. The pseudospectral Fourier method^{16,18,19} (also known as the periodic sinc Discrete Variable Representation (DVR)²⁰) is the underlying Hilbert space on which we construct the PvB method. A comprehensive exposition can be found in ref 21.

Functions with support on a finite segment $x \in [0, L]$ may be assumed, without loss of generality, to be cyclic, and reside in a Hilbert space spanned by

$$\varphi_n(x) = \frac{1}{\sqrt{L}} \exp\left(2\pi i \frac{x}{L} n\right) = \frac{1}{\sqrt{L}} \exp(ik_n x), \quad \forall n \in \mathbb{Z}, \quad k_n = \frac{2\pi}{L} n \quad (1)$$

Limiting bandwidth to K implies $n \in [-n_{\max} + 1, \dots, n_{\max}]$ where $n_{\max} := \left\lfloor \frac{KL}{2\pi} \right\rfloor$. This defines a rectangular area of phase space of area $2KL$, which is spanned by the *spectral basis*, $\{\varphi_n\}_{n=1}^N$, with $N = 2n_{\max}$. With an inner product defined as $\langle f, g \rangle := \int_0^L f^*(x)g(x)dx$ this constitutes the *Fourier grid* (FG) Hilbert space, \mathcal{H} .

Any $f \in \mathcal{H}$ can be expanded as $f(x) = \sum_{n=1}^N \langle \varphi_n, f \rangle \varphi_n(x)$, allowing us to represent f as a column vector of the expansion coefficients, $\vec{f}_{\varphi} := (\langle \varphi_1, f \rangle, \langle \varphi_2, f \rangle, \dots, \langle \varphi_N, f \rangle)^T$. We shall drop the basis designation when implied by context.

Define the *Fourier grid points*, or *sampling points*, as the set of N equidistant points $\{x_j = x_0 + L \frac{j}{N}\}_{j=0}^{N-1}$ with $x_0 \in [0, \frac{L}{N}]$.

Define the *pseudospectral basis* of \mathcal{H} as the set of *pseudospectral functions* $\Theta = \{\theta_m(x)\}_{m=1}^N \in \mathcal{H}$ such that for $f(x) \in \mathcal{H}$, $f(x) = \sum_{m=1}^N f(x_m) \theta_m(x)$. The function f may now be represented by its *sampling vector*, $\vec{f} = \vec{f}_{\theta} = (f(x_1), f(x_2), \dots, f(x_N))^T$.

By expanding the spectral basis functions in the pseudospectral basis, one may derive the explicit form of the latter,

$$\begin{aligned} \theta_m(x) &= \frac{1}{N} \sum_{n=-n_{\max}+1}^{n_{\max}} \exp(ik_n(x - x_m)), \quad \text{with } \alpha := 2\pi \frac{x - x_m}{L} \\ &= e^{i\pi(x-x_m)/L} \frac{\sin\left(\frac{N\alpha}{2}\right)}{N \sin\left(\frac{\alpha}{2}\right)} \end{aligned}$$

These are periodic *sinc* functions, which are localized around x_m with $\theta_m(x_n) = \delta_{nm}$. The pseudospectral basis functions satisfy the normalization condition $\langle \theta_n, \theta_m \rangle = \frac{N}{L} \delta_{nm}$.²³

Thus, functions in \mathcal{H} may be represented in the pseudospectral basis by their sampling vector. Unlike the spectral basis representation, this does not require integration to compute the coefficients. The existence of the pseudospectral basis, allowing reconstruction of a function from sampled values, is equivalent to the Shannon–Nyquist theorem for band-limited functions.

The projector into the FG Hilbert space is

$$\mathcal{P} := \frac{L}{N} \sum_{m=1}^N |\theta_m\rangle \langle \theta_m| = \sum_{n=1}^N |\varphi_n\rangle \langle \varphi_n| \quad (2)$$

When $f(x) \notin \mathcal{H}$, the projector \mathcal{P} minimizes the distance to the projected state, and consequently maximizes the overlap, that is, $\langle f, \mathcal{P}f \rangle / \|\mathcal{P}f\| \geq \langle f, g \rangle / \|g\| \quad \forall g \in \mathcal{H}$ (see ref 24). The pseudospectral functions are the projection of the sampling functions into \mathcal{H} , that is, $\mathcal{P}\delta(x - x_m) = \theta_m(x)$. Defining the *collocation* or *sampling pseudoprojection*

$$Qf(x) := \sum_{m=1}^N f(x_m) \theta_m(x) \quad (3)$$

generally $Qf \neq \mathcal{P}f$, unless $f \in \mathcal{H}$. For functions that are almost within \mathcal{H} , one may opt to accept the easy-to-compute Q as an approximation of \mathcal{P} , which requires costly integration.

Note that \mathcal{H} and the associated pseudospectral functions are just one possible choice for the phase space underlying PvB. See refs 25–27 for alternative possibilities.

2.2. The von Neumann Lattice and Its Projection onto the Fourier Grid. Consider a lattice of Gaussians in the (x, p) plane. Let (x_i, p_i) indicate the center of Gaussian number i , and let $(\Delta x, \Delta p)$ be the spacing between the lattice sites, with $\frac{\Delta x}{\Delta p} = \frac{\alpha}{\sigma_p}$. We define

$$g_{\bar{x}_i, \bar{p}_i}(x) = \left(\frac{1}{2\pi\sigma_x^2}\right)^{1/4} \exp\left(-\left(\frac{x - \bar{x}_i}{2\sigma_x}\right)^2 + \frac{i}{\hbar} \bar{p}_i (x - \bar{x}_i)\right) \quad (4)$$

If the lattice spans the infinite plane in the $x-p$ phase space it is known as the *von Neumann lattice*.^{3,4,28} However, in any real calculation the lattice must be truncated to a finite domain $N_x \times N_p = N$. This leads to a lack of convergence, as discovered independently in the context of quantum mechanics⁵ and the time-frequency analogue in signal processing.²⁹ However, if one projects the von Neumann lattice onto the FG basis one builds in periodic boundary conditions and obtains the same convergence as for the FG.

Define a cyclic formulation of the Gaussians,

$$\text{mod}_L x := x - L \left\lfloor \frac{x}{L} \right\rfloor, \quad g_{\bar{x}_i, \bar{p}_i}^{\text{mod}}(x) := (Qg_{0,0}(\text{mod}_L(x - \bar{x}_i))) e^{i\bar{p}_i \text{mod}_L(x - \bar{x}_i)/\hbar} \quad (5)$$

The cyclic projected Gaussians, known as the *Periodic von Neumann* or *PvN basis*, constitute a *periodic Gabor basis*, where all basis functions are related to each other by shifts in x and p .³⁰ For the conditioning of the overlap matrices (eq 11) it is beneficial to choose the von Neumann lattice points such that \bar{x}_i are a subset of the FG sample points and \bar{p}_i are a subset of the spectral basis frequencies.

The representation of the PvN basis functions in the θ basis is given by

$$G_{jk} := g_{\bar{x}_k, \bar{p}_k}^{\text{mod}}(x_j) \quad (6)$$

The FG defines an area of $(2K) L = 2\pi N$ in phase space. Therefore, one may intuitively assign a phase space area of 2π to each of the N Gaussians of the PvN basis, and consider them “phase space pixels”. Defining $P := \hbar K$, each such pixel covers a phase space area of $2\pi\hbar = h$.

2.3. Biorthogonal Bases. In this section we consider the general theory of nonorthogonal bases and their biorthogonal bases. In the next section we will specialize to the periodic von Neumann basis and its biorthogonal basis. In anticipation of that section, we use the notation G and B here.

Any set of N linearly independent vectors $\mathcal{G} = \{|g_k\rangle\}_{k=1}^N$ in \mathcal{H} may serve as a non orthogonal basis of \mathcal{H} . Let \mathcal{G} be represented in the Θ orthogonal basis of \mathcal{H} by the invertible matrix G . Let \mathcal{B} be a similarly defined nonorthogonal basis of \mathcal{H} , represented in Θ by B . The bases \mathcal{G} and \mathcal{B} are considered *biorthogonal bases* (a reciprocal relationship) if

$$\langle b_j | g_k \rangle = \delta_{jk} \Leftrightarrow B^\dagger G = \mathbf{1}_N \quad (7)$$

The relation is reciprocal, that is

$$\langle g_j | b_k \rangle = \delta_{jk} \Leftrightarrow G^\dagger B = \mathbf{1}_N \quad (8)$$

If, and only if, \mathcal{G} is orthogonal, then so is \mathcal{B} and $\mathcal{G} = \mathcal{B}$. According to eq 8, the rows of G^\dagger represent the bra states $\{\langle g_k | \}$, while the columns of B represent the ket states. The representation in the B basis of any state $|\psi\rangle \in \mathcal{H}$ associated with the sampling vector $\vec{\psi}$ is

$$\vec{\psi}_B := B^{-1}\vec{\psi} = G^\dagger\vec{\psi} \quad (9)$$

with the elements ψ_B denoting the overlaps $\langle g_k | \psi \rangle$.

The *completeness relation* for \mathcal{H} is

$$BG^\dagger = GB^\dagger = \mathbf{1}_N \Leftrightarrow \mathcal{P} = \sum_{j=1}^N |b_j\rangle\langle g_j| = \sum_{j=1}^N |g_j\rangle\langle b_j| \quad (10)$$

By construction, the projector in eq 10 spans the full FG Hilbert space, and therefore is equal to the projectors in eq 2.

We define the *overlap matrices* of the G and B bases, respectively:

$$S := G^\dagger G, \quad S^{-1} = B^\dagger B \quad (11)$$

From these relations it follows that

$$G = BS, \quad \vec{\psi}_B = S\vec{\psi}_G, \quad B = GS^{-1}, \quad \vec{\psi}_G = S^{-1}\vec{\psi}_B \quad (12)$$

Norms of vectors in B and G are computed via $\|\psi_G\|^2 = \vec{\psi}_G^\dagger S \vec{\psi}_G$ and $\|\psi_B\|^2 = \vec{\psi}_B^\dagger S^{-1} \vec{\psi}_B$. Note that the G and B bases cannot be independently normalized.

2.4. Periodic von Neumann with Biorthogonal Exchange—A Sparse Representation. Many wave functions of interest, whether bound states or traveling wavepackets, are fairly well-localized in phase space. Therefore, a representation whose coefficients are $\beta_k = \langle g_k | \psi \rangle$ is expected to be sparse, that is, to have many near-zero elements.

Consider a Fourier grid Hilbert space \mathcal{H} . Using eq 10, any state $|\psi\rangle \in \mathcal{H}$ can be represented as

$$|\psi\rangle = \left(\sum_{j=1}^N |g_j\rangle\langle b_j| \right) |\psi\rangle = \sum_{j=1}^N \langle b_j | \psi \rangle |g_j\rangle \quad (13)$$

We shall use the term PvN to denote this representation. Alternatively, any state in \mathcal{H} can be represented as

$$|\psi\rangle = \left(\sum_{j=1}^N |b_j\rangle\langle g_j| \right) |\psi\rangle = \sum_{j=1}^N \langle g_j | \psi \rangle |b_j\rangle \quad (14)$$

This defines the *biorthogonal von Neumann representation*, PvB.

Note that while the $\langle g |$ states are highly localized in phase space, the $|b\rangle$ states are highly delocalized. As a result, the PvB representation is sparse, while the PvN representation is not. The PvB and PvN bases both span \mathcal{H} , and therefore these representations contain exactly the same information. From this point onward, we shall assume all states are in \mathcal{H} , and default to the pseudospectral representation unless otherwise noted. We will also drop the explicit vector notation for states.

2.5. Schrödinger Equation in the Biorthogonal von Neumann Representation. We now turn to the form of the time-independent and time-dependent Schrödinger equations (TISE and TDSE, respectively) in the PvB basis. Starting from the TISE, $H\psi = \lambda\psi$, where λ is the energy, and using eqs 8 and 9, gives

$$(G^\dagger HB)\psi_B = \lambda\psi_B \quad (15)$$

Similarly, the TDSE $\partial_t\psi = -\frac{i}{\hbar}H\psi$ takes the form

$$\partial_t\psi_B = -\frac{i}{\hbar}(G^\dagger HB)\psi_B \quad (16)$$

The term $G^\dagger HB = B^{-1}HB$ is a similarity transformation of H , and therefore all eigenvalues are real and all evolutions are unitary. One can make Hermiticity in eq 15 explicit by multiplying it from the left by $B^\dagger B$ and using eq 10, which transforms it into a generalized eigenvalue problem

$$(B^\dagger HB)\psi_B = (B^\dagger B)\lambda\psi_B \quad (17)$$

One may rewrite the TDSE in four distinct ways, all strictly equivalent. We denote a Hamiltonian taking a state in basis X and returning a state in basis Y by H_{YX} .

$$\begin{aligned} G^\dagger HB &= B^{-1}HB =: H_{BB} &\rightarrow \partial_t\psi_B &= -\frac{i}{\hbar}H_{BB}\psi_B, \\ B^\dagger HB &= G^{-1}HB =: H_{GB} &\rightarrow \partial_t\psi_B &= -\frac{i}{\hbar}S H_{GB}\psi_B, \\ G^\dagger HG &= B^{-1}HG =: H_{BG} &\rightarrow \partial_t\psi_B &= -\frac{i}{\hbar}H_{BG}S^{-1}\psi_B, \\ B^\dagger HG &= G^{-1}HG =: H_{GG} &\rightarrow \partial_t\psi_B &= -\frac{i}{\hbar}S H_{GG}S^{-1}\psi_B. \end{aligned} \quad (18)$$

Although the forms are mathematically equivalent, they require different computational efforts. $H_{BG} = G^\dagger HG$ is quick to compute as the integrations on both sides are with the highly local Gaussians. This is counterbalanced by the need to compute S^{-1} . This issue shall be revisited in Section 4.

3. THE REDUCED HILBERT SPACE

As discussed above, many of the coefficients of ψ_B are negligible, since the phase space-localized state does not overlap with many of the localized Gaussians. We therefore define a reduced Hilbert subspace, spanned by a subset of the $|b\rangle$ vectors, whose coefficients are all above some predefined threshold (Section 3.1). Next we define the biorthogonal bases for this reduced space (Section 3.2) and the projector into it (Section 3.3). Finally we mention a different subspace, spanned by a subset of $|g\rangle$ vectors (Section 3.4), which will be useful in later discussions. The idea of defining a pruned basis in which the Schrödinger equation takes a more compact representation has a long history. Of particular relevance to this work are the matrix transformation and simultaneous diagonalization approach by the Carrington

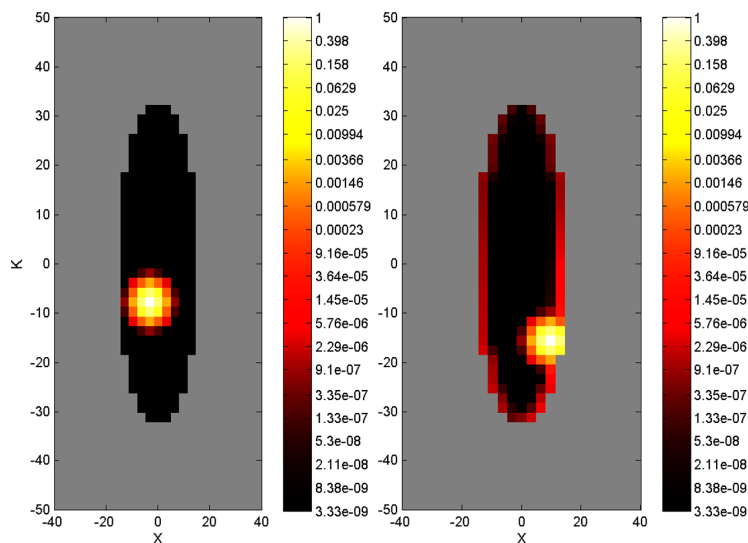


Figure 1. Depiction of modified Gaussians associated with the reduced basis. The reduced basis is the nongray area in both plots. (left) The modified Gaussian \tilde{g} , which is centered around a nonedge location in the phase space, is almost unchanged. (right) A heavily deformed Gaussian, that is, the function is delocalized throughout the edge region. This results from the projection of the G basis functions into the subspace spanned by B . The deformation is much more significant for Gaussians whose centers are near the edge. See eq 40 and the detailed discussion following eq 41 for details. The states are plotted as heat maps, where the value of each cell of the von Neumann lattice is the absolute value of the overlap of the state plotted (here the modified Gaussians), with the Gaussian centered at that cell of the lattice, $|\langle g_{\vec{r}, \tau} | \tilde{g} \rangle|$.

group,^{27,34,35} and the phase-space localized orthogonal wavelets by the Poirer group.^{6,7}

3.1. Defining the Reduced Hilbert Space, $\tilde{\mathcal{H}}$. Consider a Hilbert space \mathcal{H} , of dimension N , spanned by the orthogonal pseudospectral basis Θ and a set of biorthogonal bases \mathcal{B} , \mathcal{G} , represented in Θ by the $N \times N$ matrices B and G , with G being the periodic von Neumann Gaussian lattice, as defined in eq 6. A state $|\psi\rangle$ that is localized in phase space will be sparse in the B -representation, that is, ψ_B will have many near-zero elements. For the sake of notational convenience, let us assume the first \tilde{N} coefficients in ψ_B are significant, while the remaining $N - \tilde{N}$ are negligible. In such a case, we can save computational resources by reducing the vector ψ_B of length N to a vector $\psi_{\tilde{B}}$ of length $\tilde{N} \ll N$.

Define the *reduced subspace* $\tilde{\mathcal{H}} \subseteq \mathcal{H}$ as the Hilbert space spanned by the first \tilde{N} vectors of B , that is, all states whose B -basis representation is strictly zero in entries $(\tilde{N} + 1) \dots N$.

$$\tilde{\mathcal{H}} = \text{span}(\{|b_j\rangle\}_{j=1}^{\tilde{N}}) \quad (19)$$

Note that generally, $\tilde{\mathcal{H}}$ is quite different from

$$\check{\mathcal{H}} := \text{span}(\{|g_j\rangle\}_{j=1}^{\tilde{N}}) \quad (20)$$

as is evident when $\tilde{N} = 1$. We shall discuss $\check{\mathcal{H}}$ further in Section 3.4. Define the *complementary subspace*, $\bar{\mathcal{H}}$, by

$$\mathcal{H} = \tilde{\mathcal{H}} \oplus \bar{\mathcal{H}} \quad (21)$$

requiring that every vector in the complementary subspace $\bar{\mathcal{H}}$ is orthogonal to every vector in the reduced subspace $\tilde{\mathcal{H}}$. As the B basis is nonorthogonal, there is no partitioning of the B functions that allows one to span both subspaces separately. However, the complementary space may be written as

$$\bar{\mathcal{H}} = \text{span}(\{|g_k\rangle\}_{k=\tilde{N}+1}^N) \quad (22)$$

By construction, $\tilde{\mathcal{H}}$ is rank \tilde{N} , $\bar{\mathcal{H}}$ is rank $N - \tilde{N}$, and $\tilde{\mathcal{H}} \perp \bar{\mathcal{H}}$ due to the biorthogonality of their respective base vectors. Therefore, $\text{rank}(\tilde{\mathcal{H}}) + \text{rank}(\bar{\mathcal{H}}) = \text{rank}(\mathcal{H})$, and we conclude that indeed $\mathcal{H} = \tilde{\mathcal{H}} \oplus \bar{\mathcal{H}}$. Given any state $|\psi\rangle \in \mathcal{H}$, we may therefore decompose it as

$$|\psi\rangle = |\tilde{\psi}\rangle + |\bar{\psi}\rangle \text{ s.t. } \langle \tilde{\psi} | \bar{\psi} \rangle = 0 \text{ and } |\tilde{\psi}\rangle \in \tilde{\mathcal{H}}, |\bar{\psi}\rangle \in \bar{\mathcal{H}} \quad (23)$$

where $|\tilde{\psi}\rangle$ is the *reduced state* and $|\bar{\psi}\rangle$ is the *complementary state*. Projection may be viewed as subtracting $|\bar{\psi}\rangle$ from $|\psi\rangle$, a view that will be made explicit in Section 3.3.

3.2. Biorthogonal Bases for $\tilde{\mathcal{H}}$. We now turn to the biorthogonal bases for the reduced subspace.

$$\tilde{\mathcal{H}} = \{|b_j\rangle\}_{j=1}^{\tilde{N}}$$

We define these bases in a manner similar to that of the unreduced bases. Let us denote the first \tilde{N} columns of the B matrix with the matrix $\tilde{B}_{N \times \tilde{N}}$; that is, \tilde{B} is the Θ representation of the basis defining $\tilde{\mathcal{H}}$. \tilde{G} will be defined as a basis that is biorthogonal to \tilde{B} and spans the same Hilbert space as \tilde{B} ; that is, the pair \tilde{G} and \tilde{B} satisfy the completeness relation on the subspace. We stress that \tilde{B} is the natural basis of $\tilde{\mathcal{H}}$, while \tilde{G} is defined in terms of \tilde{B} . Note that while \tilde{B} is a truncated version of B , the \tilde{G} matrix is not a simple truncation of G , but rather that individual g functions are modified by a projection into the subspace spanned by \tilde{B} . This will be discussed in detail later in this section.

The biorthogonality requirement is

$$\tilde{G}^\dagger \tilde{B} = \mathbf{1}_{\tilde{N}} \quad (24)$$

The requirement that \tilde{B} and \tilde{G} span the same subspace is equivalent to the statement that \tilde{G} vectors are expressible as linear combinations of \tilde{B} vectors, and vice versa, that is:

$$\exists C \text{ s.t. } \tilde{B} = \tilde{G}C \quad (25)$$

$$\exists D \text{ s.t. } \tilde{G} = \tilde{B}D \quad (26)$$

(i.e., $|\tilde{g}_i\rangle = \sum_{k=1}^N C_{k,i} |\tilde{b}_k\rangle$, etc). The biorthogonality requirement is satisfied by the right pseudoinverse of \tilde{B}^\dagger

$$\tilde{G} := \tilde{B}(\tilde{B}^\dagger \tilde{B})^{-1} \quad (27)$$

and eqs 25 and 26 are satisfied by $D = \tilde{S}$ where

$$\tilde{S} := (\tilde{B}^\dagger \tilde{B})^{-1} = \tilde{G}^\dagger \tilde{G} \quad (28)$$

and $C = \tilde{S}^{-1}$ where

$$\tilde{S}^{-1} = \tilde{B}^\dagger \tilde{B} = (\tilde{G}^\dagger \tilde{G})^{-1} \quad (29)$$

Therefore, \tilde{G} and \tilde{B} are biorthogonal bases, both spanning \tilde{H} . As biorthogonality is a reciprocal relation, eq 27 is echoed by $\tilde{B} = \tilde{G}(\tilde{G}^\dagger \tilde{G})^{-1}$. Using eqs 28 and 29, we may relate \tilde{G} and \tilde{B} using \tilde{S} : $\tilde{G} = \tilde{B}\tilde{S}$ and $\tilde{B} = \tilde{G}\tilde{S}^{-1}$.

Note that the biorthogonality requirement alone, eq 24, is insufficient to uniquely define \tilde{G} . For example, both the Gaussians $|g\rangle$, and the vectors $|\tilde{g}\rangle$ of \tilde{G} are biorthogonal to the $|b\rangle = |\tilde{b}\rangle$ vectors spanning the reduced subspace, that is, $\langle g_i | b_j \rangle = \langle \tilde{g}_i | \tilde{b}_j \rangle = \delta_{jk} = \langle \tilde{g}_k | \tilde{b}_i \rangle \forall j, k \in 1 \dots \tilde{N}$. But while $\{|\tilde{b}_j\rangle\}_{j=1}^{\tilde{N}}$ and $\{|\tilde{g}_j\rangle\}_{j=1}^{\tilde{N}}$ span the same subspace, $\{|b_j\rangle\}_{j=1}^{\tilde{N}}$ and $\{|g_j\rangle\}_{j=1}^{\tilde{N}}$ do not (except when $\tilde{N} = N$). At the extreme, when $\tilde{N} = 1$, it is clear that $|b_1\rangle$ and $|g_1\rangle$ span different (trivial) Hilbert spaces.

Similarly to the definitions of \tilde{B} and \tilde{G} , we define the basis for the complementary Hilbert space \tilde{H} with \tilde{G} of size $N \times (N - \tilde{N})$ as the last $N - \tilde{N}$ columns of G , and $\tilde{B} := \tilde{G}(\tilde{G}^\dagger \tilde{G})^{-1}$.

The Deformation of the \tilde{G} Functions and the \tilde{S} Matrix on the Reduced Subspace. The discussion above, and particularly eq 27, leads to the conclusion that the columns of \tilde{G} are no longer exactly Gaussians but have been deformed as the result of the basis reduction. This is depicted in Figure 1. Note that Gaussians that are far away from the reduction boundary are not as affected as the Gaussians closer to the boundary. This is consistent with the intuitive notion that the localized Gaussians should not be affected by changes in areas of phase space into which they do not significantly extend. This intuition is made precise in the following section.

Schematically, the reduced \tilde{S} matrix is constructed from the S matrix by the following circuitous path,

$$\begin{array}{ccc} S_{N \times N}^{-1} = B^\dagger B & \xrightarrow{\text{truncation}} & \tilde{S}_{\tilde{N} \times \tilde{N}}^{-1} = \tilde{B}^\dagger \tilde{B} \\ \uparrow \text{inversion} & & \downarrow \text{inversion back} \\ S_{N \times N} = G^\dagger G & & \tilde{S}_{\tilde{N} \times \tilde{N}} = (\tilde{B}^\dagger \tilde{B})^{-1} = \tilde{G}^\dagger \tilde{G} \end{array} \quad (30)$$

One starts with the unmodified $S_{N \times N}$, inverts to get $S_{N \times N}^{-1}$, truncates to get $\tilde{S}_{\tilde{N} \times \tilde{N}}^{-1}$, and then inverts back to get $\tilde{S}_{\tilde{N} \times \tilde{N}}$. The chain of relationships suggests that, although G is simpler than B , \tilde{G} is more complicated than \tilde{B} . Specifically, in the multidimensional case the columns of the \tilde{G} matrix do not decompose into products of their one-dimensional (1D) counterparts, while the columns of the \tilde{B} matrix do decompose into 1D components. The reduced $\tilde{S}^{-1} = \tilde{B}^\dagger \tilde{B}$ matrix is a subset (of rows and columns) of the unreduced S^{-1} matrix, but the reduced $\tilde{S} = \tilde{G}^\dagger \tilde{G}$ matrix is not a subset of the full S , due to the inversion in eq 30. Non-decomposability of the multidimensional \tilde{S} and \tilde{G} matrices has significant impact on the computational resources required to

compute the reduced Hamiltonian. The issue is discussed in depth in Section 4.

We summarize the identities involving the reduced \tilde{S} matrix that are counterparts of the identities for the unreduced S matrix, eq 11:

$$\tilde{S} := \tilde{G}^\dagger \tilde{G}, \quad \tilde{G} = \tilde{B}\tilde{S}, \quad \tilde{\psi}_{\tilde{B}} = \tilde{S}\tilde{\psi}_{\tilde{G}}, \quad \tilde{S}^{-1} = \tilde{B}^\dagger \tilde{B}, \quad \tilde{B} = \tilde{G}\tilde{S}^{-1}, \quad \tilde{\psi}_{\tilde{G}} := \tilde{S}^{-1}\tilde{\psi}_{\tilde{B}} \quad (31)$$

3.3. Projecting into \tilde{H} . We can now expand a state using the reduced basis, echoing eq 14

$$|\tilde{\psi}\rangle := \sum_{j=1}^{\tilde{N}} \langle \tilde{g}_j | \psi \rangle |\tilde{b}_j\rangle = \left(\sum_{j=1}^{\tilde{N}} |\tilde{b}_j\rangle \langle \tilde{g}_j | \right) |\psi\rangle \quad (32)$$

and providing us with a representation-free form of the projector from \mathcal{H} to \tilde{H} . In Dirac notation

$$\tilde{P} := \sum_{j=1}^{\tilde{N}} |\tilde{b}_j\rangle \langle \tilde{g}_j | = \sum_{j=1}^{\tilde{N}} |\tilde{g}_j\rangle \langle \tilde{b}_j | \quad (33)$$

with the second equation following by Hermiticity of the projection. Note similarity to eqs 13 and 14. Recall that $|\tilde{b}_j\rangle = |b_j\rangle \forall j = 1 \dots \tilde{N}$.

The projector in the Θ representation (i.e., both input and output are represented on the Fourier grid) is given by

$$\tilde{P} := \tilde{B}\tilde{G}^\dagger \quad (34)$$

where we omit the basis designation Θ . One may directly show that \tilde{P} is idempotent; that is, $\tilde{P}^2 = \tilde{P}$ and Hermitian. Moreover, the projector \tilde{P} transforms a general state to the state closest to it within the subspace.²⁴ The idempotent property of \tilde{P} requires that the bra matrix in eq 34, \tilde{G}^\dagger , be biorthogonal to the ket matrix, \tilde{B} . Therefore, the projector is nonorthogonal if and only if the bases are nonorthogonal, which is the case if and only if \tilde{B} and \tilde{G} are not identical. The projection operator may be rewritten in several representations. We shall denote by \tilde{P}_{YX} the projection operator from the full Hilbert space \mathcal{H} into the reduced subspace \tilde{H} , where the Fourier grid representation of the input basis for \mathcal{H} is the matrix X , and the Fourier grid representation for \tilde{H} is the matrix Y . \tilde{P}_{YX} may be square or rectangular, depending on the choice of output basis. The projection operator transforms as do all operators, using

$$\tilde{P}_{YX} = Y^{-1} P X \quad (35)$$

When Y is not square, Y^{-1} should be taken to be the left pseudoinverse of Y .

To better understand the difference between this non-orthogonal projector and a standard orthogonal projector we shall examine two representations: $\tilde{P}_{\tilde{B}\tilde{B}}$, where the projection operation will be viewed as an additive operation, and $\tilde{P}_{\tilde{G}\tilde{G}}$, where the projection operation will be viewed as a subtractive operation.

$\tilde{P}_{\tilde{B}\tilde{B}}$ —All Basis Vectors Contribute to the Reduced Subspace. Given a state in the B basis, $|\psi\rangle = \sum_{k=1}^N \beta_k |b_k\rangle$, the application to $|\psi\rangle$ of eq 33 gives

$$\tilde{P}|\psi\rangle = \sum_{j=1}^{\tilde{N}} \sum_{k=1}^N \beta_k |\tilde{g}_j\rangle \langle \tilde{b}_j | b_k \rangle \quad (36)$$

Note that all b_k vectors contribute to the coefficients in the reduced subspace, as indicated by the $\langle \tilde{b}_j | b_k \rangle$ term of eq 36. The

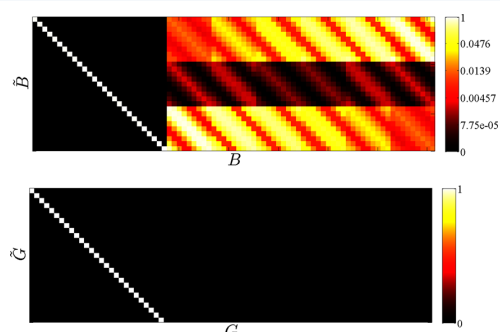


Figure 2. (top) The \tilde{P}_{BB} projector, i.e., the operator projecting the state ψ_B into the reduced Hilbert space \tilde{H} and representing the result in the \tilde{B} basis. Notice the block structure. The left square is the identity matrix, since if $|\psi\rangle = |b_{k \leq \tilde{N}}\rangle$ it remains unchanged by the projection. The right block provides insight into the unique additive contributions characteristic of nonorthogonal projections: as $\{|b_j\rangle\}_{j=1}^{\tilde{N}}$ and $\{|b_j\rangle\}_{j=\tilde{N}+1}^N$ overlap, when projecting into \tilde{H} , all b vectors have some overlap into the reduced subspace and therefore contribute to the projected vector. (bottom) The \tilde{P}_{GG} projector. The right block is empty, denoting the subtraction of all G vectors, which span the complementary subspace \tilde{H} , from the G representation of the state. The left block is the identity matrix, denoting the coefficients in this block remain unchanged. However, since $|\tilde{g}\rangle \neq |g\rangle$, the vector represented by these coefficient does change, due to the subtraction of the G subspace from the \tilde{G} vectors, resulting in the \tilde{G} basis.

participation of all b_k vectors in the coefficients is reflected in the \tilde{P}_{BB} representation of the projector, as depicted in Figure 2. We derive the explicit form of \tilde{P}_{BB} from eq 35, using eq 24, giving

$$\tilde{P}_{BB} = \tilde{G}^\dagger \tilde{P} B \quad (37)$$

Examining the top panel of Figure 2, the right block of \tilde{P}_{BB} depicts the overlap of all B vectors of the unreduced basis, including $\{|b_j\rangle\}_{j=\tilde{N}+1}^N$ with the $\{|b_j\rangle\}_{j=1}^{\tilde{N}}$ subset. This added contribution is unique to nonorthogonal projections. If this were an orthogonal projection, only the basis vectors defining the reduced basis, $\{|b_j\rangle\}_{j=1}^{\tilde{N}}$, which make up the identity matrix appearing in the left square, would play a part.

\tilde{P}_{GG} —Projection as a Subtractive Process. Recalling eq 21, $\mathcal{H} = \tilde{H} \oplus \tilde{H}$, we express the identity operator as a sum of projectors

$$I = \tilde{P} + \bar{P} \quad (38)$$

where, by analogy to \tilde{P} , we define $\bar{P} := \sum_{j=\tilde{N}+1}^N |b_j\rangle\langle \bar{g}_j|$. Using $|\bar{g}_j\rangle = |g_j\rangle \forall j = \tilde{N} + 1 \dots N$

$$\bar{P} = 1 - \sum_{j=\tilde{N}+1}^N |b_j\rangle\langle g_j| \quad (39)$$

We shall apply both sides of eq 39 to $|g_k\rangle_{k \leq \tilde{N}}$. On the left-hand side, using eq 33 gives

$$\tilde{P}|g_k\rangle = |\tilde{g}_k\rangle \quad (40)$$

Applying the right-hand side (rhs) of eq 39 to $|g_k\rangle$ and equating it with eq 40 results in

$$|\tilde{g}_k\rangle = |g_k\rangle - \sum_{j=\tilde{N}+1}^N \langle g_j | g_k \rangle |b_j\rangle \quad \forall k \leq \tilde{N} \quad (41)$$

Note that \tilde{P} , applied to $|g_k\rangle_{k > \tilde{N}}$ is zero, as the state is part of the basis spanning the complementary subspace.

We now have a new insight into the deformation of the Gaussians due to the basis reduction, as depicted in Figure 1: it is the result of subtraction of $|b_j\rangle$ vectors, weighted by the overlap of the Gaussians inside the reduced subspace with the Gaussians spanning the complementary space. This clarifies why Gaussians at the boundary of the reduced subspace are modified more—they have a larger overlap with Gaussians outside the reduced subspace.

Applying \tilde{P} to a superposition state $|\psi\rangle = \sum_{k=1}^N \gamma_k |g_k\rangle$ and using eq 40 gives

$$\tilde{P}|\psi\rangle = \sum_{k=1}^{\tilde{N}} \gamma_k |\tilde{g}_k\rangle \quad (42)$$

Gaussians spanning the complementary subset are dropped, and the coefficients of the remaining Gaussians are unchanged but now serve as coefficients of the modified Gaussians. If this were an orthogonal basis, these coefficients would have been unchanged without modifying the underlying basis.

An equivalent view is provided by examining the projector representation \tilde{P}_{GG} . Define the matrix

$$R_{N \times \tilde{N}} := \begin{pmatrix} 1 & 0 & 0 & \dots \\ 0 & 1 & \ddots & \ddots \\ \vdots & \ddots & \ddots & 0 \\ 0 & \dots & 0 & 1 \\ 0 & 0 & \dots & 0 \\ 0 & \ddots & & 0 \\ \vdots & \ddots & \vdots & \\ 0 & 0 & \dots & 0 \end{pmatrix} \quad (43)$$

allowing us to write

$$\tilde{B} := BR \quad (44)$$

Combining eqs 34, 35, and 27, and using eqs 44 and 7, we obtain

$$\tilde{P}_{GG} = R^\dagger \quad (45)$$

This uniquely simple form is depicted in the bottom panel of Figure 2.

\tilde{P}_{BB} and \tilde{P}_{GG} provide two complementary views of the nonorthogonal projection. With \tilde{P}_{BB} , projection is an additive process: The vectors of the reduced basis, $\{\tilde{b}_j\}_{j=1}^{\tilde{N}}$ are the same as their unreduced counterparts, $\{b_j\}_{j=\tilde{N}+1}^N$ as is the case for orthogonal projections. However, the projection modifies their coefficients due to additive contributions by $\{b_j\}_{j=\tilde{N}+1}^N$ which is unique to nonorthogonal projections. With \tilde{P}_{GG} , projection is a subtractive process: If $|\psi\rangle = \sum_{k=1}^N \gamma_k |g_k\rangle$, then the coefficients $\{\gamma_k\}_{k=1}^{\tilde{N}}$ are unchanged by the projection, and the rest are removed completely, as in an orthogonal projection. However, the Gaussian basis vectors are modified by subtraction proportional to their overlap with the Gaussians spanning the complementary subspace, changing $|g\rangle$ to $|\tilde{g}\rangle$. This modification is again unique to nonorthogonal projections.

Table 1. Summary of Properties of the Full, Reduced, and Complementary Hilbert Spaces

Hilbert space	dimension	b-like basis	g-like basis	biorthogonality	completeness
\mathcal{H}	N	$B = (G^{-1})^\dagger$	$G = (B^{-1})^\dagger$	$G^\dagger B = \mathbf{1}$	$GB^\dagger = \mathbf{1}$
\check{H}	\check{N}	$\check{B} = BR$	$\check{G} := \check{B}(\check{B}^\dagger \check{B})^{-1}$	$\check{G}^\dagger \check{B} = \mathbf{1}$	$\begin{cases} \check{G} = \check{B}(\check{B}^\dagger \check{B})^{-1} \\ \check{B} = \check{G}(\check{G}^\dagger \check{G})^{-1} \end{cases}$
\bar{H}	$N - \check{N}$	$\bar{B} := \bar{G}(\bar{G}^\dagger \bar{G})^{-1}$	$\bar{G} = GR$	$\bar{G}^\dagger \bar{B} = \mathbf{1}$	$\begin{cases} \bar{G} = \bar{B}(\bar{B}^\dagger \bar{B})^{-1} \\ \bar{B} = \bar{G}(\bar{G}^\dagger \bar{G})^{-1} \end{cases}$

Table 1 provides a summary of the properties of the full, reduced and complementary Hilbert spaces. Figure 3 gives a graphical representation of the transitions between the unreduced and reduced bases.

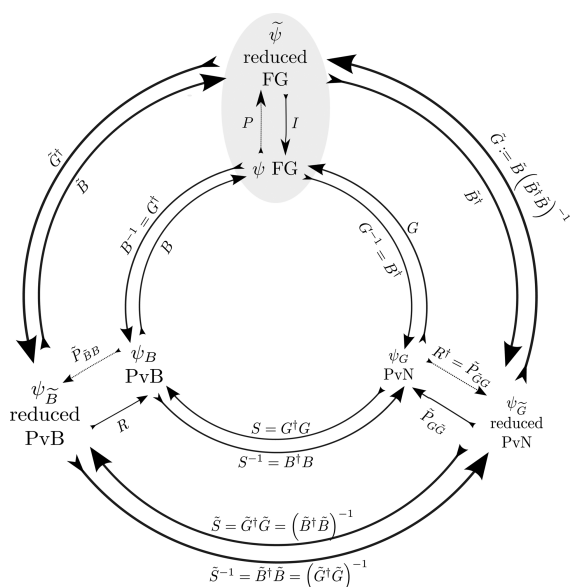


Figure 3. Transitions between the unreduced and reduced bases, represented on the middle and outer circles, respectively, with dimension N and \check{N} . Dashed arrows indicate a projection (surjective; with information loss), continuous arrows are injective (one-to-one but not necessarily on-to) mappings. The nomenclature \check{P}_{YX} is used to indicate the projection from representation X of \mathcal{H} into representation Y of \check{H} . This diagram may be used, for example, to construct \check{P}_{BB} by going through the following series of transformations: (1), from the B basis to G using the transformation matrix S^{-1} , (2) projecting with R^\dagger , (3) transforming back to \check{B} using \check{S} , (4) transforming to base B using R . Multiplying the matrices appearing from right to left gives $\check{P}_{BB} = R\check{S}R^\dagger S^{-1}$.

3.4. Projecting into the Subspace Spanned by Gaussians, \check{H} . We defined the reduced subspace \check{H} in eq 19 as the Hilbert space spanned by $\{|b_k\rangle\}_{k=1}^{\check{N}}$. One may define a different reduced subspace, $\check{H} = \text{span}(\{|g_k\rangle\}_{k=1}^{\check{N}})$, as in eq 20. As discussed in Section 3.2, these subspaces are not identical (unless $\check{N} = N$), as is evident when $\check{N} = 1$ and $\check{H} = \text{span}(|b_1\rangle)$ and $\check{H} = \text{span}(|g_1\rangle)$.

Following the discussion in Sections 3.1, 3.2, and 3.3 one may define the projector into this subspace and the subspace's biorthogonal bases. Let us denote the first \check{N} columns of the G

matrix with the matrix $\check{G}_{N \times \check{N}}$; that is, \check{G} is the Θ representation of $\{|g_k\rangle\}_{k=1}^{\check{N}}$, the basis spanning \check{H} . To satisfy the biorthogonality requirement, eq 8, in the \check{H} basis, one must define

$$\check{G} := GR \quad (46)$$

$$\check{B} := \check{G}\check{S}^{-1} \quad (47)$$

with $\check{S} = \check{G}^\dagger \check{G}$. The projector into \check{H} may then be defined as

$$\check{P} = \sum_{j=1}^{\check{N}} |g_j\rangle\langle b_j| \quad (48)$$

with $|g_j\rangle = |g_j\rangle$. Therefore, in the Θ representation the projector is

$$\check{P} = \check{G}\check{B}^\dagger \quad (49)$$

Note both \bar{H} and \check{H} are spanned by Gaussians. Specifically, \bar{H} is the reduced subspace spanned by the set of Gaussians complementary to \check{G} . It must be stressed that $\bar{H} \neq \check{H} \neq \bar{H}$.

As discussed in Section 2.4, the representation of a state as a sum of Gaussians (PvN) is not sparse. Therefore, given a well-localized state $|\psi\rangle$, if one wishes to use the \check{H} subspace, one can expect that a very large number of functions will be needed. This is in stark contrast to \bar{H} , where well-localized states are well-approximated by a small number of functions. Thus, given a fixed size of the representation, one will achieve much higher accuracies with \check{P} than with \bar{P} . This will be explicitly demonstrated when we discuss the various representations of the reduced Hamiltonian and their accuracy, in Section 4.

4. THE HAMILTONIAN AND THE SCHRÖDINGER EQUATION FOR THE REDUCED STATE

The Schrödinger equation for the reduced state requires projecting the Hamiltonian into the reduced subspace. In this section we consider three possibilities from both the theoretical and practical viewpoints: Projecting into the \bar{H} subspace (Section 4.1), into the \check{H} subspace (Section 4.2), and performing a pseudoprojection into a combination of the two (Section 4.3). Finally we benchmark the respective accuracies of the possible projections (Section 4.4).

4.1. The Equation of Motion in the \bar{H} Subspace. To arrive at the reduced Hamiltonian, we apply the \bar{P} projection on both the input and output of the Hamiltonian. As the state is represented in the \bar{B} basis, one can either convert the vector to Θ , project into \bar{H} , apply H , project the resulting state again into \bar{H} , and transform it to \bar{B} , or, equivalently, first apply the projection and then the base transformation. These two alternatives correspond to the following two expressions for H_1 :

$$H_1 := \check{G}^\dagger (\check{P}H\check{P})\check{B} = \check{P}_{\bar{B}\bar{B}}(G^\dagger HB)\check{P}_{\bar{B}\bar{B}} \quad (50)$$

Utilizing eqs 34, 37, and 27

$$H_1 = \tilde{G}^\dagger H \tilde{B} = (\tilde{B}^\dagger \tilde{B})^{-1} (\tilde{B}^\dagger H \tilde{B}) \quad (51)$$

The TISE and TDSE then take the form

$$E \psi_{\tilde{B}} = H_1 \psi_{\tilde{B}} \quad (52)$$

$$\partial_t \psi_{\tilde{B}} = -\frac{i}{\hbar} H_1 \psi_{\tilde{B}} \quad (53)$$

Equations 51, 52, and 53 will be the key working equations for the remainder of this article. See also ref 12 and ref 27 for alternative derivations.

The formulation using only \tilde{B} matrices (rhs of eq 51) is appealing, as $\tilde{B} = B R$ is the naturally reduced matrix in \tilde{P} . An equivalent, more heuristic approach, is to replace all matrices in any of the forms of eq 18 by their reduced counterparts, $B \rightarrow \tilde{B}$, $G \rightarrow \tilde{G}$, $S \rightarrow \tilde{S}$, etc. All four variations transform to the reduced Hamiltonian in eq 51.

Finally, we note that H_1 is similar to a Hermitian matrix, in that the product of matrices to the left and right of H in eq 51 produce the identity, $((\tilde{B}^\dagger \tilde{B})^{-1} \tilde{B}^\dagger) (\tilde{B}) = \mathbf{1}$. Therefore, eigenvalues are real, and evolution is unitary. Moreover, combining eqs 51 and 52 the TISE may be reformulated as a generalized eigenvalue equation with Hermitian matrices.

$$(\tilde{B}^\dagger \tilde{B}) \lambda \psi_{\tilde{B}} = (\tilde{B}^\dagger H \tilde{B}) \psi_{\tilde{B}} \quad (54)$$

thus avoiding the matrix inversion required to compute \tilde{S} . This form is solvable with an iterative eigensolver, such as Arnoldi. Unfortunately, in this form it is not possible to implement the eigensolver with just matrix-vector multiplications (i.e., it is not possible to avoid matrix–matrix multiplications).³¹ This is in contrast with the pseudoprojection discussed in Section 4.3, which can be implemented with just matrix-vector multiplications.

While accurate and mathematically rigorous, computing the H_1 form in eq 51 is time-consuming. Most significantly, calculation of elements of the reduced Hamiltonian $\tilde{B}^\dagger H \tilde{B}$ can be laborious, particularly in the multidimensional case, as the B functions are nonlocalized. Fortunately, there are symmetry considerations and numerical techniques that can accelerate this computation by several orders of magnitude. Alternatively, using eqs 51, 44, 11, and 31, one may rewrite H_1 as

$$H_1 = \tilde{S} (R^\dagger S^{-1} G^\dagger H G S^{-1} R) \quad (55)$$

Equation 55 may be quicker to compute than 50: due to the locality of G and the fact that elements of H are usually functions of either position or momentum (but rarely both), the vast majority of $G^\dagger H G$ elements are vanishingly small. Note that G and S^{-1} decompose dimensionally. Indeed, one would still need to calculate \tilde{S} , which requires the inversion of $\tilde{B}^\dagger \tilde{B}$, but this may be accelerated, if one is able to store the matrix. If we then use an iterative algorithm for solving the TISE (e.g., Arnoldi) and the TDSE (e.g., Taylor propagator), one may use only matrix-vector operations to further accelerate the process. Similar considerations have been noted in ref 27.

4.2. Alternatives to the \tilde{H} -Projected Equations of Motion. In the previous section we presented the projection of the TISE and TDSE into the \tilde{H} subspace. There are, however, additional alternatives we should consider. First, we shall examine the possible choices for state representation: In addition to the \tilde{B} representation we use, there are three additional a priori candidates: \tilde{G} , \tilde{B} , and \tilde{G} . Then, we shall consider various

projections for the Hamiltonians. This analysis is of some importance, as alternatives to eq 51 are currently in use by the community. For example, H_2 , defined in eq 62 using a hybrid of \tilde{P} and \tilde{P} , is used in 27.

The first alternative state representation, \tilde{G} , spans \tilde{H} just as \tilde{B} does and therefore provides the same accuracy. However, it has a disadvantage: the coefficients are determined by an overlap with \tilde{B} -s, which are highly nonlocal. As a result, the coefficients are not expected to drop off sharply at the boundary of the reduced subspace, where the wavepacket is absent. As a result, we cannot use their declining values to determine the selection of basis functions for the reduced subspace, as one may do with an amplitude cutoff threshold for $\psi_{\tilde{B}}$. This issue is of primary concern, especially for the TDSE, where the coefficients of the state at the boundary of the reduced phase space serves determine how to modify the subspace over time. We therefore conclude that the \tilde{G} is unfit for our purposes.

The two remaining options, \tilde{B} and \tilde{G} , are disqualified because the subspace to which such states belong, \tilde{H} , is spanned by Gaussians, and hence does not provide a sparse representation for localized states. In other words, many Gaussians (or many \tilde{B} vectors) are required to accurately represent a localized state (see Section 3.4). We therefore conclude that \tilde{B} is the only viable option for state representation.

Next we proceed to examine the possible projections of the Hamiltonian. Until now we have been considering projection into \tilde{H} . The other natural alternative is projection into \tilde{H} . This may be performed either by acting with \tilde{P} on H on the left and the right, or by using the replacement rules $G \rightarrow \tilde{G}$, $S \rightarrow \tilde{S} = \tilde{G}^\dagger \tilde{G}$, $B \rightarrow \tilde{B} = G \tilde{S}^{-1}$ on any of the Hamiltonian forms in eq 18. This leads to

$$H_4 := \tilde{G}^\dagger \tilde{P} H \tilde{P} \tilde{B} = \tilde{G}^\dagger H \tilde{B} = (\tilde{G}^\dagger H \tilde{G}) (\tilde{G}^\dagger \tilde{G})^{-1} \quad (56)$$

Note that we would like to continue to represent states in the \tilde{B} representation, in accordance with the above discussion of its compactness. Then the TISE and TDSE take the form

$$E \psi_{\tilde{B}} = H_4 \psi_{\tilde{B}} \quad (57)$$

$$\partial_t \psi_{\tilde{B}} = -\frac{i}{\hbar} H_4 \psi_{\tilde{B}} \quad (58)$$

However, because the subspace into which H_4 is projected does not span the subspace defined by the $\psi_{\tilde{B}}$, the accuracy may be significantly lower than that of H_1 (see Figure 4 and the discussion in Section 4.4). Nevertheless, H_4 greatly benefits from having a highly local Hamiltonian transform, $\tilde{G}^\dagger H \tilde{G}$, making it usable when fast low-accuracy results are acceptable.

With the strict application of \tilde{P} leading to an accurate but slow H_1 , and the application of \tilde{P} leading to an inaccurate alternative, in the following section we explore the possibility of a hybrid projection that combines some of the benefits of both.

4.3. The Equation of Motion in Hybrid Subspaces. Recall the discussion in Section 3.2 regarding the modification of the \tilde{G} Gaussians when near the edge of the reduced subspace. One may hypothesize that if we extend the reduced subspace beyond the minimal volume required to represent the state, so that Gaussians near the boundary do not have significant overlap with the state, we may achieve a good approximation while still using the unmodified Gaussians. In the nomenclature established in Section 3.4, we wish to replace \tilde{G} with G , and possibly avoid the nonlocal \tilde{B} matrix altogether.

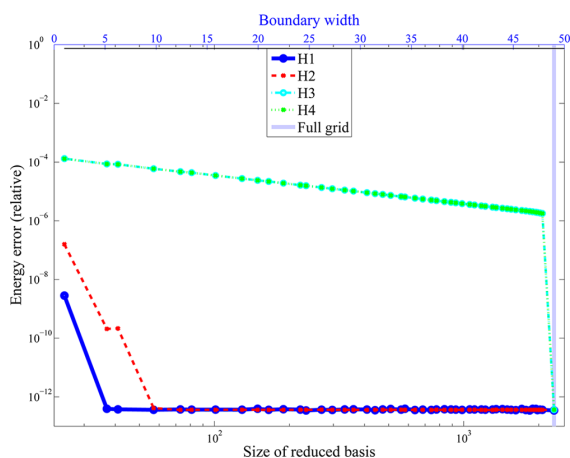


Figure 4. Accuracy of the ground-state energy of the 1D Harmonic oscillator as a function of the reduced basis size (lower x -axis) or reduced-basis boundary width (upper x -axis) computed using different reduced Hamiltonians. As expected from the theoretical discussion, $H_1 = \tilde{G}^\dagger H \tilde{B}$ is orders of magnitude more accurate than $H_2 = \check{G}^\dagger H \check{B}$, until the reduced subspace is increased to the point where the state does not significantly overlap any of the distorted Gaussians, and the distinction between \tilde{G} and \check{G} becomes moot. $H_3 = \check{G}^\dagger H \check{B}$ and $H_4 = \tilde{G}^\dagger H \tilde{B}$ are significantly less accurate.

We note that $\check{G}^\dagger \check{B} = \mathbf{1}_{\check{N}}$; that is, they are biorthogonal. However, as they do not span the same subspace the completeness relations do not hold.

Recalling eq 51, $H_1 = \tilde{G}^\dagger H \tilde{B}$, and eq 56, $H_4 = \check{G}^\dagger H \check{B}$, we shall define the hybrid form

$$H_2 := \check{G}^\dagger H \tilde{B} \quad (59)$$

with the corresponding TISE and TDSE:

$$E \psi_{\tilde{B}} = H_2 \psi_{\tilde{B}} \quad (60)$$

$$\partial_t \psi_{\tilde{B}} = -\frac{i}{\hbar} H_2 \psi_{\tilde{B}} \quad (61)$$

This form is advantageous over eq 51 in that no matrix inversion is necessary (implying there is no generalized eigenvalue problem to solve for the TISE), and the localized nature of \check{G} can be used to simplify the calculation of multidimensional terms in $\check{G}^\dagger H \tilde{B}$. H_2 is similar to a Hermitian matrix (as $\check{G}^\dagger \check{B} = \mathbf{1}_{\check{N}}$) and hence diagonalizable with real eigenvalues.

Equation 62 may be reformulated using eqs 46, 44, and 11 as

$$H_2 = R^\dagger \check{G}^\dagger H G S^{-1} R \quad (62)$$

This form allows the TDSE to be solved using only matrix-vector type operations. S^{-1} decomposes into a product of 1D matrixes, and $\check{G}^\dagger H G$ may be calculated analytically by expanding the potential term as a Taylor series around the center of the Gaussian. Such an approach may be sufficiently quick to eliminate the need to store the reduced Hamiltonian, by making use of an iterative eigensolver as described in ref 27 along with a Taylor propagator for the TDSE.

A final possible hybrid is $H_3 := \tilde{G}^\dagger H \check{B}$, but we do not see any immediate usefulness in this form.

4.4. Comparing the Accuracy of the Dynamical Formulations. We now compare the accuracy of the various

reduced Hamiltonians introduced in the previous sections. From Figure 4 we can conclude that H_1 is indeed the most accurate. This is expected as it contains no approximations beyond the amplitude cutoff used to define the reduced subspace. H_2 provides 2 orders of magnitude lower accuracy for the same reduced basis size or alternatively, requires a boundary width of five lattice cells to achieve equivalent accuracy. The latter translates to 30% to 80% larger reduced basis size for 1D problems and is expected to grow exponentially with higher dimensions, making it an unappealing option for high-dimensional problems. The lower accuracy of H_2 may be understood when we compare eq 62 to 51, that is, $\check{G}^\dagger H \check{B}$ to $\tilde{G}^\dagger H \tilde{B}$, and recall the deformation of the Gaussians by the basis reduction, as depicted in Figure 1. H_2 ignores this deformation, instead acting with the unmodified Gaussians. If we enlarge the boundary of the reduced subspace sufficiently so that there is little overlap between the state represented and the deformed Gaussians, then $\check{G}^\dagger \psi \approx \tilde{G}^\dagger \psi$. Therefore, H_2 may achieve accuracy equal to H_1 provided the reduced subspace is expanded.

H_3 and H_4 provide almost identically poor performance, never achieving an accuracy of 1×10^{-5} , except when utilizing the full grid, where the difference between the various reduced Hamiltonians disappears. This is again expected, as by using the projector \tilde{P} instead of \check{P} on the input state to the Hamiltonian, we are projecting into a subspace spanned by Gaussians (Section 3.4), which is nonsparse. As analyzed in ref 11, in this case the full Hilbert space is required to achieve highly accurate results.

To conclude, for highly accurate results, H_1 is the form of choice. In some instances where high accuracy is not paramount, or one opts for a significant increase in the reduced subspace size, H_2 may allow for greater speed.

5. EXAMPLES

We provide some illustrative examples of the use of the PvB representation for both the TISE and TDSE. The algorithms used to solve the time-dependent and time-independent Schrödinger equation are described in detail in ref 32, and an application of PvB to the challenging problem of double ionization of helium is given in ref 17.

In PvB, the process of computing eigenmodes begins with the definition of a Fourier grid prescribing an area in phase space $x \in \left[-\frac{L}{2}, \frac{L}{2}\right]$, $k \in [-K, K]$ such that all states of interest, truncated to a predefined amplitude cutoff, fit inside it. Starting from a reduced subspace containing only the potential's local minima, the eigenmode algorithm iteratively extends the reduced subspace to neighboring von Neumann grid cells. The process concludes when all eigenmode amplitudes at the boundary of the reduced subspace are below the predefined cutoff. If L or K are too small, the process will fail when reaching the edge of the FG. Therefore, eigenvalue accuracy is determined by the wave function amplitude cutoff, which in turn dictates the required FG dimensions. Dynamics proceeds by examining at every time step the amplitudes at the edge of reduced subspace, and adding or removing vectors to the reduced basis, as to maintain a thin boundary with amplitudes below the cutoff threshold. During the above processes, the algorithms construct the PvB representation of the reduced Hamiltonian, H_1 (eq 50). In some instances, this task can benefit from a dimensional decomposition of the Hamiltonian matrix. See ref 32 for details.

5.1. One-Dimensional Morse Oscillator. The Hamiltonian for the Morse oscillator, in atomic units, is

$$H_{\text{Morse}} = -\frac{\partial_x^2}{2 \times 6} + 12 \left(1 - e^{(x-2)/2} \right)^2 \quad (63)$$

The PvB representation for the 21st eigenstate is shown in Figure 5, using a von Neumann grid of size $N_k = N_x = 15$, projected into a Fourier grid with $x \in [-1, 21]$ and $k \in [-33.66, +33.66]$.

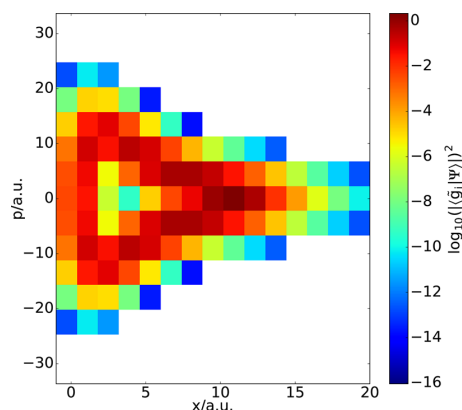


Figure 5. PvB representation of the 21st eigenstate of the 1D Morse oscillator, eq 63. The system supports 24 bound states; the size of the reduced basis is 97. Pixel colors represent the absolute value squared of the PvB expansion coefficients. Only the basis functions corresponding to colored pixels are part of the reduced subspace.

The mean error of the first 21 states as a function of the reduced basis size is depicted in Figure 6. The behavior of H_2 compared to H_1 for the Morse oscillator is similar to their behavior for the harmonic oscillator ground state (Figure 4). If the reduced basis is large enough, so that the basis functions near the subspace boundary have negligible overlap with the state, then $\tilde{G}^\dagger \psi$ is almost equal to $\check{G}^\dagger \psi$, and the results using H_2 do not differ significantly from the results using H_1 . In other words, $\check{S}_{\tilde{N} \times \tilde{N}} = (\check{B}^\dagger \check{B})^{-1}$ is similar to $\check{S} = R^T S_{N \times N} R$. At the other extreme, if the Hilbert space is pruned too drastically, parts of phase space with significant population are left out of the reduced subspace. In that

case, the errors induced by the excessive pruning become more significant than the errors caused by approximating \tilde{G} by \check{G} , and the distinction between H_1 and H_2 becomes negligible. We conclude that H_2 may be useful for low-accuracy applications.

5.2. Two-Dimensional Coupled Harmonic Oscillator.

The observations of Section 5.1 are applicable to higher-dimensional systems. We repeat the previous analysis for a coupled two-dimensional (2D) harmonic oscillator described by

$$H_{2\text{D-HO}} = -\frac{1}{2}(\partial_x^2 + \partial_y^2) + \frac{1}{2}(x^2 + y^2) - 0.3xy \quad (64)$$

Note that the Hamiltonians in this and the following example (eq 65) are in the form of a sum of products of 1D terms. In both examples, we used the fact that the Hamiltonian is dimensionally decomposable to expedite the calculation of H_1 , by evaluating the operation in each of the two dimensions sequentially, rather than as a single, multidimensional operation. A more systematic strategy for dimensional decomposition is detailed in ref 32 and used in ref 17.

Eigenmodes were computed on a von Neumann grid of size $N_k = 35$, $N_x = 37$, projected into a Fourier grid with $N = 1295$ sampling points, prescribing an area of phase space $x \in [-40, 40]$ and $k \in [-50.85, +50.85]$. Figure 7 shows the error of the first 22 eigenstates of this system as a function of the subspace size. The results are qualitatively similar to those of Figure 6. For a large reduced space, the results of H_1 and H_2 are similar, with the results of H_2 actually slightly more accurate. The slightly higher accuracy of H_2 may originate from the additional inversion of \tilde{S}^{-1} that is required for H_1 . For intermediate basis sizes, the error of H_2 is larger than for H_1 , until the error introduced by excessive pruning of the basis dominates at small basis sizes.

5.3. Two-Dimensional Double-Well Dynamics. We now turn to the time-dependent case. When propagating a wave function in time, the reduced basis changes, as the phase space occupied by the state evolves. To compare the accuracy of H_1 and H_2 , we consider a 2D double-well potential with strong coupling between x and y , with

$$H_{2\text{D-DW}} = -\frac{1}{2 \times 200}(\partial_x^2 + \partial_y^2) + 6.4(x-1)^2(x-2)^2 + 37.5(y-2)^2 + 10x^2y \quad (65)$$

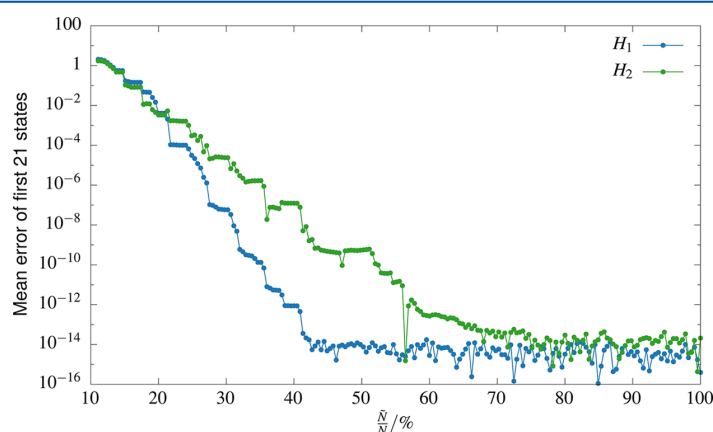


Figure 6. Mean error of the first 21 eigenstates in a 1D Morse oscillator, as a function of the ratio between the reduced and unreduced basis sizes. The error is shown for the two Hamiltonians, H_1 and H_2 . Eigenstate error is computed as the infidelity with respect to the eigenstate computed with the unreduced Hilbert space.

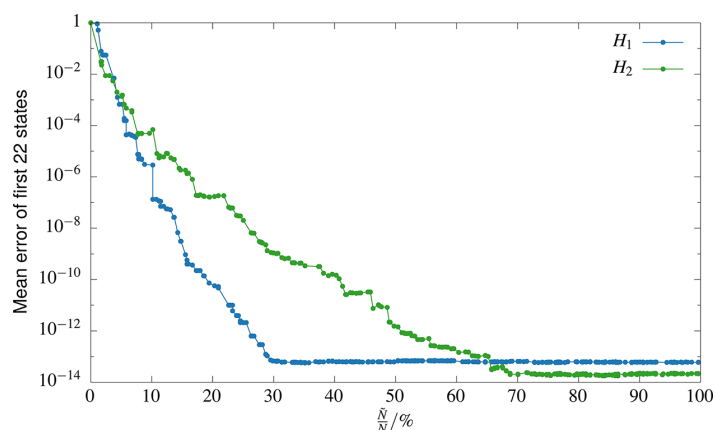


Figure 7. Mean error of the first 22 eigenstates in a 2D coupled harmonic oscillator, eq 64, as a function of the ratio of the reduced and unreduced basis sizes. The error is shown for the two Hamiltonians, H_1 and H_2 .

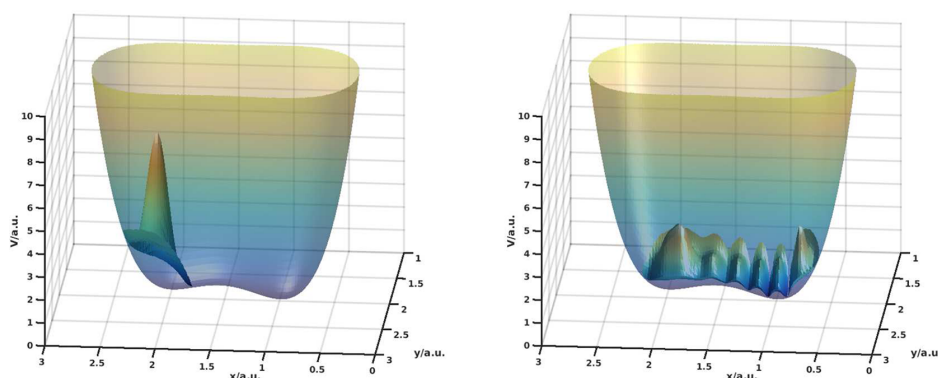


Figure 8. Potential surface for 2D double well (eq 65), overlaid with the initial (left) and final (right) state. Wave function z coordinate is proportional to the absolute value squared of its amplitude.

and the initial wave packet is given by

$$\langle xy | \psi_{\text{initial}} \rangle = \frac{\sqrt{\frac{2}{\pi}}}{(0.04 \times 0.02)^{1/4}} \exp\left(-\frac{(x-2.1)^2}{0.04} - \frac{(y-2.05)^2}{0.02}\right) \quad (66)$$

Calculations were performed on a von Neumann grid of size $N_{k_1} = N_{x_1} = 15$, $N_{k_2} = N_{x_2} = 9$, projected into a 2D Fourier grid with $N = 225 \times 81$ sampling points, prescribing an area of phase space $x_1 \in [-0.75, 3.7]$, $x_2 \in [1.0, 2.9]$, $k_1 \in [-158.8, 158.8]$ and $k_2 \in [-133.9, 133.9]$. The wave packet was propagated from $t_0 = 0$ to $t_2 = 24.6$. The potential surface and the initial and final wave packets are shown in Figure 8. At the final time, the wave packet has spread across the barrier and oscillates in x and y . The wave packet was also investigated at $t_1 = 16.6$ (not shown), when the packet is at the barrier but still retains a compact form.

Figure 9 compares the accuracy of the dynamics computed using H_1 and H_2 . Here we observe a significant deterioration in H_2 performance. Specifically, H_2 fails to achieve 10^{-4} accuracy, both at t_1 and t_2 , unless more than half of the unreduced Hilbert space is used. This is in stark contrast to H_1 , which can achieve better than 10^{-8} accuracy with less than 30% of the Hilbert space. Moreover, the $\approx 10^{-4}$ accuracy of H_2 for a very small basis size at t_1 is lost for t_2 . Both aspects of this reduction in H_2 accuracy can be explained by recognizing the importance of the low-amplitude

boundary dynamics as the wavepacket tunnels across the barrier. The Gaussians at the boundary are the first to be removed in the pruning process, as depicted in Figure 1. Therefore, H_2 may not be used where the low-amplitude boundary is essential for getting acceptable accuracy. In contrast, H_1 can be used in such situations with no difficulty, as long as the amplitude cutoff is sufficiently low so as to retain the tunneling amplitude.

6. CONCLUSIONS AND OUTLOOK

In this paper we presented the mathematical underpinnings of the PvB method for quantum mechanical simulations. The PvB method exploits the phase space localization of the von Neumann basis to provide a sparse representation of quantum mechanical states that spans only the part of phase space where there is significant amplitude. This in turn can lead to significant computational savings in both CPU and memory.

A detailed analysis was given of the subtle issues of projection onto subspaces of biorthogonal bases. Two complementary ways of understanding this projection were provided. The first focuses on the basis functions: it was shown that under projection one of the biorthogonal bases remains unchanged, while the other becomes significantly distorted. We showed that the distortions may be viewed as arising from subtraction of the \tilde{G} Gaussians that span the complementary subspace. This explains why Gaussians

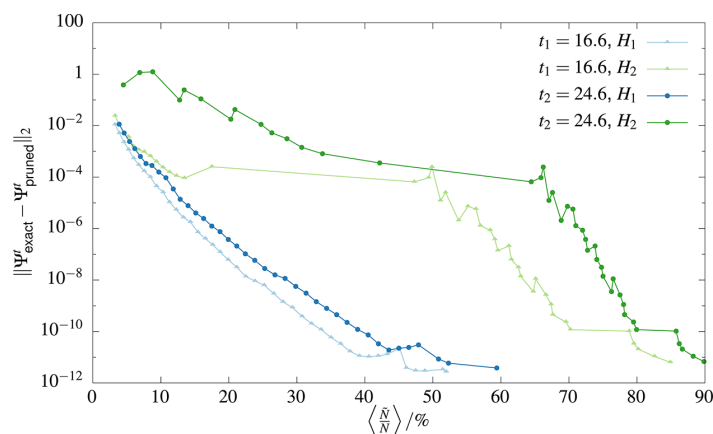


Figure 9. Accuracy of the wavepacket dynamics for the 2D double-well as a function of the ratio of the reduced and unreduced basis sizes. The fidelity is shown for the two Hamiltonians, H_1 and H_2 , at two times t_1 and t_2 .

near the boundary of the reduced phase space boundary are significantly distorted, while Gaussians far from the boundary are essentially unperturbed. The second way to understand the effect of nonorthogonal projection focuses on the coefficients: in the \tilde{G} basis all \tilde{B} basis vectors contribute to the coefficients, since all basis vectors overlap one another due to the nonorthogonality of the basis.

We then analyzed the various representations of the Schrödinger equation in the reduced basis and approximations thereto. We concluded that for high-accuracy applications $H_1 = \tilde{G}^\dagger H \tilde{B}$ (eq 50) is the preferred form, although it comes with a relatively high computational cost. For medium-to-low accuracy applications, an approximate form, $H_2 = \tilde{G}^\dagger H \tilde{B}$ (eq 62), may be used.

Several numerical examples were brought, showing the relative merits of H_1 and H_2 . A more challenging application of PvB, the double ionization of helium, is presented in ref 17.

Despite the significant methodological progress further development is possible. Specifically, one may further reduce the representation by decomposing multidimensional objects into a sum of products, and truncating the sum when the correlation is sufficiently low. This strategy is used by the POTFIT algorithm to decompose the potential, but a similar approach could be used for the wave function and the reduced Hamiltonian. This is a challenging problem, however, as the dynamics continuously modify the reduced basis, which generally is not easily decomposable.

Further areas of research include the correspondence between PvB and other phase space representations, including the discrete Husimi and Wigner representation. We also plan to explore the treatment of particle symmetries (Bosonic, Fermionic) in multiparticle implementations of the PvB method.

Beyond method development, there is a wide range of problems that are amenable to the PvB methodology, including high-harmonic generation, multielectron ionization, photodissociation, and chemical reactions. We intend to explore these applications in the near future.

To conclude, PvB is an accurate, scalable, and efficient method for quantum dynamics simulations, and it is our hope that it will find its place as part of the standard quantum numerics toolbox.

■ AUTHOR INFORMATION

Corresponding Author

*E-mail: shai.machnes@weizmann.ac.il.

Notes

The authors declare no competing financial interest.

■ ACKNOWLEDGMENTS

The authors thank T. Carrington for useful correspondence. This work was supported by the Israel Science Foundation (533/12), the Minerva Foundation with funding from the Federal German Ministry for Education and Research, and the Koshland Center for Basic Research. H.R.L. acknowledges support by the Deutscher Akademischer Austauschdienst, Studienstiftung des deutschen Volkes, and the Fonds der Chemischen Industrie.

■ REFERENCES

- (1) Cabrera, R.; Bondar, D. I.; Jacobs, K.; Rabitz, H. A. Efficient Method to Generate Time Evolution of the Wigner Function for Open Quantum Systems. *Phys. Rev. A: At, Mol., Opt. Phys.* **2015**, *92*, 042122.
- (2) Esposti, M. D.; Graffi, S. In *The Mathematical Aspects of Quantum Maps*; Esposti, M. D., Graff, S., Eds.; Springer: Berlin, Germany, 2003; pp 49–90.
- (3) von Neumann, J. Die Eindeutigkeit der Schrödingerschen Operatoren. *Mathematische Annalen* **1931**, *104*, 570–578.
- (4) Gabor, D. Theory of Communication. Part 1: The Analysis of Information. *Journal of the Institution of Electrical Engineers - Part III: Radio and Communication Engineering* **1946**, *93*, 429–441.
- (5) Davis, M. J.; Heller, E. J. Semiclassical Gaussian Basis Set Method for Molecular Vibrational Wave Functions. *J. Chem. Phys.* **1979**, *71*, 3383–3395.
- (6) Poirier, B.; Salam, A. Quantum Dynamics Calculations using Symmetrized, Orthogonal Weyl-Heisenberg Wavelets with a Phase Space Truncation Scheme. III. Representations and Calculations. *J. Chem. Phys.* **2004**, *121*, 1704–1724.
- (7) Lombardini, R.; Poirier, B. Improving the Accuracy of Weyl-Heisenberg Wavelet and Symmetrized Gaussian Representations using Customized Phase Space Region Operators. *Phys. Rev. E* **2006**, *74*, 036705.
- (8) Halverson, T.; Poirier, B. Large Scale Exact Quantum Dynamics Calculations: Ten thousand Quantum States of Acetonitrile. *Chem. Phys. Lett.* **2015**, *624*, 37–42.
- (9) Halverson, T.; Poirier, B. One Million Quantum States of Benzene. *J. Phys. Chem. A* **2015**, *119*, 12417–12433. PMID: 26418314.

- (10) Dimler, F.; Fechner, S.; Rodenberg, A.; Brixner, T.; Tannor, D. J. Accurate and Efficient Implementation of the von Neumann Representation for Laser Pulses with Discrete and Finite Spectra. *New J. Phys.* **2009**, *11*, 105052.
- (11) Shimshovitz, A.; Tannor, D. J. Phase-Space Approach to Solving the Time-Independent Schrödinger Equation. *Phys. Rev. Lett.* **2012**, *109*, 070402.
- (12) Takemoto, N.; Shimshovitz, A.; Tannor, D. J. Communication: Phase Space Approach to Laser-Driven Electronic Wavepacket Propagation. *J. Chem. Phys.* **2012**, *137*, 011102.
- (13) Whittaker, E. T. XVIII - On the Functions which are Represented by the Expansions of the Interpolation-Theory. *Proc. R. Soc. Edinburgh* **1915**, *35*, 181–194.
- (14) Nyquist, H. Certain Topics in Telegraph Transmission Theory. *Trans. Am. Inst. Electr. Eng.* **1928**, *47*, 617–644.
- (15) Shannon, C. Communication in the Presence of Noise. *Proc. IRE* **1949**, *37*, 10–21.
- (16) Kosloff, R. In *Numerical Grid Methods and Their Application to Schrödinger's Equation*; Cerjan, C., Ed.; Springer: Dordrecht, The Netherlands, 1993; pp 175–194.
- (17) Assémat, E.; Machnes, S.; Tannor, D. J. Double Ionization of Helium from a Phase Space Perspective. *arXiv:1502.05165 [quant-ph]* **2015**.
- (18) Marston, C. C.; Balint-Kurti, G. G. The Fourier grid Hamiltonian Method for Bound State Eigenvalues and Eigenfunctions. *J. Chem. Phys.* **1989**, *91*, 3571–3576.
- (19) Fattal, E.; Baer, R.; Kosloff, R. Phase Space Approach for Optimizing Grid Representations: The Mapped Fourier Method. *Phys. Rev. E: Stat. Phys., Plasmas, Fluids, Relat. Interdiscip. Top.* **1996**, *53*, 1217–1227.
- (20) Colbert, D. T.; Miller, W. H. A Novel Discrete Variable Representation for Quantum Mechanical Reactive Scattering via the S-matrix Kohn Method. *J. Chem. Phys.* **1992**, *96*, 1982–1991.
- (21) Tannor, D. J. *Introduction to Quantum Mechanics: A Time-Dependent Perspective*; University Science Books: Sausalito, CA, 2007.
- (22) Reference 11, Supporting Information 1.
- (23) Note the different definition of the norm from that in ref 21.
- (24) Genossar, T.; Porat, M. Optimal Bi-Orthonormal Approximation of Signals. *IEEE Transactions on Systems, Man and Cybernetics* **1992**, *22*, 449–460.
- (25) Tannor, D. J.; Takemoto, N.; Shimshovitz, A. Phase Space Approach to Solving the Schrödinger Equation: Thinking Inside the Box, *Advances in Chemical Physics*. In *Advances in Chemical Physics*; John Wiley & Sons, Inc: Hoboken, NJ, 2014; Vol. 156.
- (26) Shimshovitz, A.; Bacic, Z.; Tannor, D. J. The von Neumann Basis in non-Cartesian Coordinates: Application to Floppy Triatomic Molecules. *J. Chem. Phys.* **2014**, *141*, 234106.
- (27) Brown, J.; Carrington, T. Using an Iterative Eigensolver to Compute Vibrational Energies with Phase-Spaced Localized Basis Functions. *J. Chem. Phys.* **2015**, *143*, 044104.
- (28) Fechner, S.; Dimler, F.; Brixner, T.; Gerber, G.; Tannor, D. J. The von Neumann Picture: a New Representation for Ultrashort Laser Pulses. *Opt. Express* **2007**, *15*, 15387–15401.
- (29) Daubechies, I. The Wavelet Transform, Time-Frequency Localization and Signal Analysis. *IEEE Trans. Inf. Theory* **1990**, *36*, 961–1005.
- (30) The transformation from the Fourier to the PvN basis can be accomplished using approximately $N \times \ln(N)$ operations using a Fast Gabor Transform,³³ which is closely related to the Fast Fourier Transform.
- (31) Bai, Z.; Demmel, J.; Dongarra, J.; Ruhe, A.; van der Vorst, H. In *Templates for the Solution of Algebraic Eigenvalue Problems*; Bai, Z., Demmel, J., Dongarra, J., Ruhe, A., van der Vorst, H., Eds.; Society for Industrial and Applied Mathematics, 2000.
- (32) Machnes, S.; Assémat, E.; Tannor, D. J. Quantum Dynamics in Phase Space using the Biorthogonal von Neumann bases: Algorithmic Considerations. In *arXiv:1603.03963 [quant-ph]*. To be published **2016**.
- (33) Wang, L.; Chen, C.-T.; Lin, W.-C. An Efficient Algorithm to Compute the Complete set of Discrete Gabor Coefficients. *IEEE Transactions on Image Processing* **1994**, *3*, 87–92.
- (34) Dawes, R.; Carrington, T. How to choose one-dimensional basis functions so that a very efficient multidimensional basis may be extracted from a direct product of the one-dimensional functions: Energy levels of coupled systems with as many as 16 coordinates. *J. Chem. Phys.* **2005**, *122*, 134101.
- (35) Dawes, R.; Carrington, T. Using simultaneous diagonalization and trace minimization to make an efficient and simple multidimensional basis for solving the vibrational Schrödinger equation. *J. Chem. Phys.* **2006**, *124*, 054102.

I.1.2.4. Complementary Information

Unfortunately, a typo appears in the definition of the two-dimensional double-well potential H_{2D-DW} in Eq. (65) in the publication (page 63). The correct form with the correction highlighted in red is

$$H_{2D-DW} = -\frac{1}{2 \times 200}(\partial_x^2 + \partial_y^2) + 6.4(x - 1)^2(x - 2)^2 + 37.5(y - 2)^2 + 0.05x^2y. \quad (\text{I.1.6})$$

The wrong value in the coupling term x^2y was 10 instead of 0.05 (a division by 200 has been omitted). Thus, the potential is only weakly coupled. However, this does not affect the conclusions drawn from this example, because the efficiency of **PvB** does not depend on the amount of correlation but on the phase-space sparsity. This is in contrast to the **MCTDH** method.

I.1.3. Publication: Projected Weylets and Discrete Variable Representations

I.1.3.1. Own Contributions

- Implementation of a pruned quantum dynamics program from scratch (see [Chapter I.3](#)).⁷
- Identification of the nonorthogonality as the central issue of applying PvB to quantum dynamics.
- Idea of using and combining Weylets with the projection idea of PvB; development of pW.
- Development of the required algorithms, especially the efficiently scaling matrix-vector product based on permutations and the update of the set of new basis functions using hash tables.
- Reevaluation of coordinate space methods (DVR in this case) for pruning.
- Setup, execution, analysis and interpretation of all simulations. The usage of NO₂ as a test example was a suggestion by U. Manthe.
- Writing and editing of the whole article (some parts of Section I are due to B. Hartke).

I.1.3.2. Bibliographic Data

Title Efficient molecular quantum dynamics in coordinate and phase space using pruned bases

Authors Henrik R. Larsson, Bernd Hartke and David J. Tannor

Journal The Journal of Chemical Physics

Volume 145

Issue 20

Page 204108

Year 2016

DOI [10.1063/1.4967432](https://doi.org/10.1063/1.4967432)

Note Reprinted from [The Journal of Chemical Physics 145, 204108 (2016)], with the permission of AIP Publishing.

Preprint <https://arxiv.org/abs/1606.04004>

⁷Some parts related to the setup of PvB and the pruning are inspired but reimplemented by a code written by S. Machnes and E. Assémat.

I.1.3.3. Article

THE JOURNAL OF CHEMICAL PHYSICS 145, 204108 (2016)



Efficient molecular quantum dynamics in coordinate and phase space using pruned bases

H. R. Larsson,^{1,a)} B. Hartke,¹ and D. J. Tannor²¹*Institut für Physikalische Chemie, Christian-Albrechts-Universität zu Kiel, 24098 Kiel, Germany*²*Department of Chemical Physics, Weizmann Institute of Science, 76100 Rehovot, Israel*

(Received 28 June 2016; accepted 28 October 2016; published online 28 November 2016)

We present an efficient implementation of dynamically pruned quantum dynamics, both in coordinate space and in phase space. We combine the ideas behind the biorthogonal von Neumann basis (PvB) with the orthogonalized momentum-symmetrized Gaussians (Weylets) to create a new basis, projected Weylets, that takes the best from both methods. We benchmark pruned time-dependent dynamics using phase-space-localized PvB, projected Weylets, and coordinate-space-localized DVR bases, with real-world examples in up to six dimensions. For the examples studied, coordinate-space localization is the most important factor for efficient pruning and the pruned dynamics is much faster than the unpruned, exact dynamics. Phase-space localization is useful for more demanding dynamics where many basis functions are required. There, projected Weylets offer a more compact representation than pruned DVR bases. *Published by AIP Publishing.* [<http://dx.doi.org/10.1063/1.4967432>]

I. INTRODUCTION

Chemical reaction dynamics can be studied theoretically by molecular quantum dynamics.¹ Especially, quantum effects like resonances and tunneling can be very important for the correct description of molecular processes in chemical reactions.^{2–5} Classical or semi-classical methods may fail to describe this. However, the exact treatment of molecular quantum dynamics is hampered by the exponential scaling of the underlying direct-product basis with the dimensionality of the system. Exact quantum dynamics based on a direct-product basis is now possible for up to five-atomic systems or nine degrees of freedom.^{6,7} Dynamics in reduced dimensionality is possible for six atoms and has been successfully applied.^{8–10} However, in reduced dimensionality dynamics, the explicitly treated degrees of freedom and the methods for approximate treatment of the other degrees of freedom have to be selected and tested carefully, otherwise the results may deviate qualitatively from full-dimensional computations.^{11,12}

A physically motivated route towards reducing or even overcoming the exponential scaling aims at representing the wavefunction not everywhere in configuration space but only where it is needed. In a very general and hence very robust sense, this is certain to incur huge savings, since in typical chemical situations the vibrational wavefunction has many degrees of freedom but is narrowly confined in most of them—simply because chemistry is not about many electrons and bare nuclei colliding at high speeds (which corresponds to the wavefunction covering large parts of coordinate space and/or phase space) but rather about stable molecules undergoing well-defined reactions, which means that chemical energies are just above one or a few barriers. There simply is not enough energy to break arbitrary bonds in a reactant molecule. Hence,

the mathematically simple and thus appealing direct-product bases already are wasteful for dynamics of small molecules and become even more wasteful for larger molecules.

A conceptually elegant way to exploit these characteristics is to employ a basis representation of the wave packet in which the basis functions themselves move around and follow the wave packet, e.g., time-dependent Gaussians. These Gaussians are either moved in time by classical mechanics or by proper quantum treatment. There is a plethora of established methods like G-MCTDH,^{13,14} its cousin variational Multi-configurational Gaussians, vMCG,^{15,16} the matching-pursuit algorithm, MP-SOFT,¹⁷ multiple spawning dynamics,^{18,19} or the coupled coherent state approach.²⁰ However, these methods are either not fully exact or often suffer from numerical difficulties.¹⁶

Another possibility is to use an optimal time-dependent direct-product basis built upon a larger time-independent primitive basis. The outcome is then the multi-configurational time-dependent Hartree (MCTDH) algorithm.^{21,22} MCTDH and especially its multilayer variant (ML-MCTDH)^{23–25} are often an efficient way to reduce the exponential scaling. Although a direct-product basis is still used, the number of needed basis functions is drastically reduced. This achievement comes with a much more complicated algorithm and it may work less well for dynamics with strongly coupled modes. Further, to find proper mode combinations in normal MCTDH (to optimize multidimensional bases for efficiency) or tree structures in ML-MCTDH is a nontrivial task.^{26,27}

Using lower-dimensional direct-product bases to create contracted basis functions has been found to be very successful for quantum (ro-)vibrational computations.^{28–35} A contracted basis was even used for computing vibrational energy levels of 12-dimensional CH₅⁺.³⁶

Yet another possibility, which certainly can be combined with the MCTDH ansatz, is to prune a time-independent direct-product basis and choose only those functions that are

^{a)}Electronic mail: larsson@pctc.uni-kiel.de

necessary to describe the wave function. This approach is very successful for solving the time-independent Schrödinger equation, i.e., retrieving the eigenfunctions. It can be simply implemented by discarding functions that are located at points with high potential,^{28,29} or by more advanced techniques like simultaneous diagonalization,^{37,43,44} utilization of phase-space-structured basis functions^{38–41} or sparse grids.^{42,45,46} It has also been used for time-independent scattering simulations.⁴⁷

For solving the time-dependent Schrödinger equation, e.g., for simulating time-dependent quantities in a chemical reaction, pruning is much more complicated because the wavepacket moves in time. One may use static pruning.^{48,49} Especially, an L-shaped selection of basis functions localized in coordinate space has been used very successfully in quantum scattering simulations.⁵⁰ However, a more general pruning scheme that really adapts the basis in time should be much more efficient. This has been implemented and thoroughly tested by Hartke and co-workers for coordinate-space localized Gaussians⁵¹ and orthogonalized Gaussians based on collocation.⁵² McCormack showed that it is a possible avenue for coordinate-space-localized discrete variable representation (DVR) functions and phase-space-localized functions but did not present an implementation.⁵³ Pettey and Wyatt implemented pruning by a moving grid.^{54,55} An additional advantage of dynamical pruning is the ability to compute the needed points of the potential energy surface (PES) on the fly during the dynamics, instead of pre-computing the PES prior to the dynamics, which makes it hard to avoid computing PES points that are never needed and to avoid exponential scaling already at this stage.

Because the wave packet is most often not only confined in coordinate space but also exhibits structured motion in phase space (combined position x and momentum p), pruning based on phase-space-localized functions generally gives more compact representations. However, obtaining an accurate and prunable basis of a well-defined rectangular grid of phase-space-localized functions is far from trivial⁵⁶ and has only been established in the last few years.^{57–60} Until now, the so-called Weylets and momentum-symmetrized Gaussians by Poirier *et al.* have not been used for quantum dynamics simulations but only for computing eigenstates. There, they have been shown to be very successful.^{40,59,61–64} The periodic von Neumann basis with biorthogonal exchange, PvB, from Tannor and co-workers has been both successfully applied to vibrational eigenstates⁴¹ and to electronic dynamics.^{65,66} It has not yet been used in time-dependent molecular quantum dynamics.

In this contribution, we develop a very efficient implementation of dynamical, time-dependent pruning. We benchmark several bases using two-, three-, and six-dimensional examples. The bases we employ are coordinate-space-localized DVR functions, the biorthogonal von Neumann basis, PvB, and a novel method, called projected Weylets, which combines the idea behind PvB with the Weylet basis to create a basis that inherits the advantages of the PvB methods without inheriting its disadvantage, namely nonorthogonality.

Our implementation is based on Hamiltonians that are a sum of products (SoP) of one-dimensional operators. Poirier

and co-workers used SoP Hamiltonians for their computations using Weylets and symmetrized Gaussians.^{40,59,62–64} Moreover, Brown and Carrington have used the momentum-symmetrized Gaussians of Poirier together with SoP Hamiltonians for vibrational computations.⁶⁷ Many other methods require SoP Hamiltonians or are much more efficient if SoP Hamiltonians are utilized,^{22,68,69} and there are many algorithms available to fit the Hamiltonian in a SoP form efficiently, notably potfit and variants thereof,^{70–72} neural networks,^{73,74} or some interpolation techniques.^{75,76} Note, however, that pruned DVR bases do not require SoP Hamiltonians (to be precise: A SoP form of the potential) and we show that these bases can be very successfully pruned.

The remainder of this article is organized as follows: Section II A gives an overview of exact quantum dynamics with a direct-product basis. A review of the PvB method, its drawbacks in high dimensions, and the Weylets follow in Sections II B and II C, respectively. We present our new projected Weylets in Section II D, followed by details of the numerical implementation in Section II E and the Appendix. The mentioned methods and a pruned DVR basis are tested in Section III. Section IV summarizes the most important points of this work and gives an outlook.

II. THEORY

A. Overview

The standard approach in molecular quantum dynamics for solving the time-dependent Schrödinger equation is to expand the D -dimensional wave function in a direct product of time-independent basis functions $\{|\chi_{i_k}^{(\kappa)}\rangle\}_{i_k=1}^{n_\kappa}$,^{1,22}

$$|\Psi(t)\rangle = \sum_{i_1=1}^{n_1} \cdots \sum_{i_D=1}^{n_D} a_{i_1 i_2 \dots i_D} \bigotimes_{\kappa=1}^D |\chi_{i_\kappa}^{(\kappa)}\rangle. \quad (1)$$

The size of the coefficient tensor, \mathbf{a} , scales as $\prod_{\kappa=1}^D n_\kappa = \bar{n}^D$, where \bar{n} is the geometric mean of the number of basis functions. A discrete variable representation (DVR) is often used as the underlying basis, $\{|\chi_{i_k}^{(\kappa)}\rangle\}$.¹ This ansatz is then inserted into the time-dependent Schrödinger equation,

$$i \frac{\partial}{\partial t} |\Psi(t)\rangle = \hat{H} |\Psi(t)\rangle, \quad (2)$$

to obtain

$$i \frac{\partial}{\partial t} \mathbf{a}(t) = \mathbf{H} \mathbf{a}(t), \quad (3)$$

$$H_{IJ} = \bigotimes_{\kappa=1}^D \bigotimes_{\tau=1}^D \langle \chi_{i_\kappa}^{(\kappa)} | \hat{H} | \chi_{j_\tau}^{(\tau)} \rangle, \quad (4)$$

where we have introduced multi-indices $I \equiv i_1 i_2 \dots i_D$. Throughout the text, we use atomic units unless stated otherwise. Eq. (3) can be solved using standard integrators that require many tensor transformations of the type $\mathbf{H} \mathbf{a}$. Using multi-indices, this tensor transformation can be considered as a matrix-vector product. The terms “tensor transformation” and “matrix-vector product” will be taken as a synonym throughout the text.

The direct-product basis is conceptually simple and easy to implement. A DVR basis allows further simplifications due to the diagonality of the potential operator \hat{V} which leads to diagonal matrices, i.e., $V_{IJ} \propto \delta_{IJ}$. The problem is the exponential scaling of the size of the coefficient tensor, \mathbf{a} . When using a DVR as the underlying basis, the basis functions are localized in coordinate space. Since the wavepacket is normally not spread over the whole multidimensional coordinate space, the coefficient tensor \mathbf{a} is sparse and it is possible to prune the basis. By using a phase-space-localized basis, the coefficient tensor gets sparser and pruning is often more efficient. Secs. II B and II C will deal with phase-space-localized basis functions.

B. Biorthogonal projected von Neumann basis

1. Theoretical foundations

A grid of phase-space-localized basis functions is established with von Neumann functions^{77,78}

$$\langle x | \tilde{g}_{nl} \rangle = \left(\frac{2\alpha}{\pi} \right)^{\frac{1}{4}} \exp \left[-\alpha(x - x_n)^2 + i \times p_l(x - x_n) \right], \quad (5)$$

$$\alpha = \frac{\Delta p}{2\Delta x}. \quad (6)$$

The basis functions are localized at (x_n, p_l) in phase space with widths Δp and Δx in p and x . They are placed on a rectangular lattice in phase space with rectangles of widths Δp and Δx such that $\Delta x \Delta p = 2\pi$, which is the size of a unit cell in phase space. This assures that the basis is complete but not overcomplete. The von Neumann basis was used by Davis and Heller but they found very poor convergence.⁵⁶ This may be understood as a consequence of the theorem of Balian and Low which states that a phase-space-localized basis is incompatible with completeness for all practical purposes.^{79–81} Shimshovitz and Tannor have shown that projecting the von Neumann functions to a different (DVR-like) basis $\{|\chi_i\rangle\}$ solves this problem,⁶⁰

$$|g_i\rangle = \sum_j |\chi_j\rangle \langle \chi_j | \tilde{g}_i \rangle = \sum_j |\chi_j\rangle \sqrt{\omega_j} \langle \chi_j | \tilde{g}_i \rangle. \quad (7)$$

Here, the von Neumann functions are labeled by a multi-index. The last equality comes from the DVR properties of $\{|\chi_i\rangle\}$. $\omega_j = W_j/\omega(x_j)$, where W_j is the quadrature weight of the DVR point x_j and $\omega(x_j)$ the weight function of the underlying DVR polynomials.¹ Since Eq. (7) denotes just a similarity transformation, utilization of $|g_i\rangle$ to solve the Schrödinger equations gives exactly the same eigenvalues as with the DVR basis. However, the basis $\{|\chi_i\rangle\}$ has to occupy the same area in phase space to render the transformation bijective. The Fourier Grid Hamiltonian (FGH) DVR fulfills this property and is thus often used.^{1,82} This makes the $|g_i\rangle$ periodic. However, other (nonperiodic) DVR bases like the sinc DVR or Gauss-Legendre DVR (for angular coordinates) are possible (see also Section III B).^{1,41,47} Other non-DVR bases or even simple Newton-Cotes quadrature work as well.

These basis functions are localized in phase space, but their coefficients are not, because they include a linear combination of the inverse of the overlaps of the $|g_j\rangle$,

$$|\Psi\rangle = \sum_m |g_m\rangle^g a_m = \sum_{m=1}^N |g_m\rangle \sum_{n=1}^N [{}^g S^{-1}]_{mn} \langle g_n | \Psi \rangle, \quad (8)$$

$${}^g \mathbf{S} = \mathbf{G}^\dagger \mathbf{G}. \quad (9)$$

Left superscripts indicate the employed basis. Because ${}^g \mathbf{S}^{-1}$ is not sparse, the coefficients ${}^g a_m$ are dense and pruning is not possible. Shimshovitz and Tannor solved this problem by transforming to the biorthogonal basis where

$$|b_n\rangle = \sum_{m=1}^N |g_m\rangle [{}^g S^{-1}]_{mn}, \quad \langle b_n | g_m \rangle = \delta_{mn}, \quad (10)$$

$$|\Psi\rangle = \sum_{m=1}^N |b_m\rangle^b a_m = \sum_{m=1}^N |b_m\rangle \langle g_m | \Psi \rangle. \quad (11)$$

The coefficients in these representations are just the overlap of the wavefunction with phase-space-localized $|g_i\rangle$ and hence sparse. Note that $\langle x | b_i \rangle$ is anything but localized, which is a manifestation of the Balian-Low theorem.^{81,83} Indeed, it does not matter whether the basis is localized but whether the coefficients are. $\langle b_i | \Psi \rangle$ is actually the expansion coefficient in the $|g\rangle$ representation, compare with Eqs. (8) and (10). The basis $\{|b_i\rangle\}$ is called the periodic von Neumann basis with biorthogonal exchange (PvB). Because the basis was initially based on FGH functions, it was termed periodic. However, since also other basis functions can be used and because the essential part in Eq. (7) is the projection onto the DVR basis and not its periodicity, the basis may also be dubbed projected von Neumann basis.

Because the basis is nonorthogonal, the Schrödinger equation takes the form

$$i^b \mathbf{S} \frac{\partial}{\partial t} {}^b \mathbf{a} = {}^b \mathbf{H} {}^b \mathbf{a}, \quad (12)$$

where ${}^b \mathbf{H}$ is just the congruence-transformed DVR Hamiltonian ${}^x \mathbf{H}$,⁸⁴

$${}^b \mathbf{H} = \mathbf{B}^\dagger {}^x \mathbf{H} \mathbf{B}, \quad B_{ji} = \sqrt{\omega_j} \langle \chi_j | b_i \rangle \quad (13)$$

2. Drawbacks in high dimensions

In the following, we will assume that the Hamiltonian can be decomposed as a sum of direct products (SoP) of one-dimensional matrices,

$${}^x \mathbf{H} = \sum_{l=1}^g \bigotimes_{\kappa=1}^D \chi_{\mathbf{h}}^{(\kappa,l)}. \quad (14)$$

Each matrix $\chi_{\mathbf{h}}^{(\kappa,l)}$ needs then to be transformed as shown in Eq. (13), which comes with essentially no computational cost. If the Hamiltonian possesses the SoP form, the matrix-vector product scales as $\mathcal{O}(\bar{n}^{D+1})$ instead of $\mathcal{O}(\bar{n}^{2D})$, if the matrix-vector product or tensor transformation is done sequentially.^{85,86} To give an example, consider a three-dimensional problem with $g = 1$,

$$\begin{aligned} (\mathbf{H}\mathbf{a})_{pqr} &= a'_{pqr} = \sum_{i=1}^{n_1} \sum_{j=1}^{n_2} \sum_{k=1}^{n_3} h_{pi}^{(1)} h_{qj}^{(2)} h_{rk}^{(3)} a_{ijk} \\ &= \sum_{i=1}^{n_1} h_{pi}^{(1)} \underbrace{\sum_{j=1}^{n_2} h_{qj}^{(2)} \sum_{k=1}^{n_3} h_{rk}^{(3)} a_{ijk}}_{\tilde{a}_{ijr}}. \end{aligned} \quad (15)$$

The $\mathcal{O}(\bar{n}^{D+1})$ scaling is achieved by first computing all needed values of \tilde{a}_{ijr} , reusing them for computing all needed values of \tilde{a}_{iqr} , and reusing those for the final transformation to a'_{pqr} .

If one prunes the basis, some coefficients a_{abc} are neglected and only $\tilde{n}_\kappa < n_\kappa$ basis functions are used in dimension κ . The pruning can be formulated by introducing sets \mathcal{I} , $\mathcal{J}(a)$, and $\mathcal{K}(a, b)$ that store the indices of the used basis functions. Eq. (15) then takes the form

$$\begin{aligned} a'_{pqr} &= \sum_{i \in \mathcal{I}} h_{pi}^{(1)} \sum_{j \in \mathcal{J}(i)} h_{qj}^{(2)} \sum_{k \in \mathcal{K}(i,j)} h_{rk}^{(3)} a_{ijk} \\ &= \sum_{i \in \mathcal{I}} h_{pi}^{(1)} \tilde{a}_{iqr}, \quad \tilde{a}_{iqr} = \sum_{j \in \mathcal{J}(i)} h_{qj}^{(2)} \tilde{a}_{ijr}, \quad \dots \end{aligned} \quad (16)$$

Wang and Carrington used a similar form for specific index ranges.⁸⁷ Here, no assumptions about the structure in the pruning are made. In these expressions, values of \tilde{a}_{iqr} are needed for the computation of \mathbf{a}' that are not included in the index sets, i.e., q may not be an element of $\mathcal{J}(i)$ and r may not be an element of $\mathcal{K}(i, q)$. Then, in principle, almost all possible index combinations of \tilde{a}_{iqr} need to be evaluated. The same holds for the needed values of $\tilde{\mathbf{a}}$ for the computation of $\tilde{\mathbf{a}}$. However, if the coefficient tensor is sparse and the Hamiltonian transforms it to the same sparse representation, the partially transformed tensors $\tilde{\mathbf{a}}$ and $\tilde{\mathbf{a}}$ are sparse as well and the values of coefficients which are not elements of the employed set of the initial tensor can be neglected. The favorable scaling of order $\mathcal{O}(\bar{n}^{D+1})$ results. An efficient implementation for this pruned tensor transformation is presented in the Appendix.

Because the PvB representation is nonorthogonal, matrix-vector products of type $\mathbf{S}^{-1} \mathbf{H} \mathbf{a}$ are needed. Here, we cannot assume that the partially transformed tensors $\tilde{\mathbf{a}}$ and $\tilde{\mathbf{a}}$ are sparse, because $\mathbf{a}' = \mathbf{H} \mathbf{a}$ transforms the basis into the non-sparse $|g\rangle$ representation [see text below Eq. (11)],

$$a'_I = \sum_J \langle b_I | \hat{H} | b_J \rangle \langle g_J | \Psi \rangle = \langle b_I | \hat{H} | \Psi \rangle. \quad (18)$$

Only the final multiplication with \mathbf{S}^{-1} transforms the tensor back into the sparse $|b\rangle$ representation. Hence, one has to either compute all needed partially transformed coefficients which at worst results in a $\mathcal{O}(\bar{n}^{D+1})$ scaling instead of $\mathcal{O}(\bar{n}^{D+1})$, or one has to do the transformation in Eq. (15) directly to obtain a $\mathcal{O}(\bar{n}^{2D})$ scaling. None of these options are favorable.

Further, the inverse of the pruned overlap matrix is not decomposable into a SoP form. In a full basis, the overlap matrix obeys the SoP form and so does its inverse,

$$\mathbf{S} = \bigotimes_{\kappa=1}^D \mathbf{S}^{(\kappa)}. \quad (19)$$

\mathbf{S} is the multidimensional tensor and $\mathbf{S}^{(\kappa)}$ one-dimensional matrices. Pruning the basis means that some rows and columns are removed from \mathbf{S} . Then, the inverse of \mathbf{S} in the truncated basis has no structure to exploit. Either one needs to compute it explicitly and store a huge matrix of size \bar{n}^{2D} or one

needs to compute $\mathbf{S}^{-1} \mathbf{a}'$ via direct algorithms like conjugate gradient that perform many $\mathbf{S} \mathbf{a}'$ operations (typically more than 100 for numerical accuracy). We conclude that, due to its phase space locality and DVR accuracy, the PvB representation has very appealing properties. However, its nonorthogonality results in the unfavorable $\mathcal{O}(\bar{n}^{2D})$ scaling when computing the matrix-vector product.

It is possible to approximate the inverse of the pruned overlap matrix by pruning the inverse of the unpruned overlap matrix.^{67,84,88} Then, the matrix-vector product $\mathbf{S}^{-1} \mathbf{H} \mathbf{a} = \tilde{\mathbf{H}} \mathbf{a}$ can be done in one step and the favorable $\mathcal{O}(\bar{n}^{D+1})$ scaling is recovered.^{67,88} The introduced approximation is, however, difficult to control and is only useful for time-dependent quantum dynamics if very low accuracy is passable.⁸⁴ It may, however, be useful for computing vibrational eigenstates where this approximation is not severe.^{67,84,88}

C. Weylet representation

In Sec. II B 2, we have shown that the nonorthogonality causes problems if the PvB representation is employed for pruning. Due to the Balian-Low theorem, an orthogonal phase-space-localized basis is not possible.⁷⁹⁻⁸¹ However, Wilson⁸⁹ and Daubechies *et al.*⁹⁰ have shown that it is possible to obtain a momentum-symmetrized basis that can be orthogonalized without jeopardizing its locality, so called ‘‘Weyl-Heisenberg’’ wavelets (Weylets). Poirier refined this basis and found a simpler orthogonalization procedure.⁵⁷⁻⁵⁹ The momentum-symmetrized Gaussians are

$$\begin{aligned} \langle x | \tilde{\phi}_{nl} \rangle &= \left(\frac{8\alpha}{\pi} \right)^{\frac{1}{4}} \exp \left[-\alpha(x - x_n)^2 \right] \\ &\times \sin \left[p_l \left(x - x_n - \sqrt{\frac{\pi}{8\alpha}} \right) \right]. \end{aligned} \quad (20)$$

They are localized in x_n and $\pm p_l$ and real-valued. The phase factor in the sine term is crucial to greatly reduce linear dependencies. To maintain completeness, the functions are further placed on a doubly dense grid, i.e., $\Delta x \Delta p = \pi$ and $p_l \neq 0$. For further details, we refer to Refs. 58 and 59.

Although the underlying basis is symmetrized in p , because it is doubly dense it can describe states that are not symmetric in p . One unit-cell on the upper (or lower) plane in phase space has contributions from two momentum-symmetrized Gaussians and a proper linear combination can then describe states of arbitrary shape in phase space, as they occur in time-dependent quantum dynamics.

The symmetrized Gaussians are then orthogonalized via symmetric Löwdin orthogonalization, i.e., using $\mathbf{S}^{-1/2}$.⁹¹ Since this basis is infinite-dimensional, in principle, $\mathbf{S}^{-1/2}$ has to be infinite-dimensional as well. However, the basis actually sets up a ‘‘tight’’ frame, i.e., the basis functions are as orthogonal as possible and the overlap between two functions decays exponentially.⁵⁸ It is thus sufficient to obtain $\mathbf{S}^{-1/2}$ for a reasonably large basis. Poirier and Salam have listed the needed values of $\mathbf{S}^{-1/2}$ to high accuracy in Ref. 58.

Weylets have the drawback that, compared to symmetrized Gaussians, the transformation of the matrix elements to the Weylet basis can be quite cumbersome (see

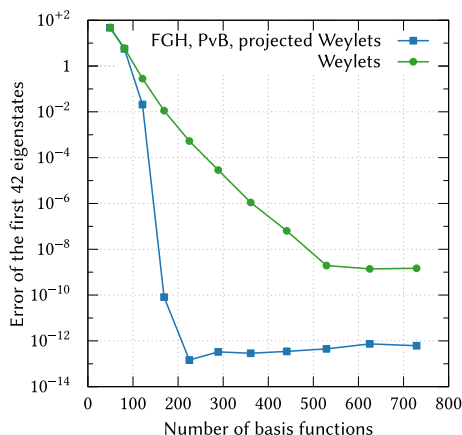


FIG. 1. Convergence of the Weylets (without projection) compared to a FGH DVR basis for the first 42 states of the harmonic oscillator, $\hat{H} = (-\partial_x^2 + x^2)/2$. The FGH-eigenvalues are identical to PvB and projected Weylets (Section II D). As the basis size is enlarged, both the x -range and the maximal momentum are increased such that a square area in phase space is covered. For each basis size, both bases span roughly the same phase-space area.

Section i of the [supplementary material](#)), especially if the Hamiltonian does not obey a SoP form.^{59,61} Even without pruning, the basis in certain situations is not as accurate as a Fourier basis. A comparison of the convergence of Weylets, PvB, FGH, and projected Weylets (pW, see Section II D) for the eigenvalues of the harmonic oscillator is shown in Fig. 1. The error is defined by the Euclidian L_2 distance between the exact and the numerical energies. It decreases much faster for FGH than for the Weylets. The asymptotic error of the Weylets stems from the limited accuracy (12 digits) of $\mathbf{S}^{-1/2}$ which has been taken from Ref. 58. In practical calculations, this does not matter. Since both PvB and projected Weylets are a similarity transformed FGH basis, they give the same eigenvalues as the FGH basis (apart from numerical noise). In Section ii of the [supplementary material](#), we show further comparisons of Weylets against FGH, PvB, and pW. We show there that for a pruned basis (no rectangular phase-space area), the error of the Weylets is almost identical to that of pW.

Poirier and co-workers avoid the transformation to the Weylet basis by working solely with the nonorthogonal symmetrized Gaussians. They soften the $\mathcal{O}(\bar{n}^{2D})$ scaling by massive parallelization.^{62,63} Note that this scaling is a function of the number of pruned direct-product basis functions, \bar{n} .

D. Projected Weylets

The relatively elaborate transformation needed for the creation of the Weylets (compared to the creation of momentum-symmetrized Gaussians) can be reduced by combining them with elements of the projected von Neumann basis. First, the momentum-symmetrized Gaussians are projected onto the DVR lattice,

$$|\phi_i\rangle = \sum_j |\chi_j\rangle \langle \chi_j | \tilde{\phi}_i \rangle = \sum_j |\chi_j\rangle \sqrt{\omega_j} \langle \chi_j | \tilde{\phi}_i \rangle, \quad (21)$$

compare with Eq. (7). The projected Weylets, $\langle x | w_i \rangle$, are then defined on the DVR grid as

$$W_{ji} = \langle \chi_j | w_i \rangle, \quad (22)$$

$$\mathbf{W} = \mathbf{\Phi} \mathbf{\Phi} \mathbf{S}^{-1/2}, \quad (23)$$

$$\Phi_{ji} = \sqrt{\omega_j} \langle \chi_j | \tilde{\phi}_i \rangle, \quad \mathbf{\Phi} \mathbf{S} = \mathbf{\Phi}^\dagger \mathbf{\Phi}. \quad (24)$$

In Ref. 67, Brown and Carrington mention in passing the possibility of projecting the momentum-symmetrized Gaussians onto a DVR grid, without implementing it. They do not consider orthogonalization. Instead of employing momentum-symmetrized Gaussians $|\tilde{\phi}\rangle$, one could also use the continuous Weylets as the initial basis. However, the numerical difference between these options is negligible. Instead of using orthogonalized functions, it is possible to use the biorthogonal basis and approximate the pruned inverse overlap matrix (see the last paragraph in Section II B 2). Due to the more banded structure of the overlap matrix on a doubly dense grid, this approximation would be less severe than for PvB.

The matrix representation of the Hamiltonian is again obtained by a similarity transformation of the DVR Hamiltonian, see Eq. (13), and DVR accuracy is maintained. \mathbf{W} represents now an orthogonal, momentum-symmetrized localized basis in phase space that has the same convergence properties as the underlying DVR basis, provided that $\{|\phi_i\rangle\}$ and $\{|\chi_i\rangle\}$ span the same area in phase space. The only drawback that remains is the transformation of the Hamiltonian if it does not possess a SoP form. However, the sparsity of the transformed Hamiltonian, $\mathbf{W}^{\dagger X} \mathbf{H} \mathbf{W}$, and the transformation matrix, \mathbf{W} , can be exploited. This cannot be done with PvB, because both $\mathbf{B}^{\dagger X} \mathbf{H} \mathbf{B}$ and \mathbf{B} are dense. The transformation of Hamiltonians without SoP form will be addressed in future publications.

To summarize, the projected Weylets reduce the effort of the more involved transformation of the Weylets because they are set up from a finite set of symmetrized Gaussians and not defined on an infinite plane, like Weylets (see Section i of the [supplementary material](#)). They show no reduction of accuracy compared to Weylets (see Fig. 1 and Figure i in the [supplementary material](#)) and the generation of the basis is as simple as the generation of the PvB basis. Nevertheless, pW should not be regarded as a replacement for Weylets but rather as an alternative in the framework of the projected von Neumann basis.

E. Numerical implementation

Since the set of used basis functions changes during pruned time-dependent dynamics, a careful implementation is required for obtaining an efficient algorithm. Notably, the tensor transformation needs special attention because this is the main bottleneck of the dynamics. A very efficient implementation optimized for operators with SoP form is given in the [Appendix](#). It takes advantage of the fact that the algorithm simplifies significantly if the tensor transformation is performed over the last dimension (assuming this dimension is represented contiguously in memory). For other dimensions, the coefficient tensor is first permuted properly which is not costly compared to the tensor transformation itself.

If a DVR basis is used, no SoP form of the potential is needed and the multiplication of the potential times the vector is just a (direct) vector-vector multiplication, see Section II A. We exploit this for exact dynamics without pruning. For our tests with pruned DVRs, we use the SoP form, for convenience. The potential is then represented as a sum of product of diagonal matrices. This introduces an overhead compared to a simple vector-vector multiplication.

The decision to add or remove basis functions is defined by a wave amplitude threshold, θ . If the absolute value of a coefficient is larger than or equal to θ , the nearest neighbors of the corresponding basis in phase space are added to the set of used basis functions. If they have not already been members of the set of used basis functions, they are included with coefficients set to zero. If the value is smaller than θ and all nearest neighbors have coefficients whose absolute value is smaller as well, the corresponding basis function is excluded from the set. Hartke used two thresholds, one for the inclusion and one for the exclusion of basis functions.^{51,52} We decided to choose only one threshold but we add the possibility to exclude basis functions only if the total number of those to exclude is larger than a certain relative threshold.^{66,92} It remains to choose how many nearest neighbors are added. This is tested numerically in Section III A.

The algorithm and the choice of data structures needed to check the coefficients are crucial. In our implementation, we simply loop over all basis function coefficients and evaluate them successively. The new set of basis function indices is stored in a hash table.^{93,94,112} If new basis functions need to be added, a lookup is required to check whether these basis functions are already elements of the set. If not, they are added to the set. The usage of the hash table is very important because lookup and insertion scale on average as $\mathcal{O}(1)$. Since all basis functions have to be checked, the whole adaption procedure scales as $\mathcal{O}(\bar{n}^D \times N_{\text{neighbor}})$, where N_{neighbor} is the number of nearest neighbors of one basis function. This number is much smaller than \bar{n}^D , see Section III A for a test of how many neighbors have to be added. If no hash table but a simple sorted list of coefficients were used, the scaling would be $\mathcal{O}(\bar{n}^D \times N_{\text{neighbor}} \times \bar{n}^D) = \mathcal{O}(\bar{n}^{2D} \times N_{\text{neighbor}})$ because insertion and removal of duplicates in a sorted array scale linearly. The adaption would then scale worse than the matrix-vector product and would hence become the computational bottleneck of the dynamics. With our implementation using hash tables, the adaption of the set of basis functions never needs more than 5% to 10% of the overall computing time during the dynamics, in the application examples shown below. It could be further optimized by storing the information whether a basis function has neighbors with large coefficient values or not.⁵² If that is the case, there is no need to check or to add neighbors to this basis function.

III. APPLICATION

A. Two-dimensional double well

We test the time-dependent dynamics within a two-dimensional double well employed in Ref. 84. The

Hamiltonian for this model potential is

$$\hat{H}_{\text{DW}} = -\frac{1}{2 \times 200} \left(\frac{\partial^2}{\partial x^2} + \frac{\partial^2}{\partial y^2} \right) + 6.4(x-1)^2 \times (x-2)^2 + 37.5(y-2)^2 + 10x^2y, \quad (25)$$

and the used initial wave packet has the form

$$\langle xy | \Psi(0) \rangle = \frac{\sqrt{2/\pi}}{(0.0008)^{1/4}} \exp[-(x-2.1)^2/0.04 - (y-2.05)^2/0.02]. \quad (26)$$

The wave packet is propagated until $t_e = 24.6$. In x we use a phase-space grid of size $n_x \times n_p = 15 \times 11$ ($x \in [-0.5, 3.7]$), and in y a grid of size 9×9 ($y \in [1.0, 2.9]$). The overall size of the basis is $165 \times 81 = 13\,365$. We use the FGH method for the pruned dynamics and as the underlying DVR of the projected Weylets and PvB. For further details, we refer to Ref. 84. We employ the short iterative Arnoldi propagator^{22,95} as implemented in the Heidelberg MCTDH package.⁹⁶

To evaluate the dynamics, we compute the autocorrelation, $C(t)$, using

$$C(t) = \langle \Psi(0) | \Psi(t) \rangle = \langle \Psi(t/2)^* | \Psi(t/2) \rangle, \quad (27)$$

where the last equality holds for real-valued initial wave functions $|\Psi(0)\rangle$.^{97,98} To compute the autocorrelation with a nonorthogonal basis like PvB, one needs to multiply the coefficient vector \mathbf{a} with $\mathbf{B}^T \mathbf{B}$, where \mathbf{B} is defined in Eq. (13). For $D = 1$, this is

$$C(2t) = \langle \Psi(t)^* | \Psi(t) \rangle = (\mathbf{a}^\dagger \mathbf{B}^\dagger)^* \mathbf{B} \mathbf{a} = \mathbf{a}^T \mathbf{B}^T \mathbf{B} \mathbf{a}. \quad (28)$$

From Section II E, it remains to show how many nearest neighbors, N_{neighbor} , should be added during the adaption of the pruned basis. At first attempt, one could add all nearest neighbors which are directly connected to the basis function of interest, i.e., also basis functions located diagonally on the phase-space grid. This means an index change of the basis of ± 1 in each dimension in phase space and all possible combinations of index changes. This corresponds to a ‘‘phase-space ball radius’’ of 2.⁹² Obviously, this is the most conservative way to add basis functions but it requires to add many basis functions in high dimension since the number of all nearest neighbors scales again exponentially, namely $3^{2D} - 1$. The factor of 2 in the exponent comes from the definition in phase space and not in coordinate space. For high-dimensional problems like 24-dimensional pyrazine,⁹⁹ this number is 3^{48} which approximately equals Avogadro’s number. A much simpler way would be to exclude all diagonally connected neighbors and add a maximum of two basis functions per dimension, i.e., only $2D$. This corresponds to a phase-space ball radius of 1 and was chosen in Ref. 52. Clearly, this way works even for high-dimensional problems but the basis adapts less quickly during the dynamics, which might be critical for tunneling processes, etc. On the other hand, this could be compensated with a smaller threshold but then, overall more basis functions may be required. An intermediate way would correspond to a phase-space radius of $\sqrt{2}$, where $2D^2$ nearest neighbors are added.⁹²

Fig. 2 compares the three choices for the double-well dynamics. We have evaluated the infidelity in the

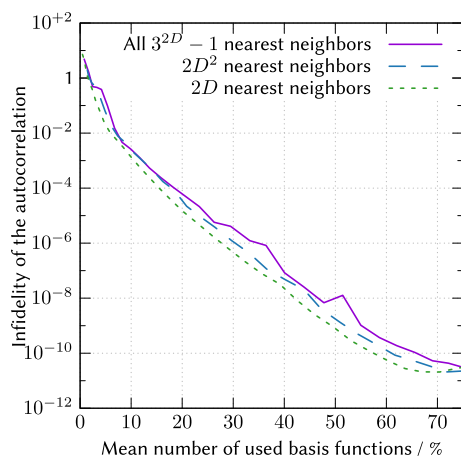


FIG. 2. Accuracy of the pruned projected Weylet dynamics for the two-dimensional double well as a function of the percentage ratio of reduced and unreduced basis sizes. The full basis size is 13 365. The accuracy is determined by the infidelity of the autocorrelation and shown for three different numbers of nearest neighbors to add to the pruned basis (see the text for details).

autocorrelation, defined by the Euclidian L_2 distance between the values of $C(t)$ of the pruned and of the unpruned, exact dynamics. We have used different wave amplitude thresholds but plot the mean number of used basis functions (in percent compared to the unpruned dynamics). The smaller the threshold, the more basis functions are added and the larger the number of used basis functions. Because the map of threshold to number of basis functions is different for each problem and depends on the dimensionality and the number of basis functions to add, it makes more sense to plot the number of actually used basis functions than the threshold employed. For the double well and NO_2 computations (Section III B), the threshold has been varied between 0.046 and 10^{-12} . Our results show that the best way is always to add only $2D$ nearest neighbors. Then, fewer basis functions are required for the same accuracy, although a smaller threshold is needed. We did the same test for the NO_2 dynamics (Section III B) and came to the same conclusion. Henceforth, we always add only $2D$ nearest neighbors (phase-space ball radius of 1) to each pruned basis function.

The accuracy of the pruned dynamics as a function of the number of used basis functions is shown in Fig. 3 for the different methods tested. The accuracy is evaluated by comparing to an exact unpruned FGH basis. For the pruned bases, we have compared a FGH basis that is pruned in coordinate space, the projected Weylets (pW), and the biorthogonal projected von Neumann basis (PvB). The accuracy is measured by the error in the autocorrelation. We have also compared the error of the final wave packet. The curves for this error measurement look very similar such that we only show the error in the autocorrelation. All computations have been performed using a single core of Intel(R) Xeon(R) CPU E5-2650 v2 processors. The accuracy of the integrator is adapted to the wave amplitude threshold. PvB requires the fewest basis functions for a given accuracy. pW in general requires more basis functions than PvB to represent a state. However, momentum-asymmetric

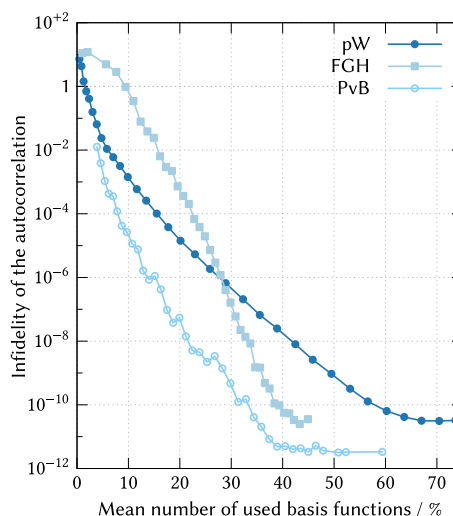


FIG. 3. Accuracy of the dynamics for the 2D double well as a function of the percentage ratio of reduced and unreduced basis sizes. The full basis size is 13 365. The accuracy is determined by the infidelity of the autocorrelation and shown for the projected Weylets (pW, filled circles), pruned FGH (squares), and PvB (rings).

states are described by pW just as well as momentum-symmetrized states (see Section iii in the [supplementary material](#) for an example).

The different accuracy limits stem from the numerical error in the creation of the bases (arising from multiplication by $S^{-1/2}$ or S^{-1}). In principle, FGH, pW, and PvB should give the same result if 100% of basis functions are used. The residual error on the order of 10^{-10} in the fidelity of the autocorrelation arises from the accumulation of numerical noise which we have not tried to reduce.

For low accuracies, the pruned FGH basis needs many more basis functions than PvB or pW to obtain the same accuracy. Surprisingly, FGH beats pW for errors smaller than 10^{-6} . In fact, the number of basis functions required to reach numerically exact results is similar to that in PvB, namely $\sim 40\%$ of the totally available basis. This comes from the choice of potential and wavepacket. The potential is quite correlated between x and y , and in certain regions the whole phase space needs to be covered. Then, it is sufficient to use a DVR basis that is not localized in phase space. Note that a FGH basis is more localized in x than a phase-space-localized basis (here, it is a factor of ~ 10 times more localized in x than the pW basis). However, we could change the ratio $\Delta x/\Delta p$ for the phase-space-localized functions to make them more localized in x and even use more complicated phase-space tiling.¹⁰⁰ We prefer not to optimize the tiling for this problem to keep the discussion more general.

Another point to consider is that some newly added nearest neighbors do not contribute to the wavepacket if it moves in another direction. This is more severe in phase space where there are four directions to consider instead of two in coordinate space. In fact, the current scheme is wasteful for phase-space dynamics. For small wave amplitude thresholds θ (high accuracy), about 20% of basis functions whose coefficient value is smaller than θ are used, i.e., they do not contribute to the description of the wavepacket but are

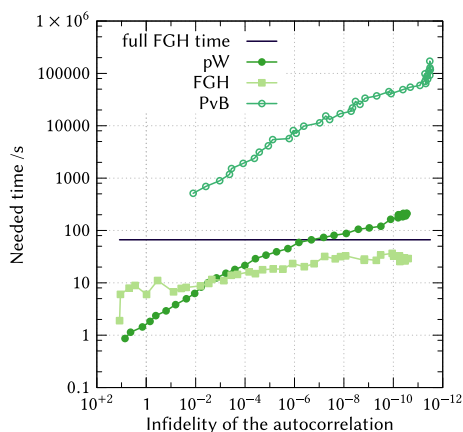


FIG. 4. Computing time of the dynamics for the 2D double well as a function of accuracy. The accuracy is determined by the infidelity of the autocorrelation and shown for the projected Weylets (pW, filled circles), pruned FGH (squares), and PvB (rings). The black horizontal line denotes the computing time of the unpruned FGH method.

included because a nearest neighbor has large coefficient values. For larger θ , this value increases even up to $\sim 50\%$. As expected, the situation is less severe for the DVR that is only localized in coordinate space. There, only $\sim 10\%$ of functions are “wasted”. This could be corrected by better schemes to add nearest neighbors. Essentially, the information where the wavepacket moves is already encoded in the phase-space structure.

We now compare the timing. Fig. 4 compares the accuracy versus computing time for the pruned dynamics. Due to the $\mathcal{O}(\bar{n}^{2D})$ scaling, PvB requires more than 600 times the computing time needed by any other method. Even though FGH needs more basis functions to reach the same accuracy, the pruned dynamics is almost always as fast or faster than pW. Only at the low-infidelity end is pW faster. Both FGH and pW use a SoP Hamiltonian and employ the same computational routines. The difference comes from the transformation of the Hamiltonian, see Eq. (13). For a DVR basis like the FGH method, all potential matrices are diagonal whereas in pW, the matrices are nondiagonal although sparse (actually banded if seen as a tensor in phase space). A multiplication of a diagonal matrix times the coefficient vector scales as $\mathcal{O}(\bar{n}^D)$ instead of $\mathcal{O}(\bar{n}^{D+1})$.

B. NO₂ dynamics on the B₂ surface

As a three-dimensional example, we study the performance of our methods with the dynamics of NO₂ on the B₂ surface. Due to its ergodicity, this dynamic is challenging for the MCTDH method.^{98,101} The wave packet spreads over many configurations in phase space and large basis sets are required. Nevertheless, as we show here, even in such a situation pruning is useful, since the wavepacket does not instantly and fully cover the full space spanned by a direct-product basis.

We follow Ref. 98 and propagate the wave function in bond coordinates (distances r_1 and r_2 for N–O and bond angle θ). In these coordinates, the vibrational Hamiltonian

takes the form of

$$\begin{aligned} \hat{H}_{\text{NO}_2} = & -\frac{1}{2\mu} \left(\frac{\partial^2}{\partial r_1^2} + \frac{\partial^2}{\partial r_2^2} \right) - \frac{\cos(\theta)}{m_N} \frac{\partial^2}{\partial r_2 \partial r_1} \\ & - \frac{1}{2\mu} \left(\frac{1}{r_1^2} + \frac{1}{r_2^2} \right) \frac{1}{\sin(\theta)} \frac{\partial}{\partial \theta} \\ & + \frac{1}{2m_N r_1 r_2} \left[\cos(\theta), \frac{1}{\sin(\theta)} \frac{\partial}{\partial \theta} \sin(\theta) \frac{\partial}{\partial \theta} \right]_+ \\ & + \frac{1}{m_N} \left(\frac{1}{r_1} \frac{\partial}{\partial r_2} + \frac{1}{r_2} \frac{\partial}{\partial r_1} \right) \frac{\partial}{\partial \theta} \sin(\theta) \\ & + V(r_1, r_2, \theta), \end{aligned} \quad (29)$$

with

$$\mu^{-1} = m_{\text{O}}^{-1} + m_{\text{N}}^{-1}, \quad (30)$$

where m_A is the mass of atom A. $[\cdot, \cdot]_+$ denotes the anticommutator. The potentials $V(r_1, r_2, \theta)$ for the A₁ and the B₂ states are taken from Ref. 102 and the latter modified as explained in Ref. 98. To compensate for inaccuracies of the potential,¹⁰³ the potential functions are held constant below $r_i < 1.95$ and below $\theta < 1$. The volume element is

$$dV = dr_1 dr_2 d\theta \sin(\theta). \quad (31)$$

The projected von Neumann basis has already been used in angular coordinates (Jacobi and Radau) with a Gauss-Legendre DVR in Refs. 41 and 88. The used grid points are $\theta_i = \arccos(z_i)$, $\theta_i \in [0, \pi]$, where $z_i \in [-1, 1]$ is a Gauss-Legendre DVR point. The grid points θ_i are almost equidistantly spaced and can thus be used just like a FGH grid. The condition numbers of \mathbf{G} (PvB) or Θ (projected Weylets) are less than 20 for a Gauss-Legendre grid with 100 grid points. A projected phase-space basis is therefore well conditioned for angular grids.¹⁰⁴

We use a FGH DVR basis of size $n_x \times n_p = 13 \times 13$ in the radial coordinates ($r_i \in [1.6, 16]$) and a Gauss-Legendre DVR of size 10×10 . In total, the unpruned basis has a size of $\sim 285 \times 10^4$. The ground state of the A₁ surface is taken as the initial wave packet and propagated on the B₂ surface until $t_e = 90$ fs. The autocorrelation, Eq. (27), is computed to evaluate the pruned dynamics.

The accuracy of the pruned dynamics is depicted in Fig. 5. We are unable to show results for PvB due to the demanding requirements in computing time. From Section III A, it should be clear that pruned orthogonal bases are faster than both PvB and pruned nonorthogonal bases, in general. pW always needs fewer basis functions than a pruned FGH/DVR basis to reach the same accuracy. Almost all basis functions are required to reach numerical accuracy because the dynamics is highly ergodic and most of the phase space is covered.

Fig. 6 shows the timing of the NO₂ dynamics. Like in the double-well example, pruned DVR almost always performs faster than pW. For accuracies lower than 7×10^{-5} (less than 38% of basis functions), pruned DVR dynamics is faster than the exact unpruned dynamics. The pruned DVR simulations could be accelerated by a better exploitation of the diagonality of the potential. This is done for the full DVR but not for the pruned DVR, see Section II E. To reach an accuracy of 10^{-4} , DVR needs 5 h computing time whereas pW requires 12 h. However, DVR also needs more basis functions to reach the

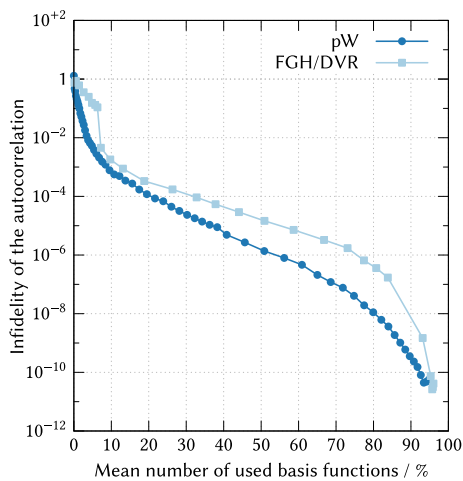


FIG. 5. Accuracy of the dynamics for NO_2 as a function of the percentage ratio of reduced and unreduced basis sizes for the pruned Weylets (circles) and pruned FGH/DVR (squares), compare with Fig. 3. The full basis size is $\sim 285 \times 10^4$.

same accuracy. For the considered accuracy, 26% of the basis functions are required for the DVR dynamics whereas only 16% are required for pW. The memory requirements are not of interest in this three-dimensional example because no more than ~ 1 GB of memory is ever needed. However, for higher-dimensional dynamics as ergodic as those of NO_2 , memory could be crucial and pW might be the method of choice.

Comparing the error in the autocorrelation to very high accuracies is a useful benchmark of pruned methods. However, for many purposes even a lower accuracy autocorrelation function is sufficient to obtain the correct qualitative behavior of the spectral observables. The autocorrelations for some simulations are shown in Fig. 7. There, we only compare the

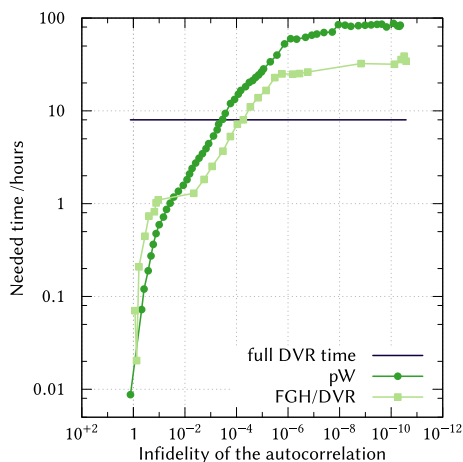


FIG. 6. Computing time of the dynamics for NO_2 as a function of the accuracy for the pruned Weylets (circles) and pruned FGH/DVR (squares), compared with Fig. 4. The black horizontal line denotes the computing time of the unpruned FGH/DVR method. Due to computational overhead, pruned DVR dynamics needs more computing time than full DVR dynamics, for many basis functions (small infidelities). To some extent, this is artificial due to the choice of implementation, see Section II E for details.

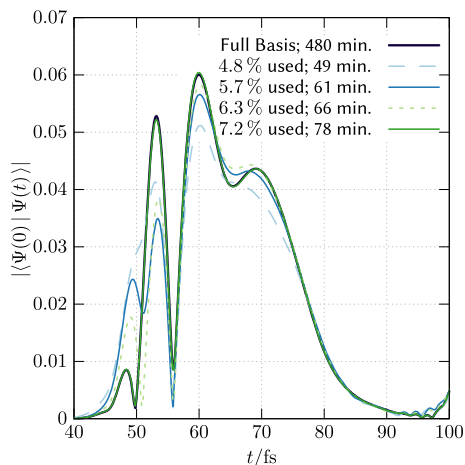


FIG. 7. Absolute value of the autocorrelation for pruned FGH/DVR dynamics compared to the exact dynamics (black line) for NO_2 .

DVR dynamics because this outperforms pW. Most of the features are reproduced even if only 4.8% of the total number of available basis functions are used during the dynamics. The autocorrelation is visually converged if 7.2% are used and the dynamics is faster by a factor of 6 compared to the full dynamics.

C. Nonadiabatic dynamics of pyrazine

As a higher-dimensional example, we consider the nonadiabatic dynamics of a six-dimensional vibronic-coupling model of pyrazine.⁹⁹ The Hamiltonian was obtained from the Heidelberg MCTDH package.⁹⁶ Compared to the dynamics of NO_2 , the wavepacket behaves much more smoothly. Hence, many fewer basis functions are needed and the dynamics is well suited for the MCTDH method. For further details of this benchmark example, we refer to the literature.^{99,105}

Again, we used a FGH basis with parameters shown in Table I. In this case, a Gauss-Hermite DVR would be better suited but to allow for an easier comparison to the other examples and to the projected Weylet method, we choose to keep the FGH method. The overall basis size, including the electronic basis consisting of two states, is $\sim 322 \times 10^6$. We have propagated until 95 fs.

The accuracy versus number of used basis functions is depicted in Fig. 8. The wave amplitude threshold θ has been varied between 10^{-3} and 10^{-8} . Only 5% of the totally available FGH basis is needed to accurately describe the dynamics. This comes primarily from the smooth dynamics where the

TABLE I. Used basis parameters of the six-dimensional pyrazine example.

Mode	n_x	n_p	x-Range
ν_{10a}	5	6	[-8.3,8.3]
ν_{6a}	6	7	[-9.4,9.4]
ν_1	5	5	[-7.0,7.0]
ν_{9a}	5	4	[-7.1,7.1]
ν_{16b}	4	4	[-6.6,6.6]
ν_{18b}	4	4	[-6.6,6.6]

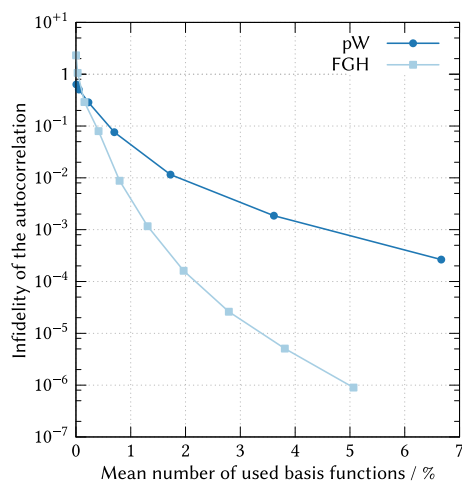


FIG. 8. Accuracy of the dynamics for the six-dimensional model of pyrazine as a function of the percentage ratio of reduced and unreduced basis sizes for the pruned Weylets (circles) and pruned FGH (squares), compare with Fig. 3. The full basis size is $\sim 322 \times 10^6$.

wavepacket retains a rather compact form in configuration space. However, it also shows the general trend that more and more basis functions are wasted if direct product bases are used in higher-dimensional spaces.^{45,52}

Surprisingly, the FGH method needs fewer basis functions than the projected Weylets for reaching the same accuracy. Obviously, localization in coordinate space is here much more important than phase-space localization. In general, fewer basis functions are needed in each mode and the wavepacket does not reach high momenta. Further, the needed “shell” of nearest neighbors is more wasteful in phase space than in coordinate space. Consider the two modes with a size of $n_x \times n_p = 4 \times 4$. In coordinate space, only two nearest neighbors are added in one dimension to one function, that is, 1/8 of the basis functions are added. In phase space, four nearest neighbors need to be added which is already 1/4. In other words, a 4×4 grid in phase space is simply too small with the current scheme. Nevertheless, adding nearest neighbors also here is wasteful for the DVR method. During the dynamics, about 50% of included basis functions have values smaller than the used threshold (compare with the discussion in Section III A). For pW, it is 80%. Note that, for slightly different reasons, Halverson and Poirier have found that a properly pruned harmonic oscillator basis can be more efficient than the symmetrized Gaussians in certain regions of the vibrational spectrum.⁴⁰ Brown and Carrington have found similar results.⁶⁷

The convergence of the autocorrelation function for selected simulations is shown in Fig. 9. Only 0.8% of the basis functions are needed for visual convergence of the autocorrelation! The computational speed-up compared to exact dynamics is a factor of more than 16. Note that the setup of the permutations and arrays, \mathcal{I} and $\mathcal{J}(i)$ (see the appendix for details), needed for an efficient matrix-vector product took significantly more computing time than before, namely $\sim 30\%$ for the largest computation. This fraction is negligible for our two- and three-dimensional examples where, in general, many fewer

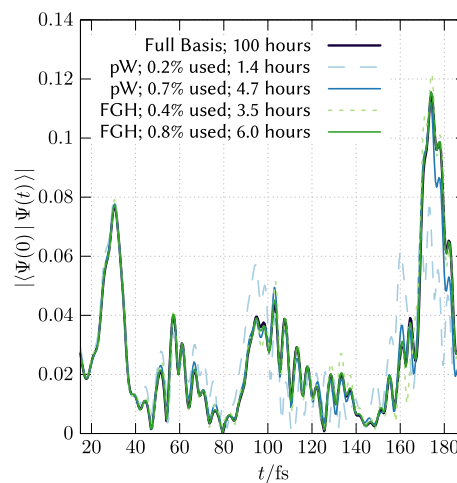


FIG. 9. Absolute value of the autocorrelation for pruned projected Weylets and FGH dynamics compared to the exact dynamics (black line) for the six dimensional model of pyrazine.

basis functions are needed. The reason for the increased computing time is that this part is currently not optimized in our implementation. Hence, the computing time could be significantly reduced.

IV. CONCLUSION AND OUTLOOK

By combining the idea behind the biorthogonal von Neumann basis (PvB), namely projecting phase-space-localized von Neumann functions to another basis, with the orthogonalized, momentum-symmetrized Gaussians (Weylets), we have established a new method, projected Weylets (pW), that inherits the advantage of PvB, namely DVR accuracy, and the advantage of Weylets, orthogonality. We have shown that orthogonality is crucial for an efficient matrix-vector product for solving the time-dependent Schrödinger equation of multi-dimensional systems. Additionally, we have developed a new, highly efficient algorithm for the matrix-vector product for sum-of-product Hamiltonians by permuting the basis such that the dimension to transform over is contiguously represented in memory.

We have compared three methods for dynamically pruning a localized basis during the wavepacket dynamics, namely PvB and pW that are localized in phase space and the FGH and Gauss-Legendre DVRs that are localized in coordinate space. Due to the nonorthogonality and the unfavorable scaling of the matrix-vector product, PvB is much more expensive than the other methods, although it is very appealing in theory. It may, however, be a very useful tool for one-dimensional simulations, since the representation in PvB is the most compact one. By examining the ergodic dynamics of NO_2 , we showed that, due to the phase-space localization of pW, it needs fewer basis functions than a pruned FGH basis for the same accuracy. However, we showed further that in general pW needs more computing time because all potential matrices are non-diagonal whereas they are diagonal in the DVR representation. For the six-dimensional dynamics of a vibronic coupling model of pyrazine, coordinate-space localization turned out to

be much more important than phase-space localization. There, FGH outperforms pW not only in computing time but also in accuracy versus number of basis functions. Fewer than 1% of all basis functions were needed to obtain almost converged dynamics, resulting in speedups of more than 16. Only a single parameter is needed to control the accuracy of the simulation.

At first sight, DVR methods seem to have more advantages than pW. The potential terms are diagonal, and in general no sum-of-product form of the potential operator is required. The pW method gives, however, more compact representations of the wavefunction if the latter covers many regions in phase space and many basis functions are needed, like for the NO₂ dynamics. A compact representation is very crucial for higher-dimensional dynamics. This might be especially useful for scattering simulations like S⁺ + H₂ or HO + CO.^{106,107} Note further that pW and a pruned DVR can of course be combined: pW can be used in modes where phase-space localization is needed and the pruned DVR can be used in spectator modes that are more well-behaved.

Our methods can, of course, be improved. At this stage, we add nearest neighbors in all directions, even if the wave packet moves only in one direction. This is wasteful, especially in phase-space. The phase-space representation of pW can be utilized to predict the movement of the wavepacket. By this, it is clear where to add nearest neighbors. In this contribution, we made use of a sum-of-product Hamiltonians. A transformed Hamiltonian of general form should, however, be very sparse in the pW representation. This could lead to a very promising tool to handle high-energy electronic dynamics, like double ionization dynamics. There, the potential of interest (Coulomb) is not decomposable. Exploiting the sparsity could be useful even if many terms are needed for the sum-of-product potentials. The phase-space view of pW and PvB offers further possibilities to reduce the size of the basis, either by contraction of the basis in the classically forbidden region or by combination with semiclassical methods.³⁵ Note that pruned dynamics also offers the possibility to compute the potential on the fly, obviating complicated global representations of the potential energy surface. These avenues will be pursued in the future.

Why bother with pruned dynamics if (ML-)MCTDH is the method of choice for high-dimensional dynamics? First of all, MCTDH has its drawbacks: it is very expensive for highly correlated systems and is inefficient if many primitive basis functions are required. But perhaps more significantly, pruned dynamics, either in coordinate space or phase space, can be combined with MCTDH, in different possible ways. One way is to use pruned functions as the underlying bases of the single-particle functions (SPFs) in MCTDH, which is quite similar to the multilayer variant of G-MCTDH.¹⁴ A second way is to prune the MCTDH coefficient tensor by transforming the SPFs to a localized basis.¹⁰⁸ Both ways can be easily combined. Work in this direction is in progress.

SUPPLEMENTARY MATERIAL

See [supplementary material](#) for more details on the transformation of the Weylet basis compared to pW, further comparisons of Weylets against FGH, PvB, and pW,

and for a comparison of a phase-space-representation of a momentum-symmetric and a momentum-asymmetric state.

ACKNOWLEDGMENTS

H.R.L. and D.J.T. thank S. Machnes and E. Assémat for enlightening discussions regarding the PvB method. We thank H. D. Meyer for providing us with the Heidelberg MCTDH package and U. Manthe for help with the NO₂ potential. We thank T. Carrington, B. Poirier, and the anonymous referees for helpful comments on the manuscript. H.R.L. acknowledges support by the Fonds der Chemischen Industrie, Studienstiftung des deutschen Volkes, and the Deutscher Akademischer Austauschdienst. D.J.T. acknowledges support from the Israel Science Foundation (No. 533/12) and from the Minerva Foundation with funding from the Federal German Ministry for Education and Research.

APPENDIX A: TENSOR TRANSFORMATIONS

Let us first consider the tensor transformation (matrix-vector product) without pruning. By doing the transformation sequentially, one always has to consider transformations in only one dimension t ,

$$\tilde{a}_{i_1 i_2 \dots i_D} = \sum_{j=1}^{n_t} h_{i_t j}^{(t)} a_{i_1 \dots i_{t-1} j i_{t+1} \dots i_D}. \quad (\text{A1})$$

To simplify the notation, we define the multi-indices $i \equiv i_1 \dots i_{t-1}$ and $k \equiv i_{t+1} \dots i_D$. We further denote the t th index as j or l and drop the superscript (t) of the matrix. Then, Eq. (A1) simplifies to

$$\tilde{a}_{ilk} = \sum_{j=1}^{n_t} h_{lj} a_{ijk}. \quad (\text{A2})$$

Assuming a row-major layout of the tensor (the last index is contiguous in memory), a possible implementation would look like

```

a'_{i::} ← 0
for i in [1, n1]:
  for l in [1, n2]:
    for j in [1, n2]:
      for k in [1, n3]:
        a'_{ilk} ← a'_{ilk} + hlj aijk.

```

A colon means an implicit loop over all indices. The order of the loops is crucial to enable an efficient caching of the values in memory. Actually, this transformation can be recast into a loop over n_1 general matrix multiplications (GEMM) without additional copying,¹⁰⁹

```

for i in [1, n1]:
  a'_{i::} ← h ai::,

```

where **a**_{*i*::} is a $n_2 \times n_3$ matrix. Because there are many efficient libraries implementing the matrix matrix product, this recasting is favorable, although, in real applications, a speed up of only up to ~10% is achieved because **a**_{*i*::} are long and skinny since $n_2 \ll n_3$. Recall that n_3 is the number of basis functions of a multi-index and therefore very large. Memory access is thus

the bottleneck of the tensor transformation—even if well tuned algorithms are employed for the matrix matrix product.¹¹⁰

For a pruned basis, the situation is much more complicated. Following the definitions introduced in Section II B 2, a straightforward implementation would look like

```

a'_{::} ← 0
for i in I:
  for l in J(i):
    for j in J(i):
      for k in K'(i,j,l):
        a'_{ik} ← a'_{ik} + h_{lj}a_{ijk}.

```

The last loop over k depends on $\mathcal{K}'(i,j,l)$ since one has to sum only over entries where k is an element of both sets $\mathcal{K}(i,l)$ (left side of the summation) and $\mathcal{K}(i,j)$ (right side of the summation). Therefore, the storage of all sets \mathcal{K}' would require a size of $\mathcal{O}(\overline{n}^{d+1})$. This is not efficient. One loophole would be to store all possible indices j in a hash table \mathcal{D} ,⁹⁴

```

a'_{::} ← 0
for i in I:
  for l in J(i):
    for k in K(i,j):
      for j in D(i,k):
        a'_{ik} ← a'_{ik} + h_{lj}a_{ijk}.

```

Using the hash table \mathcal{D} reduces the memory requirements. However, the indices of the tensor \mathbf{a} are now accessed in an arbitrary order which results in a very reduced performance.

This problem is solved if the tensor transformation is performed over the last dimension. Then, the tensor transformation reduces to one matrix matrix product, because the multi-index k does not exist,

```

a'_{::} ← 0
for i in I:
  for l in J(i):
    for j in J(i):
      a'_{il} ← a'_{il} + h_{lj}a_{ij}.

```

We assume that the pruned coefficient tensor \mathbf{a} is properly sorted. The storage of \mathcal{I} and $\mathcal{J}(i)$ scales as $\mathcal{O}(\overline{n}^d)$ but it can be reduced by utilizing the fact that many indices in $\mathcal{J}(i)$ appear in ranges. Instead of storing all individual indices, we therefore store only the ranges. To give an example, $\mathcal{J} = \{1, 2, 3, 4, 6, 7, 8, 10\}$ would be stored as $\{[1,4],[6,8],[10,10]\}$.

We have shown that the transformation over the last dimension can be implemented in a very efficient way such that no auxiliary arrays of size larger than $\mathcal{O}(\overline{n}^d)$ need to be stored. In fact, the required storage of the needed arrays is much smaller due to the storage of the index ranges. Note that the sizes of the auxiliary arrays are never larger than the size of the pruned basis.

One can use this algorithm also for the transformation over other dimensions by simply permuting the tensor in a way that the dimension to be transformed over is the last one. After the transformation, the tensor is permuted back to the original

order. Finding the proper permutation is just a sorting operation and scales as $\mathcal{O}\left[\frac{\overline{n}^d}{\overline{n}} \log\left(\frac{\overline{n}^d}{\overline{n}}\right)\right] = \mathcal{O}\left[d \times \overline{n}^d \log\left(\frac{\overline{n}^d}{\overline{n}}\right)\right]$. This is much faster than the tensor transformation. Additionally, the permutations can be stored such that the sorting operations are needed only after a change of the basis. The memory requirements and the cost of the permutations scale as $\mathcal{O}(d \times \overline{n}^d)$. Compared to the storage requirements of the Lanczos-Arnoldi-propagator and the scaling of the tensor transformation, this is justifiable. A permutation of the basis to obtain more efficient tensor transformations was already used in a different application.¹¹¹

To show the efficiency of the algorithm, we compare our approach to the unpruned algorithm that uses GEMM calls. For this, we do not prune the basis but store all possible functions of the direct-product basis. We use NO₂ (Section III B) as an example. The total size of the basis is $\sim 285 \times 10^4$. The GEMM version (unpruned variant) needed 30.1 s for computing the matrix-vector product (36 sum terms) whereas the pruned variant takes 32.5 s. The pruned variant is 8% slower. For a smaller basis with size $\sim 146 \times 10^4$, the GEMM version needs 9.80 s. The pruned variant needs 13.05 s and is 33% slower. For smaller vectors, more values fit into the cache of the CPU and the GEMM implementation is then more efficient. Of course, in real simulations, the pruned variant will only be used for a pruned and not for a full basis and will therefore be much faster.

Note that this scheme for pruned tensor transformations is completely general; no assumptions about any structure in the pruning are made. It could be further optimized by dividing the matrix into chunks that fit into the cache of the computer.¹¹⁰ Brown and Carrington have developed a different algorithm for a similar application, based on a more complicated recursive mapping strategy.⁶⁷ It remains to be seen which approach is faster.

¹D. J. Tannor, *Introduction to Quantum Mechanics: A Time-Dependent Perspective*, 1st ed. (University Science Books, 2007).

²M. Tizniti, S. D. Le Picard, F. Lique, C. Berteloite, A. Canosa, M. H. Alexander, and I. R. Sims, *Nat. Chem.* **6**, 141–145 (2014).

³T. Wu, H.-J. Werner, and U. Manthe, *Science* **306**, 2227–2229 (2004).

⁴R. Otto, J. Ma, A. W. Ray, J. S. Daluz, J. Li, H. Guo, and R. E. Continetti, *Science* **343**, 396–399 (2014).

⁵T. Westermann, J. B. Kim, M. L. Weichman, C. Hock, T. I. Yacovitch, J. Palma, D. M. Neumark, and U. Manthe, *Angew. Chem., Int. Ed.* **53**, 1122–1126 (2014).

⁶L. Chen, K. Shao, J. Chen, M. Yang, and D. H. Zhang, *J. Chem. Phys.* **144**, 194309 (2016).

⁷H. Song, J. Li, M. Yang, Y. Lu, and H. Guo, *Phys. Chem. Chem. Phys.* **16**, 17770 (2014).

⁸J. Palma and D. C. Clary, *J. Chem. Phys.* **112**, 1859 (2000).

⁹W. Zhang, Y. Zhou, G. Wu, Y. Lu, H. Pan, B. Fu, Q. Shuai, L. Liu, S. Liu, L. Zhang, B. Jiang, D. Dai, S.-Y. Lee, Z. Xie, B. J. Braams, J. M. Bowman, M. A. Collins, D. H. Zhang, and X. Yang, *Proc. Natl. Acad. Sci. U. S. A.* **107**, 12782 (2010).

¹⁰E. Baloitcha, B. Lasorne, D. Lauvergnat, G. Dive, Y. Justum, and M. Desouter-Lecomte, *J. Chem. Phys.* **117**, 727 (2002).

¹¹F. Huarte-Larrañaga and U. Manthe, *J. Phys. Chem. A* **105**, 2522 (2001).

¹²A. Vikár, T. Nagy, and G. Lendvay, *J. Phys. Chem. A* **120**, 5083 (2016).

¹³I. Burghardt, H.-D. Meyer, and L. S. Cederbaum, *J. Chem. Phys.* **111**, 2927 (1999).

¹⁴S. Römer, M. Ruckebauer, and I. Burghardt, *J. Chem. Phys.* **138**, 064106 (2013).

¹⁵G. A. Worth, M. A. Robb, and I. Burghardt, *Faraday Discuss.* **127**, 307 (2004).

- ¹⁶G. Richings, I. Polyak, K. Spinlove, G. Worth, I. Burghardt, and B. Lasorne, *Int. Rev. Phys. Chem.* **34**, 269–308 (2015).
- ¹⁷Y. Wu and V. S. Batista, *J. Chem. Phys.* **118**, 6720 (2003).
- ¹⁸T. J. Martínez, M. Ben-Nun, and R. D. Levine, *J. Phys. Chem.* **100**, 7884 (1996).
- ¹⁹M. Ben-Nun and T. J. Martínez, *J. Chem. Phys.* **108**, 7244 (1998).
- ²⁰D. V. Shalashilin and M. S. Child, *Chem. Phys.* **304**, 103 (2004).
- ²¹H.-D. Meyer, U. Manthe, and L. Cederbaum, *Chem. Phys. Lett.* **165**, 73 (1990).
- ²²M. H. Beck, A. Jäckle, G. A. Worth, and H.-D. Meyer, *Phys. Rep.* **324**, 1 (2000).
- ²³H. Wang and M. Thoss, *J. Chem. Phys.* **119**, 1289 (2003).
- ²⁴U. Manthe, *J. Chem. Phys.* **128**, 164116 (2008).
- ²⁵O. Vendrell and H.-D. Meyer, *J. Chem. Phys.* **134**, 044135 (2011).
- ²⁶R. Welsch and U. Manthe, *J. Chem. Phys.* **137**, 244106 (2012).
- ²⁷Q. Meng and H.-D. Meyer, *J. Chem. Phys.* **141**, 124309 (2014).
- ²⁸Z. Bačić and J. C. Light, *J. Chem. Phys.* **85**, 4594 (1986).
- ²⁹Z. Bačić and J. C. Light, *J. Chem. Phys.* **86**, 3065 (1987).
- ³⁰J. M. Bowman and B. Gazdy, *J. Chem. Phys.* **94**, 454 (1991).
- ³¹M. J. Bramley and N. C. Handy, *J. Chem. Phys.* **98**, 1378 (1993).
- ³²A. Viel and C. Leforestier, *J. Chem. Phys.* **112**, 1212 (2000).
- ³³D. Luckhaus, *J. Chem. Phys.* **113**, 1329 (2000).
- ³⁴X.-G. Wang and T. Carrington, *J. Chem. Phys.* **117**, 6923 (2002).
- ³⁵A. Shimshovitz, “Phase space approach to solving the Schrödinger equation,” Ph.D. thesis, Weizmann Institute of Science, 2015.
- ³⁶X.-G. Wang and T. Carrington, *J. Chem. Phys.* **129**, 234102 (2008).
- ³⁷R. Dawes and T. Carrington, *J. Chem. Phys.* **122**, 134101 (2005).
- ³⁸A. Maynard, R. E. Wyatt, and C. Iung, *J. Chem. Phys.* **106**, 9483 (1997).
- ³⁹D. Bégué, N. Gohaud, C. Pouchan, P. Cassam-Chenaï, and J. Liévin, *J. Chem. Phys.* **127**, 164115 (2007).
- ⁴⁰T. Halverson and B. Poirier, *J. Phys. Chem. A* **119**, 12417–12433 (2015).
- ⁴¹A. Shimshovitz, Z. Bačić, and D. J. Tannor, *J. Chem. Phys.* **141**, 234106 (2014).
- ⁴²R. Dawes and T. Carrington, *J. Chem. Phys.* **121**, 726 (2004).
- ⁴³I. Degani, J. Schiff, and D. J. Tannor, *Numer. Math.* **101**, 479 (2005).
- ⁴⁴I. Degani and D. J. Tannor, *J. Phys. Chem. A* **110**, 5395 (2006).
- ⁴⁵G. Avila and T. Carrington, *J. Chem. Phys.* **131**, 174103 (2009).
- ⁴⁶D. Lauvergnat and A. Nauts, *Spectrochim. Acta, Part A* **119**, 18 (2014).
- ⁴⁷D. T. Colbert and W. H. Miller, *J. Chem. Phys.* **96**, 1982 (1992).
- ⁴⁸M. McLeod and T. Carrington, *Chem. Phys. Lett.* **501**, 130–133 (2010).
- ⁴⁹V. Gradinaru, *Computing* **80**, 1 (2007).
- ⁵⁰D. H. Zhang and J. Z. H. Zhang, *J. Chem. Phys.* **101**, 1146 (1994).
- ⁵¹B. Hartke, *Phys. Chem. Chem. Phys.* **8**, 3627 (2006).
- ⁵²J. Sielk, H. F. von Horsten, F. Krüger, R. Schneider, and B. Hartke, *Phys. Chem. Chem. Phys.* **11**, 463–475 (2009).
- ⁵³D. A. McCormack, *J. Chem. Phys.* **124**, 204101 (2006).
- ⁵⁴L. R. Petey and R. E. Wyatt, *Chem. Phys. Lett.* **424**, 443 (2006).
- ⁵⁵L. R. Petey and R. E. Wyatt, *Int. J. Quantum Chem.* **107**, 1566 (2007).
- ⁵⁶M. J. Davis and E. J. Heller, *J. Chem. Phys.* **71**, 3383 (1979).
- ⁵⁷B. Poirier, *J. Theor. Comput. Chem.* **02**, 65 (2003).
- ⁵⁸B. Poirier and A. Salam, *J. Chem. Phys.* **121**, 1690 (2004).
- ⁵⁹B. Poirier and A. Salam, *J. Chem. Phys.* **121**, 1704 (2004).
- ⁶⁰A. Shimshovitz and D. J. Tannor, *Phys. Rev. Lett.* **109** (2012).
- ⁶¹R. Lombardini and B. Poirier, *J. Chem. Phys.* **124**, 144107 (2006).
- ⁶²T. Halverson and B. Poirier, *J. Chem. Phys.* **137**, 224101 (2012).
- ⁶³T. Halverson and B. Poirier, *J. Chem. Phys.* **140**, 204112 (2014).
- ⁶⁴T. Halverson and B. Poirier, *Chem. Phys. Lett.* **624**, 37 (2015).
- ⁶⁵N. Takemoto, A. Shimshovitz, and D. J. Tannor, *J. Chem. Phys.* **137**, 011102 (2012).
- ⁶⁶E. Assémat, S. Machnes, and D. Tannor, “Double ionization of Helium from a phase space perspective,” e-print [arXiv:1502.05165](https://arxiv.org/abs/1502.05165) (2015).
- ⁶⁷J. Brown and T. Carrington, Jr., “Assessing the utility of phase-space-localized basis functions: Exploiting direct product structure and a new basis function selection procedure,” *J. Chem. Phys.* **144**, 244115 (2016).
- ⁶⁸O. Christiansen, *Phys. Chem. Chem. Phys.* **14**, 6672 (2012).
- ⁶⁹A. Leclerc and T. Carrington, *J. Chem. Phys.* **140**, 174111 (2014).
- ⁷⁰A. Jäckle and H. Meyer, *J. Chem. Phys.* **104**, 7974 (1996).
- ⁷¹D. Peláez and H.-D. Meyer, *J. Chem. Phys.* **138**, 014108 (2013).
- ⁷²F. Otto, *J. Chem. Phys.* **140**, 014106 (2014).
- ⁷³S. Manzhos and T. Carrington, *J. Chem. Phys.* **125**, 194105 (2006).
- ⁷⁴W. Koch and D. H. Zhang, *J. Chem. Phys.* **141**, 021101 (2014).
- ⁷⁵G. Avila and T. Carrington, *J. Chem. Phys.* **143**, 044106 (2015).
- ⁷⁶B. Ziegler and G. Rauhut, *J. Chem. Phys.* **144**, 114114 (2016).
- ⁷⁷J. von Neumann, *Math. Annal.* **104**, 570 (1931).
- ⁷⁸J. von Neumann, *Mathematische Grundlagen der Quantenmechanik*, 2nd ed. (Springer, 1996).
- ⁷⁹R. Balian, *C. R. Acad. Sci. Paris* **292**, 1357(1981).
- ⁸⁰F. Low, “Complete sets of wave packets,” in *A Passion for Physics: Essays in Honor of Geoffrey Chew* (World Scientific, 1985), pp. 17–22.
- ⁸¹G. Battle, *Lett. Math. Phys.* **15**, 175–177 (1988).
- ⁸²C. C. Marston and G. G. Balint-Kurti, *J. Chem. Phys.* **91**, 3571 (1989).
- ⁸³I. Daubechies and A. J. E. M. Janssen, *IEEE Trans. Inf. Theory* **39**, 3 (1993).
- ⁸⁴S. Machnes, E. Assémat, H. R. Larsson, and D. J. Tannor, *J. Phys. Chem. A* **120**, 3296 (2016).
- ⁸⁵U. Manthe and H. Köppel, *J. Chem. Phys.* **93**, 345 (1990).
- ⁸⁶M. J. Bramley and T. Carrington, *J. Chem. Phys.* **99**, 8519 (1993).
- ⁸⁷X.-G. Wang and T. Carrington, Jr., *J. Phys. Chem. A* **105**, 2575 (2001).
- ⁸⁸J. Brown and T. Carrington, *J. Chem. Phys.* **143**, 044104 (2015).
- ⁸⁹K. G. Wilson, *Generalized Wannier Functions*, preprint (Cornell University, 1987).
- ⁹⁰I. Daubechies, S. Jaffard, and J.-L. Journé, *SIAM J. Math. Anal.* **22**, 554 (1991).
- ⁹¹P. Löwdin, *J. Chem. Phys.* **18**, 365 (1950).
- ⁹²S. Machnes, E. Assémat, and D. Tannor, “Quantum dynamics in phase space using the biorthogonal von Neumann bases: Algorithmic considerations,” e-print [arXiv:1603.03963](https://arxiv.org/abs/1603.03963) (2016).
- ⁹³We use `std::unordered_set` of the C++ programming language standard library as implemented in the GNU compiler collection.¹¹²
- ⁹⁴R. Sedgewick and K. Wayne, *Algorithms*, 4th ed. (Addison-Wesley Professional, 2011).
- ⁹⁵T. J. Park and J. C. Light, *J. Chem. Phys.* **85**, 5870 (1986).
- ⁹⁶G. A. Worth, M. H. Beck, A. Jäckle, and H.-D. Meyer, The MCTDH Package, Version 8.4.10, 2014, See <http://mctdh.uni-hd.de>.
- ⁹⁷V. Engel, *Chem. Phys. Lett.* **189**, 76 (1992).
- ⁹⁸U. Manthe, H.-D. Meyer, and L. S. Cederbaum, *J. Chem. Phys.* **97**, 9062 (1992).
- ⁹⁹G. A. Worth, H.-D. Meyer, and L. S. Cederbaum, *J. Chem. Phys.* **109**, 3518 (1998).
- ¹⁰⁰A. Shimshovitz and D. J. Tannor, *J. Chem. Phys.* **137**, 101103 (2012).
- ¹⁰¹T. Westermann and U. Manthe, *J. Chem. Phys.* **136**, 204116 (2012).
- ¹⁰²G. Hirsch, R. J. Buenker, and C. Petrongolo, *Mol. Phys.* **73**, 1085–1099 (1991).
- ¹⁰³E. Leonardi, C. Petrongolo, V. Keshari, G. Hirsch, and R. J. Buenker, *Mol. Phys.* **82**, 553–565 (1994).
- ¹⁰⁴Brown and Carrington noted problems with the condition number of **G**, namely numbers $\sim 10^3$ after an adaption of the width of each von Neumann function for a grid of size 48.⁸⁸ We do not experience such problems.
- ¹⁰⁵A. Raab, G. A. Worth, H.-D. Meyer, and L. S. Cederbaum, *J. Chem. Phys.* **110**, 936 (1999).
- ¹⁰⁶A. Zanchet, O. Roncero, and N. Bulut, *Phys. Chem. Chem. Phys.* **18**, 11391 (2016).
- ¹⁰⁷J. Ma, J. Li, and H. Guo, *J. Phys. Chem. Lett.* **3**, 2482 (2012).
- ¹⁰⁸G. A. Worth, *J. Chem. Phys.* **112**, 8322 (2000).
- ¹⁰⁹E. D. Napoli, D. Fabregat-Traver, G. Quintana-Ortí, and P. Bientinesi, *Appl. Math. Comput.* **235**, 454 (2014).
- ¹¹⁰K. Goto and R. A. v. d. Geijn, *ACM Trans. Math. Software* **34**(3), 1 (2008).
- ¹¹¹J. Cooper and T. Carrington, *J. Chem. Phys.* **130**, 214110 (2009).
- ¹¹²R. M. Stallman *et al.*, *Using The Gnu Compiler Collection: A Gnu Manual For GCC Version 5.3.0*, 2015.

I.1.3.4. Supplementary Information

Supplementary information for Efficient molecular quantum dynamics in coordinate and phase space using pruned bases

H. R. Larsson¹ B. Hartke¹ D. J. Tannor²

¹Institut für Physikalische Chemie, Christian-Albrechts-Universität zu Kiel,
24098 Kiel, Germany

² Department of Chemical Physics, Weizmann Institute of Science,
76100 Rehovot, Israel

Journal of Chemical Physics

i. Comparison of the basis transformations

For the transformation of the matrix elements from the momentum-symmetrized Gaussian to the Weylet basis, we closely follow Ref. 1. The Weylet functions $\langle x | \bar{w} \rangle$ are given by a linear combination of momentum-symmetrized Gaussians,

$$|\bar{w}_{st}\rangle = \sum_{m=-m_{\max}}^{m_{\max}} \sum_{n=-m_{\max}}^{m_{\max}} (-1)^{n/2+mt} S_{mn}^{-1/2} |\tilde{\phi}_{uv}\rangle, \quad (\text{i})$$

where $u = s + m$, $v = t + n$ and t is half-integer.¹ $\langle x | \tilde{\phi}_{uv} \rangle$ are given in Eq. (20) in the main article. The summation is only over even position and momentum indices, m and n .² Further, one can apply a ‘‘symplicial’’ truncation using the restriction $|m| + |n| \leq m_{\max}$.³ m_{\max} is chosen to be 10 which is the value used in Table 1 in Ref. 2. If lower accuracy is sufficient, smaller values can be used.

One transformed matrix element is then evaluated as

$$\bar{w}_{sts't'} = \sum_{m=-m_{\max}}^{m_{\max}} \sum_{n=-m_{\max}}^{m_{\max}} \sum_{m'=-m_{\max}}^{m_{\max}} \sum_{n'=-m_{\max}}^{m_{\max}} (-1)^{n/2+mt+n'/2+m't'} S_{mn}^{-1/2} S_{m'n'}^{-1/2} \tilde{\phi}_{uvv'u'}. \quad (\text{ii})$$

There are four indices to account for the indices in x and in p in phase space for each of the two basis functions. Defining $M \equiv (m_{\max} + 1)$, the transformation of one matrix scales as $N^2 [M^2/2]^2 = N^2 \bar{M}$, where N is the total number of basis functions. The prefactor $1/2^2$ stems from the symplicial truncation along the m , n and m' , n' indices. The factor $(-1)^{n/2+mt+n'/2+m't'}$ prevents a sequential summation. Note that N is independent of M . Even if a small basis is used, \bar{M} can be significantly larger and is 3721 for $m_{\max} = 10$. This value may not be large enough if very high accuracies are needed, see the asymptotic behavior in Fig. i. However, in Ref. 1, a lower accuracy was sufficient and the authors used $m_{\max} = 6$ ($\bar{M} = 625$) to reach a relative error of 10^{-6} . Further, a value of $m_{\max} = 4$ ($\bar{M} = 169$) has been used to give an accuracy of the eigenvalues within $\pm 0.02 \text{ cm}^{-1}$, compared to $m_{\max} = 6$ for the Ne_2 potential.¹ One can do a further symplicial truncation of the sum requiring $|m| + |n| + |m'| + |n'| \leq m_{\max}$. Then, \bar{M} would be 681 ($m_{\max} = 10$), 129 ($m_{\max} = 6$) or 41 ($m_{\max} = 4$). However, we found a decrease in accuracy from $\sim 10^{-10}$ to 10^{-7} including violation of the variational principle ($m_{\max} = 10$, error of the first eigenvalue in the harmonic oscillator) if this additional truncation is used. We found improved results by using the restriction $|m| + |n| + |m'| + |n'| \leq 1.5 \times m_{\max}$.

In the projected Weylet basis, the integral transformation is $\mathbf{W}^\dagger \mathbf{H} \mathbf{W}$, where \mathbf{W} is given in Eq. (23) in the main article. This scales as N^3 , independent of the required accuracy, because the definition of the projected Weylets is based on a finite basis whereas the Weylets are defined from an infinite-dimensional basis.

If a SoP form of the Hamiltonian is used, the transformation needs to be done only for matrices of one-dimensional bases. However, the number of sum terms of the Hamiltonian can be quite large and the $N^2 \bar{M}$ scaling can become a bottleneck. For example, the number of terms required in a POTFIT expansion of a six-dimensional HONO potential energy surface is 3750 for a basis of with sizes {20, 20, 45, 35, 30, 35} (without mode-combination).⁴ A transformation of the POTFIT terms to the Weylet basis would require $3750 \times \bar{M} \times (2 \times 20^2 + 45^2 + 2 \times 35^2 + 30^2) = 8.6 \times 10^{10}$ summations. In the case of the projected Weylets, only $3750 \times (2 \times 20^3 + 45^3 + 2 \times 35^3 + 30^3) = 8.2 \times 10^8$ summations are needed – more than 100 times less than for the Weylets. For $m_{\max} = 6$ (4), the factor in saved summations is still 18 (4.7). Using the additional symplectic truncation, the factor would be 19 ($m_{\max} = 10$), 3.6 ($m_{\max} = 6$) or 1.2 ($m_{\max} = 4$). If $N > \bar{M}$, the Weylet transformation would be faster. However, a basis of this size is rarely needed, and at most in one or two dimensions. Further, the pW transformations can be readily implemented using BLAS calls. Due to the highly optimized matrix-matrix multiplication routines in BLAS implementations, an additional saving in computing time of ~ 10 – 10^2 (depending on the hardware) is possible. For very large basis sizes, one can also make use of sparse matrix-matrix multiplication.

ii. Comparison between the Weylet basis and FGH

We compare a pruned Weylet basis for the simple harmonic oscillator,

$$\hat{H}_{\text{HO}} = -\frac{1}{2} \frac{d^2}{dx^2} + \frac{1}{2} x^2 \quad (\text{iii})$$

against the Fourier Grid Hamiltonian. There are many ways to prune a phase-space basis. Here, we use the simple energy-cutoff formula and restrict the Weylet basis by

$$|p_{\max}| = \sqrt{[E_{\text{cut}} - V(x)]2m} \quad (\text{iv})$$

and $E_{\text{cut}} = 90$, $m = 1$. We further used a FGH which has the *same* basis size as the *pruned* Weylet basis and $x \in [-13.29, 13.29]$, which corresponds to the maximal x -range of the pruned Weylets. That is, the FGH describes a rectangle in phase space and the pruned Weylet basis an ellipse. The results are depicted in Table i. The FGH results are much more accurate, even though the basis size is not larger. Our pruned Weylet computation is in perfect agreement with a similar calculation of B. Poirier.⁵ A pW computation based on the FGH-setup would yield the *same* eigenvalues as the FGH (up to rounding errors). However, the pW setup can be chosen to be identical to the pruned Weylets. Then, they exhibit almost the same eigenvalues as the pruned Weylets.

Table i: Comparison of the eigenenergies of the simple harmonic oscillator using a pruned Weylet basis and a Fourier Grid Hamiltonian that has the *same* size as the *pruned* Weylet basis, 92. For the pruned Weylet basis, an energy cutoff criterion of $E_{\max} = 90$ has been chosen. Shown are the exact and numerical eigenenergies and the absolute error.

E(exact)	E(pruned Weylet)	absolute error	E(FGH)	absolute error
0.5	0.500 000 000	3.98×10^{-10}	0.500 000 000	8.10×10^{-15}
1.5	1.500 000 001	1.05×10^{-9}	1.500 000 000	3.77×10^{-15}
2.5	2.500 000 004	4.50×10^{-9}	2.500 000 000	1.02×10^{-14}
3.5	3.500 000 011	1.08×10^{-8}	3.500 000 000	4.44×10^{-15}
4.5	4.500 000 019	1.93×10^{-8}	4.500 000 000	-3.55×10^{-15}
5.5	5.500 000 030	3.02×10^{-8}	5.500 000 000	8.88×10^{-15}
6.5	6.500 000 043	4.31×10^{-8}	6.500 000 000	8.88×10^{-15}
7.5	7.500 000 057	5.65×10^{-8}	7.500 000 000	1.78×10^{-15}
8.5	8.500 000 073	7.26×10^{-8}	8.500 000 000	1.42×10^{-14}
9.5	9.500 000 093	9.33×10^{-8}	9.500 000 000	-7.11×10^{-15}
10.5	10.500 000 124	1.24×10^{-7}	10.500 000 000	-8.88×10^{-15}
11.5	11.500 000 176	1.76×10^{-7}	11.500 000 000	-1.60×10^{-14}
12.5	12.500 000 278	2.78×10^{-7}	12.500 000 000	-3.55×10^{-15}
13.5	13.500 000 483	4.83×10^{-7}	13.500 000 000	-7.11×10^{-15}
14.5	14.500 000 870	8.70×10^{-7}	14.500 000 000	-7.11×10^{-15}
15.5	15.500 001 520	1.52×10^{-6}	15.500 000 000	7.11×10^{-15}
16.5	16.500 002 496	2.50×10^{-6}	16.500 000 000	-2.84×10^{-14}
17.5	17.500 003 820	3.82×10^{-6}	17.500 000 000	-1.42×10^{-14}
18.5	18.500 005 484	5.48×10^{-6}	18.500 000 000	-7.11×10^{-15}
19.5	19.500 007 484	7.48×10^{-6}	19.500 000 000	-2.49×10^{-14}
20.5	20.500 009 834	9.83×10^{-6}	20.500 000 000	-1.07×10^{-14}
21.5	21.500 012 564	1.26×10^{-5}	21.500 000 000	-7.11×10^{-15}
22.5	22.500 015 680	1.57×10^{-5}	22.500 000 000	-1.78×10^{-14}
23.5	23.500 019 107	1.91×10^{-5}	23.500 000 000	-2.84×10^{-14}
24.5	24.500 022 633	2.26×10^{-5}	24.500 000 000	-1.42×10^{-14}
25.5	25.500 025 958	2.60×10^{-5}	25.500 000 000	-1.07×10^{-14}
26.5	26.500 028 840	2.88×10^{-5}	26.500 000 000	-1.78×10^{-14}
27.5	27.500 031 306	3.13×10^{-5}	27.500 000 000	-2.49×10^{-14}
28.5	28.500 033 920	3.39×10^{-5}	28.500 000 000	-1.78×10^{-14}
29.5	29.500 037 999	3.80×10^{-5}	29.500 000 000	-1.07×10^{-14}
30.5	30.500 045 676	4.57×10^{-5}	30.500 000 000	-4.62×10^{-14}
31.5	31.500 059 659	5.97×10^{-5}	31.500 000 000	1.88×10^{-13}
32.5	32.500 082 783	8.28×10^{-5}	32.500 000 000	-1.00×10^{-12}
33.5	33.500 117 681	1.18×10^{-4}	33.500 000 000	4.91×10^{-12}
34.5	34.500 166 917	1.67×10^{-4}	34.500 000 000	-2.35×10^{-11}
35.5	35.500 233 806	2.34×10^{-4}	35.500 000 000	1.05×10^{-10}
36.5	36.500 323 380	3.23×10^{-4}	36.500 000 000	-4.63×10^{-10}
37.5	37.500 442 936	4.43×10^{-4}	37.500 000 002	1.89×10^{-9}
38.5	38.500 602 055	6.02×10^{-4}	38.499 999 992	-7.63×10^{-9}
39.5	39.500 812 058	8.12×10^{-4}	39.500 000 028	2.84×10^{-8}
40.5	40.501 084 992	1.08×10^{-3}	40.499 999 894	-1.06×10^{-7}
41.5	41.501 435 088	1.44×10^{-3}	41.500 000 357	3.57×10^{-7}
42.5	42.501 871 271	1.87×10^{-3}	42.499 998 775	-1.22×10^{-6}

Further, we have compared both PvB, pW and the Weylets for the harmonic oscillator using different values of E_{cut} resulting in different basis sizes. Fig. i shows the results. The error is evaluated by the Euclidian L_2 distance between the exact and the numerical energies. PvB is the most efficient scheme, followed by pW and the Weylets. Because of the same phase-space tiling, the errors of pW and the Weylets are very similar. Of course, these results cannot be generalized and it does not mean that, in general, PvB is more efficient than Weylets in the time-independent context.

The $\mathbf{S}^{-1/2}$ values for the creation of the Weylets have been taken from Ref. 2. There, they are listed up to 12 digits. Hence the asymptote of the Weylets which exhibit an error of $\sim 10^{-9}$ (accumulated for the first 42 eigenvalues) in the basis limit. In practice, this error does not matter.

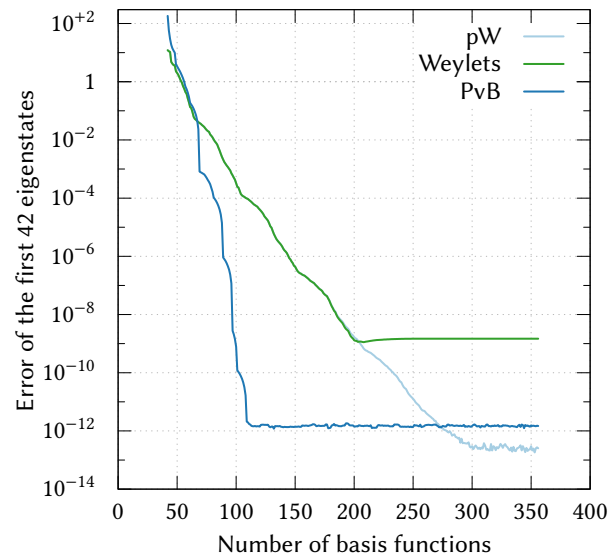


Figure i: Comparison of pruned pW, Weylets and PvB for the simple harmonic oscillator.

iii. Phase-space representation of symmetric or asymmetric states

We represent the following two states

$$f_1(x) = \exp[-(x - 28.83)^2 + i \times 14x] \times \frac{\exp(49)}{\pi}, \quad (\text{v})$$

$$f_2(x) = \{\exp[-(x - 28.83)^2 + i \times 14x] + \exp[-(x - 28.83)^2 - i \times 14x]\} \times \frac{\exp(49)}{2\sqrt{\pi}} \quad (\text{vi})$$

using PvB and pW. $|f_1\rangle$ is momentum-asymmetric whereas $|f_2\rangle$ is momentum-symmetric in phase-space. The phase-space-representation is shown in Fig. ii. Both states span roughly the same area in the pW representation whereas they span twice the area in PvB representation. With pW, the information about momentum-symmetry seems to be almost only described by the phase of the complex-valued coefficients. The needed area to describe the space is larger for pW than for PvB. This is also the case for a Weylet calculation. It seems that this is due to the inclusion of $\mathbf{S}^{-1/2}$ in the wavefunction expansion coefficients (compare with the discussion below Eq. (8) in the main article). If one uses the biorthogonal basis of the projected symmetrized Gaussians, the needed area is much more confined.

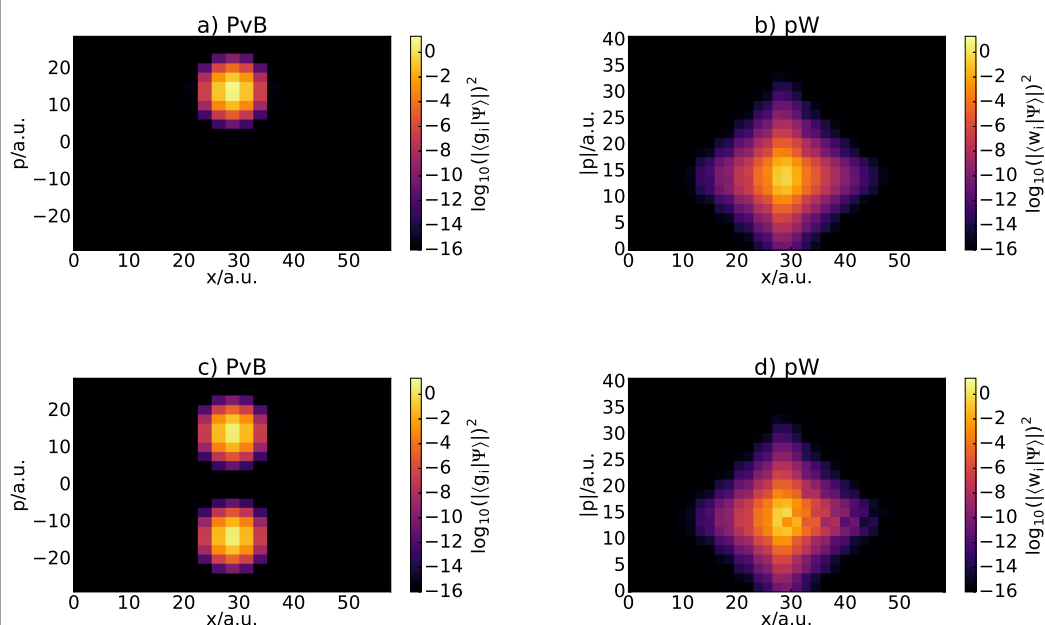


Figure ii: Phase-space-representation of the states $|f_1\rangle$, Eq. (v), in a) and b) and $|f_2\rangle$, Eq. (vi), in c) and d) using PvB and pW.

References

- ¹ Lombardini, R.; Poirier, B. *J. Chem. Phys.* **2006**, *124*, 144107.
- ² Poirier, B.; Salam, A. *J. Chem. Phys.* **2004**, *121*, 1690.
- ³ Poirier, B.; Salam, A. *J. Chem. Phys.* **2004**, *121*, 1704.
- ⁴ Peláez, D.; Meyer, H.-D. *J. Chem. Phys.* **2013**, *138*, 014108.
- ⁵ Poirier, B. private communication.

I.1.3.5. Complementary Information

The typo regarding the double-well potential (see Section I.1.2.4) has been propagated to this publication. That is, \hat{H}_{DW} , Eq. (25) in the publication (page 74), should be replaced by Eq. (I.1.6). Again, this does not affect any conclusions drawn from the results of the simulations.

Further, a term in the kinetic energy operator of NO_2 is shown incorrectly in Eq. (29) in the publication (page 76). The correct Hamiltonian takes the form of

$$\begin{aligned} \hat{H}_{\text{NO}_2} = & -\frac{1}{2\mu} \left(\frac{\partial^2}{\partial r_1^2} + \frac{\partial^2}{\partial r_2^2} \right) - \frac{\cos(\theta)}{m_{\text{N}}} \frac{\partial^2}{\partial r_2 \partial r_1} - \frac{1}{2\mu} \left(\frac{1}{r_1^2} + \frac{1}{r_2^2} \right) \frac{1}{\sin(\theta)} \frac{\partial}{\partial \theta} \sin(\theta) \frac{\partial}{\partial \theta} \\ & + \frac{1}{2m_{\text{N}}r_1r_2} \left[\cos(\theta), \frac{1}{\sin(\theta)} \frac{\partial}{\partial \theta} \sin(\theta) \frac{\partial}{\partial \theta} \right]_+ + \frac{1}{m_{\text{N}}} \left(\frac{1}{r_1} \frac{\partial}{\partial r_2} + \frac{1}{r_2} \frac{\partial}{\partial r_1} \right) \frac{\partial}{\partial \theta} \sin(\theta) \quad (\text{I.1.7}) \\ & + V(r_1, r_2, \theta), \end{aligned}$$

where the red part is missing in the publication. The implementation of the Hamiltonian in the program was correct. Thus, this typo did not affect any results shown in the publication.

Configurational Space Methods

“Every revolutionary idea — in science, politics, art, or whatever — seems to evoke three stages of reaction. They may be summed up by the phrases:

- (1) “It’s completely impossible — don’t waste my time”
- (2) “It’s possible, but it’s not worth doing”;
- (3) “I said it was a good idea all along.”

— Arthur C. Clarke

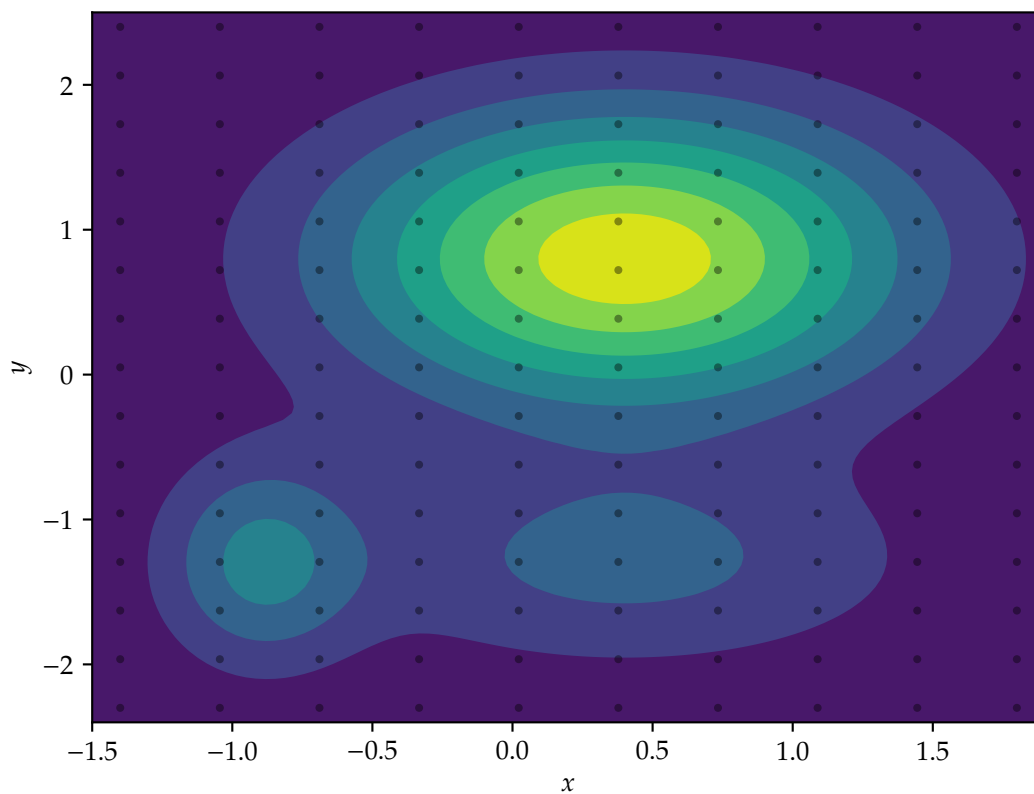
The simplicity of the TD-FCI methods described in the previous Chapter I.1 comes with the drawback that the employed basis functions are not the most optimal in the sense of a compact description of the wavefunction. Even when the functions are pruned, too many of them are needed because the inner region of a wavefunction is still of direct-product type and the hypervolume of the outer, classically forbidden region leads to exponential scaling.^[80]

More compact descriptions of the wavefunction can be obtained by judiciously chosen basis functions. Consider for example the two-dimensional wavefunction shown in Fig. I.2.1a. Clearly, a simple description by a grid or DVR-like basis (black dots) is wasteful, even if the grid is pruned.¹ Being of static nature, even phase-space bases like PvB or pW do not give the most compact representation. Indeed, the wavefunction can be expressed by a direct product of the functions $\{\phi_1, \phi_2\}$ and $\{\zeta_1, \zeta_2\}$ shown in Fig. I.2.1b and I.2.1c. That is, the wavefunction can be compactly expressed as

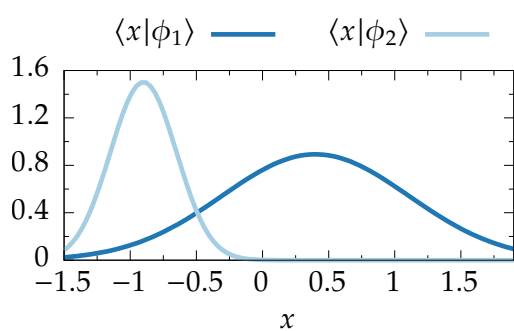
$$|\Psi\rangle \approx A_{11}|\phi_1\rangle \otimes |\zeta_1\rangle + A_{12}|\phi_1\rangle \otimes |\zeta_2\rangle + A_{21}|\phi_2\rangle \otimes |\zeta_1\rangle + A_{22}|\phi_2\rangle \otimes |\zeta_2\rangle, \quad (\text{I.2.1})$$

$$\mathbf{A} = \begin{pmatrix} 0.95 & 0.24 \\ 0.00 & 0.19 \end{pmatrix}. \quad (\text{I.2.2})$$

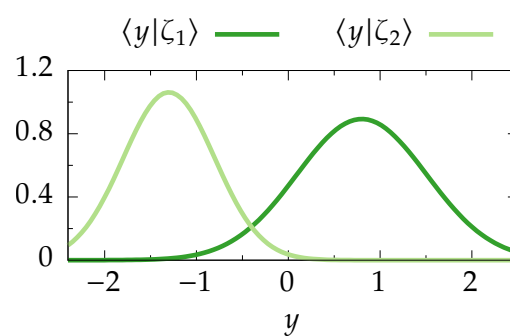
¹This might contradict the motivation of Chapter I.1 where it is stated that the wavepacket will never cover the full region in coordinate space. Here, this two-dimensional example might be a cut through a high-dimensional wavefunction or a cut from a larger coordinate space region where other parts are covered during later propagation times.



(a) Contour plot of the two-dimensional wavefunction. The magnitude of the values is increased from blue to yellow color. An underlying direct-product grid is shown as black dots.



(b) Optimal direct-product basis for dimension x .



(c) Optimal direct-product basis for dimension y .

Figure I.2.1.: Cartoon-like comparison of a grid-like description of the two-dimensional wavefunction shown in panel (a) with an optimized direct-product basis [panels (b) and (c)].

The multi-configuration time-dependent Hartree (**MCTDH**) *ansatz* is similar: At each time step, the underlying direct-product basis is variationally optimized. The corresponding basis functions are called single-particle functions (**SPFs**). This compactness comes with the price of an additional complexity because an equation of motion (**EOM**) has to be solved both for the coefficient tensor **A** and the **SPFs**. For the latter, another basis is needed which is typically a **DVR** and called primitive basis in this context.

Dynamical pruning (**DP**) can be introduced in **MCTDH** in two ways: One way is to prune the direct-product space spanned by the **SPFs**, i. e., the sparsity of **A** is exploited. In the example above, one out of four coefficients is zero [Eq. (I.2.2)]. In higher dimensions, many more coefficients are zero.² The other way is to prune the space of the primitive basis. This is especially useful if higher-dimensional **SPFs** are propagated which is called *mode combination*.

The publication presented in the next Section I.2.1 shows the implementation and benchmark of these two strategies in **MCTDH** and thus introduces dynamically pruned multi-configuration time-dependent Hartree (**DP-MCTDH**). It is the first time that pruning is applied to the primitive basis in **MCTDH** and the first time that **DP** is applied to the **SPF** space for solving the **TDSE**. The achievements from the work presented in Chapter I.1 have been successfully converted to the **MCTDH** methodology, making **DP-MCTDH** competitive but simpler than the state-of-the-art **ML-MCTDH** method.

Another method that utilizes a statically pruned configuration space of antisymmetrized configurations is presented in Chapter II.4.

²The two-dimensional case is special because one can apply a singular value decomposition (**SVD**) to **A**, which corresponds to a transformation into natural orbitals. Then, **A** is diagonal. In higher dimensions, **A** can, in general, never be transformed such that it takes a diagonal form.^[114,115] The choice of representation is discussed in Section I.2.1.4.2.

I.2.1. Dynamically Pruned Multi-Configuration Time-Dependent Hartree

I.2.1.1. Own Contributions

- Idea of pruning the primitive basis and generalizing the static pruning of the SPFs, as established by WORTH,^[116] to DP.
- Implementation of a MCTDH program from scratch (see Chapter I.3).³
- Adapting the algorithms from Section I.1.3 to the needs of the MCTDH method as pointed out in the publication.
- Setup, execution, analysis and interpretation of all simulations, if not mentioned otherwise in the publication.
- Writing and editing of the whole article.

I.2.1.2. Bibliographic Data

Title Dynamical pruning of the multiconfiguration time-dependent Hartree (DP-MCTDH) method: An efficient approach for multidimensional quantum dynamics

Authors Henrik R. Larsson and David J. Tannor

Journal The Journal of Chemical Physics

Volume 147

Issue 4

Page 044103

Year 2017

DOI [10.1063/1.4993219](https://doi.org/10.1063/1.4993219)

Note Reprinted from [The Journal of Chemical Physics 147, 044103 (2017)], with the permission of AIP Publishing.

Preprint <https://arxiv.org/abs/1705.02769>

³Some parts are inspired by the Heidelberg MCTDH package^[117] but reimplemented.

I.2.1.3. Article

THE JOURNAL OF CHEMICAL PHYSICS **147**, 044103 (2017)**Dynamical pruning of the multiconfiguration time-dependent Hartree (DP-MCTDH) method: An efficient approach for multidimensional quantum dynamics**H. R. Larsson^{1,2,a)} and D. J. Tannor²¹*Institut für Physikalische Chemie, Christian-Albrechts-Universität zu Kiel, 24098 Kiel, Germany*²*Department of Chemical Physics, Weizmann Institute of Science, 76100 Rehovot, Israel*

(Received 8 May 2017; accepted 27 June 2017; published online 25 July 2017)

We present two strategies for combining dynamical pruning with the multiconfiguration time-dependent Hartree (DP-MCTDH) method, where dynamical pruning means on-the-fly selection of relevant basis functions. The first strategy prunes the primitive basis that represents the single-particle functions (SPFs). This is useful for smaller systems that require many primitive basis functions per degree of freedom, as we will illustrate for NO₂. Furthermore, this allows for higher-dimensional mode combination and partially lifts the sum-of-product-form requirement onto the structure of the Hamiltonian, as we illustrate for nonadiabatic 24-dimensional pyrazine. The second strategy prunes the set of configurations of SPF at each time step. We show that this strategy yields significant speed-ups with factors between 5 and 50 in computing time, making it competitive with the multilayer MCTDH method. *Published by AIP Publishing.* [<http://dx.doi.org/10.1063/1.4993219>]

I. INTRODUCTION

The aim of theoretical molecular quantum dynamics is to describe chemical reactions and molecular dynamics more generally by solving the time-dependent Schrödinger equation (TDSE).¹ The standard approach to solve the TDSE is to expand the wavefunction in a direct product of one-dimensional basis functions. This transforms the partial differential equation into a linear algebra problem that can be solved efficiently on a computer. This simple approach works well for lower-dimensional systems but the exponential scaling with dimension of the size of the direct-product basis leads to intractable computational effort for systems with more than five atoms.^{2,3}

Therefore, more sophisticated methods are required to avoid the exponential scaling. For computing (ro-)vibrational spectra, that is, solving the time-independent molecular Schrödinger equation (TISE), several techniques have been developed to circumvent the exponential scaling, see Ref. 4 for a recent review. However, circumventing the exponential scaling is easier in this case because the wavefunctions do not change in time and their shape is often simpler.

For the TDSE, the multiconfiguration time-dependent Hartree (MCTDH) method^{5–7} has had tremendous success. It does not eliminate the exponential scaling but it reduces the base. The method employs a time-dependent direct-product basis that is evolved variationally at each time step. These basis functions are called single-particle functions (SPFs). The MCTDH method allowed for the simulation of 12-dimensional systems.⁸ It leads to significant reduction of computational effort, but only for weakly coupled systems (between weakly

coupled groups of modes). Moreover, the direct application of the MCTDH *Ansatz* is still affected by exponential scaling. This was alleviated by so-called “mode combination,” where a direct-product basis of not one-dimensional but higher-dimensional basis functions are used and variationally optimized.^{7,9} With this, even 24-dimensional problems were tractable already almost 20 years ago.^{9,10} More recently, the MCTDH *Ansatz* has been used to describe higher-dimensional SPFs, leading to the multilayer MCTDH (ML-MCTDH) method.^{11–14} For model systems, the treatment of hundreds or even thousands of degrees of freedom (DOF) is then possible.^{11,13,15,16} Despite its success, the MCTDH method with mode-combination and its ML variant have their drawbacks. Finding optimal combinations of modes or ML-“trees” is difficult.^{17–19} Furthermore, the MCTDH approach is only advantageous if the Hamiltonian is in the form of a sum of products (SoP) of operators acting on only one degree of freedom.⁷ Fitting the Hamiltonian into this form is possible but adds an additional layer of complexity and approximation.^{20–26} Fitting the Hamiltonian into the SoP form for higher-dimensional systems is still challenging. With mode-combination, the Hamiltonian may be expressed as a sum of products of operators acting on more DOF.²⁷ Correlation discrete-variable-representation (DVR) is an alternative but it is approximate and challenging to use within the context of ML-MCTDH.^{12,28–30}

Building on previous ideas,^{31–36} we have recently proposed an alternative method to implement the TDSE for higher-dimensional systems.³⁷ We use the standard *Ansatz* of a time-independent direct-product basis but employ basis functions that lead to a sparse representation of the wavefunction. The basis functions are either coordinate-space-localized discrete-variable-representation (DVR) functions,^{1,38} phase-space-localized projected von Neumann functions, PvB,^{35,39–42}

^{a)}Electronic mail: larsson@pctc.uni-kiel.de

or phase-space-localized but momentum-symmetric projected Weylets, pW.^{37,43–48} If the wavefunction is expanded in one of these bases, large parts of the wavefunction coefficient tensor have negligible amplitude, i.e., they are sparse and the values are below a certain threshold. The corresponding terms in the wavefunction expansion can then be dropped, i.e., the basis is pruned. The time-dependence requires an adaptive scheme where basis functions are added and removed during the propagation of the wavepacket. The three mentioned bases can be pruned very efficiently. DVR and pW turned out to be useful also for higher-dimensional systems. We showed the efficiency of our approach for up to six-dimensional systems,³⁷ and we believe that this pruning strategy can be an alternative to MCTDH for systems with intermediate dimensionality. Because the pruning is not based on exploiting weak correlation, it might be especially useful for highly correlated systems. Despite the tremendous decrease of effort compared to unpruned dynamics, simple pruning of a direct-product grid will not suffice for applications with more than about nine or twelve DOF without further development. This is due to the exponential increase of the size of the boundary of the wavefunction in higher dimension.⁴⁹ Note, however, that systems with more than twelve DOF can indeed be treated within this approach if (ro-)vibrational spectra are of interest.^{41,42,50–55}

Clearly, pruning can be combined with the MCTDH *Ansatz*, because, in principle, any direct-product Hilbert space can be pruned, as long as the representation of the wavefunction is sufficiently sparse. There are two ways to use the pruning strategy within (ML-)MCTDH. Both will be considered in this contribution. The SPFs are normally described by a so-called primitive direct-product basis. Thus, the first way to combine pruning with the MCTDH approach is to prune this primitive basis. This allows for a straightforward combination of our pruning methodology from Ref. 37 with the MCTDH method. It might be useful for SPFs that require many primitive basis functions. Moreover, pruning the SPF representation allows for higher-dimensional mode combination, making MCTDH more favorable for higher-dimensional systems. Furthermore, higher-dimensional mode coupling relaxes the requirements regarding the form of the Hamiltonian. Pruning is particularly useful for complicated and highly correlated dynamics.

Note that the primitive bases DVR, PvB, and pW,³⁷ which we will use for pruning the SPF representation, are grid-based methods. As an alternative, one could also regard the two-layer version of G-MCTDH⁵⁶ as a compact representation of the SPFs.⁵⁷ G-MCTDH, however, adds an additional layer of complexity.

The second way is to prune the wavefunction in SPF representation, i.e., the MCTDH coefficient tensor. Often, the most time-consuming parts of a MCTDH computation is the handling of the coefficient tensor, and therefore the savings can be significant. Consequently, this idea is not new and was first successfully implemented by Worth.⁵⁸ It can be regarded as an alternative to ML-MCTDH but it can also be combined with the ML-MCTDH strategy. The earlier cousins of the MCTDH methods, namely, multiconfiguration time-dependent self-consistent field *Ansätze*,^{59–61} might also be considered as pruned MCTDH methods.⁵⁸

The work of Worth was extended by Haxton and McCurdy in the context of electron dynamics.⁶² The time-dependent Restricted-Active-Space Self-Consistent-Field (TD-RASSCF)^{63–65} methodology and the occupation-restricted multiple-active-space model (TD-ORMAS)⁶⁶ may also be viewed as pruned MCTDH methods for fermions. The former has recently been formulated for bosonic systems.⁶⁷

Variational Multiconfigurational Gaussians, vMCG,^{68,69} might be considered as a radical way to prune the SPF space. There, the SPFs are not a direct-product basis but a selection of time-dependent Gaussians.⁵⁶ However, this method is challenging to implement numerically.⁶⁹

In the context of computing vibrational levels, i.e., solving the TISE, one can use the MCTDH *Ansatz* within the so-called “improved diagonalization” approach developed by Meyer *et al.*⁷⁰ This approach can be considered as vibrational Complete-Active-Space Self-Consistent-Field, vCASSCF⁷¹ or as a special case of vibrational Multi-Configurational Self-Consistent-Field, vMCSCF.^{72,73} Pruning the configurational space in vMCSCF has been thoroughly studied by Rauhut *et al.* and Mizukami and Tew,^{73–76} including a further perturbative treatment.^{75,77} Recently, also Wodraszka and Carrington followed this path and presented an efficient algorithm for the required pruned tensor transformations.⁷⁸

In all the above methods, the SPF space is not pruned dynamically and the size of the pruned space is not allowed to change. In this contribution, we introduce, for the first time, dynamic pruning as presented in Ref. 37 for standard time-independent direct-product bases into MCTDH, called DP-MCTDH. This greatly increases the effectivity of pruning. By defining a wave amplitude threshold θ , which determines the accuracy of the pruning, one avoids the need to predetermine the number of SPFs in each dimension. Essentially, this yields the MCTDH method with just one parameter. This might be an alternative to ML-spawning where the parameters in ML-MCTDH are determined dynamically, and again one effective parameter is used.¹⁹ We compare DP-MCTDH against conventional MCTDH and ML-MCTDH using well-established benchmark systems.

After submitting this paper, Wodraszka and Carrington published another article about pruned vCASSCF (MCTDH with improved diagonalization).⁷⁹ There, they use an adaptive pruning for solving the TISE, similar in spirit of Ref. 80. They refined their algorithm from Ref. 78 for the pruned matrix-vector product using our ideas from Ref. 37 and compared their method with ML results. There are three key differences from the present work. (1) They do not prune the primitive basis, just the coefficient tensor; (2) they do not use mode combination; (3) in contrast with the present paper, they are not solving the TDSE. Using adaptive or dynamic pruning for solving the TDSE is more difficult than using it for the TISE because the basis has to be adapted at each time step. This makes it necessary to develop efficient algorithms for updating the pruned basis.³⁷ Additionally, the error of the pruning depends on the wavefunction at previous times, whereas, for solving the TISE, pruned bases can always be refined without the dependence on previous results. By analyzing reduced densities, we will show why it is important to use dynamical/adaptive instead of static pruning.

In the following, we briefly restate the MCTDH theory in Sec. II A. Then, we describe the pruning of the SPF representation and of the coefficients in detail in Secs. II B 1 and II B 2, respectively. More details regarding our implementation are given in Sec. III. This is followed by examples in which the primitive basis is pruned (Sec. IV A), the set of configurations of SPFs is pruned (Sec. IV B), and where both pruning strategies are combined (Sec. IV C). The reduced density in DP-MCTDH is analyzed in Sec. IV D. We conclude in Sec. V.

II. THEORY

A. General MCTDH theory

In MCTDH,⁵⁻⁷ the D -dimensional wavefunction $|\Psi(t)\rangle$ is expanded in a direct-product of a so-called single-particle basis $\{|\varphi_{j_k}^{(\kappa)}(t)\rangle\}_{j_k=1}^{n_\kappa}$,

$$|\Psi(t)\rangle = \sum_{j_1=1}^{n_1} \sum_{j_2=1}^{n_2} \cdots \sum_{j_D=1}^{n_D} A_{j_1 j_2 \dots j_D}(t) \bigotimes_{\kappa=1}^D |\varphi_{j_\kappa}^{(\kappa)}(t)\rangle, \quad (1)$$

$$\equiv \sum_J A_J(t) |\Phi_J(t)\rangle, \quad (2)$$

where we have introduced the multi-index $J = j_1 j_2 \dots j_D$. Both the coefficient tensor \mathbf{A} and the single-particle functions (SPFs) $|\varphi_{j_k}^{(\kappa)}\rangle$ are time-dependent. Mathematically, this corresponds to a Tucker decomposition of the full tensor of $|\Psi\rangle$ in a primitive basis representation (see below).⁸¹ In the context of quantum chemistry, this form is known as Complete-Active-Space Self-Consistent-Field, CASSCF.⁸² Throughout the text, we use atomic units unless stated otherwise.

Inserting this *Ansatz* into the time-dependent Schrödinger equation, $i\partial_t |\Psi(t)\rangle = \hat{H} |\Psi(t)\rangle$, employing the Dirac-Frenkel-McLachlan variational principle,⁸³⁻⁸⁶ $\langle \delta\Psi | i\partial_t - \hat{H} | \Psi \rangle = 0$, and restricting the variations of the SPFs to satisfy

$$\langle \varphi_i^{(\kappa)} | \varphi_j^{(\kappa)} \rangle \stackrel{!}{=} \delta_{ij} \quad \text{and} \quad (3)$$

$$\langle \varphi_i^{(\kappa)} | \partial_t \varphi_j^{(\kappa)} \rangle \stackrel{!}{=} 0 \quad (4)$$

gives⁵⁻⁷

$$i\partial_t A_J = \sum_L \langle \Phi_J | \hat{H} | \Phi_L \rangle A_L \equiv \sum_L H_{JL} A_L, \quad (5)$$

$$i\partial_t |\varphi_j^{(\kappa)}\rangle = (\hat{1} - \hat{P}^{(\kappa)}) \sum_{k,l=1}^{n_\kappa} [\hat{\rho}_{jl}^{(\kappa)}]^{-1} \langle \hat{H} \rangle_{lk}^{(\kappa)} |\varphi_k^{(\kappa)}\rangle. \quad (6)$$

$\hat{P}^{(\kappa)}$ projects onto the space spanned by the SPFs,

$$\hat{P}^{(\kappa)} = \sum_{i,j=1}^{n_\kappa} |\phi_i\rangle [S_\phi^{-1}]_{ij} \langle \phi_j|, \quad (7)$$

with $[S_\phi]_{ij} = \langle \varphi_i^{(\kappa)} | \varphi_j^{(\kappa)} \rangle$. Initially, \mathbf{S}_ϕ is a unit matrix but the limited precision of the numerical solver of the system of ordinary differential equations (ODE) leads to spurious nonorthogonalities that need to be taken into account.⁷

Introducing the so-called single-hole functions

$$|\Psi_l^{(\kappa)}\rangle \equiv \langle \varphi_l^{(\kappa)} | \Psi \rangle, \quad (8)$$

the so-called mean-field matrix and density matrix can be written as

$$\langle \hat{H} \rangle_{jl}^{(\kappa)} = \langle \Psi_j^{(\kappa)} | \hat{H} | \Psi_l^{(\kappa)} \rangle, \quad (9)$$

$$\rho_{jl}^{(\kappa)} = \langle \Psi_j^{(\kappa)} | \Psi_l^{(\kappa)} \rangle. \quad (10)$$

The rank of the $n_\kappa \times n_\kappa$ density matrix, $\rho^{(\kappa)}$, might be less than n_κ and an inversion is not possible. To solve this issue, the density matrix is regularized using⁷

$$\tilde{\rho}^{(\kappa)} = \rho^{(\kappa)} + \epsilon \exp(-\rho^{(\kappa)}/\epsilon). \quad (11)$$

Depending on the parameter ϵ , this regularization can decrease the efficiency of the ODE solver for too low values and can sometimes cause inaccuracies and instabilities.⁸⁷ Recently, new formulations that either “hide” the rank-deficiency^{88,89} or remove it using a perturbative treatment^{30,90} have been developed.

To solve the equations for the SPFs, Eq. (6), the SPFs are expanded in a so-called primitive basis $\{|\chi_a^{(\kappa)}\rangle\}_{a=1}^{N_\kappa}$,

$$|\varphi_i^{(\kappa)}(t)\rangle = \sum_{a=1}^{N_\kappa} U_{ai}^{(\kappa)}(t) |\chi_a^{(\kappa)}\rangle. \quad (12)$$

The primitive basis is normally a time-independent discrete variable representation (DVR) basis.^{1,38,91,92} Other bases like PvB can be used as well. In the latter case, the primitive basis becomes nonorthogonal, and the overlap matrix of the primitive basis has to be included in the equations of motion (EOM) for the matrix $\mathbf{U}^{(\kappa)}$.

The memory-requirement is proportional to $DnN + n^D$, where n is the geometric mean of the set of the numbers of SPFs, $\{n_\kappa\}_{\kappa=1}^D$, and N is similarly defined for the number of primitive basis functions. If we assume that the Hamiltonian, \hat{H} , can be decomposed as a sum of products of one-dimensional operators (see Sec. III A), the computational effort is proportional to $e_1 DnN^2 + e_2 D^2 n^{D+1}$, where e_1 and e_2 are some coefficients.⁷ Note the exponential scaling with respect to the number of SPFs. This scaling limits the applicability of MCTDH to $D \leq 12$.

If so-called mode combination is employed,^{7,9} some degrees of freedom are described by higher-dimensional single-particle functions. The primitive basis functions, $\{|\chi_a^{(\kappa)}\rangle\}_{a=1}^{N_\kappa}$, are then multidimensional. This decreases the dimension of the coefficient tensor \mathbf{A} and hence leads to a reduction in computational effort and storage requirement. However, the effort and storage needed for the description of the single-particle functions is increased.⁹³ Nevertheless, if not too many modes are combined, the overall computational effort and storage requirement can be reduced. This is because the required number of multidimensional SPFs is typically less than the product of the required numbers of one-dimensional SPFs, especially if highly correlated modes are combined. Mode combination led to the successful simulation of 24-dimensional pyrazine,^{9,10} see also Secs. IV B and IV C. In ML-MCTDH,¹¹⁻¹³ the multidimensional SPFs are described recursively using the MCTDH approach itself, which corresponds mathematically to a hierarchical Tucker decomposition.^{94,95} Finding the best mode combination can be a nontrivial task.¹⁷⁻¹⁹

B. Pruning within the MCTDH method

There are several ways to apply pruning to the MCTDH method and the different strategies can be combined. One can prune the primitive basis used for expanding the SPFs and/or the set of configurations of the SPF basis, i.e., the coefficient tensor. These pruning strategies are described in the following.

1. Pruning the primitive basis

The most straightforward application of possibly multidimensional wavefunction pruning as introduced in Ref. 37 to MCTDH consists in pruning the representation of the (multidimensional) SPFs, i.e., to prune the expansion in Eq. (12) like

$$|\varphi_i^{(k)}(t)\rangle = \sum_{a \in \mathcal{A}_i^{(k)}} U_{ai}^{(k)}(t) |\chi_a^{(k)}\rangle, \quad (13)$$

where $\mathcal{A}_i^{(k)}$ is the subset of employed indices. Because the shapes of the SPFs change in time, the subsets should be time-dependent. For mode combination, a can be a multi-index and the primitive basis functions $|\chi_a^{(k)}\rangle$ can be a Hartree-product of one-dimensional functions. For efficient pruning, a judicious choice of primitive functions is paramount. In Ref. 37 we benchmarked coordinate-space-localized DVR functions, phase-space-localized projected von Neumann functions, PvB, and phase-space-localized momentum-symmetrized projected Weylets, pW. We found that PvB gives the most compact representation but exhibits in higher dimensions an unfavorable computational scaling with respect to the basis size. The representation in pW is less compact but the scaling is as good as in the DVR. However, the latter was found to have a smaller prefactor in the scaling due to the diagonality of the matrix representation of the potential, even though the representation is less compact than pW.

In many applications of MCTDH, the propagation of the SPFs is not the most time-consuming part. However, this changes if many primitive basis functions in one (combined) mode are required. This is typically the case in lower-dimensional systems with photodissociation or reaction dynamics for at least one or two coordinates. For larger systems, it may happen if many modes are combined. By pruning the SPFs, the effort required to propagate the SPFs is decreased and it becomes possible to combine more modes to propagate even higher-dimensional SPFs.

2. Pruning the configurations of single-particle basis functions

In most applications, the propagation of the coefficient tensor, \mathbf{A} , and the setup of the mean-field matrices, Eq. (9), are the most time- and memory-consuming parts. It is therefore natural to try to prune the configurational space spanned by the SPFs. This was successfully done by Worth,⁵⁸ including a careful analysis of the consequences of pruning. See Sec. I for further examples where this approach or variants of it have been used.

Until now, only static pruning conditions have been used to prune MCTDH for solving the TDSE (see Ref. 79 for adaptively pruned vCASSCF). However, the number of required configurations that contribute to the wavefunction normally

changes (and often increases) during the propagation. Furthermore, it may happen that previously important configurations become negligible at later times. Therefore, static pruning is not the best choice although the easiest to implement. Instead, we use our dynamic pruning method described in Ref. 37; see also Refs. 36, 80, and 96: At each time step, all configurations with a coefficient magnitude larger than a specified wave amplitude threshold, θ , get nearest neighbors in configuration space added. All configurations that have magnitudes smaller than θ and that have no nearest neighbors with magnitudes larger than θ are discarded.

If natural SPFs (natural orbitals), i.e., SPFs or orbitals that diagonalize the density matrices, Eq. (10),^{7,97,98} are used, the SPFs can be ordered by their natural population or weight. This provides for a well-defined order of configuration space. In the context of electronic structure theory, it was shown that natural orbitals give the sparsest representation.⁹⁹

Because our selection of significant configurations is dynamical, the overall number of SPFs required generally changes with time. Hence, there is no requirement to specify the number of SPFs, n_k , in advance. This means that pruned MCTDH has essentially just one parameter, the wave amplitude threshold.

Haxton and McCurdy noticed that in an arbitrarily pruned MCTDHF method, the different variational principles are not identical.⁶² They tried different approaches to find the best EOM in a reduced configurational space. Here, we simply follow Worth⁵⁸ and use the MCTDH EOM as described in Sec. II A without further modifications. To the extent that our dynamic pruning scheme selects the most important configurations up to a given threshold θ , the standard MCTDH equations will be sufficient up to that chosen level of accuracy.

III. IMPLEMENTATION

We have implemented the MCTDH and the DP-MCTDH methods in a new computer code. The basis, the Hamiltonian, and the initial state are set up using the Python programming language. This is then interfaced to a compiled code, written in the C++ programming language. The object-orientation of the two languages allowed for a simple implementation of the pruned and unpruned variants of our code without creating significant overhead. For the unpruned parts of the code, we use the Eigen linear algebra library¹⁰⁰ that is interfaced against the Intel® MKL library.¹⁰¹ The tensor transformations (see next Sec. III A) of both the unpruned and pruned bases follow Ref. 37. Our (DP-)MCTDH implementation is as fast or slightly faster than implementations in the Fortran programming language but currently not parallelized.

A. Pruned tensor transformation

An efficient implementation of matrix-vector products or tensor transformations $\mathbf{H}\mathbf{A}$ as found in Eqs. (5) and (9) is of pivotal importance. Assuming \hat{H} to be decomposed in a sum of direct products of one-dimensional operators (SoP),

$$\hat{H} = \sum_{l=1}^g c_l \bigotimes_{k=1}^D \hat{h}^{(k,l)}, \quad (14)$$

the tensor transformation scales as gn^{D+1} instead of n^{2D} .^{102–104} By introducing one approximation, this scaling is retained in the pruned case, even if the pruning is without any structure. We will review this procedure as introduced in Refs. 37 and 42 briefly. Assuming a two-dimensional Hamiltonian like

$$\hat{H} = \hat{h}^{(1)} \otimes \hat{h}^{(2)}, \quad (15)$$

one can write it as

$$\hat{H} = (\hat{h}^{(1)} \otimes \hat{1}^{(2)})(\hat{1}^{(1)} \otimes \hat{h}^{(2)}), \quad (16)$$

or, in matrix representation,

$$\mathbf{H} = (\mathbf{h}^{(1)} \otimes \mathbf{1}^{(2)})(\mathbf{1}^{(1)} \otimes \mathbf{h}^{(2)}) = \mathbf{H}^{(1)}\mathbf{H}^{(2)}. \quad (17)$$

\mathbf{H} might be dense but $\mathbf{H}^{(\kappa)}$ are permuted block-diagonal matrices of size $n^D \times n^D$. Each block has a size of $n \times n$. Thus, successive multiplication of $\mathbf{H}^{(\kappa)}$ with \mathbf{A} takes n^{D+1} operations.

Pruning can be introduced by a matrix \mathbf{R} that is a rectangular matrix of size $n^D \times \tilde{n}^D$ with ones on the diagonal, where \tilde{n} is the size of the *pruned* one-dimensional basis. Projection into the pruned subspace then gives

$$\mathbf{R}^\dagger \mathbf{H} \mathbf{R} = \mathbf{R}^\dagger \mathbf{H}^{(1)} \mathbf{H}^{(2)} \mathbf{R} \quad (18)$$

$$\approx [\mathbf{R}^\dagger \mathbf{H}^{(1)} \mathbf{R}] [\mathbf{R}^\dagger \mathbf{H}^{(2)} \mathbf{R}] = \tilde{\mathbf{H}}^{(1)} \tilde{\mathbf{H}}^{(2)}. \quad (19)$$

The last approximation is used in our implementation;^{37,42} see also Ref. 105, where this concept was first used for a pruned basis. This type of approximation is known as the product approximation in DVR theory.^{1,105,106} It leads to nonhermitian matrices^{42,105} but the error introduced by the approximation is generally lower than the error introduced by the pruning.

This approximation reintroduces the favorable scaling of order \tilde{n}^{D+1} . We emphasize that no arrays of size larger than \tilde{n}^D are required and that the number of basis functions in each dimension can differ. No scaling with respect to the size of the unpruned tensor is involved. In practice, no matrix $\tilde{\mathbf{H}}^{(\kappa)}$ is explicitly stored. However, we need to permute the vectors between the successive application of $\tilde{\mathbf{H}}^{(\kappa)}$. This simplifies the algorithm and makes each operation local in memory.³⁷ By allowing intermediate arrays of size larger than \tilde{n}^D (and thus a slightly less favorable scaling), the product approximation can be avoided.^{78,79} We found the product approximation not to be severe, see above and Sec. III C.

The computation of mean-field and density matrices, Eqs. (9) and (10), can be done using the same permutation strategy. The density-like matrix \mathbf{D} , $D_{lm}^{(\tau)} = \langle \Psi_l^{(\tau)} | \tilde{\Psi}_m^{(\tau)} \rangle$, can be evaluated as $\mathbf{A}^\dagger \tilde{\mathbf{A}}$, where \mathbf{A} is the matricized and permuted pruned coefficient tensor of size $(\prod_{\kappa \neq \tau} \tilde{n}_\kappa) \times \tilde{n}_\tau$. In our implementation, both the tensor and the matricized tensor are stored in memory as one-dimensional arrays of the same size. The only difference is the dimension that is represented contiguously in memory. No product form is required. More details are given in Ref. 37. Only a minor adjustment of the algorithm described in the Appendix of Ref. 37 is needed to compute density matrices. Here, no approximation is involved.

B. Pruning the primitive basis

Each SPF typically occupies a slightly different region in phase space. Therefore, the most compact representation is

obtained by using different subsets $\mathcal{A}_i^{(\kappa)}$ for each single-particle function i in mode κ . However, to ease the implementation, we use a common subset for all SPFs in one (combined) mode. It turns out that this still leads to a compact representation.

After each time step, we prune the primitive basis again. Once primitive basis functions have been removed or added (by setting their coefficient to zero), the SPFs are no longer orthogonal, and Löwdin's symmetric orthogonalization procedure is used to restore orthogonality.¹⁰⁷ We have tested different orthogonalization methods and found no significant instability caused by the orthogonalization. We prefer Löwdin orthogonalization because it retains the shape of the SPFs as closely as possible.

C. Pruning the configurations of single-particle basis functions

1. Propagation

We closely follow Worth⁵⁸ and use a constant mean-field (CMF) propagator.¹⁰⁸ The Bulirsch-Stoer solver¹⁰⁹ is used for propagating the SPFs and the short-iterative Lanczos solver^{7,110} for propagating the coefficient tensor. Both have been taken from the Heidelberg package¹¹¹ and interfaced against our C++ code.

After each time step of the propagator, we transform to natural SPFs (natural orbitals).^{7,97,98} Changing the propagation equations to fulfill the natural orbital requirement turned out to be numerically unstable and required more time steps,⁵⁸ even if a variable mean-field propagator⁷ is used.

Once we transform the orbitals into the natural orbital representation, the orbitals are ordered by their occupation number or natural population. Hence, our dynamical pruning scheme might be too general because nearest neighbors are added in all directions in configuration space, regardless of the natural population. An improvement might be considered in the future.

2. Pruning

The SPFs are pruned before each transformation into natural orbitals. Our dynamical pruning does not assume any structure; therefore, our pruned tensor transformation cannot use the algorithms described in Refs. 58 and 78 without jeopardizing the favorable scaling of the transformation. We used our implementation from Ref. 37, which is based on permutations; see Sec. III A. The cost of the additional permutation operations was negligible in our examples in Ref. 37. It is not negligible in our examples considered in Secs. IV B and IV C because few SPFs are required in each dimension and there are many unit operators in the SoP form of the considered Hamiltonians. In our original, cyclic permutation scheme, we need to permute the basis in order to apply the unit operation in dimension τ and afterwards permute it again to apply the next operator in dimension $\tau - 1$. This requires the storage of D vectors of permutation indices. To avoid unnecessary permutations, we introduce noncyclic permutations and thereby reduce the computational cost for applying unit operators. This is implemented in practice by saving all possible permutations between each dimension, storing $(D - 1)(D - 2)/2$ additional vectors of the size of the *pruned* coefficient tensor. Wodraszka

and Carrington also needed to adapt their algorithm to handle Hamiltonians with many unit operators.⁷⁸

We note that our pruned tensor transformation leads to nonhermitian mean-field matrices; see Sec. III A. Nevertheless, the numerical propagation turned out to be stable while an explicit symmetrization of the matrices actually decreased the stability. If a symmetrized pruned product of type $[\tilde{\mathbf{H}}^{(1)}\tilde{\mathbf{H}}^{(2)} + \tilde{\mathbf{H}}^{(2)}\tilde{\mathbf{H}}^{(1)}]/2$ [compare with Eq. (19)] is used,¹⁰⁵ hermiticity is restored but the error of the product approximation in the matrix-vector product remains and is only slightly decreased. Hence, we did not use this symmetrized product. Hermiticity is attained by increasing the size of the reduced SPF subspace.

3. Newly added SPFs

Dynamical pruning requires the removing and adding of SPFs. Removing SPFs is not difficult but the initial representation of newly added SPFs can be problematic because they do not contribute to the wavefunction, at the given timestep. Mendive-Tapia *et al.* used a random representation and orthogonalized the SPFs afterwards.¹⁹ We prefer to use the first Krylov vectors obtained by multiplying the uncorrelated part of the Hamiltonian with the SPFs in that dimension. We have also tried other Krylov spaces like that generated by the position operator but found no significant advantage. The optimal way would be to use the scheme by Lee and Fischer⁹⁰ and Manthe,³⁰ but it is computationally expensive as the scaling is $\mathcal{O}[(N^{(\kappa)})^2]$ for each degree of freedom κ .

All steps involved in the pruning procedure are summarized as a pseudo-code in the Appendix.

IV. EXAMPLES

A. Pruning the primitive basis: NO₂

To test the pruning of the primitive basis, we use the example of NO₂ dynamics on the B_2 surface¹¹² and closely follow Ref. 37. This three-dimensional example has been claimed to exhibit ergodic dynamics. Many (20 in each coordinate) SPFs are needed to correctly describe the autocorrelation function. Further, many primitive functions are needed: We use 250 Fourier Grid Hamiltonian functions^{1,113} in the radial coordinates and 100 Gauss-Legendre-DVR functions in the angular coordinate; see Ref. 37 for further details of our setup. For this system, more than 60% of the computing time is spent on solving the SPF EOM.

We compare the pruning of both coordinate-space-localized DVR and phase-space-localized PvB. The latter is formed by a similarity transformation of the DVR basis. Without pruning, it leads to exactly the same results (within machine accuracy).^{37,40,41} We have previously shown that PvB is not optimal for higher-dimensional dynamics due to a less favorable scaling.³⁷ Here, no mode combination is used, and the SPFs are one-dimensional. Therefore, the scaling in higher dimensions does not matter.

Figure 1 shows the autocorrelation function ($\langle\Psi(0)|\Psi(t)\rangle = \langle\Psi(t/2)^*|\Psi(t/2)\rangle$) obtained from unpruned dynamics (using the DVR basis), and pruned dynamics using either DVR or PvB. The accuracy of the CMF propagator was set to 10^{-6} .

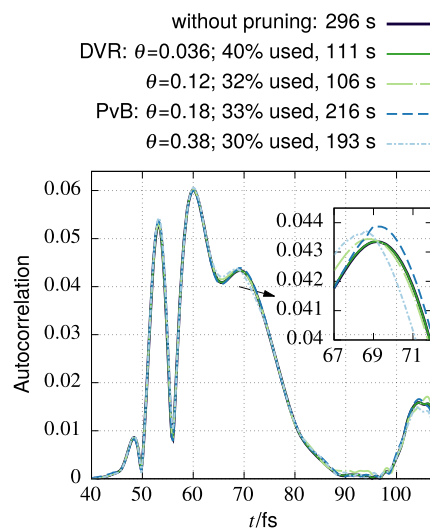


FIG. 1. Autocorrelation function of NO₂ dynamics without pruning (black) compared to pruned DVR (green lines) and pruned PvB (blue lines) dynamics. The percentages denote the average fraction of the total basis size used for all coordinates. 100% corresponds to a basis size of $(256 + 256 + 100)$. The times denote the overall runtime and θ denotes the wave amplitude threshold.

The computation was done on a single core of an Intel(R) Core(TM) i7-6700 processor. We used the same wave amplitude threshold, θ , in all coordinates. Using different thresholds for the angular and for the radial coordinates would maybe give an improvement. Note that the values of θ for a requested accuracy level depend on the dimensionality and the choice of basis. Better definitions of θ might be considered in the future. In all of our pruned benchmark calculations, we simply scanned various values of θ on a logarithmic scale to find appropriate values. Throughout, we use a regularization parameter of $\epsilon = 10^{-8}$ [see Eq. (11)].

The unpruned dynamics (black line) took 296 s runtime. If 40% of the overall basis is used on average (green line), pruned DVR can accurately reproduce the unpruned dynamics and 62% of the overall runtime can be saved (111 s runtime). PvB is less efficient. If 33% of the overall basis is used (dashed blue line), the autocorrelation function is less accurately reproduced and only 27% of runtime is saved (216 s runtime). This is a result of the nondiagonality of the potential matrices in the PvB representation, see Ref. 37.

B. Pruning the configurations of single-particle basis functions: Pyrazine

Here, we consider the quadratic vibronic-coupling model of 24-dimensional (plus an electronic degree of freedom, DOF) pyrazine.^{9,10} To simplify the implementation, we use the so-called single-set mode⁷ where the same SPF basis is used for both electronic states. The SPFs are expanded in Gauss-Hermite-DVRs.^{1,91,92} Including the electronic DOF, the coefficient tensor, \mathbf{A} , is nine-dimensional.

The basis parameters and mode combinations are shown in Table I. There, we show two variants for the number of SPFs, A and B. Variant A corresponds to the numbers used in Refs. 10 and 58 whereas variant B corresponds to the ‘‘MCTDH-3’’

TABLE I. Mode combination and basis parameters of the (24+1)-dimensional pyrazine example. Two variants for the number of SPFs are shown, see the text for details.

DOF	Combined normal modes	Number of SPFs variants {A, B}	Primitive basis size
0	Electronic	{2,2}	2
1	$[\nu_{10a}, \nu_{6a}]$	{14,21}	[40, 32]
2	$[\nu_1, \nu_{9a}, \nu_{8a}]$	{8,12}	[20, 12, 8]
3	$[\nu_2, \nu_{6b}, \nu_{8b}]$	{6,7}	[4, 8, 24]
4	$[\nu_4, \nu_5, \nu_3]$	{6,8}	[24, 8, 8]
5	$[\nu_{16a}, \nu_{12}, \nu_{13}]$	{5,7}	[24, 20, 4]
6	$[\nu_{19b}, \nu_{18b}]$	{7,12}	[72, 80]
7	$[\nu_{18a}, \nu_{14}, \nu_{19a}, \nu_{17a}]$	{5,7}	[6, 20, 6, 6]
8	$[\nu_{20b}, \nu_{16b}, \nu_{11}, \nu_{7b}]$	{4,5}	[6, 32, 6, 4]

variant from Ref. 13. Many more SPFs are used in variant B. We closely follow Ref. 10 and first use variant A that also allows for a comparison with Ref. 58 (Sec. IV B 1). The spectrum computed from the dynamics with variant A is already converged to a reasonable level but the autocorrelation function is not. Therefore, we also show results from variant B and later compare also with ML-MCTDH results (Sec. IV B 2). Comparing variants A and B provides insights into the scalability of DP-MCTDH. If the reader is more interested in the general performance and comparison to ML-MCTDH, the studies on variant A (Sec. IV B 1) may be skipped. Finally, we present unrestricted simulations (no limit regarding the number of SPFs) in Subsection IV B 3.

1. Variant A (fewer SPFs)

For variant A, almost 95% of runtime is spent on routines where **A** is involved. Hence, pruning only **A**, that is, the SPF space, makes sense. Because the unpruned propagation is not fully converged with respect to the number of SPFs, we have limited the maximal number of SPFs in the pruned dynamics to the number of SPFs in the unpruned dynamics.

We stress that variant A is not converged with respect to the number of SPFs, n_k . Compared to variant B, the autocorrelation function differs. The restricted values for n_k in variant A lead to a strong dependence of the dynamics on the choice of the initially unoccupied SPFs. Depending on their shape, the SPFs and thus the wavefunction “drift” into different spaces. In particular, values of the autocorrelation function at the maxima are sensitive to this choice, whereas the positions of the maxima are not. Even minor perturbation of the unoccupied SPFs has a strong influence on the autocorrelation function at later times. The sensitivity of the values can be considered as an indicator of the accuracy. The better converged variant B is much less sensitive to the choice of the initial SPFs. There, a perturbation yields almost no difference in the autocorrelation function for the first 80 fs. For larger times, the difference is less than for variant A.

Following the implementation in the Heidelberg MCTDH package,¹¹¹ we prepare the initially unoccupied SPFs by generating an orthonormal Krylov space of the operator \hat{x} : $|\varphi_j^{(k)}\rangle = \hat{x}^{j-1}|\varphi_1^{(k)}\rangle$ for $j > 1$. To measure the sensitivity, we compare unpruned dynamics with those where the initially unoccupied SPFs are perturbed by adding higher order Krylov vectors:

$|\varphi_j^{(k)}\rangle^{\text{pert.}} = |\varphi_j^{(k)}\rangle + r|\varphi_{j+n_k}^{(k)}\rangle$, for $j > 1$, where r is a random number in the range $[-0.01, 0.01]$. This procedure follows a suggestion by Meyer.¹¹⁴ As only initially unoccupied SPFs are perturbed, this procedure has no influence on the initial wavefunction. The autocorrelation function is shown in Fig. 2, where the continuous black line corresponds to unpruned dynamics and the dashed red line corresponds to dynamics with perturbed initial SPFs.

This sensitivity to the choice of the initial SPFs renders a comparison of accuracy with the pruned dynamics difficult. In our pruned variant, SPFs that are dynamically added at later time steps are prepared differently from the unpruned variant; see Sec. III C. Even if the newly added SPFs were generated by the same procedure, the dynamics would differ because they would not be generated by the SPFs at $t = 0$. To make the comparison with our pruned dynamics easier, we propagate until $t = t_S$ and restart the propagation again at $t = 0$ with the subset of configurations from $t = t_S$. The SPFs at $t = 0$ do not differ for the pruned and unpruned variants. Note that this still corresponds to pruned dynamics for *all* propagation times. It only means that we use a minimum pruned set of configurations for $t \leq t_S$ but adding and removing other configurations is still allowed during this initial period. We chose $t_S = 7$ fs, well within the initial decay of the autocorrelation function. At least for dynamics with lower wave amplitude thresholds, during the first 7 fs, almost all SPFs are used somewhere in **A** such that the number of initial SPFs is the same, compared to unpruned dynamics. The full coefficient tensor is never required for the pruned dynamics. Hence, this initialization procedure is negligible with respect to runtime because, compared to later times, not many configurations contribute to the wave function within the first 7 fs.

In general, this procedure increases the stability of the dynamics. Only a single configuration is occupied at $t = 0$ and many other configurations will become important within the

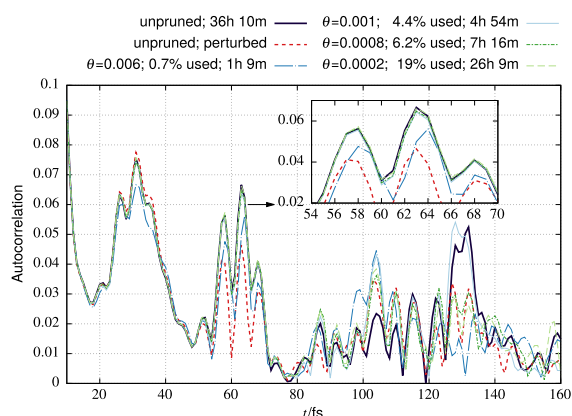


FIG. 2. Autocorrelation function of unpruned pyrazine dynamics compared to dynamics with a pruned coefficient tensor. The (maximal) number of SPFs corresponds to variant A in Table I. The percentages denote the average size of the pruned configuration space used. 100% corresponds to a size of $5.6 \cdot 10^6$. The times denote the overall runtime and θ denotes the wave amplitude threshold. The dashed red curve shows unpruned dynamics where the initial and unoccupied SPFs are randomly perturbed and illustrates the general accuracy of the unpruned dynamics.

first femtoseconds. Therefore, a dynamically pruned dynamics may require short time steps during the initial period of propagation. For the pruning of the coefficient tensor, we use a “configuration-space radius” of $\sqrt{2}$,⁸⁰ where $2D^2$ nearest neighbors are added for each non-negligible configuration. This further increased the stability, compared to the radius of 1 used for pruning DVR,³⁷ that only adds $2D$ nearest neighbors.

All computations were performed using a single core of Intel(R) Xeon(R) CPU E5-2650 v2 processors. The accuracy of the CMF propagator was set to 10^{-6} , and the accuracy of the propagators for the EOM of \mathbf{A} and that of the SPFs were set to 10^{-7} . Like Ref. 58, we propagated until 80 fs.

Figure 2 depicts the autocorrelation function for the pruned and unpruned dynamics (black line). Until approximately 80 fs, the autocorrelation function can be well described using pruned dynamics. At later times, the autocorrelation function is still in good agreement, compared to the difference of unpruned dynamics with and without perturbed unoccupied SPFs (dashed red line), see above. In particular, the positions of the maxima of the autocorrelation function are generally in excellent agreement with those from the unpruned dynamics. If 4.4% of all possible configurations are used (pale blue line), the runtime can be reduced from 36 h to approximately 5 h. However, even if only 19% of the configuration space is needed (dashed pale green line), the pruned dynamics takes 72% of the runtime of the dynamics without pruning. This is caused by the additional overhead of the pruned tensor transformation. In general, pruning is more favorable if larger numbers of SPFs are required. Since, on average, only six SPFs in each degree of freedom are used, pruning cannot be fully efficient. Even so, a significant decrease in runtime is possible. We note that our pruned calculations achieve larger speed-ups than those found in the ML-spawning scheme.¹⁹ Furthermore, these timings are much better than those presented by Worth.⁵⁸ There, the static pruning led to *larger* CPU time even if only 16% of the totally available configurations are used (compare configuration 24a3 to 24a in Table II in Ref. 58). Worth reported a speed-up of 4.6 if only 0.5% of configurations are used. We gain a speed-up of 5.1 if 6.2% of configurations are used and obtain a better converged spectrum, see below (Fig. 3). Of course, these comparisons have to be taken with care because the computations were done on different hardware. Wodraszka and Carrington used a pruning similar to that of Worth and developed a new algorithm that should improve performance.⁷⁸ However, they did not try to solve the TDSE, so no direct comparison can be done.

In many applications, not the autocorrelation function but the absorption spectrum is of importance. In general, this quantity is easier to converge than the autocorrelation function. We follow Worth⁵⁸ and compute the spectrum as

$$I(\omega) \propto \omega \int_0^T dt \Re [\langle \Psi(0) | \Psi(t) \rangle \exp(i\omega t) \times \exp(-t/\tau) \cos(\pi t/(2T))], \quad (20)$$

with the damping parameter $\tau = 150$ fs, using the `autospec` utility of the Heidelberg MCTDH package.¹¹¹ The shifted and scaled spectra of the autocorrelation functions of Fig. 2 are shown in Fig. 3. Compared to the spectrum of the unpruned

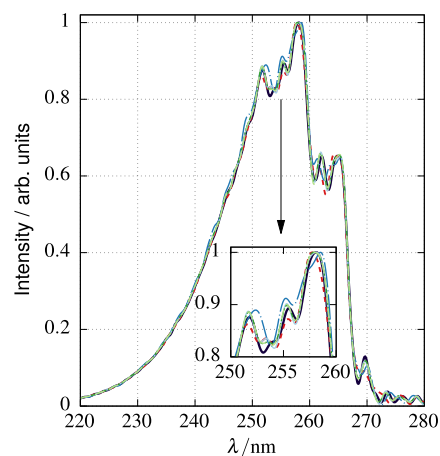


FIG. 3. Shifted absorption spectrum of pyrazine using (DP)-MCTDH with variant A (Table I) for the number of SPFs in each DOF: unpruned (black line), unperturbed pruned with perturbed SPFs (red dashed line), pruned with an average usage of 0.7% (blue, long dashed-dotted line), 4.4% (pale blue, continuous line), 6.2% (dashed-dotted green line), and 19% (pale green, dashed line). See Fig. 2 and text for further details.

dynamics with perturbed unoccupied SPFs, the agreement is excellent. Even using only 0.7% of the full configuration space (blue line) gives a qualitatively correct behavior within the uncertainty of the spectrum introduced by the damping of the autocorrelation function (1 nm at 250 nm; see Ref. 58). If this accuracy is sufficient, the runtime can be reduced from 36 h to 1 h. Note that the spectrum slightly differs from that shown in Ref. 58 because we use the single-set approach and most likely a different accuracy of the propagator (no accuracy threshold is mentioned by Worth).

2. Variant B (more SPFs)

We now turn to variant B where more SPFs in each DOF are used. Now, the sensitivity to the initially unoccupied SPFs is not severe. The autocorrelation functions for pruned and unpruned dynamics are shown in Fig. 4. Here, the unpruned MCTDH dynamics was performed with the Heidelberg package¹¹¹ in order to exploit shared-memory parallelization (16 threads).¹¹⁵ Since the speed-up with respect to the number of threads is not ideal,¹³ we have estimated the total runtime on a single core to be 692 h (see Fig. 4) based on a speed-up factor of 5.2 for the parallel computation. Until approximately 80 fs, the autocorrelation function can be well described with pruned dynamics using only 0.53% of the totally available configurations (blue curve). The runtime is then below 10 h—much less than even the runtime from unpruned dynamics of variant A! With only 0.75% of all configurations (dashed-dotted green line), the autocorrelation function is accurately reproduced at almost all times. The deviation should be compared with that of the more accurate ML-MCTDH result (gray line); see next paragraph. The runtime was only about 14 h, representing a speed-up of 49. Even if many more configurations are used, e.g., 4% (dashed pale green line), a significant speed-up of 7 is obtained.

In Fig. 4, we also compare to a ML-MCTDH calculation (gray curve). The setup corresponds to that of the (largest)

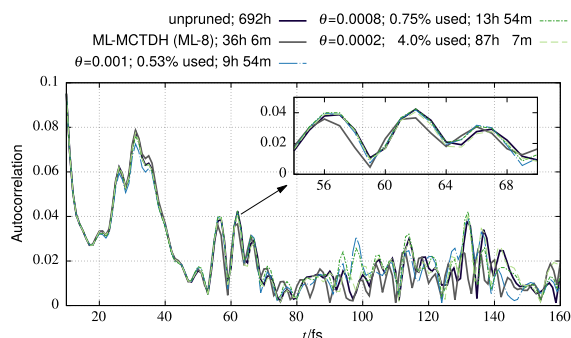


FIG. 4. Same as Fig. 2, except that the maximal number of SPFs corresponds to variant B in Table I. The gray curve shows the result of ML-MCTDH (configuration ML-8 in Ref. 13) for further comparisons. 100% corresponds to an average size of the pruned configuration tensor of $8.3 \cdot 10^7$.

“ML-8” configuration in Ref. 13 but we use a lower accuracy of the propagator (10^{-6}), like we use in our other simulations. We employ the Heidelberg ML-MCTDH package¹¹⁶ for this simulation. This calculation is considered to be more accurate than variant B.¹³ Despite the efficiency of the multilayer method, almost all of our pruned simulations are faster than the (unpruned) ML-MCTDH. Only if 4% of the configurations are used is the pruned dynamics a factor of 2.4 slower than the ML-8 simulations. A simulation of the “ML-6” configuration from Ref. 13 (not shown) took only 14 h and 46 min but this configuration is less accurate than variant B and still needs slightly more computing time than our more accurate pruned dynamics with usage of 0.75%, which took 13 h and 54 min. Note, however, that Vendrell and Meyer comment that their ML-tree is not optimal.¹³

The results of variants A and B are summarized in Table II. For evaluating the error, we follow Worth⁵⁸ and evaluate the error as

$$\Delta_{AR} = \|\tilde{I}_A(\omega) - \tilde{I}_R(\omega)\|_2, \quad \tilde{I}_X = I_X / \|I_X\|_2, \quad (21)$$

where R is the reference calculation. The norm is computed by discretizing the spectrum $I(\omega)$ on a grid of size 10^3 .

3. No restriction on the number of SPFs

As a final test, we lift the SPF constraint almost completely by setting the maximum number of SPFs in each DOF to be 50, not including the electronic DOF. The restriction to 50 SPFs was chosen for convenience. Except for dimension 1, this number does not restrict the pruning. The resulting autocorrelation functions are shown in Fig. 5. Comparing to the unpruned variant B and the more accurate “ML-8” variant, it shows that the autocorrelation function can be systematically converged within our pruning scheme. Notably, the positions of the maxima of the autocorrelation functions for the pruned dynamics [continuous blue, dashed(-dotted) green, and dotted yellow lines] are generally different from variant B (black line) but resemble the more accurate ML-8 variant (gray line). Only after 120 fs, one can notice a more significant deviation. At these times, even the ML-8 variant is not converged and one might speculate that our pruned dynamics are more accurate. To verify this, a more systematic

TABLE II. Comparison of the performance of variants A and B of DP-MCTDH dynamics of pyrazine with the ML variants from Ref. 13. The errors are defined according to Eq. (21). Error 1 uses the ML-8 calculation as a reference whereas error 2 uses the corresponding unpruned calculation as a reference. $\langle N_{\text{coeff}} \rangle$ denotes the (average) number of coefficients used to describe the configuration tensor.

Setup	$\langle N_{\text{coeff}} \rangle$	Runtime (h:m)	Error 1	Error 2
ML-8	$1.5 \cdot 10^5$	36:60
ML-7	$1.1 \cdot 10^5$	27:00	0.005	...
ML-6	$5.1 \cdot 10^4$	14:47	0.015	...
A: unpruned	$5.6 \cdot 10^6$	36:10	0.044	...
A: "-", perturbed	$5.6 \cdot 10^6$	36:10	0.044	0.029
A: $\theta = 0.006$	$3.9 \cdot 10^4$	1:09	0.043	0.033
A: $\theta = 0.001$	$2.5 \cdot 10^5$	4:54	0.042	0.014
A: $\theta = 0.0008$	$3.5 \cdot 10^5$	7:16	0.043	0.012
A: $\theta = 0.0002$	$1.1 \cdot 10^6$	26:09	0.045	0.014
B: unpruned	$8.3 \cdot 10^7$	692:00	0.011	...
B: $\theta = 0.001$	$4.4 \cdot 10^5$	9:54	0.016	0.016
B: $\theta = 0.0008$	$6.2 \cdot 10^5$	13:54	0.013	0.011
B: $\theta = 0.0002$	$3.3 \cdot 10^6$	87:07	0.010	0.009

convergence study would be required. This is beyond the scope of this work.

Here, all of our pruned simulations need more runtime than the ML simulation. However, the runtimes are of similar magnitude while including a substantially larger configuration space. As discussed above, by constraining the number of SPFs to a lower limit, faster runtimes may be obtained if some accuracy is sacrificed.

C. Pruning both the primitive and the SPF basis with higher-dimensional mode combination: Pyrazine

As a proof of principle, we show that pruning both the SPF and the primitive basis can be combined. We show further that pruning the primitive basis allows for higher-dimensional mode combination. We use again the pyrazine model (variant A in Table I) but now combine the modes ν_2 , ν_{6b} and ν_{8b} together with ν_4 , ν_5 and ν_3 using twelve SPFs. This decreases the dimension of the coefficient tensor by one but requires propagating

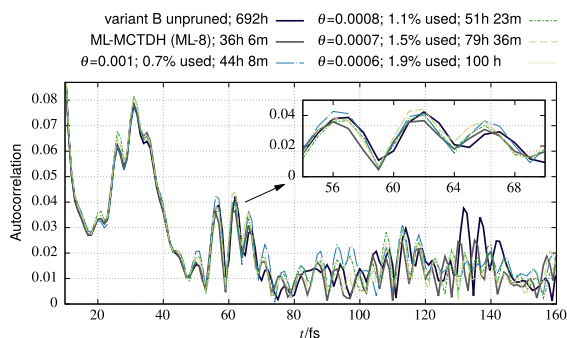


FIG. 5. Same as Fig. 2, except that the maximal number of SPFs is allowed to be as high as 50 in each dimension (except for the electronic DOF) for the pruned dynamics. Except for dimension 1, this large number does not restrict the pruning. For further comparisons, the black line shows unpruned dynamics of variant B; see Table I. The gray curve shows result of ML-MCTDH (configuration ML-8 in Ref. 13). 100% corresponds to an average size of the pruned configuration tensor of $7.8 \cdot 10^{13}$.

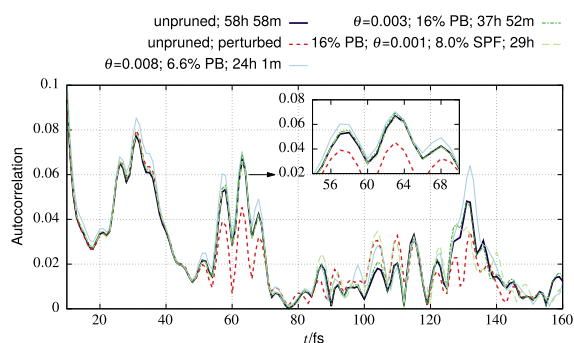


FIG. 6. Same as Fig. 2 but with higher-dimensional mode combination and with a pruned primitive basis (PB) in the first DOF; see text. The percentages denote the average usage of PB. 100% of PB corresponds to a size of $1.2 \cdot 10^6$. The dashed pale green line shows dynamics where both the primitive basis and the configuration space are pruned. The SPFs span a space of size $1.3 \cdot 10^6$.

six-dimensional SPFs. Additionally, this increases the overall runtime for the unpruned propagation by 60%. The propagation of the SPFs in this mode is then the dominant part (70% of runtime) of the propagation.

Hence, it makes sense to prune the primitive basis. We prune only the DVR representation of these six-dimensional SPFs. Note that the Gauss-Hermite DVR gives a non-equidistant grid. Nevertheless, our pruning methodology from Ref. 37 works here. All other SPFs are propagated without pruning their representation. The result is shown in Fig. 6. If only 16% of the primitive basis is used (dashed-dotted green line in Fig. 6), the autocorrelation function can be reproduced accurately and the runtime can be reduced from 59 h to 38 h. This almost matches the runtime of the unpruned dynamics from Sec. IV B, thus offsetting the unfavorable mode combination setup.

If both the primitive basis and the SPF basis are pruned, the runtime can be decreased to 29 h while retaining a reasonable accuracy (dashed pale green line). Then, solving the SPF

EOM again becomes the dominant part of the runtime. The contributions of the parts of the code dealing with \mathbf{A} are then less than 8%.

D. Analysis of the pruned configuration space

We now turn to an analysis of the pruned configuration space used in Subsection IV B 3. It is clear that this nine-dimensional configuration space cannot be analyzed in detail everywhere. It is instructive, however, to examine the diagonal of the two-“particle” reduced density matrix in configuration space, i.e., we have integrated the absolute square of the wavefunction in configuration space for all but two combined modes in the pruned subspace. One “particle” then corresponds to the combined modes used for setting up the SPFs in the corresponding DOF. For example, the particle of the DOF 6 would represent the modes ν_{19b} and ν_{18b} , compare with Table I. Figure 7 (Multimedia view) shows two examples of the diagonal of the reduced density matrix of the underlying wavefunction in Fig. 5 with 1.1% usage (dashed-dotted green curve) at $t = 59$ fs and $t = 80$ fs. Since natural orbitals, ordered by their weight, are used for the dynamics, a triangle-shaped occupation of the ordered orbitals is expected. The smaller the orbital index, the larger is the weight of the corresponding orbital. This shape approximately appears in panels (c) and (d) in Fig. 7 (Multimedia view). However, the structure is more complex and contains some “islands” in this two-dimensional space. This is more pronounced in panels (a) and (b), showing DOF 1 and 6. Because natural orbitals diagonalize only the one-particle density matrix, the natural populations (eigenvalues of the density matrix) are highly averaged quantities. It is still possible that configurations corresponding to orbitals with small natural populations may become significant during the dynamics. Note that the structure of these plots changes during time and can become more complex for intermediate times, as can be seen by comparing panels (a) with (b) or (c) with (d). Furthermore, note that the two-dimensional reduced densities vastly understate the sparsity of the full

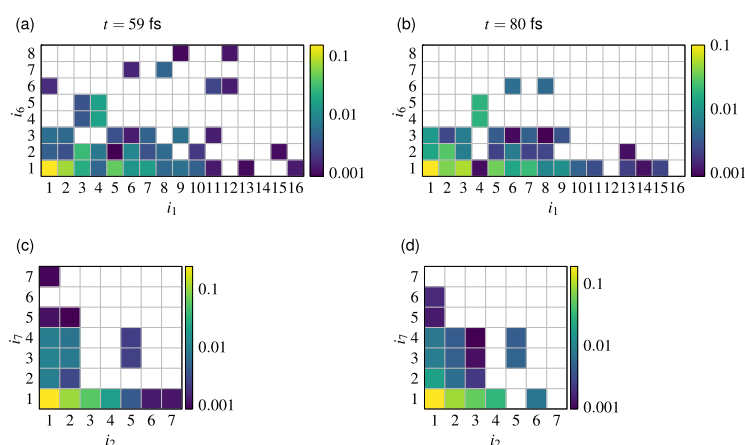


FIG. 7. Graphical representation of the diagonal of the two-“particle” reduced density matrix in configuration space of pyrazine at $t = 59$ fs for (a) and (c) and at $t = 80$ fs for (b) and (d). The density corresponds to unconstrained DP-MCTDH dynamics of Fig. 5 with a mean-usage of 1.1%. Each pixel corresponds to one configuration. White pixels correspond to configurations whose values are below the employed wave amplitude threshold, 0.0008. Lower indices of the SPFs correspond to natural orbitals with larger populations. Panels (a) and (b) show the (combined) DOF 1 (modes $[\nu_{10a}, \nu_{6a}]$) and 6 ($[\nu_{19b}, \nu_{18b}]$); see Table I. Panels (c) and (d) show the DOF 2 ($[\nu_1, \nu_{9a}, \nu_{8a}]$) and 7 ($[\nu_{18a}, \nu_{14}, \nu_{19a}, \nu_{17a}]$). (Multimedia view) [URL: <http://dx.doi.org/10.1063/1.4993219.1>]

nine-dimensional density. An analysis of the diagonal of the three-“particle” density matrices forms a similar picture. Additionally, an analysis of the DP-MCTDH dynamics with 0.7% usage (dashed-dotted blue curve in Fig. 5) and of unpruned dynamics of variant A does not significantly change the structure presented in Fig. 7 (Multimedia view). Clearly, a simple static pruning as used in Refs. 58 and 78 would be suboptimal as it would have to be vastly overextended to describe the structure of this non-direct-product configuration space for all simulation times.

V. CONCLUSIONS AND OUTLOOK

We have presented two approaches for dynamical pruning MCTDH (DP-MCTDH). The first method prunes the primitive basis used to represent the SPFs whereas the second method prunes the set of configurations in the SPF space. The former method is useful for dynamics where a large, possibly multi-dimensional primitive basis set is required, as in NO₂. There, pruning the primitive bases leads to speed-up factors between two and three without jeopardizing accuracy. We showed further that pruning the primitive basis makes higher-dimensional mode combination feasible, taking the 24-dimensional nonadiabatic dynamics of pyrazine as an example. Note that this partially relaxes the constraint that the Hamiltonian be of SoP form.

Pruning the space of SPF configurations often allows for even larger time-savings. We again used pyrazine dynamics as an example and showed that, while retaining accuracy, pruning leads to speed-ups between 5 and 50. The more the SPFs are needed in MCTDH, the larger is the speed-up in DP-MCTDH. Depending on the setup, the runtime of the DP-MCTDH dynamics is comparable to or even faster than ML-MCTDH. We also showed that both pruning methods can be combined, again using pyrazine with higher-dimensional mode combination as an example.

Pruning the SPF space dynamically introduces an MCTDH variant, DP-MCTDH, with just one single parameter, the wave amplitude threshold. By analyzing the reduced densities, we showed that dynamic instead of static pruning is crucial for a most effective reduction of the number of used configurations. The result is a more powerful alternative to the ML-spawning scheme. Further, both pruning strategies might be useful for solving the TISE as well. There, an adaptive or iterative pruning like it is used in our time-independent simulations⁸⁰ should, in principle, be more efficient than simple static pruning, as was recently shown.⁷⁹ The achievement of efficiency comparable to ML-MCTDH is promising. Combining pruning strategies with ML-MCTDH, giving DP-ML-MCTDH, should give an even faster method without jeopardizing accuracy.

ACKNOWLEDGMENTS

We thank H.-D. Meyer for providing us with the Heidelberg MCTDH package and for helpful discussions. H.R.L. thanks W. Koch for helpful discussions and comments on the manuscript. H.R.L. acknowledges B. Hartke for his continuous support, helpful discussions, and comments on the

manuscript. H.R.L. acknowledges support from the Fonds der Chemischen Industrie and the Studienstiftung des deutschen Volkes. D.J.T. acknowledges support from the Israel Science Foundation (1094/16) and the German-Israeli Foundation for Scientific Research and Development (GIF).

APPENDIX: PSEUDO-CODE OF THE PRUNING PROCEDURE

After each CMF step, the pruning proceeds as follows:
if prune primitive basis **then**

- update primitive basis
- set newly added coefficients to zero
- do Löwdin orthogonalization of SPFs
- update data structures for tensor transformation

end if

if prune coefficient tensor **A then**

- update **A**
- set newly added coefficients of **A** to zero
- set new SPFs to Krylov vectors of uncorrelated Hamiltonian
- do Gram-Schmidt orthogonalization of new SPFs
- transform to natural orbitals
- update data structures for tensor transformation

end if

¹D. J. Tannor, *Introduction to Quantum Mechanics: A Time-Dependent Perspective*, 1st ed. (University Science Books, 2007).

²L. Chen, K. Shao, J. Chen, M. Yang, and D. H. Zhang, *J. Chem. Phys.* **144**, 194309 (2016).

³H. Song, J. Li, M. Yang, Y. Lu, and H. Guo, *Phys. Chem. Chem. Phys.* **16**, 17770 (2014).

⁴T. Carrington, Jr., *J. Chem. Phys.* **146**, 120902 (2017).

⁵H.-D. Meyer, U. Manthe, and L. Cederbaum, *Chem. Phys. Lett.* **165**, 73 (1990).

⁶U. Manthe, H. Meyer, and L. S. Cederbaum, *J. Chem. Phys.* **97**, 3199 (1992).

⁷M. H. Beck, A. Jäckle, G. A. Worth, and H.-D. Meyer, *Phys. Rep.* **324**, 1 (2000).

⁸F. Huarte-Larrañaga and U. Manthe, *J. Phys. Chem. A* **105**, 2522 (2001).

⁹G. A. Worth, H.-D. Meyer, and L. S. Cederbaum, *J. Chem. Phys.* **109**, 3518 (1998).

¹⁰A. Raab, G. A. Worth, H.-D. Meyer, and L. S. Cederbaum, *J. Chem. Phys.* **110**, 936 (1999).

¹¹H. Wang and M. Thoss, *J. Chem. Phys.* **119**, 1289 (2003).

¹²U. Manthe, *J. Chem. Phys.* **128**, 164116 (2008).

¹³O. Vendrell and H.-D. Meyer, *J. Chem. Phys.* **134**, 044135 (2011).

¹⁴H. Wang, *J. Phys. Chem. A* **119**, 7951 (2015).

¹⁵Y. Xie, J. Zheng, and Z. Lan, *J. Chem. Phys.* **142**, 084706 (2015).

¹⁶J. Schulze, M. F. Shibl, M. J. Al-Marri, and O. Kühn, *J. Chem. Phys.* **144**, 185101 (2016).

¹⁷R. Welsch and U. Manthe, *J. Chem. Phys.* **137**, 244106 (2012).

¹⁸Q. Meng and H.-D. Meyer, *J. Chem. Phys.* **141**, 124309 (2014).

¹⁹D. Mendive-Tapia, T. Firmino, H.-D. Meyer, and F. Gatti, *Chem. Phys.* **482**, 113 (2017).

²⁰A. Jäckle and H.-D. Meyer, *J. Chem. Phys.* **104**, 7974 (1996).

²¹D. Peláez and H.-D. Meyer, *J. Chem. Phys.* **138**, 014108 (2013).

²²F. Otto, *J. Chem. Phys.* **140**, 014106 (2014).

²³S. Manzhos and T. Carrington, *J. Chem. Phys.* **125**, 194105 (2006).

²⁴W. Koch and D. H. Zhang, *J. Chem. Phys.* **141**, 021101 (2014).

²⁵G. Avila and T. Carrington, *J. Chem. Phys.* **143**, 044106 (2015).

²⁶B. Ziegler and G. Rauhut, *J. Chem. Phys.* **144**, 114114 (2016).

²⁷O. Vendrell, F. Gatti, D. Lauvergnat, and H.-D. Meyer, *J. Chem. Phys.* **127**, 184302 (2007).

²⁸U. Manthe, *J. Chem. Phys.* **105**, 6989 (1996).

- 044103-12 H. R. Larsson and D. J. Tannor J. Chem. Phys. **147**, 044103 (2017)
- ²⁹U. Manthe, *J. Chem. Phys.* **130**, 054109 (2009).
³⁰U. Manthe, *J. Chem. Phys.* **142**, 244109 (2015).
³¹B. Hartke, *Phys. Chem. Chem. Phys.* **8**, 3627 (2006).
³²D. A. McCormack, *J. Chem. Phys.* **124**, 204101 (2006).
³³L. R. Petey and R. E. Wyatt, *Chem. Phys. Lett.* **424**, 443 (2006).
³⁴L. R. Petey and R. E. Wyatt, *Int. J. Quantum Chem.* **107**, 1566 (2007).
³⁵N. Takemoto, A. Shimshovitz, and D. J. Tannor, *J. Chem. Phys.* **137**, 011102 (2012).
³⁶E. Assémat, S. Machnes, and D. Tannor, "Double ionization of helium from a phase space perspective," e-print [arXiv:1502.05165](https://arxiv.org/abs/1502.05165) (2015).
³⁷H. R. Larsson, B. Hartke, and D. J. Tannor, *J. Chem. Phys.* **145**, 204108 (2016).
³⁸J. C. Light, "Discrete variable representations in quantum dynamics," in *Time-Dependent Quantum Molecular Dynamics*, edited by J. Broeckhove and L. Lathouwers (Springer, 1992), pp. 185–199.
³⁹M. J. Davis and E. J. Heller, *J. Chem. Phys.* **71**, 3383 (1979).
⁴⁰A. Shimshovitz and D. J. Tannor, *Phys. Rev. Lett.* **109**, 070402 (2012).
⁴¹S. Machnes, E. Assémat, H. R. Larsson, and D. J. Tannor, *J. Phys. Chem. A* **120**, 3296 (2016).
⁴²D. J. Tannor, S. Machnes, E. Assémat, and H. R. Larsson, "Phase space vs. coordinate space methods: Prognosis for large quantum calculations," in *Advances in Chemical Physics*, Vol. 163 (John Wiley & Sons, Inc., in press).
⁴³K. G. Wilson, *Generalized Wannier Functions* (Cornell University, 1987).
⁴⁴I. Daubechies, S. Jaffard, and J.-L. Journé, *SIAM J. Math. Anal.* **22**, 554 (1991).
⁴⁵B. Poirier, *J. Theor. Comput. Chem.* **02**, 65 (2003).
⁴⁶B. Poirier and A. Salam, *J. Chem. Phys.* **121**, 1690 (2004).
⁴⁷B. Poirier and A. Salam, *J. Chem. Phys.* **121**, 1704 (2004).
⁴⁸R. Lombardini and B. Poirier, *J. Chem. Phys.* **124**, 144107 (2006).
⁴⁹A. Shimshovitz, "Phase space approach to solving the Schrödinger equation," Ph.D. thesis, Weizmann Institute of Science, 2015.
⁵⁰A. Shimshovitz, Z. Bačić, and D. J. Tannor, *J. Chem. Phys.* **141**, 234106 (2014).
⁵¹J. Brown and T. Carrington, *J. Chem. Phys.* **143**, 044104 (2015).
⁵²T. Halverson and B. Poirier, *J. Chem. Phys.* **140**, 204112 (2014).
⁵³T. Halverson and B. Poirier, *Chem. Phys. Lett.* **624**, 37 (2015).
⁵⁴T. Halverson and B. Poirier, *J. Phys. Chem. A* **119**, 12417–12433 (2015).
⁵⁵J. Brown and T. Carrington, Jr., *J. Chem. Phys.* **144**, 244115 (2016).
⁵⁶I. Burghardt, H.-D. Meyer, and L. S. Cederbaum, *J. Chem. Phys.* **111**, 2927 (1999).
⁵⁷S. Römer, M. Ruckebauer, and I. Burghardt, *J. Chem. Phys.* **138**, 064106 (2013).
⁵⁸G. A. Worth, *J. Chem. Phys.* **112**, 8322 (2000).
⁵⁹N. Makri and W. H. Miller, *J. Chem. Phys.* **87**, 5781 (1987).
⁶⁰A. D. Hammerich, R. Kosloff, and M. A. Ratner, "Time dependent quantum mechanical calculations of the dissociation dynamics of the cluster He_n-I₂," in *Large Finite Systems: Proceedings of the Twentieth Jerusalem Symposium on Quantum Chemistry and Biochemistry Held in Jerusalem*, edited by J. Jortner and A. Pullman (Springer, 1987), Vol. 20.
⁶¹A. D. Hammerich, R. Kosloff, and M. A. Ratner, *Chem. Phys. Lett.* **171**, 97 (1990).
⁶²D. J. Haxton and C. W. McCurdy, *Phys. Rev. A* **91**, 012509 (2015).
⁶³H. Miyagi and L. B. Madsen, *Phys. Rev. A* **87**, 062511 (2013).
⁶⁴H. Miyagi and L. B. Madsen, *Phys. Rev. A* **89**, 063416 (2014).
⁶⁵H. Miyagi and L. B. Madsen, *Phys. Rev. A* **95**, 023415 (2017).
⁶⁶T. Sato and K. L. Ishikawa, *Phys. Rev. A* **91**, 023417 (2015).
⁶⁷C. Lévesque and L. B. Madsen, *New J. Phys.* **19**, 043007 (2017).
⁶⁸G. A. Worth, M. A. Robb, and I. Burghardt, *Faraday Discuss.* **127**, 307 (2004).
⁶⁹G. Richings, I. Polyak, K. Spinlove, G. Worth, I. Burghardt, and B. Lasorne, *Int. Rev. Phys. Chem.* **34**, 269–308 (2015).
⁷⁰H.-D. Meyer, F. L. Quéré, C. Léonard, and F. Gatti, *Chem. Phys.* **329**, 179 (2006).
⁷¹F. Culot, F. Laruelle, and J. Liévin, *Theor. Chim. Acta* **92**, 211 (1995).
⁷²F. Culot and J. Liévin, *Theor. Chim. Acta* **89**, 227 (1994).
⁷³S. Heislbetz and G. Rauhut, *J. Chem. Phys.* **132**, 124102 (2010).
⁷⁴S. Heislbetz, F. Pfeiffer, and G. Rauhut, *J. Chem. Phys.* **134**, 204108 (2011).
⁷⁵W. Mizukami and D. P. Tew, *J. Chem. Phys.* **139**, 194108 (2013).
⁷⁶P. Meier, D. Oschetzki, F. Pfeiffer, and G. Rauhut, *J. Chem. Phys.* **143**, 244111 (2015).
⁷⁷F. Pfeiffer and G. Rauhut, *J. Chem. Phys.* **140**, 064110 (2014).
⁷⁸R. Wodraszka and T. Carrington, *J. Chem. Phys.* **145**, 044110 (2016).
⁷⁹R. Wodraszka and T. Carrington, *J. Chem. Phys.* **146**, 194105 (2017).
⁸⁰S. Machnes, E. Assémat, and D. Tannor, "Quantum dynamics in phase space using the biorthogonal von Neumann bases: Algorithmic considerations," e-print [arXiv:1603.03963](https://arxiv.org/abs/1603.03963) (2016).
⁸¹T. G. Kolda and B. W. Bader, *SIAM Rev.* **51**, 455 (2009).
⁸²T. Helgaker, J. Olsen, and P. Jørgensen, *Molecular Electronic-Structure Theory*, 1st ed. (Wiley, 2013).
⁸³P. A. M. Dirac, *Math. Proc. Cambridge Philos. Soc.* **26**, 376–385 (1930).
⁸⁴J. Frenkel, *Wave Mechanics: Advanced General Theory* (Clarendon Press, Oxford, 1934).
⁸⁵A. McLachlan, *Mol. Phys.* **8**, 39 (1964).
⁸⁶J. Broeckhove, L. Lathouwers, E. Kesteloot, and P. V. Leuven, *Chem. Phys. Lett.* **149**, 547 (1988).
⁸⁷C. M. Hinz, S. Bauch, and M. Bonitz, *J. Phys.: Conf. Ser.* **696**, 012009 (2016).
⁸⁸C. Lubich, *Appl. Math. Res. eXpress* **2015**, 311–328.
⁸⁹B. Kloss, I. Burghardt, and C. Lubich, *J. Chem. Phys.* **146**, 174107 (2017).
⁹⁰K.-S. Lee and U. R. Fischer, *Int. J. Mod. Phys. B* **28**, 1550021 (2014).
⁹¹D. Baye and P. H. Heenen, *J. Phys. A: Math. Gen.* **19**, 2041 (1986).
⁹²D. Baye, *Phys. Rep.* **565**, 1 (2015).
⁹³For mode combination, the scaling in computational effort for the description of the SPFs can be implemented as gDn^2M^{P+1} , where P is the dimension of the SPFs and M is the geometric mean of the numbers of one-dimensional primitive functions describing the SPFs. This is often more favorable than a $gDnM^{2P} = gDnN^2$ scaling.
⁹⁴W. Hackbusch and S. Kühn, *J. Fourier Anal. Appl.* **15**, 706 (2009).
⁹⁵L. Grasedyck, *SIAM J. Matrix Anal. Appl.* **31**, 2029 (2010).
⁹⁶J. Sielk, H. F. von Horsten, F. Krüger, R. Schneider, and B. Hartke, *Phys. Chem. Chem. Phys.* **11**, 463–475 (2009).
⁹⁷A. P. J. Jansen, *J. Chem. Phys.* **99**, 4055 (1993).
⁹⁸U. Manthe, *J. Chem. Phys.* **101**, 2652 (1994).
⁹⁹P.-O. Löwdin, *Phys. Rev.* **97**, 1474 (1955).
¹⁰⁰G. Guennebaud, B. Jacob *et al.*, Eigen v3.3, 2017, <http://eigen.tuxfamily.org>.
¹⁰¹Intel Corporation, Intel® Math Kernel Library, version 11.3.3, 2016, <http://software.intel.com/en-us/articles/intel-mkl/>.
¹⁰²R. A. Friesner, R. E. Wyatt, C. Hempel, and B. Criner, *J. Comput. Phys.* **64**, 220 (1986).
¹⁰³U. Manthe and H. Köppel, *J. Chem. Phys.* **93**, 345 (1990).
¹⁰⁴M. J. Bramley and T. Carrington, *J. Chem. Phys.* **99**, 8519 (1993).
¹⁰⁵J. Cooper and T. Carrington, *J. Chem. Phys.* **130**, 214110 (2009).
¹⁰⁶J. C. Light and T. Carrington, "Discrete-variable representations and their utilization," in *Advances in Chemical Physics* (John Wiley & Sons, Inc., 2007), pp. 263–310.
¹⁰⁷P. Löwdin, *J. Chem. Phys.* **18**, 365 (1950).
¹⁰⁸M. Beck and H.-D. Meyer, *Z. Phys. D: At., Mol. Clusters* **42**, 113 (1997).
¹⁰⁹J. Stoer and R. Bulirsch, *Numerische Mathematik 2*, 5th ed. (Springer, 2006).
¹¹⁰T. J. Park and J. C. Light, *J. Chem. Phys.* **85**, 5870 (1986).
¹¹¹G. A. Worth, M. H. Beck, A. Jäckle, and H.-D. Meyer, the MCTDH package, version 8.4.10, <http://mctdh.uni-hd.de>, 2014.
¹¹²U. Manthe, H.-D. Meyer, and L. S. Cederbaum, *J. Chem. Phys.* **97**, 9062 (1992).
¹¹³C. C. Marston and G. G. Balint-Kurti, *J. Chem. Phys.* **91**, 3571 (1989).
¹¹⁴H.-D. Meyer, private communication (2017).
¹¹⁵H.-D. Meyer and B. Brill, "Shared memory parallelization of the multiconfiguration time-dependent Hartree method," in *Multidimensional Quantum Dynamics*, 1st ed., edited by H.-D. Meyer, F. Gatti, and G. A. Worth (Wiley-VCH, 2009).
¹¹⁶G. A. Worth, M. H. Beck, A. Jäckle, O. Vendrell, and H.-D. Meyer, the MCTDH package, version 8.5.6.1, 2016, <http://mctdh.uni-hd.de>.

I.2.1.4. Complementary Information

I.2.1.4.1. Additional Spectrum

Table II in the publication (page 101) might be complemented with the spectrum of variant B shown in Fig. I.2.2. Clearly, the result of the pruned computation is closer to the unpruned reference than the ML-6 result but needs less computing time.

However, WORTH^[118] pointed out that the Quantics^[119] package is faster than the Heidelberg MCTDH package.^[120] The latter was employed in this calculation. Hence, a ML-MCTDH calculation with Quantics might still be faster than a DP-MCTDH calculation with the current implementation. Nevertheless, both timescales are similar and the current implementation of DP is not fully optimal such that the timing can be further improved; see Chapter III.2 for some thoughts about that.

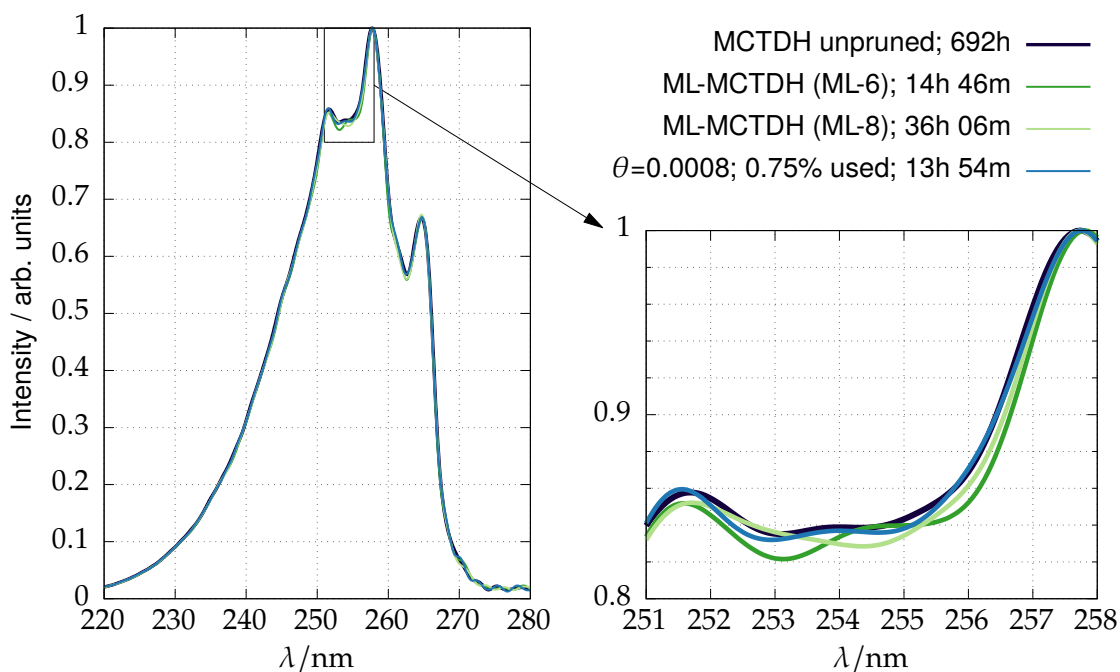


Figure I.2.2.: Like Fig. 3 in the publication (page 100) but for variant B, comparing unpruned (ML-)MCTDH with DP-MCTDH.

I.2.1.4.2. Choice of Representation

In the publication, natural orbitals were used as the representation. It was argued that they are the best choice with respect to sparsity of \mathbf{A} (Section II.B.2 in the publication; page 96). There are two questions to discuss: Is this statement correct? Does the scheme of adding nearest neighbors works in general; in other words, do natural orbitals lead to a spontaneous appearance of nonnegligible configurations that are not connected to other nonnegligible configurations (“islands” in configuration space)? First, the second question is discussed.

Do Islands Appear? In the current implementation, DP cannot take a spontaneous appearance of nonnegligible “islands” into account. This is because DP relies on a neighboring relationship: Only nearest neighbors of important configurations are added. This does not mean that the reduced subspace needs to be connected (in terms of a topology analysis) but it does mean that a disconnected space must have been evolved from a previously connected space.

Since Fig. 7 in the publication (page 102) looks like an appearance of “islands” of important configurations in configuration space could happen in practice, one might argue that DP is errorprone. However, Fig. 7 in the publication shows the diagonal of particular two-particle density matrices and not the full coefficient tensor. Care must be taken not to draw wrong conclusions from this type of plot. Indeed, these “islands” appear both for simulations of unpruned and of DP calculations. Hence, they *are* connected to other configurations but this connection is “hidden” (or just smaller below the color scale of the plot) in this particular presentation.

A spontaneous appearance of “islands” would correspond to a strong coupling of configurations far apart from each other in configuration space, i. e., large off-diagonal elements of the Hamiltonian in natural orbital representation. Indeed, this *can* occur, at least for specifically constructed examples. Consider a model system with three electronic states with the Hamiltonian in matrix representation given as

$$\hat{H} = \mathbf{1}_{3 \times 3} \otimes \hat{H}_0 + \begin{pmatrix} 0 & 0 & 1 \\ 0 & 0 & 0 \\ 1 & 0 & 0 \end{pmatrix} \otimes \hat{1}, \quad (\text{I.2.3})$$

where \hat{H}_0 is the Hamiltonian for the nuclear motion, for example, a two-dimensional harmonic oscillator. Assume, that the initial wavefunction is in the first electronic state:

$$|\Psi(t_0)\rangle = (1, 0, 0)^T \otimes |\psi^{(\text{nu})}(t_0)\rangle. \quad (\text{I.2.4})$$

Its evolution after a very small time step δt is then given by

$$|\Psi(t_0 + \delta t)\rangle = \exp(-i\hat{H}\delta t)|\Psi(t_0)\rangle \approx |\Psi(t_0)\rangle - i\hat{H}\delta t|\Psi(t_0)\rangle \quad (\text{I.2.5})$$

$$= |\Psi(t_0)\rangle - i\delta t \left[(1, 0, 0)^T \otimes \hat{H}_0 |\psi^{(\text{nu})}(t_0)\rangle + (0, 0, 1)^T \otimes |\psi(t_0)^{(\text{nu})}\rangle \right]. \quad (\text{I.2.6})$$

$i = \sqrt{-1}$ is the imaginary unit. An immediate population transfer from the first to the third state happens. Assuming a single-set setup of MCTDH,^[48] this can hardly be captured by DP if just the directly connected nearest neighbors are added to significant configurations. Further, the strong coupling will lead to a rapid change in the nuclear degrees of freedom for the other electronic states, making this model a really challenging test-case for DP.

Nevertheless, there are at least four ways to improve DP for this problem: First, the natural orbital representation of the electronic degree of freedom is arbitrary because all population is in

the first electronic state and an arbitrary orthogonal electronic basis can be used for the other two electronic states. A judiciously chosen basis could mix the off-diagonal coupling between the first and the third electronic states to the second, allowing for a population transfer *via* the second state.⁴ Second, the amount of nearest neighbors added in configuration space can always be increased. This could be done dynamically by checking the off-diagonal terms of the Hamiltonian in natural orbital representation at each time step. Third, for the electronic state, the multi-set setup^[48] could help with this particular problem. The multi-set setup is generally often more efficient than the single-set setup but currently not implemented in my program. Fourth, one could also use other representations than natural orbitals, see below.

It should be emphasized, that DP works surprisingly well for the bilinear vibronic coupling model of pyrazine. Thus, in many practical applications, the problem of sudden appearances of islands in configuration space might not be so severe or it might not even appear. In any case, Fig. 7 in the publication clearly shows that DP is preferable over static pruning.

Do Natural Orbitals Lead to the Sparsest Representation? Another aspect to consider for natural orbitals is that they might *not* give the sparsest representation. There are two aspects to distinguish: Convergence with respect to the size of a direct-product basis that is smaller than the primitive basis and sparsity with respect to the *full* space of the primitive basis in a natural orbital representation. In electronic structure theory and electron dynamics, the former property of natural orbitals has been tested in many applications;^[99,121-124] see also Section II.4.1.1 and Section II.4.1.4. Here, however, the latter property is more important. Natural orbitals might give an optimal truncation order but within that direct-product space, they might not be most optimal in terms of sparsity.

This has been found for MCTDH for Bosons by STRELTISOV ET AL.^[125] and for FCI for Fermions by GIESBERTZ,^[126] LAIN ET AL.^[127] and ALCOBA ET AL.,^[128] for example.⁵ STRELTISOV ET AL.^[125] have done numerical optimization of the SPFs such that a particular variance (Eq. (43) in that reference) is minimized. GIESBERTZ^[126] minimized the distance to the exact wavefunction for a representation in a reduced subspace. One could think of a minimization of the L_1 norm to obtain SPFs that lead to a sparser coefficient tensor. Variants of the L_1 norms that are more regular and do not contain absolute values and as such are easier to use might also be useful.

This has not been done and applied to DP-MCTDH yet. Even if such a representation were obtained, it would remain to be seen whether this would give a *much* sparser representation than those obtained from natural orbitals. Further, the aforementioned sudden appearance of nonnegligible and disconnected configurations should not appear in such a representation. Compared to coordinate or phase-space bases, natural orbitals are already a significant improvement; see Fig. I.2.3, where the sparsity of natural orbitals are compared with position, momentum and PvB representations.⁶

⁴However, whether this transformation can be implemented robustly and generally needs to be investigated.

⁵I am thankful to Sven Krönke for helpful discussions and for pointing me to Refs. [125, 126].

⁶Surprisingly, the momentum representation gives a sparser coefficient tensor than the coordinate representation. Hence, one could also try DP dynamics using TD-FCI with DVR functions in momentum space.

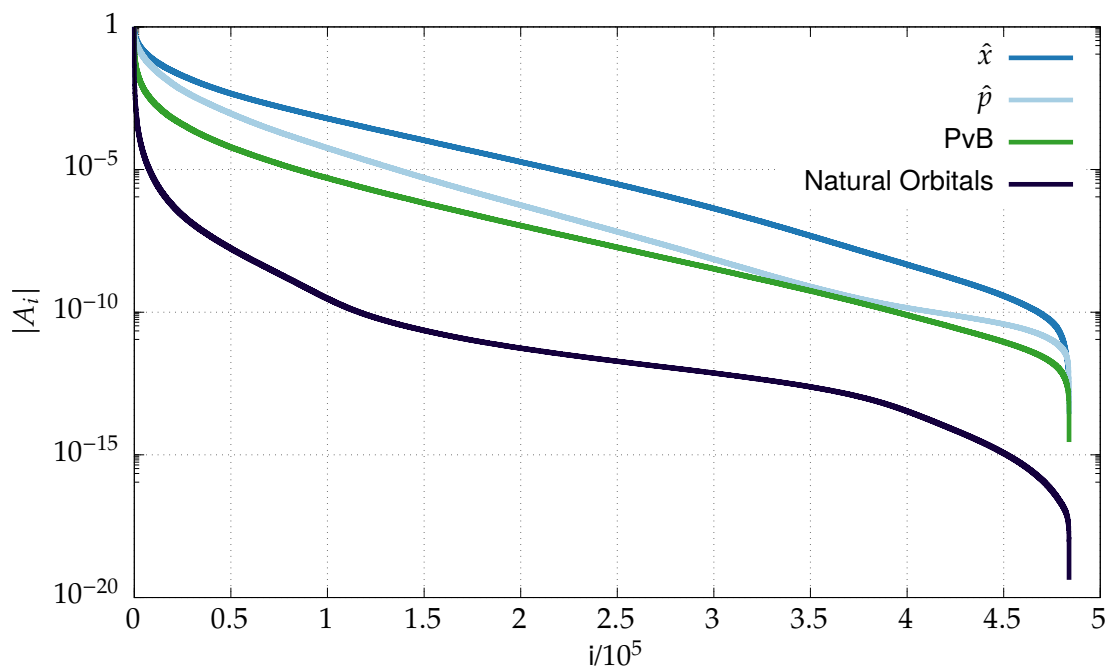


Figure I.2.3.: Sparsity analysis of the wavefunction coefficient tensor \mathbf{A} in TD-FCI for different representations. \hat{x} and \hat{p} stand for the corresponding basis that diagonalize the particular operator. \mathbf{A} is taken from dynamics of the four-mode pyrazine model from Ref. [129]. The size of the DVR is the same as in that publication and the wavepacket has been propagated until 120 fs. The coefficient tensors for all representations are normalized in the sense that the maximum absolute value is 1. The entries are sorted such that $|A_i|$ for $i = 0$ is maximal.

I.2.1.5. Implementation of the Equations of Motion for the Single-Particle Functions

Here, the implementation of the EOMs for the SPFs is described; see Eq. (6) in the publication on page 95. If the SPFs are expanded in the primitive basis (Eq. (12) in the publication), one obtains

$$i \sum_b^N \dot{U}_{bj} |\chi_b\rangle = (\hat{1} - \hat{P}) \left[\hat{h} \sum_b^N U_{bj} |\chi_b\rangle + \sum_{k,l=1}^n [\tilde{\rho}^{-1}]_{jl} \langle \hat{H} \rangle_{lk} \sum_b^N U_{bk} |\chi_b\rangle \right], \quad \dot{U}_{bj} \equiv \frac{\partial}{\partial t} U_{bj}. \quad (\text{I.2.7})$$

\hat{h} is the uncorrelated part of the Hamiltonian in dimension κ . For simplicity, the dimension label κ is omitted in all expressions. Projecting onto a specific primitive function $\langle \chi_a |$ and inserting the completeness relationship $\hat{1} = \sum_{cd} |\chi_c\rangle [Z^{-1}]_{cd} \langle \chi_d |$ with $Z_{cd} = \langle \chi_c | \chi_d \rangle$ between the projector

⁷Note that the notation used in this Section differs from the rest of the thesis. In particular, the overlap matrix \mathbf{Z} has nothing to do with a biorthogonal basis.

\hat{P} and the expression in brackets leads to⁷

$$i \sum_b^N \dot{U}_{bj} Z_{ab} = \sum_b^N \left\{ h_{ab} U_{bj} + \sum_{k,l=1}^n [\tilde{\rho}^{-1}]_{jl} [\langle \hat{H} \rangle_{lk}]_{ab} U_{bk} \right\} - \sum_{bcd}^N P_{ac} [Z^{-1}]_{cd} \left\{ h_{db} U_{bj} + \sum_{k,l=1}^n [\tilde{\rho}^{-1}]_{jl} [\langle \hat{H} \rangle_{lk}]_{db} U_{bk} \right\}, \quad (\text{I.2.8})$$

with

$$h_{ab} \equiv \langle \chi_a | \hat{h} | \chi_b \rangle, \quad (\text{I.2.9})$$

$$[\langle \hat{H} \rangle_{lk}]_{ab} \equiv \langle \chi_a | \langle \hat{H} \rangle_{lk} | \chi_b \rangle, \quad (\text{I.2.10})$$

$$P_{ac} \equiv \langle \chi_a | \hat{P} | \chi_c \rangle. \quad (\text{I.2.11})$$

For a Hamiltonian of sum of products (SoP) form, the matrix elements of the mean fields, Eq. (I.2.10), can be separated into

$$\langle \chi_a | \langle \hat{H} \rangle_{lk} | \chi_b \rangle = \tilde{h}_{ab} \mathcal{H}_{ij}, \quad (\text{I.2.12})$$

where \tilde{h}_{ab} is the matrix-element of the correlated part of the Hamiltonian acting in the dimension κ of the primitive basis. For simplicity, it is assumed that the Hamiltonian only has one sum-term such that the equations are not further complicated by the introduction of many sum-terms. A generalization is straightforward. With that, Eq. (I.2.8) can be written in more compact matrix notation as

$$i \mathbf{Z} \dot{\mathbf{U}} = (\mathbf{1}_{n \times n} - \mathbf{P} \mathbf{Z}^{-1}) \left[\mathbf{h} \mathbf{U} + \left(\tilde{\rho}^{-1} \mathcal{H} (\tilde{\mathbf{h}} \mathbf{U})^T \right)^T \right] \quad (\text{I.2.13})$$

$$= (\mathbf{1}_{n \times n} - \mathbf{P} \mathbf{Z}^{-1}) \{ \mathbf{h} \mathbf{U} + \tilde{\mathbf{h}} \mathbf{U} \mathcal{H}^T [\tilde{\rho}^{-1}]^T \}. \quad (\text{I.2.14})$$

The term $\mathcal{H}^T [\tilde{\rho}^{-1}]^T$ appearing in Eq. (I.2.14) can be understood as an expression involving the right pseudoinverse of the tensor \mathbf{A} viewed as a matrix with column size being equal to n .^[130] New implementations of the EOM with a different treatment of regularization can be achieved with this interpretation.^[131,132] Further, it is easier to see which terms act on the level of the SPF (to the right of \mathbf{U}) and which terms act on the level of the primitive basis (to the left of \mathbf{U}). Here, I focus on Eq. (I.2.13) because this is how the equations are currently implemented in my program (Chapter I.3).

The projector \hat{P} , Eq. (I.2.11), deserves some further attention. Assuming that the SPF basis is nonorthogonal ($\langle \phi_i | \phi_j \rangle = S_{ij} \neq \delta_{ij}$ due to numerical errors), the matrix elements of the projector

can be evaluated as

$$\hat{P} = \sum_{ij}^n |\phi_i\rangle [S^{-1}]_{ij} \langle \phi_j| = \sum_{ab}^N \sum_{ij}^n U_{ai} |\chi_a\rangle [S^{-1}]_{ij} \langle \chi_b| U_{bj}^*, \quad (\text{I.2.15})$$

$$\langle \chi_c | \hat{P} | \chi_d \rangle \equiv P_{cd} = \sum_{ab}^N \sum_{ij}^n U_{ai} Z_{ca} [S^{-1}]_{ij} Z_{bd} U_{bj}^*, \quad (\text{I.2.16})$$

$$S_{ij} = \langle \phi_i | \phi_j \rangle = \sum_{ab} U_{ai}^* \langle \chi_a | \chi_b \rangle U_{bj} = [\mathbf{U}^\dagger \mathbf{ZU}]_{ij}. \quad (\text{I.2.17})$$

In matrix form, the whole expression for the projector can be written as

$$\mathbf{P} = \mathbf{ZU}[\mathbf{U}^\dagger \mathbf{ZU}]^{-1} \mathbf{U}^\dagger \mathbf{Z}. \quad (\text{I.2.18})$$

Inserting this in Eq. (I.2.13) gives

$$i\mathbf{Z}\dot{\mathbf{U}} = (\mathbf{1}_{n \times n} - \mathbf{ZU}[\mathbf{U}^\dagger \mathbf{ZU}]^{-1} \mathbf{U}^\dagger \mathbf{Z}\mathbf{Z}^{-1}) \left[\mathbf{hU} + \left(\tilde{\rho}^{-1} \mathcal{H}(\tilde{\mathbf{hU}})^T \right)^T \right], \quad (\text{I.2.19})$$

$$= (\mathbf{1}_{n \times n} - \mathbf{ZU}[\mathbf{U}^\dagger \mathbf{ZU}]^{-1} \mathbf{U}^\dagger) \left[\mathbf{hU} + \left(\tilde{\rho}^{-1} \mathcal{H}(\tilde{\mathbf{hU}})^T \right)^T \right]. \quad (\text{I.2.20})$$

This equation has to be implemented carefully. To be more specific, the term

$$\check{\mathbf{U}}\mathbf{U}^\dagger \check{\mathbf{U}}, \quad \check{\mathbf{U}} = \mathbf{U}[\mathbf{U}^\dagger \mathbf{ZU}]^{-1}, \quad \check{\mathbf{U}} = \mathbf{hU} + \left(\tilde{\rho}^{-1} \mathcal{H}(\tilde{\mathbf{hU}})^T \right)^T \quad (\text{I.2.21})$$

arises. It can be either evaluated as

$$(\check{\mathbf{U}}\mathbf{U}^\dagger)\check{\mathbf{U}} \quad (\text{I.2.22})$$

or as

$$\check{\mathbf{U}}(\mathbf{U}^\dagger \check{\mathbf{U}}), \quad (\text{I.2.23})$$

where the brackets show the order of evaluation. Since these matrices are of size $n \times N$, Eq. (I.2.22) scales as $\mathcal{O}(N^2 n)$, whereas Eq. (I.2.23) scales as $\mathcal{O}(n^2 N)$ and is the preferred way of implementation. Especially for mode combination, N can be of size $\sim 10^5$ such that an evaluation given by Eq. (I.2.22) would be the bottleneck of the whole MCTDH propagation!⁸

⁸See also footnote/Ref. 93 in the publication (page 104).

Chapter 1.3

The LAGOM package

“ We have seen that computer programming is an art, because it applies accumulated knowledge to the world, because it requires skill and ingenuity, and especially because it produces objects of beauty.

— Donald E. Knuth

During the course of the doctoral studies, it became clear that the aforementioned methodological developments required also the development of a newly written program package tailored to the needs of method development in (pruned) quantum dynamics and with the focus on molecular systems. To allow for more advanced applications of pruned dynamics, the package grew during time and can now be considered as a full-fledged quantum dynamics package for distinguishable particles.

The package is called LAGOM. LAGOM stands for “Local and Adaptive bases for Globally Optimal Molecular quantum propagation”. *Lagom* is a Swedish word that is barely translatable. Roughly, it means “not too little, not too much”, “just right” or “in balance”. *La gomme* is a french word meaning “the eraser”.¹ Both meanings perfectly describe the main spirit of the methods used and developed in this thesis: To allow for *fast* and high-dimensional quantum dynamics simulations, not too many basis functions should be used. However, to allow for *accurate* quantum dynamics, also not too few basis functions should be used. Indeed, the employed basis should be “in balance” and “just right”. Here, this is accomplished by employing dynamical pruning, i. e., by “erasing” negligible basis functions.

Although an all-embracing explanation of the package cannot be given, the following Sections both describe some details about the code and the implementation of scientific methods. This is because, in my opinion, in many scientific publications and theses, not much attention is paid to the explanation of the implementation, even though this is often a major part of the actual work. Given some mathematical equations or algorithms, it is often unclear to the programmer

¹I am thankful to Alexandra Viel for pointing this out.

how to express these equations/algorithms in efficient code — both in terms of performance of the program and in terms of code quality. Given electronic structure theory as an example, it has been evolved so much that the complexity of the equations and the hardware render manual implementations of new methods almost impractical. Thus, code is now often generated automatically, sometimes based on only the mathematical expressions of the wave function *ansatz* or the required integrals to compute (just to give *some* exemplary references, see Ref. [133-140]). As a side note, computer-generated code even led to the detection of a wrong implementation in a well-established electronic structure package.^[141]

Additionally, while intertwined with the implementation details of LAGOM, some of the Sections are written in a tutorial manner and are about the choice of programming languages and used programming principles. This is because writing good code is not a task that can be easily accomplished. This is especially true for natural scientists that often have no formal training in computer science. Being aware of modern programming concepts, languages and data structures can have a significant impact on the success of a project — not to mention the challenges introduced with the rise of heterogeneous hardware (accelerators, general-purpose graphics processing unit (GPGPU) and field-programmable gate arrays (FPGAs)) and massively parallel computing. Since the focus of this thesis is on method development, no attention has been paid to heterogeneous hardware and massively parallel computing.² As a scientist with background in chemistry, I faced the same challenge of how to implement mathematical expressions such that execution is fast on the one hand and to write robust, general and reusable code on the other hand.

In the following, the capabilities of the program will be briefly described in [Section I.3.1](#). Afterwards, the requirements of the package are described ([Section I.3.2](#)), already available packages are briefly mentioned ([Section I.3.3](#)) and the choice of programming languages is detailed ([Section I.3.4](#)). Independently of LAGOM, ways to implement quantum dynamics methods are presented in [Section I.3.5](#). The programming concepts used in LAGOM are outlined in [Section I.3.6](#) and the structure of the program is sketched in [Section I.3.7](#). This Chapter ends with an input example in [Section I.3.8](#). It is hoped that some of the Sections will enable future quantum dynamics developers of this or other codes a smoother introduction to modern scientific computing.

I.3.1. Capabilities of the Package

LAGOM is able to perform the following tasks:

- Pruned and unpruned standard [TD-FCI](#) and [MCTDH](#) dynamics for systems with arbitrary dimensionality (limited by computational resources), [SoP](#) operators and arbitrary potential operators (for [DVRs](#)).

²Developing a new method that is 50 times faster than an old method on one central processing unit (CPU) seems to be at least as useful as trying to parallelize the old method. Hardware can barely beat exponential scaling.

- Propagation *via* various propagators:^[14] Standard short iterative Lanczos (SIL),^[142] SIL with adaptive stepsize and dimension of the Krylov space (one own implementation and one taken from the Heidelberg MCTDH package),^[117,143] standard ordinary differential equation (ODE) solvers like Adams-Bashforth-Moulton or Runge-Kutta (as implemented in `scipy`^[144] or the Heidelberg package),^[145,146] symplectic integrators^[147] and Taylor expansion.^[148] For MCTDH, variable mean field (VMF) propagation, the standard constant mean field (CMF) scheme^[143] and CMF “scheme 2” from Ref. [149] are implemented.
- Eigenstate calculations *via* propagation in imaginary time,^[150] Lanczos algorithm,^[146] filter diagonalization^[151,152] and, for MCTDH, an initial implementation of improved relaxation.^[153]
- Setup of various DVRs:^[14,154-156] FGH,^[157] sinc DVR,^[158] sine DVR,^[158] radial sine DVR,^[158] standard DVRs based on Gauß quadrature^[159-161] and finite element discrete variable representation (FE-DVR).^[162-165]
- Scattering dynamics *via* the Møller operator formalism by TANNOR AND WEEKS.^[166-169]
- Dissociation dynamics and fragmentation analysis *via* the analysis line method; see Chapter II.1 for details.
- Optimal control *via* the Krotov algorithm and basis-expansion of the field (Galerkin) and local optimization (with and without using gradients); see Chapter II.3 for details.
- Many utility scripts, for example, for computing the spectrum from the autocorrelation^[14,96] or for plotting wavefunctions or (reduced) density matrices^[96] in various representations, e. g., position, momentum, PvB, Husimi Q and Wigner.^[170]
- Routines for efficient propagation of special systems like coupled electron-nuclear dynamics of H_2^+ ,^[171-173] electron dynamics in one-dimensional He and for photoelectron momentum distribution (PMD) computations of atomic three-dimensional Hydrogen,³ see Chapter II.2 and II.3 for details.

As of November 2, 2017, and *excluding* comment lines, empty lines and external libraries, the core code of LAGOM has almost 15000 lines of code written in Python, almost 20000 lines written in C++, more than 1000 lines written in Fortran and a few lines written in Cython. Auxiliary Python code for special tasks (scattering, dissociation dynamics, plotting etc.) consists of more than 19000 lines of code.

³In H_2^+ and hydrogen, a SoP form is not available.

I.3.2. Requirements of the Package

LAGOM is definitely not the first program that aims to perform (molecular) quantum dynamical simulations for arbitrary systems. Thus, the reader may ask why there was a need for developing LAGOM.

On the one hand, for method development and the amount of additional capabilities mentioned in the previous [Section I.3.1](#), the structure of the package needs to be very flexible and the programming language needs to be both easy to use and powerful. This is accomplished by scripting languages which enable an interactive use. This is extremely useful when it comes to method development where it is not clear from the beginning how the method to be implemented will look like. There are just two available programs I am aware of that are programmed in a scripting language; see the next [Section I.3.3](#). Neither have [MCTDH](#) implemented.

On the other hand, the implementation needs to be fast in execution such that it is able to compete with existing and already highly optimized codes. Further, during the procedure of developing dynamical pruning, it became clear that efficient and more advanced data structures (see [Section I.3.6.6](#)) and algorithms like set operations are required to enable a fast handling of the bookkeeping involved in the [DP](#) approach. To avoid cumbersome and error-prone reimplementations, the data structures should already be implemented in the programming language as part of a standard library or a similar concept. These needs are not fulfilled in the currently available programs; see next [Section I.3.3](#). In contrast, it was found that not even the usage of only a single programming language is enough to satisfy all requirements. The available programs are mostly written in one language.

I.3.3. Already Available Packages

For allowing an overview of what is already available, other codes are briefly mentioned. This overview is focused on programs that are not tailored to specific systems and to programs that are easily available and not in-house codes from other groups. LAGOM is partially inspired by some of these codes.

MrPropa This [TD-FCI](#) program was developed in the [HARTKE](#) group by [VON HORSTEN](#)^[174] and was later generalized to dynamically pruned [proDG](#) dynamics^[89,90] by [SIELK](#)^[79] and [STEFFEN](#).^[78] It is currently not maintained. The program is written in Fortran 90 and is specialized to the use of numerical kinetic energy operators in arbitrary coordinate systems *via* an interface to the [Tnum](#) program which sets up this operator.^[175] It includes many features like scattering calculations or optimal control. The pruned dynamics does not exploit the favorable $\mathcal{O}(\tilde{n}^{D+1})$ scaling of the matrix-vector product and the handling of the active basis set is not well-implemented.^[79]

BvN This program is tailored to [PvB](#) dynamics and was written by [MACHNES](#) and [ASSÉMAT](#) in the [TANNOR](#) group.^[83,84] It is written in Matlab and it is focused on non-decomposable potentials.

It does not exploit the favorable $\mathcal{O}(\tilde{n}^{D+1})$ scaling of the matrix-vector product. I made initial attempts to refactor the code to enable molecular dynamics and mixed representations of P_vB with spherical harmonics to enable electronic dynamics in 3D. These attempts have been abandoned in favor of developing LAGOM. B_vN is currently not maintained.

Wavepacket This TD-FCI code is specialized to conventional low-dimensional dynamics with DVRs and is written in Matlab by SCHMIDT AND LORENZ.^[87,176] A C++ library of the program is still in its infancy. It includes many features like optimal control or the treatment of open quantum systems.

Heidelberg MCTDH package This suite of programs is tailored to MCTDH dynamics and also implements ML-MCTDH in its newer version.^[117,120] The MCTDH part is written in Fortran 77 while the ML-MCTDH part is written in Fortran 90. It includes many features like eigenspectrum calculations, filter diagonalization, initial-state selected scattering calculations or optimal control. The static pruning of the SPFs of WORTH^[116] is implemented in an older version but has been removed in the newer version. The implementation of the pruning is known to have a high overhead and is not always competitive to unpruned MCTDH dynamics.^[116,177]

Quantics This package^[119] wraps the Heidelberg MCTDH and ML-MCTDH packages into a common Fortran 90 code and it includes further codes to enable, among others, variational multi-configuration Gaussian (vMCG)^[178,179] and real-valued wavepacket propagations.^[180-182]

Bielefeld MCTDH package This in-house code from the MANTHE group is specialized to ML-MCTDH dynamics with correlation discrete variable representation (CDVR)^[183-185] for the application to molecular rate constants and scattering calculations.^[186] It is programmed in Fortran 77/90 and not written for a broader user base. However, a new version is currently in development.^[187] This is written in C++ and tailored to easily enable method development.

I.3.4. Choice of Programming Languages

As already pointed out in Section I.3.2, the requirements of LAGOM are quite challenging. The choice of the programming language turned out to be crucial for enabling both fast developing processes and fast program executions. In fact, a single programming language did not fulfill all the requirements. Thus, LAGOM is written mostly in Python 3 and C++ 14. Some parts, however, are written in Fortran 90, Fortran 77 and Cython.^[188]⁴ The dynamical pruning part is solely written in C++, but the initial method development has been done in Python.

⁴Cython is a combination of C and Python.

I.3.4.1. Python

Python is a scripting language and easy to learn, use and debug.^[189,190] Powerful libraries for scientific computation like numpy^[191] and scipy^[144] are available. However, note that not all parts of numpy and scipy are equally well implemented and it sometimes makes sense to reimplement some routines. The combination with compilable languages like Fortran and C++ is straightforward. The structure of the language, its generic programming style and its object orientation make it very easy to use *and* to develop even very large packages with hundred thousands lines of codes. Python is therefore well-suited for method development and serious scientific computation. This is indicated by a growing use in other scientific communities. Just to mention electronic structure theory, at least six packages are available: PySCF,^[192] psi4,^[193] GPAW,^[194] PyQuante,^[195] molsturm^[196] and HORTON.^[197] These packages are either mainly written in Python or have powerful interfaces to Python scripts. For the description of nuclear motion, a modern vibrational configuration interaction (VCI) code, PyVCI, has recently been developed.^[198]

Certainly, Python has some disadvantages. Since it is a scripting language, loops are executed slowly and one should try to implement all computing-intensive procedures in terms of calls to numpy and scipy.⁵ However, effort is taken to enable just-in-time compilation for Python^[199-201] or even to automatically translate Python code to C++ code.^[202] Besides, parallelization is not easily accomplished (especially shared-memory parallelization) and the optimization of memory demands can be difficult.

I.3.4.2. C++

C++ features powerful generic programming *within* a compilable programming language *via* its template approach, enabling programming not tailored to one specific data type or data structure (see [Section I.3.6.3](#)).^[203,204] It comes with a flexible standard library that includes many data structures, algorithms for set operations, sorting etc. (see [Section I.3.6.6](#)). It also enables the use of so-called smart pointers and other concepts that render the use of explicit memory handling as unessential. Besides the standard library, powerful general purpose libraries like boost^[205] and numerical libraries like Trilinos^[206] or Eigen^[207] are available.⁶ In fact, modern scientific libraries are almost exclusively written in C++ or C.⁷ Interfacing C++ with C or Fortran is very straightforward. Other useful features of this multi-paradigm language are aspects of functional programming ([Section I.3.6.2](#)) and object orientation ([Section I.3.6.4](#)). Despite all these advanced concepts, there is typically no difference in the performance of the code compared to established Fortran code (given a proper implementation). However, the inclusion of all these features into a

⁵This might be considered as an advantage and not a disadvantage because it forces the programmer to think in a more abstract way (e. g. matrix-matrix products instead of sums) and many loop expressions can be recast to highly optimized Basic Linear Algebra Subprograms (BLAS) calls. This is also the case for the sequential matrix-vector product, see [Section I.1.3](#).

⁶LAGOM makes intense use of Eigen.

⁷Also the core part of numpy and the mostly used Python compiler are written in C.

compilable language comes with the price of high complexity and with the difficulty to master C++.

I.3.4.3. Other Languages

In the context of scientific computing, the most common alternatives to Python are Matlab^[208] and Julia.^[209] Matlab has powerful just-in-time compilation and an extensive library but it is hard to develop larger packages with thousands of lines, the application programming interface (API) of the library is not uniform and it is a commercial language.⁸ Julia is a new language and, like Matlab and unlike Python, specifically made for scientific computations. This language is quite new and the API is not yet stable.

Many packages in quantum chemistry are written in Fortran. Although a classical language for scientific computation, Fortran lacks a powerful standard library such that everyday tasks like sorting have to be implemented by the user. It lacks features of generic programming like C++-like template programming and the object orientation of modern Fortran 2003/2008 are, to my eyes, too clumsy. However, for standard linear algebra problems often encountered in computational quantum mechanics, it is and remains a powerful and easy-to-learn language.

I.3.5. Elements and their Implementation of Quantum Dynamics Methods

In the following, the requirements of typical DVR, MCTDH and DP codes in terms of needed algorithms and routines are described in an abstract way. It turns out that many parts can be implemented in Python and only minor parts, aside from DP, need to be programmed in a compilable language for optimal performance.

Although this Section does not focus on LAGOM, the related parts of the program are mostly based on the concepts presented here. These concepts can also be used elsewhere.

I.3.5.1. Conventional Discrete Variable Representation Dynamics

A conventional DVR TD-FCI code for molecular quantum dynamics in arbitrary dimensions consists of the following four parts: Routines for setting up the DVR representation, a propagator, a routine for the matrix-vector product and post-processing routines. They are described in the following paragraphs.

The setup of the DVR representation consists of computing the DVR grid and weights and the matrix elements of the operators (\hat{p} , \hat{p}^2 and so on). Depending on the type of the DVR, this can be quite involved. However, the setup of the DVR basis almost never requires much computational time since, for typical applications, only one-dimensional DVRs are used such that the computational scaling is independent of dimensionality. Hence, an implementation in

⁸Open-source replacements for Matlab are available but they lack some features like just-in-time compilation.

Python can be conveniently done, without thinking too much about performance. Available scientific libraries like `numpy` and `scipy` simplify the implementation due to routines for getting Gauß quadrature grid points, etc.

For standard quantum dynamics, powerful and elaborate propagators exist.^[14,142,147,148,210-221] Although programming these propagators can be quite involved, the main parts of the propagators can be reduced to a combination of calls to `BLAS` and Linear Algebra Package (`LAPACK`) routines.^[222,223] A fast implementation in Python is therefore possible. Again, Python simplifies some tasks, e. g., the computation of complicated mathematical functions that are already implemented in `scipy`.

However, the *main* part of a `DVR` program is the application of \hat{H} to $|\Psi\rangle$, i. e., the matrix-vector product or tensor transformation. For a `DVR`, the potential matrix is diagonal and thus secondary.⁹ The primary computational bottleneck is the application of the kinetic energy operator, \hat{T} , to the wavefunction. \hat{T} is normally in `SoP` form and details about an efficient implementation of applying an operator in `SoP` form to a wavefunction are given in APPENDIX A of Publication 3 (Section I.1.3). The implementation is, essentially, a loop over matrix-matrix multiplications and has to be programmed in a compilable language like `Cython` or `Fortran`. However, new libraries that perform these tensor transformations are already available — even for automatic distributed memory parallelization.^[207,224-229] In principle, the `einsum` routine of `numpy`^[191] can do tensor transformations as well but my tests revealed poor performance.¹⁰ The `bohrium` library might be an alternative to `numpy`, also for parallel and `GPGPU` computations.^[201,230]

The complexity of the post-processing steps depends on the task to perform. Often, it can be reduced to tensor transformations like multidimensional Fourier transforms or applications of `SoP` operators to the state of interest. In that case, the post-processing can be efficiently computed in Python with calls to the aforementioned tensor transformation routine.

To summarize, it is possible to program a conventional `DVR` program in Python with the help of a single routine (written in a compilable language) that does the tensor transformation/matrix-vector product and *without* jeopardizing performance. Indeed, Python libraries like `numpy` and `scipy` reduce the burden of implementing complex linear algebra and analysis tasks.

1.3.5.2. Conventional Multi-Configuration Time-Dependent Hartree Dynamics

Most elements of `MCTDH` codes can be reduced to tasks described in the previous Section I.3.5.1. The evaluation of the right-hand side of the `EOM` for the `SPFs` is a standard linear algebra problem and can thus be implemented in Python as well (cf. Section I.2.1.5). An additional part of `MCTDH` is the evaluation of reduced single-particle density matrices. This can be achieved in a similar vein as the matrix-vector operation and an implementation is described in Section III A of Publication 4 (Section I.2.1) (page 96 in this thesis). As for the matrix-vector operation, a compilable language is needed.

⁹It is assumed that the system of interest is already described by a fitted or interpolated potential energy surface.

¹⁰The recent version of `numpy` (1.14 which was released on January 7, 2018) has some significant improvements but this has not yet been tested for my applications.

I.3.5.3. Dynamically Pruned Dynamics

An additional complexity to both [DVR](#) and [MCTDH](#) dynamics is added by dynamical pruning. There, almost all dense linear algebra problems are replaced by sparse problems. Additional bookkeeping and the development of new algorithms are required, see [Publication 3 \(Section I.1.3\)](#) and [Publication 4 \(Section I.2.1\)](#). As it is detailed in these publications and in [Section I.3.6.6](#), this requires a compilable programming language with a powerful standard library and advanced data structures. Hence, this part needs to be programmed in a language like C++. Nevertheless, it can be done in a modular fashion: Changing a conventional code to a [DP](#) code means that routines for updating the set of active basis functions need to be added and that routines for the tensor transformation need to be replaced by special routines described in APPENDIX A of [Publication 3 \(Section I.1.3\)](#). Nevertheless, the program can still be driven through a Python or even a Fortran interface. The structure of the [MCTDH](#) algorithm and the propagator in a [DVR](#) code remain unchanged.

I.3.6. Used Programming Concepts

In the following, a few elements of general concepts in software design and concepts used in the development of LAGOM are briefly described in an introductory manner. The concepts and design principles are described in the context of the used programming languages Python and C++ and sometimes not in a formally correct way (i. e., in a perspective of a computer scientist). The implementation, advantages and disadvantages of programming concepts and design principles may differ in other languages. The given examples for the programming concepts clarify how some parts of the program are designed and written.

I.3.6.1. Combining Various Programming Languages

It became clear in the previous Sections [I.3.4](#), [I.3.5](#) and [I.3.2](#) that LAGOM is heavily based on the combination of different programming languages. This is easily accomplished by tools and libraries like `f2py`^[231] (interfacing Fortran \leftrightarrow Python) and `pybind11`^[232] (C++ \leftrightarrow Python). Combining Python with Fortran is crucial because almost all available [PES](#) routines are written in Fortran, see the [PES](#) library `POTLIB` for an example.^[233] Only recently, some [PES](#) have directly been written in Python.^[234]

I.3.6.2. Functional Programming

Although being mainly procedural and object-oriented languages, both Python and C++ have elements of functional programming implemented.^[204] Among functional programming features, so-called functors and lambda expressions are heavily used throughout LAGOM. Functors are full-blown classes in a functional style paradigm. They are callable and can thus be used like normal functions. The benefit is that they can have “memory” (a “state”) and can even fulfill

other tasks, i. e., they may have other methods defined. Lambda expressions are “on-the-fly” specified functions that can have access to local data. Another benefit is that functors and lambda expressions allow for an *external* change of specific parts of an otherwise static algorithm. This enables flexibility and avoids hard-coded expressions that “bloat” the implementation of the algorithm.

A simple example for its use are propagator routines that require functors computing the application of the Hamiltonian to quantum states as input. Another example is the criterion when to add nearest neighbors in DP dynamics. The default criterion is to check whether the absolute value of a coefficient of the corresponding basis function is larger than the wave amplitude threshold (WAT), see Publication 3 (Section I.1.3). However, one might want to have a different criterion. For example, in Publication 4 (Section I.2.1), during the initial phase of the propagation, a small direct product space should be included in the pruned subspace. This could easily be accomplished by providing the update routine with a functor that replaces the default criterion *without* changing the update routine. All changes are done locally on the user level without touching the update routine.¹¹ Another example about the use of lambda expressions is given in Section I.3.8.

I.3.6.3. Generic Programming

Generic programming is an essential part of many scripting languages like Python, because those languages are agnostic about concrete data types. In C++, generic programming is mainly achieved through so-called templates. In an object-oriented way of thinking, template programming can be regarded as compile-time polymorphism.

Generic programming is heavily used in LAGOM. To give only a simple example, the C++ part of LAGOM is completely implemented with different generic integer types that are used for different tasks.¹² In DP, the location of an active Hartree product is stored using the indices of the corresponding one-dimensional basis functions as a vector of integers. To reduce the cost of memory accesses and to reduce the memory requirements in general, one may want to use different types of integers with different numbers of bytes. For a small problem with less than 256 basis functions per dimension, only one byte is enough to store the location in one dimension. For integers indicating locations within the overall coefficient vector, larger integer types need to be used. Hence, the integer type used for specific tasks is implemented generically and the code can be compiled with different types, without creating any overhead at runtime. Also the complex floating point number type is programmed generically. This allows to compile the code

¹¹This is actually a way to implement the so-called template method pattern^[235] (this has nothing to do with C++ templates); see Section I.3.6.5.

¹²Fortran compilers often have options to change the default integer or real type but this is error prone if the program contains “static” calls to libraries that then use different data types. For example, the names of BLAS functions depend on the employed real type which is not the case for generic C++ libraries; for using different integer types, different libraries need to be linked typically. Further, these options do not allow for the simultaneous usage of different data types in different parts of the program. Although this can be conveniently done in Fortran 90 with the kind feature, it is restricted to primitive data types.

with a real type for the coefficient tensor. Changing from complex to real algebra is useful for [MCTDH](#) with improved relaxation, i. e., for solving the [TISE](#) which often does not require complex algebra, because it reduces the amount of required [CPU](#) instructions and registers and it reduces the memory requirements and thus also the required memory bandwidth. [WODRASZKA AND CARRINGTON](#)^[236] mentioned this but did not make use of it, probably because their Fortran code is based on complex numbers and does not allow for generic programming.

I.3.6.4. Object Orientation

Object orientation helps to structure the code and to avoid code duplication. Structuring is achieved by encapsulating and decoupling of code that is subject to changes from stable code that should not be touched in so-called classes. Avoiding code duplication is achieved by inheriting routines from another class. Another powerful feature is polymorphism where the actual choice which class is used during a program run is done during runtime.

It is a common misconception that object oriented code cannot be as fast as standard procedural code. This criticism comes from the feature of polymorphism because the program has to check at runtime which class is actually used. This creates a computational overhead.¹³ However, this part is highly optimized by modern compilers. Further, in the context of scientific computing, it is very common that more than 90 percent of runtime is spent in less than 10 percent of the code. These fractions of the code are typically either calls to linear algebra routines or self-implemented loops. In properly programmed code, no polymorphism is needed within this critical fraction. Indeed, in scientific computing, polymorphism is normally only needed during the initialization of the program. Once the input file is read in, the used class instances are known and are typically not changed during the remaining phase of the program execution. Polymorphism is therefore typically only used in the outer layers of the code where the “administration” takes place. In those rare instances where polymorphism is useful in time-critical parts of the code, one can use template or generic programming as a static compile-time polymorphism; see [Section I.3.6.3](#). To put it in other words: Just because a language is known to be object-oriented, this does not mean that one should always use this feature. Functional ([Section I.3.6.2](#)) and generic programming ([Section I.3.6.3](#)) are powerful alternatives, see also the comment in [Section I.3.6.5](#).

A simple example of object orientation in a quantum dynamics code is the creation of a basis class. A basis like a [DVR](#) consists of attributes like basis size, grid points (in the case of a [DVR](#)), functions for their representation in position, momentum and phase space and matrices representing typical quantum-mechanical operators (\hat{x} , \hat{p} and so on) in this basis. Therefore, [LAGOM](#) consists of an abstract base class, containing these attributes and routines as abstract items, which needs to be implemented. It further consists of typical operations that are common for all basis classes, as, in the case of a [DVR](#), the calculation of the grid length from the grid range. This needs to be implemented only once. The actual basis classes (electronic basis, [FGH](#)

¹³This discussion is focused on standard C++ code. With just-in-time compiling, the overhead can sometimes be overcompensated, giving actually better performance. This is not used in [LAGOM](#).

etc.) are then child classes of this abstract base class and implement the aforementioned routines. This gives the program structure and allows the user to quickly change the type of basis and even to implement a new basis that can be straightforwardly used in the code because the interface of the class is well-defined by the abstract base class.

The State Classes To give a slightly more complex example in C++, the structure of the classes representing the wavefunction is described. The relationship of the classes described in the remainder is shown in Fig. I.3.1. For a FCI state, only a big coefficient array and additional information like dimensionality need to be stored. If more states should be stored (e.g., for computing several eigenstates), it can be done in a matrix format. This can be wrapped together in one class, called States.

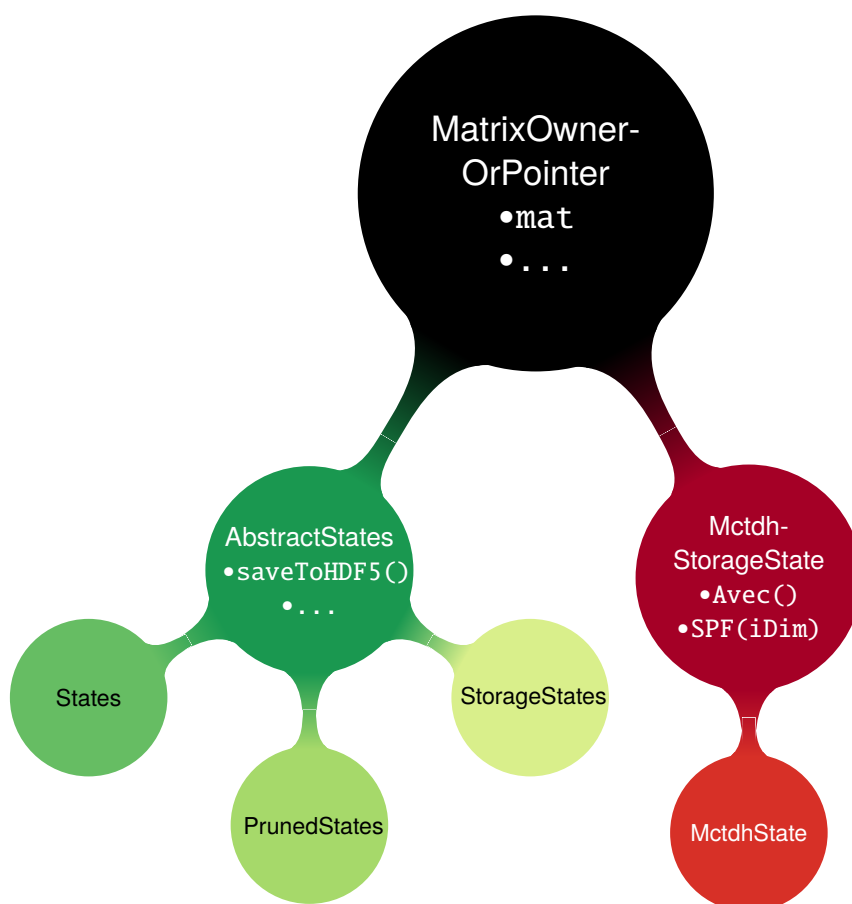


Figure I.3.1.: Hierarchy for state classes representing wavefunctions in the C++ code. The functions *Avec* and *SPF* return an *AbstractStates* implementation for the coefficients of the *SPFs* or the *DVRs*, respectively. The input of *SPF* is the dimension. Note that the actual implementation is slightly more complex.

Dynamically Pruned States If a state is pruned dynamically, additional routines are required for the pruning. Further, additional arrays storing the subset of active basis function and lookup

data are necessary. It is useful to define a separate class, `PrunedStates`, for this. `PrunedStates` shares many aspects with a `FCI States` class. For example, both classes should implement a function `saveToHDF5` that saves all data to disk in HDF5 format.^[237] It thus makes sense to use inheritance/polymorphism and to define an abstract base class `AbstractStates` that can either be `States` or `PrunedStates`.

Auxiliary Memory However, for the sequential efficiently scaling matrix-vector product, two additional auxiliary arrays need to be stored; see Publication 3 (Section I.1.3). They should explicitly be marked as “storage” objects because they have less memory requirements. For example, they do not need to store the subset of active basis functions provided by the class `PrunedStates`. Further, they should also not implement all the methods. It does not make sense that an auxiliary object should, e. g., be written to disk for postprocessing. Hence, an additional class `StorageStates` is defined. This is a lightweight object and, essentially, just provides additional memory.

More Flexibility Regarding Memory With that, there are three classes, `States`, `PrunedStates` and `StorageStates`, that are all child classes of the `AbstractStates` class. However, some propagators (and a `MCTDH` state; see below) require specific memory layouts. For example, many propagators need additional storage for several states and this should often be provided in matrix form. To allow for full flexibility, it is useful that the states either own the memory that is used for storing the wavefunction coefficients, or that the states use memory provided by another routine, for example the propagator. To implement this, the `AbstractStates` class is actually again a child class of `MatrixOwnerOrPointer`. The latter class is just an object that either stores an array `mat` or it points to an array. This is implemented using the Eigen library.^[207] Note that this is the *only* part in the code where memory handling is done manually. One could have implemented these features also directly in `AbstractStates`. However, to encapsulate the memory handling (to *hide* the details) and to make these features available for `MCTDH` classes, `MatrixOwnerOrPointer` is a class of its own.¹⁴

Multi-Configuration Time-Dependent Hartree States Finally, also an `MCTDH` state needs to be programmed. Here, an additional complexity arises, because both the `SPF` coefficient tensor \mathbf{A} and the coefficients $\mathbf{U}^{(\kappa)}$ of the primitive basis for the representation of the `SPFs` need to be stored. Further, if pruning is introduced, *some* `SPFs` are pruned and some are not. The same holds for \mathbf{A} . Additionally, `VMF` propagators require *all* coefficients, \mathbf{A} and $\mathbf{U}^{(\kappa)}$, to be stored in one big array. To handle these requirements, `MatrixOwnerOrPointer` comes in handy: All coefficients are stored in one big array and additional states for \mathbf{A} and for $\mathbf{U}^{(\kappa)}$ are defined that are instances of *either* `States` or `PrunedStates` and *point* to the specific location in the big array. For `PrunedStates`, the class still stores the set of active basis functions separately. For also allowing the usage of

¹⁴Actually, the data type of the matrix is a template such that both complex and real or even other types can be used.

auxiliary memory, a storage class `MctdhStorageState` is defined and the final `MctdhState` class is based on it. In principle, one could also first define an abstract `MCTDH` base class and let both `MctdhStorageState` and `MctdhState` be children from this abstract base class, as it is the case for `AbstractStates`. However, this is currently not needed as it does not simplify anything. In contrast, too much abstraction makes it more difficult for new users to understand the code.

A similar class hierarchy is used for the operator state. There, an `AbstractOperator` class is defined and other subclasses are used for the description of, among others, one-dimensional or `SoP` operators.

I.3.6.5. Design Patterns

Design patterns describe solution strategies for recurring problems in software design.^[235,238] They are commonly related to object-oriented programming. Often, they arise due to the lack of features in programming languages. Indeed, with modern C++ 11/14 and the rise of new standard library tools and additional concepts like functional programming (Section I.3.6.2), many design patterns have become obsolete.^[239] Nevertheless, some design patterns are still needed for good (C++) code.

In the following, I will only give one example of the usage of a design pattern in LAGOM, namely the visitor pattern. The visitor pattern is defined as follows:^[235]

Represent an operation to be performed on elements of an object structure. Visitor lets you define a new operation without changing the classes of the elements on which it operates.

In object-oriented polymorphism, functions of an abstract class whose actual implementation is unknown at compile time can be called at runtime where the proper call to the function is chosen according to the current implementation. This is called *single dispatch*. To give an example, consider the `AbstractStates` class and its actual implementation, see Section I.3.6.4 and Fig. I.3.1. At compile time, it is not known whether the class is `States` or `PrunedStates`. If the function `saveToHDF5` is called in a code, the compiler inserts proper code that finds out whether the class is a `States` or a `PrunedStates` implementation and calls the proper implementation of `saveToHDF5` in one of the classes.¹⁵

In LAGOM, polymorphism is also used for the quantum operator. At compile time, it is not known, whether an operator is of `SoP` form, of some other form or some special operator, as for a one-dimensional problem where the `SoP` form can be optimized. All implementations of an `AbstractOperator` class have their own `MatrVecProd` routine that takes a state as input and applies the operator to the state. However, different routines exist for different implementations of `AbstractStates`, i. e., a `FCI` state or a pruned state. For the `TD-FCI` code, it is clear that the operator will always be of `SoP` form and polymorphism is only applied to the state object. A single dispatch is enough. However, for `MCTDH`, both the operator *and* the state should be polymorph. This leads to a problem because then a *double dispatch* is needed: One wants to have to call a

¹⁵To be precise: A specific instance of the actual implementation is called.

function of a polymorphic class, `MatrVecProd` of `AbstractOperator` in this case, but the *function argument* is also polymorph, namely it is an `AbstractStates` object. This double dispatch is not supported by C++ (and most other languages) but can be implemented with the help of the visitor pattern.

In the language of the visitor pattern, the `AbstractStates` class is an element and the `AbstractOperator` class is the visitor. The implementation of the visitor pattern is as follows. In `AbstractStates`, one defines a function `acceptForMatrVecProd`, that takes an `AbstractOperator` as input. In a call to `acceptForMatrVecProd`, the first dispatch takes place: Once the function is called at runtime, it is clear to which actual implementation the class belongs (either `States` or `PrunedStates`). Then, in `acceptForMatrVecProd` one just calls the `MatrVecProd` of the `AbstractOperator` with a reference of the actual implementation as input. There, the second dispatch takes place and the actual implementation of the operator class is chosen. In other words, the visitor pattern achieves the double dispatch with two sequential single dispatches.

To give an example, the scheme is pictorially described in the following for a particular call sequence:

$$\begin{aligned}
 \text{(A)} & \begin{pmatrix} \text{States} \\ \text{PrunedStates} \\ \dots \end{pmatrix} .\text{acceptForMatrVecProd} \begin{pmatrix} \text{SoPOperator} \\ \text{Operator1D} \\ \dots \end{pmatrix} : \text{first dispatch: PrunedStates} \\
 \text{(B)} & \begin{pmatrix} \text{SoPOperator} \\ \text{Operator1D} \\ \dots \end{pmatrix} .\text{MatrVecProd}(\text{PrunedStates}) : \text{second dispatch: SoPOperator}
 \end{aligned}$$

In (A), `acceptForMatrVecProd` is called and the first dispatch happens: The user chose `DP` dynamics and an instance of `PrunedStates` is selected and its implementation of `acceptForMatrVecProd` is called. There, line (B), the final `MatrVecProd` is called with a reference to the actual instance of `PrunedStates` as input. The second dispatch happens and an instance of `SoPOperator` is called.

During the development of LAGOM, an additional complication arose: First, an `MCTDH` program using only unpruned `States` object was written and a single dispatch was enough. All matrix-vector products were implemented as calls to `MatrVecProd` routines of `AbstractOperator` classes. When the program should be generalized to both pruned and unpruned dynamics, the visitor pattern was needed. However, the call structure is *inverted*: First, a call to the function `acceptForMatrVecProd` of `AbstractStates` takes place and then a call to `MatrVecProd`. This would mean to change each single line where `MatrVecProd` is called into a call to `acceptForMatrVecProd`. Instead, I changed the `MatrVecProd` routine such that it just calls `acceptForMatrVecProd`. There, the actual implementation of the matrix-vector product is then called. With that, only minor changes to the code were needed in the operator and state classes and the `MCTDH` code could remain completely unchanged without introducing an unmanageable number of `if` clauses in various locations of the code.¹⁶ The adaption of the visitor pattern to this

¹⁶I am grateful to Mark Dittner for helpful discussions.

particular problem exemplifies that design patterns are solution strategies and not fixed solution templates.

I.3.6.6. Data Structures

Data structures are different ways to store and organize data in memory.^[240] As such, they are not related to programming concepts in software engineering like object orientation or functional programming but rather algorithmic solutions to data-related problems. The standard library in C++ has many data structures already implemented as templates such that they can be used without the burden of writing own implementations.

The choice of proper data structures turned out to be crucial for dynamical pruning. To give an example, consider the problem of updating the set of active neighbors, see Section II.E in Publication 3 (Section I.1.3) for details. A simplified version of the initial $\mathcal{O}(\tilde{n}^{2D})$ scaling code using sorted lists (vector in the language of C++ standard library) is shown in Listing I.3.1. The new $\mathcal{O}(\tilde{n}^D)$ scaling version using hash tables (unordered_set in the language of the C++ standard library) is given in Listing I.3.2. Note that only two lines are changed (plus a simple implementation of a functor idxVecHasher that computes the hash value of the list of basis functions that is here simply the index of the corresponding entry of the full, unpruned tensor, viewed as a one-dimensional array). For the NO₂ dynamics (see Publication 3 (Section I.1.3)), the runtime of the code using sorted lists was 4580 seconds for one specific parameter set whereas the runtime of the code using hash tables was only 24 seconds, giving a speedup of more than 190!

Listing I.3.1: Simplified code showing the update of the set of active basis functions, newBasisSet, using sorted lists/arrays as implementation.

```

1 vector<vector<int>> newBasisSet; //1D array of 1D arrays of basis function locations
2 LOOP over used (multidimensional) basis functions i:
3   if (abs(vec(i)) > waveAmplitudeThreshold) {
4     auto idxToAdd = createNeighbors(idx[i]); // idxToAdd is a sorted list of all neighbors for function i
5     newBasisSet.merge_unique(idxToAdd); // Merges idxToAdd into newBasisSet and does a unique operation
6     afterwards
7   }

```

Listing I.3.2: Simplified code showing the update of the set of active basis functions, newBasisSet, using a hash table as implementation.

```

1 unordered_set<vector<int>,idxVecHasher> newBasisSet; //Hash table of 1D arrays of basis function locations
2 LOOP over used (multidimensional) basis functions i:
3   if (abs(vec(i)) > waveAmplitudeThreshold) {
4     auto idxToAdd = createNeighbors(idx[i]);
5     newBasisSet.insert(idxToAdd);
6   }

```


I.3.7. Overall Structure of the Package

As already pointed out in [Section I.3.5](#) and [Section I.3.4](#), LAGOM mainly consists of a Python and a C++ part. Both parts are almost independent from each other. The setup of the operator and basis is done in Python. The matrix elements and the initial state are then transferred to the C++ part via files in HDF5 format. The C++ program can be executed as a standalone program for [TD-FCI](#) or [MCTDH](#) (pruned or unpruned) or it can be driven through Python *via* an interface using pybind11. That is, Python has access to all the data stored in the C++ part but the computationally intense processes are done in C++. Currently, only the [TD-FCI](#) part is interfaced with Python but the writing of a [MCTDH](#) interface could easily be achieved. Further, the Python part offers unpruned [TD-FCI](#) and [MCTDH](#) dynamics. Indeed, this means code duplication and redundancy. This happened because in the initial phase of writing the program, it was not clear where LAGOM would stand now and it was not clear that [MCTDH](#) can be efficiently implemented almost exclusively using Python (see [Section I.3.5.2](#)).

It is planned to leave only the very essential parts in C++ and to drive the program completely in Python, both for [TD-FCI](#) and [MCTDH](#), *via* pybind11 and without auxiliary files. This allows for an easier implementation since the flexibility of Python makes it easier to design proper software.

I.3.8. Input Example

Consider the propagation of a two-dimensional coupled harmonic oscillator with [TD-FCI](#). The [SoP](#) operator of this specific example is given by

$$\hat{H} = \hat{T}_1 \otimes \hat{1} + \hat{1} \otimes \hat{T}_2 + \hat{x}^2 \otimes \hat{1} + 2 \cdot \hat{1} \otimes \hat{x}^2 + 0.2 \cdot \hat{x} \otimes \hat{x}, \quad (\text{I.3.1})$$

$$\hat{T}_1 = \frac{1}{2 \cdot 9} \hat{p}^2, \quad (\text{I.3.2})$$

$$\hat{T}_2 = \frac{1}{2 \cdot 16} \hat{p}^2. \quad (\text{I.3.3})$$

The operator is represented by a sinc [DVR](#) (40 basis functions in the range $[-6, 6]$) in the first dimension and by a [FGH](#) in the second dimension (64 basis functions in the range $[-4, 4]$). Apart from a normalization factor, the initial state is given by

$$|\Psi(0)\rangle = \exp[-\alpha(\hat{x} - x_{0,1})^2 + ip_{0,1}(x - x_{0,1})] \otimes \exp[-\alpha(\hat{x} - x_{0,2})^2 + ip_{0,2}(x - x_{0,2})], \quad (\text{I.3.4})$$

$$x_{0,1} = 0.4, \quad p_{0,1} = 0.1, \quad x_{0,2} = -0.8, \quad p_{0,2} = 0. \quad (\text{I.3.5})$$

$|\Psi(0)\rangle$ is propagated until 1 fs and the autocorrelation at time $2t$ given by $\langle \Psi(t)^* | \Psi(t) \rangle$ (see [Section III.A](#) in [Publication 3 \(Section I.1.3\)](#)) is computed every 0.01 fs. Afterwards, it is plotted and shown on the screen.

This task performed by LAGOM is shown in [Listing I.3.3](#). The [DVR](#) is set up in lines 12 to 16. To avoid a large list of input parameters, the Python classes are implemented with auxiliary

option classes that define all parameters and their default values. Given a certain option class, the function `basisFactory` selects the corresponding `DVR` class (line 16).¹⁷

The Hamiltonian is set up in lines 19 to 34. First, it is defined in an abstract way without an actual basis. Note that the potential functions (the lambda functions in lines 22 to 25) are again examples of functional programming (Section I.3.6.2). The matrix representation of the abstract operator is created in line 29. Several sum-terms that differ in only one dimension are contracted in line 31 and the potential term is separated from the rest of the operator in line 33. This is to optimize for `DVR` dynamics. Note the commented line 30 where the kinetic energy matrix of the first dimension is perturbed by random numbers. This is just to show that simple tests and method development can easily be done in Python without changing the code of the actual implementation.

Instead of the direct definition in Python, the Hamiltonian can be conveniently defined in the format of the Heidelberg `MCTDH` package and read in and parsed to the LAGOM format (commented line 26). The corresponding operator file is shown in Listing I.3.4. Note that the definition and usage of the parameters of the operator is a bit obfuscated in Listing I.3.4. This is to show that the parsing can handle also more complex tasks like different units and arithmetic operations. This is also the case for the Heidelberg `MCTDH` package.

The initial state is set up in lines 38 to 43 and a wrapper object, `Hamilt`, is created in line 46. This wrapper just provides additional functions like the computation of the energy etc.

The propagation is then set up and performed using a `SIL` propagator in lines 50 to 73 and the autocorrelation function is finally plotted in lines 76 to 79. These lines should be self-explanatory. LAGOM provides also a function that already implements a simple propagation. This has not been used in this example.

Listing I.3.3: Example input of the program.

```

1  """ Simple 2D coupled harmonic oscillator example:
2     Propagation in a DVR basis and plot of the autocorrelation """
3  from magic import * # Imports numpy, scipy etc. and sets default values
4  import basis
5  import operator1D
6  import operatornD
7  import hilbert
8  from propagation import propagators
9  import mctdh_stuff
10
11 # Set up DVR
12 DVROpts = [
13     basis.SincInfInf.getOptions(N=40, xRange= [-6,6]),
14     basis.FGH.getOptions(N=64, xRange= [-4,4])
15 ]
16 bases = [basis.basisFactory(opt) for opt in DVROpts]

```

¹⁷The usage of “factory” functions is also a design pattern (Section I.3.6.5).

```

17
18 # Set up Hamiltonian
19 Hop = operatornD.operatorSumOfProduct(nDim=2, nSum=5)
20 Hop[0,0] = operator1D.KE(mass=9) # Kinetic energy operator
21 Hop[1,1] = operator1D.KE(mass=16) # Hop[i,s] accesses dimension i and sum-term s
22 Hop[0,2] = operator1D.fx(lambda x: x**2) # Potential function
23 Hop[1,3] = operator1D.fx(lambda x: 2 * x**2)
24 Hop[0,4] = operator1D.fx(lambda x: 0.2 * x) # Coupling term
25 Hop[1,4] = operator1D.fx(lambda x: x) # --
26 #Hop = mctdh_stuff.translateOperatorFile("c2dho.op")
27
28
29 Hop.storeMatrices(bases)
30 #Hop[0,0].mat += 0.01 * np.random.rand(*Hop[0,0].mat.shape) #random perturbation
31 Hop = operatornD.contractSoPOperatorSimpleUsage(Hop)
32
33 potential, opRest = operatornD.separatePotentialFromSoP(Hop,
34                                                         [bas.N for bas in bases])
35
36
37 # Initial state
38 g1 = basis.misc.Gaussian(x0=+0.4, p0=0.1, alpha=1)
39 g2 = basis.misc.Gaussian(x0=-0.8, p0=0.0, alpha=1)
40
41 # bases[i].xi are the DVR grid points of dimension i
42 psiInit = np.kron( g1.xRepr(bases[0].xi), g2.xRepr(bases[1].xi) )
43 psiInit /= la.norm(psiInit) # Normalize to DVR representation
44
45 # Create wrapper
46 Hamilt = hilbert.HilbertOrthogonalnD(bases, opRest,
47                                     potential=potential, wave=psiInit)
48
49 # Set up propagation
50 sil = propagators.sil_heidelberg(
51     propagators.sil_heidelberg.getOptions(KrL=20, tol=1e-6) )
52 t = 0
53 dt = util.unit2au(0.01, "fs")
54 tend = util.unit2au(1, "fs")
55 NpropSteps = math.ceil(tend / dt)
56
57
58 times = [0] # Array for autocorrelation function
59 autoCorrelation = [1] # Array for autocorrelation function
60
61 # Do the propagation
62 for m in range(NpropSteps):
63     # Propagate one time step
64     Hamilt.states = sil.march(Hamilt.Hvec, Hamilt.states, dt)

```

```

65     t += dt
66     # Compute properties and print them in different units
67     norm = Hamilt.getNorm()
68     energy = Hamilt.getEnergy()
69     print( util .au2unit(t, "fs"), util .au2unit(energy, "eV"), norm)
70
71     # Autocorrelation function;  $C(2t) = \langle \Psi(t)^* | \Psi(t) \rangle$ 
72     times.append(2 * t)
73     autoCorrelation.append( np.vdot(Hamilt.states.conj(), Hamilt.states) )
74
75 # Plot result
76 plt .plot( util .au2unit(np.array(times), "fs"), np.abs(autoCorrelation))
77 plt .xlabel("t/fs")
78 plt .ylabel(r"|⟨Ψ(0)|Ψ(t)⟩|")
79 plt .show()

```

Listing I.3.4: Operator file for the example input (Listing I.3.4) in the format of the Heidelberg MCTDH package.

```

1 PARAMETER-SECTION
2 one = 1.0, au
3 xFac    = one
4 couplFac = 0.2
5 mass_v1 = 9.0
6 mass_v2 = 16.0
7 end-parameter-section
8
9 HAMILTONIAN-SECTION
10 -----
11 modes   | v1 | v2
12 -----
13 1.0     | KE | 1
14 1.0     | 1  | KE
15 xFac    | q^2 | 1
16 2.0*one | 1  | q^2
17 couplFac | q  | q
18 end-hamiltonian-section

```

Part II

Applying Pruning Methods

Resonance Decay Dynamics of the Deuterated Formyl Radical

“*The atoms are eternal and always moving. Everything comes into existence simply because of the random movement of atoms, which, given enough time, will form and reform, constantly experimenting with different configurations of matter from which will eventually emerge everything we know.*

— **Titus Lucretius Carus**
about 99 BC – 55 BC

The article shown in the following Section presents the first larger application of dynamically pruned discrete variable representation (DP-DVR). It sheds light on the decay mechanism of vibrationally highly excited resonance states of the deuterated formyl radical, DCO, and compares to experimental velocity map imaging results. Due to strong anharmonic coupling, this is an important benchmark example but the number of studies on DCO is limited. This article makes an initial attempt to fill this gap. We could confirm results from a polyad model.^[241] We further show that DP-DVR is a promising new method for this challenging test case, covering high-energy resonance calculations and long-time dissociation dynamics up to 180 ps.

II.1.1. Publication

II.1.1.1. Own Contributions

- Implementation, setup, execution and analysis of all simulations.¹
- Writing and editing of the whole manuscript, excluding Sections II and IV.A.

II.1.1.2. Bibliographic Data

Title Resonance dynamics of DCO (\tilde{X}^2A') simulated with the dynamically pruned discrete variable representation (DP-DVR)

Authors Henrik R. Larsson, Jens Riedel, Jie Wei, Friedrich Temps, Bernd Hartke

Journal The Journal of Chemical Physics

Volume 148

Note In press

DOI [10.1063/1.5026459](https://doi.org/10.1063/1.5026459)

Preprint <https://arxiv.org/abs/1802.07050>

¹The initial idea to perform the simulations for this system is due to Friedrich Temps. Bernd Hartke and Friedrich Temps were involved in the discussions of the analysis. The idea of using filter diagonalization is due to Bernd Hartke.

II.1.1.3. Article

Resonance dynamics of DCO (\tilde{X}^2A') simulated with the dynamically pruned discrete variable representation (DP-DVR)

Henrik R. Larsson,^{1, a)} Jens Riedel,^{1, b)} Jie Wei,¹ Friedrich Temps,¹ and Bernd Hartke¹
Institut für Physikalische Chemie, Christian-Albrechts-Universität zu Kiel, Olshausenstraße 40, 24098 Kiel, Germany

(Dated: 20 February 2018)

Selected resonances of the deuterated formyl radical in the electronic ground state \tilde{X}^2A' are computed using our recently introduced dynamically pruned discrete variable representation (DP-DVR) [H. R. Larsson, B. Hartke and D. J. Tannor, *J. Chem. Phys.*, **145**, 204108 (2016)]. Their decay and asymptotic distributions are analyzed and, for selected resonances, compared to experimental results obtained by a combination of stimulated emission pumping (SEP) and velocity-map imaging of the product D atoms. The theoretical results show good agreement with the experimental kinetic energy distributions. The intramolecular vibrational energy redistribution (IVR) is analyzed and compared with previous results from an effective polyad Hamiltonian. These results could mainly be confirmed. The C=O stretch quantum number is typically conserved, while the D-C=O bend quantum number decreases. Differences are due to strong anharmonic coupling such that all resonances have major contributions from several zero-order states. For some of the resonances, the coupling is so strong that no further zero-order states appear during the dynamics, even after propagating for 300 ps.

Keywords: quantum dynamics, pruning, non-direct-product bases, resonance decay, dissociation, DCO, filter diagonalization, stimulated emission pumping, velocity map imaging

I. INTRODUCTION

One of the fundamental processes in molecular reaction dynamics is the unimolecular dissociation of vibrationally excited molecules.¹⁻⁴ Depending on the molecular system, their decay dynamics can span the range from mode-specific to statistical. For intermediate cases, the dissociation mechanism in terms of intramolecular vibrational energy redistribution (IVR) of bound and metastable resonance states provides considerable insight into the dynamic properties of the molecular system under study.

One standard benchmark system is the formyl radical HCO which plays an important role in many combustion processes as well as in atmospheric and interstellar chemistry; see, e.g., Ref. 5. In its electronic ground state \tilde{X}^2A' , HCO shows many resonance states whose decays follow very systematic mode-specific pathways.

In contrast to HCO, its deuterated counterpart DCO shows more statistical behavior. This is due to an accidental, strong $\nu_1 : \nu_2 : \nu_3 \approx 1 : 1 : 2$ Fermi resonance in the D-CO stretching vibration ν_1 (1910 cm^{-1}), the DC=O stretching vibration ν_2 (1795 cm^{-1}), and the D-C=O bending vibration ν_3 (847 cm^{-1}). The Fermi resonance leads to strong mixing between zero-order states, already for the lowest vibrational states.⁶⁻⁹ Strong mixing is an essential prerequisite for statistical dynamics. Keller *et al.* thus consider DCO a ‘precursor of ‘chaos’ in more

complicated systems’.⁷ Consequentially, the normal assignments in terms of the associated vibrational quantum numbers (v_1, v_2, v_3) lose their meanings, although they may still be used economically as ‘nominal labels’ to indicate possible predominating vibrational character. The only conserved quantity at short times is the polyad quantum number, $P = v_1 + v_2 + v_3/2$, which describes the total vibrational excitation.^{6,10-12}

Due to their strikingly different characteristics, there has been strong interest in both HCO and DCO, from both experiment and theory. Due to the amount of work on these systems, we briefly mention only some of the most important contributions. Energies and widths of resonances of HCO and DCO have been measured to high resolution by dispersed fluorescence and stimulated emission pumping.^{6,13-17} For HCO, Neyer *et al.* also measured the rovibrational product distribution of CO.¹⁸

Likewise, energies and widths of HCO have been computed using various methods, establishing this system as a benchmark for computing resonance states.¹⁹⁻²⁸ Rovibrational CO state distributions and resonance decays have been analyzed by various researchers, also for nonzero total angular momentum.^{21,22,29-34} However, less attention has been paid to DCO.^{6,7,35-37} Although DCO shows close to statistical behavior, it is not fully irregular. The decay constants show strong state-to-state fluctuations. Microcanonical statistical rate theory thus cannot predict the state-specific decay constants. Due to strong anharmonic couplings, an IVR analysis is much less straightforward but still desirable. Clear indications that remaining regularities may be strong enough for such an approach were provided by the aforementioned polyad model that turned out to be applicable to DCO and quite useful.⁷ The group of Temps fitted an effec-

^{a)}Electronic mail: larsson@pctc.uni-kiel.de

^{b)}Present address: Federal Institute for Materials Research and Testing (BAM), Unter den Eichen 87, 12205 Berlin, Germany

tive polyad Hamiltonian to experimental data and did an analysis of different IVR pathways within this polyad model.^{8,38} This model Hamiltonian was then used for further semiclassical analysis.^{39–41} However, many of these analyses still lack comparison with quantum calculations on an *ab-initio* potential energy surface (PES).

Here, we make an initial attempt to fill this gap by a joint experimental and theoretical study of the observed and calculated resonances of DCO in polyads 5 and 5.5. In particular, we present experimental measurements of the kinetic energy release (KER) spectra of the D atoms from the decay of the resonances and the associated CO vibration-rotation product state distributions. The results were obtained using the method of Stimulated Emission Pumping (SEP)⁶ for the preparation of selected excited DCO resonance states in combination with velocity-map imaging⁴² of the D atoms. In addition, we computed the CO state distributions using our dynamically pruned discrete variable representation (DP-DVR) approach^{43–45} and analyzed the computed resonance decays. As critical tests of the theory, we compare our computational results with the experimental data taking either the PES of Werner *et al.* (WKS)^{21,22} or the PES of Song *et al.* (SAG).⁴⁶

We thereby use this study as a real-life application of our new method for performing molecular quantum dynamics. The standard method in molecular quantum dynamics is to employ a direct-product basis of discrete variable representation (DVR) functions.⁴⁷ However, this approach suffers from an exponential scaling of basis size with dimensionality. Even for lower-dimensional problems like the one studied here, it is not the most efficient method. For dissociation problems like DCO, long coordinate ranges need to be described, but the wavefunction typically does not occupy the whole direct-product coordinate space. Such a problem is well-suited for only using DVR grid points where the wavepacket has non-negligible amplitudes. This leads to significant savings in computational resources (both regarding number of operations and memory requirements). Since the wavepacket moves in time, the set of active basis functions needs to be dynamically adapted. Exactly this capability is provided by our dynamically pruned DVR approach (DP-DVR).^{43–45} The accuracy is controlled by a so-called wave-amplitude threshold.^{43,48} The smaller the threshold, the more basis functions are added and the more accurate the simulation becomes. In Ref. 45 we have introduced a very efficient algorithm for DP simulations and have done careful benchmarks of the DP-DVR and other methods. We have shown that DP-DVR can be more efficient than conventional dynamics already for two-dimensional systems.

For the dissociation dynamics of DCO, phase-space bases would be other useful candidates for our DP approach.^{44,45,49,50} One could use such a phase-space basis in the coordinate describing the dissociation. However, efficient use of phase-space bases requires that the potential operator has the form of a sum of products of one-dimensional terms (SOP form). This requires an ad-

ditional fitting of the potential into this form.

Recently, we have combined our DP approach with the Multiconfiguration Time-Dependent Hartree method (MCTDH), giving DP-MCTDH.⁵¹ There, DP can be used either for pruning the time-dependent basis functions (single-particle functions) or their DVR representation. The former is most useful for higher-dimensional systems (see also Refs. 52–54) whereas the latter is useful whenever many DVR functions are needed for describing the (multidimensional) single-particle functions. This is the case for DCO dissociation dynamics such that DP-MCTDH could be a useful method for our study. MCTDH itself has been used for computing resonances of HCO.^{27,28} However, the MCTDH algorithm is more complicated than a DVR code. Furthermore, as with phase-space bases, an efficient use of MCTDH requires a SOP form of the potential. Although methods for combining arbitrary potentials with MCTDH exist,^{55,56} they are less well established and require more careful convergence tests. Further, MCTDH is most useful for weakly correlated systems and short-time dynamics, but for HCO²⁷ many single-particle functions are needed and the wavepacket has to be propagated for tens of picoseconds.

Here, we resort to our standard DP-DVR algorithm to make our simulations as simple as possible, without jeopardizing computational efficiency, and also to test the capabilities of our DP-DVR approach in an application involving resonances and their decay.

The remainder of this Article is organized as follows: The experimental and theoretical setups are described in Sections II and III, respectively. The latter provides more details on the DP-DVR method (Section III A), on the methods to obtain resonance states (Section III B) and asymptotic product distributions (Section III C), and on the employed PES (Section III D). Our results are presented and discussed in Section IV. The experimental velocity map images are presented in Section IV A. Section IV B details the simulation parameters and Section IV C compares our computed resonance energies and widths with literature values. The PES is analyzed in terms of an adiabatic picture in Section IV D, the experimental and theoretical asymptotic distributions are presented and compared in Section IV E, and the decay processes of the studied resonances are analyzed in Section IV F. We summarize in Section V.

II. EXPERIMENT

The experimental measurements required four spatially and temporally controlled laser pulses to be focused into a supersonic seeded molecular beam in a differentially pumped stainless steel vacuum chamber. Fig. 1 shows a sketch of the employed installation. The SEP part of the setup for preparation of the DCO (\tilde{X}) radicals in their highly excited states^{6,17} and the photofragment imaging part for measuring the kinetic energy release to

the D atoms^{57,58} have been described in some detail separately before. The exact experimental conditions varied slightly from those to record optimal SEP spectra by the need of the present experiment for a high number density of highly vibrationally excited radicals.⁵⁹

A pulsed supersonic free jet containing $\sim 0.5\%$ deuterated acetaldehyde (CD_3CDO) in He was generated by flowing the carrier gas at a backing pressure of ~ 2 bar through a stainless steel reservoir with freshly distilled CD_3CDO (Fluka, $> 99\%$) at -78°C and expanding it into the first vacuum chamber of the imaging apparatus through a 0.8 mm diameter solenoid-actuated valve (General Valve) at 20 Hz repetition rate. Photolysis of the CD_3CDO with a XeCl excimer laser at $\lambda = 308$ nm in the high-pressure region of the free jet expansion ~ 3 mm behind the pulsed nozzle produced the desired DCO radicals. A molecular beam of the radicals shaped by a 1.5 mm diameter conical skimmer then entered the test volume between the repeller and extractor plates of the imaging electrode assembly in the second vacuum chamber, where it was crossed by the pump, dump and probe laser beams. A liquid- N_2 cryo-pump surrounding the assembly minimized the background ion signal.

Two dye lasers (Lambda Physik) were optically pumped by the dichroically separated third resp. second harmonic output beams of a Nd:YAG laser (Spectra Physics) and frequency-doubled in BBO crystals to obtain the required ~ 259 nm pump (1.5 mJ) and 336–362 nm dump (5–7 mJ) pulses. The precise wavelengths were set by recording the $\tilde{B}(^2A') \leftarrow \tilde{X}(^2A')$ fluorescence excitation and $\tilde{B} \rightarrow \tilde{X}$ SEP spectra in a separate molecular beam apparatus with fluorescence detection.^{6,17} Both beams were focused into the test volume at a small angle with respect to each other through a $f = 500$ mm fused silica lens. The 308 nm excimer-pumped probe dye laser (both Lambda Physik) for imaging of the D atoms from the D–CO dissociation reaction by 2+1 resonance-enhanced multi-photon ionization (REMPI) via the $2^2S \leftarrow 1^2S$ transition was frequency-doubled to the required $\lambda = 243$ nm (1 mJ) and focused into the detection region counter-propagating to the pump and dump with a short delay of ~ 10 ns. The exact probe wavelength was set by optimizing the D^+ ion yield. All laser polarizations were set parallel to the plane of the imaging detector using combinations of Fresnel double rhombs and Rochon or Wollaston prisms.

The imaging measurements were made under velocity mapping conditions.⁴² The probe laser was periodically scanned over the Doppler profile of the recoiling D atoms. The resulting D^+ ions were monitored on a microchannel plate (MCP) detector coupled to a phosphor screen. The obtained signals were recorded on a CCD camera and accumulated over up to 200 000 laser shots using single ion counting and centroiding⁶⁰ to improve the detection sensitivity and spatial resolution and to discriminate against noise. Background images with the dump laser blocked on alternate shots were subtracted to eliminate contributions to the D atoms from the CD_3CDO photolysis and

from predissociation of the DCO (\tilde{B}) state. Mass selectivity was achieved using a fast transistor switch (Behlke) to gate the MCP. The timing of the pulsed valve, all lasers and the MCP voltage was controlled by a digital delay generator (Stanford Research).

III. THEORY

A. Dynamically pruned discrete variable representation (DP-DVR)

The propagation is performed in Jacobi coordinates $\{R, r, \theta\}$. R is the distance of D to the center of mass of C–O, r is the C–O distance and θ the angle between the corresponding vectors \vec{R} and \vec{r} . As usual,⁶¹ the wavefunction is divided by Rr such that the volume element takes the form of $dV = dR dr \sin(\theta)d\theta$. In our propagation, we consider only the $\tilde{X}(^2A')$ ground state and neglect nonadiabatic and Renner-Teller couplings. The couplings only play an important role if the wavefunction has non-negligible contributions at linear geometries.²¹ This requires high excitation in the bending mode and only occurs for a minority of the resonances studied; we will mention them in Section IV F.

The wavefunction is represented by a Gauß-Legendre DVR for the angular coordinate and by a sinc DVR for the radial coordinates.^{47,62} This direct-product basis is then pruned using our DP-DVR approach.⁴⁴ If the absolute value of a coefficient of a direct-product basis function is larger than a predefined wave-amplitude threshold, this basis function and its nearest neighbors become active. Otherwise, this function is removed from the set of active functions. This procedure is repeated at each time step, ensuring a compact representation of the wavefunction for all propagation times. For further details we refer to Ref. 44.

In the following, we mention two improvements of our code introduced in Ref. 44 (the reader who is not interested in technical details may skip the rest of this Subsection). The first improvement is a (straightforward) implementation of standard shared-memory parallelization. For the second improvement, we take advantage of the fact that the momentum and kinetic energy operators in sinc DVR representation give Toeplitz matrices with elements $T_{i,j} = T_{i+1,j+1} = t_{i-j}$. Instead of storing all matrix elements $T_{i,j}$, we only store one row t_{i-j} of the matrix. This reduces the memory needed to be loaded into the cache of the central processing units and thus gives large speed-ups, especially for shared-memory parallelization. In standard molecular quantum dynamics applications with basis sizes smaller than 100, the storage of the one-dimensional matrices is negligible, compared to the storage of the (pruned) multidimensional wavefunction. However, the exploitation of the Toeplitz structure becomes useful whenever the one-dimensional basis size is large. This is the case for the dissociation dynamics considered here. For a basis that is not pruned, the

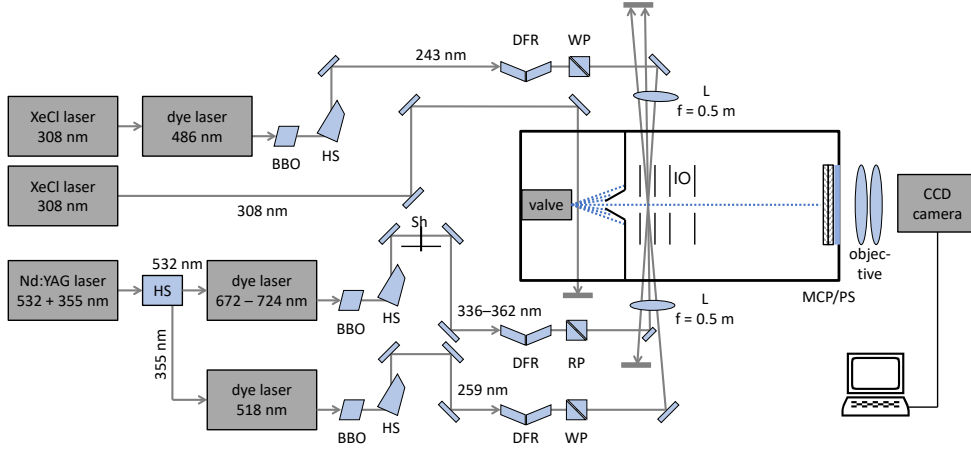


FIG. 1. Schematic diagram of the experimental setup. BBO: doubling crystal, DFR: double-Fresnel rhomb, HS: harmonic separator, IO: ion optics electrode assembly, L: lens, MCP: multi-channel plate, PS: phosphor screen, RP: Rochon prism, Sh: shutter, WP: Wollaston prism.

action of a Toeplitz matrix onto a vector can be implemented with a scaling of $\mathcal{O}(N \log(N))$ using fast Fourier transforms (FFTs).⁶³ However, when the basis is pruned, some structure of the pruned matrix is lost and an implementation in terms of FFTs is not straightforward. Nevertheless, the matrix-vector product in a pruned basis is much faster than a FFT in an unpruned basis if pruning reduces the size of the objects sufficiently, which typically is the case.

B. Retrieval of resonances

Previously, HCO and DCO resonances have been computed using, among others, Lanczos procedures,^{24,26} a log-derivative version of Kohn's variational principle,^{7,22} MCTDH,²⁷ projection theory,⁶⁴ and filter diagonalization.^{25,32} Many applications utilize the time-independent Schrödinger equation (TISE). In principle, our DP-DVR code would work as well for the TISE using an algorithm that iteratively adds and removes new basis functions after each Lanczos iteration.⁴⁸ However, Lanczos and other iterative diagonalization algorithms require a good preconditioner for efficient usage,^{24,65,66} especially when eigenstates are searched in the middle of a dense eigenspectrum, as is the case in this application. The search for a good preconditioner for a Hamiltonian is not trivial and depends on the employed basis. We tested the preconditioner proposed in Ref. 65 and some standard preconditioners like diagonal matrices but found no satisfying results.

Thus, instead of using a Lanczos approach, we use filter diagonalization.^{67,68} Since the standard form of filter diagonalization is based on propagation, it allows for a straightforward integration into a DP code for solving the time-dependent Schrödinger equation. This worked

without any adjustments or tuning of parameters, and the bottleneck of our simulations was then not the retrieval of the eigenstates but the subsequential simulation of their decay. Thus, we did not try to use further improvements of filter diagonalization.^{25,69,70}

In standard filter diagonalization, a real-time dynamics of an initial wavepacket with absorbing boundary conditions is performed and the wavepacket is stored at intermediate times. Afterwards, the wavepacket is filtered at (typically equidistantly spaced) energies E_n via Fourier transform:⁶⁸

$$|\Phi_F(E_n)\rangle = \frac{1}{2\pi\hbar} \int_0^\infty \exp(iE_n t/\hbar) |\Psi(t)\rangle F(t) dt, \quad (1)$$

where $F(t)$ is a filter function of the form

$$F(t) = \exp[-(t - \tau)^2 W^2/\hbar^2]. \quad (2)$$

W is the energy bandwidth, here taken as $E_{n+1} - E_n$. The duration τ is set such that $W\tau \gg 1$. Afterwards, the Hamiltonian is represented in the nonorthogonal basis of filtered states $\{|\Phi_F(E_n)\rangle\}_{n=1}^N$ and diagonalized. The size of the basis is typically less than 100, such that diagonalization can be performed using standard procedures.

C. Rovibrational product distribution

For obtaining the KER spectra of the D atom and the asymptotic rovibrational distributions of the CO fragment, we employ the analysis-line method developed by Balint-Kurti *et al.*⁷¹ It has previously been used for HCO by both Gray and Dixon.^{30,33,34} The retrieval of the asymptotic distribution is performed by Fourier-transforming cuts of $\Psi(R, r, \theta; t)$ along the "analysis line" $R = R_\infty$, where the cuts $\Psi(R_\infty, r, \theta; t)$ are represented in

the basis of asymptotic rovibrational states, $\{|\psi_{vj}\rangle\}$. v and j are the CO stretch and rotational quantum numbers, respectively. The working expression is

$$C_{vj}(R_\infty, t) = \langle R_\infty | \langle \psi_{vj} | \Psi(t) \rangle,$$

$$A_{vj}(R_\infty, E) = \frac{1}{2\pi} \int_0^\infty \exp(iEt/\hbar) C_{vj}(R_\infty, t) dt.$$

The KER spectrum $P(E_D)$ is then given by

$$P(E_D) = \sum_{v,j=0}^{\infty} P_{vj}(E_D), \quad (3)$$

$$P_{vj}(E_R) = \lim_{t \rightarrow \infty} |\langle \Psi_{kvj}^{(-)} | \Psi(t) \rangle|^2 \quad (4)$$

$$= \frac{16\pi^3 k}{\mu_R} |A_{vj}(R_\infty, E_R)|^2, \quad (5)$$

$$E = E_{vj} + E_R, \quad E_D = \frac{m_{\text{CO}}}{m_{\text{DCO}}} E_R, \quad (6)$$

where $k = \sqrt{2\mu_R E_R/\hbar^2}$ and E_R is the kinetic energy in the internal Jacobi coordinate R . The corresponding kinetic energy of the D atom in the laboratory frame (without translation and rotation of the DCO system) is then given by mass-weighting E_R (Eq. (6)), as obtained from the standard center-of-mass transformation of a two-body system.⁷² E_{vj} is the internal energy of the CO fragment. μ_R is the reduced mass of D–CO in Jacobi coordinates. $|\Psi_{kvj}^{(-)}\rangle$ is the outgoing scattering state for dissociation into D and CO.³ Integrating $P_{vj}(E_R)$ over all E_R gives the rovibrational distributions of the CO product.

Combining this method with our DP-DVR approach is straightforward because the only quantity that needs to be stored during the dynamics calculation is the wavefunction evaluated at R_∞ which is a DVR grid point in the asymptote. When no basis function at R_∞ is active at a specific time step, the wavefunction there is simply zero.

D. Potential energy surfaces

To the best of our knowledge, there are three accurate and more recent potential energy surfaces (PES) for HCO. The (modified) WKS surface of Werner, Keller and Schinke^{21,22} has been applied in many studies; for example Refs. 6,7,24–27,64. This PES quite accurately describes both the dissociation and the interaction region, including the conical intersection at linear geometry. It is based on multireference configuration interaction (MRCI) calculations. Another recent PES is that developed by Song, van der Avoird and Groeneboom (SAG).⁴⁶ It is based on unrestricted coupled-cluster calculations and focuses on the asymptotic and lower-energy regions. It has been used for scattering calculations.⁷³ The third recent PES was developed by Ndengué, Dawes and Guo and is based on explicitly correlated MRCI

calculations.²⁸ It was used for unraveling the effects of Renner-Teller coupling on the resonance levels.

Only the WKS surface has been used in studies of DCO.^{6,7} To connect to those previous studies, we mainly use this well-established PES in our calculations. In order to estimate the sensitivity of the observables to changes of the potential, we also employed the SAG surface for selected resonances. Figures i and ii in the supplementary material show cuts of the two PES. Since none of those PES were constructed with decay dynamics of high-energy resonances far out into the asymptote in mind, none of the utilized PES can be expected to give quantitative agreement between theoretical and experimental results in this present application.

IV. RESULTS AND DISCUSSION

A. Experimental Results

Four DCO (\tilde{X}) resonances were picked at random for investigating the KER spectra and CO (v, j) product state distributions by the D atom velocity map imaging experiment. Two states were taken from polyad $P = 5$ (at energies $E_v = 8902$ and 8942 cm^{-1}) and two from polyad $P = 5.5$ ($E_v = 9896$ and 10065 cm^{-1}). SEP spectra illustrating the observed vibrational states belonging to both polyads are shown in Fig. 2.

Following Keller *et al.*,⁷ the four resonances are nominally labeled as (0,4,2), (0,5,0), (2,3,1) and (1,4,1), in order of increasing energy for reference below. We emphasize, however, that these “assignments” have to be taken with caution. For example, the 8902 cm^{-1} resonance was reported as a mixture of 48% (2,2,2) and 32% (0,4,2), while the neighboring 8821 cm^{-1} resonance was found as a mixture 41% (2,2,2) and 32% (0,4,2). Further, the resonance at $E_v = 10065 \text{ cm}^{-1}$ nominally assigned as (1,4,1) is special because it shows pronounced interpolyad mixing with a highly dissociative resonance belonging to polyad $P = 6$, most likely (4,2,0).¹⁷

The recorded D atom velocity mapped images after excitation of the 2_{02} and 2_{12} rotational states of the above four DCO (\tilde{X}) resonances are printed in Fig. 3 a) together with their Abel inversions in Fig. 3 b). The depicted meridional slices through the three-dimensional (3D) D atom recoil distributions were obtained using the iterative regularization method with the projected Landweber algorithm.⁷⁴ As can be seen, the raw images and the associated slices through the 3D recoil distributions differ substantially from vibrational resonance to resonance, while the results for the two rotational states are very similar, indicating the good reproducibility of the data. For (0,5,0) and (1,4,1), the 3D slices show D atoms with comparably low recoil velocities. The allowed maximal available energies E_{av1} is determined by the energy balance

$$E_r + \nu_{\text{pump}} - \nu_{\text{dump}} = \Delta H_0^0(\text{D-CO}) + E_{\text{av1}}, \quad (7)$$

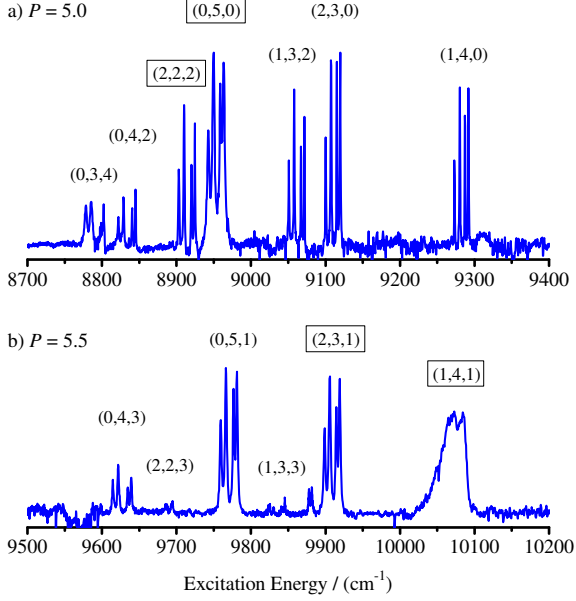


FIG. 2. SEP scans over a) polyad 5.0 and b) polyad 5.5 with nominal assignments of the observed resonances according to Ref. 7. The four resonances selected for D atom imaging are highlighted by frames around the state labels. With the pump laser tuned to the $\tilde{B} \leftarrow \tilde{X}, 0_0^0, {}^aR_0(0)$ line at $\nu_{\text{pump}} = 38\,631.60\text{ cm}^{-1}$, state, the dump transition can reach four different rotational states, $N_{K_a K_c} = 0_{00}, 2_{02}, 1_{10}$ and 2_{12} , in each \tilde{X} vibrational state, explaining the four-line patterns observed in the SEP scans.

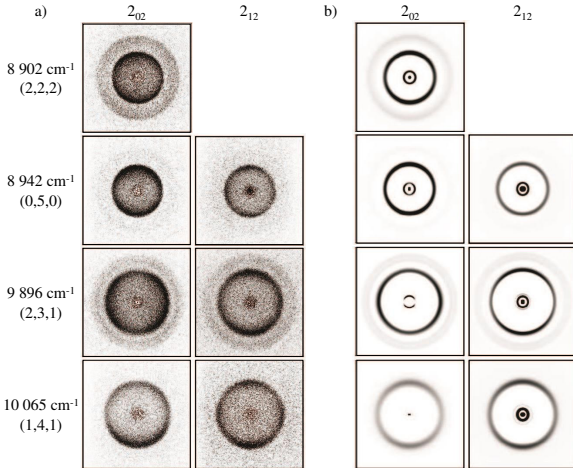


FIG. 3. a) Measured two-dimensional (2D) D atom velocity map images after excitation of the (0,4,2), (0,5,0), (2,3,1) and (1,4,1) DCO (\tilde{X}) resonances in the 2_{02} and 2_{12} rotational states and b) reconstructed meridional slices through the respective three-dimensional (3D) D atom recoil distributions.

where E_r is the initial state's rotational state (here $E_r = 0$ for $N_{K_a K_c} = 0_{00}$), $\Delta H_0^0(\text{D-CO})$ is the asymptotic D-CO dissociation energy, and ν_{pump} and ν_{dump} are the energies supplied by the pump and dump laser pulses. Thus, dissociation of the (2,2,2) and (0,5,0) resonances may lead to CO in $v = 0$ and $v = 1$, while the (2,3,1) and (1,4,1) resonances may also give CO in $v = 2$. Evidently, however, (0,5,0) and (1,4,1) give mainly CO in $v = 1$. Further, as indicated by the narrow recoil widths, the CO ($v = 1$) acquires relatively low rotational excitation (quantum number j). In contrast, the images obtained from the (2,2,2) and (2,3,1) resonances show the formation of CO in $v = 1$ and in $v = 0$, with broader rotational excitation in $v = 0$. The observed recoil anisotropies are negligible within experimental errors, consistent with resonance lifetimes ($\tau = 0.8\text{--}5\text{ ps}$ inferred from the measured resonance widths) longer than the DCO rotational period.

Subsequent integration of the D atom images over the angular coordinates and transformation of the resulting recoil velocity distributions to the recoil translational energies with account of the fragment mass ratio and the appropriate Jacobian finally gave the total kinetic energy release (KER) spectra for the decaying resonances. The corresponding CO vibrational and rotational product state distributions follow by the energy balance. The experimental KER spectra will be presented and compared with the present theoretical predictions in Section IV E. The asymptotic D-CO dissociation energy was assumed to have a value of $\Delta H_0^0 = 5\,450\text{ cm}^{-1}$.

B. Simulation parameters

For the filter diagonalization, the initial wavefunction is taken from Ref. 7 and takes the form of the following Gaussian (excluding normalization)

$$\Psi^{\text{FD}}(R, r, \theta; t = 0) \propto \exp\{-[(R - R_0)/\alpha_R]^2\} \times \exp\{-[(r - r_0)/\alpha_r]^2\} \exp\{-[(\theta - \theta_0)/\alpha_\theta]^2\}, \quad (8)$$

with the parameters $R_0 = 3.05 a_0$, $r_0 = 2.57 a_0$, $\theta_0 = 138^\circ$, $\alpha_R = 0.256 a_0$, $\alpha_r = 0.195 a_0$, and $\alpha_\theta = 7.19^\circ$. This initial wavepacket is propagated for 2 ps. The filter function is a Gaussian with duration of $\tau = 1\text{ ps}$ (see Eq. (2)), and the energy region of interest (see Section IV C) was divided into four regions, each with a width of $\sim 400\text{ cm}^{-1}$ and with typically 10 energy-filtered basis functions. For each region, the number of basis functions was adapted to avoid an overcomplete basis.

The DVR basis set parameters are given in Table I. For the filter diagonalization, a smaller range in R up to $R = 10 a_0$ is used. Due to a wrong asymptote of the SAG potential, a smaller coordinate range in r was used for all simulations on that PES. In coordinate R , we use the transmission-free complex absorbing potential of Ref. 75 (taking the rational form, Eq. (2.25) in that reference) with a width of $5 a_0$ for the filter diagonalization and

a width of $10 a_0$ for the decay dynamics. We use the following atomic masses: 12.0096 Da for C,⁷⁶ 15.99977 Da for O and 2.01410178 Da for D.⁷⁷

The wave-amplitude threshold used for the pruning of the filter diagonalization dynamics is 10^{-11} , although a threshold of 10^{-8} would give the same results. This looser threshold is used for the decay dynamics. There, a threshold of 10^{-6} would have been sufficient. The analysis line (Section III C) is placed at $R_\infty = 16 a_0$. For all propagations, we employ a short iterative Arnoldi propagator^{78,79} with an accuracy of 10^{-10} , in the form in which it is also implemented in the Heidelberg MCTDH package.⁸⁰ For each resonance, the final propagation time and the norm of the wavefunction at that time can be found in Table I in the supplementary material.

We note that all parameters were chosen conservatively and are not well-optimized. Especially, the employed coordinate ranges are probably too large. They do not require an in-depth optimization because our DP algorithm does this automatically: If the wavepacket will not enter a certain region in coordinate space, no basis function will become active in that region during the propagation and computational costs will not increase, compared to a carefully optimized coordinate range. Further, this means that the CAP width needs not be tuned to increase computational efficiency (although, the stronger the CAP, the earlier the wavefunction is absorbed in the CAP region, and the fewer basis functions are needed). This gives the DP-DVR algorithm more of a black-box character than conventional DVR dynamics. However, the other parameters still required convergence tests. The number of DVR functions, which determines the maximum momentum that can be described, can be easily determined by checking reduced densities of the wavefunction in momentum space. For the filter diagonalization and decay dynamics of selected resonances, careful convergence tests with tighter parameters have been pursued and the stated final parameters were chosen based on conservative conclusions from these tests.⁸¹

TABLE I. Basis sizes N and coordinate ranges for the three Jacobi coordinates R, r and θ for the two employed PES. Atomic units are used.

PES	R		r		θ	
	N	range	N	range	N	range
WKS ^{21,22}	210	[1.5, 28]	78	[1.5, 6]	60	[0, π]
SAG ⁴⁶	-	-	34	[1.5, 3.49]	-	-

C. Energies and widths

The computed resonance energies and widths on the WKS surface are given in Table II and compared with both our theoretical values and the experimental and theoretical values from Refs. 6,7.

Note that some energetically low-lying resonances (below $\Delta E = 8770 \text{ cm}^{-1}$, ΔE is the vibrational resonance energy relative to the ground state energy) in polyad 5 and one in polyad 5.5 are not included in our simulations. They were also not experimentally accessible. Here, we consider resonances in polyad 5 and 5.5 that are within a ΔE range of 8770 cm^{-1} and 10050 cm^{-1} .

Compared to the computed energies from Ref. 7, ours are systematically smaller but agree within $\sim 5 \text{ cm}^{-1}$. The decay widths have a better agreement; there, except for resonance (0,3,4), the maximal absolute deviation is 1 cm^{-1} . Note that Keller *et al.* reported that their basis was probably too small to yield accurate calculations.⁷ Their basis used in the calculations for HCO²² was significantly larger. To our knowledge, there are no further calculations done for DCO on the WKS surface. However, theoreticians have used resonance calculations for HCO on the WKS surface as a benchmark case.^{23–28} There, the deviations from the results of Ref. 22 have a similar magnitude as the deviations shown here. To conclude, our DP-DVR method with filter diagonalization gives results that are within reasonable agreement with the results from Keller *et al.* To allow for a better comparison, more extensive tests with HCO should be done but this is not within the scope of this work.

In Table III, vibrational energies and widths for five selected resonances are shown for the SAG surface and compared against experiment and results using the WKS surface. For four of them, experimental KER spectra are available as well (Section IV A). Compared to our WKS results, the energies differ from those obtained with the SAG surface by up to 54 cm^{-1} . The widths differ by up to 3 cm^{-1} . The WKS energies are closer to the experimental values and so are most of the widths — except for resonance (0,5,0). Note that some SAG states have components of the wavefunctions at linear geometries where Renner-Teller coupling and a conical intersection occur; see Section III A. Using single-reference coupled-cluster calculations, the SAG surface was not optimized for linear geometries. Since both the energies and rovibrational distributions (Section IV E) from the WKS surface are typically closer to the experiment, we focus in the following on the WKS surface but mention the SAG results where they are available.⁸²

D. Adiabatic rovibrational states

To shed more light on the coupling of the different states, we look at the adiabatic potential energy curves in R defined by the following eigenvalue problem in $\{r, \theta\}$:

$$\left[-\frac{\hbar^2}{2\mu_{\text{CO}} r^2} \frac{\partial^2}{\partial r^2} + \left(\frac{1}{2\mu_R R^2} + \frac{1}{2\mu_r r^2} \right) \hat{j}^2 + V(R, r, \theta) \right] |\chi_n(r, \theta; R)\rangle = E_n(R) |\chi_n(r, \theta; R)\rangle, \quad (9)$$

TABLE II. Comparison of computed relative resonance energies ΔE (relative to the ground state energy) and widths Γ from this work (DP) with the experimental (Exp.) and theoretical (WKS) results from Refs. 6,7.

P. ^a	label ^b	$\Delta E/\text{cm}^{-1}$				Γ/cm^{-1}				decomposition of wavefunction ^f							
		Expt. ^c	WKS ^b	DP ^d	Δ^e	Expt. ^c	WKS ^b	DP ^d	Δ^e								
5	((034))	8778	8780	8775	5	3.50	7.6	5.6	2	38:	034	30:	(411)	16:	222	16:	124
5	((042))	8821	8832	8830	2	<2.00	1.1	1.1	0	41:	222	32:	042	23:	132		
5	((222))	8902	8901	8895	6	1.06	1.9	1.2	0.7	48:	222	32:	042				
5	(050)	8942	8953	8950	3	1.79	0.14	0.13	0.01	44:	050	33:	(140)	15:	230		
5	(132)	9050	9031	9029	2	0.34	0.28	0.28	0	59:	132	24:	042	11:	222		
5	(230)	9099	9099	9096	3	0.20	0.32	0.32	0	57:	230	32:	050				
5.5	027	—	9235	9234	1	—	14	13	1	100:	027						
5.5	((140))	9272	9251	9248	3	0.29	0.32	0.31	0.01	64:	140	20:	230	14:	050		
5.5	((321))	—	9496	9494	2	—	17	17	0	57:	(321)	32:	035				
5.5	(043)	9614	9630	9629	1	2.30	1.5	1.4	0.1	38:	(223)	29:	043	27:	133		
5.5	(223)	9686	9690	9688	2	<5.00	5.6	5.5	0.1	52:	(223)	25:	043	13:	035		
5.5	((051))	9757	9764	9762	2	0.83	0.66	0.64	0.02	26:	051	24:	231	22:	141	22:	043
5.5	((133))	9819	9807	9805	2	<3.00	1.9	1.8	0.1	45:	133	21:	043	21:	051	11:	(223)
5.5	(231)	9896	9893	9891	2	1.22	1.6	1.6	0	56:	231	29:	051				
5.5	((141))	10065	10046	10044	2	6.00	3.9	3.9	0	46:	141	21:	420	21:	231		

^a Polyad quantum number.

^b Assignment according to Ref. 7. The more parentheses the assignment has, the more complicated the shape and the more difficult the assignment; see Ref. 7 for details.

^c According to Ref. 6 and as given in Ref. 7.

^d This work with the PES from Refs. 21,22.

^e Difference between the theoretical results from Ref. 7 and ours.

^f Each entry: First part is contribution in percent, second part is zero-order state assignment; taken from Ref. 7.

 TABLE III. Comparison of computed relative resonance energies ΔE and widths Γ from this work with the PES from Refs. 21,22 (WKS) and the PES from Ref. 46 (SAG), together with the experimental (Exp.) results from Refs. 6,7.

P. ^a	Label ^b	$\Delta E/\text{cm}^{-1}$					Γ/cm^{-1}				
		Expt. ^c	DP:WKS ^d	DP:SAG ^e	Δ_{WKS}^f	Δ_{SAG}^g	Expt. ^c	DP:WKS ^d	DP:SAG ^e	Δ_{WKS}^f	Δ_{SAG}^g
5	((042))	8821	8830	8849	-9	-28	<2.00	1.1	0.77	<0.90	<1.2
5	((222))	8902	8895	8925	7	-23	1.06	1.2	0.53	-0.2	0.5
5	(050)	8942	8950	8957	-8	-15	1.79	0.13	1.2	1.7	0.59
5.5	(231)	9896	9891	9928	5	-32	1.22	1.6	0.36	-0.38	0.86
5.5	((141))	10065	10044	10098	21	-33	6.00	3.9	0.85	2.1	5.2

^a Polyad quantum number.

^b According to Ref. 7.

^c According to Ref. 6.

^d This work with the PES from Refs. 21,22.

^e This work with the PES from Ref. 46.

^f Difference between Exp. and WKS results.

^g Difference between Exp. and SAG results.

where \hat{j}^2 is the angular momentum operator in θ and $V(R, r, \theta)$ is the WKS potential. μ_r is the reduced mass of CO. A similar but one-dimensional Hamiltonian, averaged over θ , was considered for HCO in Ref. 21. For DCO, the agreement found with this angle-averaged potential is less satisfactory.

Selected adiabatic potential energy curves are shown in Fig. 4. For $R < 4 a_0$, there are many avoided crossings and as such strong couplings between states that have a different v_2 number. For example, the curve for $v_2 = 3, v_3 = 0$ shows a coupling with $v_2 = 0, v_3 = 5$ and, at small R , even with $v_2 = 0, v_3 = 4$. These curves can be used to qualitatively understand the mixing of the zero-order states: State (0,5,1) has contributions of (2,3,1),

(1,4,1) and (0,4,3) (see Table II). The avoided crossing at $R \approx 3.3 a_0$ for $v_2 = 5, v_3 = 1$ and $v_2 = 4, v_3 = 3$ explains the mixing of states (0,5,1) and (0,4,3). Although the curve also overlaps with $v_2 = 3, v_3 = 5$, the mixing is less significant because the difference in the character of the two states is larger such that the coupling is reduced. Due to the excitation in v_1 , states (2,3,1) and (1,4,1) mix with (0,5,1) as well.

It would strongly simplify the analysis of the decomposition of the states if the adiabatic states $|\chi_n(r, \theta; R)\rangle$ were (quasi-)diabatized such that the character of the states does not change for all considered values of R . A projection of the resonance states onto the diabatic states would give a quantitative decomposition in terms

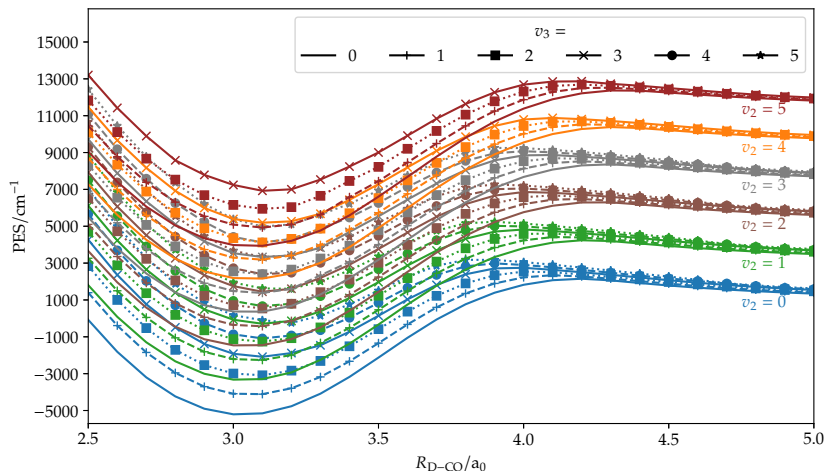


FIG. 4. Adiabatic potential energy curves for the CO vibrational problem as a function of D–CO distance R in Jacobi coordinates; see Eq. (9). The adiabatic curves are assigned DC=O stretch v_2 and D–C=O rotation v_3 quantum numbers according to the character of the eigenstates. Note the occurrence of many avoided crossings where the character of the adiabatic states is ambiguous. Further, note that only a selection of curves ($v_2 \leq 5$ and $v_3 \leq 5$) is depicted, i.e., there are many more curves in this energy region. For $v_2 \geq 4$, only curves for $v_3 \leq 3$ are shown and they should be regarded as qualitative in the interaction region.

of quantum numbers v_2 and v_3 . However, we were not able to obtain useful diabatic states that have a conserved nodal pattern for all values of R ; see Section iii in the supplementary material for more details.

E. Product distributions

The experimental and convoluted theoretical KER spectra for resonances (2,2,2), (0,5,0), (2,3,1) and (1,4,1) are shown in Fig. 5. All theoretical KER spectra without convolution are shown in the supplementary information (Figures iv – xv). The agreement between the theoretical and the experimental spectra is good. For (0,5,0) the spectrum from the SAG surface agrees better with experiment. Whereas the spectrum from the WKS surface shows a bimodal distribution, both experimental and SAG spectra show a monomodal rotational distribution for $v = 0$. This is in accord with the better agreement of the resonance width. For the WKS surface, the width is too small; compare with Table III. However, for the other three resonances, the WKS surface shows better agreement with the experiment, both in terms of peak positions and intensities. Compared to the experimental results, some, but not all, peaks exhibit a minor shift. This cannot be explained simply by a different asymptotic dissociation energy because there is no consistent trend. Instead, the shifts probably arise because the KER spectra are very sensitive to the shape of the PES, in particular near the transition region.

To allow for a easier comparison of the theoretical

results, we have converted the energetically resolved spectra to distributions resolved rovibrationally by the asymptotic CO fragment (see Section III C). Two of the distributions (for resonances (2,3,1) and (0,5,0)) are shown in Fig. 6 (black/darker bars). The rest of the distributions is shown in the supplementary material (Figures xvi – xxv). Except for (0,2,7), all computed resonances have major contributions for $v = 1$ (compared to $v = 0$) and negligible contributions for $v = 2$. As in HCO,^{21,33} the distributions typically are multimodal. Especially the resonances with large initial quantum numbers in v_2 and v_3 show a complicated multimodal pattern for a CO stretch quantum number of $v = 0$. The multimodal pattern is in agreement with semiclassical estimates used for H₂O and HCO.^{21,31,83}

To evaluate the changes of these distributions during the decay, we projected the part of the initial ($t = 0$) resonance that lies in the dissociation region (we chose $R \geq 5 a_0$) onto the asymptotic rovibrational states; see Eq. (4). Characteristic examples of such distribution changes are shown as gray/brighter bars in Fig. 6. The relative amount of the initial wavepacket that lies in this asymptotic region ranges from 7% (resonance (0,5,0)) to 33% (resonance (3,2,1)). For most resonances, this ratio lies between 13% and 20%. In most cases, the qualitative features of these asymptotic distributions do not change during the dynamics, hence the projection at $t = 0$ provides a very reasonable estimate of the rovibrational product distribution, even though the major part (typically more than 80%) of the initial wavepacket resides in the interaction region. Some resonances exhibit

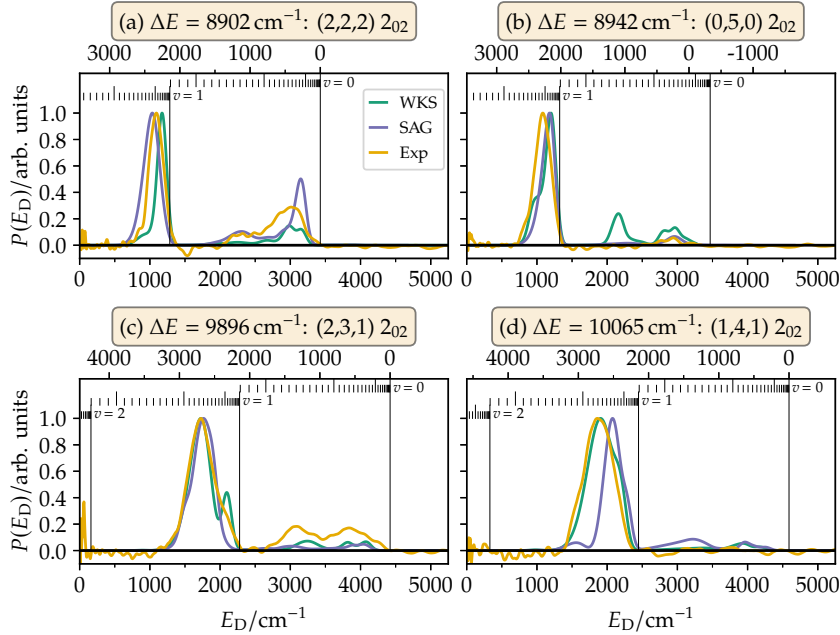


FIG. 5. Experimental (Exp) and convoluted theoretical (WKS and SAG) total kinetic energy release spectra $P(E_D)$ and corresponding CO rovibrational product state distributions for the experimentally investigated DCO (\tilde{X}) resonance states. WKS^{21,22} and SAG⁴⁶ stands for the two employed PES. The vertical lines indicate the maximal available energies E_{av1} for formation of CO in $v = 0, 1$ and 2 and the energies of the CO product rotational (j) states. The CO rovibrational energies corresponding to the vertical lines are obtained from computations with the WKS PES. The theoretical curves are convoluted with a Gaussian, $\exp[-(E/\sigma)^2/2]$, with an arbitrarily chosen width of $\sigma = 60 \text{ cm}^{-1}$.

a shift to higher (lower) j values for $v = 0$ ($v = 1$).

Only for those resonances that have a small decay width ((0,5,0), (1,3,2), (2,3,0) and (1,4,0); (2,3,1) on the SAG surface), we see larger deviations, see, e.g., resonance (0,5,0) in Fig. 6. A small decay width means a large decay time and as such more time for interference processes etc. which lead to these more significant asymptotic pattern changes. This follows from an investigation of the non-adiabatic coupling elements of the adiabatic, R -dependent rovibrational states (see Section IV D). It shows that the different states couple with each other even for $R > 4.5 a_0$, especially those with the same quantum number v_2 ; compare with Fig. 4 and Section iii in the supplementary material. Further, the stated resonances are those where less than 10% of the initial wavepacket lies in the interaction region (naturally, a small decay width causes a smaller fraction of that resonance in the asymptotic region).

F. Decay processes

We now analyze and discuss mechanisms of resonance decay, i.e., the occurrence of IVR during the decay. Using a polyad model Hamiltonian, the Temps group has already done an IVR analysis.^{8,38} During dissociation,

the bending motion (quantum number v_3) turns into rotational motion of the CO fragment (quantum number j). Semiclassically, four quanta need to be transferred to the D–C stretch degree of freedom. The C–O stretch quantum number v_2 remains (approximately) conserved and turns into v .

Here, we consider the *ab initio* Hamiltonian, where an in-depth and quantitative analysis is not possible. As already mentioned in Section I, the assignment in terms of zero-order eigenstates and their vibrational quantum numbers is problematic. This was already visible in Table II above, and it becomes even more obvious when analyzing the time-dependent wavefunctions further: Already counting the number of nodes (by plotting $\Re(\Psi)$) or counting the number of pronounced lobes (by plotting $|\Psi|^2$) can lead to different assignments because the intensities of the lobes vary significantly. In this sense, any assignment should be regarded as approximate, and the IVR mechanism should be regarded as qualitative.

In the following, the assignment is performed based on counting the number of lobes. Qualitatively, we reproduced the assignment from Ref. 7 (see Table II). The assignment was done based on cuts of Jacobi coordinates that have been shifted and rotated such that the first excited adiabatic state retained its orientation for different cut values (see also Section IV D). Further, we

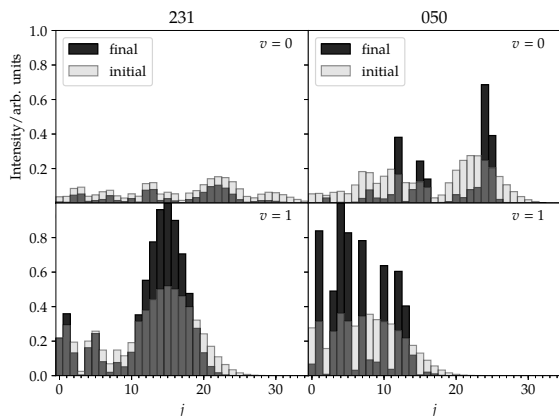


FIG. 6. Asymptotic distributions resolved by CO vibration-rotation quantum numbers, for resonances (2,3,1) (left) and (0,5,0) (right) using the WKS PES.^{21,22} The upper (lower) panels show the distributions for stretch quantum number $v = 0$ ($v = 1$) versus different rotational quantum numbers j of the asymptotic CO fragment (bend quantum numbers for the undissociated state). The distributions are scaled such that the maximal value is 1. The darker bars show the distributions for the final wavepacket, $|\Psi(t \rightarrow \infty)\rangle$, the brighter bars for the initial wavepacket, $|\Psi(t = 0)\rangle$, both in the asymptotic region.

plotted cuts in Eckart bond coordinates, i.e., coordinates $\{X, Y, \phi\}$, where X (Y) is the C–D (C–O) distance and ϕ the angle \sphericalangle (DCO) between the corresponding vectors \vec{X} and \vec{Y} . Here, we solely show cuts of the wavefunction in Eckart coordinates, since they provide clearer nodal patterns in the decisive interaction region. Throughout, all cuts are performed along coordinate values that show significant contributions to the wavefunction.

Note that we analyze the wavefunction in the interaction region, that is, we analyzed that part of the wavefunction that remains bounded during the studied propagation times. Hence, the following analysis is not directly comparable with the rovibrational product state distributions shown in Section IV E. The direct conversion of the bound to the unbound part in the continuum is hard to analyze since it happens over a wide coordinate range and over long propagation times and since the initial wavefunctions already extends into the dissociation region. Indeed, already the initial wavefunctions qualitatively contains all required components in the asymptotic region (see Section IV E), although these asymptotic parts typically contribute only 13–20% to the total resonance wavefunction.

1. Polyad 5

Cuts of the decay of the (0,3,4) resonance in the plane of C–O stretching (D–C stretching) and D–C–O bend-

ing are shown in Eckart bond coordinates in Fig. 7 (Fig. 8). The upper left panel of Fig. 7 shows a part of the initial resonance that can be assigned as $v_1 = 3$ and $v_3 = 4$ (there are four lobes in the C–O distance Y and five lobes in the bending angle ϕ). Here, the assignment is already ambiguous, because there is no contiguous nodal pattern. However, an inspection of different cuts and in different coordinates (see Section IV F) verifies the assignment. The upper left panel of Fig. 8 shows a part of the initial resonance that can clearly be assigned as $v_0 = 0$ and $v_3 = 4$. Note that the other zero-order components are typically visible in different coordinate ranges such that there are regions where the different components do not significantly overlap.

A distinctive change in the vibrational structure happens only after the norm of the wavefunction has decreased to 0.15 or less. This is also the case for the other resonances studied. Before IVR takes place, there are oscillations between the different zero-order components of the wavefunction, that is, the intensities of the lobes change. This can be seen in the plots shown in the upper two panels of Fig. 7, although the oscillations are typically less intensive.

At propagation times when the norm is below 0.15, a decrease of the bending quantum number v_3 from 4 to 2 happens; see Fig. 7 and 8. Neither an increase in v_1 nor a change in v_2 is visible in the interaction region. This is valid also for other cuts of the wavefunction where other zero-order states show contributions. For the zero-order 411 contribution to the 034 resonance, there is an additional decrease of v_1 to 2. The oscillations of the different zero-order states, the approximate conversion of quantum number v_2 and the decay of v_3 are all in agreement with the analysis done by a polyadic model Hamiltonian.^{8,38} Note that we analyze here what remains in the interaction region. A loss in a quantum number means that the corresponding energy is moved from the interaction region to the continuum.

For the resonances (0,4,2), (2,2,2), (0,5,0), (1,3,2), (2,3,0), (1,4,0) (polyad 5) and (0,4,3) (polyad 5.5), only minor oscillations of the lobes occur.⁸⁴ No IVR is visible and the oscillations are much less pronounced than that shown in the upper panels of Fig. 7 for (0,3,4). To some extent, this can be explained by the small decay rate of the resonances. Except for (0,4,3) (polyad 5.5), they all have a decay width of $\Gamma \leq 0.32 \text{ cm}^{-1}$. In polyad 5.5, resonance (0,4,3) has the second smallest value of Γ . A small reaction rate is correlated with a hindered IVR.³⁸ However, resonance (0,5,1), the resonance with the smallest value of Γ (0.64 cm^{-1}) in polyad 5.5, does show a decay mechanism (see Section IV F 2) but also lies higher in energy and has an evenly spread-out distribution of four zero-order components such that the coupling to other states may be larger; see also below.

To show how insignificant the temporal change in wavefunction structure can be, consider the cut of the (0,5,0) resonance shown in Fig. 9. Even after propagating for 175 ps and after decay of the norm to a value of

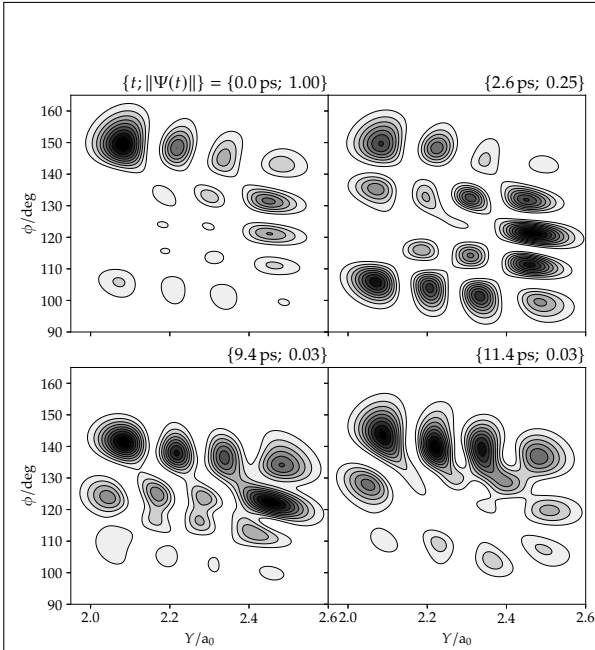


FIG. 7. Contour values of $|\Psi(X, Y, \phi; t)|^2$ at $X = 2.2 a_0$ and different times, for the $(0,3,4)$ resonance. X is the D–C distance, Y the C≡O distance and ϕ the D–C=O bending angle in Eckart bond coordinates. For each panel, the shown function is normalized to have the maximal value of 1. For a comparison of the relative intensity, see the norm values in the panel captions.

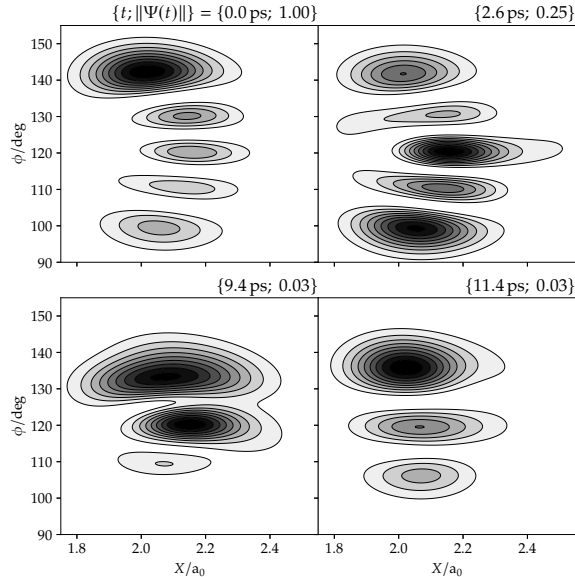


FIG. 8. Same as Fig. 7 but showing cuts of $|\Psi(X, Y, \phi; t)|^2$ at $Y = 2.53 a_0$. X is the D–C distance, Y the C≡O distance and ϕ the D–C=O bending angle in Eckart bond coordinates.

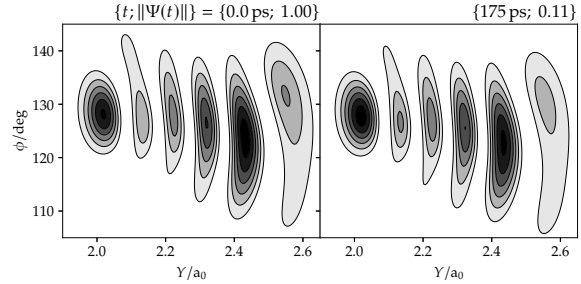


FIG. 9. Same as Fig. 7 but showing cuts of $|\Psi(X, Y, \phi; t)|^2$ at $X = 2.15 a_0$ for the $(0,5,0)$ resonance.

0.11, the structure does not change. For checking our results, we have propagated the $(0,5,0)$ state using smaller coordinate ranges and a higher propagator accuracy with a standard DVR code (without DP) until 300 ps, where the norm has dropped down to a value of 0.02. Even then, no significant change in the structure of the wavefunction is visible. Additionally, our DP-DVR results are confirmed by this conventional DVR run.

For a polyadic model Hamiltonian, Temps *et al.* studied the decay of a *pure* $(0,5,0)$ state.³⁸ The state turned, among others, into $(1,4,0)$ and $(2,3,0)$ within less than 0.5 ps. Here, already the *initial* resonance state consists of these components (not seen in the cuts shown in Fig. 9); see Table II. Hence, the *initial* state already has all main zero-order components needed for the IVR to happen. This explains the small oscillations in the nodal pattern.

This further means that the zero-order states included in the initial resonance states are strongly coupled whereas they couple weakly to other states. The strong coupling of the states within one polyad is stressed in Ref. 6. Indeed, resonances $(0,4,2)$, $(2,2,2)$ and $(1,3,2)$ consist of the corresponding zero-order states and so do resonances $(0,5,0)$, $(1,4,0)$ and $(2,3,0)$; see Table II. In contrast, resonance $(0,3,4)$ shows an IVR. However, its decay rate is much larger and the resonance has components of $(2,2,2)$ but also of the different zero-order states $(4,1,1)$ and $(1,2,4)$. The strong coupling between states $\{(0,4,2), (2,2,2), (1,3,2)\}$ and $\{(0,5,0), (1,5,0), (2,3,0)\}$ is in agreement with the parameters from the polyadic model Hamiltonian.⁸

Considering the insignificant changes of the wavefunction within the interaction region, it may seem counter-intuitive that for a subset of these states the asymptotic rovibrational distributions of the CO fragment do change significantly in time. However, as pointed out in Section IV E, the rovibrational states still couple outside the typical interaction region where $R < 4.5 a_0$, such that the dynamics in the asymptote and in the interaction regions are, to first order, not directly related. In fact, from Fig. 4, it may be argued that the distribution of the adiabatic states on the energy axis, and thus also their couplings, strongly change between $R < 4.0 a_0$ and

$R > 4.0 a_0$, supporting different dynamical behaviors.

As a side remark: On the SAG surface, resonance (0,5,0) does show an IVR with an increase in v_3 to 1 (with intermediate numbers up to $v_3 = 3$) and a decrease in v_2 up to $v_2 = 2$. However, the character of this resonance state also differs from the state computed on the WKS surface. Most importantly, the initial state already has some contributions of $v_3 = 1$ which the state on the WKS surface does not have (see Table II). Note that, in this case, Γ is larger and, like the KER, closer to the experimental value on the SAG surface. Resonances with excitations in both v_2 and v_3 exhibit larger decay rates than those with excitations only in v_3 .⁷

2. Polyad 5.5

In polyad 5.5, resonance (0,2,7) decays rapidly with a decrease in v_2 . However, it has a strong contribution at the linear geometry. Due to the neglect of Renner-Teller coupling in this simulation and since resonances with high bending motion are experimentally hard to measure, we have not analyzed this state further in the present study.

As already mentioned in Section IV F 1, resonance (0,4,3) shows only minor oscillations between the zero-order components of the initial state. Resonance (2,2,3) shows a decrease in v_3 from 3 to $\{1, 0\}$ (both 1 and 0) and an increase in v_2 from 4 to 5. However, due to a component of $v_3 = 5$, it shows also contributions at linear geometry and the results have to be taken with caution. As for the previous resonances where a clear IVR takes place, (0,5,1) shows a decrease in v_3 whereas v_2 remains mostly conserved. Likewise, 133 decays to $v_3 = \{2, 1\}$ and the zero-order (0,5,1) state initially contributing by $\sim 21\%$ (Table II) gets more populated.

A decrease in v_3 to 0 while the other quantum numbers are approximately conserved is clearly seen also in state (2,3,1), see Fig. 10 and Fig. 11. Both cuts in Y and X show a decrease in v_3 whereas the $v_2 = 3$ and $v_1 = 2$ components are constant. At 26 ps, the cut shown in Y (right panel in Fig. 11) is more difficult to analyze because contributions from other zero-order states become more visible.

The corresponding state on the SAG surface shows no significant IVR. There, the state has similar zero-order components except for a reduced $v_1 = 2$ component. This decreases the decay width which is smaller, compared to experiment; see Table III). The hindered IVR due to the smaller decay width ($\Gamma = 0.36 \text{ cm}^{-1}$) is in agreement with the discussion in Section IV F 1.

As (2,3,1), state (1,4,1) decays in v_3 . Here, the $v_2 = 5$ component (see Table II) becomes more pronounced. The contribution of the (4,2,0) zero-order state shows a decay from $v_1 = 4$ to $v_1 = 1$, see Fig. 12. There, the wavefunction looks like it has increased in v_3 but an inspection of the phase cannot clearly confirm this.

State (1,4,1) computed on the SAG surface shows a

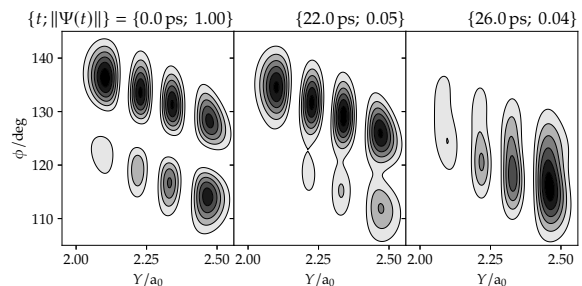


FIG. 10. Same as Fig. 7 but showing cuts of $|\Psi(X, Y, \phi; t)|^2$ at $X = 1.85 a_0$ for the (2,3,1) resonance.

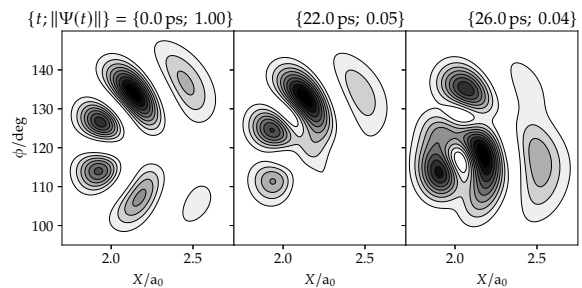


FIG. 11. Same as Fig. 7 but showing cuts of $|\Psi(X, Y, \phi; t)|^2$ at $Y = 2.5 a_0$ for the (2,3,1) resonance.

similar initial state (with a reduced component of the (2,3,1) state) and a similar decay mechanism. There, Γ is lower (0.85 cm^{-1} compared to the experimental value of 6 cm^{-1} ; see Table III), but not too low for IVR, compared to the resonances that show no pronounced IVR.

A sequential decay from $v_1 = 3$ via $v_1 = 2$ to $v_1 = \{1, 0\}$ in conjunction with a decay of $v_3 = 1$ to $v_3 = 0$ can be observed for resonance (3,2,1). Again, v_2 remains conserved. Note that this resonance in polyad 5.5 has the highest D–C stretch excitation. Due to the large decay width of $\Gamma = 17 \text{ cm}^{-1}$, the IVR begins quickly and there are intermediate states with contributions from

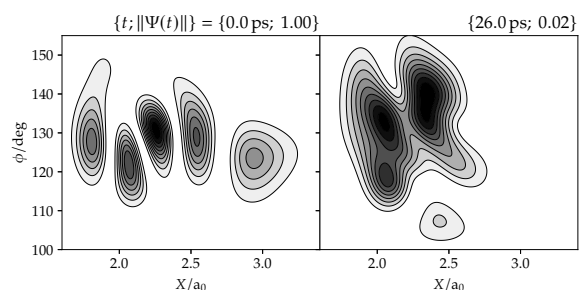


FIG. 12. Same as Fig. 7 but showing cuts of $|\Psi(X, Y, \phi; t)|^2$ at $Y = 2.09 a_0$ for the (1,4,1) resonance.

many zero-order states that are hard to analyze. Note that this state has some contributions of $v_3 = 5$ and, due to this high excitation in the bending mode, contributions at linear geometries. However, they are less pronounced than for the other states with similar contributions.

While a decrease in bending quantum number v_3 can be seen in all resonances where a clear IVR occurs, a decrease in D–C stretch quantum number v_1 can only be seen for $v_1 > 2$, namely in states (3,2,1), (1,4,1) and (0,3,4) where the latter two have zero-order states with $v_1 = 4$.

V. CONCLUSIONS

To summarize, we have employed our newly developed dynamically pruned DVR (DP-DVR) for computing resonance states in DCO of polyads 5 and 5.5 using filter diagonalization and for subsequential propagation to analyze their decay mechanisms. For selected resonances, the kinetic energy release (KER) spectra were compared to experimental results obtained from velocity-map images.

For this challenging test case where the wavefunction has to be propagated in the asymptotic region for up to 180 picoseconds, DP-DVR works well and the computed resonance energies and widths show good agreement with results from the literature. The computed KER spectra are in good agreement with the experimental spectra. Two PES have been compared. For many states, the WKS surface²¹ gives slightly better results than the SAG surface.⁴⁶ Since no PES was constructed with this particular application in mind (decay dynamics of energetically high-lying resonances far out into the asymptote), no quantitative agreement between theoretical and experimental results can be expected. Also, the importance of including $J > 0$ and Renner-Teller couplings to higher electronic states at linear geometries still has to be elucidated.

The rovibrational distribution of the asymptotic CO states shows major contributions only for C≡O stretch quantum numbers $v = 0$ and 1. The distribution in the CO rotational quantum number j is multimodal. For states with larger decay widths of $\Gamma > 0.6 \text{ cm}^{-1}$, the initial state already shows the qualitatively correct shape of the distributions. Due to a coupling of the rovibrational states even in the near-asymptotic region, states with smaller decay rates show qualitatively different distributions after long propagation times.

Analyses of the decay processes confirm the results from a polyad model Hamiltonian.⁸ For the studied resonance states, the v_2 quantum number typically is a conserved quantity while the wavefunction part in the interaction region shows a decrease in quantum number v_3 . For high D–CO stretch excitations with corresponding quantum number $v_2 > 2$, a decay in this quantum number is possible as well. In contrast to the polyad model, all resonances show significant mixing of zero-

order states.

Some resonances, in particular in polyad 5, show very strong coupling with each other. Almost all zero-order components needed for an IVR are already contained in the initial state and, for these states, no appearance or disappearance of additional zero-order components can be observed.

The qualitative agreements between a polyad model and full quantum dynamics confirm that there are analyzable residues of orderly IVR mechanisms present in the strongly anharmonic DCO system. However, not surprisingly, our full quantum dynamics also indicate where and how a mechanistic understanding has to transcend a zero-order model picture.

SUPPLEMENTARY MATERIAL

See supplementary material for plots of the PES, the propagation times, details on the diabaticization and the asymptotic distributions of all resonances.

ACKNOWLEDGMENTS

We thank R. Schinke, L. Song, A. van der Avoird and G. C. Groeneboom for providing us with their PES. H. R. L. thanks R. Welsch for helpful discussions. H. R. L. acknowledges support by the Studienstiftung des deutschen Volkes. J. R., J. W. and F. T. gratefully acknowledge the financial support of the experimental part of this work by the Deutsche Forschungsgemeinschaft. J. R. is indebted to F. Renth for discussions regarding the analysis of the photofragment images. J. W. thanks the Alexander von Humboldt-Stiftung for a research fellowship.

¹P. J. Robinson and K. A. Holbrook, *Unimolecular Reactions* (Wiley, 1972).

²T. Baer and W. L. Hase, *Unimolecular Reaction Dynamics* (Oxford University Press, 1996).

³R. Schinke, *Photodissociation Dynamics* (Cambridge University Press, 1995).

⁴M. Stumpf, A. J. Dobbyn, D. H. Mordaunt, H.-M. Keller, H. Fluethmann, R. Schinke, H.-J. Werner, and K. Yamashita, *Faraday Discuss.* **102**, 193 (1995).

⁵A. J. Ocaña, E. Jiménez, B. Ballesteros, A. Canosa, M. Antiñolo, J. Albaladejo, M. Agúndez, J. Cernicharo, A. Zanchet, P. del Mazo, O. Roncero, and A. Aguado, *Astrophys. J.* **850**, 28 (2017).

⁶C. Stöck, X. Li, H.-M. Keller, R. Schinke, and F. Temps, *J. Chem. Phys.* **106**, 5333 (1997).

⁷H.-M. Keller, M. Stumpf, T. Schröder, C. Stöck, F. Temps, R. Schinke, H.-J. Werner, C. Bauer, and P. Rosmus, *J. Chem. Phys.* **106**, 5359 (1997).

⁸A. Troelsch and F. Temps, *Z. Phys. Chem.* **215**, 207 (2001).

⁹C. Jung, H. S. Taylor, and E. Atilgan, *J. Phys. Chem. A* **106**, 3092 (2002).

¹⁰H.-R. Dübal and M. Quack, *Mol. Phys.* **53**, 257 (1984).

¹¹A. Amrein, H.-R. Dübal, and M. Quack, *Mol. Phys.* **56**, 727 (1985).

¹²M. E. Kellman and V. Tyng, *Acc. Chem. Res.* **40**, 243 (2007).

¹³G. Adamson, X. Zhao, and R. Field, *J. Mol. Spectrosc.* **160**, 11 (1993).

- ¹⁴D. W. Neyer, X. Luo, P. L. Houston, and I. Burak, *J. Chem. Phys.* **98**, 5095 (1993).
- ¹⁵J. D. Tobiasson, J. R. Dunlop, and E. A. Rohlfing, *J. Chem. Phys.* **103**, 1448 (1995).
- ¹⁶J. D. Tobiasson, J. R. Dunlop, and E. A. Rohlfing, *Chem. Phys. Lett.* **235**, 268 (1995).
- ¹⁷J. Wei, A. Tröllsch, C. Tesch, and F. Temps, *J. Chem. Phys.* **120**, 10530 (2004).
- ¹⁸D. W. Neyer, X. Luo, I. Burak, and P. L. Houston, *J. Chem. Phys.* **102**, 1645 (1995).
- ¹⁹J. M. Bowman, J. S. Bittman, and L. B. Harding, *J. Chem. Phys.* **85**, 911 (1986).
- ²⁰H. Romanowski, K.-T. Lee, J. M. Bowman, and L. B. Harding, *J. Chem. Phys.* **84**, 4888 (1986).
- ²¹H.-J. Werner, C. Bauer, P. Rosmus, H.-M. Keller, M. Stumpf, and R. Schinke, *J. Chem. Phys.* **102**, 3593 (1995).
- ²²H.-M. Keller, H. Floethmann, A. J. Dobbyn, R. Schinke, H.-J. Werner, C. Bauer, and P. Rosmus, *J. Chem. Phys.* **105**, 4983 (1996).
- ²³H.-M. Keller and R. Schinke, *J. Chem. Phys.* **110**, 9887 (1999).
- ²⁴B. Poirier and T. Carrington, *J. Chem. Phys.* **116**, 1215 (2002).
- ²⁵V. A. Mandelshtam and A. Neumaier, *J. Theor. Comput. Chem.* **1**, 1 (2002).
- ²⁶J. C. Tremblay and T. Carrington, *J. Chem. Phys.* **122**, 244107 (2005).
- ²⁷S. A. Ndengué, R. Dawes, F. Gatti, and H.-D. Meyer, *J. Phys. Chem. A* **119**, 12043 (2015).
- ²⁸S. A. Ndengué, R. Dawes, and H. Guo, *J. Chem. Phys.* **144**, 244301 (2016).
- ²⁹J. Qi and J. M. Bowman, *J. Chem. Phys.* **105**, 9884 (1996).
- ³⁰C.-Y. Yang and S. K. Gray, *J. Chem. Phys.* **107**, 7773 (1997).
- ³¹H.-M. Keller and R. Schinke, *J. Chem. Soc., Faraday Trans.* **93**, 879 (1997).
- ³²U. Brandt-Pollmann, J. Weiß, and R. Schinke, *J. Chem. Phys.* **115**, 8876 (2001).
- ³³R. N. Dixon, *J. Chem. Soc. Faraday Trans.* **88**, 2575 (1992).
- ³⁴S. K. Gray, *J. Chem. Phys.* **96**, 6543 (1992).
- ³⁵D. Wang and J. M. Bowman, *Chem. Phys. Lett.* **235**, 277 (1995).
- ³⁶A. Loettgers and R. Schinke, *J. Chem. Phys.* **106**, 8938 (1997).
- ³⁷S. Stamatiadis, S. C. Farantos, H.-M. Keller, and R. Schinke, *Chem. Phys. Lett.* **344**, 565 (2001).
- ³⁸F. Renth, F. Temps, and A. Tröllsch, *J. Chem. Phys.* **118**, 659 (2003).
- ³⁹C. Jung, H. S. Taylor, and E. Atilgan, *J. Phys. Chem. A* **106**, 3092 (2002).
- ⁴⁰J. Huang and G. Wu, *Chem. Phys. Lett.* **439**, 231 (2007).
- ⁴¹A. Semparathi and S. Keshavamurthy, *Phys. Chem. Chem. Phys.* **5**, 5051 (2003).
- ⁴²A. T. J. B. Eppink and D. H. Parker, *Rev. Sci. Instrum.* **68**, 3477 (1997).
- ⁴³B. Hartke, *Phys. Chem. Chem. Phys.* **8**, 3627 (2006).
- ⁴⁴H. R. Larsson, B. Hartke, and D. J. Tannor, *J. Chem. Phys.* **145**, 204108 (2016).
- ⁴⁵D. J. Tannor, S. Machnes, E. Assémat, and H. R. Larsson, "Phase space vs. coordinate space methods: Prognosis for large quantum calculations," in *Advances in Chemical Physics*, Vol. 163 (John Wiley & Sons, Inc., 2018) p. in press.
- ⁴⁶L. Song, A. van der Avoird, and G. C. Groenenboom, *J. Phys. Chem. A* **117**, 7571 (2013).
- ⁴⁷D. J. Tannor, *Introduction to Quantum Mechanics: A Time-Dependent Perspective*, 1st ed. (University Science Books, 2007).
- ⁴⁸S. Machnes, E. Assémat, and D. Tannor, "Quantum dynamics in phase space using the biorthogonal von neumann bases: Algorithmic considerations," (2016), arXiv:1603.03963.
- ⁴⁹A. Shimshovitz and D. J. Tannor, *Phys. Rev. Lett.* **109**, 070402 (2012).
- ⁵⁰S. Machnes, E. Assémat, H. R. Larsson, and D. J. Tannor, *J. Phys. Chem. A* **120**, 3296 (2016).
- ⁵¹H. R. Larsson and D. J. Tannor, *J. Chem. Phys.* **147**, 044103 (2017).
- ⁵²G. A. Worth, *J. Chem. Phys.* **112**, 8322 (2000).
- ⁵³R. Wodraszka and T. Carrington, *J. Chem. Phys.* **145**, 044110 (2016).
- ⁵⁴R. Wodraszka and T. Carrington, *J. Chem. Phys.* **146**, 194105 (2017).
- ⁵⁵U. Manthe, *J. Chem. Phys.* **105**, 6989 (1996).
- ⁵⁶R. Wodraszka and T. Carrington, *J. Chem. Phys.* **148**, 044115 (2018).
- ⁵⁷J. Wei, A. Kuczmann, J. Riedel, and F. Temps, *Phys. Chem. Chem. Phys.* **5**, 315 (2003).
- ⁵⁸J. Riedel, S. Dziarzhyski, A. Kuczmann, F. Renth, and F. Temps, *Chem. Phys. Lett.* **414**, 473 (2005).
- ⁵⁹J. Riedel, *Untersuchung photoinduzierter molekularer Zerfallsprozesse mittels Photofragment-Geschwindigkeitskartographie*, Ph.D. thesis, Christian-Albrechts-Universität zu Kiel (2006).
- ⁶⁰B.-Y. Chang, R. C. Hoetzlein, J. A. Mueller, J. D. Geiser, and P. L. Houston, *Rev. Sci. Instrum.* **69**, 1665 (1998).
- ⁶¹F. Le Quéré and C. Leforestier, *J. Chem. Phys.* **92**, 247 (1990).
- ⁶²D. T. Colbert and W. H. Miller, *J. Chem. Phys.* **96**, 1982 (1992).
- ⁶³I. Gohberg and V. Olshevsky, *Linear. Algebra. Appl.* **202**, 163 (1994).
- ⁶⁴X. Wang and J. M. Bowman, *Int. J. Quantum Chem.* **117**, 139 (2017).
- ⁶⁵S.-W. Huang and T. Carrington, *J. Chem. Phys.* **112**, 8765 (2000).
- ⁶⁶B. Poirier and T. Carrington, *J. Chem. Phys.* **114**, 9254 (2001).
- ⁶⁷D. Neuhauser, *J. Chem. Phys.* **93**, 2611 (1990).
- ⁶⁸D. Neuhauser, *J. Chem. Phys.* **95**, 4927 (1991).
- ⁶⁹K. Takatsuka and N. Hashimoto, *J. Chem. Phys.* **103**, 6057 (1995).
- ⁷⁰V. A. Mandelshtam and H. S. Taylor, *J. Chem. Phys.* **106**, 5085 (1997).
- ⁷¹G. G. Balint-Kurti, R. N. Dixon, and C. C. Marston, *J. Chem. Soc., Faraday Trans.* **86**, 1741 (1990).
- ⁷²P. F. Bernath, *Spectra of Atoms and Molecules*, 2nd ed. (Oxford University Press, 2005).
- ⁷³L. Song, N. Balakrishnan, A. van der Avoird, T. Karman, and G. C. Groenenboom, *J. Chem. Phys.* **142**, 204303 (2015).
- ⁷⁴F. Renth, J. Riedel, and F. Temps, *Rev. Sci. Instrum.* **77**, 033103 (2006).
- ⁷⁵D. E. Manolopoulos, *J. Chem. Phys.* **117**, 9552 (2002).
- ⁷⁶J. Meija, T. B. Copen, M. Berglund, W. A. Brand, P. De Bièvre, M. Gröning, N. E. Holden, J. Irgeher, R. D. Loss, T. Walczyk, and T. Prohaska, *Pure Appl. Chem.* **88**, 265 (2016).
- ⁷⁷M. Wang, G. Audi, F. G. Kondev, W. Huang, S. Naimi, and X. Xu, *Chin. Phys. C* **41**, 030003 (2017).
- ⁷⁸T. J. Park and J. C. Light, *J. Chem. Phys.* **85**, 5870 (1986).
- ⁷⁹M. H. Beck, A. Jäckle, G. A. Worth, and H.-D. Meyer, *Phys. Rep.* **324**, 1 (2000).
- ⁸⁰G. A. Worth, M. H. Beck, A. Jäckle, and H.-D. Meyer, The MCTDH Package, Version 8.4.14 (2017). See <http://mctdh.uni-hd.de>.
- ⁸¹To avoid unnecessary computational costs, not all the resonances have been propagated with the final parameters. Further, the propagation for the filter diagonalization has been performed with a larger basis but the results with the basis from Table I are virtually identical.
- ⁸²The PES of Ndengué *et al.* shows a better agreement to experimental data for many but not all resonances in HCO. Some energies and widths are actually still better described by the WKS surface. Thus, it cannot be expected that this PES would give much improved results than the two PES studied here.
- ⁸³R. Schinke, R. L. Vander Wal, J. L. Scott, and F. F. Crim, *J. Chem. Phys.* **94**, 283 (1991).
- ⁸⁴For (0,4,2), the resonance computed with the SAG PES does show an IVR with a decrease in v_3 to 2 and 1, but the initial state has a significant contribution near the linear configuration of DCO. Since linear configurations are not properly described (see text), this result has to be taken with caution.

II.1.1.4. Supplementary Information

Supplementary material for
**Resonance dynamics of DCO (\tilde{X}^2A') simulated with the
dynamically pruned discrete variable representation
(DP-DVR)**

Henrik R. Larsson Jens Riedel Jie Wei Friedrich Temps Bernd Hartke

Institut für Physikalische Chemie, Christian-Albrechts-Universität zu Kiel,
Olshausenstraße 40
24098 Kiel, Germany

Journal of Chemical Physics

Contents

i. Potential energy surfaces	2
ii. Propagation times	4
iii. Diabatization of rovibrational states	4
iv. Kinetic energy release spectra	6
v. Rovibrational CO product distributions	10

i. Potential energy surfaces

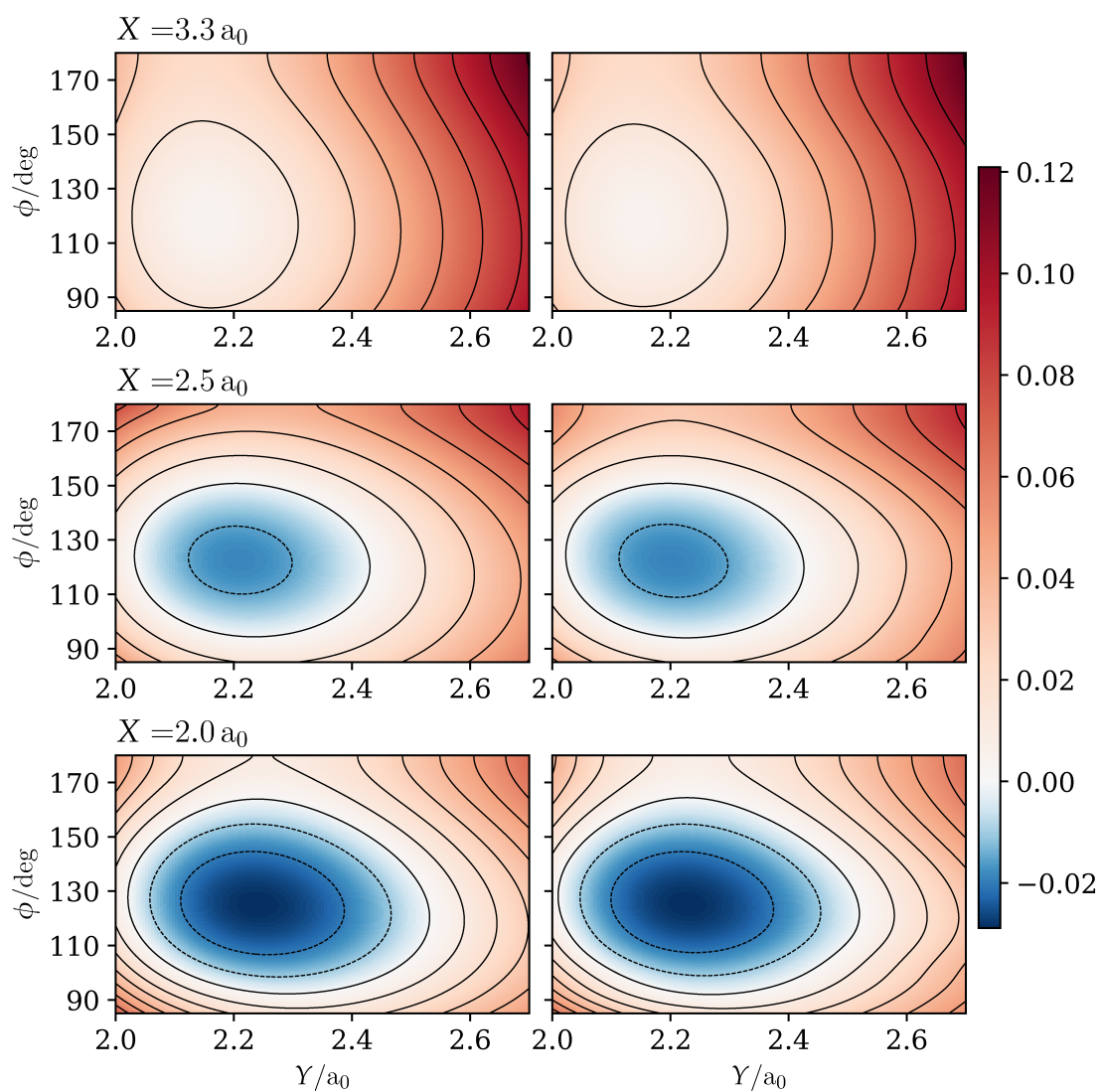


Figure i: Cuts through the WKS^{1,2} (left) and SAG³ (right) PES in Eckart bond coordinates. X is the D-CO distance, Y the DC=O distance and ϕ the D-C=O bending angle. The values of the potential are given in Hartree.

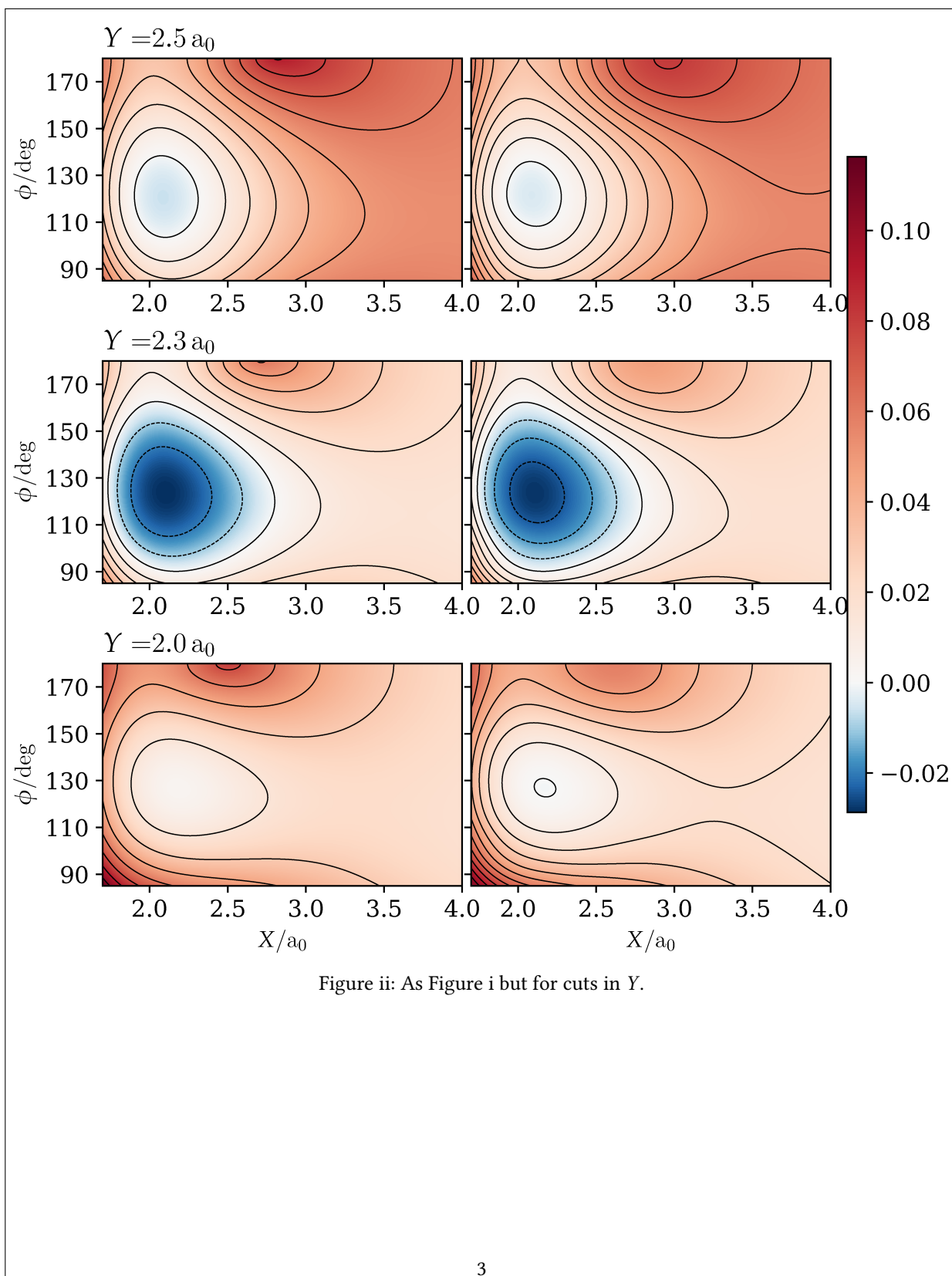


Figure ii: As Figure i but for cuts in Y .

ii. Propagation times

Table i: Final propagation time t_{end} and norm of the wavefunction at that time for the simulations.

label	WKS PES ^{1,2}		SAG PES ³	
	t_{end}/ps	norm	t_{end}/ps	norm
034	27	0.02		
042	27	0.06	80	0.02
222	24	0.07	53	0.07
050	175	0.1	80	0.005
132	89	0.1		
230	80	0.09		
027	22	0.03		
140	80	0.1		
043	27	0.03		
223	30	0.01		
051	60	0.04		
133	30	0.04		
231	28	0.03	75	0.08
141	27	0.02	30	0.1
321	30	0.01		

iii. Diabatization of rovibrational states

Although we tried many different diabaticization schemes,⁴⁻⁷ taking either the nonadiabatic coupling matrix elements explicitly into account or using other approaches solely based on the potential energy curves (diabatization by *ansatz*^{8,9} or minimizing the curvature of the diabatic curves), we were not able to obtain useful (quasi-)diabatic states that have proper nodal patterns. Besides requiring the diabaticization of *many* states (up to ~ 250 are required for $v_2 \leq 5$ and $v_3 \leq 8$), the Hamiltonian introduces an “artificial” nonadiabatic coupling between the states. The coupling is artificially increased by the R -dependent part of the kinetic energy operator in Eq. (9) of the paper and by non-trivial changes in the potential. For example, an inspection of Fig. 4 shows that the adiabatic ground state does not strongly couple to other states and, of course, it does not change its character in terms of number of nodes. In other words, the adiabatic ground state can already be considered as a proper diabatic state that would suffice for further analysis. However, the shape of the ground-state wavefunction for different values of R differs drastically, because the cut of the potential changes significantly. For large R , the wavefunction has a prolate shape. With decreasing R , the function becomes more confined and the coordinates of the maximum describes a complicated path. The change of the shape introduces the “artificial” coupling such that the obtained diabatic states have a very complicated nodal pattern and are useless for a further analysis. This is shown in Figure iii.

One way to circumvent this “artificial” coupling is to remove the part from the nonadiabatic coupling that is due to the change in shape/location of the eigenstates, such that only the coupling remains that accounts for the mixing of the nodal pattern. This is similar to the procedure suggested by Esry and Sadeghpour.¹⁰ It can be easily done for the R -dependent part of the kinetic energy operator. For the potential, this is much more difficult. We tried different R -dependent coordinate transforms trying to retain the shape of the ground state. This gave no satisfactory results for all R values because the changes in the potential are too complicated. Especially, an affine coordinate transformation does not suffice.

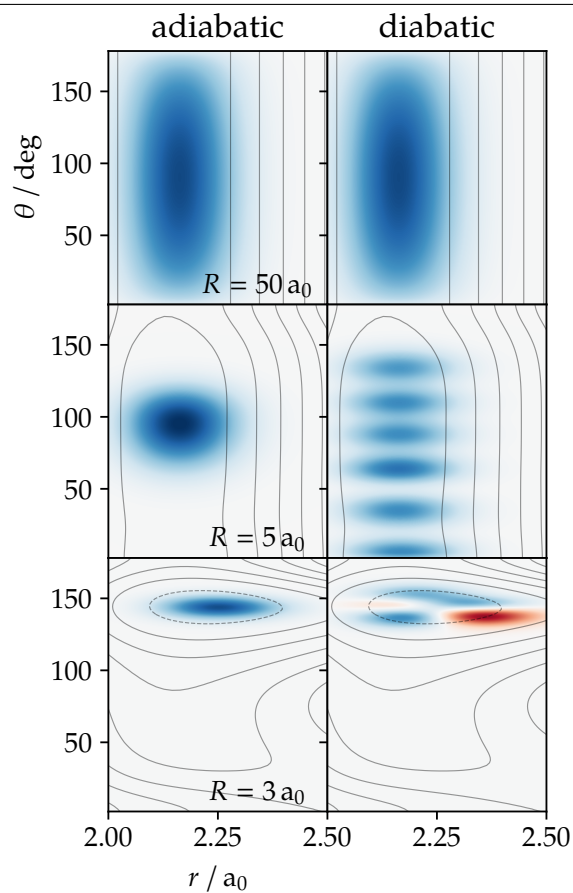


Figure iii: First adiabatic and diabatic state of the CO vibrational problem for different D–CO distances R in Jacobi coordinates; see Eq. (9) in the paper. Red color shows lobes of the wavefunction with a different sign. The contours denote the potential. Dashed contours correspond to negative values. The diabaticization is done by solving a differential equation for the rotation matrix.⁴ Only the first 10 states are included in the diabaticization procedure and the coupling due to the R^{-2} term in the kinetic energy is omitted.

iv. Kinetic energy release spectra

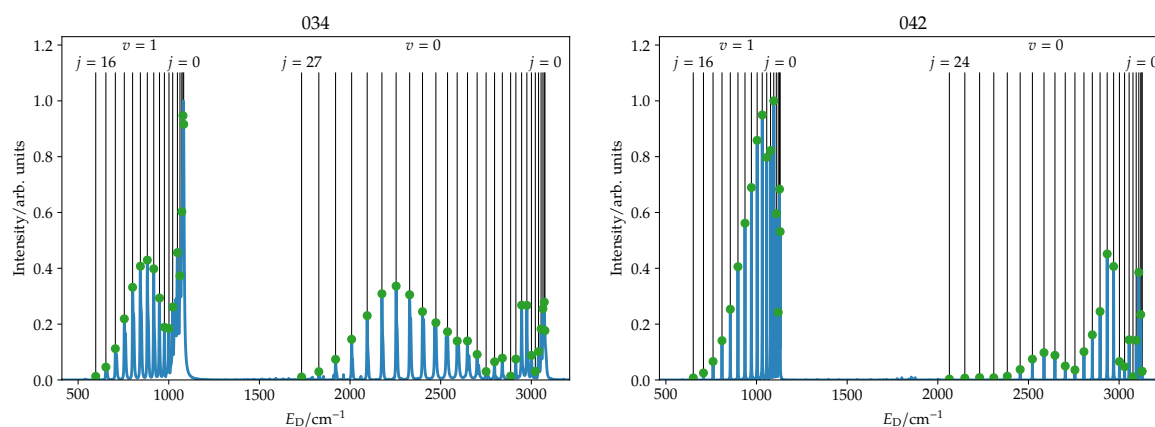


Figure iv: Kinetic energy release spectra of the D atom for resonances (0,3,4) (left) and (0,4,2) (right) using the WKS PES.^{1,2} The vertical lines show the assignment of the quantum numbers of the asymptotic CO fragment. The first upper line shows the CO stretch quantum number ν and the second line the minimal and maximal shown rotational/bend quantum number j . The distributions are scaled such that the maximal value is 1.

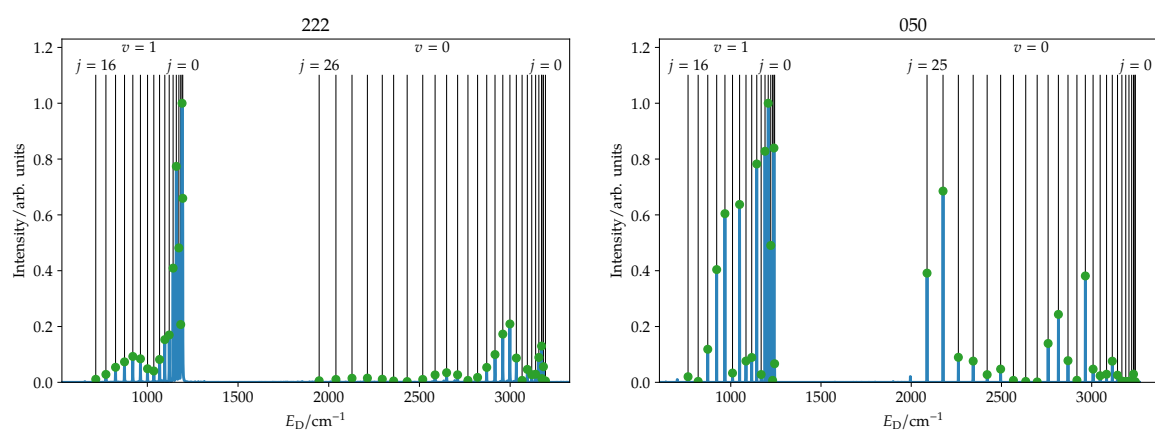


Figure v: Same as Figure iv but with resonances (2,2,2) (left) and (0,5,0) (right).

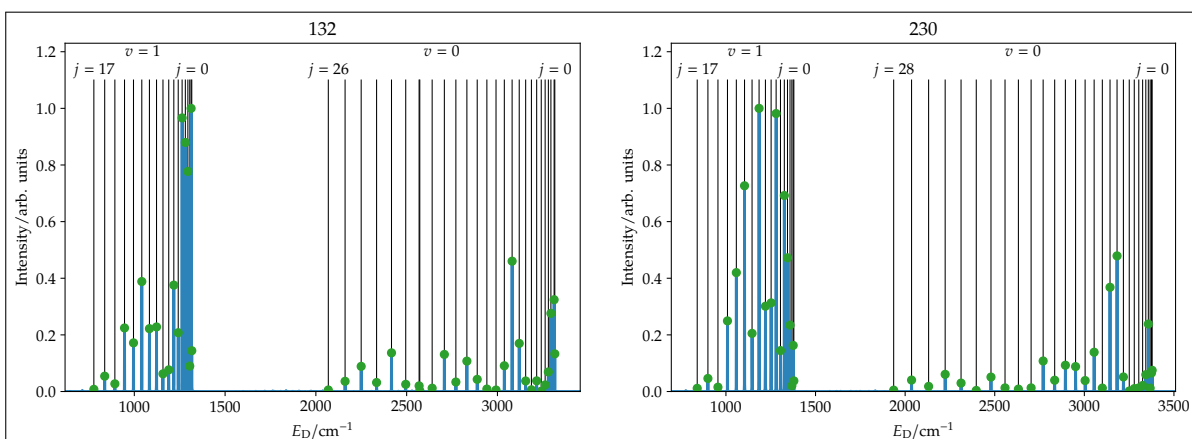


Figure vi: Same as Figure iv but with resonances (1,3,2) (left) and (2,3,0) (right).

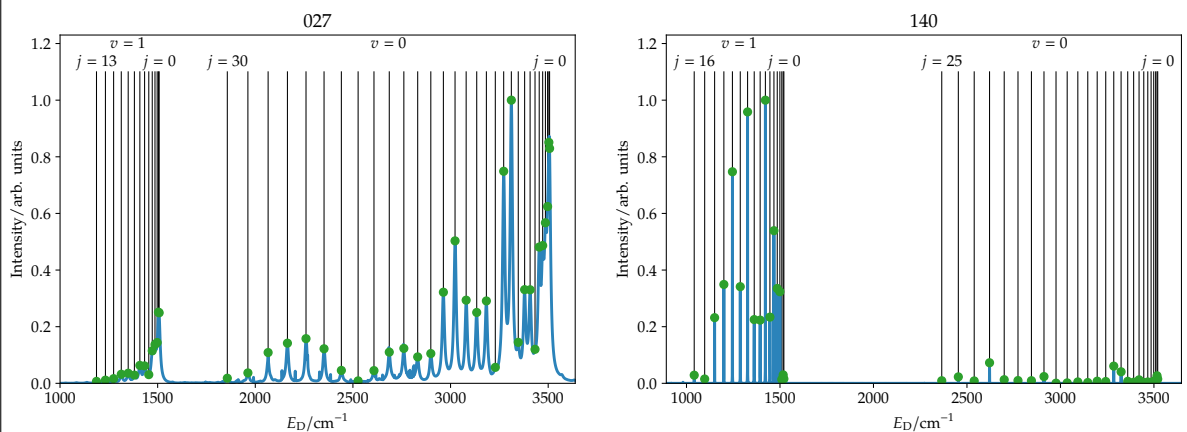


Figure vii: Same as Figure iv but with resonances (0,2,7) (left) and (1,4,0) (right).

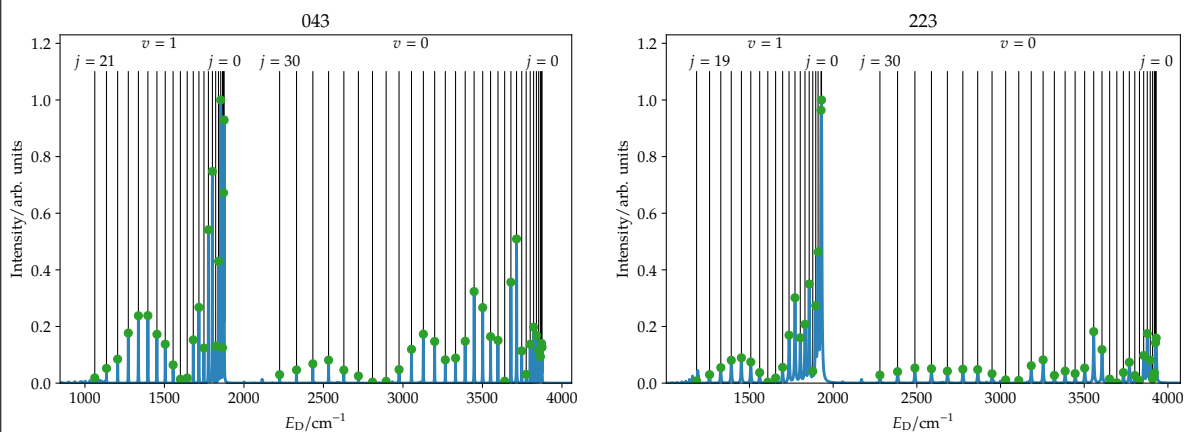


Figure viii: Same as Figure iv but with resonances (0,4,3) (left) and (2,2,3) (right).

Figure ix: A figure

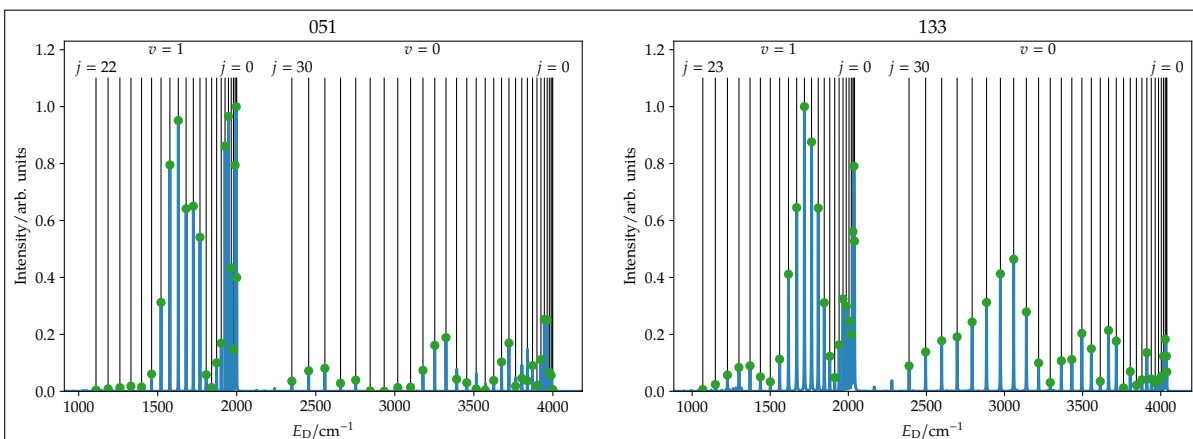


Figure x: Same as Figure iv but with resonances (0,5,1) (left) and (1,3,3) (right).

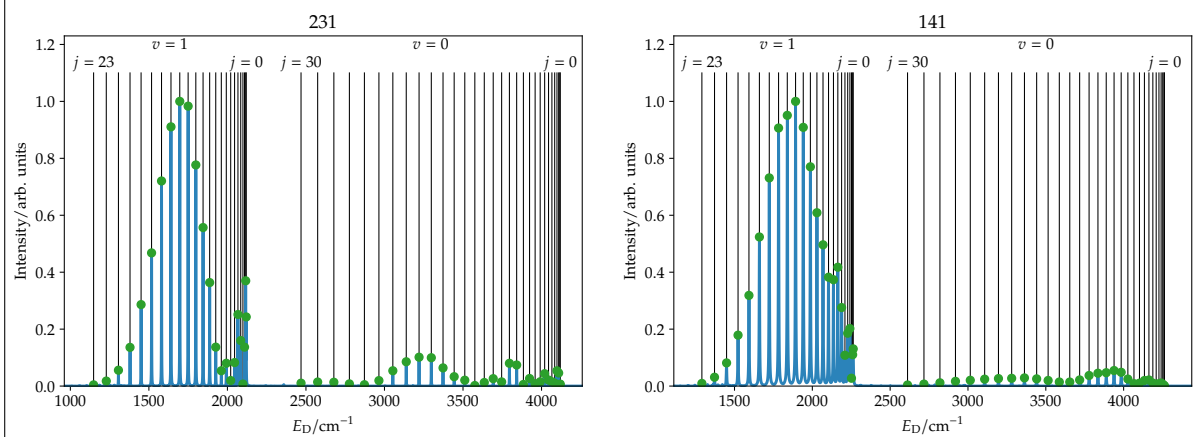


Figure xi: Same as Figure iv but with resonances (2,3,1) (left) and (1,4,1) (right).

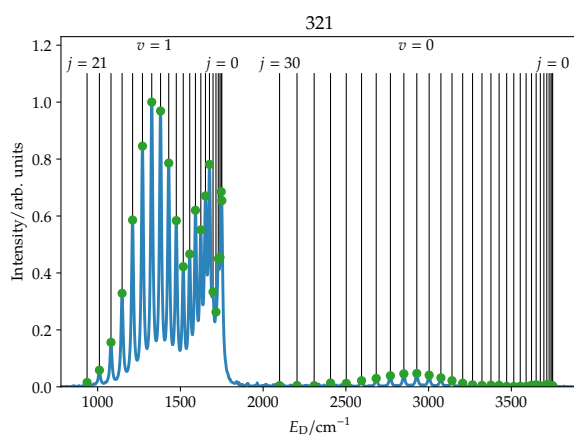


Figure xii: Same as Figure iv but with resonance (3,2,1).

II.1. Resonance Decay Dynamics of the Deuterated Formyl Radical

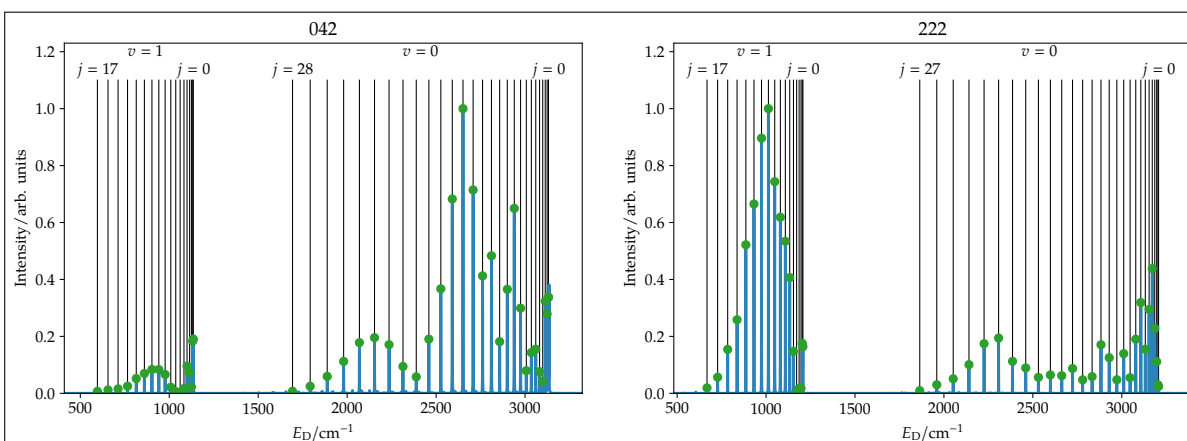


Figure xiii: Same as Figure iv but for resonances (0,4,2) (left) and (2,2,2) (right) using the SAG PES.³

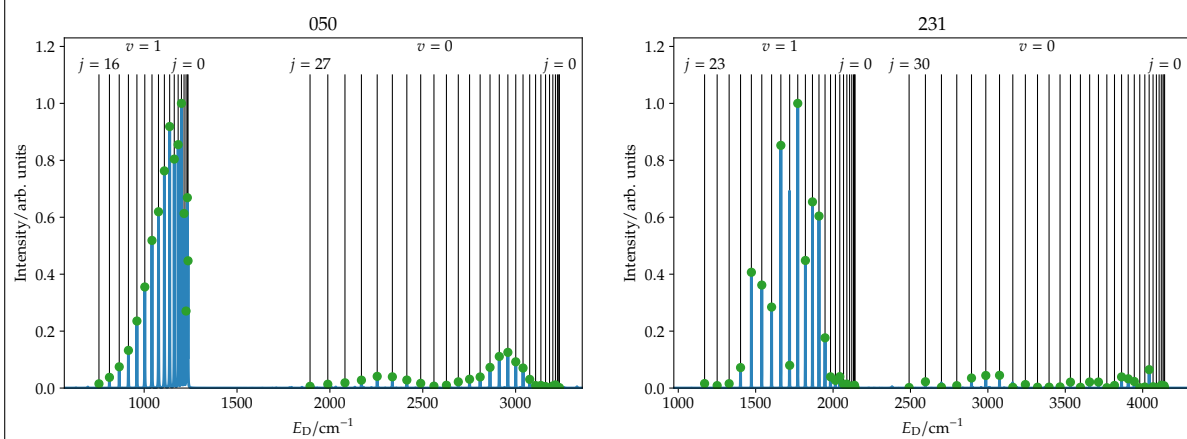


Figure xiv: Same as Figure iv but for resonances (0,5,0) (left) and (2,3,1) (right) using the SAG PES.³

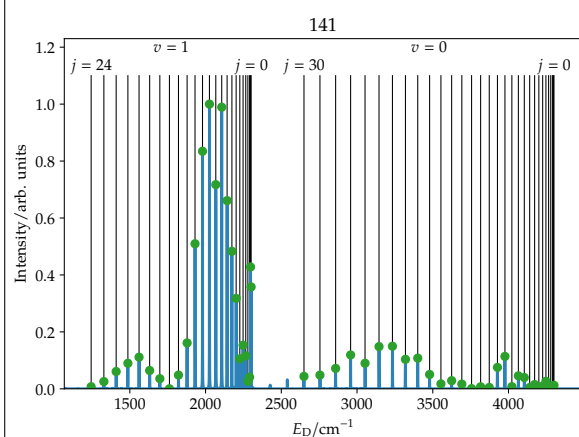


Figure xv: Same as Figure iv but for resonance (1,4,1) using the SAG PES.³

v. Rovibrational CO product distributions

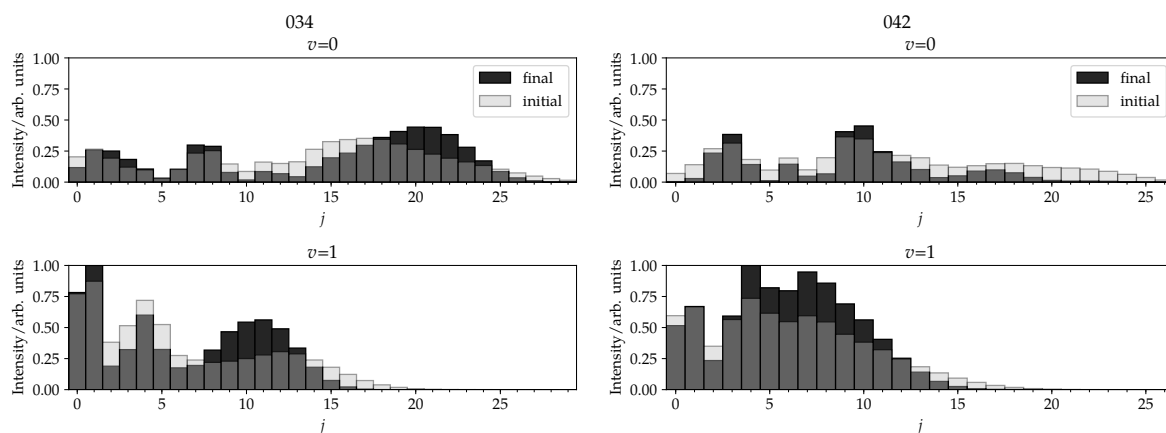


Figure xvi: Asymptotic CO quantum-number resolved distributions for resonances (0,3,4) (left) and (0,4,2) (right) using the WKS PES.^{1,2} The upper (lower) panels show the distributions for stretch quantum number $v = 0$ ($v = 1$) versus different rotational quantum numbers j of the asymptotic CO fragment. The distributions are scaled such that the maximal value is 1. The darker bars show the distributions for the final wavepacket, $|\Psi(t \rightarrow \infty)\rangle$. The brighter bars show the distributions for the *initial* wavepacket, $|\Psi(t = 0)\rangle$, in the asymptotic region.

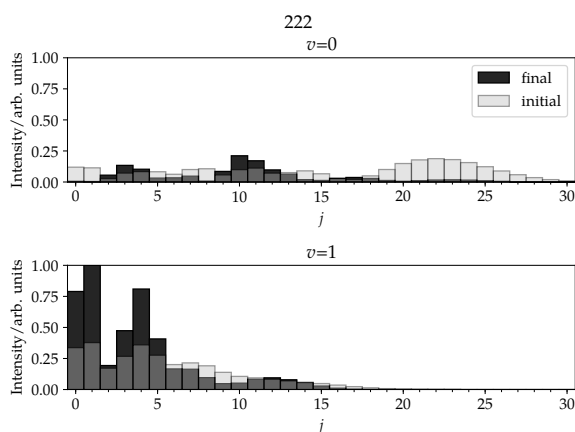


Figure xvii: Same as Figure xvi but with resonance (2,2,2).

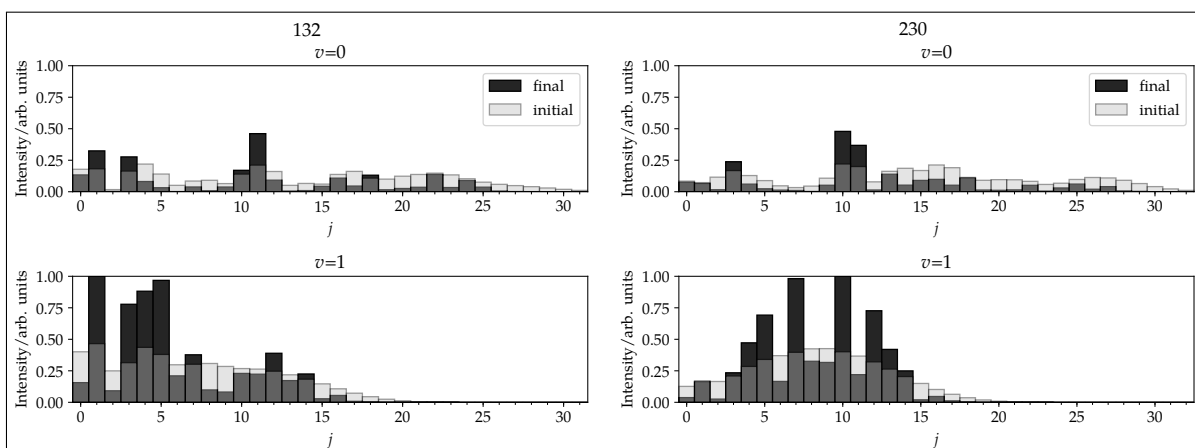


Figure xviii: Same as Figure xvi but with resonances (1,3,2) (left) and (2,3,0) (right).

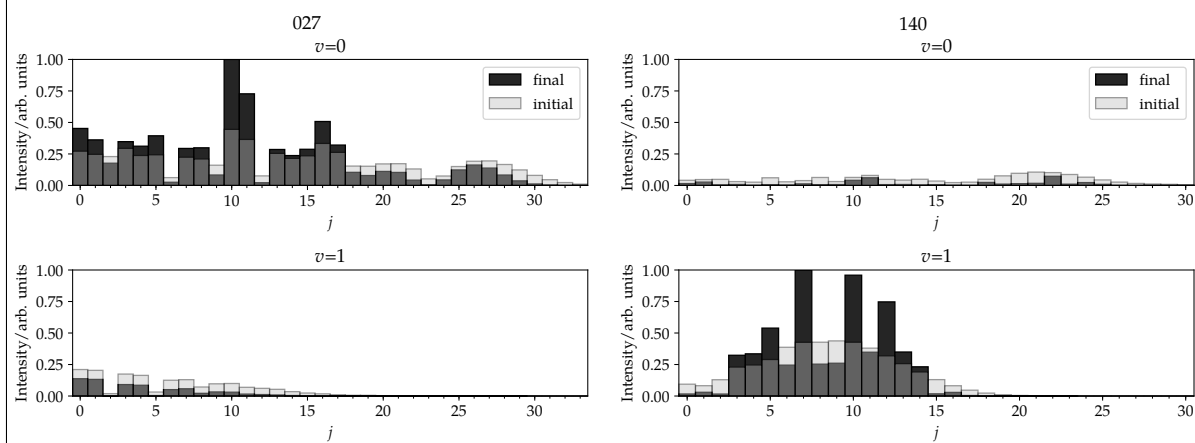


Figure xix: Same as Figure xvi but with resonances (0,2,7) (left) and (1,4,0) (right).

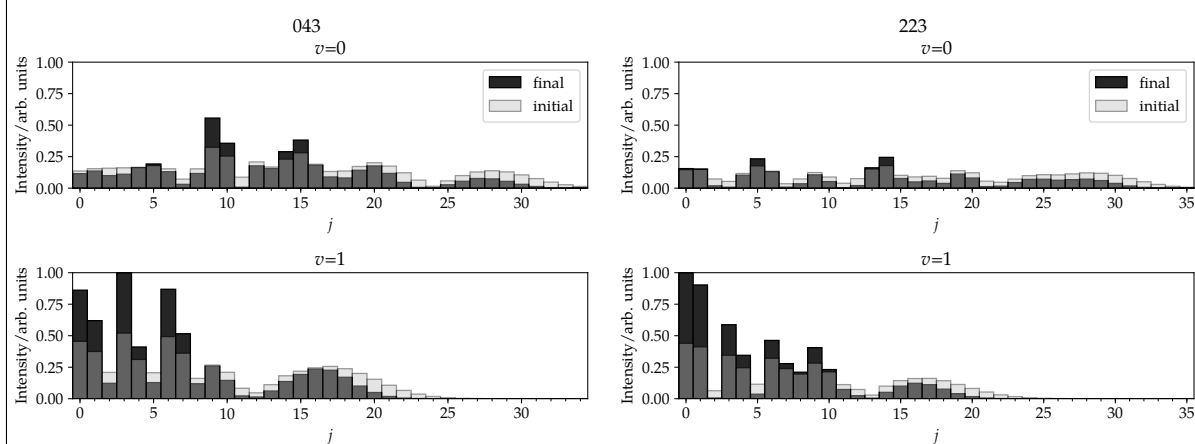


Figure xx: Same as Figure xvi but with resonances (0,4,3) (left) and (2,2,3) (right).

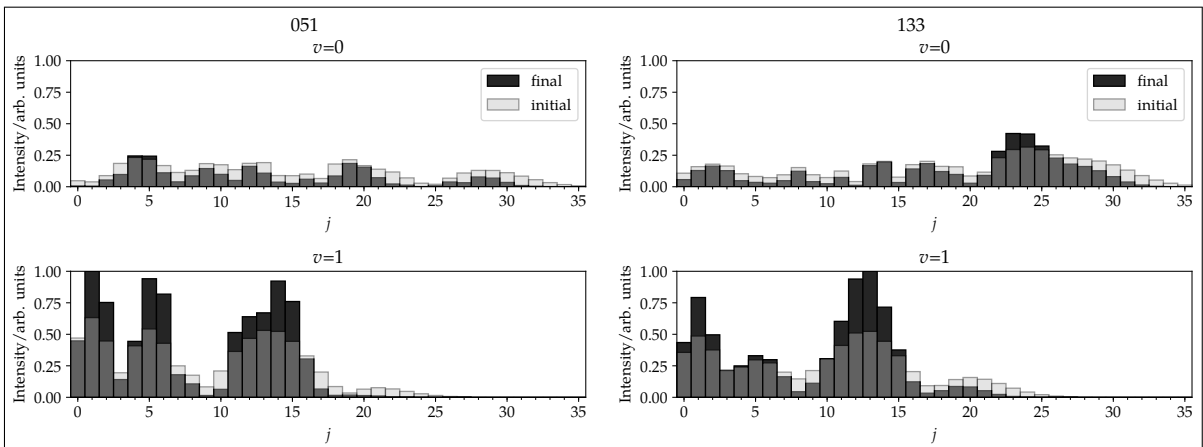


Figure xxi: Same as Figure xvi but with resonances (0,5,1) (left) and (1,3,3) (right).

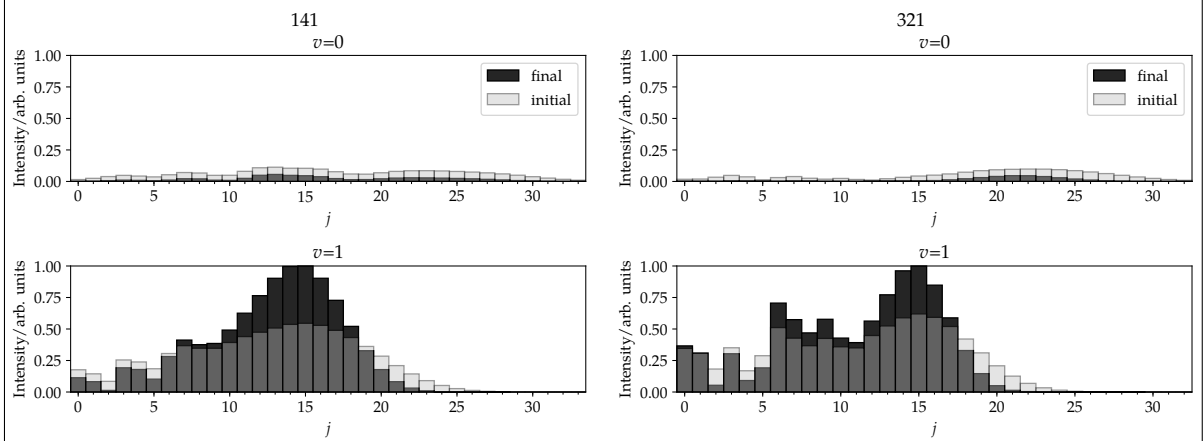


Figure xxii: Same as Figure xvi but with resonances (1,4,1) (left) and (3,2,1) (right).

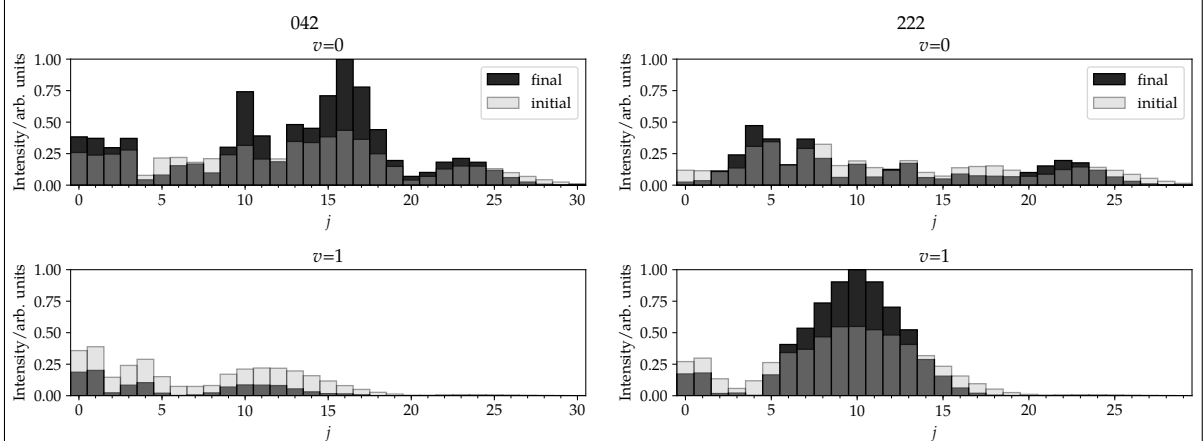


Figure xxiii: Same as Figure xvi but for resonances (0,4,2) (left) and (2,2,2) (right) using the SAG PES.³

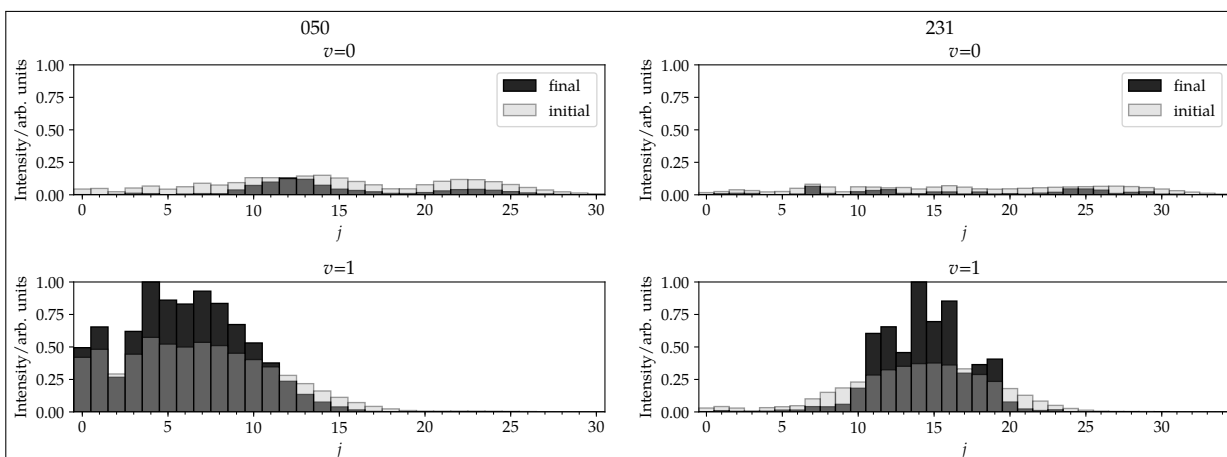


Figure xxiv: Same as Figure xvi but for resonances (0,5,0) (left) and (2,3,1) (right) using the SAG PES.³

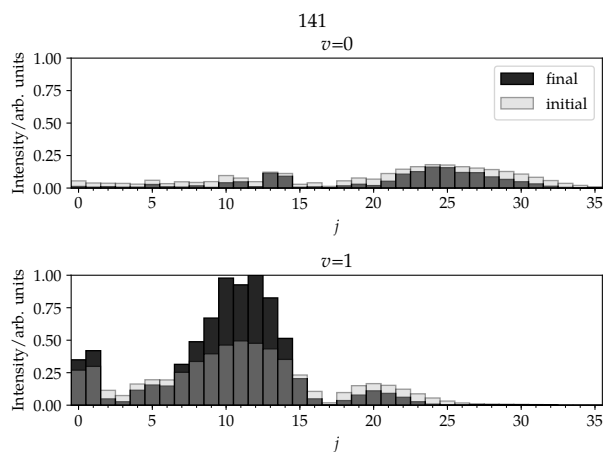


Figure xxv: Same as Figure xvi but for resonance (1,4,1) using the SAG PES.³

References

- ¹ Werner, H.-J.; Bauer, C.; Rosmus, P.; Keller, H.-M.; Stumpf, M.; Schinke, R. *J. Chem. Phys.* **1995**, *102*, 3593–3611.
- ² Keller, H.-M.; Floethmann, H.; Dobbyn, A. J.; Schinke, R.; Werner, H.-J.; Bauer, C.; Rosmus, P. *J. Chem. Phys.* **1996**, *105*, 4983–5004.
- ³ Song, L.; van der Avoird, A.; Groenenboom, G. C. *J. Phys. Chem. A* **2013**, *117*, 7571–7579.
- ⁴ Baer, M. *Chem. Phys. Lett.* **1975**, *35*, 112–118.
- ⁵ Pacher, T.; Köppel, H.; Cederbaum, L. S. *J. Chem. Phys.* **1991**, *95*, 6668–6680.
- ⁶ Simah, D.; Hartke, B.; Werner, H.-J. *J. Chem. Phys.* **1999**, *111*, 4523–4534.
- ⁷ Mitrushenkov, A. O.; Palmieri, P.; Puzzarini, C.; Tarroni, R. *Mol. Phys.* **2000**, *98*, 1677–1690.
- ⁸ Köppel, H.; Domcke, W.; Cederbaum, L. S. *Adv. Chem. Phys.* *57*, 59–246.
- ⁹ Wittenbrink, N.; Venghaus, F.; Williams, D.; Eisfeld, W. *J. Chem. Phys.* **2016**, *145*, 184108.
- ¹⁰ Esry, B. D.; Sadeghpour, H. R. *Phys. Rev. A* **2003**, *68*.

Photoelectron Momentum Distributions of Atomic Hydrogen

“ You’re bound to be unhappy if you optimize everything.

— Donald E. Knuth

In contrast to the previous application in [Chapter II.1](#), the following Chapters present applications of pruned dynamics for electrons in strong electromagnetic fields. They show that pruned dynamics is not restricted to the simulation of nuclear motion. This Chapter starts with applications in single-electron dynamics whereas the other Chapters show applications in two-electron dynamics. New and exciting effects arise when an electronic system is subjected to a strong external field. Since electron dynamics and strong field physics are not standard topics in theoretical chemistry, the theory will be briefly described.

This Chapter starts with a description of the handling of external fields in [Section II.2.1](#). Some phenomena and theory for strong external fields are presented in [Section II.2.2](#). One of the important quantities in strong-field physics are photoelectron momentum distributions (PMDs). How to obtain them is shown in [Section II.2.3](#). This Chapter ends with a benchmark study for getting PMDs for the hydrogen atom with DP in [Section II.2.4](#).

II.2.1. External Fields

Neglecting spin-dependency, the nonrelativistic Hamiltonian of a particle of charge q and mass m in an external electromagnetic field represented by the operator \hat{V}_{ext} is^[242]

$$\hat{H} = \hat{T} + \hat{V} + \hat{V}_{\text{ext}} = -\frac{\nabla^2}{2m} + \hat{V} + \underbrace{\frac{1}{2m}(iq(\nabla \cdot \vec{A} + \vec{A} \cdot \nabla)/c + q^2 \vec{A}^2/c^2)}_{\hat{V}_{\text{ext}}} + q\phi, \quad (\text{II.2.1})$$

¹This Section is based on my Master’s thesis.^[99]

where ϕ and \vec{A} are the scalar and vector potential of the field and are functions of coordinates \vec{r} and time t .¹ c is the speed of light. Here, these quantities are treated classically because the quantization of the field is negligible for high intensities produced by a light amplification by stimulated emission of radiation (LASER).^[243] The SE is invariant under the gauge transformations

$$\vec{A}(\vec{r}, t) = \vec{A}(\vec{r}, t) + \nabla\chi(\vec{r}, t), \quad (\text{II.2.2})$$

$$\phi(\vec{r}, t) = \phi(\vec{r}, t) - \partial_t\chi(\vec{r}, t), \quad (\text{II.2.3})$$

$$\Psi(\vec{r}, t) = \tilde{\Psi}(\vec{r}, t) \exp(iq\chi(\vec{r}, t)). \quad (\text{II.2.4})$$

In the *Coulomb gauge*, the condition $\nabla \cdot \vec{A} \stackrel{!}{=} 0$ is further imposed and ϕ is normally taken to be zero. Accordingly, Eq. (II.2.1) reduces to

$$\hat{H} = \frac{1}{2m}(-\nabla^2 + 2iq\vec{A} \cdot \nabla/c + q^2\vec{A}^2/c^2) + \hat{V}. \quad (\text{II.2.5})$$

For monochromatic light, \vec{A} is described by^[242,244]

$$\vec{A}(\vec{r} + \vec{r}_0, t) = \vec{A}(t) \frac{1}{2} \exp(i\vec{k}(\vec{r}_0 + \vec{r})) + \text{c.c.} \quad (\text{II.2.6})$$

c.c. means the complex conjugated part. In the following, $\vec{r}_0 \equiv \vec{0}$ is chosen in order to get rid of a phase term. In the *dipole approximation*, $\exp(i\vec{k} \cdot \vec{r})$ is assumed to be 1:

$$\vec{A}(t) \frac{1}{2} (1 + i\vec{k} \cdot \vec{r} + \dots) + \text{c.c.} \approx \vec{A}(t). \quad (\text{II.2.7})$$

This is valid if the wavelength of the incident light is much larger than the molecule. The length scale of small molecules is of order $\sim 10^{-10}$ m whereas the wave number of infrared light is $k = 2\pi/\lambda \sim 8 \times 10^6 \text{ m}^{-1}$. Hence, $|\vec{k} \cdot \vec{r}|$ is small ($\sim 8 \times 10^{-3}$) and $|\exp(i\vec{k} \cdot \vec{r})|$ is approximately 1. Thus, within the dipole approximation, the vector potential solely depends on the time t and not on the spatial coordinates \vec{r} such that the magnetic field ($\vec{B} = \nabla \times \vec{A}$) is neglected which is a valid approximation for “weak” fields up to strengths of $\sim 10^{15} \text{ W/cm}^2$ (assuming a wave length of 800 nm).^[245-247] Even for extreme ultraviolet (XUV) radiation with a wavelength of 10 nm, $\exp(i\vec{k} \cdot \vec{r})$ becomes $0.998 + 0.0628i$ which is still close to 1. However, for high intensities, the dipole approximation can break down for radiation with long wavelengths.^[248] This is due to magnetic field effects. Fig. 1 in Ref. [248] gives an overview of the field parameters and their boundaries for a valid dipole approximation.

The \vec{A}^2 -term in Eq. (II.2.5) can be eliminated within the dipole approximation by applying the gauge transform^[242]

$$\Psi(\vec{r}, t) = \exp\left(-i \frac{q^2}{2mc^2} \int_{-\infty}^t d\tilde{t} \vec{A}^2(\tilde{t})\right) \Psi^V(\vec{r}, t). \quad (\text{II.2.8})$$

This is the *velocity gauge*, where the interaction is described by

$$\hat{V}_{\text{ext}}^V = -i \frac{q}{mc} \vec{A}(t) \cdot \nabla = \frac{q}{mc} \vec{A}(t) \cdot \hat{p}. \quad (\text{II.2.9})$$

The dependence on the momentum operator, $\hat{p} = -i\nabla$, explains its name. The transformation

$$\Psi^L(\vec{r}, t) = \exp\left(-i \frac{q}{c} \vec{A}(t) \cdot \vec{r}\right) \Psi^V(\vec{r}, t) \quad (\text{II.2.10})$$

leads to the *length gauge* with

$$\hat{V}_{\text{ext}}^L = qE(t) \cdot \hat{r}, \quad (\text{II.2.11})$$

$$= -E(t) \cdot \hat{\mu}, \quad (\text{II.2.12})$$

$$\vec{E} = -\frac{1}{c} \frac{d\vec{A}(t)}{dt}. \quad (\text{II.2.13})$$

Eq. (II.2.12) can also be obtained straightforwardly by applying the identity $\nabla_x = -m[\hat{H}, \hat{x}]$, where \hat{x} is some spatial coordinate operator, to $\vec{A} \cdot \nabla$ in the dipole approximation. By defining a scaled vector potential $\vec{\tilde{A}} = c\vec{A}$, the speed of light c can be omitted in the final working expressions since both Eq. (II.2.9) and Eq. (II.2.13) contain c^{-1} . Thus, similar to atomic units, c is “set to 1” in the following and when writing \vec{A} , the scaled vector potential $\vec{\tilde{A}}$ is assumed. This is a usual convention.^[249]

II.2.2. Electron Dynamics and Strong Field Physics

If very strong and very short time-dependent external fields are applied to an electronic system, new and interesting phenomena arise. This sets the stage for a new scientific area — attosecond and strong field physics. Some of the fundamentals are briefly described in the following Subsections that are mostly based on my Master’s thesis.^[99] The equations presented here are mainly formulated in terms of classical principles. Interestingly, quantum mechanics qualitatively gives the same results within the classical field approximation. For more comprehensive reviews and perspectives on the phenomena and applications of attosecond and strong field physics the reader is referred to Refs. [250-256].

II.2.2.1. Ponderomotive Potential

The potential that an electron experiences in an inhomogeneous, oscillating electromagnetic field is called ponderomotive potential.^[251,257] The kinetic energy of the electron in the continuum that is subjected to the external field is classically formulated as

$$T_{\text{cl}} = \frac{p^2}{2} = \frac{E_0^2}{2\omega^2} \sin^2(\omega t), \quad (\text{II.2.14})$$

where ω and E_0 are the frequency and the strength of the field. Due to the oscillations of the field, the electron performs a “quiver motion” with an amplitude of

$$x_0 = \frac{E_0}{\omega^2}. \quad (\text{II.2.15})$$

The ponderomotive potential is the mean value of the kinetic energy,

$$U_p = \langle T \rangle_{\text{cl}} = \frac{E_0^2}{4\omega^2} = \frac{1}{4}\omega^2 x_0^2. \quad (\text{II.2.16})$$

To give an example,^[257] the ponderomotive potential induced by a titanium-sapphire LASER with a wave length of $\lambda = 800$ nm and an intensity of $I = 10^{14}$ W/cm² is $U_p \approx 6$ eV = 0.22 E_h . This corresponds to a very large amplitude of $x_0 = 164 a_0 = 8.7$ nm.

II.2.2.2. Keldysh Parameter

The above example shows that current experimentally available electromagnetic fields can create external potentials that have the same magnitude as molecular or atomic potentials. To classify the strength of the external field, the *Keldysh parameter* is defined as^[255,257,258]

$$\gamma = \sqrt{\frac{I_p}{2U_p}}, \quad (\text{II.2.17})$$

where I_p is the ionization potential. $\gamma < 1$ corresponds to a “field with an atom” (the field dominates) and $\gamma > 1$ to an “atom with a field” (the Coulomb potential dominates). For the hydrogen atom, the example considered in the previous Subsection corresponds to a Keldysh parameter of approximately 1. Since $\gamma \propto U_p^{-1/2} \propto \lambda^{-1}$, the Keldysh parameter *decreases* (the tunnel-ionization probability increases) with increasing wave length, i. e., decreasing energy of the external field.

II.2.2.3. Tunnel Ionization

A very important effect in electron dynamics is the ionization process *via* tunneling through a barrier effectively created by the external field. Assuming a linearly polarized field in z-direction and the validity of the dipole approximation (Section II.2.1), a single electron in an atom of charge Z is affected by the overall potential

$$V(\vec{r}, t) = -\frac{Z}{r} - E(t)z, \quad z = r \cos(\theta), \quad (\text{II.2.18})$$

where spherical coordinates $\vec{r} = (r, \theta, \phi)^T$ are used. As $V(\vec{r}, t)$ gets “tilted” by the applied field, the electrons can tunnel through the barrier. A critical field strength, E_{cr} , is reached if the saddle

point of the barrier approaches the negative ionization energy, I_p . For an atomic field,

$$E_{\text{cr}} = \frac{I_p^2}{4Z}. \quad (\text{II.2.19})$$

For the hydrogen atom, E_{cr} is 0.0625 (intensity of $1.4 \times 10^{14} \text{ W/cm}^2$). If the critical field intensity is exceeded, the electron can move over the barrier without the need of tunneling. This is called above-barrier ionization. A sketch of these processes is shown in Fig. II.2.1.

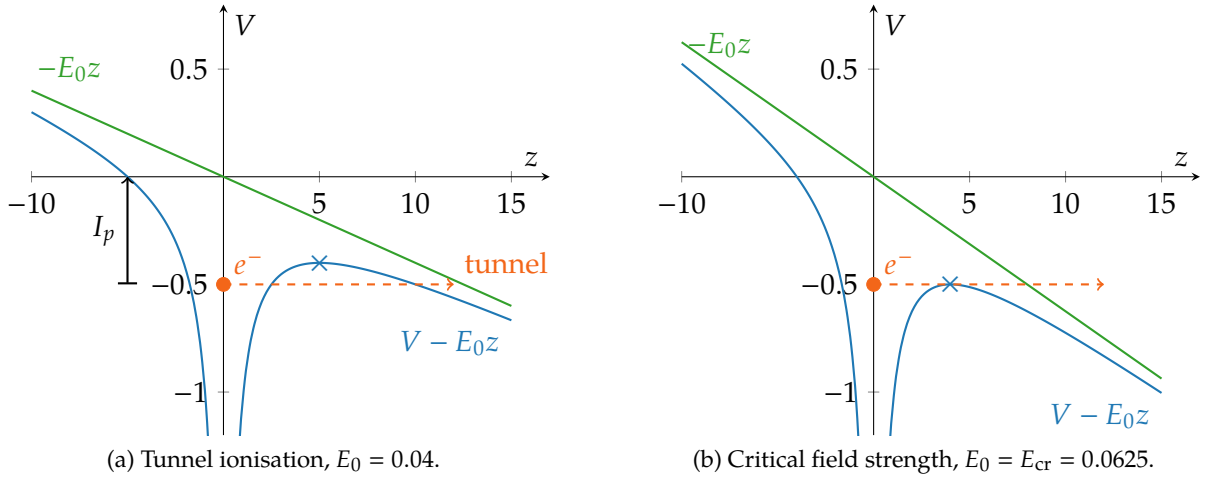


Figure II.2.1.: Example of strong-field ionization in hydrogen with two different field strengths leading to tunneling- or the beginning of above-barrier ionization. The blue curve displays the molecular potential including the interaction potential (green curve) along the spherical coordinate z . The top of the tunnel barrier is marked by “ \times ”.^[257] Atomic units are used.

The Keldysh parameter (Section II.2.2.2) can also be defined by the process of tunnel ionization because $\gamma \equiv 2\omega t_{\text{tu}}$, where t_{tu} is the “classical tunneling time” of an electron, i. e. the classical time needed to move with speed v through the potential barrier of length l_{tu} .^[257]

$$t_{\text{tu}} = \frac{l_{\text{tu}}}{v} = \frac{\sqrt{I_p}}{\sqrt{2}E_0}. \quad (\text{II.2.20})$$

This explains why the field becomes more effective with increasing wave length/decreasing frequency: The smaller the frequency, the more time the electron has to tunnel through the barrier.

For high intensities and in an energy picture, it is possible that the electron absorbs more photons than actually needed for ionization. Assuming sufficiently long LASER pulses, the photoelectron spectrum exhibits peaks separated by the photon energy ω and appearing at positions $E_s = (n + s)\omega - I_p$; $s \in \mathbb{N}_0$.^[242] n is the minimum number of photons needed to exceed the ionization potential I_p .

II.2.2.4. High Harmonic Generation

As an example of an application of tunnel ionization, the process of HHG is considered here.^[250-252,256,257,259] In an intense infrared (IR) LASER field, radiation is emitted with high frequencies that are odd multiples of the applied field frequency, so-called high harmonics.² The occurrence of the harmonics can be explained by a three-step model: First, an electron tunnels through the barrier and is accelerated by the external field. Second, the sign of the field changes and the electron is scattered back to the atom. Third, it recombines with the atom under emission of light with a final energy that is the sum of the (accumulated) kinetic energy and the ionization energy, see Fig. II.2.2.

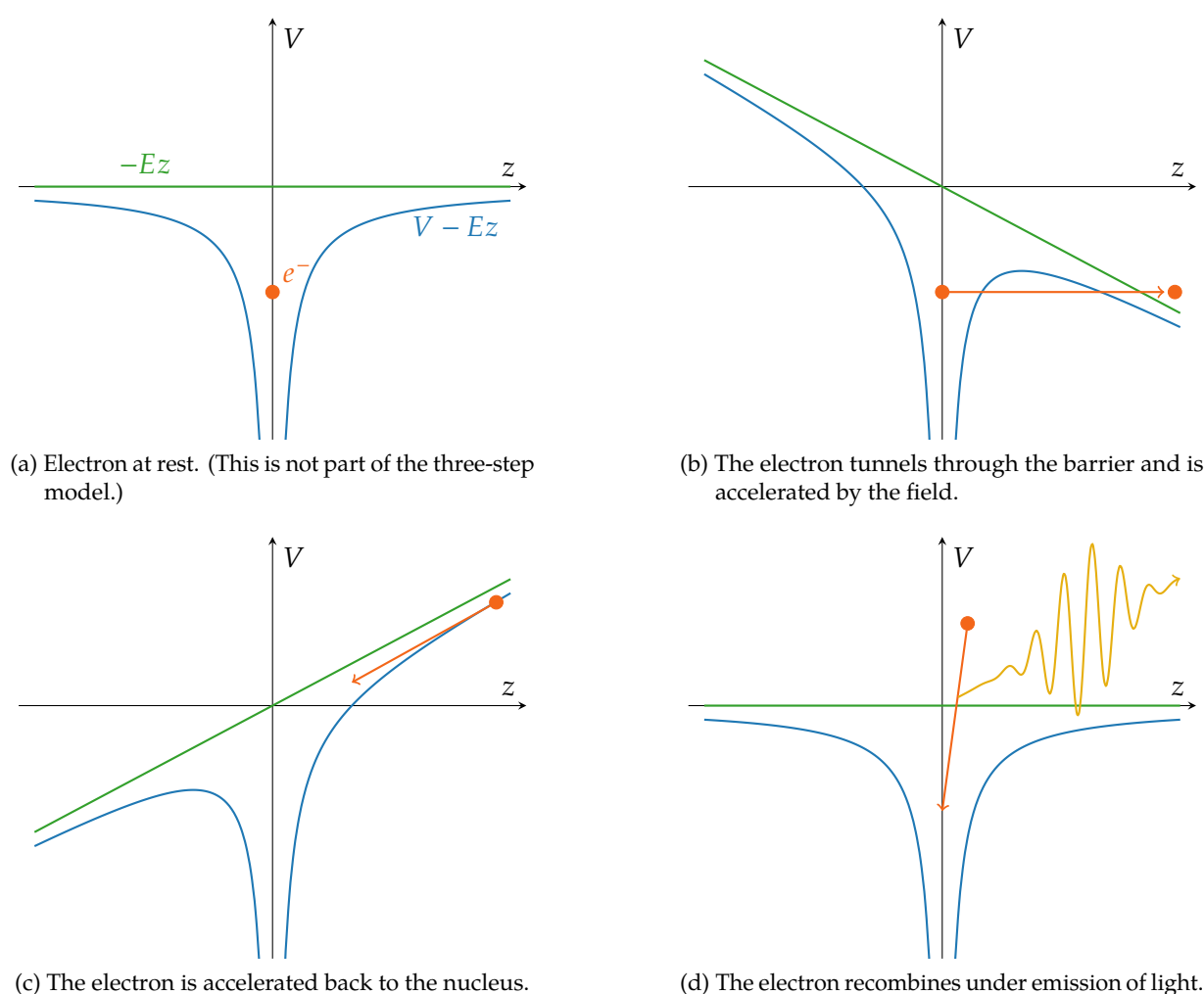


Figure II.2.2.: Cartoon of the HHG generation process (three step model), see text for details. During the recollision process, panel (d), a re-ejection or an ejection of another electron is possible for multi-electron systems.

²For reasons of symmetry, only odd multiples occur for atoms. If the field is perturbed, also even harmonics occur; see also Publication 7 (Section II.4.2) for a study.

Due to the acceleration of the electron by the external field, the emitted light has much more energy than the incident light. The HHG spectrum has a long plateau with peaks of similar intensity and a displacement of 2ω . The cutoff of the plateau can be calculated and is equal to $3.17U_p + I_p$.^[259] A coherent superposition of these high harmonics yields attosecond pulses. In Publication 7 (Section II.4.2), the first step of the three-step process is replaced by a direct ionization by a high-energy pulse.

II.2.3. Computation of Photoelectron Momentum Distributions

Besides HHG, one of the key observables in strong field physics are photoelectron momentum distributions (PMDs) (momentum-resolved photoelectron spectra). They offer a direct connection to experiment and a more or less simple means of interpretation. PMDs are defined in terms of a differential as the projection of the wavefunction $|\psi\rangle$ at infinite time onto the outgoing scattering states $|\psi_{\vec{k}}^{(-)}\rangle$ with momentum values \vec{k} :^[260]

$$\frac{\partial^3 P}{\partial \vec{k}^3} = \left| \langle \psi_{\vec{k}}^{(-)} | \psi(t \rightarrow \infty) \rangle \right|^2. \quad (\text{II.2.21})$$

In the following, most commonly used methods for the computation as well as general remarks on the latter are given. The theory will be restricted to central potentials, that is, potentials that only depend on the distance between the particles and not on their individual Cartesian components. Central potentials occur both for molecules in the long-distance limit and for atoms.

II.2.3.1. How to Obtain Scattering States

Typically, it is difficult to obtain $|\psi_{\vec{k}}^{(-)}\rangle$ because they are not square-integrable and they often need to be computed approximately. In general, the asymptotic form of the outgoing wavefunction for a scattering event in a central potential can be written as^[245,261,262]

$$\lim_{r \rightarrow \infty} \psi_{\vec{k}}^{(-)}(\vec{r}) = A(k) \left[\exp(i\vec{k} \cdot \vec{r}) + f_k(\Omega) \frac{\exp(ikr)}{r} \right], \quad (\text{II.2.22})$$

where Ω is the solid angle and $r \equiv |\vec{r}|$, $k \equiv |\vec{k}|$. $\exp(i\vec{k} \cdot \vec{r})$ can be expanded in partial waves:

$$\exp(i\vec{k} \cdot \vec{r}) = 4\pi \sum_{l=0}^{\infty} \sum_{m=-l}^l i^l R_l(kr) Y_{lm}^*(\hat{\mathbf{k}}) Y_{lm}(\hat{\mathbf{r}}), \quad (\text{II.2.23})$$

where the symbol $\hat{\mathbf{x}}$ denotes a unit vector and Y_{lm} are the spherical harmonics. $R_l(kr)$ is the solution of the one-dimensional TISE with the scattering potential $U(r)$:

$$\left[\frac{d^2}{dr^2} + k^2 - \frac{l(l+1)}{r^2} - U(r) \right] R_l(r) = 0. \quad (\text{II.2.24})$$

For the Coulomb potential, $R_l(r)$ are the Coulomb wavefunctions. For molecular problems, the asymptotic part of the potential is usually flat ($U(r) = 0$ for $r \gg 1$) and the solution of Eq. (II.2.24) corresponds to the Bessel functions. In this case, the projection onto the scattering states corresponds to the Fourier transform in spherical coordinates. Hence, one way to obtain ionization probabilities is to propagate for a long enough time such that the scattering part of the wavefunction is located in the asymptotic region where $U(r) \approx 0$. The projection onto Bessel polynomials is then only done in this region.^[263] The disadvantage of this method is the long propagation time. The lower the momentum values to be computed, the longer the propagation time. Long propagation times are especially important for getting the angular distributions right.

II.2.3.2. Surface Flux Methods

In the family of surface flux methods, the wavepacket is projected onto the continuum states *during* the appearance of the external field.^[264-268] The continuum states are time-dependent and are the solutions of a TISE that includes the external field. For $U(r) = 0$, these solutions are called Volkov states and are used for the projection. As the wavepacket in the inner region is continuously moving towards the continuum during the appearance of the external field, the projection has to be done during the whole time of the appearance of the external field. This is achieved by keeping track of the flux through a surface and by absorbing the wavefunction at this surface by a good complex absorbing potential (CAP) or by complex scaling.^[269,270] With this, the numerical description of the wavefunction is restricted to a confined region. Typically, surface flux methods neglect or only approximately describe the Coulomb potential in the continuum part. Further, a very good CAP is needed to ensure that no artifacts due to reflections at the boundary of the simulation box appear. If low momenta should be described, the wavefunction has to be propagated until the part of the wavefunction with the requested momentum components reaches the CAP.

II.2.3.3. Window Operator Method

Another way to approximately compute the PMD is to apply a so-called window operator to the wavefunction at the end of the laser pulse at time $t = T$:^[271-273]

$$|\chi(E)\rangle \equiv \hat{W}(E)|\psi(T)\rangle, \quad (\text{II.2.25})$$

$$\hat{W}(E) = \frac{\gamma^{2n}}{(\hat{H}_0 - E)^{2n} + \gamma^{2n}}. \quad (\text{II.2.26})$$

\hat{H}_0 is the field-free Hamiltonian. \hat{W} extracts the components of the wavefunction in the energy range $[E - \gamma, E + \gamma]$ for $n \rightarrow \infty$ and the energy-differentiated PMD is given as

$$\frac{\partial P}{\partial E} = \langle \chi(E) | \chi(E) \rangle. \quad (\text{II.2.27})$$

In contrast to simple projection onto Bessel functions, Eq. (II.2.27) provides a correct description directly after the end of the laser pulse. By leaving out the integration over the angles in Eq. (II.2.27), angle-differential momentum distributions as shown in Eq. (II.2.21) can be obtained. However, this typically requires further propagation into the continuum in order to have the angular distribution sufficiently converged.^[260] The specific form of \hat{W} allows for the following decomposition which enables an efficient implementation of the inverse that appears in $\hat{W}(E)$:^[274]

$$(\hat{H}_0 - E)^{2^n} + \gamma^{2^n} = \prod_{k=1}^{2^{n-1}} [\hat{H}_0 - E + \gamma \exp(i\nu_{nk})] [\hat{H}_0 - E - \gamma \exp(i\nu_{nk})], \quad (\text{II.2.28})$$

$$\nu_{nk} = (2k - 1)\pi 2^{-n}. \quad (\text{II.2.29})$$

Choices of $n = 2$ or $n = 3$ are usually sufficient. The optimal value of γ can be estimated by^[273]

$$\gamma = \frac{\pi \sqrt{2E}}{r_{\max}}, \quad (\text{II.2.30})$$

where r_{\max} is the boundary of the discretized radial coordinate.

II.2.4. Publication: Benchmark of Time-Dependent Schrödinger Equation Solvers

While there is a plethora of different (variants of) methods and codes to compute PMDs, currently, there is a lack of proper comparisons and benchmark standards. With the requirements of large grids and small wavelengths to be represented, PMD calculations are difficult to implement and the available codes and methods can differ in computational resource requirements by orders of magnitudes. To give a comparison of PMD calculations for a typical problem, a benchmark has been initiated by Brett Esry (Kansas State University), where several groups compared runtimes for a well-defined problem, namely, PMD calculations for a hydrogen atom subject to a linearly-polarized external field. The linear polarization leads to a constant magnetic quantum number, making the computational problem two-dimensional. With the given field parameters (see Section II.2.4.3), this problem is simple enough to allow for many simulation runs in order to optimize all required simulation parameters. Nevertheless, the problem is not too simple and is close to the requirements of typical experiments. One of the requirements of the benchmark is to obtain the observables to high accuracy (see Eq. (II.2.34)). In conjunction with the need to describe the continuum, the high accuracy makes this problem a challenging test case for dynamical pruning. Besides DP-DVR, here, also dynamical pruning of a polynomial basis is performed.

Currently, the writing of the publication is still in progress such that no final manuscript can be presented. Instead, selected aspects of the benchmark with focus on the performance of the DP approach are shown.

II.2.4.1. Own Contributions

Setup, optimization, execution and analysis of the DP dynamics.

II.2.4.2. Bibliographic Data

Title Comparing the performance of time-dependent-Schrödinger-equation solvers for the 800-nm, one-electron-atom, strong-field problem

Authors Preliminary: Jens Svensmark, Yujun Wang, D. Ursrey, Henrik R. Larsson, D. J. Tannor, Nicolas Douguet, Klaus Bartschat, A. N. Grum-Grzhimailo, Bruno Schulz, Alejandro Saenz, A. Scrinzi, F. Morales, T. Bredtmann, H. G. Muller, S. Patchkovskii, Xiao Wang, F. Robicheaux, V. Mosert, D. Bauer, X. M. Tong and B. D. Esry

Journal To be submitted to The Journal of Physics B

Note In preparation

II.2.4.3. Problem Definition

For one electron with mass $m = 1$, and \vec{k} described in spherical coordinates, Eq. (II.2.21) takes the form of

$$\frac{\partial^3 P}{\partial k \partial \theta_k \partial \phi_k} = \left| \langle \psi_{k\theta_k\phi_k}^{(-)} | \psi(t \rightarrow \infty) \rangle \right|^2. \quad (\text{II.2.31})$$

Here, the energy-resolved PMD, integrated over the azimuthal angle ϕ_k and described by the cosine of the polar angle, $\cos(\theta_k)$, is the observable of interest. With $d^3\vec{k} = k^2 dk d\Omega_k = \sqrt{2E} dE d\Omega_k$, where Ω is the solid angle, this gives

$$\left. \frac{\partial^2 P}{\partial E \partial \cos(\theta_k)} \right|_{E=\tilde{E}, \theta_k=\tilde{\theta}_k} = \sqrt{2\tilde{E}} \int_0^{2\pi} d\phi_k \left| \langle \psi_{\tilde{k}, \tilde{\theta}_k, \phi_k}^{(-)} | \psi(t \rightarrow \infty) \rangle \right|^2 \equiv O_{\tilde{E}}(\tilde{\theta}_k). \quad (\text{II.2.32})$$

In the following, the subscript k and the tildes are dropped, for simplicity.

The vector potential of the employed field (along the Cartesian z direction) is described by

$$A(t) = \frac{E_0}{\omega} \sin^2\left(\frac{\pi t}{\tau}\right) \sin(\omega t), \quad t \in [0, \tau], \quad (\text{II.2.33})$$

with $\omega = 0.05695 \hat{=} 800 \text{ nm}$, $\tau = 331 \hat{=} 8 \text{ fs}$ and $E_0 = 0.05338$ (corresponding to an intensity of $10^{14} \text{ W cm}^{-2}$).³ This leads to a ponderomotive potential of $U_p = 0.2196 \hat{=} 6 \text{ eV}$.

The definition of the benchmark problem is to compute the PMD as defined in Eq. (II.2.32) for two energies $E = 0.1U_p$ and $E = 10U_p$, covering both small and large momentum components.

³Again, atomic units are used unless mentioned otherwise.

The accuracy of the **PMD** is defined by

$$\eta_E = \sqrt{\frac{1}{2} \int_{-1}^1 d(\cos(\theta)) \left[\frac{O_E(\theta) - O_E^{\text{ref}}(\theta)}{O_E^{\text{ref}}(\theta) + \Delta \cdot O_E^{\text{ref,max}}} \right]^2}, \quad (\text{II.2.34})$$

where $O_E^{\text{ref,max}}$ is the maximal value of the reference $O_E^{\text{ref}}(\theta)$, which has been computed to very high accuracy. The cutoff $\Delta = 10^{-4}$ is included to reduce the influence of numerical noise from small values. The goal is to compute $O_E(\theta)$ on a fine grid in θ (501 points) such that η_E is not larger than 10^{-2} . The first phase of the benchmark has been carried out as a blind test, that is, the values of $O_E(\theta)$ and runtimes have been submitted without knowing the reference $O_E^{\text{ref}}(\theta)$ and without knowing the timings from the other groups. This requires own convergence tests in order to fulfill the goal of having $\eta_E \leq 10^{-2}$.

II.2.4.4. Outgoing Scattering States

For atomic hydrogen, the outgoing scattering states can be calculated analytically. They are given by^[263,275]

$$\psi_{\vec{k}}^{(-)}(\vec{r}) = \sum_{lm} \sqrt{\frac{2}{\pi}} i^l \exp(-i\sigma_l(k)) \frac{F_l(kr, \eta)}{kr} Y_{lm}^*(\hat{\mathbf{k}}) Y_{lm}(\hat{\mathbf{r}}), \quad (\text{II.2.35})$$

$$\sigma_l(k) = \arg[\Gamma(l+1+i\eta)], \quad (\text{II.2.36})$$

$$\eta = -1/k, \quad (\text{II.2.37})$$

where $F_l(\rho, \eta)$ is the regular Coulomb wavefunction and the solution of^[276,277]

$$\frac{d^2 F_l}{d\rho^2} + \left[1 + \frac{2\eta}{\rho} + \frac{l(l+1)}{\rho^2} \right] F_l = 0, \quad (\text{II.2.38})$$

compare with Eq. (II.2.24).

The knowledge of $|\psi_{\vec{k}}^{(-)}\rangle$ simplifies the problem a lot because the propagation needs only to be done during the appearance of the field until $t = \tau = 8$ fs. For comparison, some tests with the window operator method required the propagation for more than 140 fs in order to have the **PMD** computed accurately enough. However, some groups chose to use standard surface flux methods instead of using the exact solution of $|\psi_{\vec{k}}^{(-)}\rangle$. Other groups used surface flux methods only during the appearance of the field and then projected the state onto $|\psi_{\vec{k}}^{(-)}\rangle$.

⁴For simplicity, the basis function coefficients are absorbed in $|\chi_{lm}\rangle$ in this particular notation.

II.2.4.5. Setup

The wavefunction is expanded in a direct-product basis consisting of a radial part $|\chi_{lm}\rangle$ and spherical harmonics Y_{lm} (in spherical coordinates):⁴

$$|\psi\rangle = \sum_{lm} \frac{|\chi_{lm}\rangle}{r} |Y_{lm}\rangle. \quad (\text{II.2.39})$$

Due to the linear polarization of the field, only $m = 0$ needs to be considered because the initial state is the ground state. Thus, the TDSE becomes^[278]

$$i \frac{\partial}{\partial t} |\chi_{l0}\rangle = \left[-\frac{1}{2} \frac{\partial^2}{\partial r^2} + \frac{l(l+1)}{2r^2} - \frac{1}{r} \right] |\chi_{l0}\rangle + \sum_{l'} \langle Y_{l0} | W | Y_{l'0} \rangle |\chi_{l'0}\rangle, \quad (\text{II.2.40})$$

$$\langle Y_{l0} | W | Y_{l'0} \rangle = \sqrt{\frac{4\pi}{3}} \langle Y_{l0} | Y_{10} | Y_{l'0} \rangle W_{ll'}, \quad (\text{II.2.41})$$

$$W_{ll'} = -\frac{i}{2} A(t) \left\{ \frac{1}{2r} [l(l+1) - l'(l'+1)] + \frac{\partial}{\partial r} \right\}. \quad (\text{II.2.42})$$

Note that the operators have a SoP form.

Dynamical pruning is performed for both the r -dependent part (described by a DVR) and the spherical harmonics. Note that this is the first application where also a finite basis representation (FBR) in terms of spherical harmonics/Legendre polynomials is pruned. As usual in the DP scheme, the absolute value of the wavefunction coefficient for a specific DVR point x_i^l and harmonic Y_{l0} is checked. If it is larger than the WAT θ , the basis functions corresponding to the nearest neighbors $\{x_{i-\{1,2\}}^l, x_{i+\{1,2\}}^l, x_i^{l+1}, x_i^{l-1}\}$ are added to the set of active functions, \mathcal{A} . Otherwise, the basis function corresponding to x_i^l is removed from \mathcal{A} . This procedure is repeated for every time step δt . Note that here, not only the direct nearest neighbors $\{x_{i-1}^l, x_{i+1}^l\}$ on the DVR grid are added but also $\{x_{i-2}^l, x_{i+2}^l\}$. This makes the DP scheme more stable for the rapid ionization process.

The efficient algorithm for the pruned matrix-vector product described in Publication 3 (Section I.1.3) is optimized further and takes into account that the interaction operator only couples basis functions for which $\Delta l = 1$, that is, the corresponding matrix is tridiagonal. Instead of retrieving the values on-the-fly from a big matrix as it is done in Publication 3, for each combination of l and $l' = l \pm 1$, the matrix representation in the pruned subset consisting of the intersection of the active DVR functions for l and l' is set up.

As the DVR, the FE-DVR is used.^[162,163] There, the radial coordinate is discretized into N_e elements with $N_{p/e}$ Gauß-Lobatto DVR functions in each element. This discretization into elements makes the kinetic energy matrix banded. It can be decomposed into a sum of block-diagonal matrices enabling the use of efficient matrix-vector-product routines.^[164] $N_e = 570$ elements distributed equidistantly up to $r_{\max} = 510$ are used. In each element, $N_{p/e} = 5$ DVR functions are used, resulting overall in 2275 basis functions in the radial coordinate. This number is smaller than

$N_e \cdot N_{p/e}$ due to shared basis functions at the element boundaries and the removal of the basis functions at the end of the grid points (Dirichlet boundary condition). The maximal angular momentum is restricted to $l^{\max} = 24$. The set \mathcal{A} is updated every $\delta t = 0.1$ with a WAT of $\theta = 10^{-17}$.

The initial state is found by diagonalizing the Hamiltonian in the unpruned FE-DVR representation for $l = 0$ using a Lanczos algorithm. The SIL propagator^[142] with an adaptive step-size and adaptive Krylov dimension^[143] is used. The error tolerance of the propagator is set to $\epsilon = 5 \cdot 10^{-8}$. $\delta t = 0.1$ is also the minimal step size of the propagator, although, in general, this is not necessary. The PMDs are retrieved by projecting the wavefunction at the end of the propagation onto $|\psi_{\vec{k}}^{(-)}\rangle$. No surface flux method is used, although DP-DVR could be combined with these kinds of methods.

To allow for a better comparison of the various methods, a scaling of the method with respect to CPU-time was demanded. Because the size of the active basis changes during the propagation and the pruned subspace is of non-direct-product type, it is hard to estimate the CPU-time scaling. Roughly, the CPU-time scales as

$$T_{\text{CPU}} \propto \frac{\tilde{l}_{\max} \tilde{N}_e \tilde{N}_{p/e}^2}{\delta t} \log_{10}(\epsilon^{-1}), \quad (\text{II.2.43})$$

where the quantities decorated with a tilde denote the maximal number of basis functions in \mathcal{A} during the dynamics and ϵ is the accuracy of the propagator.

II.2.4.6. Results

The computed PMDs are shown in Fig. II.2.3. The accuracy goal of $\eta \leq 10^{-2}$ is achieved for the presented results. The computed curve for $E = 0.1U_p$ is accurately described for all values of $\cos(\theta)$. For $E = 10U_p$ and values below $\sim 10^{-12}$, deviations between DP-DVR calculations and the accurate references occur. Due to the very low values, the accuracy goal is still fulfilled. This curve accounts for fast electrons with very high energies. High accuracy requires a large number of DVR points (to take the high momentum into account) and a small WAT (to take the fast motion into account such that many nearest neighbors are added).

The accuracy as a function of the WAT θ is shown in Fig. II.2.4. For $\theta > 10^{-15}$, a double exponential decay of the accuracy with decreasing WAT is visible. Due to the fast electrons that require a rapid addition of nearest neighbors to the set of active basis functions, the values of η are larger for $E = 10U_p$. This is in agreement to Fig. II.2.3. For $\theta \leq 10^{-15}$ and $E = 10U_p$, a plateau in accuracy is reached because other parameters (accuracy of the propagator, number of basis functions, ...) begin to restrict the accuracy. Note that the reference was converged with $\eta \leq 10^{-4}$ such that the curve for $E = 0.1U_p$ and $\theta \leq 10^{-15}$ is probably as accurate as the used reference.

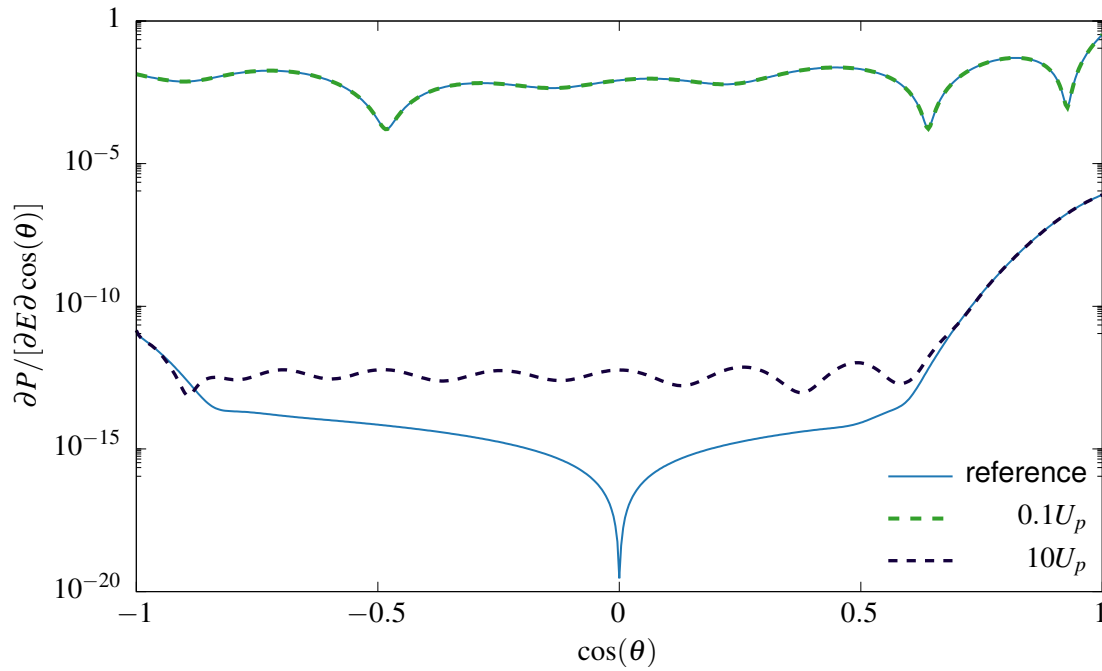


Figure II.2.3.: Computed photoelectron momentum distributions for the two energies $E = \{10U_p, 0.1U_p\}$. The blue curves show the accurate reference values and the dashed curves the DP-DVR results. Note the logarithmic scale.

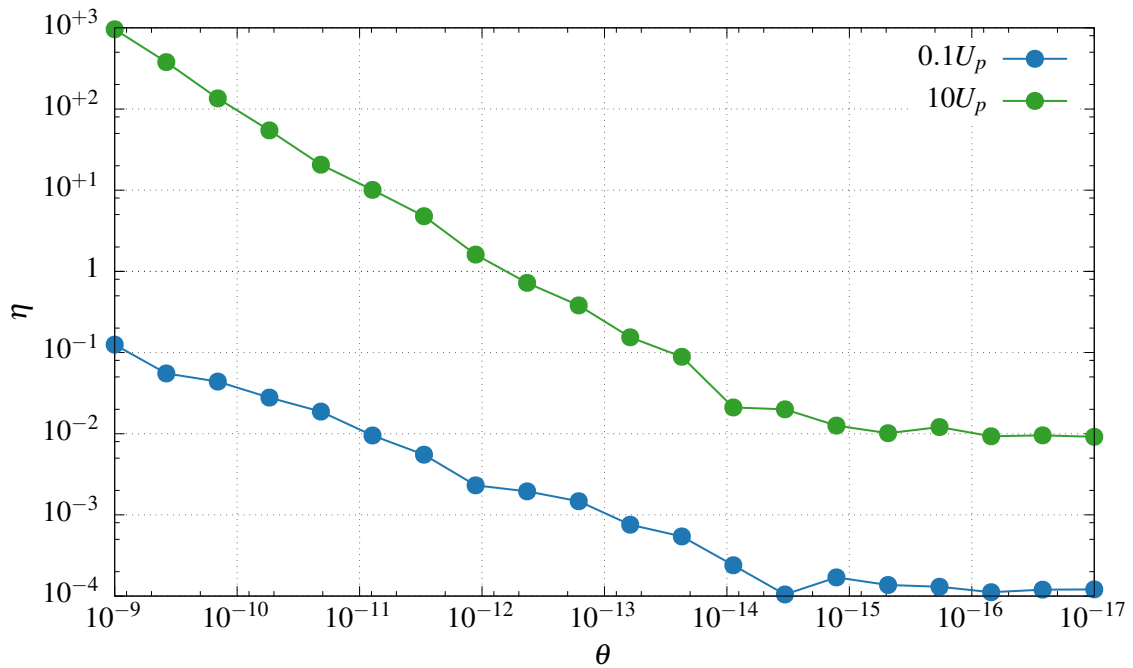


Figure II.2.4.: Accuracy η of the photoelectron momentum distributions as a function of wave amplitude threshold θ for DP-DVR. η is defined in Eq. (II.2.34). Note the logarithmic scales.

The runtime of the **DP-DVR** code is compared against the other methods/codes in [Tab. II.2.1](#). Note that many of the methods employ a “direct-product pruning”. That is, the number of basis functions in the two coordinates is gradually increased during the dynamics by defining something similar to the **WAT**. However, only **DP-DVR** uses a fully non-direct-product pruned space.

Table II.2.1.: Preliminary runtimes for computing the photoelectron momentum distributions. The times are given in minutes:seconds. Here, the methods are presented in an anonymous form and labeled alphabetically. The gauge is either length (L) or velocity (V). Some methods have been used with both gauges. More details will be presented in the final publication. All runs were performed on a single core of an Intel Xeon E5-2687W v3 processor. A subscript F denotes a surface-flux-based method. A superscript l or r denotes a method that uses an adaptive direct-product basis for spherical harmonics (l) and/or the radial expansion (r).

method	gauge	runtime
A_F^r	V	00:13
B^l	L	00:16
C_F	V	00:45
D_F^{lr}	V	00:51
E_F	V	00:59
F_F	V	01:23
F_F	L	02:55
DP-DVR	V	06:18
H	L	08:34
I^l	V	09:45
J^r	L	22:22
K^r	L	31:21
L_F	V	33:15
K^r	V	56:29

The runtime varies dramatically between 13 seconds and one hour. With six minutes and 18 seconds, the runtime of **DP-DVR** gives almost the median value. There are several reasons why **DP-DVR** is not the fastest method. One major reason is probably that the used **SIL** propagator is not the best one for this particular case. As a high grid density is required, the **TDSE** becomes stiff such that standard propagators become less useful. Indeed, many of the methods use Crank-Nicolson-type propagators,^[279] which are implicit differential equation solvers and as such well-suited for stiff problems.^[280] For **DP-DVR**, other propagators than **SIL** have not yet been tested.

Another reason is that not all parts of the code have been optimized. The very fast runtime of only 13 seconds of method A_F^r can only be explained by a careful optimization to this particular problem, including lookup tables for the initial, analytically known wavefunction etc. Indeed,

⁵This was allowed.

during the course of the benchmark, some groups have further optimized the code such that the timing changed drastically.⁵ For example, method E_F has now a runtime of 59 seconds and is faster than DP-DVR (about 6 minutes). Initially, the runtime was about 7 minutes, that is, slower than DP-DVR. Method I^l has now a runtime of almost 10 minutes whereas the initial runtime was 7.5 hours. Since many parts of the DP-DVR code are still written in unoptimized Python, it can be expected that the runtime of DP-DVR can be optimized by a factor of 5 or even more but this only shows how a particular method can be tuned to a very specific problem. Generality gets lost.

Further, DP-DVR currently does not use any surface-flux method which reduces the grid range and thus the amount of required basis functions. Additionally, it should be stressed that DP-DVR works best for higher-dimensional problems where direct-product-like bases become more wasteful.

II.2.4.7. Conclusions and Outlook

To conclude, accurate calculations of PMDs were computed for the hydrogen atom with DP-DVR. Besides a DVR, also spherical harmonics were pruned. It shows that DP is able to perform very accurate calculations and that it is not restricted to DVRs or phase-space bases. The runtimes of the methods in this benchmark study differ drastically and range from 13 seconds to almost one hour. With a runtime of about six minutes, DP-DVR is in between these two extrema. The main reasons why it is not the fastest method are the stiffness of the equations of motion and a not fully optimized code. The former can be handled by using an implicit propagator.

The runtime could further be improved by combining surface-flux methods with DP. This should give major speedups. For this problem, DP-MCTDH dynamics is not useful because the rank of the two-dimensional wavefunction is quite large. This changes when multi-electron systems, including molecules, are considered; see also the following Chapters.

Control of Double Ionization Dynamics of Helium

“Hofstadter’s Law: It always takes longer than you expect, even when you take into account Hofstadter’s Law.”

— Douglas R. Hofstadter

Helium is the simplest atom that shows many-body effects. Already a system this small can lead to puzzling effects in strong laser fields and can be used for introducing new phenomena.¹ One interesting process that appears in strong laser fields is double ionization. It is caused by different mechanisms of the three main types, namely direct, sequential, and nonsequential double ionization. In direct ionization, the energy of one photon is sufficient to ionize both electrons directly. In sequential ionization, one photon ionizes the first electron and a second photon ionizes the remaining electron. For that, the energy of the photon needs to be high (larger than the second ionization potential, $I_2 = 54.4$ eV for helium^[281]) or the intensity needs to be very large such that over-the-barrier ionization can occur.² Nonsequential double ionization appears when the energy of the photon is smaller than the second ionization potential but larger than the first ionization potential, $I_1 = 24.6$ eV. There, similar to the semi-classical three-step model in HHG (Section II.2.2.4), one electron first tunnels through the potential barrier (or is ionized directly), is accelerated into the continuum, is then rescattered back and collides with the remaining electron such that both electrons are ionized. There is also a recollision-excitation mechanism where the remaining electron is first excited into a higher-lying bound state. In a second step, it tunnels through the barrier. This occurs for smaller intensities. There is a vast literature on double ionization in helium and an in-depth review is not within the scope of this thesis. Instead, the reader is referred to recent reviews.^[282-284]

¹See also the next Chapter II.4.

²This is due to the “tilt” of the potential by the amplitude of the field in length gauge; see Section II.2.2.3 for more information.

Another way to look at the mechanism of double ionization is to consider the final relative motion of the electrons. Are they accelerated to the same or to opposite directions? The latter solely arises due to the electronic repulsion and thus is a pure electron-electron correlation effect. Without a phase change, an external field can only accelerate the electrons to the same direction. Thus, the effect of double ionization to opposite directions is controlled only to higher order and indirectly by the laser field. The control of ejection into opposite directions by an external field is the objective of this Chapter. It combines the topics of strong-field physics, many-particle physics, quantum control and, here as an application, dynamical pruning. As such, this is a difficult but fascinating research area.

Due to the singularity of the Coulomb potential, the treatment of the continuum, and the time-dependence of the Hamiltonian, the theoretical simulation is very challenging. In the group of TANNOR, ASSÉMAT ET AL. studied double ionization of a one-dimensional helium model with `PvB` and compared its performance with that of `MCTDH`.^[83] Although they were able to study double ionization dynamics of helium with `PvB`, they could not perform optimizations of the laser field parameters with quantum control algorithms because this requires the ability to perform many different propagations with different fields. This requires short runtime that `PvB`, at its current state, cannot fulfill. In contrast, `DP-DVR` allows for very fast simulation and enabled an in-depth control study. On a standard `CPU`, `DP-DVR` performs even faster than a fast-Fourier-transform-based^[285] propagation on a `GPGPU`. However, it is noted that only preliminary work is presented. There remains much to do to fully understand the system and to obtain useful expressions of external fields that lead to the requested wavefunction dynamics.

In the following, the general formalism of optimal control theory is described in [Section II.3.1](#). Its cousin, local control theory, is briefly described in [Section II.3.2](#). Since helium is a two-electron system, many-particle systems in general are discussed in [Section II.3.3](#). This Section is also needed for [Chapter II.4](#). The particular one-dimensional model system is discussed in [Section II.3.4](#), including more details on the control targets and strategies in [Section II.3.4.3](#). The results are presented and discussed in [Section II.3.5](#) and finally summarized in [Section II.3.6](#).

II.3.1. Quantum Optimal Control Theory

In this Chapter, a term involving a “control operator” $\hat{B}e(t)$ is added to the `TDSE`:

$$i \frac{\partial}{\partial t} |\psi(t)\rangle = \hat{H} |\psi(t)\rangle + \hat{B}e(t) |\psi(t)\rangle, \quad e(t) \in \mathbb{C}. \quad (\text{II.3.1})$$

The time-dependence of the complex- or real-valued scalar function $e(t)$ (the “pulse”) allows the control of the system described by $|\psi\rangle$. Typically, it is controlled by an external electromagnetic field, see [Section II.2.1](#). For example, assuming a linearly polarized field and the dipole approximation, \hat{B} would be proportional to either \hat{x} (length gauge) or \hat{p} (velocity gauge). $e(t)$ would then either be the external field or the external vector potential, respectively. In general, a sum of control operators/fields can be added to the `TDSE`, for example, for describing light

without polarization. Here, without losing generality, only one term is used for the discussion.

In quantum optimal control, the objective is to find an *optimal* function $e(t)$ such that the evolution of $|\psi(t)\rangle$ leads to a predefined goal. Typically, this means that $|\psi\rangle$ at final propagation time T should take a certain form or should give a maximal value for some observable. To give an example, the goal could be to control the dissociation of the molecule ABC either to A + BC or to AB + C, depending on the field parameters.^[286] Other, more complicated goals like optimizing a high harmonic generation (HHG) spectrum are possible as well; see, e. g., Ref. [287]. Further, the field $e(t)$ is often restricted, e. g., to avoid nonphysical solutions (too large values of $e(t)$) or to take experimental constraints into account when determining the optimal field.

Optimal control theory is actually much more general and can be applied to any partial differential equation. Together with feedback control, optimal control is widely used in engineering and cybernetics in general. As such, there is a vast literature on control theory. Just to mention a few, see Refs. [288-291]. Examples of applications in engineering are the control of the movement of an industrial robot^[292,293] and the control of renewable energy source networks.^[294,295] Software packages like CasADi^[296] or GPOPS-II^[297] allow for the control of almost any system of differential equations, treating the control problem as a nonlinear numerical optimization task.

However, as often in numerical applications, a specialization of the numerical procedure to the problem of interest is better than applying a multi-purpose algorithm. Indeed, the TDSE as formulated in Eq. (II.3.1) is actually a so-called bilinear control problem. Rewriting Eq. (II.3.1) as

$$\frac{\partial}{\partial t}|\psi\rangle \equiv |\dot{\psi}\rangle = -i\hat{H}|\psi\rangle - i\hat{X}e(t)|\psi\rangle, \quad (\text{II.3.2})$$

and expressing the operators and state in a basis gives the following matrix-vector equation

$$\dot{\vec{x}} = \mathbf{A}\vec{x} + \mathbf{B}e(t)\vec{x}. \quad (\text{II.3.3})$$

\vec{x} is the vector of basis function coefficients of $|\psi\rangle$. Without absorbing boundary conditions (no CAP), \mathbf{A} and \mathbf{B} are anti-Hermitian matrices. For general matrices, this form is the typical formulation of a bilinear control problem.^[14,288] For comparison, in a linear control problem, the product of $\mathbf{B}e(t)$ with \vec{x} is replaced by $e(t)\vec{b}$, where \vec{b} is constant such that

$$\dot{\vec{x}} = \mathbf{A}\vec{x} + e(t)\vec{b}. \quad (\text{II.3.4})$$

This is much simpler than bilinear control.

The form of bilinear control enables a development of very efficient algorithms. This and a more thorough quantum formulation are described in the next subsections.

II.3.1.1. General Formulation

In the following, only targets will be considered that depend on $|\psi\rangle$ at final propagation time T . This is the most typical application of quantum optimal control. A wide variety of physical

optimization goals can be formulated in terms of a control functional J of the form

$$J = \langle \psi(T) | \hat{O} | \psi(T) \rangle, \quad (\text{II.3.5})$$

which should be maximized.^[14,298-300] \hat{O} is Hermitian and typically a projection operator but this is not required. In the most simple case where $|\psi(t = T)\rangle$ should approach a target state $|\phi\rangle$, \hat{O} takes the form of $|\phi\rangle\langle\phi|$. Loosely speaking, the standard initial-value problem of propagating the TDSE is then broadened to a double-ended boundary value problem where both $|\psi(t = 0)\rangle$ and $|\psi(t = T)\rangle$ are fixed and both $e(t)$ and $|\psi(t \in (0, T))\rangle$ are to be determined.³

The control problem is typically formulated as a variational optimization problem.^[289,291] Additional constraints on the field $e(t)$ and the constraint that $|\psi(t)\rangle$ must be restricted to be a solution of the TDSE can be formulated in terms of Lagrange multipliers. There are different actual formulations of this variational approach. The following form is based on Refs. [301, 302]. It can be derived directly from the so-called Pontryagin's maximum principle which establishes necessary conditions for optimality.^[289,291] Sufficient conditions are given by the more complicated Hamilton-Jacobi-Bellman equation which follows a different approach^[289,291] and is not considered here.

To simplify the equations, the TDSE given in Eq. (II.3.2) is abbreviated as

$$|\dot{\psi}(t)\rangle = |f[\psi, e](t)\rangle. \quad (\text{II.3.6})$$

To take the constraints due to the TDSE and those of the fields into account, a new functional \bar{J} is defined as

$$\bar{J} = J + J_1 + J_2 + J_3, \quad (\text{II.3.7})$$

where

$$J_1 = -2\Re \int_0^T \langle \chi(t) | \dot{\psi}(t) \rangle dt, \quad (\text{II.3.8})$$

$$J_2 = +2\Re \int_0^T \langle \chi(t) | f[\psi, e](t) \rangle dt, \quad (\text{II.3.9})$$

$$J_3 = + \int_0^T \lambda(t) g[e](t) dt. \quad (\text{II.3.10})$$

The functional J_3 constrains the field. Typically, the penalty functional $g[e]$ takes the form

$$g[e](t) = -[e(t) - e^{\text{ref}}(t)]^2, \quad (\text{II.3.11})$$

³With J as formulated as in Eq. (II.3.5), $|\psi(t = T)\rangle$ is *not* fully determined because the rank of \hat{O} can be larger than

where $e^{\text{ref}}(t)$ is some reference field. Particular choices of e^{ref} are discussed later in [Section II.3.1.3](#). $g[e](t)$ in the form of [Eq. \(II.3.11\)](#) restricts the fluence of $e(t)$. $\lambda(t)$ is a Lagrange multiplier. However, typically it is treated as a preset penalty function with $\lambda(t) > 0$ and not optimized, thus acting as a restraint. The smaller $\lambda(t)$, the smaller the contribution of J_3 to \bar{J} and the larger the deviations from e^{ref} that are allowed. J_3 makes the maximization problem overall concave. Without J_3 , $|e(t)|$ could approach infinity.

The second Lagrange multiplier, $\langle \chi(t) |$, is called dual function or costate. When \bar{J} approaches its maximum value, $\langle \chi(t) |$ approaches $\langle \psi(t) |$. Due to [Eq. \(II.3.6\)](#), $J_1 + J_2 = 0$, provided that the TDSE is propagated to high accuracy; compare with the Lagrange formulation of the Dirac-Frenkel variational principle.^[303] The prefactor 2 is introduced to simplify the final expressions.

Requiring $\frac{\partial \bar{J}}{\partial \langle \psi |} \stackrel{!}{=} 0$ yields the following constraints for the dual function:^[302]

$$|\dot{\chi}(t)\rangle = -\frac{\delta J_2}{\delta \langle \psi(t) |} = -i[\hat{H} + \hat{B}e(t)]|\chi(t)\rangle, \quad (\text{II.3.12})$$

$$|\chi(T)\rangle = \frac{\delta J}{\delta \langle \psi(T) |} = \hat{O}|\psi(T)\rangle. \quad (\text{II.3.13})$$

That is, $|\chi(t)\rangle$ must satisfy the TDSE. Together with [Eq. \(II.3.13\)](#), the evolution of the dual function is fully determined as a final-value boundary problem that can be solved by backward propagation. This already hints at an optimization scheme where the initial-value boundary problem for $|\psi(t)\rangle$ is solved by forward propagation, thereby determining $|\chi(T)\rangle$, which in turn allows for a subsequent backward propagation to obtain $|\chi(t \in [0, T])\rangle$. What remains is to find an expression for the values of the field, $e(t)$.

Dropping the explicit time dependence of all quantities, the gradient of \bar{J} with respect to e is then evaluated as

$$\frac{\delta \bar{J}}{\delta e} = 2\Re \left\langle \chi \left| \frac{\delta f[\psi, e]}{\delta e} \right. \right\rangle + \lambda \frac{\delta g[e]}{\delta e}. \quad (\text{II.3.14})$$

Note that the gradient is a function of time and is valid only for a particular $|\psi(t)\rangle$.

Until now, all equations have been written in a functional form. This is useful for obtaining analytical expressions for very simple problems. For solving the equations numerically on the computer, it is more appropriate either to expand $e(t)$ in a basis (Galerkin method^[280]) or to discretize the problem in time, that is, to expand $e(t)$ in a basis of piecewise constant (rectangular) functions. This is the more common approach and described in the following.

II.3.1.2. Time Discretization

Since a propagation of a wavefunction is typically done using short-time propagation for small equidistant time intervals, it is natural to perform a discretization of the field $e(t)$ as well. Thus, the interval $[0, T]$ is discretized in N typically equidistant pieces t_i of spacing $\Delta t = t_1 - t_0$. Using

1. With $\hat{O} = |\phi\rangle\langle\phi|$, $|\psi(t = T)\rangle$ is determined up to a global phase; see also [Section II.3.4.3](#) for another formulation of J .

the notation $\psi(t_i) \equiv \psi_i$, Eq. (II.3.5), (II.3.6) and (II.3.8) – (II.3.10) take the form of

$$J = \langle \psi_N | P | \psi_N \rangle, \quad (\text{II.3.15})$$

$$|\psi_j\rangle = F_{j-1} |\psi_{j-1}\rangle, \quad (\text{II.3.16})$$

$$J_1 = -2\Re \sum_{j=1}^N \langle \chi_j | \psi_j \rangle \Delta t, \quad (\text{II.3.17})$$

$$J_2 = +2\Re \sum_{j=1}^N \langle \chi_j | F_{j-1} | \psi_{j-1} \rangle \Delta t, \quad (\text{II.3.18})$$

$$J_3 = + \sum_{j=1}^{N-1} \lambda_j g_j[e] \Delta t. \quad (\text{II.3.19})$$

F_{j-1} is the propagator; compare with Eq. (II.3.6). Note the upper limit $N - 1$ in Eq. (II.3.19). Since the interval is discretized into N time points, there are $N - 1$ piecewise constant functions defining e . F_{j-1} depends on e_j .

Consequently the gradient of J with respect to e is evaluated as

$$\frac{\delta \bar{J}}{\delta e_i} = 2\Delta t \left[\Re \left\langle \chi_i \left| \frac{\delta F_{i-1}}{\delta e_i} \right| \psi_{i-1} \right\rangle + \lambda_i \frac{\delta g_i[e]}{\delta e_i} \right]. \quad (\text{II.3.20})$$

Note that the magnitude of the gradient depends on the grid spacing Δt .

This definition of the gradient is all one needs to optimize the field e_i using standard optimization routines like conjugate gradient or BFGS.^[304,305] However, there are typically better strategies to perform the optimization task. In particular, if the form of the penalty functional $g[e]$ is that of Eq. (II.3.11) and demanding that Eq. (II.3.20) equals 0 (requiring a stationary point) yields

$$\frac{\delta \bar{J}}{\delta e_i} = 2\Delta t \left[\Re \left\langle \chi_i \left| \frac{\delta F_{i-1}}{\delta e_i} \right| \psi_{i-1} \right\rangle - \lambda_i (e_i - e_i^{\text{ref}}) \right] \stackrel{!}{=} 0, \quad (\text{II.3.21})$$

$$\Leftrightarrow e_i = e_i^{\text{ref}} + \frac{1}{\lambda_i} \Re \left\langle \chi_i \left| \frac{\delta F_{i-1}}{\delta e_i} \right| \psi_{i-1} \right\rangle. \quad (\text{II.3.22})$$

This is equation needs to be solved iteratively because both the optimal e_i and the corresponding ψ_{i-1} are unknown. e_i can be retrieved by means of fixed-point iterations. Using superscripts (p) that denote the iteration, Eq. (II.3.22) is formulated as

$$e_i^{(p)} = e_i^{\text{ref}} + \frac{1}{\lambda_i} \Re \left\langle \chi_i^{(p-1)} \left| \frac{\delta F_{i-1}}{\delta e_i} \right| \psi_{i-1}^{(p-1)} \right\rangle. \quad (\text{II.3.23})$$

This form (with $e_i^{\text{ref}} = 0$) has been used in the early phase of quantum optimal control.^[298] Now, the convenient factor of 2 in Eq. (II.3.8) and (II.3.9) can be explained: It cancels with the factor of 2 stemming from the derivative of the fluence constraint. It is remarkable that this expression is

independent of the grid spacing Δ_t , whereas the expression for the gradient itself involves the spacing. Although the fixed-point iteration is known to be rapidly convergent, Eq. (II.3.23) is costly to evaluate. For that, one needs to know both $|\chi\rangle$ and $|\psi\rangle$ at a given iteration. This means that two propagations are required if $|\psi_i\rangle$ can be stored on disc. Otherwise, another (backward) propagation is required where $|\psi_i\rangle$ is evaluated on the fly. The Krotov method provides an improvement on the above theory and this is explained in the following.

II.3.1.3. Krotov Method

In the Krotov method,^[291] $e^{(p)}$ is computed “on the fly” using the dual function from the *previous* iteration:

$$e_i^{(p)} = e_i^{\text{ref}} + \frac{1}{\lambda_i} \Re \left\langle \chi_i^{(p-1)} \left| \frac{\delta F_{i-1}}{\delta e_i} \right| \psi_{i-1}^{(p)} \right\rangle, \quad (\text{II.3.24})$$

where the only difference compared to Eq. (II.3.23) has been highlighted with red color. Inserting the explicit form of F_{i-1} (see Eq. (II.3.1) and (II.3.6)) gives

$$e_i^{(p)} = e_i^{\text{ref}} + \frac{1}{\lambda_i} \Im \left\langle \chi_i^{(p-1)} \left| \hat{B} \right| \psi_{i-1}^{(p)} \right\rangle. \quad (\text{II.3.25})$$

Although the change compared to the fixed-point iteration is minimal, the effect is huge. In the fixed-point iteration, two propagations have to be performed with the old field $e^{(p-1)}$ before it gets updated. The feedback of the algorithm to the field is delayed. In the Krotov method, $e_i^{(p)}$ is computed on the fly using $|\psi_{i-1}^{(p)}\rangle$ and the previously obtained $|\chi_i^{(p-1)}\rangle$. The feedback is immediate.^[306]

The actual derivation of the Krotov method is more involved and is shown in Refs. [291, 302, 307]. Provided that \hat{O} is a positive semidefinite operator, e. g. a projector, it is shown there that the Krotov method gives monotonic convergence with respect to \bar{J} . If the reference field e^{ref} is set to the field of the previous iteration, $e^{(p-1)}$, the method is even monotonically convergent both with respect to \bar{J} and J .^[302] Otherwise, it can happen that only J_3 is optimized. The property of monotonic convergence is remarkable because black-box gradient-based optimization algorithms like conjugate gradient typically need line searches in the direction of the gradient to obtain monotonic convergence. This is avoided in the Krotov method.

The actual algorithm takes the following form:

$$\text{iteration } 0 : \quad |\psi^{(0)}(0)\rangle \xrightarrow{e^{(0)}(t)} |\psi^{(0)}(T)\rangle, \quad (\text{forward propagation}), \quad (\text{II.3.26})$$

$$\hat{O}|\psi^{(0)}(T)\rangle = |\chi^{(0)}(T)\rangle \xrightarrow{e^{(0)}(t)} |\chi^{(0)}(0)\rangle, \quad (\text{backward propagation}), \quad (\text{II.3.27})$$

$$\text{iteration } p : \quad [|\chi^{(p-1)}(0)\rangle \xrightarrow{e^{(p-1)}(t)} |\chi^{(p-1)}(T)\rangle], \quad (\text{forward propagation}), \quad (\text{II.3.28})$$

$$|\psi^{(p)}(0)\rangle \xrightarrow{e^{(p)}(t)} |\psi^{(p)}(T)\rangle, \quad (\text{forward propagation}), \quad (\text{II.3.29})$$

$$\hat{O}|\psi^{(p)}(T)\rangle = |\chi^{(p)}(T)\rangle \xrightarrow{e^{(p)}(t)} |\chi^{(p)}(0)\rangle, \quad (\text{backward propagation}). \quad (\text{II.3.30})$$

The term in brackets, Eq. (II.3.28), is optional and only needed when there is not enough disk space to save all $|\chi_i^{(p-1)}\rangle$. If there is no better guess, the initial field $e^{(0)}(t)$ can often be set to 0, provided that the initial state, $|\psi(0)\rangle$, is not stationary and that the gradient is large enough.

II.3.1.4. Variants and Extensions

A variant of the Krotov algorithm has been developed by ZHU and RABITZ. For the backward propagation of χ , Eq. (II.3.30), they use Eq. (II.3.23) such that the field is updated twice per iteration.^[300,308] It can be shown that the Krotov and the Zhu-Rabitz variants are two extrema of a more general formulation where, essentially, the expressions from both variants are combined.^[309]

Both variants have convergence problems when J approaches the maximum value. There, methods based on (approximate) Hessians are hard to beat. Consequently, the Krotov method has been combined with the BFGS algorithm in Ref. [302] *without* introducing a costly line search.

A variant for nonlinear Schrödinger equations, that is, formulations like time-dependent Hartree, MCTDH or their formulations for Bosons or Fermions, have been introduced to quantum dynamics in Refs. [310, 311].

More general formulations of field constraints are given in Ref. [312] and expressions for the Hessian/second derivatives with respect to the field are given in Ref. [313]. Extensions to allow more involved field constraints without jeopardizing the monotonic convergence are found in Refs. [314-318].

II.3.1.5. Alternatives

One of the disadvantages of the Krotov method or their variants is the requirement to have a backward propagation. For example, this renders the combination with absorbing boundary conditions difficult because parts of the wavefunction are lost during the propagation and cannot be used for evaluating $|\chi(T)\rangle$. The discretization is a very simple approach and too large a grid density is required if $e(t)$ covers high frequencies for certain times. Adaptive grids are used in engineering control problems but,^[297] to my knowledge, not used in quantum control, although a combination with the Krotov method should be more or less straightforward.

In some situations, the field should/can be described by simple analytic expressions where only a few parameters are to be optimized. Then, a Galerkin-like scheme is much more useful for the optimization. Standard algorithms like conjugate gradient or BFGS that use gradient information have the drawback that a backward propagation is still needed to compute the gradient. Further, these algorithms are very sensitive to numerical noise of the gradient. Hence, derivative-free optimization algorithms^[319] like the Nelder-Mead simplex method or the BOBYQA algorithm^[320] have become popular. In particular, the “chopped random basis”/CRAB scheme has gained increased interest.^[321-323] Therein, the Nelder-Mead method is applied to some basis. To overcome local maxima, the basis parameters are randomly perturbed in each iteration. A hybrid approach that first uses derivative-free optimization and then performs

Krotov iterations on a preoptimized field has been introduced in Ref. [324]. Using heuristic global optimization schemes like genetic algorithms are possible as well.^[325-328] Recently, a new and efficient formulation of a gradient-based approach has been introduced.^[329] See Ref. [330] for a recent review on further developments in quantum optimal control.

II.3.2. Local Quantum Control Theory

In optimal control as described in the previous Section, one searches for a *global* expression of the field $e(t)$ for the full simulation period, $t \in [0, T]$. In contrast, the idea of local control theory is to optimize $e(t)$ *locally* at time t_0 for a small time-interval $t \in [t_0, t_0 + \Delta_t]$.^[331] Local control has already been discussed in 1989 when the research area was founded in molecular quantum dynamics.^[298] There are many different flavors and names (like “tracking”) for local control.^[332-335] In principle, one could already use the Krotov algorithm subsequentially for small time intervals to get some local control scheme, and some expressions actually are derived with this idea in mind.^[332,333] Here, I will follow the simplest and probably most popular variant.^[14,331,336]

Consider again the TDSE as stated in the previous Section in Eq. (II.3.1) on page 182. Consider further some operator \hat{O} whose expectation value $\langle \hat{O} \rangle$ should be optimized. According to the Ehrenfest theorem, the rate of $\langle \hat{O} \rangle$ becomes^[14]

$$\frac{d}{dt} \langle \hat{O} \rangle = i \langle \psi(t) | [\hat{H}, \hat{O}] | \psi(t) \rangle + ie(t) \langle \psi(t) | [\hat{B}, \hat{O}] | \psi(t) \rangle + \left\langle \frac{\partial \hat{O}}{\partial t} \right\rangle. \quad (\text{II.3.31})$$

Provided that \hat{O} does not commute with the control operator, \hat{B} , the temporal change of $\langle \hat{O} \rangle$ can be controlled by an appropriately chosen $e(t)$. This is local control.

In most applications, it is assumed that \hat{O} commutes with \hat{H} and that \hat{O} is time-independent.^[331,332] Then, Eq. (II.3.31) takes the form of

$$\frac{d}{dt} \langle \hat{O} \rangle = ie(t) \langle \psi(t) | [\hat{B}, \hat{O}] | \psi(t) \rangle = e(t) Z(t). \quad (\text{II.3.32})$$

By setting $e(t)$ to $Z^*(t)$, $d\langle \hat{O} \rangle/dt$ is always positive such that $\langle \hat{O} \rangle$ is maximized. Note that this requires a complex-valued $e(t)$. This corresponds to the rotating wave approximations and real fields can be obtained, for example, by taking the average of e and its complex conjugate.^[331] More general forms of local control are discussed in Section II.3.4.3.2.

Compared to optimal control, there is another important difference that needs to be discussed: In local control, a field $e(t)$ is searched for that typically leads to a monotonic increase of $\langle \hat{O} \rangle$ for all propagation times $t \in [0, T]$. In optimal control, a field $e(t)$ is searched for that maximizes $\langle \hat{O} \rangle$ at the *final* propagation time T .^[336] In other words, optimal control algorithms may allow for a *decreasing* $\langle \hat{O} \rangle$ during intermediate times if that helps to maximize its value at final propagation time. An extreme example is discussed in Ref. [337]. This often leads to different pulse shapes and different mechanisms. Another, more practical difference is that local control is not iterative.

No backward propagation and typically only one propagation is required. This makes local control applications very “cheap”.

II.3.3. Many-Particle Systems

In order to apply control theory to the two-particle system helium, common molecular many-particle systems are discussed in the following.⁴ In general, the nonrelativistic, molecular electronic Hamiltonian reads

$$\hat{H}_M = \sum_{i=1}^{N_{\text{el}}} \hat{h}(\vec{r}_i, t) + \sum_{i<j=1}^{N_{\text{el}}} \hat{W}(\vec{r}_i, \vec{r}_j) + \underbrace{\sum_{A<B=1}^{N_{\text{nu}}} \frac{Z_A Z_B}{R_{AB}}}_{=h_{\text{nuc}}}, \quad (\text{II.3.33})$$

$$\hat{h}(\vec{r}_i, t) = -\frac{\Delta_i}{2} - \sum_{A=1}^{N_{\text{nu}}} \frac{Z_A}{r_{iA}} + \hat{v}_{\text{ext}}(\vec{r}_i, t), \quad (\text{II.3.34})$$

$$\hat{W}(\vec{r}_i, \vec{r}_j) = \frac{1}{r_{ij}}, \quad (\text{II.3.35})$$

$$r_{ij} = \|\vec{r}_j - \vec{r}_i\|_2, \quad R_{AB} = \|\vec{r}_B - \vec{r}_A\|_2. \quad (\text{II.3.36})$$

N_{el} is the number of electrons, N_{nu} is the number of nuclei and Δ is the Laplacian. A and B denote indices for the nuclei and i and j indices for the electrons. Z_X is the nuclear charge of atom X . \hat{v}_{ext} is the operator for an external, time-dependent potential, coming from, e. g., an electromagnetic field (see Section II.2.1). It corresponds to $\hat{B}e(t)$ in Eq. (II.3.1). \hat{h} is the one-particle Hamiltonian. The main difficulty arises from the two-particle interaction, \hat{W} , and the resulting electron correlation in the wavefunction.^[338] Note that \hat{W} is *not* of SoP form.

Due to their Fermionic character, the many-electron wavefunction has to be antisymmetric with respect to permutations:⁵

$$\hat{P}_{12}|\varphi_{i_1}\varphi_{i_2}\dots\varphi_{i_{N_{\text{el}}}}\rangle \stackrel{!}{=} -|\varphi_{i_2}\varphi_{i_1}\dots\varphi_{i_{N_{\text{el}}}}\rangle, \quad (\text{II.3.37})$$

where \hat{P}_{ij} permutes particle i with particle j . $|\varphi_i\rangle$ denotes here a *spin orbital* that is composed of a spatial part $|\phi_i\rangle$ and a spin-dependent part $|\omega\rangle$: $|\alpha\rangle$ for spin up and $|\beta\rangle$ for spin down:

$$|\varphi_i\rangle = |\phi_i\rangle \otimes |\omega\rangle, \quad |\omega\rangle \in \{|\alpha\rangle, |\beta\rangle\}, \quad (\text{II.3.38})$$

$$\langle\omega_1|\omega_2\rangle = \delta_{\omega_1\omega_2}. \quad (\text{II.3.39})$$

Antisymmetry can be achieved by using a (normalized) linear combination of Hartree products, that is, by Slater determinants:^[122]

⁴This Section is mostly taken from Ref. [99].

⁵For simplicity, only one particular configuration is shown.

$$|\varphi_{i_2}\varphi_{i_1}\dots\varphi_{i_{N_{\text{el}}}}\rangle_S \equiv \frac{1}{\sqrt{N_{\text{el}}!}} \sum_{\omega \in N_{\text{el}}} \left(\text{sign}(\omega) \bigotimes_{i=1}^{N_{\text{el}}} |\varphi_{\omega(i)}\rangle \right). \quad (\text{II.3.40})$$

$\text{sign}(\omega)$ is equal to 1 if the number of permutations ω is even. Otherwise, it is equal to -1 . The matrix elements of \hat{H}_M , Eq. (II.3.33), represented in a basis of Slater determinants, is called configuration interaction (CI) matrix. Its elements can be evaluated by the so-called Slater-Condon rules;^[122,278] see also Section II.4.1.

In this thesis, only up to two-electron systems, no spin-dependent operators and only singlet states are considered. Then, simplifications arise by formally separating the spin-dependent part from the spatial part:

$$|\varphi_1, \varphi_2\rangle_S = |\Phi_{12}\rangle \otimes |\Omega_{12}\rangle, \quad (\text{II.3.41})$$

where $|\Phi_{12}\rangle$ and $|\Omega_{12}\rangle$ only depend on either the spatial or spin-dependent part, respectively.

Applying the permutation operator yields

$$\hat{P}_{12}|\varphi_1, \varphi_2\rangle_S = -|\varphi_2, \varphi_1\rangle_S \stackrel{\text{either}}{=} [-|\Phi_{21}\rangle] \otimes |\Omega_{21}\rangle \stackrel{\text{or}}{=} |\Phi_{21}\rangle \otimes [-|\Omega_{21}\rangle]. \quad (\text{II.3.42})$$

Depending on the spin quantum number (singlet or triplet state), the sign can be put either in the spatial- or in the spin-dependent part. Assuming a singlet state, $|\Omega_{21}\rangle$ takes the form of^[339]

$$|\Omega_{21}\rangle \stackrel{\text{singlet}}{=} 2^{-1/2}[|\alpha_1\beta_2\rangle - |\beta_2\alpha_1\rangle]. \quad (\text{II.3.43})$$

This is a Slater determinant and as such antisymmetric. Hence, the remaining spatial part in Eq. (II.3.42) has to be symmetric. In contrast, for triplet states and a spin projection number M_S of 0, $|\Omega_{21}\rangle$ takes the form of

$$|\Omega_{21}\rangle \stackrel{\text{triplet}}{=} \begin{cases} 2^{-1/2}[|\alpha_1\beta_2\rangle + |\beta_1\alpha_2\rangle], & M_S = 0, \\ |\alpha_1\alpha_2\rangle, & M_S = +1, \\ |\beta_1\beta_2\rangle, & M_S = -1, \end{cases} \quad (\text{II.3.44})$$

for a particular spin projection number M_S . In all cases, the spin part of a triplet state is symmetric and the spatial part in Eq. (II.3.42) has to be antisymmetric.

Since \hat{H}_M does not depend on spin and singlet states are typically of interest, all calculations can be solely performed with a spatial description of the wavefunction, provided that the spatial part is symmetric.

II.3.4. The One-Dimensional Helium Model

In three-dimensional helium, the motion of the electrons is governed by a central potential, that is, a potential that only depends on the distance between the particles and not their individual Cartesian components; see Eq. (II.3.33). Thus, it should be possible to describe some of the essential features of the three-dimensional system by a one-dimensional model potential. This is described in the following Section II.3.4.1. Afterwards, an appropriate coordinate system for taking the Fermionic symmetry into account is described in Section II.3.4.2 and the combination with control discussed in Section II.3.4.3.

II.3.4.1. Model

The one-dimensional model potential cannot be simply a cut through the three-dimensional Cartesian potential because the singularity of the Coulomb potential divides the one-dimensional coordinate into two pieces. This hinders the electrons to move from one piece to the other. Instead, a somewhat arbitrary regularization of the Coulomb potential is performed and the one-dimensional two-electron Hamiltonian takes the overall two-dimensional form of

$$\hat{H}^a = -\frac{1}{2} \frac{\partial^2}{\partial x_1^2} - \frac{1}{2} \frac{\partial^2}{\partial x_2^2} + V^a(x_1, x_2), \quad (\text{II.3.45})$$

$$V^a(x_1, x_2) = \sum_{i \in \{1,2\}} -\frac{c_n}{\sqrt{x_i^2 + \alpha_n^2}} + \frac{c_e}{\sqrt{(x_1 - x_2)^2 + \alpha_e^2}}, \quad (\text{II.3.46})$$

$$\hat{B}_l^a = c_e(x_1 + x_2), \quad (\text{II.3.47})$$

$$\hat{B}_v^a = -i c_e \left(\frac{\partial^2}{\partial x_1^2} + \frac{\partial^2}{\partial x_2^2} \right), \quad (\text{II.3.48})$$

where x_i is the coordinate of electron i . \hat{B}_l^a (\hat{B}_v^a) describes the perturbation by the external field in length (velocity) gauge. α_n and α_e are the regularization parameters. In this model, the nuclear and electronic charges, c_n and c_e , are additional parameters. Typically, these parameters are fitted to match the lowest energies of the full three-dimensional helium atom. See Ref. [340] for particular parameters. In principle, the regularization is only needed at the singularity. To avoid a perturbation of the long-range part of the Coulomb potential, BANDE ET AL. have modified α^2 with a distance-dependent exponential damping:^[341] $c/\sqrt{(x_1 - x_2)^2 + \alpha^2} \exp[-\beta|x_1 - x_2|]$. Here, a simpler form without any damping is considered where $c_n = 2$, $c_e = 1$, $\alpha_n = \alpha_e = 0.739707902 \equiv \alpha$.^[83] This regularization leads to a match of the exact ground state energy of the helium atom.

II.3.4.2. Coordinate System

As elaborated in Section II.3.3, the Fermionic nature of a two-electron singlet system leads to a symmetric spatial wavefunction with respect to coordinate exchange:

$$\psi(x_1, x_2) \stackrel{!}{=} \psi(x_2, x_1). \quad (\text{II.3.49})$$

Symmetry can be straightforwardly exploited by rotating the coordinate system by 45° . New rotated coordinates u and v are defined as:

$$u = \frac{x_1 + x_2}{2}, \quad v = \frac{x_1 - x_2}{2}, \quad (\text{II.3.50})$$

$$u + v = x_1, \quad u - v = x_2. \quad (\text{II.3.51})$$

Exchange of x_1 and x_2 leads to a sign flip in v . Accordingly, the wavefunction is axially symmetric in v ,

$$\psi(u, v) = \psi(u, -v). \quad (\text{II.3.52})$$

Besides the revelation of symmetry, this coordinate system allows for a very easy interpretation of the wavefunction in terms of the movement of the electrons with respect to each other; see Fig. II.3.1. v describes a symmetric stretch (Fig. II.3.1a) and u an antisymmetric stretch (Fig. II.3.1b). Large values of v (compared to u) mean large separations of the two electrons: They are on different sites of the nucleus. In contrast, large values of u (compared to v) mean that they are on the same site of the nucleus and they approach each other with decreasing v .

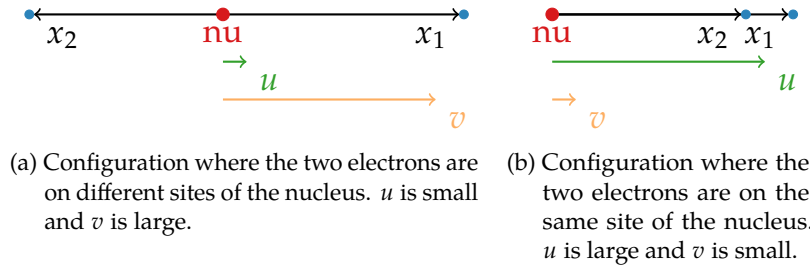


Figure II.3.1.: Depiction of the rotated coordinates for one-dimensional helium; see Eq. (II.3.50). The red filled circle marks the point of origin where the nucleus is located. x_i corresponds to the coordinate of electron i .

The Hamiltonian and the field-interaction operators in this rotated coordinate system are given as

$$\hat{H}^s = -\frac{1}{4} \left(\frac{\partial^2}{\partial u^2} + \frac{\partial^2}{\partial v^2} \right) + V^s(u, v), \quad (\text{II.3.53})$$

$$V^s(u, v) = \frac{1}{\sqrt{(2v)^2 + \alpha^2}} - \frac{2}{\sqrt{(u+v)^2 + \alpha^2}} - \frac{2}{\sqrt{(u-v)^2 + \alpha^2}}, \quad (\text{II.3.54})$$

$$\hat{B}_l^s = 2u, \quad (\text{II.3.55})$$

$$\hat{B}_v^s = -i \frac{\partial}{\partial u}. \quad (\text{II.3.56})$$

Compared to Eq. (II.3.46), the used charge parameters have already been inserted in these equations.

The potential $V^s(u, v)$ is shown in Fig. II.3.2. Compared to the unrotated system, the repulsive electron-electron interaction is peaked along the $v = 0$ line and the attractive electron-nuclear interaction is peaked along the diagonal $u = v$ lines. Along these diagonals, one electron is ionized and another remains near the nucleus. At the origin, both electrons stay at the nucleus.

As a side note: Since the electron-nuclear interaction is larger in magnitude, this coordinate system actually increases the amount of correlation in MCTDH wavefunctions. However, this is unimportant for FCI calculations as they occur with DP-DVR.

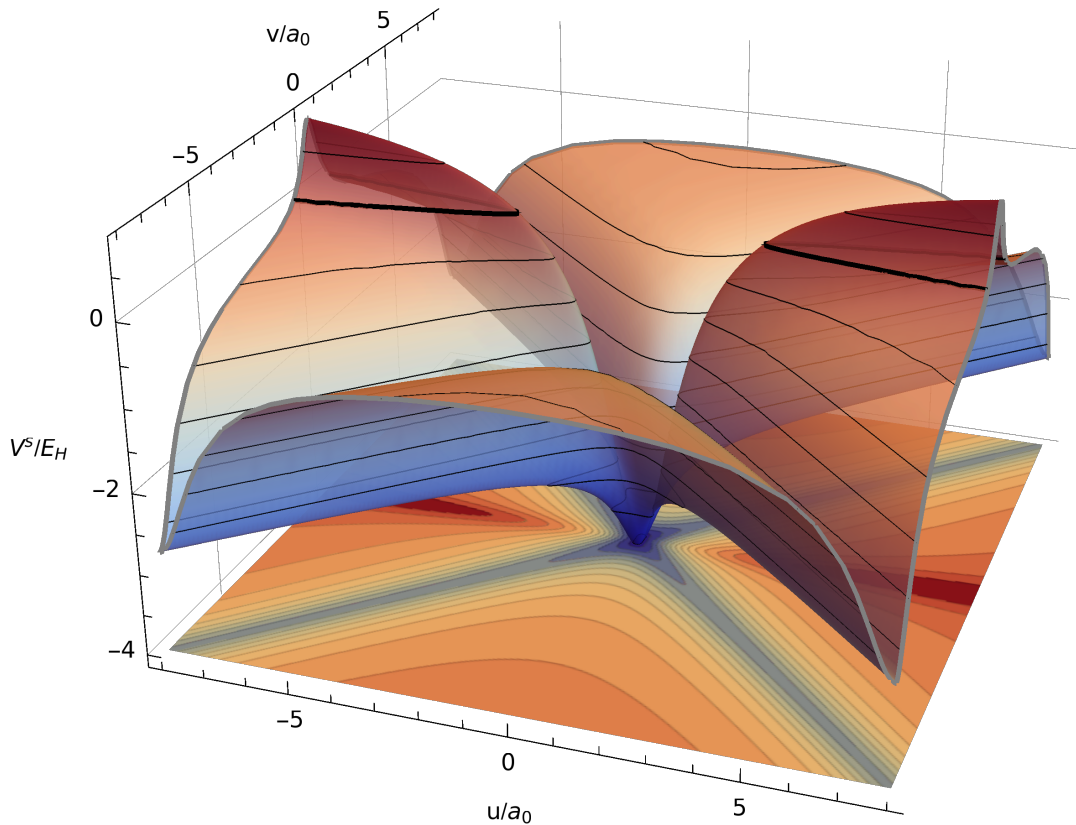


Figure II.3.2.: Potential $V^s(u, v)$ of the helium model in the rotated coordinate system. The contour line at $V^s(u, v) = 0$ is highlighted by thicker lines. Note the axial symmetry of the potential.

II.3.4.3. Control Targets and Control Strategies

In the continuum, there are three regions with different characteristics. They are shown schematically in Fig. II.3.3. S corresponds to single ionization. D_1 (D_2) corresponds to double ionization where the electrons are ionized into different (same) directions. When double ionization occurs, S is typically occupied as well. An external field only couples with the u direction. That is, both electrons are accelerated into the same direction; compare with Eq. (II.3.55) and (II.3.56). If the perturbation induced by the external field is stronger than the Coulomb repulsion of the electrons, they mainly occupy region D_2 . Typically, both regions D_2 and D_1 are

occupied but, due to the perturbation induced by the field, there is a substantially larger fraction of the wavepacket in region D_2 or the fraction in region D_2 has not its main component along the $u = 0$ line.

Here, the objective is to revert this situation and to increase the occupancy of region D_1 , compared to region D_2 . The optimal target would be a wavepacket that is doubly ionized but centered at the $u = 0$ line. Since the external laser field couples only with the u direction, this can solely be achieved by a tricky interplay between the laser field and the repulsion of the electrons.

In the following, possible target states are discussed for both optimal and local control. The initial state is always the ground state of helium.

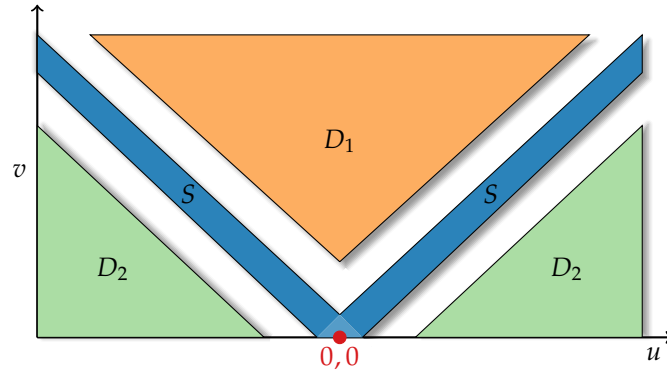


Figure II.3.3.: Regions of the one-dimensional helium atom in the continuum for the rotated coordinate system. The red dot marks the origin where the ground-state density is peaked. The blue region S corresponds to single ionization and the two regions $D_{\{1,2\}}$ denote double ionization and are not connected. D_1 (D_2) corresponds to double ionization where the electrons are ionized into different (same) directions. The white region in between denotes an intermediate between single and double ionization. The regions are only shown for values of v larger or equal to zero. For negative values, the schematic is mirrored; compare with the plot of the potential in Fig. II.3.2.

II.3.4.3.1. Optimal Control

With the goal to increase the occupancy in region D_1 in mind, it is natural to use a target state, called $|\phi\rangle$, as an optimization goal. With a target state, the operator for the field optimization corresponds to a projector $\hat{O} = |\phi\rangle\langle\phi|$ and the functional \bar{J} becomes

$$\bar{J} = \langle\psi(T)|\hat{O}|\psi(T)\rangle = |\langle\psi(T)|\phi\rangle|^2, \quad (\text{II.3.57})$$

see Eq. (II.3.5). In the Krotov algorithm, the dual function at time T is then formed by

$$\hat{O}|\psi(T)\rangle = \langle\phi|\psi(T)\rangle \cdot |\phi\rangle. \quad (\text{II.3.58})$$

This causes a vanishing dual function if $|\langle \phi | \psi(T) \rangle|$ approaches 0 which can occur for bad initial fields. To avoid this, one can minimize

$$\|\psi(T) - \phi\|^2 = \langle \psi(T) | \psi(T) \rangle - \langle \phi | \phi \rangle - 2\Re \langle \psi(T) | \phi \rangle, \quad (\text{II.3.59})$$

which corresponds to a maximization of $\Re \langle \psi(T) | \phi \rangle$.^[300] Then, $|\chi(T)\rangle$ is simply $|\phi(T)\rangle$ and there is no trouble with vanishing overlap between the final wavefunction and the target state. Further, this particular goal fixes the global phase of the target.

Possible forms of $|\phi\rangle$ that have been tried out in this study are now discussed. To increase the occupancy in region D_1 , it is useful to use a Gaussian located in region D_1 and centered along $u = 0$ as target state:

$$\langle uv | \phi \rangle = N \exp(-\alpha u^2) \exp[-\alpha(v - v_0)^2 + ip_0(v - v_0)], \quad (\text{II.3.60})$$

where N is an appropriate normalization factor. Since the electrons should move into opposite directions, there should be no momentum in u but a positive momentum in v . The Gaussian should be located in v somewhere in the continuum. Different parameters were tested and they were typically set to $v_0 = 70$, $\alpha \sim 2/39$ and $p_0 \sim 1-3$.⁶

A Gaussian might be a useful starting point but may not be very physical because neither the initial wavepacket nor final wavepackets obtained from typical laser pulses have forms that look like Gaussians. As an alternative, the wavepacket was propagated with an actual external field and the part of the final wavefunction located in D_1 was used as a target state. The used field was (in length gauge)

$$e(t) = E_0 \sin(\omega t) \sin(\pi t/T)^2, \quad (\text{II.3.61})$$

with $E_0 \approx 0.17$ (corresponding to a field intensity of $10^{15} \text{ W cm}^{-2}$), $T \approx 28$ (that is, a full width at half maximum of 0.25 fs) and $\omega = 2.57$ (corresponding to 70 eV) and the wavefunction has been propagated for $T = 60 \hat{\approx} 1.45$ fs. It is shown on the left panel of Fig. II.3.4. The right panel shows the normalized target state. It is the final wavefunction multiplied with a mask function $M_{\square}(u, v)$ based on tanh functions:

$$M_{\square}(u, v) = \{-[\tanh(u - u_0) + 1] + [\tanh(u + u_0) + 1]\} / 2 \cdot \{-[\tanh(v - v_s) + 1] + [\tanh(v - v_e) + 1]\} / 2, \quad (\text{II.3.62})$$

with $u_0 = -40$, $v_s = 50$ and $v_e = 90$.

Another way to formulate a target state would be to make it *dependent* on $|\psi(T)\rangle$. After each propagation, parts of $\psi(T)$ that lie inside the region of D_1 are extracted by the mask function $M_{\square}(u, v)$ or a Gaussian to define a new target state.

All three discussed targets try to maximize the wavefunctions occupancy in region D_1 . It

⁶As noted in Chapter I.1, atomic units are used unless explicitly stated otherwise.

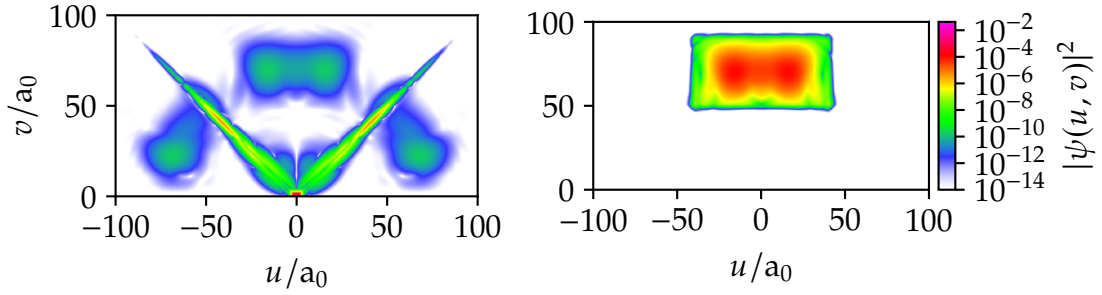


Figure II.3.4.: Square of the wavefunction (left panel) after the propagation with the field shown in Eq. (II.3.61). The right panel shows the wavefunction after the application of a mask function and subsequent renormalization. This is used as a target state for optimal control. Note the logarithmic scale of the colormap. The colormap is taken from Ref. [342] and applies to both panels.

turned out that an additional minimization of the occupancy in region D_2 is important to get more useful results (see Section II.3.5.1.1). Then, the target operator is $\hat{O} = |\phi_1\rangle\langle\phi_1| - |\phi_2\rangle\langle\phi_2|$, where $|\phi_i\rangle$ is located in region D_i . This corresponds to a min-max optimization. Note that this operator is not positive and as such, the Krotov algorithm is not monotonically convergent, although there are ways to retain monotonicity.^[311] More problematic is that it is not clear how $|\phi_2\rangle$ should look like. A Gaussian has been tried with the following form

$$\langle uv | \phi_2 \rangle = N \exp[-(|u| - v - v_0)^2/\alpha - (v - v_0)^2/\alpha], \quad (\text{II.3.63})$$

with $v_0 = 25$ and $\alpha = 1/80$. Additionally, a $|\psi(T)\rangle$ -dependent state has been tested for $|\phi_2\rangle$. Triangular functions like those shown in Fig. II.3.3 are inappropriate because they occupy a large area in coordinate space and are not very physical. The former property decreases the performance of DP-DVR.

II.3.4.3.2. Local Control

Similar to optimal control, one first needs to define an appropriate operator \hat{O} for the local control optimization. From the previous discussion (and from the results presented in Section II.3.5.1.1), it makes sense to maximize the expectation value of a function defined in coordinate space, $o(u, v)$.

In length gauge, \hat{B} commutes with operators defined in coordinate space such that no field-dependent expressions are obtained to first order. In velocity gauge, this is not the case and Eq. (II.3.31) takes the form of

$$\begin{aligned} \frac{d\langle o(u, v) \rangle}{dt} = & e(t)\langle o_u(u, v) \rangle \\ & - \frac{i}{4} (2\langle o_v(u, v) \partial_v \rangle + \langle o_{vv}(u, v) \rangle + 2\langle o_u(u, v) \partial_u \rangle + \langle o_{uu}(u, v) \rangle), \end{aligned} \quad (\text{II.3.64})$$

where $o_{uu}(u, v) = \frac{\partial^2 o(u, v)}{\partial u^2} \equiv \partial_u^2 o(u, v)$ and so on. As noted in Section II.3.4.3, the field only couples with the u direction. This is evident from the form of Eq. (II.3.64), where $e(t)$ solely couples with $\langle o_u(u, v) \rangle$.

Forms of $o(u, v)$ like $v^2 - u^2$ lead to *no* coupling to first order with the field. Then, coupling appears only to second order. The expression of the second derivative of an expectation value leads to

$$\begin{aligned} \frac{d^2 \langle \hat{O} \rangle}{dt^2} = & - \langle [[\hat{O}, \hat{H}], \hat{H}] \rangle - i \frac{de(t)}{dt} \langle [[\hat{O}, \hat{B}]] \rangle \\ & - e(t) \{ \langle [[\hat{O}, \hat{H}], \hat{B}] \rangle + \langle [[\hat{O}, \hat{B}], \hat{H}] \rangle \} \\ & - e(t)^2 \langle [[\hat{O}, \hat{B}], \hat{B}] \rangle. \end{aligned} \quad (\text{II.3.65})$$

The derivation is straightforward by applying the Ehrenfest theorem to $d\langle \hat{O} \rangle/dt$ (see Eq. (II.3.31)). Since $d\langle \hat{O} \rangle/dt$ contains $e(t)$, $de(t)/dt$ appears in the second derivative of $\langle \hat{O} \rangle$. Further, a term with $e(t)^2$ appears. In an actual optimization scheme, $de(t)/dt$ can be approximated by finite differences. This gives a quadratic equation for $e(t)$ that can be used for requiring that $\frac{d^2 \langle \hat{O} \rangle}{dt^2}$ is always a constant value. However, this scheme turned out to be very unstable in this study and is not pursued further.

Instead, forms that look like $o(u, v) = \tilde{o}(u) \cdot \check{o}(v)$ are discussed where Eq. (II.3.64) can be used directly. This equation has the form of

$$\frac{d\langle o(u, v) \rangle}{dt} \equiv C = e(t)\mathcal{A}(t) + \mathcal{Y}(t). \quad (\text{II.3.66})$$

Since $\mathcal{Y}(t)$ is not zero, the simple strategy of setting $e(t)$ to $\mathcal{A}^*(t)$ does not work. Instead, C needs to be taken as a constant, giving

$$e(t) = \lambda \frac{C - \mathcal{Y}(t)}{\mathcal{A}(t)}. \quad (\text{II.3.67})$$

Here, $\mathcal{A}(t)$ often can take very low values below 10^{-11} such that a scaling factor λ is introduced in order to have a reasonable magnitude of $e(t)$.

The fact that $e(t)$ is complex leads to further difficulties because this means that $e(t)\hat{B}$ is not Hermitian. As a simple example, consider the length gauge where $\hat{B} \propto u$. Then, $e(t)\hat{B}$ is actually a complex potential. For negative values of $\Im u$, it behaves like a CAP and for positive values, it does the opposite and leads to a dramatic increase of the norm. To avoid this, $e(t)$ is made real-valued by modifying it to $[e(t) + e^*(t)]/2$.

Due to the complex-valuedness and the division by $\mathcal{A}(t)$, this approach of local control has some flaws. Another disadvantage is that only the first derivative is optimized. For high-frequency fields, this requires very small time steps. As another local control algorithm, a “simple man” approach was followed and the increase of the expectation value from time t_0 to $t_0 + \Delta_t$ was

maximized:

$$\max \langle \psi(t_0 + \Delta_t) | \hat{O} | \psi(t_0 + \Delta_t) \rangle, \quad (\text{II.3.68})$$

where

$$|\psi(t_0 + \Delta_t)\rangle = \exp[-i(\hat{H} + e(t_0 + \Delta_t/2) \cdot \hat{B})\Delta_t] |\psi(t_0)\rangle. \quad (\text{II.3.69})$$

It means that at each time step t_0 the field $e(t_0 + \Delta_t/2)$ is varied such that the expectation value of \hat{O} at time $t_0 + \Delta_t$ is maximized. This is a simple one-dimensional optimization problem and there are methods like Brent's algorithm that solve this problem within a few iterations.^[144,343] Nevertheless, this requires the application of many short-time propagations (typically 5 to 10 for each time step) until the optimal field is found. However, it has the advantage that there are no further parameters like λ and its implementation is straightforward. To the best of my knowledge, such a simple strategy has not been tried before. In order to avoid too large values and too rapid increases of $e(t)$, the optimization is performed such that $e(t_0 + \Delta_t/2)$ is bounded by

$$e_{\max} \geq |e(t_0 + \Delta_t/2)| \leq 2|e(t_0)|. \quad (\text{II.3.70})$$

II.3.5. Results and Discussion

In the following, some results from the optimization procedures are presented. As already mentioned in the introduction, the use of DP-DVR was crucial to do many propagations in a small amount of time. To give a comparison of runtimes, the ground state of the one-dimensional helium system was propagated with the field from Ref. [83] on a grid with range $[-400, 400]$ and with a basis size of 4098^2 . A fast-Fourier-transform-based^[285] propagation until $T = 450$ on a Nvidia Tesla K80 GPGPU took almost two and a half days of runtime whereas DP dynamics with a sinc DVR propagation on six cores of Intel(R) Xeon(R) CPU E5-2650 v2 processors (where other computations ran simultaneously on other cores on that computing node) took only about one day and reproduced the essential features of the wavefunction. This was *before* the symmetrized coordinate system was used and before the Toeplitz structure of the matrices was exploited (see Publication 5 (Section II.1.1), Section III.A). Especially the latter is very important in this case because the one-dimensional basis size is big and a one-dimensional operator matrix is as large as the unpruned two-dimensional wavefunction. Note that only the DVR in the u coordinate has operator matrices with Toeplitz structure because the symmetrization in v destroys this structure. Symmetrization is done by centering the grid around $v = 0$ and using appropriate linear combinations of DVR functions peaked at positive and negative coordinate values.

As a side note: Also DP dynamics using pWs has been tried, representing the potential matrix either in SoP form or as a full two-dimensional operator. In any case, the propagation is much

slower than DP-DVR. However, it should be noted that the performance of DP-DVR heavily depends on the occupancy in coordinate space. For particular external fields with small intensities that do not lead to major ionization, a propagation takes only minutes to a few hours. However, once major regions in coordinate space are covered, the runtime can be more than two days. This is especially a problem for the Krotov method because for bad initial fields or some operators \hat{O} , $|\chi(t)\rangle$ often covers large regions in coordinate space. Calculations using DP-MCTDH have been initially performed but were not further used to avoid an increase in complexity of the methodology. For these kind of problems, MCTDH is very sensitive to the regularization parameter which increases the level of noise in the wavefunction and thus has to take very low values.⁷

It should be emphasized that the following results are not final. The optimization is very difficult and the problem and choice of optimal targets is not yet fully understood. A plethora of optimization runs (more than 500 individual runs for both optimal and local control, resulting in several months of computation) was performed but only some selected results are shown, mostly because many of them were not satisfactory.

II.3.5.1. Optimal Control

In the following, the aforementioned basis on a grid of $u \in [-400, 400]$ and $v \in [0, 400]$ (symmetrized) is used with a sinc DP-DVR together with a WAT of typically 10^{-8} . Only the velocity gauge is used for the propagation because this gauge is typically very efficient for ionization dynamics,^[249] although for few-cycle pulses, the length gauge might be preferable.^[345]

The propagation time is set to $T = 60 \hat{\approx} 1.45$ fs. Clearly, this is a very short time duration. However, the initialization of the electron ejection is important in this control study. For the control target, it does not make sense to control the motion of the electrons when they are already ionized and are located far out in the continuum. There is also a practical aspect of this short time, namely a faster runtime which is important for optimal control because typically, many iterations are required. Once the mechanism is better understood, larger propagation times can be tested.

II.3.5.1.1. Krotov Optimization

Although some variants mentioned in Section II.3.1.5 were tested, the standard Krotov algorithm is used for the following results. The Lagrange multiplier for the field constraints is taken as

$$\lambda(t) = \lambda_0 + 100\{\exp(-12t) + \exp[-12(T - t)]\}. \quad (\text{II.3.71})$$

The smaller λ_0 , the larger the changes in the field amplitude can be. The term with the exponentials ensures that the field starts and ends with negligible values. A zero amplitude of the vector potential $e(t)$ (velocity gauge) at the end of the propagation is important to ensure time-integrated zero area of the field in length gauge. A vanishing vector potential at a certain

⁷There is new work on MCTDH where the coefficient tensor and not the density matrices is regularized.^[344] This could be useful for ionization dynamics.

time means that the integral of the field up to that time is zero; compare with Eq. (II.2.13) on page 167. A non-zero integral of the field is not physical.^[346]

As mentioned in Section II.3.1.3, it is crucial to set e^{ref} to the solution from the previous iteration. Otherwise, it can happen that only J_3 is optimized and \bar{J} decreases during the optimization, especially for bad initial pulses where $\bar{J} \approx 0$.

In the following, results for the target state $|\phi\rangle$ from Fig. II.3.4 are presented. Here, the initial pulse is the same as that used for computing the target state. Thus, it already has enough overlap with the wavefunction at final time such that the standard projector $|\phi\rangle\langle\phi|$ is applicable for the optimization procedure. However, $|\chi(T)\rangle$ is normalized in order to ensure having always the same accuracy for DP-DVR propagations with constant WAT. A normalization of $|\chi(T)\rangle$ corresponds to a change in λ for each iteration.

The various $e^{(p)}$ and values of the objectives as a function of the iteration number are depicted in Fig. II.3.5. Note how the maximum of the field shifts to larger time (panel II.3.5a) and how the maximal field amplitude increases (panel II.3.5b) with each iteration. The field amplitudes might be too large for the dipole approximation. $E = 1$ corresponds to $3.5 \times 10^{16} \text{ W cm}^{-1}$ and $E = 4$ corresponds to $5.6 \times 10^{17} \text{ W cm}^{-1}$. Too large values are ignored in this initial study of this model system and it is assumed that the dipole approximation is valid.

The objectives are shown in panel II.3.5c. Note that both \bar{J} and $J = \bar{J} + J_3$ increase monotonically with each iteration. However, a plateau is reached at iteration 50 and no significant increase in the objective is notable, even though the amplitude of the field amplitude still increases, but the shape of the field does not change drastically beyond iteration 50; compare with panel II.3.5a.

Hence, it seems that the optimization procedure is near the supremum with $J \sim 0.2$. The square of the wavefunction for the optimized field at different propagation times is shown in Fig. II.3.6. Although the optimization procedure is near the supremum, the wavefunction at final time looks not as expected with a clear maximum in region D_1 (and S). As the wavefunction propagated with the initial pulse (left panel in Fig. II.3.4), the wavefunction at final propagation time (panel II.3.6d) has equal contributions in *both* regions D_1 and D_2 even though the target has only contributions in region D_1 (see right panel in Fig. II.3.4).

As an alternative, the min-max optimization explained in Section II.3.4.3.1 was tried. There, the overlap with a target state in region D_1 (D_2) should be maximized (minimized). Although different targets have been tried, the goal of obtaining a wavefunction that clearly is localized in region D_1 could not be reached.

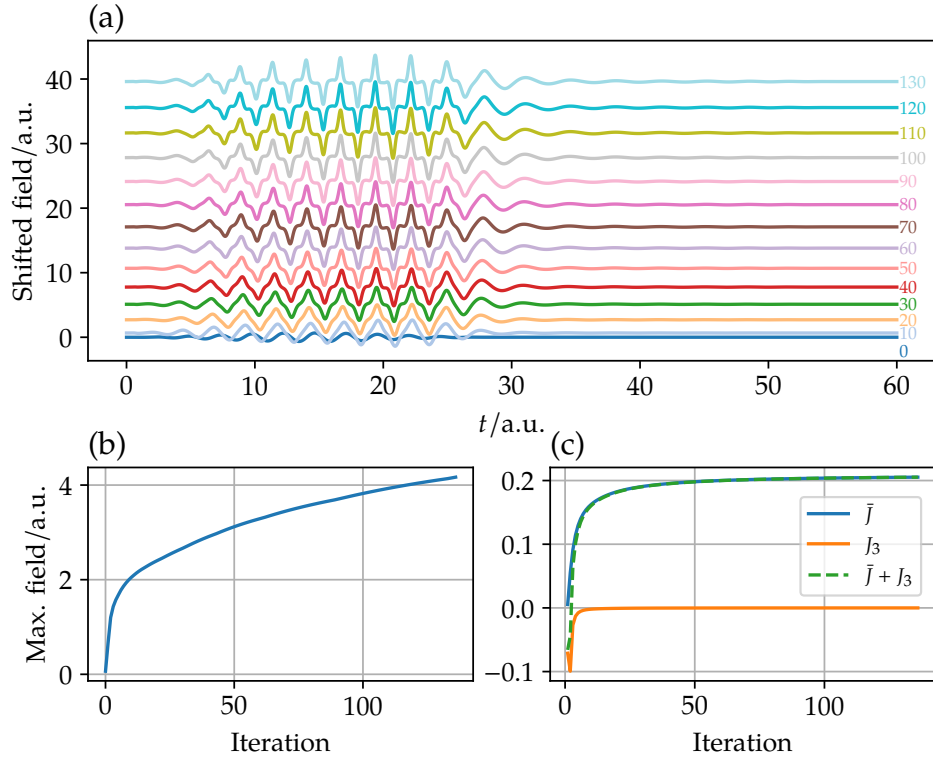


Figure II.3.5.: Behavior of the Krotov optimization for the target state shown in the right panel of Fig. II.3.4. Panel (a) shows the scaled field (vector potential in velocity gauge) for different iterations (numbers to the right). The magnitude and shift is arbitrary. Panel (b) shows the maximal amplitude of the field versus iteration. Panel (c) shows the functionals \bar{J} and J_3 as a function of iteration. Note that $J_1 + J_2 \approx 0$. For J_3 , the reference field e^{ref} is the field from the previous iteration e^{p-1} . The multiplier λ from Eq. (II.3.71) was used with $\lambda_0 = 0.05$.

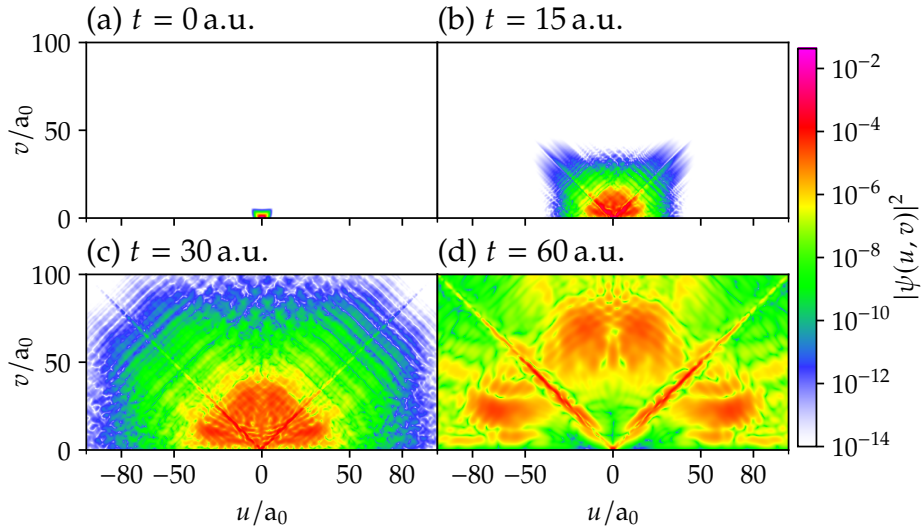


Figure II.3.6.: Square of wavefunction for different propagation times for the field shown in Fig. II.3.5 (a) (iteration 130). Note that the actual coordinate range is larger and ranges up to 400; see text for details.

As a side note: Many of the optimization procedures are quite sensitive and it happened often that the field took very unphysical forms with extremely large values and/or many oscillations. One example is shown in Fig. II.3.7, where the field “explodes” within two control iterations. This leads to numerical instabilities for both the pruning procedure and the propagator. Changing the optimization procedure to avoid too large amplitudes with too large frequency components is possible^[316] but leads to a very slow convergence (at least in this particular case).

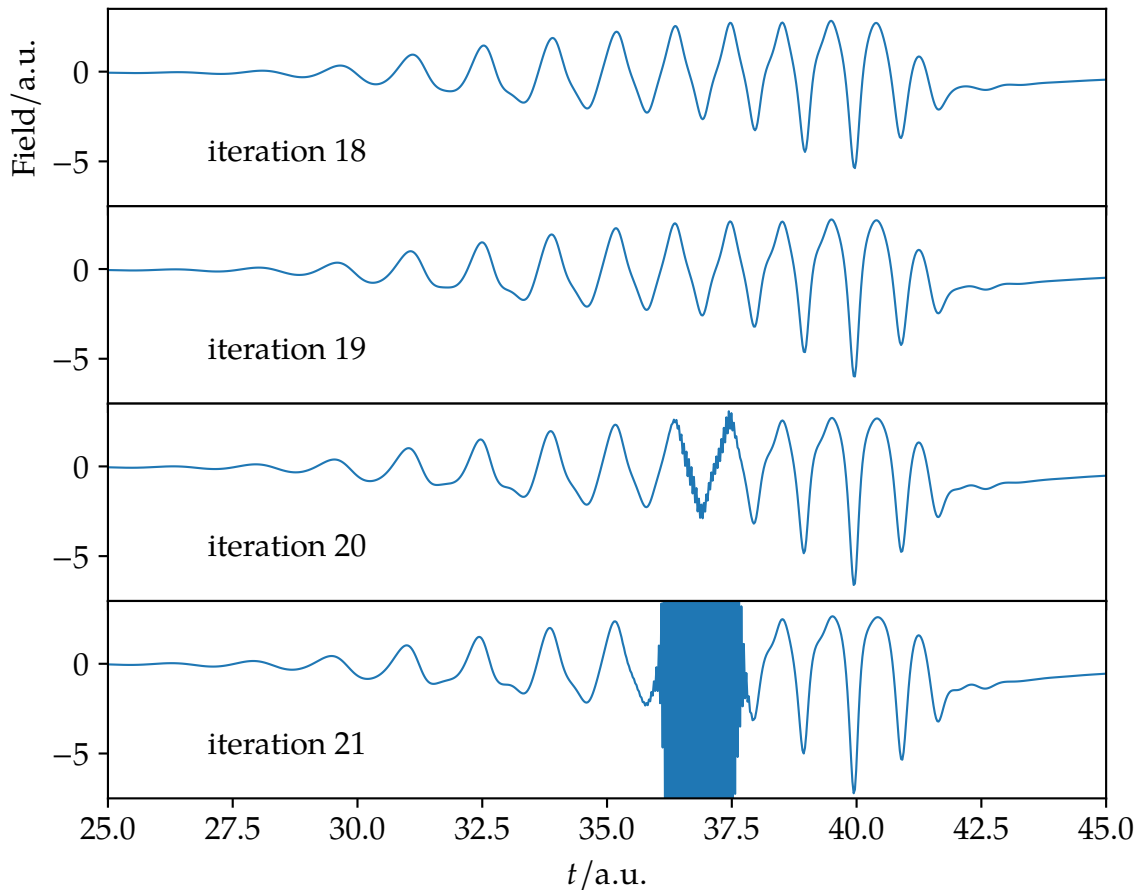


Figure II.3.7.: Exemplary field for different Krotov iterations where the field quickly takes on very large values and very large frequency components. The field at iteration 21 reaches values of up to 27 a.u.

II.3.5.1.2. Gradient-Free Optimizations

Since the Krotov algorithm leads not to the expected results (with the used targets and parameters), optimizations based on a basis expansion of the field were tried. As noted in Section II.3.1.5, black-box gradient-based optimization routines are not optimal. In this case, they do lead to an increase of J but, compared to the Krotov procedure, the increase is marginal and the rate of convergence is significantly decreased. This was also shown in other applications.^[347] Instead, derivative-free optimization routines were used. Many derivative-free optimization algorithms are very robust and not sensitive to noise.⁸ An additional advantage is that *any* optimization target can be defined, including targets that cannot be formulated in terms of operators.

As a basis for the field, both a Fourier basis and a sum of vN functions with complex width parameter α (see Publication 1 (Section I.1.1) on page 23) were tried. The choice of a vN function was inspired by Ref. [351]. It turned out that optimizing one vN function with variable phase-space location is sufficient. For the parametrization, only the real part of a vN function is used, that is

$$g(t) = A_0 \exp[-\Re\alpha(t - t_0)^2] \cos[(t - t_0)(\omega_0 - \Im\alpha(t - t_0))]. \quad (\text{II.3.72})$$

Using a complex width α enables a chirp of the field, that is, the shape in time-frequency representation is tilted. The form of Eq. (II.3.72) leads to the following five parameters $\{A_0, \Re\alpha, \Im\alpha, \omega_0, t_0\}$ to be optimized. Essentially, this type of basis expansion means that the search space is constrained because not all functional forms are possible. This leads to the occurrence of different maxima on the optimization landscape and the best way to optimize would be to employ global optimization algorithms like evolutionary algorithms. However, since the derivative-free algorithms do not explicitly use gradients, it is possible that they overcome adjacent local maxima.⁹ Further, they are robust with respect to a noisy optimization landscape.¹⁰ Anyway, both local and global optimization algorithms are used in the following. As local optimization algorithms, BOBYQA^[320] and its cousin COBYLA^[352] as implemented in `nlopt`^[353] were used. As a global optimization algorithm, differential evolution, as implemented in `scipy`^[144] was used. Differential evolution is a special type of evolutionary algorithm.^[327] As such, it is nondeterministic and typically, many separate optimization runs are required in order to get to the (global) optimum.^[350] Here, only one run with about 600 iterations was performed. The aim of this study was not to find the global maximum but to explore possible fields in order to find interesting mechanisms.

⁸In my Bachelor's thesis, more than 60 parameters of a reactive force field with a very noisy and complicated optimization landscape were successfully optimized with the help of derivative-free optimization procedures (the local BOBYQA algorithm and evolutionary algorithms).^[348-350]

⁹Typically, the term optimization is used as a synonym for minimization. Here, optimization means maximization.

¹⁰Of course, there are also gradient-based algorithms that can handle noisy landscapes. However, they are less common.

Five obtained pulses and the wavefunction at the end of the propagation time are shown in Fig. II.3.8. The parameters for Eq. (II.3.72) are stated in Tab. II.3.1. For pulses (c) to (e), A_0 is fixed and not optimized. For pulses (a) and (b), the objective is to maximize the overlap with $|\phi_1\rangle - w_2|\phi_2\rangle$, where $w_2 = 10$ and $|\phi_1\rangle$ is a Gaussian (see Eq. (II.3.60); $\alpha = 2/39$, $p_0 = 3$, $v_0 = 70$) located in region D_1 . $|\phi_2\rangle$ is a smooth triangle located in region D_2 (compare with Fig. II.3.3):

$$\phi_2(u, v) = \{\tanh[s \sin(\pi/4)(a(u) - v - v_0)] + 1\}/2, \quad (\text{II.3.73})$$

$$a(u) = u^2/\sqrt{u^2 + 0.004}, \quad (\text{II.3.74})$$

$$v_0 = 65, \quad s = 0.3. \quad (\text{II.3.75})$$

$a(u)$ is a “regularized” function for taking the absolute value of u . The COBYLA algorithm is used and the two pulses (a) and (b) correspond to the outcome at different iterations. For the other pulses, $|\phi_1\rangle$ is replaced by a smooth triangle located in region D_1 ,

$$\phi_1(u, v) = 1 - \{\tanh[s \sin(\pi/4)(a(u) - v + v_0)] + 1\}/2, \quad (\text{II.3.76})$$

with $v_0 = 40$ and $w_2 = 1$. Pulses (c) and (d) are outcomes of global optimization *via* differential evolution and pulse (e) is a result of local optimization *via* BOBYQA. Note that these five pulses are only a selection of a plethora of different pulses but their shapes are characteristic for the other pulses as well.

All shown pulses lead to an increase of the wavefunction in region D_1 , compared to region D_2 , such that they fulfill the requested task. It is remarkable that the more sophisticated Krotov procedure did not lead to satisfactory results and that the optimization of only five parameters, of which one is just a time shift, are enough to represent useful pulses. However, except for pulse (b), all pulses have in common that they are asymmetric and peaked at either a negative or a positive value. Pulse (c) is the most radical pronunciation of this characteristic. Compared to the other pulses, pulse (b) has much larger amplitudes. The mechanism of the ionization procedure is discussed in the following paragraph.

Table II.3.1.: Rounded values of the optimized parameters for the pulses depicted in Fig. II.3.8.

The equation for the pulse is shown in Eq. (II.3.72). Atomic units are used unless stated otherwise.

pulse	A_0	$A_0[\text{W}/\text{cm}^2]$	$\Re\alpha$	$\Im\alpha$	t_0	ω_0	$\omega_0[\text{eV}]$
(a)	-2.22	$2 \cdot 10^{17}$	0.21	-15	6	6.66	181
(b)	46.6	$8 \cdot 10^{19}$	0.13	-0.15	7	5.90	160
(c)	-4.43	$7 \cdot 10^{17}$	12	0.74	2	1.43	38.8
(d)	-4.43	$7 \cdot 10^{17}$	13	61	1	0.151	4.10
(e)	-4.43	$7 \cdot 10^{17}$	0.24	-0.85	5	2.19	59.3

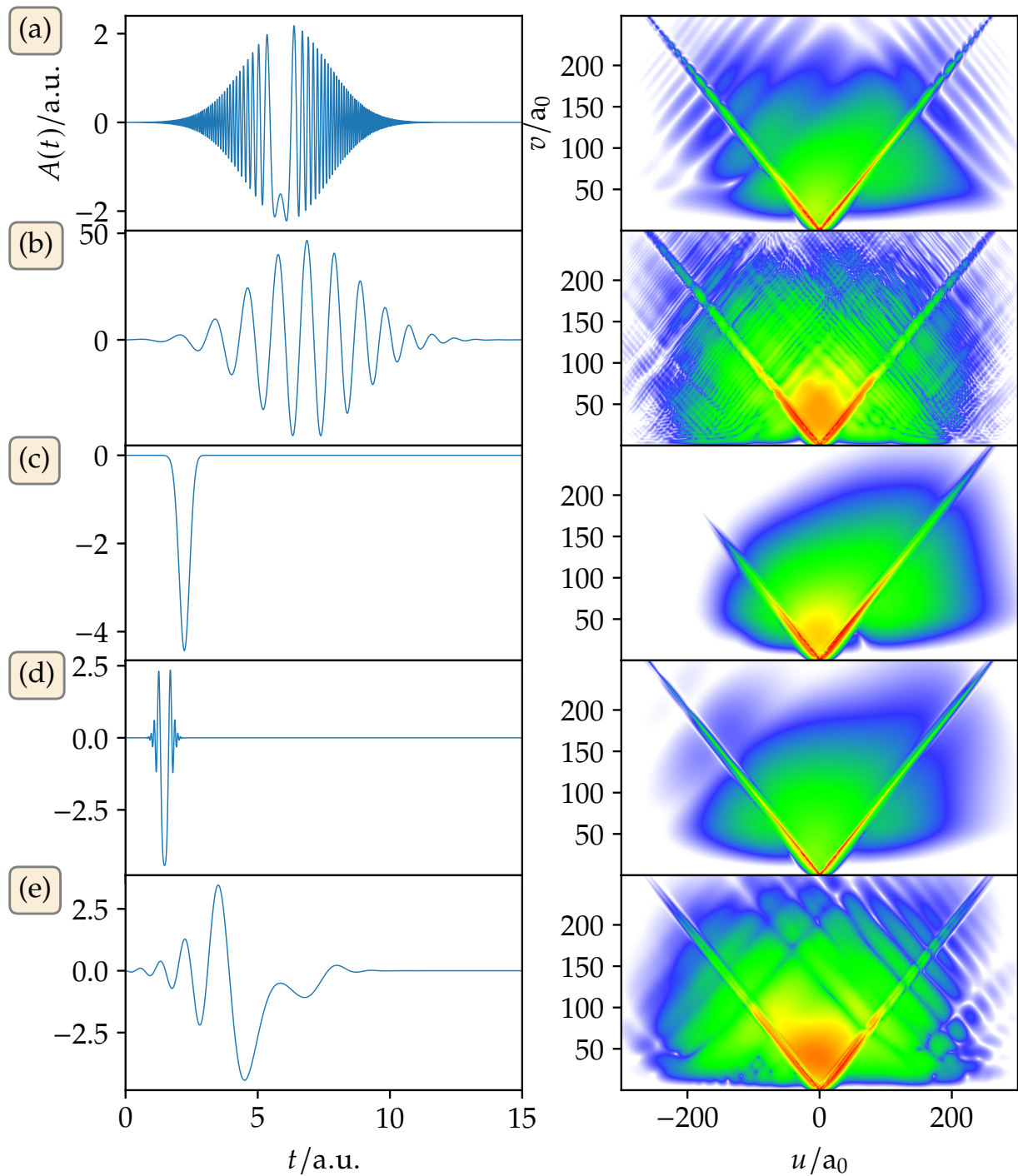


Figure II.3.8.: Optimized pulses (left) and square of the wavefunction at final propagation time $T = 60$ a.u. (right). For $t > 15$ a.u., all pulses have vanishing values. See Tab. II.3.1 for the pulse parameters and Fig. II.3.4 for the colormap.

Discussion The discussion starts with pulse (c) that has the simplest structure and consists just of a pronounced peak to negative values.¹¹ This means that, during the times of nonzero pulse values, the wavepacket is accelerated in u direction, because, in velocity gauge, the field couples with the momentum in u . Since the final wavepacket is mainly localized in regions S and D_1 (small u values) but *not* in D_2 (large u values), this pulse is, at first sight, counterintuitive. Nevertheless, an analysis of the wavepacket at different propagation time unravels a clear mechanism.

For an analysis, both the wavepacket in coordinate space and its reduced densities in phase space are shown for selected times. For the phase-space analysis, the Husimi Q representation is used, that is, a projection of the state onto vN functions:^[170]

$$Q(x, p) = \frac{1}{\pi} |\langle \mathcal{G}_{x_0, p_0} | \psi \rangle|^2. \quad (\text{II.3.77})$$

Essentially, the Husimi Q representation is a continuous version of the “pixelated” vN representation.^[354] Note that this representation depends on the width parameter α (compare with Publication 1 (Section I.1.1) on page 23). Here, it is set to $1/2$, resulting in $\sigma_x = \sigma_p$.

For the following discussion, it needs to be kept in mind that large (small) u values with small (large) v values means that both electrons are on the same (opposite) side of the nucleus; compare with Fig. II.3.1. For pulse (c) in Fig. II.3.8, the wavepacket in coordinate space and phase-space representations of the reduced densities are shown in Fig. II.3.9. Plotting the wavepacket in momentum space is not useful for an analysis because it does not reveal any coordinate-dependent information. The acceleration in u direction of the pulse leads, essentially, to a displacement of the wavepacket in u ; compare t_1 and t_2 (first and second row) of Fig. II.3.9. Some parts of the wavepacket are scattered at the potential valley but the main part of the wavepacket is simply displaced. The acceleration in u is visible in the Husimi Q distribution of that coordinate. Note that the maximum of the wavepacket is still at $v \sim 0$ where the electrons are affected strongly by their Coulomb repulsion. Therefore, once the wavepacket is displaced and the field vanishes, the wavepacket is driven to larger v values to avoid the Coulomb repulsion. Additionally, it is attracted by the nucleus and thus driven to smaller u values, compare with Fig. II.3.2. In total, the motion is diagonal and in direction to region D_1 . This is evident from t_3 (the third row of Fig. II.3.8). At that time, the wavepacket is again centered around $u \sim 0$ with large components at larger v values. Interference phenomena due to the scattering by the potential valley (along the diagonal) are visible. Note how the wavepacket has gained large positive components in momentum p_v for larger v values; as is evident from the Husimi Q distribution in coordinate v .¹² The components in p_v are enough to drive the wavepacket to into the continuum along the v direction. The nuclear attraction (the potential valley) hinders the wavepacket from moving to large negative u values. The phase-space distribution in u becomes almost point symmetric. Thus, the total movement is to large v values; see the last row.

¹¹Note that the field in length gauge would have components for both positive and negative values.

¹²The larger momentum components for $v = 0$ are due to the form of the potential and as such “ground state quantities” and not very interesting for this study.

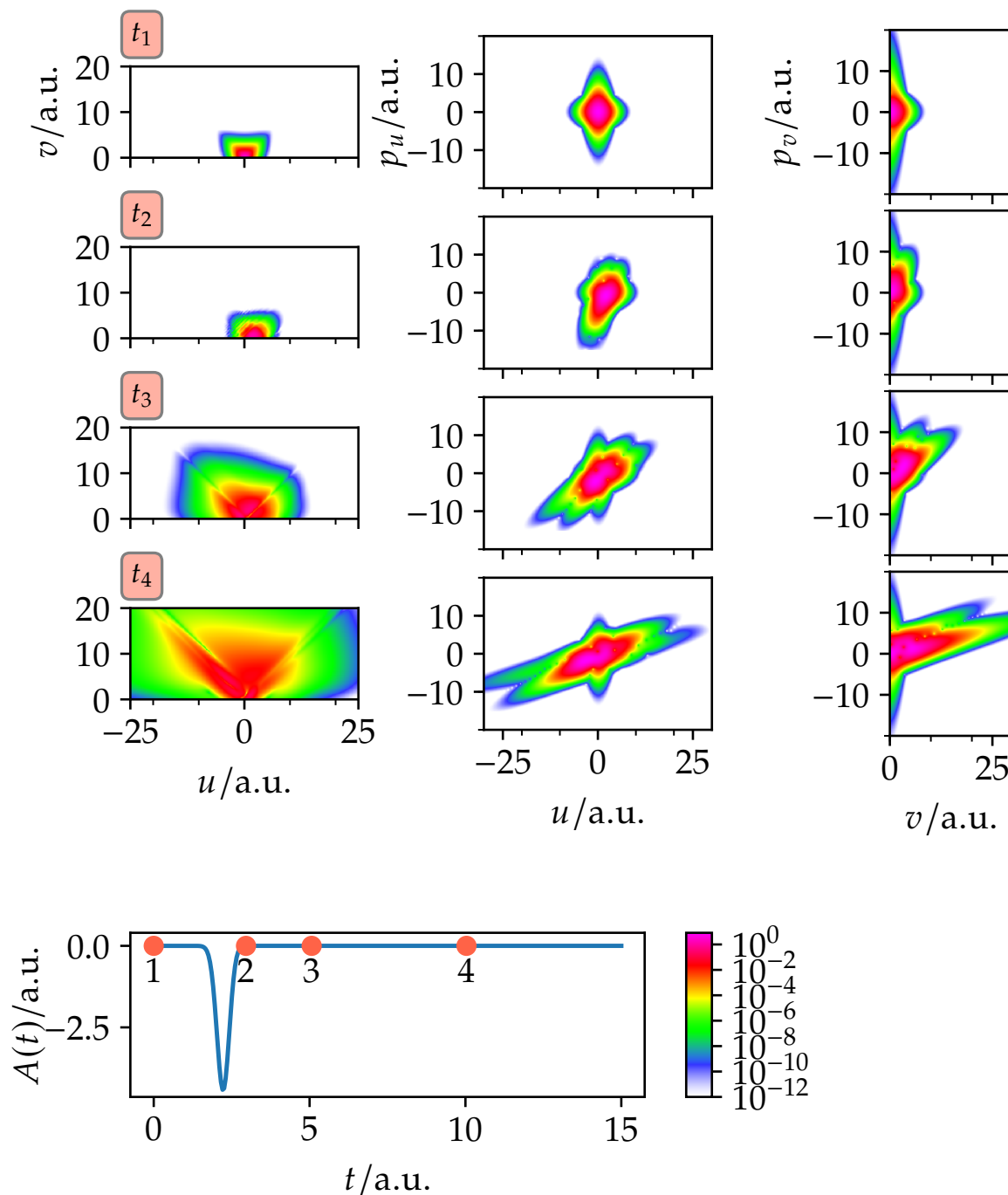


Figure II.3.9.: Square of the wavefunction in coordinate space (left panels) and Husimi Q distribution (Eq. (II.3.77)) of the reduced densities (wavefunction integrated over the other coordinate) in u (middle panels) and v (right panels) for the pulse (c) shown in Fig. II.3.8. Each row corresponds to a different time t_i . The lower left panel shows the pulse and the chosen time points t_i . The lower right panel shows the used colormap.

To show that just the displacement of the wavepacket in u leads to the desirable occupancy in region D_1 , the propagation of an initially displaced wavepacket without the appearance of an external field is shown in Fig. II.3.10. As expected, the occupancy in region D_1 is visible after a propagation for a short time (t_2 ; lower row). At that time, there are also major components in region D_2 but the strong asymmetry of the phase-space distribution in v (lower right panel) will drive the wavepacket to larger v values such that the occupancy in D_2 will vanish.

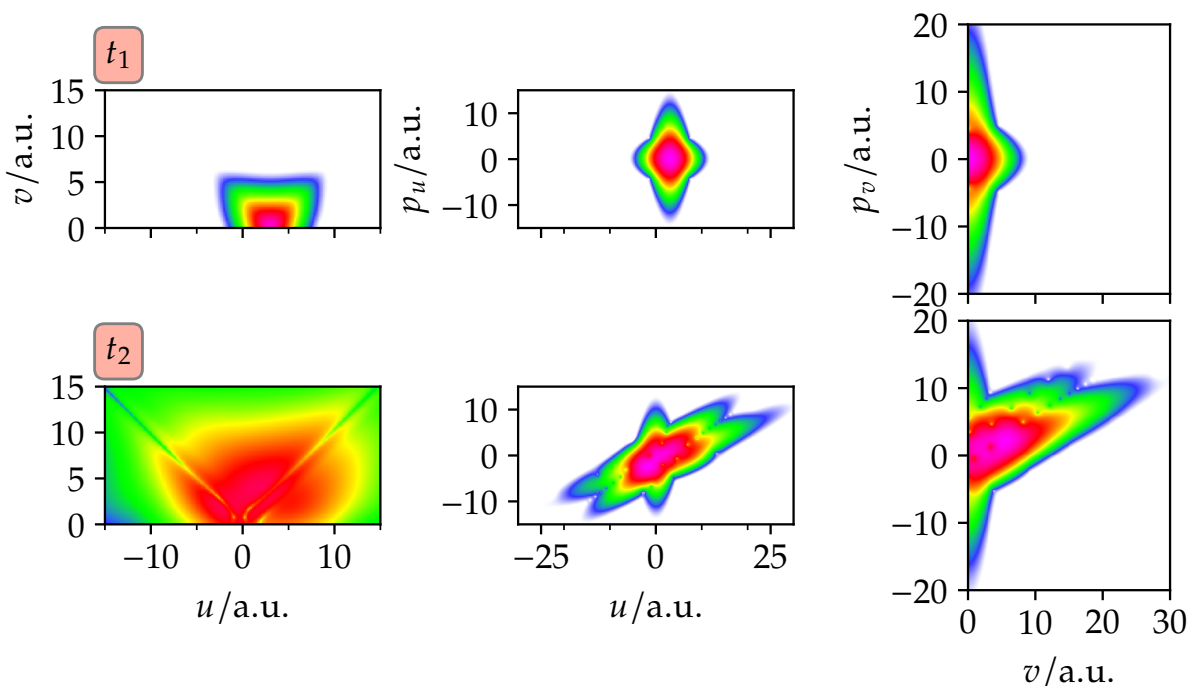


Figure II.3.10.: Same as Fig. II.3.9 but without a field and with a initial wavepacket displaced in u and centered at $u = 3$ a.u. The propagation times are $t_1 = 0$ and $t_2 = 5.02$ a.u. See Fig. II.3.9 for the colormap.

To summarize, there is a simple two-step procedure that leads to the increased occupancy in region D_1 . Pictorially, this two-step procedure is summarized in Fig. II.3.11: The wavepacket starts at the origin (position I) and the large values of the pulse in one direction leads to a displacement in u in the first step. Once the field vanishes, the wavepacket is at position II and the repulsion by the electron-electron Coulomb potential and the attraction by the nuclear Coulomb potential leads, in the second step, to a movement to region D_1 (position III).

As a side note: Pulses with one dominant peak have been used elsewhere as well. In my Master's thesis, few-cycle pulses (in length gauge) were used with a dominant peak to singly ionize LiH in a particular direction.^[99,355]

Further tests were performed by scanning the amplitude of the pulse. An increase in region D_1 is already visible for a field with amplitude of $1 \hat{=} 3.5 \cdot 10^{16} \text{ W cm}^{-2}$. For lower intensities, only single ionization occurs. For amplitudes larger than $10 \hat{=} 3.5 \cdot 10^{18} \text{ W cm}^{-2}$, the displacement is so large that the wavefunction gains enough momentum components in u to overcome the nuclear attraction by the Coulomb potential. This leads to an increase of the occupancy in region D_2 .

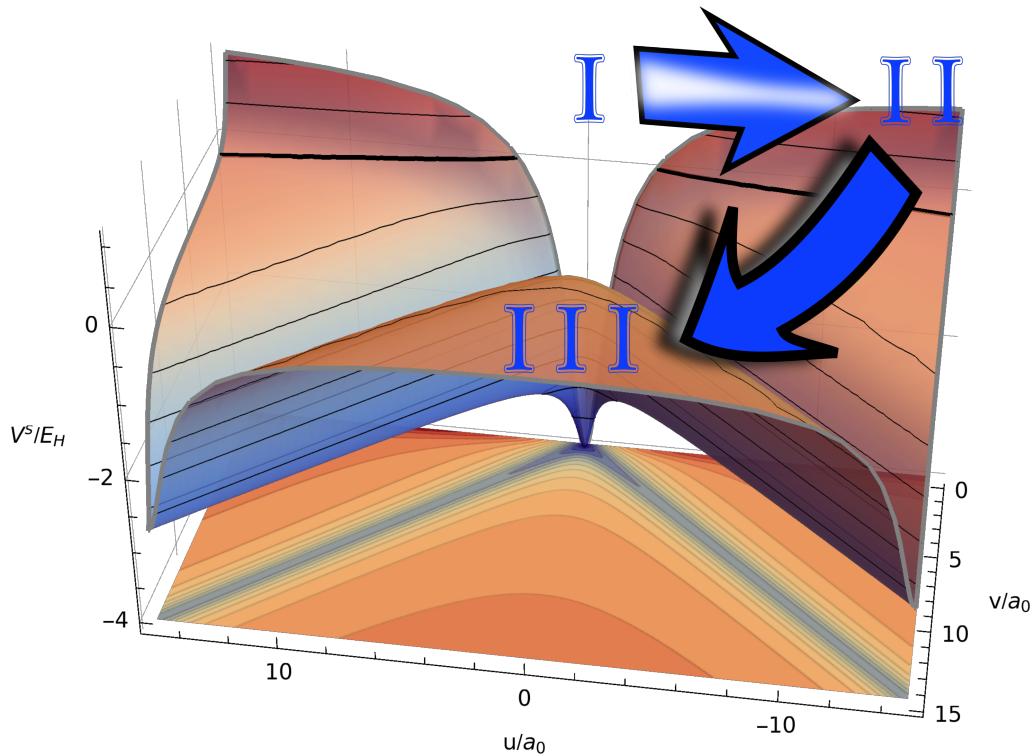


Figure II.3.11.: Schematic of the mechanism of the ionization dynamics that leads to an increased occupancy in region D_1 (see Fig. II.3.3). Shown are the potential, the initial (I), intermediate (II) and final (III) locations of the wavepacket. The two-step procedure is shown by the arrows that represent the movement of the wavepacket; see text for details. Note that the potential is symmetric in v and only non-negative values of v are shown.

What is with the other pulses shown in Fig. II.3.8? Actually, they all follow the same mechanism. Except for pulse (b), all pulses have one dominant peak or asymmetry such that a similar mechanism is more or less evident and an analysis confirms this. For pulse (b), this is not very clear because it exhibits no evident asymmetry. Instead, it is the only pulse that has many, “symmetric” cycles (as more standard pulses) but an extremely large amplitude of almost $8.8 \cdot 10^{19} \text{ W cm}^{-2}$. The wavefunctions at different times for that pulse are shown in Fig. II.3.12. The times roughly correspond to different zero-crossings of adjacent half-cycles. At these times, the wavepacket has the maximal displacement. Comparing the wavepacket for subsequent times shows that the center of the wavepacket is moving more and more to larger v values. This is also evident from the Husimi Q distribution in v . The amplitude of the field is large enough that, in u direction, the wavepacket is mostly driven by the continuously oscillating field such that the Husimi Q distribution in u is almost point symmetric (at a displaced point). Once the field vanishes, the wavepacket has enough positive momentum components in v such that the dominant occupancy in region D_1 remains.

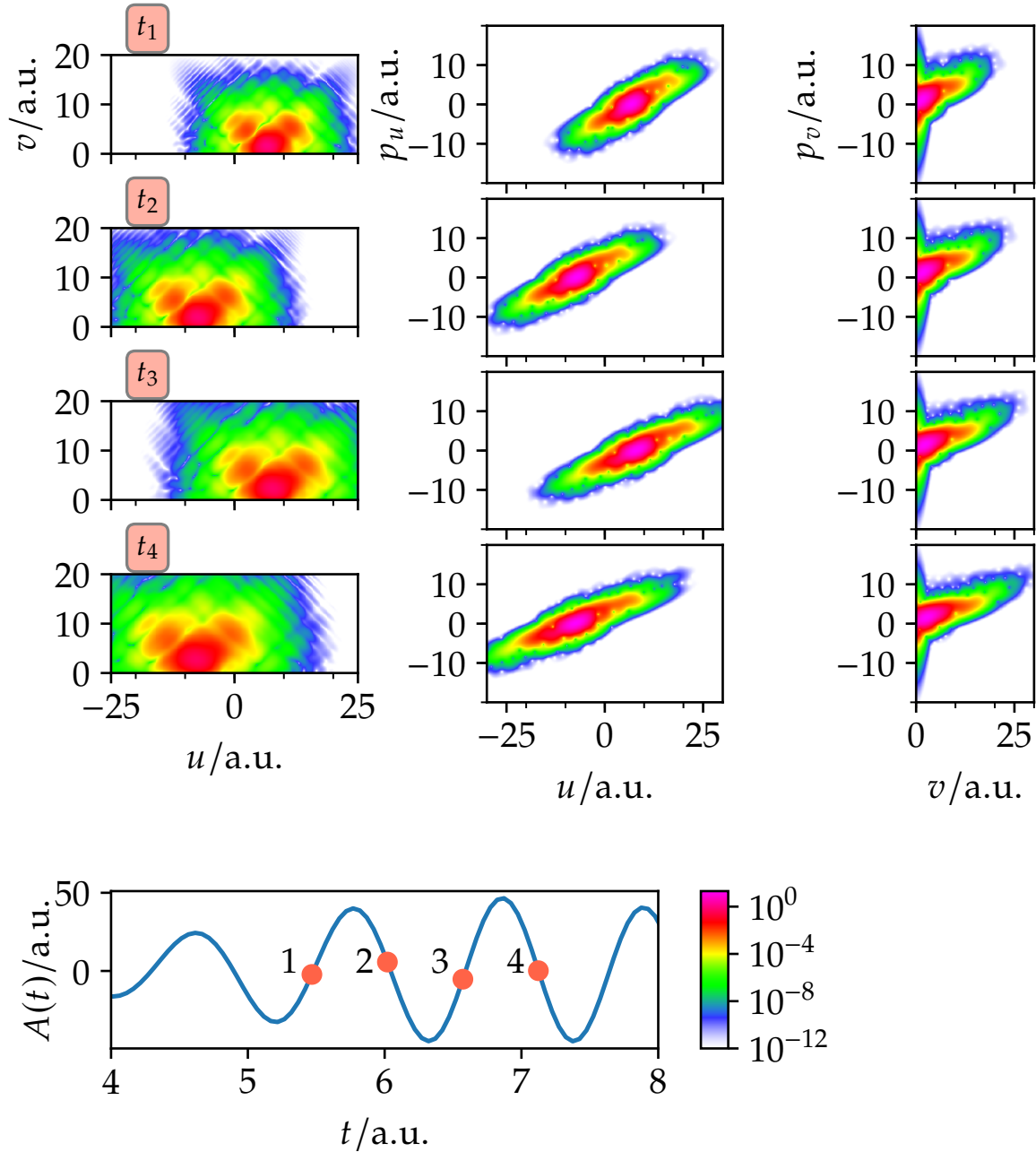


Figure II.3.12.: Same as Fig. II.3.9 but with pulse (b) shown in Fig. II.3.8. The shown times roughly correspond to the zero-crossings of the 7th, 8th, 9th and 10th half-cycle.

II.3.5.2. Local Control

In the following, two results from different local control algorithms are presented. The first result, (x), uses the form from Eq. (II.3.67) (page 198) and the second result, (y), the “simple man approach”; see Section II.3.4.3.2 for more details. For (x), the operator to be optimized is in coordinate representation

$$o^{(x)}(u, v) = N|v| \exp[-\alpha^{(x)}u^2], \quad (\text{II.3.78})$$

where N is a normalization factor (for the u -dependent Gaussian) and $\alpha^{(x)} = 2/39$. This function should drive the wavefunction to larger and larger v values while having small u values. Here, a displaced Gaussian in v is not used because the expectation value of its derivative, $\langle \partial_u o^{(x)}(u, v) \rangle$ (see Eq. (II.3.64)), vanishes for vanishing overlap of $|\psi\rangle$ with the Gaussian such that $\langle o^{(x)}(u, v) \rangle$ cannot be controlled by the field. Other functional forms like $-|v|u^2$ have not yet been tried. For the control expression, the scaling parameter λ is set to 500, $dt \langle o^{(x)} \rangle / dt = C$ is set to 1 and a maximal allowed absolute value of 50 is taken for the field. A small time step of $\Delta_t = 0.0125$ is used.

For (y), the operator is

$$o^{(y)}(u, v) = Nv^2 \exp[-\alpha^{(y)}u^2], \quad (\text{II.3.79})$$

with $\alpha^{(y)} = 2/5$. A time step of $\Delta_t = 0.05$ is used and for each time step, the amplitude of the field can only be doubled; compare with Eq. (II.3.70). Note that this makes the outcome of the optimization dependent on the choice of the time step. Different time steps have been tried.

The local control optimization is only done for a short time. For that, *no* pruning but a small direct-product basis with coordinate range $[-90, 90]$ is used. For highly oscillating fields, the pruning is only stable if many nearest neighbors are added to the active basis functions. After the local control optimization, the wavepacket is propagated field-free using pruning. The results for (x) and (y) are presented in Fig. II.3.13. The obtained fields are much more complex than those obtained from optimal control and show many oscillations with almost δ -distribution-like peaks.¹³ For *both* procedures, the expectation value of \hat{O} is not monotonically increasing. This is due to the scaling factor λ for (x) and due to the restrictions onto the maximal field amplitude for (y). Nevertheless, there is a clear increase in the objective and there is larger occupancy in region D_1 , compared to region D_2 . However, for (x), this is only marginally the case and for (y), mostly single ionization occurs.

Further, different expectation values have been tried for optimizations, in particular $\partial_u^2 - \partial_v^2$, that is, maximizing the kinetic energy in v and minimizing it in u . Although the Husimi Q distributions of the obtained wavefunction look similar to those presented in Section II.3.5.1.2, the occupancy in region D_1 is not increased. Additional tests with different expressions are needed in order to get a more detailed understanding of the optimization procedure.

¹³Further constraints to make the fields experimentally better accessible can be added in later.

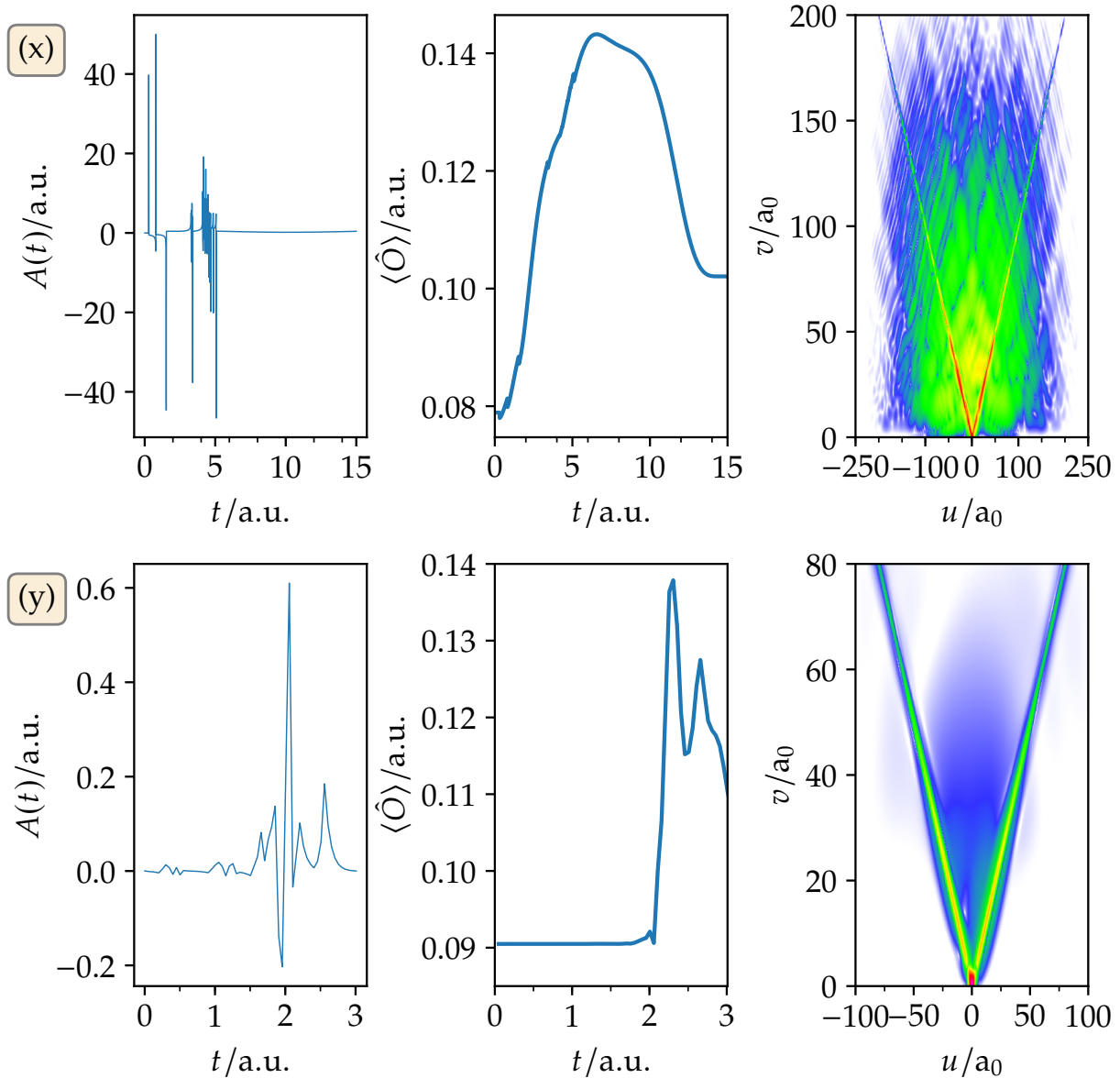


Figure II.3.13.: Optimized pulses (left), expectation value *versus* time (middle) and square of the wavefunction at final propagation time $T = 40$ a.u. (right) for the two local control procedures (x) and (y); see text for details. The pulse has only nonvanishing values for the shown propagation times. Afterwards, it is explicitly set to 0. For the pulse in (x), the values are between 0.2 and 0.4 for $t \in [5, 15]$. See Fig. II.3.4 for the colormap.

Discussion For pulse (y), the mechanism is similar to the two-step procedure explained in Section II.3.5.1.2. For pulse (x), the mechanism is also related to the two-step procedure but it happens several times and the displacement is not so large. Further, for a considerable fraction of the pulse, there only is single ionization. Then, the wavepacket is double-ionized from the single-ionized part along the diagonal, similar to what is analyzed in Ref. [83]. Snapshots of the wavepacket are shown in Fig. II.3.14. There, at time t_1 , the three main peaks in the beginning of the pulse are over and the wavepacket is slightly displaced. At t_2 , major parts of the wavefunction are in region S and some in D_1 which becomes more occupied at t_3 . This clearly comes from a part of the wavefunction that first was single-ionized. It slowly drifts away, as can be seen by comparing t_4 to t_7 . With a similar mechanism, another part of the wavepacket is generated during times t_4 to t_7 , noticeable by the pink fraction near the origin that is first occupying region S_1 at times t_4 and t_5 . At t_6 , it is moving to D_1 where it appears at t_7 as a larger red “cloud”.¹⁴ Hence, this mechanism seems to follow a sequential ionization.

¹⁴Admittedly, this is hard to see on the graphics but it becomes more clear by comparing plots of the wavefunction at different times and using different color scales and coordinate ranges. Too many figures would be required. Nevertheless, the overall procedure should become obvious from Fig. II.3.14.

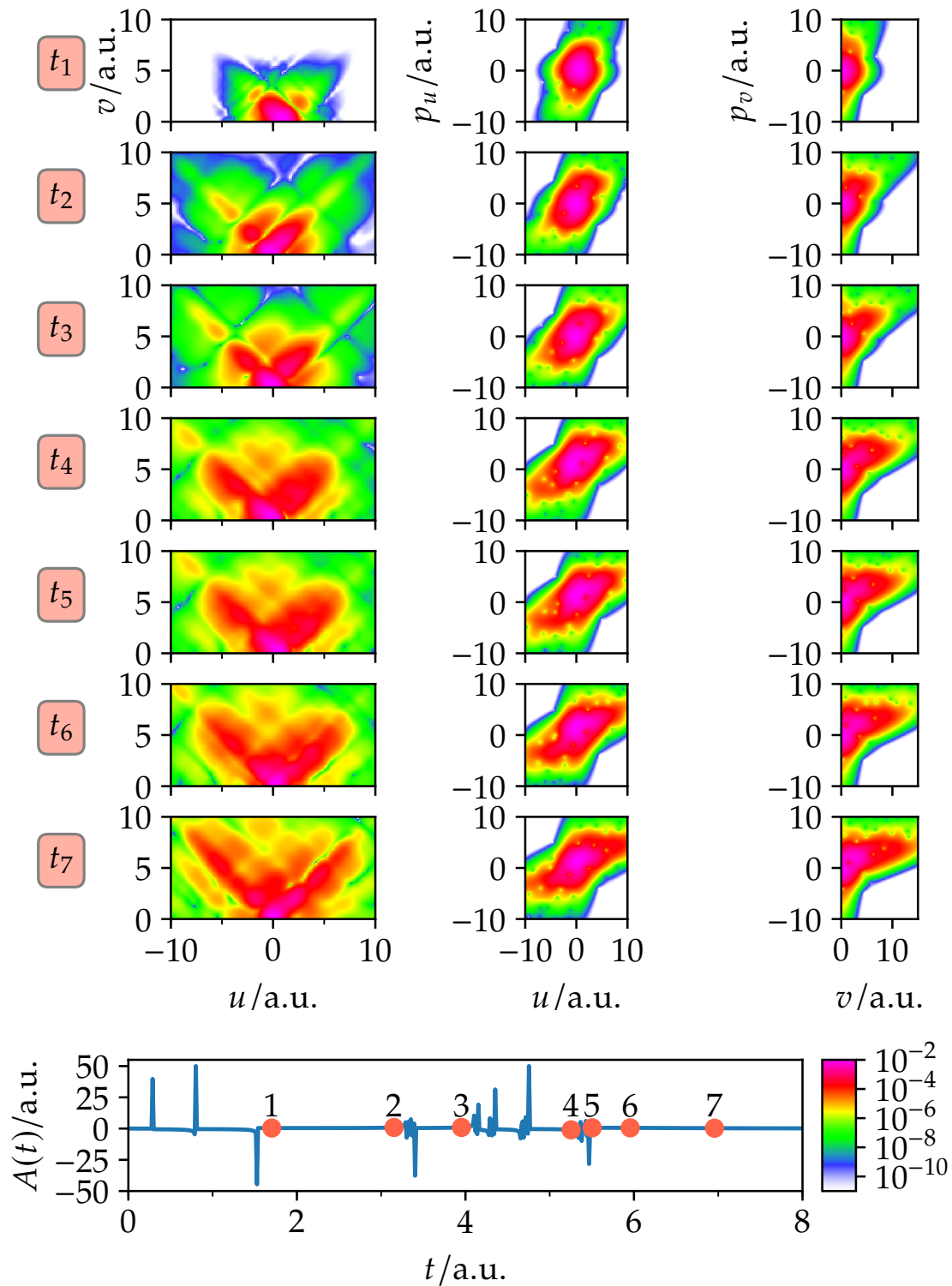


Figure II.3.14.: Coordinate and phase-space analysis of the local control propagation (x); see Fig. II.3.9 and text for details. Here, a different colormap is used (lower right panel). The obtained field (lower left panel) is for $t > 4$ a.u. slightly different than that shown in Fig. II.3.13, due to numerical issues.

II.3.6. Conclusions and Outlook

This Chapter presented the optimization of the direction of ejection of the double ionization in a one-dimensional helium model. It served as a very useful test case for DP-DVR. Indeed, DP-DVR was needed to enable these studies. However, the optimization problem itself turned out to be quite difficult. Many different optimization strategies have been tried: 1a) Optimal control with the Krotov algorithm, 1b) gradient-based and 1c) gradient-free optimizations with a basis expansion of the field and 2) two variants of local control. The optimization with the Krotov algorithm was not successful. Since the algorithm itself works, probably the “wrong” control targets have been used. More work is required in order to find the appropriate target. In contrast, gradient-free optimizations gave pulses with distinct features: Either, there is an asymmetry and a clear peak to negative or positive values, or the pulse contains many cycles with very large amplitudes. In both cases, the mechanism can easily be explained by a two-step model where the field first ionizes the electrons in the same direction. When the field vanishes, the electron-electron repulsion and the electron-nuclear attractions drive the wavepacket to the desired area in coordinate space. Initial optimization attempts have been performed with local control. In contrast to previous local control applications, the optimization is not straightforward because 1) the operator whose expectation value should be optimized does not commute with the field-free Hamiltonian, 2) an operator containing only the coordinate that describes the electronic movement away from each other couples only to second order in time with the field, and 3) the local control expressions lead to complex-valued fields that causes numerical problems as the total Hamiltonian becomes non-Hermitian. It is not clear how averaging the complex-valued field to make it real-valued changes the optimization outcome. A new, straightforward, and simple local control procedure has been proposed that does a black-box maximization of the expectation value by finding the optimal field value iteratively using short-time propagations. The obtained fields optimized by local control procedures have rugged features with δ -distribution-like peaks. Nevertheless, the mechanism is similar to the two-step model, but main parts of the double-ionization happens sequentially.

Of course, there remains much to be done. The pulses from the derivative-free optimization should be used as initial starting pulses for the Krotov procedure and different targets should be tried there. In particular, the targets used for the local control procedure should be tried out. Initial work in that direction is in progress and seems to be promising. It would be interesting to see whether there are different mechanisms that lead to the same target. Once the system is better understood, it would be illuminating to compare the outcome of this one-dimensional model with full three-dimensional calculations to ensure that electron-correlation effects are not overestimated in the one-dimensional model. This could be done with close-coupling approaches^[244] and/or using DP-MCTDH.

High Harmonic Generation of Helium Initiated by Extreme Ultraviolet Radiation

” *There is no quantum world. There is only an abstract physical description. It is wrong to think that the task of physics is to find out how nature is. Physics concerns what we can say about nature.*

— Niels H. D. Bohr

In this Chapter, the challenging process of simulating a HHG spectrum in the two-electron helium system in full three dimensions is discussed. In contrast to [Chapter II.3](#), only single ionization occurs. Nevertheless, due to the three-dimensionality of the two electrons (adding up to six dimensions) and the additional need to describe the continuum, sophisticated methods are required for solving the TDSE for this system. It turned out that the DP approaches of [Chapter I.1](#) are (currently) not suitable for an efficient simulation, which will be discussed in [Section II.4.1.4](#). Instead, the so-called time-dependent generalized active space configuration interaction (TD-GAS-CI) method has been used for this particular simulation.

Actually, the TD-GAS-CI method is a statically pruned method where the pruning is based on physical principles that are different from the concept of adding nearest neighbors introduced in [Chapter I.1](#). The employed methodology will be briefly presented in the next Sections. For more details on the generalized active space (GAS) methodology and its applications, also to diatomic systems, it is referred to my Master’s thesis^[99] and Refs. [124, 278, 355, 356]. The application to interesting HHG simulations, where the first step of the HHG process (see [Section II.2.2.4](#)) is replaced by a direct ionization with the help of a pulse with energies in the XUV region, is described in detail in the publication presented in [Section II.4.2](#).

II.4.1. The Time-Dependent Generalized Active Space Configuration Interaction Approach

In truncated/pruned CI approaches, the wavefunction is expanded in a linear combination of time-independent configurations/Slater determinants or spin-adapted so-called configuration state functions that span a part of the FCI space:^[30,122]

$$|\Psi(t)\rangle = \sum_{i \in \mathcal{A}} A_i(t) |i\rangle_S. \quad (\text{II.4.1})$$

\mathcal{A} is the set of used configurations; see also Section II.3.3 on page 190 for more details. This setup is similar to that described in Chapter I.1 except that $|\Psi\rangle$ describes Fermions and that the pruning is done statically and based on a different concept. Although only two-electron systems are studied, the following description is more general and based on any electronic system with N_{el} electrons. First, the employed orbitals describing the configurations $|i\rangle_S$ are explained in Section II.4.1.1. Afterwards, the methodology of statical pruning is described in Section II.4.1.2. A comparison to multi-configuration time-dependent Hartree-Fock (MCTDHF) and DP is done in Section II.4.1.3 and Section II.4.1.4, respectively.

II.4.1.1. Choice of Orbitals

In a truncated/pruned configuration space, $|\Psi\rangle$ is variant under a unitary transformation of the single-particle or orbital basis $\{\phi_i\}$;^[122] see also Section II.3.3 and I.2.1.4.2. Here and unlike in MCTDH (Chapter I.2), the orbital basis is not optimized at each time step. It is therefore imperative to select a properly transformed orbital basis such that the number of configurations for describing $|\Psi\rangle$ is close to minimal *during all propagation times*. The Hartree-Fock (HF) procedure generates the optimal orbitals for a *single* Slater determinant by minimizing its energy.^[122] However, only the occupied HF orbitals provide a good base for the determinantal basis. The unoccupied orbitals are typically too delocalized. Better behaving (i. e., giving a faster convergent truncated CI expansion) so-called pseudo-orbitals have been developed for ionization dynamics.^[124,278,355] The pseudo-orbitals are the solutions of the system containing $N_{\text{el}} - 2$ or, here, $N_{\text{el}} - 1$ electrons. They are then orthogonalized against the occupied orbitals of the N_{el} electronic system. The total positive charge of the system leads to more localized orbitals. BAUCH ET AL.^[124] showed that this procedure gives a faster convergent set of orbitals than natural orbitals which I could confirm also for diatomic systems in three dimensions.^[99]

HF and pseudo-orbitals provide a good description for the interaction region close to the nuclei. However, they form a poor basis in the continuum. There, a “crude” DVR basis performs much better. It is therefore useful to employ a “mixed” or partially rotated basis:¹ In the interaction region, pseudo-orbitals are used and in the continuum, DVR orbitals are used. The FE-DVR basis

¹In this context, rotation means a unitary transformation of the primitive basis. In a more abstract setting (second quantization and Fock space), unitary transformations can be understood as a rotation operation.^[30]

(see Publication 6 (Section II.2.4)) turns out to be very convenient for this setup because the coordinate is discretized into so-called elements and in each element a Gauß-Lobatto DVR is used. In the partially rotated basis, the dividing point between the pseudo-orbital and the DVR basis can be conveniently chosen to be an element boundary. Fig. II.4.1 shows an example of such a partially rotated basis.

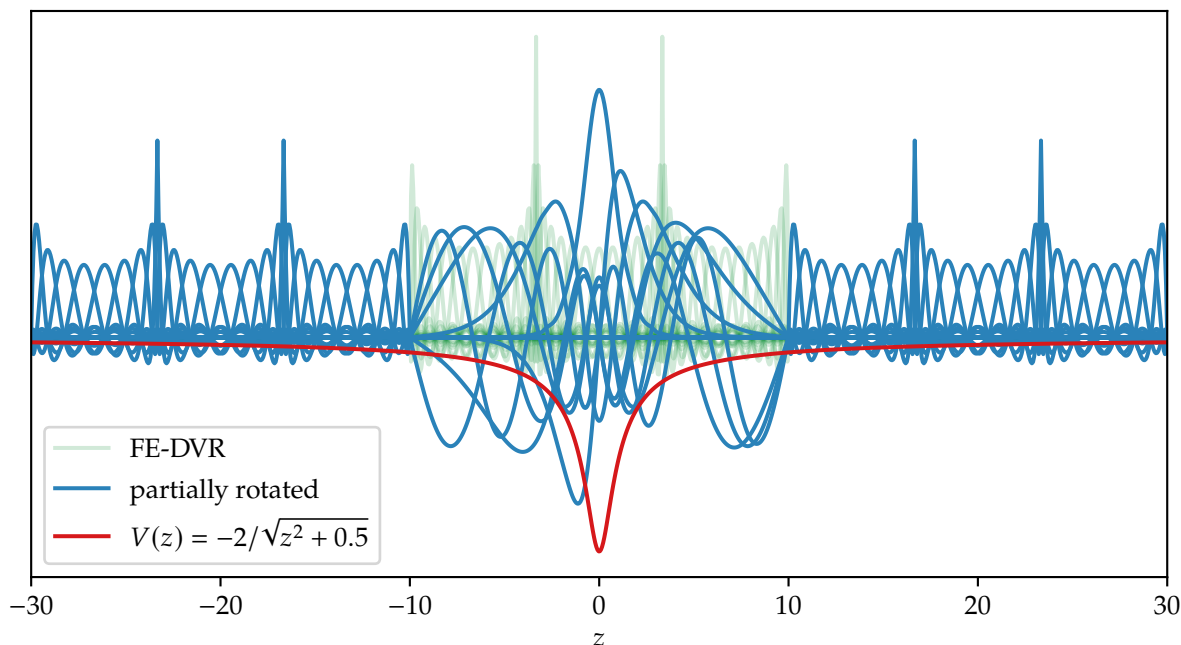


Figure II.4.1.: Example of a partially rotated basis (blue). Nine elements are used for the FE-DVR and only the region with $|z| \leq 10$ is rotated (not all rotated functions are shown). The used soft Coulomb potential is shown in red. The unrotated basis in the inner region is shown in pale green. This graphic as inspired by Ref. [357].

Besides the faster convergence of the CI expansion, the partially rotated basis leads to a significant speed-up of the calculation because the scaling of the required transformation of the electronic integrals (the matrix representation of \hat{H}_M shown in Eq. (II.3.33) on page 190) is reduced and the CI matrix is sparser in DVR than in a rotated orbital representation.^[99,124] Note again that the electronic Hamiltonian is not of SoP form.

II.4.1.2. Determining the Pruned Configuration Space

It remains to discuss how the statically pruned space is actually set up. This is explained in the following.²

²The following is based on my Master's thesis.^[99]

II.4.1.2.1. Configuration Interaction Singles Doubles

The easiest *ansatz* is to include configurations that differ from the HF configuration only in X orbitals. For example, configuration interaction singles doubles (CISD) denotes the solution where all configurations are included that differ by maximally two orbital occupations. Because the HF configuration is specified by the occupation of the single-particle orbitals with the lowest energy (in a one-particle picture), one speaks of the additionally included configurations as *excited* configurations, see Fig. II.4.2. A configuration that differs in one orbital is said to be a singly excited configuration and so on, therefore the name CISD.

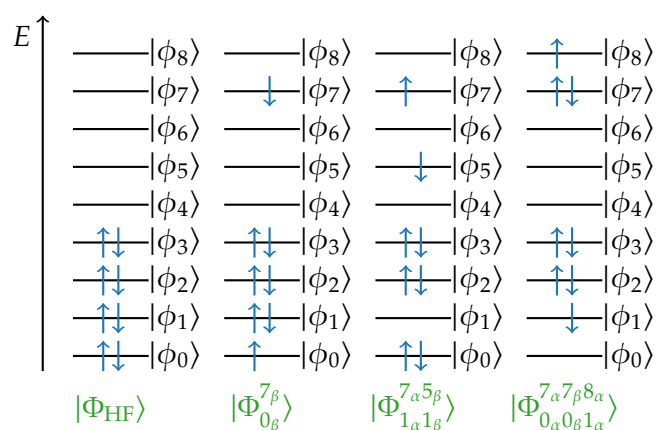


Figure II.4.2.: Example of several configurations/determinants. The orbitals $|\phi_i\rangle$ are sorted by energy. For simplicity, it is assumed that the spatial orbitals do not differ for spin up and down. The reference state, $|\Phi_{\text{HF}}\rangle$, is the HF configuration. Singly, doubly and triply excited configurations are shown as well using the nomenclature $|\Phi_{ij\dots}^{ab\dots}\rangle$, where formerly occupied orbitals i, j, \dots are excited to formerly unoccupied orbitals a, b, \dots

CISD has several drawbacks. The most obvious is that it does not take static correlation into account, i. e., situations where several configurations are equally important for the description of the wavefunction.

Further, CISD lacks so-called size consistency and size extensivity. Size extensivity means that the energy of several monomers is not proportional to the number of monomers.^[30] In truncated CI, the correlation energy goes to zero by increasing the number of electrons. Size consistency means that the energy of two non-interacting systems is not the sum of the energies of the individual systems.^[358] Hence, truncated CI is nowadays not used any more in quantum chemistry.³

As a side note: Size-extensivity and size-consistency are not well-defined properties and there has been much confusion about these terms since the beginning of their definition.^[359,360] Especially size-consistency is often only stated in the context of the description of bond dissociation.

³CIS is used for the determination of excited states, especially in approximations of so-called (linear response) time-dependent density functional theory.

The wavefunctions obtained from non-size-consistent methods have then an unphysical “memory” of the nuclear configurations.^[360]

II.4.1.2.2. Complete Active Space Configuration Interaction

A different way to include more configurations is to select a subspace consisting of n electrons and m spatial orbitals (i. e. $2m$ spin orbitals). A FCI-calculation is carried out in this subspace. This method is called complete active space configuration interaction (CAS-CI) and one uses the notation CAS(n,m)-CI. With the inclusion of relevant orbitals, size-consistency (but not size-extensivity) is at least approximately established.^[30] Only the correlation coming from the electrons in the active space is handled — but then exactly in the space of the single-particle basis. CAS-CI is therefore well suited if a few configurations are of equal, high importance in the molecular problem, i. e., if the system of interest exhibits static correlation. Correlation coming from the “dynamic” repulsion of the electrons becomes manifest in minor contributions of *many* configurations and is called *dynamic correlation*. The latter cannot be properly handled by CAS-CI.

II.4.1.2.3. Generalized Active Space Configuration Interaction

Because the number of configurations in a complete active space (CAS) is still growing factorially, more elaborate models need to be used instead in order to limit the factorial growth. This can be achieved by further restricting the number of configurations. One way to realize this is to divide the CAS into several subspaces and to apply different restrictions to them. In the restricted active space (RAS) method, the CAS is divided into three subspaces, namely RAS1, RAS2 and RAS3. A lower limit on the allowed number of electrons is placed on RAS1 and an upper limit on RAS3. RAS2 has no restrictions. This *ansatz* is much more flexible regarding the adaption of the included configurations to the problem at hand and allows the inclusion of both static and dynamic correlation. If, for example, RAS1 has up to two electron “holes” and RAS3 at most two electrons, one obtains a multireference CISD calculation, where single and double excitations are generated from several reference configurations, and not only one as in normal CISD.^[30,361,362]

When an arbitrary number of subspaces and arbitrary restrictions (number of orbitals, maximal and minimal number of electrons) are allowed, one speaks of generalized active space (GAS).^[363] GAS-CI and self-consistent field (SCF) variants where the orbitals are optimized simultaneously have also been developed under the name occupation-restricted multiple active space (ORMAS).^[364-366] A schematic of the concept is depicted in Fig. II.4.3.

For the TD-GAS-CI approach, a highly efficient algorithm has been developed by SØRENSEN ET AL.^[367] that is well-suited for the employed partially rotated basis (Section II.4.1.1).

The TD-GAS-CI approach is particularly useful for ionization dynamics. Since we know that for low enough field intensities and energies, only single ionization occurs, the GAS divisions can be chosen such that the configurations corresponding to electrons located in the continuum are only singly occupied. The multireference character of the partially ionized wavepacket can be

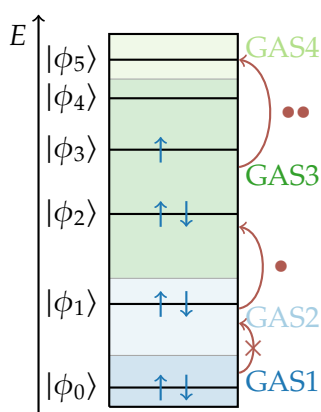


Figure II.4.3.: Example of a GAS division. There are four GASs. As in Fig. II.4.2, orbitals are the same for spin up and spin down. The red arrows with the dots exemplify the allowed excitations (the number of dots). No excitations are allowed from GAS1 — the electrons in that space are “frozen”.

accounted for by a CAS occupied with orbitals of low energy. The larger the size of the CAS, the more electronic correlation is taken into account and the more accurate and time-consuming the simulation becomes. The particular setup is motivated and discussed in Publication 7 (Section II.4.2); see also Ref. [99].

II.4.1.3. Comparison to Multi-Configuration Time-Dependent Hartree-Fock

Chapter I.2 showed how powerful the MCTDH approach is — already without DP. Also a variant of MCTDH for Fermionic systems, dubbed MCTDHF, has been developed.^[278,368-372] Although MCTDHF is a powerful method as well, it is not as easily applicable to electronic ionization dynamics as MCTDH is easily applicable to molecular dynamics. There are two main reasons: More difficult EOMs to solve and the non-decomposable form of the Coulomb potential.

In ionization dynamics, the continuum needs to be described. If high momenta need to be covered in the continuum, the EOM becomes very stiff.^[146]⁴ Further, only a small fraction of the wavepacket is actually ionized and quantities with values of the order $\sim 10^{-10}$ need to be described. This requires a small regularization parameter of the density matrices in the EOM of the SPF (see also Publication 4 (Section I.2.1)). The smaller the parameter, the more effort it takes to solve the EOM.

However, the main reason why MCTDHF is challenging to apply is that the Coulomb interaction (Eq. (II.3.35) on page 190) cannot be decomposed into a SoP form.⁵ Thus, the aforementioned integral transformation (Section II.4.1.1) is required *at each time step*. This is often the bottleneck of typical MCTDHF simulations.

In contrast, in TD-GAS-CI, the TDSE remains a linear equation in time that is much easier to

⁴Note that a reduction of the stiffness is possible.^[278]

⁵To be precise: *Any* potential can be decomposed into a SoP form but the number of sum-terms is sometimes too large.

solve. Since the orbital basis is constant in time, the integral transformation and the setup of the CI matrix need only to be done in the beginning of the simulation. Because the basis is only partially rotated, the scaling of the integral transformation is drastically reduced such that this is not the bottleneck of the simulation. Indeed, the transformation and the setup of the CI matrix do not need to be repeated for various simulations with different field parameters. Instead, the CI matrix can be stored on disk and read in for each simulation run. However, the static character of the basis has the drawback that, compared to MCTDHF, many more configurations are needed to describe the wavefunction during all simulation times. An in-depth comparison of the performance of both methods remains to be done.

Anyway, note that pruned multi-configurational SCF approaches that *do* optimize the orbitals at each time step are available.^[366,373-375] Already MCTDHF can be regarded as a time-dependent complete active space self-consistent field (CAS-SCF) method, that is, the configuration space is given by a CAS. Instead of a CAS one can also use a RAS, a GAS or, as in DP-MCTDH, even an arbitrary pruning.^[376] However, this complicates the EOM further and all downsides of the MCTDHF method are inherited.

II.4.1.4. Comparison to Dynamical Pruning

In the DP approach, a direct-product basis is pruned dynamically in phase, coordinate or some other configuration space. In DP-MCTDH, the configuration space is spanned by natural orbitals, but this is just one possible space; cf. Section I.2.1.4.2 on page 105 for an in-depth discussion.

In GAS-CI as it is used here, the space is spanned by a partially rotated basis consisting of HF-like (pseudo-)orbitals and DVR functions. The HF-like orbitals are similar to the natural orbitals in the sense that they span a more abstract configuration space and that they yield a sparse representation of typical wavefunctions as they occur during the simulation.

As pointed out in Section II.4.1.1, too many basis functions are required if unrotated “raw” DVR bases are used. This makes DP-DVR not favorable.⁶ Due to the non-decomposable Coulomb potential, phase-space bases are even more difficult to apply than DVR bases (compare with Publication 3 (Section I.1.3)) and give a less compact representation than HF-like orbitals; see also Section I.2.1.4.2 for a comparison of some representations.

How can pruning be applied to configurations spanning the (partially) rotated basis? In electron dynamics, the initial wavepacket is typically the ground state of the unperturbed system that is then driven and controlled by an external electromagnetic field. Due to the well-working classical principles mentioned in Section II.2.2 and the rather simple form of the interaction potentials, the general behavior of the wavepacket is predictable. If the field intensity is not too large, it is clear that single ionization is the dominant process and no double ionization occurs. Due to the energetic ordering of the pseudo-orbitals, it is also clear that energetically low-lying orbitals are the most important ones for the description of the ground and the first

⁶Here and in contrast to Chapter II.3, single ionization dynamics of electronic systems in three dimensions is discussed. DP-DVR is useful for electron double-ionization dynamics simulations; see also below.

excited states. These are needed for describing the part of the wavepacket that remains in the vicinity of the nucleus. Based on this, it is more clear how to prune the CI space than how to prune the configuration space for molecular wavepackets described by MCTDH.

In principle, one could also employ dynamical pruning. However, after each update of the set of used configurations, one would need to update the CI matrix as well. Since the matrix is more complicated and cumbersome to evaluate, it is better to only do that once for a particular set of configurations. Further, the algorithm implemented for setting up the CI matrix works in such a way that the used configurations must obey the GAS conditions and cannot be of arbitrary non-direct-product type.^[367] This makes an optimization of the code much easier but jeopardizes an application to completely arbitrary sets of configurations.

However, dynamical pruning might be more useful for double ionization dynamics. In Chapter II.3, DP-DVR was very useful for describing two-electron dynamics in a one-dimensional system. For double ionization, the statically pruned configuration space (*via* the GAS approach) would be too large and dynamical pruning could be one way to avoid this issue, provided that the algorithms for setting up the CI matrix and for transforming the integrals are adjusted to this. For example, one could only prune the configurations localized in the continuum dynamically.

II.4.2. Publication: Extreme Ultraviolet-Initiated High Harmonic Generation

II.4.2.1. Own Contributions

- Setup, execution and analysis of the TDSE simulations.⁷
- Writing of the text related to the TDSE simulations (Section “Integration of the time-dependent Schrödinger equation” and Supplementary Note 2).
- Optimization of an atomic TD-GAS-CI code written by S. Bauch and, for the GAS part, L. K. Sørensen; adaption of the code to HHG simulations.

II.4.2.2. Bibliographic Data

Title Self-probing spectroscopy of XUV photo-ionization dynamics in atoms subjected to a strong-field environment

Authors Doron Azoury, Michael Krüger, Gal Orenstein, Henrik R. Larsson, Sebastian Bauch, Barry D. Bruner and Nirit Dudovich

Journal Nature Communications

Volume 8

Issue 1

Page 1453

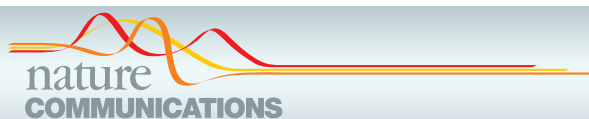
Year 2017

DOI [10.1038/s41467-017-01723-w](https://doi.org/10.1038/s41467-017-01723-w)

Note This article is licensed under a Creative Commons Attribution 4.0 International License. It permits use, sharing, adaptation, distribution and reproduction in any medium or format, as long as appropriate credit to the original authors, the source and a link to the Creative Commons License is given and as long as it is indicated if changes were made; see <http://creativecommons.org/licenses/by/4.0/>.

⁷The time-frequency analysis was performed together with M. Krüger who also created Fig. 6.

II.4.2.3. Article





ARTICLE

DOI: [10.1038/s41467-017-01723-w](https://doi.org/10.1038/s41467-017-01723-w)

OPEN

Self-probing spectroscopy of XUV photo-ionization dynamics in atoms subjected to a strong-field environment

Doron Azoury¹, Michael Krüger ¹, Gal Orenstein¹, Henrik R. Larsson ², Sebastian Bauch³, Barry D. Bruner¹ & Nirit Dudovich¹

Single-photon ionization is one of the most fundamental light matter interactions in nature, serving as a universal probe of the quantum state of matter. By probing the emitted electron, one can decode the full dynamics of the interaction. When photo-ionization is evolving in the presence of a strong laser field, the fundamental properties of the mechanism can be significantly altered. Here we demonstrate how the liberated electron can perform a self-probing measurement of such interaction with attosecond precision. Extreme ultraviolet attosecond pulses initiate an electron wavepacket by photo-ionization, a strong infrared field controls its motion, and finally electron-ion collision maps it into re-emission of attosecond radiation bursts. Our measurements resolve the internal clock provided by the self-probing mechanism, obtaining a direct insight into the build-up of photo-ionization in the presence of the strong laser field.

¹Department of Physics of Complex Systems, Weizmann Institute of Science, Rehovot 76100, Israel. ²Institut für Physikalische Chemie, Christian-Albrechts-Universität zu Kiel, D-24098 Kiel, Germany. ³Institut für Theoretische Physik und Astrophysik, Christian-Albrechts-Universität zu Kiel, D-24098 Kiel, Germany. Azoury D and Krüger M contributed equally to this work. Correspondence and requests for materials should be addressed to N.D. (email: nirit.dudovich@weizmann.ac.il)

Ultrafast spectroscopy has advanced significantly during the past decades as a fundamental tool that manipulates and probes the temporal evolution of a quantum system. One of the most important breakthroughs in ultrafast science was achieved with the production of attosecond (10^{-18} s) laser pulses in the extreme ultraviolet (XUV) wavelength range via a process known as high harmonic generation (HHG)^{1,2}. These developments opened the door to a new time regime that had previously been considered inaccessible, allowing one to follow multi-electron dynamics in atoms³, molecules⁴, surfaces⁵ and solids⁶.

The high nonlinearity that underlies the attosecond pulse generation process offers a unique path for ultrafast measurements. This spectroscopic approach, known as attosecond self-probing or HHG spectroscopy, exploits a built-in pump-probe process driven by an intense infrared (IR) laser field every half-cycle of its oscillation⁷. Here strong-field tunneling ionization acts as a pump, removing an electron and creating a hole in the system. Driven by the laser field, the liberated electron wavepacket returns to the parent ion and probes the hole via radiative recombination, which leads to the emission of high-order harmonics of the driving laser field (Fig. 1a). This nonlinear parametric process, which starts and ends at the ground state of the system, serves as an internal clock, encoding the evolution of the system between ionization and recollision with attosecond precision. In addition, this scheme provides a high spatial resolution

since the de-Broglie wavelength associated with the recolliding electron wavepacket is on an Ångström length scale⁸. The combination of extremely high temporal and spatial accuracy allows the observation of a range of fundamental phenomena—for example, proton motion⁹, valence orbital hole and electron dynamics in molecules⁴, hole rotation in chiral molecules¹⁰, and tunneling¹¹.

Although attosecond self-probing holds great promise for ultrafast spectroscopy and control of matter, the main limitations are imposed by its starting point—strong-field tunneling ionization. Since the tunneling probability decays exponentially with electron binding energy, it allows probing of only a narrow range of valence shell orbitals. Moreover, in systems with multiple orbitals, the tunneling mechanism dictates their relative amplitudes and phases. Finally, tunneling is temporally constrained to the peak of the optical field—imposing a major limitation on the ability to manipulate the temporal properties of the dynamics under study.

An alternative approach to generate high harmonics applies a photo-ionization process as the initial step of the recollision mechanism. This approach is called XUV-initiated HHG,^{12,13} which decouples the ionization step from the subsequent steps of the interaction by replacing strong-field-induced tunnel ionization with photo-ionization driven by an attosecond XUV pulse, as schematically shown in Fig. 1b. Photo-ionization serves as a

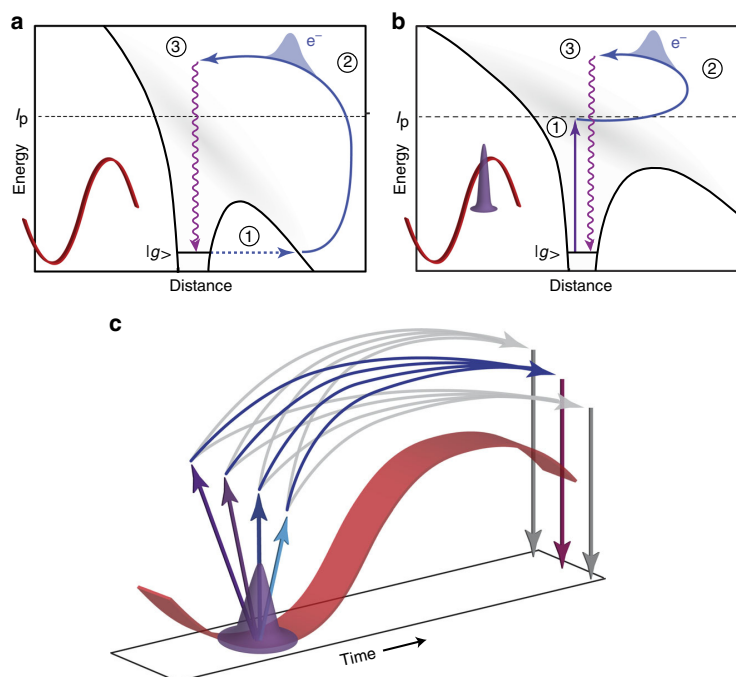


Fig. 1 Photo-ionization self-probing spectroscopy. **a** Schematic diagram of tunneling-initiated high harmonic generation (HHG). The first step is tunnel ionization from the ground state $|g\rangle$ through a suppressed Coulomb barrier (solid black line) induced by a strong laser field (illustrated in red). **b** Schematic diagram of extreme ultraviolet (XUV)-initiated HHG. In addition to the strong laser field, the atom is driven by a synchronized XUV attosecond pulse (illustrated in purple) that creates an electron wavepacket through direct photo-ionization (step 1). In both schemes, blue arrows represent strong-field-driven electron trajectories (step 2) that terminate in recollision with the parent ion (step 3), leading to the emission of high harmonics. **c** Interferometric picture of the XUV-initiated HHG mechanism. The photo-ionization attosecond pulse (purple) creates an electron wavepacket through several quantum paths (arrows pointing up), acting as the starting point of each arm of the interferometer. The infrared (IR) field (red) accelerates the wavepacket and defines the phase evolution of the paths through strong-field electron trajectories (blue and gray arrows). All quantum paths leading up to the same recollision energy interfere, determining the intensity of the corresponding harmonic emission (arrows pointing down). The XUV-IR delay controls which paths will interfere constructively (blue arrows) or destructively (gray arrows). Measurements of the intensity of the new harmonics as a function of XUV-IR delay allow the reconstruction of the photo-ionization dynamics

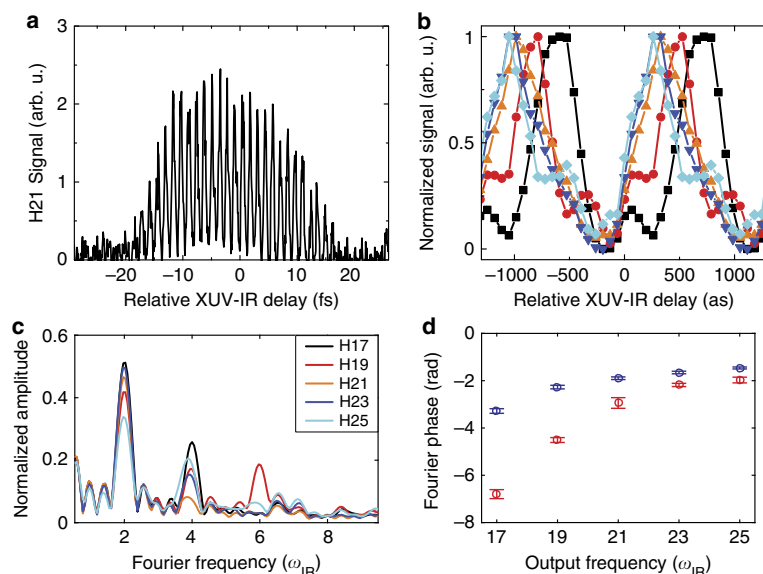


Fig. 2 Spectral analysis of multi-quantum-path beating in XUV-initiated HHG. **a** Intensity of harmonic 21 as function of the relative XUV-IR delay. Zero delay is defined arbitrarily. **b** Intensity of harmonics 17–25 as a function of the relative XUV-IR delay. All harmonics oscillate with a dominant frequency of $2\omega_{\text{IR}}$ and peak at different delays in a descending order. For better visibility, the signal is integrated over seven oscillation cycles, normalized and displayed over several cycles. The different harmonics are represented by colors as in **c**. **c** Fourier analysis of the oscillating signal of harmonics 17–25. Strong anharmonic components at $4\omega_{\text{IR}}$ are visible, as well as signatures of $6\omega_{\text{IR}}$ oscillations. **d** Measured Fourier phases (circles) as a function of harmonic order at Fourier frequencies of $2\omega_{\text{IR}}$ and $4\omega_{\text{IR}}$ in blue and red, respectively (error bars: standard deviation; for details, refer to Methods section)

universal probe of a large range of quantum systems. Ionization by single photons accurately probes, in a linear manner, the quantum state of the matter under scrutiny and produces photoelectrons, which are commonly measured far away and long after the interaction. Biegert et al.¹⁴ performed a pioneering demonstration of XUV-initiated HHG showing that the HHG mechanism can be triggered by an external XUV field. Brizuela et al.¹⁵ showed that low-order harmonics can lead to enhancement of the HHG yield, and it has been suggested that XUV-initiated HHG contributes to the gain in other HHG enhancement experiments^{16,17}. Gademann et al.¹⁸ demonstrated the ability to manipulate the temporal and spectral properties of the HHG process by controlling the XUV-IR delay (see also related work with photoelectrons^{19,20}). The establishment of the XUV-initiated HHG mechanism as a new spectroscopic approach requires a significant step forward. XUV-initiated HHG is a highly nonlinear phenomenon that couples XUV and IR frequencies to generate a new set of XUV frequencies. Its application as a spectroscopic scheme raises the following questions: Can we describe the strong-field interaction via recollision trajectories, as required for a self-probing approach? What is the spectroscopic insight provided by XUV-initiated HHG?

In this paper, we integrate single-photon ionization—one of the most fundamental light–matter interactions—with self-probing spectroscopy, demonstrating a unique spectroscopic approach in attosecond science. We combine the universality provided by single-photon ionization with the high resolution provided by the recollision self-probing mechanism. Our study reveals the rich, multiple quantum path nature of the underlying mechanism, demonstrating that it opens a route in attosecond time-resolved spectroscopy. The establishment of photo-ionization self-probing spectroscopy is based on several fundamental steps. First, we identify and control the main quantum paths that contribute to the process—each path is initiated by the

incoming XUV field and coupled to the other paths by the strong-field interaction. Next, we perform an independent measurement of the primary steps of the interaction. By applying a weak perturbative field, we independently probe either the XUV excitation step or the strong-field interaction. The measurement identifies the underlying dynamics associated with each step in XUV-initiated HHG. The complete and detailed understanding of the interplay between the XUV excitation and the strong-field interaction enables us to proceed into the final stage of our spectroscopic study. Here we reconstruct both the amplitude and phase associated with each XUV excitation path. The coherent superposition of these paths represents the temporal build-up of the photo-ionized wavepacket at its origin.

Results

Photo-ionization self-probing spectroscopy. We demonstrate photo-ionization self-probing spectroscopy in a collinear scheme composed of two main stages (for a detailed description, see Methods section and Supplementary Note 3). In the first stage, an attosecond pulse train (APT) is generated by focusing an intense IR laser pulse into a source gas cell filled with xenon. The IR and APT beams co-propagate and are refocused by a curved two-segment mirror, which controls their relative delay Δt , into a target gas cell filled with helium in order to produce XUV-initiated HHG. For an IR intensity of $8 \times 10^{13} \text{ W cm}^{-2}$, tunnel ionization and, hence, direct HHG by the IR field is strongly suppressed in helium, providing a background-free measurement. The APT consists of 4 discrete odd harmonics in the XUV ranging from $11\omega_{\text{IR}}$ to $17\omega_{\text{IR}}$, where ω_{IR} is the angular frequency of the IR field. When the APT and the IR pulse are temporally overlapped in the target gas cell, we observe the generation of at least five odd harmonics at photon energies above the field free helium ionization threshold (see Supplementary Fig. 8 and

Supplementary Note 5). We tested the generality of this observation by performing the experiment with neon atoms and found similar results (see Supplementary Fig. 9). Scanning Δt leads to high-contrast oscillations of the new harmonics (Fig. 2a, b), at a dominant frequency of $2\omega_{\text{IR}}$ ¹⁸. Each individual harmonic can be associated with an optimal delay for which the signal is maximized. As can be clearly observed, this delay gradually increases with descending harmonic order over a range of ~ 500 as (see Fig. 2b).

A closer examination of the oscillating signal shows a significant anharmonicity, manifested in higher-order oscillations at frequencies of $4\omega_{\text{IR}}$ and $6\omega_{\text{IR}}$ (see Fig. 2c, d). These oscillations reveal the interferometric nature of the mechanism (see Fig. 1c). XUV photo-ionization initiates an electron wavepacket that spreads over several quantum paths (denoted as n), with initial amplitude and phase a_n and ϕ_n , respectively. The IR field accelerates the wavepacket and defines the phase evolution of the paths through strong-field electron trajectories. Upon recollision with the parent ion, the quantum paths interfere and lead to the new set of harmonics. Essentially, multiple harmonic frequencies $n\omega_{\text{IR}}$ injected by the initial XUV field are projected through the interaction into a set of new harmonic frequencies $N\omega_{\text{IR}}$. We manipulate the phase between the different paths in a linear manner by controlling Δt . Accordingly, an interferogram which represents the emission of one new harmonic can be described as:

$$I_N(\Delta t) \propto \left| \sum_n a_n \cdot \exp\{-i\phi_n + i\Theta_{n,N} + in\omega_{\text{IR}}\Delta t\} \right|^2, \quad (1)$$

where $\Theta_{n,N}$ represents the phase that is associated with the electron trajectory that maps an initial harmonic $n\omega_{\text{IR}}$ into a new harmonic of order $N\omega_{\text{IR}}$. Scanning Δt leads to a beating of the interferogram's signal. Figure 2d shows the phases of the beating as a function of $N\omega_{\text{IR}}$. Beating at $2\omega_{\text{IR}}$ is associated with the interference between pairs of neighboring paths separated by $2\omega_{\text{IR}}$, e.g., those initiated by 13 and $15\omega_{\text{IR}}$. Higher-order beating at $4\omega_{\text{IR}}$ and $6\omega_{\text{IR}}$ is associated with the interference between paths separated by $4\omega_{\text{IR}}$ and $6\omega_{\text{IR}}$, respectively. It indicates that, in addition to harmonic 17 whose energy is above helium's ionization threshold, harmonics 11–15 have a significant contribution to the photo-ionization mechanism. This observation is striking; in the presence of the strong infrared field, the atom is ionized by a broad spectral range of XUV light well below the ionization threshold and far from any atomic resonance. This is one of the main results of our work and will be investigated in detail further below. The final step of the interferometer encodes the temporal evolution of the ionized electronic wavepacket via the coupling between the ionization frequencies to the new HHG frequencies. In order to decode this information, we need a better understanding of the dynamics associated with each of the interferometer's arms. Can we think here in the language of recollision trajectories? Can we identify their starting point? Answering these questions experimentally requires a deep study of the basic components that comprise the interferometer—ionization and recollision.

Perturbative study of the mechanism. We study the interferometer's dynamics by adding an additional degree of freedom, provided by a weak second harmonic (SH) field of the IR pulse. This approach has been previously applied to probe the internal dynamics of the conventional HHG mechanism²¹. The total field is given by $E(t) = E_0^{\text{IR}}[\cos(\omega_{\text{IR}}t) + \varepsilon \cos(2\omega_{\text{IR}}t + \varphi)]$, where E_0^{IR} is the IR field strength, $\varepsilon \ll 1$ is the SH-IR field ratio and φ is their relative phase. In the first experiment, we synchronize the SH and the IR pulses in the target gas cell in order to perturb the strong-

field interaction with helium (see Methods section and Supplementary Note 4). The presence of the perturbative SH field breaks the symmetry of the interaction, which manifests itself in the generation of even harmonics²¹. The mechanism for symmetry breaking is based on the perturbation of the electron trajectories in subsequent half-cycles (see Fig. 3a). The perturbation modifies the phase proportional to the semiclassical action S , which accumulates as the electron wavepacket interacts with the strong field. Such a perturbation, expressed by a small phase shift dS , is complex in general^{22,23}. The imaginary component is associated with a small modification of the ionization probability, whereas its real component is associated with the perturbation of electron propagation in the continuum. The intensity \tilde{I}_N of a given harmonic N now depends on dS as

$$\tilde{I}_N = I_N \begin{cases} |\cos(\varepsilon dS(N, \varphi)/\hbar)|^2, & N \text{ odd} \\ |\sin(\varepsilon dS(N, \varphi)/\hbar)|^2, & N \text{ even}, \end{cases} \quad (2)$$

where I_N is the unperturbed harmonic intensity. Since dS depends on all the different steps of the strong-field interaction, it serves as an accurate probe of the electron dynamics associated with each trajectory.

Applying the perturbative scheme, we measured the HHG spectrum as a function of both the XUV-IR and SH-IR delays. The intensity of each harmonic oscillates with half periodicity of the IR field in both degrees of freedom. The optimal XUV-IR delay of each harmonic order is equivalent to the one-dimensional results. Following the harmonic signal as a function of the SH-IR phase, we clearly observe out-of-phase oscillations of the even and odd harmonics (see Fig. 3b). According to Eq. 2, our results indicate that dS is predominantly real, therefore the mechanism is not dominated by field-induced tunneling. A closer examination shows that the SH-IR phase, which is associated with both even and odd harmonics, slowly drifts with the harmonic order (Fig. 3c). Such response reflects the variation of the electron trajectory length, providing a direct evidence for electron trajectories as the fundamental mechanism of the strong-field interaction. Following the excitation by the XUV field, electrons face the atomic potential barrier modified by the IR laser field. The instantaneous shape of the barrier, and therefore the ionization mechanism itself, changes on a sub-optical-cycle time scale. Here the internal clock provided by the self-probing scheme plays an important role; it provides a direct mapping between the ionization time and the emitted energy, enabling us to probe the evolution of this mechanism within the optical cycle. Specifically, our experiment is able to distinguish if electrons undergo tunneling or over-the-barrier emission (OBE) when launched on their recollision trajectories at a specific time within the cycle. In contrast to OBE, tunneling will lead to a non-vanishing imaginary dS , which in turn will cause a deviation from the out-of-phase behavior and strong correlation between XUV-IR and SH-IR oscillations. Neither of these signatures are observed for the XUV-initiated harmonics in our experiment. Ionization by XUV light creates a regime where HHG is dominated by OBE, an effect previously only observed in IR-driven below-threshold HHG^{24,25}.

A comprehensive understanding of the spectroscopic scheme requires an independent study of the ionization mechanism. To this end, we synchronize the SH and IR pulses in the source gas cell, allowing a direct control over the spectral components of the ionizing APT (see Methods section and Supplementary Note 4). The ionizing attosecond pulses, generated by the SH-IR field, are composed of both even and odd harmonics. We control their balance by manipulating the SH-IR delay according to Eq. 2 (Fig. 3d). Initiating ionization with even harmonics opens up new

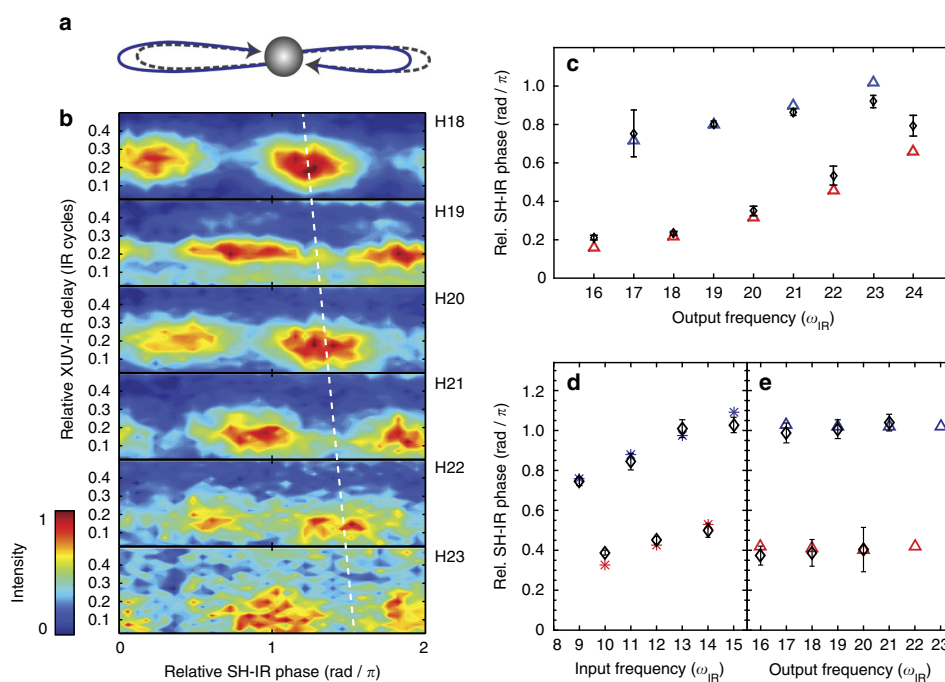


Fig. 3 Perturbative probing of the XUV-initiated HHG dynamics. **a** Illustration of symmetry breaking between consecutive electron trajectories. For a specific SH-IR delay, the symmetric picture (dashed line) is broken: in one IR half cycle (right), the electron trajectory is shorter than in the consecutive half cycle (left). **b** Probing of the strong-field interaction. Normalized intensity of XUV-initiated harmonics as a function of both SH-IR phase and XUV-IR delay. Here the SH and IR pulses are synchronized in the target gas cell. In addition to XUV-IR delay-dependent oscillations, out-of-phase oscillations between odd and even harmonics are observed as a function of SH-IR phase. The white line is a guide to the eye to highlight the phase slope of the SH-IR oscillations of the even harmonics. **c** SH-IR phases that optimize the intensity of individual harmonics after integrating over the XUV-IR delay, for the experiment (black diamonds) and the Coulomb-corrected model (triangles). **d** Probing of the ionization step. Optimal SH-IR phases of the ionizing harmonics, when the SH and IR fields are synchronized in the source gas cell. The experimental results (black diamonds) show out-of-phase oscillations of odd and even harmonics throughout the entire spectrum. Both the odd and the even phase slopes follow the classical prediction (Eq. 2, stars). **e** Optimal SH-IR phases for XUV-initiated harmonics above the helium ionization threshold. The flat-phase behavior is in good agreement with the Coulomb-corrected model (triangles). All error bars on experimental data correspond to standard deviation

quantum paths that consequentially lead to the generation of XUV-initiated even harmonics. Even and odd XUV-initiated harmonics oscillate out of phase when scanning the SH-IR phase and the oscillation phase of each parity group is uniform as a function of harmonic number (Fig. 3e). These two observations reveal two important properties of the ionization mechanism. First, out-of-phase oscillations indicate that the process retains the SH-IR phase behavior of the ionizing harmonics—odd and even harmonics correspond to two sets of independent quantum paths. Second, the uniform phase response shows that all the quantum paths that contribute to the new harmonics' generation process are initiated by the same ionized electronic wavepacket. These observations raise the following challenge: Can we reconstruct the XUV-initiated electron wavepacket, revealing its attosecond evolution in the presence of the strong IR field?

Reconstructing the build-up of the electron wavepacket. Perturbing both the ionization step and the strong-field recollision trajectories resolves the underlying dynamics that defines the different quantum paths in the XUV-initiated HHG process. As we have demonstrated, the ionization is dominated by broadband XUV photo-ionization. The ionized electronic wavepacket populates several independent paths. Finally, the evolution of the wavepacket follows well-established strong-field trajectories²⁶, mapping its nonlinear dynamics into a new set of HHG

frequencies. These fundamental steps can be integrated into a Coulomb-corrected three-step model (CCTSM; see Methods section and Supplementary Note 1). The CCTSM describes the nonlinear dipole response of an atomic system to a combined XUV-IR field. The model does not assume anything about the XUV excitation or the excited states involved in the mechanism; this allows for an investigation of these dynamics within the framework of self-probing spectroscopy. Electrons are liberated by OBE and uniformly populate strong-field electron trajectories; here the barrier is formed by the combined laser-Coulomb potential²⁵. An excellent agreement of the model with the SH-perturbative measurements strongly supports our approach (see Fig. 3c, e). We also performed a numerical integration of the time-dependent Schrödinger equation (TDSE) using the time-dependent generalized-active-space configuration-interaction (TD-GAS-CI) method^{27,28} for helium, taking electronic correlation effects into account. The simulation shows XUV-IR oscillations, similar to the experiment. In addition, it allows us to visualize the electron trajectories, confirming our understanding of the mechanism (see Methods section and Supplementary Note 2).

Revealing the primary paths of the nonlinear mechanism provides us with the opportunity to trace the attosecond build-up of the electronic wavepacket, directed by the interplay of the XUV and the strong IR fields' interaction with the atomic system. The

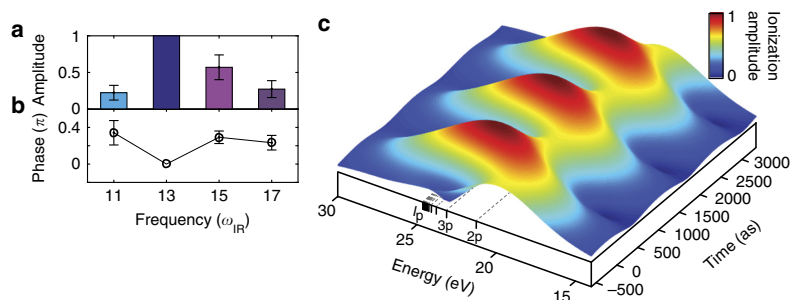


Fig. 4 Reconstruction of the ionization dynamics in strongly driven helium. Spectral **a** amplitude and **b** phase. We fix the amplitude and phase of the frequency component at $13\omega_{IR}$ since the absolute amplitude and phase of the wavepacket are unknown (error bars: standard deviation). **c** Time-energy (Gabor) representation of the ionized electron wavepacket build-up; ionization amplitude as a function of time and energy. The energy range of the ionization spans from about 9 eV below the field-free ionization potential (I_p) of helium to the continuum. We display the field free excited p -state manifold of helium for orientation

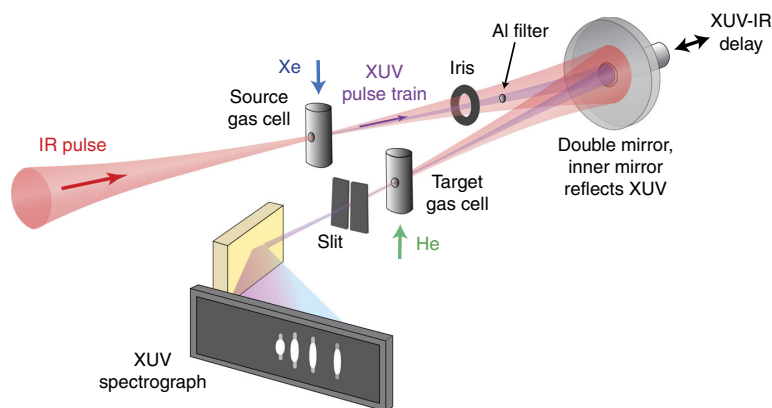


Fig. 5 Experimental setup. The IR beam is focused into the source gas cell where an attosecond pulse train (APT) is generated. The inner part of the IR beam is filtered out with a thin Al foil in order to obtain spatially independent pump (APT) and probe (IR) beams. The temporal delay between the beams is controlled by moving the inner segment of the concave focusing mirror. Both beams are refocused into a target gas cell, generating XUV-initiated HHG. The spectrum resulting from the interaction is measured in a grating-based XUV spectrograph

spectral components of this wavepacket, defined by a_n and ϕ_n (see Eq. 1), are mapped into the observed beating patterns at frequencies of $2\omega_{IR}$, $4\omega_{IR}$ and $6\omega_{IR}$. We decompose the complex contribution of each path by applying a reconstruction procedure to the Fourier data displayed in Fig. 2. In this scheme, the quantum path propagation and interference are evaluated by the CCTSM model while a_n and ϕ_n are unknown (see Methods section). These parameters depend on both phase and amplitude of the harmonics that form the ionizing XUV pulses and the transition dipole from the ground state to the excited states. Fig. 4a, b show the reconstructed amplitude and phase, respectively. Figure 4c displays a time-energy (Gabor) representation of the reconstructed ionization dynamics in helium. The ionization bandwidth reaches as deep as 9 eV below the field-free ionization potential of helium and shows an approximately uniform response in both amplitude and phase to the attosecond pulse. These observations indicate the lack of pronounced resonances and hence strongly support the picture of a continuum-like excited state manifold in helium, as it is driven by an intense IR field. Since the infrared laser field strongly dresses the excited-state manifold of the atom and leads to pronounced broadening of resonance lines due to a strong coupling to the continuum^{29,30}, the excited states can be

approximated by a continuum of states. As such, all the incoming XUV harmonics can excite the atom and populate this continuum of states. Our findings reveal the strong-field limit of a range of phenomena observed in attosecond transient absorption experiments at IR intensities $<10^{13}$ W cm⁻², such as light-induced states³¹ and AC Stark shifts³².

Discussion

In this paper, we have established a spectroscopic scheme in attosecond science. An independent control over both ionization and strong-field propagation enables us to selectively initiate an electron wavepacket in an extreme strong-field environment and reconstruct its temporal evolution following several coupled quantum paths. The precise attosecond dynamics of the wavepacket and its corresponding hole are encoded in the new, background-free, up-converted XUV frequencies and can be extracted using an interferometric method. The highly anharmonic response of the new harmonics to the XUV-IR delay scan is a clear sign of photo-ionization by photons carrying significantly lower energy than the helium ionization threshold; electrons are liberated by OBE rather than tunneling. These spectroscopic measurements provide hitherto inaccessible

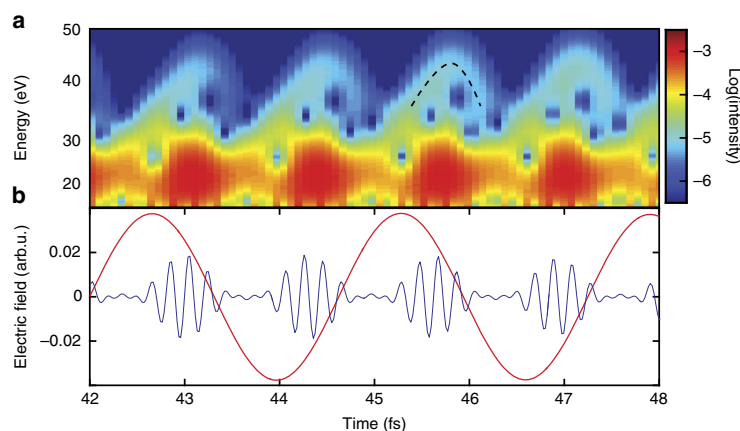


Fig. 6 Time-frequency analysis of the Schrödinger equation simulation. **a** Gabor time-frequency distribution as a function of time and photon energy for $\Delta t = -1575$ as (-0.6 IR cycles), presented in logarithmic scale. At high energies >30 eV, the arch-like structures indicate that XUV emission occurs predominantly as a result of strong-field acceleration. Qualitatively, we find agreement of the emission time from the analysis with recombination times of a classical three-step model (illustrated by the dashed black curve). **b** Input IR and XUV fields in arbitrary units

dynamic information on strongly driven systems on a sub-optical-cycle time scale. Coherent nonlinear spectroscopic methods involving frequency up-conversion in the optical and IR regime are at the heart of vibrational and rotational spectroscopy. Applying background-free frequency up-conversion in the XUV regime can significantly advance electronic spectroscopy.

Looking forward, combining the accuracy provided by the self-probing approach with the versatility provided by attosecond photo-ionization in XUV-initiated HHG opens up exciting directions in ultrafast science. While our work studies XUV-initiated HHG in a simple system, the helium atom, we believe that the concept is general and can be applied in future research to probe more complex systems, such as the study of hole dynamics in inner shells^{33,34}. The main limitation of the approach lies in the competition of XUV photo-ionization with tunneling ionization, which can create a significant background HHG signal; however, our spectroscopic method can be readily applied to atomic and molecular ions due to their higher ionization potential. The unique combination of attosecond resolution with Ångström precision, provided by the recollision process, will resolve the structural information in such systems and will shed light on fundamental phenomena that are at the heart of attosecond science.

Methods

Experimental setup. Figure 5 shows a schematic description of the experimental setup for XUV-initiated HHG. An amplified Ti:Sapphire laser system operated at 1 KHz repetition rate delivers ~ 23 fs pulses at a central wavelength of 787 nm. Focusing the beam into a continuous flow source gas cell (xenon, ~ 12 Torr) generates an APT. We spatially separate the co-propagating IR and APT beams with the help of a thin aluminum filter (200 nm thickness). Both beams are then refocused by a curved two-segment mirror (600 mm focal length) into the continuous flow target gas cell (helium, ~ 20 Torr) in order to produce XUV-initiated HHG. The inner part of the focusing mirror reflects the APT in the spectral range of 17–27 eV. A piezo stage controls the relative delay of IR and APT with 60 as accuracy. The IR intensity at the target gas cell is adjusted with the help of a motorized iris. The generated harmonic radiation is spectrally resolved by a flat-field aberration-corrected concave grating and recorded by a micro-channel plate detector. The spectrum is imaged by a CCD camera. We integrated over each harmonic on the detector in order to obtain its intensity and subtracted the background that is insensitive to the XUV-IR delay (see Supplementary Note 6 and Supplementary Fig. 10).

For the XUV-IR delay scan experiment (Fig. 2), the local laser intensity was $8.7 \pm 1.9 \times 10^{13}$ and $7.8 \pm 1.9 \times 10^{13}$ W cm⁻² in the source and target gas cell, respectively (see Supplementary Note 3). The Fourier transformation of the XUV-IR delay dependent signal includes five oscillation cycles after subtracting the

background. The errors of the Fourier amplitudes and phases represent the obtained standard deviation when varying the offset of the transformation window by ± 2 oscillation cycles.

For the SH perturbative measurements (see Supplementary Note 4 and Supplementary Fig. 7), we used ~ 32 fs pulses in a different configuration of the laser system and generated weak SH radiation by propagating the beam prior to focusing through a Type-I barium boron oxide crystal (100 μ m thickness). Due to the low conversion ratio (below 5 and 0.5% in the measurements of Fig. 3b and Fig. 3d, respectively), the chirp and the spectrum of the SH can be regarded as locked to the IR. A combination of calcite plates and a half-wave plate ensures group delay compensation and common polarization state for the co-propagating IR and SH beams. We control the SH-IR delay with the help of a fused silica wedge pair. We inserted a fused silica window between source and target gas cells in order to allow synchronization either in the source or in the gas cell; the window has a small hole to allow propagation of the APT. For the perturbative measurements, the peak IR intensities in the source and target gas cells were $7.1 \pm 1.9 \times 10^{13}$ and $7 \pm 3 \times 10^{13}$ W cm⁻², respectively.

We estimated the spectral phase of the APT from well-known attochirp values of HHG in xenon gas and the subsequent propagation in the experimental setup; the APT is close to its transform limit (see Supplementary Fig. 11). The perturbative measurement with SH field synchronized with the IR in the source gas cell observed the slope of even harmonics, as predicted by the three-step model (see Fig. 3d). This also provides strong evidence that indeed an APT is generated²¹.

Coulomb-corrected three-step model. The CCTSM describes XUV-initiated HHG in three steps (see Fig. 1b and Supplementary Fig. 1 for an illustration): photo-ionization by the XUV field via OBE, propagation of the electron in the combined laser-Coulomb potential, and recombination into the ground state. Starting from a strong-field approximation approach^{26,33,35}, we generalize the model to include OBE and the influence of the atomic potential²⁵. OBE essentially enables photo-ionization by XUV absorption and subsequent electron emission over the potential barrier lowered by the IR field. In addition, the excited states under the influence of the strong IR field are treated as a quasi-continuum, motivated by theoretical predictions^{29,30}. These modifications are essential since we experimentally observe a strong contribution of the full spectral bandwidth of the APT to the photo-ionization—although H11–H15 are not able to directly ionize helium by themselves when ignoring the effects of the IR field and the Coulomb potential. Although we simplify the interplay of XUV (driving transitions to a quasi-continuum) and IR (creation of a potential barrier that can be passed by an electron without tunneling), the model captures the essential features of the experiment. For a detailed derivation and description, we refer the reader to Supplementary Note 1. Here we only present the essential equations and definitions in atomic units (a.u.).

In the CCTSM, the frequency dipole d along the reaction coordinate z defined by the polarization axis of the laser field is given by

$$d(N\omega_{\text{IR}}) \propto \sum_n \sum_{j=1}^M a_n \exp(-i\phi_n) \left(\frac{\pi}{\eta + \frac{1}{2} \left(t_1^{(n,j)} - t_0^{(n,j)} \right)} \right)^{3/2} \exp \left[i\Theta_{\text{XUV-OBE}} \left(t_1^{(n,j)}, t_0^{(n,j)} \right) \right]. \quad (3)$$

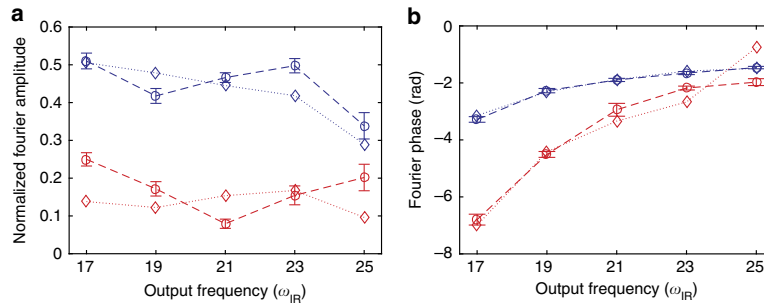


Fig. 7 Comparison of experimental and reconstructed Fourier data. **a** Normalized Fourier amplitudes as a function of output harmonic frequency and Fourier frequency (Circles and dashed lines: experiment, diamonds and dotted lines: theory reconstruction, error bars on experimental data: standard deviation). **b** Like **a**, but showing the Fourier phase

Here a_n is defined as the amplitude of the ionization channel associated with harmonic $n\omega_{\text{IR}}$ and ϕ_n is the corresponding phase—the object of the reconstruction (see below). Several quantum paths contribute to $d(N\omega_{\text{IR}})$, expressed by the two sums over all ionization channels corresponding to input harmonics of frequency $n\omega_{\text{IR}}$ and different trajectory classes, numbered with index j . This defines the multiple-path quantum interferometer (see Eq. 1). In accordance with the experiment, we take only short trajectories into account; these are subdivided into downhill (extra kick away from nucleus) and uphill trajectories (extra kick towards the nucleus)^{18,25}, so $M = 2$. The term in large brackets describes quantum diffusion³⁶, i.e., the decrease of overlap of ground state and emitted wavepacket as it undergoes transversal spread between the times of ionization $t_0^{(n,j)}$ and recollision $t_1^{(n,j)}$. Quantum diffusion leads to a suppression of uphill trajectories since the electron spends a longer time in the continuum compared to downhill trajectories. $\eta \ll 1$ is a small regularization parameter. The quasi-classical action $\Theta_{\text{XUV-OBE}}(t_1^{(n,j)}, t_0^{(n,j)})$ describes the quantum evolution of the system in terms of phase and is given by

$$\Theta_{\text{XUV-OBE}}(t, t') = -n\omega_{\text{IR}}t' + n\omega_{\text{IR}}\Delta t - S_{\text{OBE},cl}(t, t') - I_p(t - t') + N\omega_{\text{IR}}t, \quad (4)$$

with the ionization time t' , the recollision time t , the classical action along the corresponding trajectory $S_{\text{OBE},cl}(t, t')$ and the ionization potential $I_p = 24.59\text{eV}$. The physical meaning corresponds to the three-step picture, with photon absorption ($-n\omega_{\text{IR}}t'$) and its XUV-IR delay dependence ($+n\omega_{\text{IR}}\Delta t$), electron propagation ($S_{\text{OBE},cl}(t, t')$), and ground state evolution ($-I_p(t - t')$), and finally photon emission ($+N\omega_{\text{IR}}t$). A crucial feature of our model is the classical action. It takes the Coulomb force into account and hence must be determined numerically²⁵. We use a Runge-Kutta scheme to solve the equations of motion in the combined laser-Coulomb potential. The helium potential is given by a softcore potential³⁷

$$V(z) = -\frac{Z_{\text{eff}}}{\sqrt{a^2 + z^2}}, \quad (5)$$

with $Z_{\text{eff}} = 1.353$ and $a^2 = 0.001$. We explicitly allow for OBE and exclude tunneling. Excitation to states below the ionization threshold is treated effectively as ionization to a continuum.

The APT and the IR field are treated as infinitely extended in time, a sufficiently good approximation for 25 fs IR pulses. The IR intensity used for the reconstruction is $8 \times 10^{13} \text{ W cm}^{-2}$, and the wavelength is 787 nm. Supplementary Fig. 2 displays ionization and recollision times calculated for these parameters. In the calculations of the SH perturbative experiments, the SH-IR field ratio ϵ was taken as 0.05 and the IR intensity as $7.5 \times 10^{13} \text{ W cm}^{-2}$.

Integration of the time-dependent Schrödinger equation. We performed numerical calculations in order to solve the non-relativistic two-electron TDSE for the helium atom (for more details see Supplementary Note 2). Macroscopic phase matching effects have been omitted. We employed the TD-GAS-CI framework^{27,38,39}, whose accuracy has recently been demonstrated by simulating ionization dynamics in diatomic molecules²⁸. In brief, the many-particle wave function is expanded into a selection of time-independent Slater determinants via the GAS concept. The expansion allows for approximations based on physical arguments; in our case, we ignore double ionization. For the GAS division, we use a complete-active-space (CAS) with single excitations out of the active space^{27,28} (see Supplementary Fig. 3). It contains a variable amount of orbitals ν and is denoted CAS^(2, ν). The more orbitals are included in the CAS, the more electronic correlations effect are taken into account and the better the accuracy of the simulation. In particular, ionization from excited states is then possible. We found good convergence with a CAS^(2,12), where orbitals up to the third shell with a maximum magnetic quantum number $m_{\text{max}} = 1$ are included.

In order to model our experiment, we used a sine-square IR pulse with a peak intensity of $8 \times 10^{13} \text{ W cm}^{-2}$ and a full-width half-maximum (FWHM) intensity duration of 32.5 fs (see Supplementary Fig. 4 and Supplementary Table 1). The XUV field comprising harmonics $n = \{11, 13, 15, 17\}$ is given by normalized amplitudes $b_n = \{0.2214, 0.4227, 0.3127, 0.0432\}$ and flat phase and exhibits a \sin^4 -envelope with a FWHM duration of 15.12 fs. Its peak intensity is $5 \times 10^{10} \text{ W cm}^{-2}$, low enough to suppress two-photon effects. Compared to HHG driven by the IR only, the XUV-initiated HHG creates up to seven orders of magnitude stronger signal (see Supplementary Fig. 5). Scanning the XUV-IR delay leads to a signal similar to the experiment (see Supplementary Fig. 6).

We performed a time-frequency analysis of the dipole acceleration using a short-time Fourier (Gabor) transformation. Figure 6 shows the results of the analysis, plotting the attosecond emission as a function of time and photon energy for $\Delta t = -1575$ as (-0.6 IR cycles). Arch-like structures appear above photon energies of about 30 eV. These structures can be identified with recombination times of the classical three-step model. The arch contains two branches, we find both short trajectories (left branch) and long trajectories (right branch). The prominence of long trajectories in the TDSE results indicates that a quantitative comparison of TDSE and experiment is strongly limited. In our experiment, macroscopic pulse propagation effects favor the short trajectories.

Reconstruction of the build-up of the electron wavepacket. The build-up of the XUV-initiated electron wavepacket is characterized by the complex ionization amplitudes $a_n \exp(-i\phi_n)$, where n denotes a quantum path associated with an input harmonic $n\omega$. It is given by

$$a_n \exp(-i\phi_n) = b_n \exp(-i\beta_n) \times d_{\text{ion}}, \quad (6)$$

and contains both relative amplitude b_n and phase β_n of the XUV field and the (complex) dipole matrix element d_{ion} associated with the transition from the ground state to an effectively ionized excited state. Such reconstruction enables us to resolve the spectro-temporal properties of the XUV-initiated electron wavefunction.

Our measurement represents a multiple path quantum interferometer, controlled by the XUV-IR delay Δt . Using the CCTSM we can link the experimental results—Fourier amplitudes and phases—to the amplitudes $a_n \exp(-i\phi_n)$, where each amplitude corresponds to an absorption channel initiated by a given input harmonic n . We employ a least-square fitting procedure, minimizing the deviation between experimental and theoretical Fourier phases and amplitudes, the latter normalized to the DC amplitude. Since the reconstruction yields relative amplitudes and phases for the wavepacket, we fix the phase of the H13 ionization channel to be $\phi_{13} = 0$ and its amplitude a_{13} to unity, without any associated uncertainty. The calculation does not provide a trajectory from $n = 17$ to $N = 25$; the absence of this trajectory is associated with the error in determining the IR intensity. Although partially visible, the $6\omega_{\text{IR}}$ Fourier component does not reach above the noise level compared to the $2\omega_{\text{IR}}$ and $4\omega_{\text{IR}}$ components (see Fig. 2). Therefore we decided to exclude the $6\omega_{\text{IR}}$ Fourier data from the reconstruction procedure; the remaining data are sufficient for the least-square fit. The strong $6\omega_{\text{IR}}$ component of H19 has a different origin; it is due to interference between the XUV-initiated harmonic light and the background harmonic from the ionizing APT⁴⁰.

We obtain a good agreement between experiment and theory as evidenced by the error bars (standard deviation) in Fig. 4a, b. Figure 7 shows a comparison of experimental Fourier amplitudes and phases with the reconstructed values. $6\omega_{\text{IR}}$ oscillations are also obtained from the reconstruction (not shown), but their amplitudes are not able to overcome the experimental noise floor.

Data availability. The data that support the findings of this study are available from the corresponding author on request.

Received: 27 April 2017 Accepted: 10 October 2017

Published online: 13 November 2017

References

- Paul, P. M. et al. Observation of a train of attosecond pulses from high harmonic generation. *Science* **292**, 1689–1692 (2001).
- Krausz, F. & Ivanov, M. Attosecond physics. *Rev. Mod. Phys.* **81**, 163–234 (2009).
- Ott, C. et al. Reconstruction and control of a time-dependent two-electron wave packet. *Nature* **516**, 374–378 (2014).
- Smirnova, O. et al. High harmonic interferometry of multi-electron dynamics in molecules. *Nature* **460**, 972–977 (2009).
- Cavalieri, A. L. et al. Attosecond spectroscopy in condensed matter. *Nature* **449**, 1029–1032 (2007).
- Schultze, M. et al. Controlling dielectrics with the electric field of light. *Nature* **493**, 75–78 (2013).
- Kim, K. T., Villeneuve, D. M. & Corkum, P. B. Manipulating quantum paths for novel attosecond measurement methods. *Nat. Photon.* **8**, 187–194 (2014).
- Itatani, J. et al. Tomographic imaging of molecular orbitals. *Nature* **432**, 867–871 (2014).
- Baker, S. et al. Probing proton dynamics in molecules on an attosecond time scale. *Science* **312**, 424–427 (2006).
- Cireasa, R. et al. Probing molecular chirality on a sub-femtosecond timescale. *Nat. Phys.* **11**, 654–658 (2015).
- Shafir, D. et al. Resolving the time when an electron exits a tunnelling barrier. *Nature* **485**, 343–346 (2012).
- Schafer, K. J., Gaarde, M. B., Heinrich, A., Biegert, J. & Keller, U. Strong field quantum path control using attosecond pulse trains. *Phys. Rev. Lett.* **92**, 023003 (2004).
- Gaarde, M. B., Schafer, K. J., Heinrich, A., Biegert, J. & Keller, U. Large enhancement of macroscopic yield in attosecond pulse train-assisted harmonic generation. *Phys. Rev. A* **72**, 013411 (2005).
- Biegert, J. et al. Control of high-order harmonic emission using attosecond pulse trains. *J. Mod. Opt.* **53**, 87–96 (2006).
- Brizuela, F. et al. Efficient high-order harmonic generation boosted by below-threshold harmonics. *Sci. Rep.* **3**, 1410 (2013).
- Takahashi, E. J., Kanai, T., Ishikawa, K. L., Nabekawa, Y. & Midorikawa, K. Dramatic enhancement of high-order harmonic generation. *Phys. Rev. Lett.* **99**, 053904 (2007).
- Seres, J. et al. Parametric amplification of attosecond pulse trains at 11 nm. *Sci. Rep.* **4**, 4254 (2014).
- Gademann, G. et al. Attosecond control of electron-ion recollision in high harmonic generation. *New J. Phys.* **13**, 033002 (2011).
- Johnsson, P., Mauritsson, J., Remetter, T., L'Huillier, A. & Schafer, K. J. Attosecond control of ionization by wave-packet interference. *Phys. Rev. Lett.* **99**, 233001 (2007).
- Mauritsson, J. et al. Coherent electron scattering captured by an attosecond quantum stroboscope. *Phys. Rev. Lett.* **100**, 073003 (2008).
- Dudovich, N. et al. Measuring and controlling the birth of attosecond XUV pulses. *Nat. Phys.* **2**, 781–786 (2006).
- Dahlström, J. M., L'Huillier, A. & Mauritsson, J. Quantum mechanical approach to probing the birth of attosecond pulses using a two-colour field. *J. Phys. B At. Mol. Opt. Phys.* **44**, 095602 (2011).
- Pedatzur, O. et al. Attosecond tunnelling interferometry. *Nat. Phys.* **11**, 815–819 (2015).
- Soifer, H. et al. Near-threshold high-order harmonic spectroscopy with aligned molecules. *Phys. Rev. Lett.* **105**, 143904 (2010).
- Hostetter, J. A., Tate, J. L., Schafer, K. J. & Gaarde, M. B. Semiclassical approaches to below-threshold harmonics. *Phys. Rev. A* **82**, 023401 (2010).
- Lewenstein, M., Balcou, P., Ivanov, M. Y., L'Huillier, A. & Corkum, P. B. Theory of high-harmonic generation by low-frequency laser fields. *Phys. Rev. A* **49**, 2117–2132 (1994).
- Bauch, S., Sørensen, L. K. & Madsen, L. B. Time-dependent generalized-active-space configuration-interaction approach to photoionization dynamics of atoms and molecules. *Phys. Rev. A* **90**, 062508 (2014).
- Larsson, H. R., Bauch, S., Sørensen, L. K. & Bonitz, M. Correlation effects in strong-field ionization of heteronuclear diatomic molecules. *Phys. Rev. A* **93**, 013426 (2016).
- He, F., Ruiz, C., Becker, A. & Thumm, U. Attosecond probing of instantaneous ac Stark shifts in helium atoms. *J. Phys. B At. Mol. Opt. Phys.* **44**, 211001 (2011).
- Singh, K. P. & Rost, J. M. Global control of attosecond photoionization of atoms through XUV dispersion. *Phys. Rev. A* **91**, 013415 (2015).
- Beck, A. R., Neumark, D. M. & Leone, S. R. Probing ultrafast dynamics with attosecond transient absorption. *Chem. Phys. Lett.* **624**, 119–130 (2015).
- Chini, M. et al. Subcycle ac stark shift of helium excited states probed with isolated attosecond pulses. *Phys. Rev. Lett.* **109**, 073601 (2012).
- Leeuwenburgh, J., Cooper, B., Averbukh, V., Marangos, J. P. & Ivanov, M. Y. High-order harmonic generation spectroscopy of correlation-driven electron hole dynamics. *Phys. Rev. Lett.* **111**, 123002 (2013).
- Brown, A. C. & van der Hart, H. W. Extreme-ultraviolet-initiated high-order harmonic generation: driving inner-valence electrons using below-threshold-energy extreme-ultraviolet light. *Phys. Rev. Lett.* **117**, 093201 (2016).
- Figueira de Morisson Faria, C. & Salieres, P. High-order harmonic generation with a strong laser field and an attosecond-pulse train: the Dirac-Delta comb and monochromatic limits. *Laser Phys.* **17**, 390–400 (2007).
- Skruzewicz, S. et al. Two-color strong-field photoelectron spectroscopy and the phase of the phase. *Phys. Rev. Lett.* **115**, 043001 (2015).
- Chen, S., Ruiz, C. & Becker, A. Double ionization of helium by intense near-infrared and VUV laser pulses. *Phys. Rev. A* **82**, 033426 (2010).
- Hochstuhl, D. & Bonitz, M. Time-dependent restricted-active-space configuration-interaction method for the photoionization of many-electron atoms. *Phys. Rev. A* **86**, 053424 (2012).
- Olsen, J., Roos, B. O., Jørgensen, P. & Jensen, H. J. A. Determinant based configuration interaction algorithms for complete and restricted configuration interaction spaces. *J. Chem. Phys.* **89**, 2185–2192 (1988).
- Simpson, E. R. et al. Polarisation response of delay dependent absorption modulation in strong field dressed helium atoms probed near threshold. *New J. Phys.* **18**, 083032 (2016).

Acknowledgements

We thank Yann Mairesse, Mette B. Gaarde, Kenneth J. Schafer, Albert Stolow, David J. Tannor, and Andreas Kaldun for helpful discussions. N.D. is the incumbent of the Robin Chermers Neustein Professorial Chair. N.D. acknowledges the Minerva Foundation, the Israeli Science Foundation, the Crown Center of Photonics, and the European Research Council for financial support. M.K. acknowledges financial support by the Minerva Foundation and the Koshland Foundation. H.R.L. acknowledges financial support by the DAAD (German Academic Exchange Service), the Studienstiftung des Deutschen Volkes, and the Fonds der Chemischen Industrie. S.B. acknowledges financial support from the BMBF (Federal Ministry of Education and Research, Germany) in the frame of the Verbundprojekt FSP 302.

Author Contributions

N.D. conceived and supervised the study. D.A. designed the experimental setup. D.A. and M.K. built the experimental setup, performed the experiment, and analyzed the data. M.K., G.O. and D.A. devised the theory model. B.D.B. supported the operation of the laser system. H.R.L. and S.B. conceived and performed the time-dependent Schrödinger equation calculations. All authors discussed the results and contributed to the final manuscript.

Additional information

Supplementary Information accompanies this paper at doi:10.1038/s41467-017-01723-w.

Competing interests: The authors declare no competing financial interests.

Reprints and permission information is available online at <http://npg.nature.com/reprintsandpermissions/>

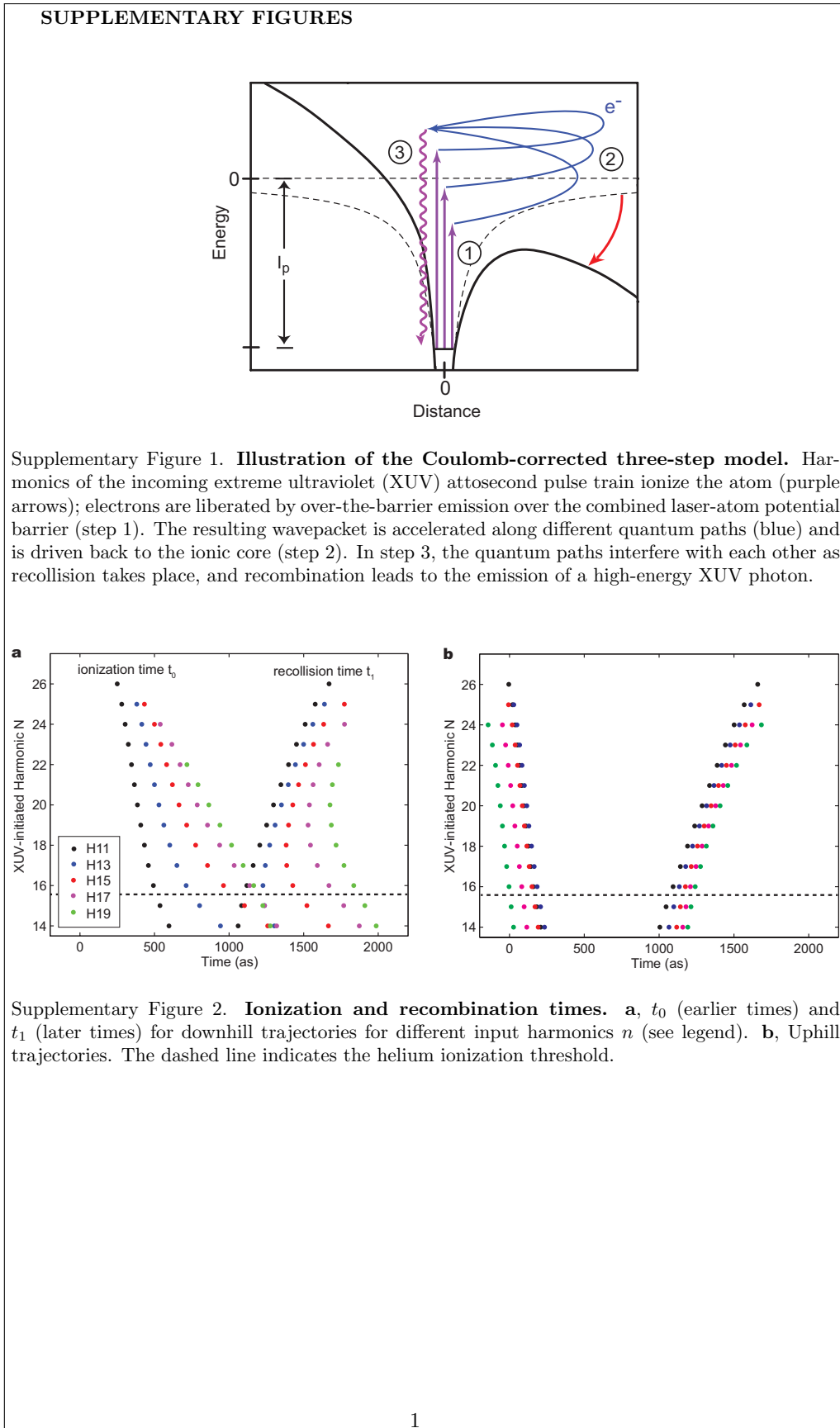
Publisher's note: Springer Nature remains neutral with regard to jurisdictional claims in published maps and institutional affiliations.

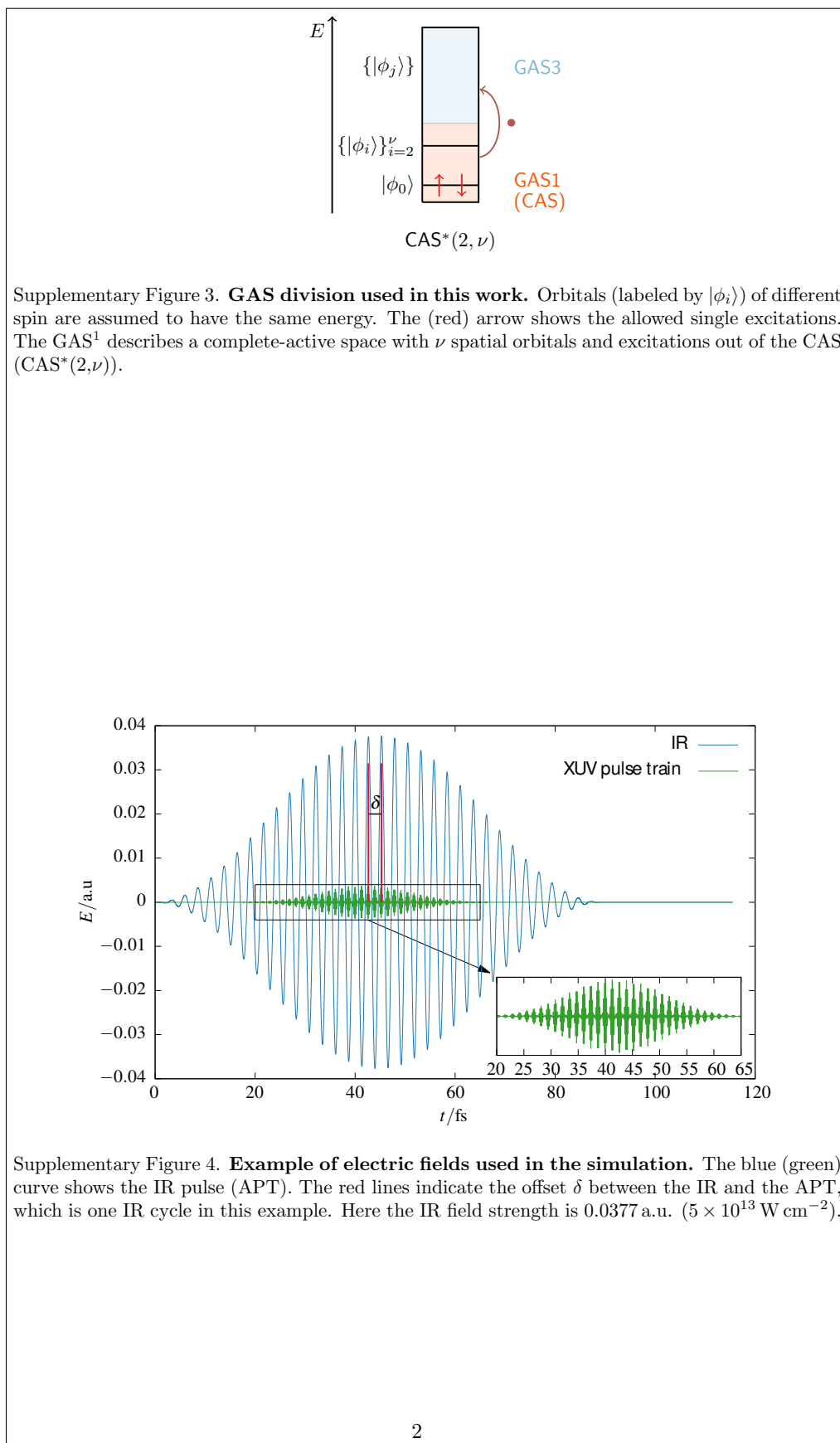


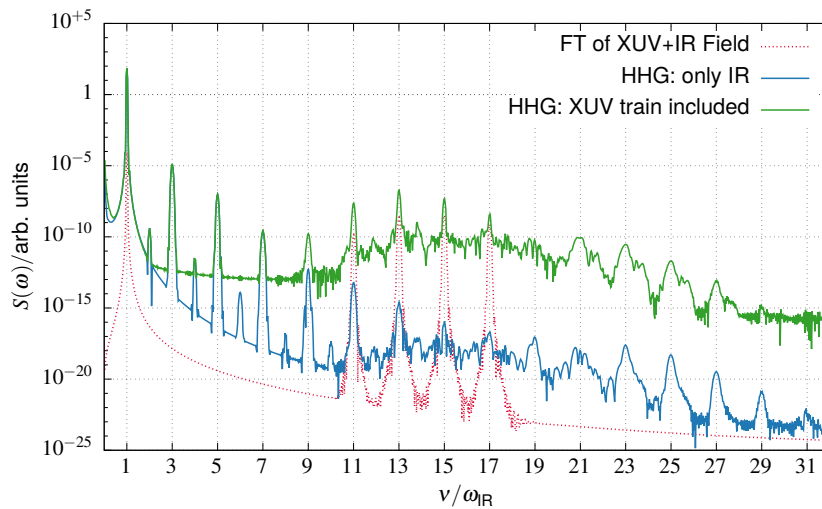
Open Access This article is licensed under a Creative Commons Attribution 4.0 International License, which permits use, sharing, adaptation, distribution and reproduction in any medium or format, as long as you give appropriate credit to the original author(s) and the source, provide a link to the Creative Commons license, and indicate if changes were made. The images or other third party material in this article are included in the article's Creative Commons license, unless indicated otherwise in a credit line to the material. If material is not included in the article's Creative Commons license and your intended use is not permitted by statutory regulation or exceeds the permitted use, you will need to obtain permission directly from the copyright holder. To view a copy of this license, visit <http://creativecommons.org/licenses/by/4.0/>.

© The Author(s) 2017

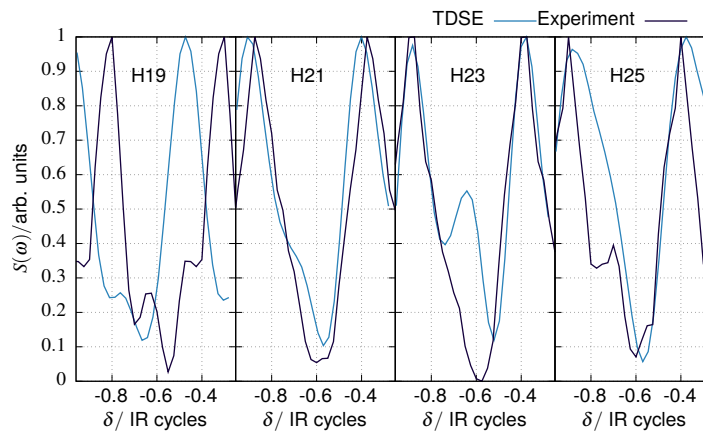
II.4.2.4. Supplementary Information



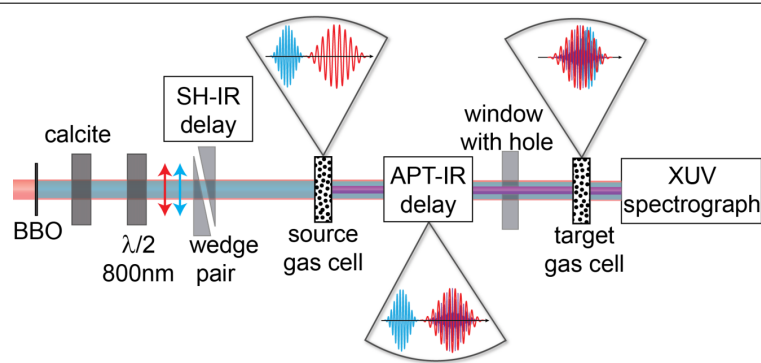




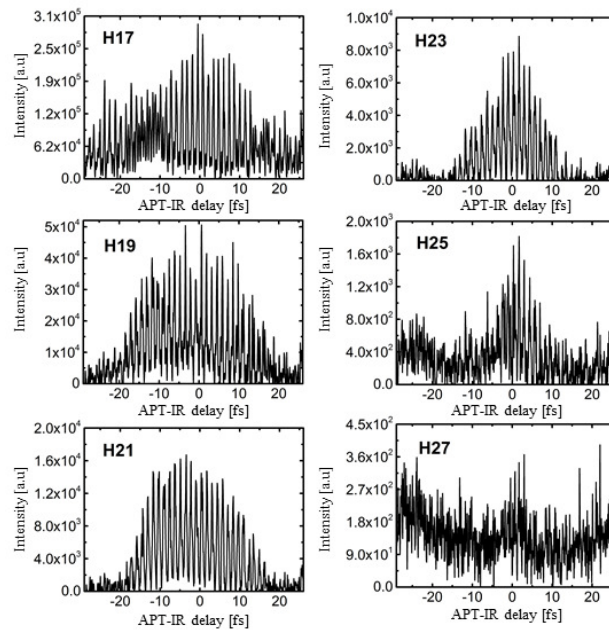
Supplementary Figure 5. **Simulated HHG spectra.** At zero delay ($\delta = 0$) for an IR field strength of 0.0377 a.u. ($5 \times 10^{13} \text{ W cm}^{-2}$). Shown is the spectrum for the simulation with only the IR pulse and the APT (green). For clarification, the Fourier transform of the field of the IR pulse and the APT is shown as well (red). Note the logarithmic scale of the spectrum.



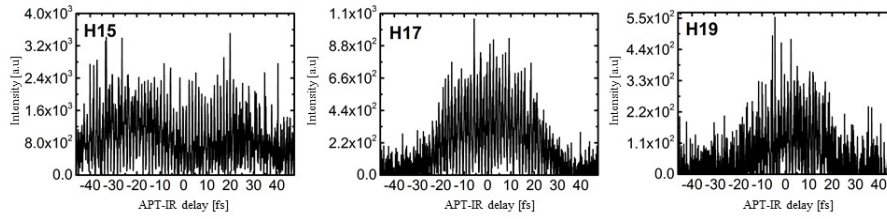
Supplementary Figure 6. **Simulated XUV-IR delay scan results.** We show the results of the TDSE simulations (blue) and the experimental data (black) for harmonics 19 to 25. The IR field strength is 0.0477 a.u. ($8 \times 10^{13} \text{ W cm}^{-2}$).



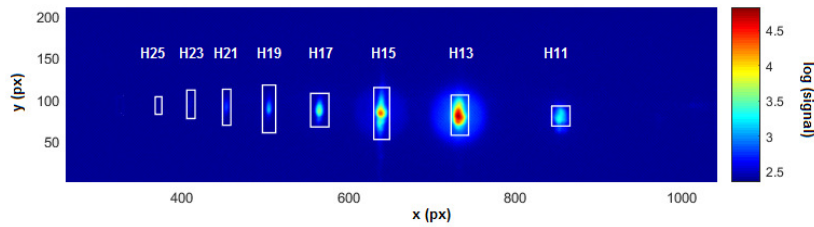
Supplementary Figure 7. **Experimental set-up for perturbative measurements.** Before the IR beam (red lines) enters the source gas cell, it is frequency doubled by a thin BBO crystal (blue lines). Calcite windows in conjunction with a fused silica window after the source gas cell control the place in which the SH and IR pulses are synchronized (synchronization in the target gas cell is exemplified here). The fused silica window has a central hole in order to allow transmission of the APT (purple lines). Following the calcite windows, a half wavelength waveplate is used for rotating the IR polarization to match the SH polarization direction. The sub-cycle SH-IR delay is controlled by a fused silica wedge pair. The XUV-IR delay control and the spectrum measurement are the same as in the one-dimensional measurement.



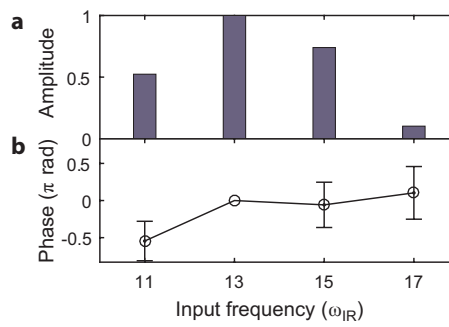
Supplementary Figure 8. **Long range delay scan with helium in the target gas cell.** Intensity of harmonics 17 to 27 as function of the relative XUV-IR delay. Zero delay is defined arbitrarily.



Supplementary Figure 9. **Long range delay scan with neon in the target gas cell.** Intensity of harmonics 17 to 27 as function of the relative XUV-IR delay. Zero delay is defined arbitrarily.



Supplementary Figure 10. **Example spectrum.** Image of the MCP detector screen with the CCD camera. The XUV-IR delay is set so that the intensity of the new harmonics is maximized. All harmonics and the corresponding regions of interest are denoted by white boxes.



Supplementary Figure 11. **Spectral properties of the APT.** Relative amplitudes (a) and relative phases (b) of the input harmonics, with H13 as reference. The error bars indicate the standard deviation.

SUPPLEMENTARY TABLES

Description	Definition
Phase of the XUV components	$\beta_n \in \{0, \pi, 0, \pi\}$
Weights of the XUV components	$b_n \in \{0.2214, 0.4227, 0.3127, 0.0432\}$
Frequency of the IR field	$\omega = 0.0579$ (787 nm)
Amplitude of the IR field	$E_0^{\text{IR}} = 0.0477$ (8×10^{13} W cm $^{-2}$)
Amplitude of the XUV field	$E_0^{\text{XUV}} = 0.00119$ (5×10^{10} W cm $^{-2}$)
Duration of the IR field	$T^{\text{IR}} = 3.6896 \times 10^3$ (32.49 fs FWHM in intensity)
Duration of the XUV field	$T^{\text{XUV}} = 2.3931 \times 10^3$ (15.12 fs FWHM in intensity)

Supplementary Table 1. **Time-dependent Schrödinger equation simulation parameters.**
Parameters for the fields corresponding to Supplementary Equations 26, 27, 28

SUPPLEMENTARY NOTES
Supplementary Note 1: Coulomb-corrected three-step model

In this section, we detail the Coulomb-corrected three-step model (CCTSM), a simple model for XUV-initiated high-harmonic generation (HHG). It is motivated by the fact that the semi-classical three-step model² needs to be extended in order to describe photoionization by an XUV attosecond pulse train (APT) and the resulting XUV-IR delay oscillations.

The CCTSM describes XUV-initiated HHG in three steps (see Supplementary Figure 1 for an illustration): Photoionization by the XUV field via over-the-barrier emission (OBE), propagation of the electron in the combined laser-Coulomb potential and recombination into the ground state. Starting from a strong-field approximation approach³⁻⁵, we generalize the model to include OBE and the influence of the atomic potential⁶. OBE essentially enables photoionization by XUV absorption and subsequent electron emission over the potential barrier lowered by the IR field. In addition, the excited states under the influence of the strong IR field are treated as a quasi-continuum, motivated by theoretical predictions^{7,8}. These modifications are essential since we experimentally observe a strong contribution of the full spectral bandwidth of the APT to the photo-ionization – although H11 to H15 are not able to directly ionize helium by themselves when ignoring the effects of the IR field and the Coulomb potential. Although we simplify the interplay of XUV (driving transitions to a quasi-continuum) and IR (creation of a potential barrier that can be passed by an electron without tunneling), the model captures the essential features of the experiment.

Lewenstein-like ansatz to the problem

We begin our derivation of the model based on the Lewenstein's seminal paper³, closely following the work of Leeuwenburgh and co-authors⁵. Throughout this section we use atomic units (a.u.). The IR field $\mathbf{E}_{\text{IR}}(t)$ and the XUV field $\mathbf{E}_{\text{XUV}}(t)$ are defined as

$$\mathbf{E}_{\text{IR}}(t) = \mathbf{e}_z E_{\text{IR}}(t) = \mathbf{e}_z E_0^{\text{IR}} \cos(\omega t), \quad (1)$$

$$\mathbf{E}_{\text{XUV}}(t) = \mathbf{e}_z E_{\text{XUV}}(t) = \mathbf{e}_z E_0^{\text{XUV}} \sum_n b_n \cos(n\omega t - \beta_n). \quad (2)$$

Note that the XUV APT is decomposed into a Fourier series with individual weights, b_n , and phases, β_n . Both fields are linearly polarized along axis z (unit vector \mathbf{e}_z). The IR vector potential is defined as $\mathbf{A}_{\text{IR}}(t) = -\mathbf{e}_z E_{\text{IR}}/\omega \sin \omega t$.

Next, we formulate the time-dependent dipole along the laser polarization axis

$$d(t) = i \int_{-\infty}^t dt' \int d^3\mathbf{p} E_{\text{XUV}}(t') d_z(\mathbf{p} + \mathbf{A}_{\text{IR}}(t')) \exp[iS(\mathbf{p}, t, t')] d_z^*(\mathbf{p} + \mathbf{A}_{\text{IR}}(t)) + c.c. \quad (3)$$

First, we assume that ionization is dominated by the APT; hence, we only consider transitions from the ground state to Volkov states, mediated by the rapidly oscillating XUV electric field $\mathbf{E}_{\text{XUV}}(t)$. Here we define $d_z(\mathbf{v})$ as the projection of the dipole matrix element connecting the ground state to a Volkov state \mathbf{v} onto the polarization axis. Hence the term $E_{\text{XUV}}(t') d_z(\mathbf{p} + \mathbf{A}_{\text{IR}}(t'))$ describes the photoionization step. Second, we assume that the propagation of the ionized electron wavepacket is dominated by the slowly varying IR field. The quasi-classical action S describes the phase evolution of the photoelectron and the ground state and is given by

$$S(\mathbf{p}, t, t') = - \int_{t'}^t dt'' \left(\frac{[\mathbf{p} + \mathbf{A}_{\text{IR}}(t'')]^2}{2} + I_p \right). \quad (4)$$

Last, the term $d_z^*(\mathbf{p} + \mathbf{A}_{\text{IR}}(t))$ in Supplementary Equation 3 accounts for the recombination step.

We now apply the saddle point approximation in the canonical momentum \mathbf{p} and find

$$d(t) = i \int_{-\infty}^t dt' \left(\frac{\pi}{\eta + \frac{i}{2}(t - t')} \right)^{3/2} E_{\text{XUV}}(t') d_z(\mathbf{p}_{\text{st}} + \mathbf{A}_{\text{IR}}(t')) \\ \times \exp[iS(\mathbf{p}_{\text{st}}, t, t')] d_z^*(\mathbf{p}_{\text{st}} + \mathbf{A}_{\text{IR}}(t)) + c.c., \quad (5)$$

with $\eta \ll 1$ and the saddle point momentum

$$\mathbf{p}_{\text{st}}(t, t') = - \frac{1}{t - t'} \int_{t'}^t dt'' \mathbf{A}_{\text{IR}}(t''). \quad (6)$$

Note that the first term of Supplementary Equation 5 in large brackets is identified with the spreading of the free electron wavepacket during propagation, decreasing the overlap with the ground state with increasing time. The harmonic spectrum follows from $I(N\omega) \propto (N\omega)^4 |d(N\omega)|^2$, with the frequency dipole

$$d(N\omega) = i \int_{-\infty}^{+\infty} dt \exp(iN\omega t) \int_{-\infty}^t dt' \left(\frac{\pi}{\eta + \frac{i}{2}(t - t')} \right)^{3/2} E_{\text{XUV}}(t') d_z(\mathbf{p}_{\text{st}} + \mathbf{A}_{\text{IR}}(t')) \\ \times \exp[iS(\mathbf{p}_{\text{st}}, t, t')] d_z^*(\mathbf{p}_{\text{st}} + \mathbf{A}_{\text{IR}}(t)) + c.c., \quad (7)$$

where N can be identified with the harmonic order of the emitted XUV light.

Saddle point approximation for XUV-initiated HHG

The natural interpretation of t' and t (Supplementary Equation 7) are ionization time and recollision time, respectively. Carrying out a saddle point approximation with t and t' naturally leads to the notion of electron trajectories. Owing to the high-frequency XUV field, a saddle point approach for t' cannot be applied for S as defined earlier, unlike tunneling-initiated HHG. However, we can include the rapidly oscillating XUV field in S and hence circumvent this issue. A similar approach was chosen independently in another work⁴. After completing the following derivation, we will discuss the absence of IR-induced tunneling in XUV-initiated HHG as evidenced by the experiment.

For simplicity we will focus only on a single ionizing XUV frequency $n\omega$. The term in the exponent for the saddle point approach with the rotating component $\exp(-in\omega t')$ of the XUV field then becomes:

$$\Theta_{\text{XUV}}(\mathbf{p}_{\text{st}}, t, t') = -n\omega t' - \int_{t'}^t dt'' \left(\frac{[\mathbf{p}_{\text{st}}(t, t'') + \mathbf{A}_{\text{IR}}(t'')]^2}{2} + I_p \right) + N\omega t. \quad (8)$$

Together with the saddle point equation for \mathbf{p}_{st} , we retrieve a set of three equations:

$$\frac{\partial \Theta_{\text{XUV}}(\mathbf{p}, t, t')}{\partial t'} \Big|_{\mathbf{p}_{\text{st}}, t_1, t_0} \rightarrow \frac{1}{2} [\mathbf{p}_{\text{st}} + \mathbf{A}_{\text{IR}}(t_0)]^2 = -I_p + n\omega, \quad (9)$$

$$\frac{\partial \Theta_{\text{XUV}}(\mathbf{p}, t, t')}{\partial \mathbf{p}} \Big|_{\mathbf{p}_{\text{st}}, t_1, t_0} \rightarrow \int_{t_0}^{t_1} dt'' [\mathbf{p}_{\text{st}} + \mathbf{A}_{\text{IR}}(t'')] = 0, \quad (10)$$

$$\frac{\partial \Theta_{\text{XUV}}(\mathbf{p}, t, t')}{\partial t} \Big|_{\mathbf{p}_{\text{st}}, t_1, t_0} \rightarrow \frac{1}{2} [\mathbf{p}_{\text{st}} + \mathbf{A}_{\text{IR}}(t_1)]^2 = -I_p + N\omega, \quad (11)$$

where t_0 and t_1 are the obtained saddle times from t' and t , respectively. We also obtain a solution $\Theta_{\text{XUV}+}(\mathbf{p}, t, t')$ that includes $\exp(+in\omega t')$ of the XUV field. This counterrotating solution does not play any role because of the extremely large imaginary part of the corresponding saddle value t_0 .

Transversal components of p do not contribute to the dipole along the laser polarization axis \mathbf{e}_z , so we confine it to one dimension ($\mathbf{p} \rightarrow p$, etc.). The resulting saddle point equations give us a natural insight into the physical mechanism: First, we ionize the atom by XUV photoionization, then the electron is driven back to the ionic core, and it finally recombines, leading to the emission of a high-energy photon. The ionization step is mediated by an XUV photon, which results in a modified initial energy $n\omega - I_p$. If the energy of the incoming XUV photon is larger than the ionization energy I_p , we retrieve a real-valued saddle time t_0 . The solution naturally provides us with the excess energy of the liberated electron. Since linear single-photon ionization shows no directionality in electron velocity, we obtain two branches of solutions for t_0 (and also for the other saddle variables), denoted as $t_{0(+)}$ and $t_{0(-)}$:

$$p_{\text{st}} + A_{\text{IR}}(t_{0(\pm)}) = \pm \sqrt{2(-I_p + n\omega)}. \quad (12)$$

This means that the XUV photon energy has a strong influence on the timings of the electron trajectory via the excess kinetic energy of the photoelectron. The two classes (+) and (-) can be identified with downhill (extra kick away from the nucleus) or uphill (extra kick towards the nucleus), respectively, in line with earlier findings^{6,9-11}. If the energy of the XUV photon cannot liberate the electron, then the first step of the HHG process is brought about by a combination of XUV excitation and IR tunneling ionization. Here the saddle times and the momentum acquire imaginary components.

Finally, we obtain the following expression for the frequency dipole:

$$d(N\omega) = \frac{1}{2} \sum_{j=1}^M \frac{2\pi}{\sqrt{\det \mathcal{H} \Theta_{\text{XUV}-}(t, t')|_{t_1^{(j)}, t_0^{(j)}}}} \left(\frac{\pi}{\eta + \frac{i}{2}(t_1^{(j)} - t_0^{(j)})} \right)^{3/2} E_0^{\text{XUV}} b_n \exp(-i\beta_n) \\ \times d_z(p_{\text{st}}^{(j)} + A_{\text{IR}}(t_0^{(j)})) \exp[i\Theta_{\text{XUV}-}(p_{\text{st}}^{(j)}, t_1^{(j)}, t_0^{(j)})] d_z^*(p_{\text{st}}^{(j)} + A_{\text{IR}}(t_1^{(j)})), \quad (13)$$

where M indicates the number of trajectories within a full cycle of the IR and \mathcal{H} indicates the Hessian of the function that follows it.

In the experiment, the majority of input harmonics can't directly ionize the helium atom without the assistance of the IR field. However, the experimental results clearly show that all input harmonics lead to photoionization. Hence, within the framework of the present model, IR-induced tunneling ionization from a transiently excited state must necessarily take place, leading to imaginary saddle times and imaginary S . However, depending on the magnitude of the effective ionization potential given by the difference of the XUV photon energy and the binding energy, these imaginary components will induce a strong dampening of the resulting dipole. If we take multiple input harmonics into consideration, this will also result in dampening of the XUV-IR oscillations. In the experiment, however, we do not observe strong dampening; the contrast of the oscillations is very high (see Supplementary Figure 8). Thus, we conclude that the contribution of IR-induced tunneling ionization is likely to be very small or even non-existent. This is confirmed by the second harmonic perturbative experiments (see Figure 3 in the main text). An alternative approach to describe the interplay between XUV and IR is provided by OBE. In the following section we will outline the necessary modifications to the theoretical model.

Over-the-barrier emission in the combined laser-atom-potential

Here we consider OBE, closely following Ref. 6 and modifying the model that we formulated in the last paragraph. OBE is an alternative way to describe the interplay of IR and XUV in the process. Here electrons undergo transitions from the ground state to transiently excited states. There they possess sufficiently large kinetic energy to overcome the potential barrier created by the IR field and the Coulomb potential, hence they can be considered as ionized. Note that throughout the main text and from this point in this Supplementary Note we employ the term XUV photoionization although the ionization process technically is a combination of XUV photoexcitation and subsequent OBE.

Because the electrons are propagating in the combined laser-atom potential, the canonical momentum p is no longer well-defined; recollision trajectories and the associated ionization and recombination times have to be determined numerically. We calculate short electron trajectories in the combined laser-atom potential by numerically integrating Newton's equations of motion. Here we use a 4th order Runge-Kutta-Fehlberg algorithm¹², considering a 1D softcore-Coulomb potential of the form

$$V(z) = -\frac{Z_{\text{eff}}}{\sqrt{a^2 + z^2}}, \quad (14)$$

representing helium with effective nuclear charge $Z_{\text{eff}} = 1.353$ and softening parameter $a^2 = 0.001$ ¹³. For a set of ionization times t_0 we launch electrons at $z_0 = 0$ with initial velocity $v_0 = \pm\sqrt{2(-I_p - V(z_0) + n\omega)}$, corresponding to the kinetic energy of a photoionized electron within the atomic potential. For those electrons subjected to OBE we also have to consider both downhill (+) and uphill (-) trajectories. We propagate electrons of both trajectory classes and calculate the first return time $t_{1(+)}$ for downhill trajectories and the second return time, denoted as $t_{1(-)}$, for uphill trajectories. For each trajectory we determine the corresponding final kinetic energy and the accumulated classical action $S_{\text{OBE,cl}}(t, t')$. We register final kinetic energies corresponding to the emission of a harmonic photon (energy $N\omega$) and thus obtain a full solution with emission time, recombination time and action, linking an input harmonic n to an output harmonic N .

Having obtained OBE trajectory solutions, we now make use of Supplementary Equation 13 which was derived in the previous subsection, but in a strongly reduced form. For simplicity we retain only the essential term that describes the broadening of the electron wavepacket during (Coulomb-free) propagation¹⁴ and the exponential term containing the (numerically calculated) action, the evolution of the ground state and the frequency of the absorbed and emitted photons. A strong modification, however, is neglecting the momentum dependence of the dipole matrix elements. Therefore we make no distinction between ionization to continuum states and excitation to states below the ionization threshold – everything is treated effectively as ionization to a continuum. At IR intensities similar to those applied in our experiment ($5 \dots 10 \times 10^{13} \text{ W cm}^{-2}$), bound-state resonances in singly-excited helium are strongly shifted and broadened by the laser field^{7,8}. In the experiment, we do not observe signatures of pronounced excited state or continuum resonances. A full treatment of these resonances including transient absorption phenomena can be performed with extensive *ab-initio* modeling, but a conclusive measurement, for example with attosecond transient absorption, remains elusive to date to the best of our knowledge. For our purposes a simple model based on the aforementioned approximations was sufficient. The frequency dipole now reads,

$$d(N\omega) \propto \sum_{j=1}^M a_n \exp(-i\phi_n) \left(\frac{\pi}{\eta + \frac{i}{2}(t_1^{(j)} - t_0^{(j)})} \right)^{3/2} \exp[i\Theta_{\text{XUV}, \text{OBE}}(t_1^{(j)}, t_0^{(j)})], \quad (15)$$

with the redefined term in the exponent

$$\Theta_{\text{XUV},\text{OBE}}(t, t') = -n\omega t' - S_{\text{OBE,cl}}(t, t') - I_{\text{p}}(t - t') + N\omega t. \quad (16)$$

Here we integrated the complex dipole matrix element for XUV photoionization and the XUV's amplitude and phase into new parameters a_n and ϕ_n which form together the complex ionization amplitude

$$a_n \exp(-i\phi_n) = b_n \exp(-i\beta_n) d_z(\mathbf{p}_{\text{st}} + \mathbf{A}_{\text{IR}}(t')). \quad (17)$$

a_n and ϕ_n effectively describe the XUV photoionization process and ultimately the build-up of the XUV-initiated electron wavepacket. As it can be seen from Supplementary Equation 16, we recover the intuitive three-step picture of photon absorption ($-n\omega t'$), electron propagation ($S_{\text{OBE,cl}}(t, t')$) and ground state evolution ($-I_{\text{p}}(t - t')$), and finally photon emission ($+N\omega t$). No tunneling is involved; the electron trajectories are treated in a completely classical way.

Dependence of XUV-initiated HHG on XUV-IR delay

We will now examine the case of multiple XUV frequencies where we sum over their respective contributions to the final spectrum. This is required for XUV-IR delay dependence within our model. With two neighboring harmonics of one kind (even or odd), the final dipole frequency spectrum $|d(N\omega)|^2$ is a result of XUV-IR delay dependent quantum interference of the respective trajectory pair. For the sake of illustration we assume input harmonics n and $n + 2$ with equal excitation amplitudes $a_n = a_{n+2}$ and equal prefactor $f = \pi / \left[\eta + i/2 \left(t_1^{(n)} - t_0^{(n)} \right)^{3/2} \right]$ and calculate the intensity of an XUV-initiated harmonic N :

$$\begin{aligned} |d(N\omega)|^2 = C |f a_n|^2 & \left| \exp \left\{ -n\omega(t_0^{(n)} - \Delta t) - S_{\text{OBE,cl}}(t_1^{(n)}, t_0^{(n)}) - I_{\text{p}}(t_1^{(n)} - t_0^{(n)}) + N\omega t_1^{(n)} \right\} \right. \\ & \left. + \exp \left\{ -(n+2)\omega(t_0^{(n+2)} - \Delta t) - S_{\text{OBE,cl}}(t_1^{(n+2)}, t_0^{(n+2)}) - I_{\text{p}}(t_1^{(n+2)} - t_0^{(n+2)}) + N\omega t_1^{(n+2)} \right\} \right|^2 \end{aligned} \quad (18)$$

We see that the interference term is proportional to $\cos(\Delta n\omega\Delta t - \varphi_{\text{osc}}(N))$, where $\Delta n = 2$ is the difference in harmonic number, Δt is the XUV-IR delay and $\varphi_{\text{osc}}(N)$ is the oscillation phase that mainly originates from the difference in ionization times. This introduces a simple half-cycle delay dependence into the model. The phase $\varphi_{\text{osc}}(N)$ and the corresponding optimal XUV-IR delay are related, but not identical, to the average ionization time of the trajectory pair. A Fourier analysis clearly shows an oscillatory behavior with the main component oscillating at twice the IR frequency, but also weaker oscillations at 4ω and 6ω (see Figure 2 in the main text). These higher frequency components arise from the interference of trajectories from harmonics with $\Delta n = 4$ and $\Delta n = 6$, respectively. This defines the multiple path quantum interferometer, the main focus of the of this work. Even higher frequencies can result from interference of an ionizing harmonic with an XUV-initiated harmonic of the same frequency¹⁵. However, this type of oscillation was not observed in the experiment since most XUV-initiated high harmonics are background-free; the only exception is H19.

Conservation of parity

In the following we will evaluate how parity is transferred from the input harmonics to the XUV-initiated harmonics. We assume that ionization is triggered either by an even or an odd harmonic n . We consider two OBE trajectories in subsequent half cycles (A) and (B), all corresponding to a trajectory leading to the emission of harmonic N – one trajectory being the exact mirror image of the other. Evaluating $|d(N\omega)|^2$ then yields

$$|d(N\omega)|^2 \propto \cos^2 [(n - N)\pi/2 + (S_{\text{OBE,cl}}^{(A)} - S_{\text{OBE,cl}}^{(B)})/2], \quad (19)$$

with $S_{\text{OBE,cl}}^{(A)}$ and $S_{\text{OBE,cl}}^{(B)}$ being the corresponding action terms. Due to the symmetry of the trajectories, the action terms are equal and cancel each other. It is obvious that only for even $(n - N)$ constructive interference is obtained. Therefore, the parity of the harmonics is conserved in the process. This is in line with the experimental observation that the parity of the input harmonics is transferred directly to the output harmonics (see Figure 3d and e in the main text). Hence the effects of even and odd input harmonics can be treated separately in the model.

Calculation details

In order to apply the model to describe the experiment, we will consider short trajectories only. We take into account both downhill and uphill trajectories, with the former naturally dominating over the latter due to shorter excursion times. We target the helium atom ($I_p = 24.59$ eV), the IR intensity is 8×10^{13} W cm⁻², and the wavelength is 787 nm for the strong-field model calculation used in the reconstruction of a_n and ϕ_n (see Figure 4 in the main manuscript).

First, we describe trajectory calculations for a set of odd input harmonics n ranging from H11 to H19. Supplementary Figure 2 displays ionization times t_0 and recollision times t_1 of output harmonics H14 to H26 for downhill and uphill electrons, respectively. The harmonic cut-off averaged over all input harmonics is in agreement with the simple three-step picture², $N_{\text{max}}\omega \sim I_p + 3U_p$. Also the cut-off observed in the experiment agrees with the three-step picture. Note that in our specific experiment the downhill trajectory initiated by H13 dominates over all other channels. It is this trajectory that mainly defines the time-energy mapping of XUV-initiated HHG.

In the following, we will consider the experiment with the second harmonic (SH) of the IR present in the target gas cell (see Figure 3a-c, main text). The symmetry breaking between initially left- and right-moving trajectories by the SH field cannot be described in the simple phase perturbation picture (Eq. 2, main text), since the canonical momentum p is not well-defined for propagation in the Coulomb potential. Instead, we include the SH field directly into the trajectory calculations and repeat the simulation for a set of SH-IR phases. A 2D scan yields the SH-IR oscillation phases shown in Figure 3c in the main text after integration over XUV-IR delay. Here ε was taken as 0.05 and the IR intensity as 7.5×10^{13} W cm⁻². We use the ionization amplitudes $a_{11} = 0.2055$, $a_{13} = 0.3584$, $a_{15} = 0.3831$ and $a_{17} = 0.0530$. We determine the ionization amplitudes by measuring the intensity difference of each harmonic when the APT and the IR pulse overlap in time compared to the case when helium is absent in the target gas cell. Furthermore, we assume a flat phase because the choice of the phase does not affect the response of XUV-initiated HHG to the SH field once we integrate over XUV-IR delay.

For simulating the XUV-initiated HHG with a pulse train consisting of even and odd harmonics (Figure 3d and e, main text), we extracted the SH-IR-phase-dependent ionization amplitudes $a_n(\varphi)$ from the measurements of the xenon harmonics. The coefficients

are defined as $a_n(\varphi) = \bar{a}_n + c_n \cos 2(\varphi - \varphi_{n,0})$, where \bar{a}_n is the phase-averaged (DC) amplitude corresponding to the harmonic n , c_n the (AC) amplitude of the oscillation and $\varphi_{n,0}$ the optimal SH-IR phase as extracted from the experiment. We calculated a full XUV-IR delay scan for each SH-IR phase φ and the corresponding input spectrum, yielding the results shown in Figure 3e in the main text after integration over XUV-IR delay. The IR intensity was taken as $7.5 \times 10^{13} \text{ W cm}^{-2}$.

Supplementary Note 2: Integration of the time-dependent Schrödinger equation

In the following section, we will detail our calculations using the time-dependent Schrödinger equation (TDSE) that includes two-electron correlations.

Theory

For computing the HHG process, we focus on the non-relativistic, quantum-mechanical theory of a single helium atom, thereby neglecting macroscopic phase effects¹⁶. The dynamics are governed by the TDSE for the two-electron wave function. In atomic units ($m_e = e = 4\pi\epsilon_0 = 2|E_{\text{Ryd}}| = a_0 = 1$), it reads as

$$i\frac{\partial}{\partial t} |\Psi(t)\rangle = \hat{H}(t) |\Psi(t)\rangle, \quad (20)$$

with the time-dependent Hamiltonian in spatial representation

$$\hat{H}(t) = \sum_{i=1}^2 \hat{h}_i(t) + \frac{1}{|\mathbf{r}_1 - \mathbf{r}_2|}, \quad (21)$$

where \mathbf{r}_i is the position operator of electron i . The single-particle Hamiltonian $\hat{h}_i(t)$ is

$$\hat{h}_i(t) = -\frac{1}{2}\nabla_i^2 - \frac{2}{|\mathbf{r}_i - \mathbf{R}|} + W(\mathbf{r}, t), \quad (22)$$

where \mathbf{R} denotes the position operator of the nucleus. In the calculation, $\mathbf{R} = \mathbf{0}$ is fixed. The interaction with the field, $W(\mathbf{r}, t)$, is treated within the dipole approximation using the velocity gauge,

$$W(\mathbf{r}, t) = -i\mathbf{A}(t) \cdot \nabla. \quad (23)$$

Here, $\mathbf{A}(t)$ is the vector potential of the corresponding electric field which is assumed to be linearly polarized in z direction. In order to exploit symmetry, Supplementary Equation (20) is transformed to spherical coordinates^{17–19}.

The HHG spectrum is computed by the Fourier transform of the dipole acceleration in the z direction, \ddot{z} ^{19,20}

$$S^z(\omega) \propto \omega^{-4} \left| \int_0^{t_{\text{final}}} dt \langle \Psi(t) | \ddot{z} | \Psi(t) \rangle \exp(-i\omega t) \right|^2. \quad (24)$$

Owing to the numerical complexity of the two-electron ionization dynamics, e.g., the HHG process, we approximate Supplementary Equation (20) using the time-dependent generalized-active-space configuration-interaction (TD-GAS-CI) framework^{21–24}. Its accuracy has recently been demonstrated by simulating ionization dynamics in diatomic molecules¹. In the TD-GAS-CI approximation, the many-particle wave function is expanded into a selection of time-independent Slater determinants $|\Phi_I\rangle$ via the GAS concept. This allows for an approximation based on physical assumptions, namely, that

double ionization is ignored. The Slater determinants themselves are antisymmetrized linear combinations of single-particle-functions (orbitals), following a partition-in-space-concept^{22,23}. Thereby, an inner region in the vicinity of the nucleus and an outer region is defined. The outer region consists of a primitive basis, in particular spherical harmonics for the angular part and a finite-element discrete-variable-representation (FE-DVR) for the radial part^{25,26}. The inner region consists of a linear combination of the primitive basis whose expansion coefficients are determined by a Hartree-Fock-like procedure²². We refer to Ref. 1, 22, 23 for details of our approach.

Numerical set-up

The primitive basis consists of spherical harmonics with quantum number l up to 10 and $|m|$ up to 1. The inner region of the basis consists of two finite elements, the first with 8 DVR functions within $r \in [0, 2)$ and the second element with 15 functions within $r \in [2, 15)$ (in atomic units). The outer region consists of 76 equally distributed elements containing 10 functions from $r = 15$ to $r < r_{\text{end}} = 600$. The total number of basis functions is then 21824. The convergence of the used basis has been carefully checked.

To avoid rescattering at the boundary, we use a complex absorbing potential (CAP) of the form^{27,28}

$$V_{\text{CAP}} = -i \left\{ 1 - \cos \left[\frac{\pi(|r| - r_{\text{CAP}})}{2(r_{\text{end}} - r_{\text{CAP}})} \right] \right\}, \quad r > r_{\text{CAP}}, \quad (25)$$

with $r_{\text{CAP}} = 500$ as the start of the CAP.

For the GAS division, we follow the work of Refs.^{1,22} and use a complete-active-space (CAS) with single excitations out of the active space approximations, depicted schematically in Supplementary Figure 3. It contains a variable amount of orbitals ν and is denoted CAS*(2, ν). The more orbitals are included in the CAS, the more electronic correlations effect are taken into account and the better the accuracy of the simulation. In particular, ionization from excited states is then possible. In the context of quantum chemistry, CAS*(2, ν) would be denoted as multi-reference CIS. Regarding the selection of the orbitals in the CAS, we found good convergence with a CAS*(2,12), where orbitals up to the third shell with $m_{\text{max}} = 1$ are included. This corresponds to approximately half a million Slater determinants. In the following, we denote the CAS*(2,12) as TDSE to simplify the notation.

The laser field utilized in the simulations consists of two parts stemming from the IR field and from the APT,

$$E(t) = E_{\text{IR}}(t) + E_{\text{XUV}}(\Delta t). \quad (26)$$

The IR field is described by a \sin^2 envelope,

$$E_{\text{IR}}(t) = \begin{cases} E_0^{\text{IR}} \sin(\omega t) \sin^2(\pi t/T_{\text{IR}}) & , t < T_{\text{IR}}, \\ 0 & , \text{else.} \end{cases} \quad (27)$$

The APT is modeled by a linear combination of phase-shifted XUV pulses with \sin^4 -envelope:

$$E_{\text{XUV}}(\Delta t) = \sum_{n \in \{11,13,15,17\}} E_0^{\text{XUV}} b_n \sin(n\omega\Delta t + \beta_n) \sin(\pi\Delta t/T_{\text{XUV}})^4 \times E_{\text{XUV}}^{\text{U}}(\Delta t), \quad (28)$$

$$E_{\text{XUV}}^{\text{U}}(\Delta t) = \begin{cases} 1 & , \Delta t > T^{\text{XUV}} \wedge \Delta t > 0 \wedge t < T^{\text{IR}}, \\ 0 & , \text{else.} \end{cases} \quad (29)$$

The APT is shifted in units of IR cycles, t_{cycl} ,

$$\Delta t = t - \delta_{\text{XUV}} t_{\text{cycl}} - \frac{T_{\text{IR}} - T_{\text{XUV}}}{2}. \quad (30)$$

The last term in Supplementary Equation (30) is required to shift the maximum of the APT so that it coincides with the maximum of the IR pulse at $\delta_{\text{XUV}} = 0$. The parameters are listed in Supplementary Table 1. The weights of the XUV components, b_n , are taken from the experiment. An example is shown in Supplementary Figure 4.

Simulation Results

Here we present the results of our simulations of XUV-initiated HHG. In order to illustrate the effect of the APT, we first compute the HHG spectrum from a simulation without the APT ($E_0^{\text{XUV}} = 0$), and compare it to a simulation with the APT at zero delay ($\delta = 0$). Supplementary Figure 5 compares the two cases – tunneling-initiated and XUV-initiated HHG. The presence of the APT results in a pronounced increase of the intensities of harmonics 19 to 29, here up to eight orders of magnitude. Indeed, no trace of tunneling-initiated HHG was observed in the experiment.

The results from the XUV-IR delay scans are depicted in Supplementary Figure 6. We compare the calculated curves to the experimental data. Because delay zero, $\delta = 0$, cannot be retrieved from the experiment, the theory curves are shifted uniformly to match the first peak of harmonic 23. In order to obtain the intensity of a given harmonic from the simulations, we integrated over a spectral range of $\pm 0.1\omega$ around the central frequency of the harmonic. The agreement of the simulations and the experimental results is fair. We also observe significant anharmonicity of the oscillations, with a strong Fourier component at 4ω .

Supplementary Note 3: Preparatory measurements

Prior to the XUV-IR delay scan experiment, we performed a series of preparatory experiments. First, we recorded the spectrum of the xenon harmonics in the absence of helium gas. We optimized both the laser parameters and the focus position relative to the source gas cell for generating the brightest and least divergent harmonics. The local laser intensity in the cell was $8.7 \pm 1.9 \times 10^{13} \text{ W cm}^{-2}$. Second, we recorded the HHG spectrum of argon instead of helium atoms at the target gas cell (without xenon in the source gas cell). According to the measured cutoff energy, we evaluated the peak IR intensity at the target gas cell to be $7.8 \pm 1.9 \times 10^{13} \text{ W cm}^{-2}$. Third, we performed an absorption measurement of the xenon harmonics in helium by recording the spectrum while scanning the XUV-IR delay over a wide range of 300 fs so that we could observe the two extreme cases in which the IR pulse precedes the APT, and vice versa. According to the wide range absorption scan, we chose a narrow range (60 fs) for the high-resolution XUV-IR delay scan (see Supplementary Figure 8). We repeated the measurement for neon instead of helium atoms in the target gas cell (see Supplementary Figure 9), with a peak IR intensity of $5.2 \pm 1.9 \times 10^{13} \text{ W cm}^{-2}$ at the source gas cell and $5 \pm 2 \times 10^{13} \text{ W cm}^{-2}$ in the target gas cell.

Supplementary Note 4: Perturbative measurement experimental set-up

For the SH perturbative measurements, we used the laser system in a different configuration, with a pulse duration of 32 fs. We perturbed the interaction by adding the

second harmonic (SH) of the IR pulse (see Supplementary Figure 7). For that purpose, we generated the SH by propagating the IR beam through a barium boron oxide (BBO) crystal (thickness of $100\ \mu\text{m}$) followed by a half-wave plate, which matches the polarization of the pulses, before focusing them into the source gas cell. We control the relative sub-cycle temporal delay between the IR beam and the SH by a fused silica wedge pair with an accuracy of 80 as. The synchronization of the IR and the SH pulses is controlled by a series of calcite windows before the source gas cell, in conjunction with a fused silica window (thickness of 2 mm) between the gas cells, so that we can synchronize both pulses either solely in the source gas cell or in the target gas cell, by adding or reducing calcite thickness, respectively. We drilled a 3 mm diameter hole in the center of the fused silica window in order to allow propagation of the APT.

In addition to the preliminary experiments described above, we verified that the SH field is delayed sufficiently with respect to the IR pulse, so that the SH field does not affect HHG of xenon in the source gas cell. For this purpose, we performed an SH-IR delay scan while we recorded xenon HHG (no gas in the target gas cell). We could not detect even harmonics for a large range of SH intensities, which indicates that the SH perturbative HHG experiments are completely self-contained. We repeated these tests for the experiments in which we synchronized the SH and IR pulses in the source gas cell.

In the perturbative measurements in which we synchronized the SH and IR pulses in the target or the source gas cell, the SH-IR intensity ratio ε^2 was below 5% and 0.5%, respectively. For both measurements, the peak IR intensities in the source and target gas cells were $7.1 \pm 1.9 \times 10^{13}\ \text{W cm}^{-2}$ and $7 \pm 3 \times 10^{13}\ \text{W cm}^{-2}$, respectively. We typically scanned over 2-3 IR cycles for both the XUV-IR and SH-IR dimensions, with 60 as and 80 as accuracy, respectively. Since the measurement duration is relatively long (about two hours), it is prone to temporal and intensity drifts. In some cases, we observed systematic temporal drifts in the XUV-IR delay dimension, which we corrected.

Supplementary Note 5: Wide-range delay scans in helium and neon

Supplementary Figure 8 shows the intensity of harmonics 17 to 27 as a function of the XUV-IR delay over a delay range of 60 fs, in addition to the result we presented in Figure 2a in the main text. One can see that the envelope of the oscillations becomes narrower in time with ascending harmonic order. This response is expected since the generation of higher harmonics requires higher field intensities and the field intensity in the IR pulse gradually increases towards its temporal center. All harmonics oscillate with high contrast, motivating the use of Coulomb-corrected three-step model (see Supplementary Note 1). As described above, we repeated the experiment with neon instead of helium in the target gas cell. Supplementary Figure 9 shows the intensity oscillations of harmonics 15-19 as a function of XUV-IR delay. Here we generated 3 harmonics above the neon ionization threshold since we used a lower IR peak intensity. Using the same IR peak intensity as in the helium experiment, the lower ionization threshold of neon already allows tunneling-initiated HHG from its ground state, which adds a significant background.

Supplementary Note 6: Data acquisition and analysis

All results from the experiments are based on spectroscopic measurements. For every XUV-IR delay, we measured the average spectrum over 100 IR pulses. Next, for each harmonic we set a specific region of interest (ROI) and integrated over it (see Supplementary Figure 10). We used the ROI mask to extract the intensity of each harmonic as a function of XUV-IR delay. The constant background for each harmonic was determined according

to the measured intensity at large XUV-IR delays where the APT and the IR pulse do not overlap temporally, and it was subsequently subtracted. We Fourier transformed the data within a window of 5 oscillation cycles and varied the offset delay of the window by ± 2 oscillation cycles in order to obtain statistics of the signals. We extracted the average values of Fourier amplitudes and phases which form the basis of the reconstruction procedure. In this approach, the error bars are given by the standard deviations of the amplitudes and phases (see Figure 7 in the Methods section of the main text), and hence indicate how robust the signal is to the choice of the integration window.

In the SH perturbative measurements, we raster scanned over both the XUV-IR and SH-IR delays, and recorded the spectrum for every delay point. For each harmonic (including the even harmonics in these experiments), we followed the same steps described above for integration and background subtraction. Accordingly, we created a two-dimensional intensity map for each harmonic, as a function of both delays. Next, we summed over the dimensions cycle wise, forming an integrated map (typically we scan over 3 oscillation cycles for each dimension). We followed the same steps in order to extract the optimal delays for the XUV-IR dimension as described above. For the SH-IR phases, we integrated over all the XUV-IR delays, fit a sinusoidal function to the oscillating harmonics intensity and extracted the associated SH-IR phase. The errors for the XUV-IR delay scans are dominated by the position accuracy of the piezo stage, which moves the XUV mirror and hence, control the XUV-IR delay. The errors in the SH-IR phases are calculated according to the standard deviation of the sinusoidal fit.

SUPPLEMENTARY REFERENCES

-
- ¹ Larsson, H. R., Bauch, S., Sørensen, L. K. & Bonitz, M. Correlation effects in strong-field ionization of heteronuclear diatomic molecules. *Phys. Rev. A* **93**, 013426 (2016).
 - ² Corkum, P. B. Plasma perspective on strong field multiphoton ionization. *Phys. Rev. Lett.* **71**, 1994–1997 (1993).
 - ³ Lewenstein, M., Balcou, P., Ivanov, M. Y., L’Huillier, A. & Corkum, P. B. Theory of high-harmonic generation by low-frequency laser fields. *Phys. Rev. A* **49**, 2117–2132 (1994).
 - ⁴ Figueira de Morisson Faria, C. & Salières, P. High-order harmonic generation with a strong laser field and an attosecond-pulse train: The Dirac-Delta comb and monochromatic limits. *Laser Physics* **17**, 390–400 (2007).
 - ⁵ Leeuwenburgh, J., Cooper, B., Averbukh, V., Marangos, J. P. & Ivanov, M. Y. High-order harmonic generation spectroscopy of correlation-driven electron hole dynamics. *Phys. Rev. Lett.* **111**, 123002 (2013).
 - ⁶ Hostetter, J. A., Tate, J. L., Schafer, K. J. & Gaarde, M. B. Semiclassical approaches to below-threshold harmonics. *Phys. Rev. A* **82**, 023401 (2010).
 - ⁷ He, F., Ruiz, C., Becker, A. & Thumm, U. Attosecond probing of instantaneous ac Stark shifts in helium atoms. *J. Phys. B: At. Mol. Opt. Phys.* **44**, 211001 (2011).
 - ⁸ Singh, K. P. & Rost, J. M. Global control of attosecond photoionization of atoms through XUV dispersion. *Phys. Rev. A* **91**, 013415 (2015).
 - ⁹ Schafer, K. J., Gaarde, M. B., Heinrich, A., Biegert, J. & Keller, U. Strong field quantum path control using attosecond pulse trains. *Phys. Rev. Lett.* **92**, 023003 (2004).
 - ¹⁰ Gaarde, M. B., Schafer, K. J., Heinrich, A., Biegert, J. & Keller, U. Large enhancement of macroscopic yield in attosecond pulse train-assisted harmonic generation. *Phys. Rev. A* **72**, 013411 (2005).
 - ¹¹ Gademann, G. *et al.* Attosecond control of electron-ion recollision in high harmonic generation. *New J. Phys.* **13**, 033002 (2011).
 - ¹² Fehlberg, E. Classical Runge–Kutta formulas of fourth and lower order with stepsize control and their use for heat problems. *Computing* **6**, 61–71 (1970).

- ¹³ Chen, S., Ruiz, C. & Becker, A. Double ionization of helium by intense near-infrared and VUV laser pulses. *Phys. Rev. A* **82**, 033426 (2010).
- ¹⁴ Skruszewicz, S. *et al.* Two-color strong-field photoelectron spectroscopy and the phase of the phase. *Phys. Rev. Lett.* **115**, 043001 (2015).
- ¹⁵ Simpson, E. R. *et al.* Polarisation response of delay dependent absorption modulation in strong field dressed helium atoms probed near threshold. *New J. Phys.* **18**, 083032 (2016).
- ¹⁶ Gaarde, M. B., Tate, J. L. & Schafer, K. J. Macroscopic aspects of attosecond pulse generation. *J. Phys. B: At. Mol. Opt. Phys.* **41**, 132001 (2008).
- ¹⁷ McCurdy, C. W., Baertschy, M. & Rescigno, T. N. Solving the three-body coulomb breakup problem using exterior complex scaling. *J. Phys. B: At. Mol. Opt. Phys.* **37**, R137–R187 (2004).
- ¹⁸ Hochstuhl, D., Hinz, C. & Bonitz, M. Time-dependent multiconfiguration methods for the numerical simulation of photoionization processes of many-electron atoms. *Eur. Phys. J. Special Topics* **223**, 177–336 (2014).
- ¹⁹ Han, Y.-C. & Madsen, L. B. Comparison between length and velocity gauges in quantum simulations of high-order harmonic generation. *Phys. Rev. A* **81**, 063430 (2010).
- ²⁰ Bandrauk, A. D., Chelkowski, S., Diestler, D. J., Manz, J. & Yuan, K.-J. Quantum simulation of high-order harmonic spectra of the hydrogen atom. *Phys. Rev. A* **79**, 023403 (2009).
- ²¹ Sørensen, L. K., Bauch, S. & Madsen, L. B. The integral screened configuration interaction method (2016). arXiv:1609.07757.
- ²² Bauch, S., Sørensen, L. K. & Madsen, L. B. Time-dependent generalized-active-space configuration-interaction approach to photoionization dynamics of atoms and molecules. *Phys. Rev. A* **90**, 062508 (2014).
- ²³ Hochstuhl, D. & Bonitz, M. Time-dependent restricted-active-space configuration-interaction method for the photoionization of many-electron atoms. *Phys. Rev. A* **86**, 053424 (2012).
- ²⁴ Olsen, J., Roos, B. O., Jørgensen, P. & Jensen, H. J. A. Determinant based configuration interaction algorithms for complete and restricted configuration interaction spaces. *J. Chem. Phys.* **89**, 2185–2192 (1988).
- ²⁵ Balzer, K., Bauch, S. & Bonitz, M. Efficient grid-based method in nonequilibrium Green's function calculations: Application to model atoms and molecules. *Phys. Rev. A* **81**, 022510 (2010).
- ²⁶ Rescigno, T. & McCurdy, C. Numerical grid methods for quantum-mechanical scattering problems. *Phys. Rev. A* **62**, 032706 (2000).
- ²⁷ Zanghellini, J., Jungreuthmayer, C. & Brabec, T. Plasmon signatures in high harmonic generation. *J. Phys. B: At. Mol. Opt. Phys.* **39**, 709 (2006).
- ²⁸ Miyagi, H. & Madsen, L. B. Time-dependent restricted-active-space self-consistent-field theory for laser-driven many-electron dynamics. *Phys. Rev. A* **87**, 062511 (2013).

II.4.2.5. Complementary Information

In Fig. II.4.4, the HHG spectrum is compared at different levels of approximation. In general, the convergence is slow and electronic correlation effects significantly affect the shape and amplitude of the peaks. Taking correlation effects into account (more electronic repulsion is described in configuration interaction singles (CIS) and CAS*) significantly increases the amplitude compared to the spectrum computed by the single active electron (SAE) approximation (red curve). CIS shows a partial overestimation, see below.

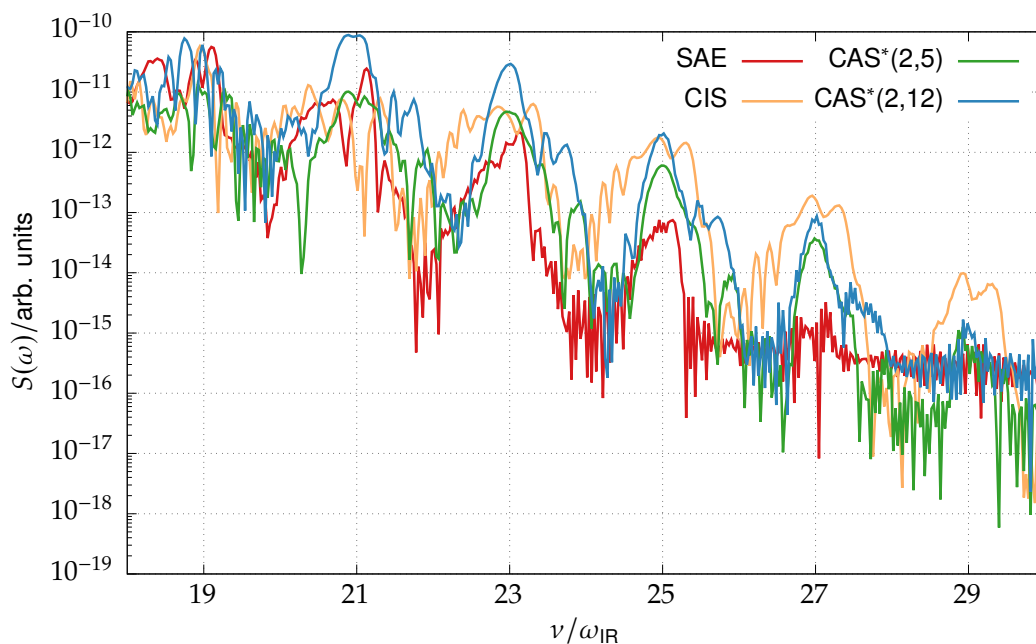


Figure II.4.4.: Comparison of several GAS approximations of the HHG spectra in the region of interest. The field parameters are the same as those shown in Supplementary Figure 5 in Section II.4.2.4.

The results from the scan of time delays are depicted in Fig. II.4.5 for SAE, CIS (upper panel), CAS*(2,5) and CAS*(2,12) (lower panel) simulations. The curves are compared to the experimental values. Note that here, compared to the publication, a weaker field intensity is used.

Comparing just the theoretical data, CIS shows more erratic results than SAE, although the CI space includes more configurations than SAE; see also Fig. II.4.4. Error cancellation effects in SAE may give an answer to this paradox; see also Ref. [355], where a similar behavior has been found in a quite different theoretical setup.

In the SAE approximation (red curve), the side-maxima at $\delta \approx 0$ are much more pronounced (i. e. a higher oscillation frequency; compare with Fig. 2 in Publication 7 (Section II.4.2) on page 228), especially for harmonics 23 and 25. Taking electronic correlation effects into account, these maxima are weakened. The curves obtained from the CAS*(2,5) approximation (green curve) still exhibit saddles (harmonics 23 and 25) or small side maxima (harmonic 21) but otherwise match the experimental curves very well. Taking even more correlation effects into account (CAS*(2,12), blue curve), the saddles or side-maxima disappear. For a higher intensity (Supplementary

Figure 6 in Section II.4.2.4), the side maxima reappear, also for CAS*(2,12). As already noted in Publication 7 (Section II.4.2), a quantitative comparison between theory and experiment is limited. Besides taking into account macroscopic phase effect, one should also take into account the intensity profile of the experimental field. This, however, is hard to retrieve and would require many simulations for different field intensities.

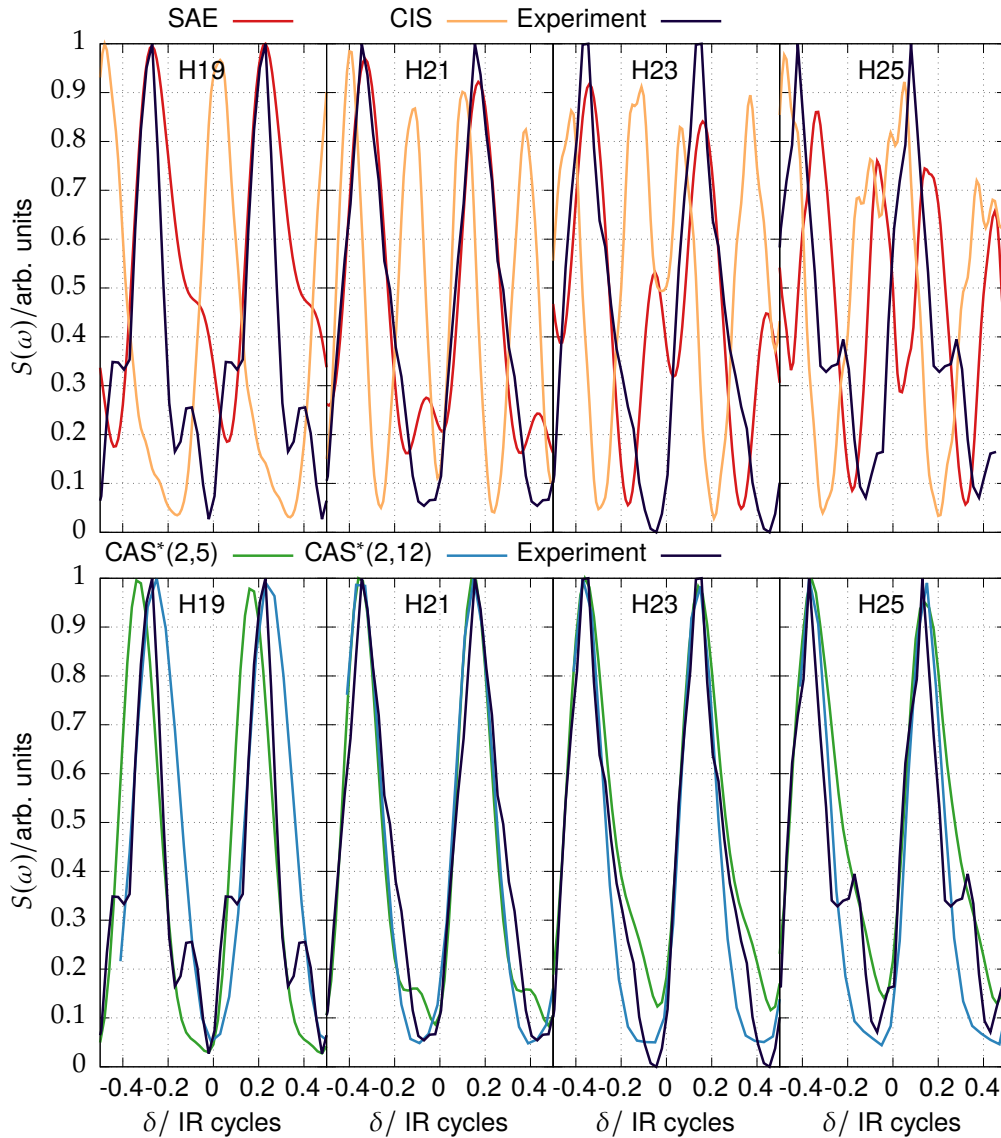


Figure II.4.5.: HHG intensities as a function of the delay between infrared and XUV pulse. Shown are the results for harmonics 19 to 25 from the SAE (red), CIS (orange), CAS*(2,5) (green), CAS*(2,12) (blue) simulations and the experiment (black). Here and in contrast to Supplementary Figure 6 of Section II.4.2.4, the infrared field intensity in all simulations is $5 \times 10^{13} \text{ W cm}^{-2}$.

Further, also two-dimensional intensity scans like those (from experiment) shown in Fig. 3 of Publication 7 (Section II.4.2) (page 230) have been tried. Compared to experiment, the oscillation frequency is higher by a factor of two. Up to now, this could not be explained. Therefore, the results are not shown here.

Part III

Conclusions

Chapter III.1

Résumé

” *Have no fear of perfection — you’ll never reach it.*

— Salvador Dalí
(attributed)

This thesis dealt with the development of dynamical pruning (DP) for multidimensional quantum dynamics in Part I and its application to molecular and electronic systems in Part II. The term DP refers to a dynamical, that is time-dependent, selection of basis functions from a direct-product basis, resulting in non-direct-product type subspaces. In Section I.1.1 and I.1.2, the mathematical structures were reviewed, and new findings about projectors onto various subspaces presented. Further, the phase-space-localized projected von Neumann with biorthogonal exchange (PvB) basis was reviewed. PvB is the biorthogonal von Neumann (vN) basis, projected onto the space spanned by Fourier grid hamiltonian (FGH) or similar discrete variable representation (DVR) functions. In the original formulation, PvB required a DVR basis with an equidistantly distributed grid. Section I.1.1.4.2 discussed the generalization to other DVRs with nonequidistantly distributed grids. The accuracy of the original vN basis was discussed in Section I.1.1.4.1.

In Section I.1.1 and I.1.3, the applicability of dynamically pruned PvB to the treatment of multidimensional systems was discussed. Nonorthogonality was identified as the key problem that hinders the usage of favorably scaling matrix-vector products (tensor transformations). Discussions of possible approximations of the inverse of the overlap matrix to introduce the favorable scaling were done in Section I.1.1 and I.1.2. The approximations turned out to be not satisfying for solving the time-dependent Schrödinger equation (TDSE).

Consequently, a new, phase-space localized, but orthogonal basis, the projected Weylets (pWs), has been developed in Section I.1.3. pW combines DVR accuracy and ease of usage of PvB with the orthogonality and phase-space locality of the Weylet basis developed by PORIER ET AL.^[104-106] pW is less localized than PvB but its orthogonality leads to a favorably scaling matrix-vector product. pW has been thoroughly tested and compared with coordinate-space localized DVR for real-world

examples in [Section I.1.3](#). The examples covered ergodic dynamics of three-dimensional NO₂ and up to six-dimensional dynamics of a vibronic coupling model of pyrazine. Although [DVR](#) needs more basis functions than [pW](#), [DVR](#) bases turned out to be typically faster and easier to use than [pW](#). This is due to the diagonality of the potential energy operator in [DVR](#) representation, which lowers the prefactor of the computational scaling of the matrix-vector product. Further, in contrast to both [pW](#) and [PvB](#), no sum-of-products (SoP) form of the potential is required in a [DVR](#). Compared to unpruned [DVR](#) dynamics, speedups of up to 25 were obtained. Later, in [Part II](#), the [DP-DVR](#) was thoroughly tested for challenging applications, namely 1) resonance calculations of DCO using filter diagonalization, 2) resonance decay dynamics covering propagation times up to almost 200 picoseconds into the asymptotic region, 3) accurate photoelectron momentum distribution (PMD) computations for essentially two-dimensional hydrogen and 4) two-electron control dynamics in a one-dimensional helium model in strong external fields. The last two applications showed that [DP-DVR](#) is not only useful for molecular but also electron dynamics, including the description of the two-electron continuum.

The success of [DP](#) was only possible due to extensive algorithmic improvements. The usage of hash tables and similar data structures enabled an efficient scheme for adding neighboring basis functions in [DP](#), as shown in [Section I.1.3](#). There, an algorithm for the matrix-vector product with pruned bases was developed. In this algorithm, the product is performed sequentially and in each sequence, the pruned basis is permuted to obtain contiguous access to the required elements of the basis function coefficient vector. This results in an efficient three-loop structure. It has later been used by WODRASZKA AND CARRINGTON.^[236]

In [Section I.2.1](#), [DP](#) was combined with the multi-configuration time-dependent Hartree ([MCTDH](#)) algorithm in two ways, namely [DP](#) of the primitive basis and/or of the single-particle functions ([SPFs](#)). While the former was more or less straightforward, the latter required the generalization of the developed algorithm to the handling of density matrices and similar quantities. In [Section I.2.1 \(I.2.1.4.2\)](#), the pruned configurational [SPF](#) space was analyzed and the usability of natural orbitals was discussed. The resulting [DP-MCTDH](#) was tested using NO₂ for pruning the primitive basis either with a [DVR](#) or with [PvB](#) and using 24-dimensional pyrazine with mode combination. In the latter case, this resulted in the pruning of a nine-dimensional [SPF](#) space. Speedups of up to 50 were obtained, making [DP-MCTDH](#) competitive and often easier to apply than multilayer multi-configuration time-dependent Hartree ([ML-MCTDH](#)). Compared to the latter, [DP-MCTDH](#) requires fewer parameters and allows for more mode combinations such that the requirements for specific forms of the potential operator are reduced.

The method development and applications were performed with a newly developed, full-fledged quantum dynamics package (for distinguishable particles), called LAGOM. It is mostly written in Python and C++ and its implementation was discussed in [Chapter I.3](#).

As an application in molecular quantum dynamics, the resonance decay dynamics of the deuterated formyl radical, DCO, was studied with [DP-DVR](#) for polyads 5 and 5.5 in [Chapter II.1](#). Due to an accidental Fermi resonance of the three vibrational modes, this system exhibits strong coupling and the majority of resonance states consists of a combination of several zero-order

states which is in strong contrast to HCO. Kinetic energy release spectra of selected resonances were compared with spectra obtained from velocity-map imaging experiments performed in the TEMPS group. Good agreement was found between the theoretical predictions using DP-DVR and the experimental data. The computed asymptotic rovibrational distributions of the CO fragment show a strong multimodal behavior. Compared to the distributions of the initial state (without decay), the asymptotic distributions for larger resonance widths are qualitatively similar. They only differ for very small resonance widths, that lead to a larger vibrational energy redistribution in the near-asymptotic region. Further, mechanisms of resonance decay were identified and previously published results from a polyadic model Hamiltonian were confirmed.^[241,377] Typically, the decay happens *via* a sequential decrease of the D–C=O bending quantum number while the DC=O stretch quantum number and, for lower excitations, the D–CO stretch quantum number are almost conserved. For resonances with strong coupling of the zero-order states and typically small resonance widths, the initial distribution of zero-order states does not change. There, changes do not occur even after propagating for 300 picoseconds, after which less than 2 % of the wavefunction is left in the interaction region.

In Section II.2.4, DP of spherical harmonics/Legendre polynomials in combination with DP-DVR was performed for the computation of PMDs in atomic hydrogen and the results were compared in a benchmark study. DP led to accurate calculations of the required PMDs with values covering orders of magnitudes from ~ 1 to $\sim 10^{-12}$. Compared to other methods, the runtime was average. An improved optimization of the code and a combination with surface flux methods would decrease the runtime further.

DP-DVR leveraged the optimization of an external field to control double ionization dynamics in an one-dimensional model of helium. This is discussed in Chapter II.3. The aim was to find a field that leads to an ejection of both electrons into opposite directions. Since, to first order, the external field leads to an ejection into the same direction, the target behavior is solely an effect that arises due to the electronic repulsion. As optimization procedures, the Krotov algorithm, derivative-free algorithms for a basis expansion of the field and local control algorithms were studied. Despite its monotonic convergence, the Krotov algorithm did not lead to the expected wavefunctions at the end of the pulse. The quest of finding properly defined target functions turned out to be quite difficult. However, the derivative-free optimization algorithms worked and several field parameters were found that lead to the requested behavior of the concerted movement of the electrons. A common mechanism could be identified where the field first displaces the wavepacket such that both electrons are ejected into the same direction while they are close to each other. When the field vanishes, the repulsion of the electrons and the attraction by the nucleus lead to the desired movement of the electrons into opposite directions. Initial results were also presented for local control procedures. Fields that lead to a similar mechanism were found but more work is required in order to fully understand the system.

In Section II.4.2, two-electron single-ionization dynamics of three-dimensional helium was studied. Instead of DP-DVR, the time-dependent generalized active space configuration interaction

(TD-GAS-CI) method was employed. Based on physical insight into the system of interest, it prunes a configurational space statically and is more mature for multi-electron single-ionization problems. Its capabilities were contrasted with both pruned MCTDH and DVR approaches in Section II.4.1.3 and II.4.1.4. As an application, extreme ultraviolet (XUV) initiated high harmonic generation (HHG) was studied. The intensity of the harmonics can be controlled by changing the delay between an XUV pulse and an infrared (IR) pulse. Accurate TD-GAS-CI calculations showed good agreement with experimental data. Remaining deviations were mostly due to macroscopic phase effects.

Chapter III.2

Prospects

“Twenty years from now you will be more disappointed by the things you didn't do than by the ones you did do. So throw off the bowlines. Sail away from the safe harbor. Catch the trade winds in your sails. Explore. Dream. Discover.

— Sarah F. Brown
(attributed)

Although significant progress in the development of DP has been obtained, much remains to be done. As always, the exploration of one single idea leads to the rise of ten new ideas. Some of them are described in the following. Possible avenues for DP for full configuration interaction (FCI) are described in Section III.2.1. The applicability of on-the-fly dynamics is discussed in Section III.2.1.1. Future directions for DP-MCTDH are elaborated on in Section III.2.2. Prospects for electron dynamics and molecular dynamics in general are briefly discussed in Section III.2.3 and III.2.4, respectively.

III.2.1. Full Configuration Interaction

The simulations done in Section I.1.3 treated up to six-dimensional systems while, for MCTDH, nine-dimensional systems were pruned. Thus, the simulation of nine-dimensional systems with DP-DVR should be possible with the current methodology. Systems that large are also state-of-the-art for time-dependent full configuration interaction (TD-FCI) computations.^[378,379] One of the most exciting goals would be to push the limits of DP-DVR to describe scattering or reaction rate calculations of twelve-dimensional systems like $\text{CH}_4 + \text{H}$. Currently, only MCTDH is able to perform such a large calculation.^[36] Using DP-DVR instead of MCTDH has several advantages like simplicity (only one convergence parameter is needed) and, most importantly, no particular form of the potential energy surface (PES) is required. The MCTDH calculations of $\text{CH}_4 + \text{H}$ were performed with correlation discrete variable representation (CDVR) which is approximate

and it would be interesting to compare those calculations with DP-DVR calculations in order to benchmark accuracy and performance of both methods.

Further, scattering calculations of smaller systems but with nonzero total angular momentum would be very interesting. This typically requires the usage of Wigner-D functions for describing rotational motion in three dimensions.^[380] Section II.2.4 showed that Legendre polynomials can be successfully pruned together with DVR bases. It should be more or less straightforward to generalize this to Wigner-D functions. This requires an adaption of the algorithm for the pruned matrix-vector product.

Besides time-dependent scattering calculations, it would also be very useful to consider time-independent scattering calculations with pruned bases. Currently, no favorably scaling matrix-vector products are exploited in time-independent scattering calculations, even for conventional direct-product-like bases.^[381]

In order to describe such large systems efficiently, the scheme of adding important basis functions needs to be improved. As shown in Section I.1.3, the current scheme of adding nearest neighbors is wasteful and, in six dimensions, the majority of functions in the active set is actually not important. This is because nearest neighbors are added in all directions, even if the wavepacket is moving only into one particular direction. There are several ways to improve this. One promising way would be to use approximate short-time dynamics in order to predict the sparsity of the wavefunction. This could be done using flux expressions, Bohmian trajectories,^[14] Gaussian-based dynamics or separate dynamics of small chunks of the total wavefunction. Some of these ideas are related to previous work on moving grids^[92,93] and moving basis functions.^[179,382] Another, more costly way would be to use backward propagation^[143] to estimate the error that is introduced by neglecting some basis functions. This increases the computational effort but would allow for dynamics with a fully automatic error control where no predefined wave amplitude threshold (WAT) but simply an allowed error is needed as user input. It could even be combined with an adaptive grid density. However, it is of utmost importance to implement such schemes without jeopardizing the favorable scaling with respect to the pruned basis size. This is not trivial.

Another way to improve DP-DVR would be to improve the algorithm for the sparse tensor transformation (matrix-vector product). Novel data structures for sparse tensors and other algorithms should be tested.^[383] Further, the inclusion of sparse fast Fourier transform (FFT) algorithms could speed up the calculations for systems where many basis functions are required in one dimension.^[384-386] For example, this is the case for the dissociation and ionization dynamics studied in Part II.

One of the intrinsic drawbacks of DP-DVR is that the pruned subspace that describes a hypervolume in coordinate space is still spanned by a basis with a direct-product like structure. This is related but not identical to the exponential scaling of the “shell” of the wavefunction in phase space.^[80] To reduce the basis size, it could be useful to combine DP with sparse grids.^[387-392] This means that a sparse grid is used for the pruned subspace. Since the wavepacket moves in time, the shape of the sparse grid needs to change at each time step, making the implementation far from trivial.

In the applications in Part II, no phase-space bases were used. Nevertheless, the pW basis is promising and should be further tested and improved. It could already improve performance for describing the dissociative coordinate in DCO. For PvB , more work on finding good approximations for the inverse overlap matrix is required. Work on how to use PvB for nondecomposable potentials using fast Gabor transforms is ongoing.^[393] One of the unique advantages of phase-space bases and PvB in particular is the close connection to semiclassical methodology; see, e. g., Refs. [14, 101, 102, 170, 382, 394, 395]. Initial work to combine fully quantum PvB dynamics with semiclassical approximations has been done^[80] but more work is needed. Besides semiclassical approximations, phase space could also be sampled *via* Monte-Carlo techniques, that is, performing random walks^[396,397] in phase space represented by PvB . PvB could also be interesting for density functional theory (DFT) applications of (periodic) materials. There, only three-dimensional bases are required and there is a close connection to Fourier-based DFT methods.^[59]

III.2.1.1. On-The-Fly Potential Calculation

It is common to relate on-the-fly calculations of the potential by electronic structure calculations *during* the dynamics simulations with DP or similar approaches.^[89,90,178,398-400] Here, the usefulness of on-the-fly calculations *within the context of DP-DVR* are further discussed. Although a simple-minded connection of on-the-fly potential calculations and $DP-DVR$ is straightforward, both methodologies are not directly related. Indeed, the potential can already be calculated on-the-fly during dynamics using full direct-product DVR bases: Similar to the DP scheme, at each time-step, the wavefunction is scanned for the most important contributions in coordinate space where the potential is calculated. For the remaining points on the direct-product grid, the potential can be extrapolated using, for example, simple Taylor-expressions like the local harmonic approximation.^[178,382,398] Indeed, such a scheme would even work for standard $MCTDH$ calculations (assuming a SoP form of the interpolating functions), where the most important configurations (in natural orbital representation) are selected to find the dominant occupancy in coordinate space. The only step that is avoided in $DP-DVR$ is the extrapolation to grid points where the wavefunction currently has vanishing contributions.

However, the main problem is that *too many* DVR grid points are active during the dynamics calculations. This is in stark contrast to Gaussian-based methods where the potential (and its derivatives) needs to be evaluated only at the centers of moving Gaussians.^[178,179,398,399] To give an example, $DP-DVR$ still required $\sim 10^6$ grid points for the simple six-dimensional vibronic coupling model of pyrazine (see Section I.1.3). A similar order of magnitude was required for DCO (see Chapter II.1), even though the potential is based on *only* 480 potential energy evaluations.^[401] Sophisticated algorithms that combine “local” interpolation with a clever selection of new grid points are needed; see, for example, Refs. [402, 403]. On the one hand, given the vast amount of required DVR points, for high-dimensional calculations, this might be as difficult as finding “global” potential energy surfaces without on-the-fly calculations. Already the implementation of

a useful database for previously computed grid points can be challenging, as exponential scaling can easily be reintroduced when nearest neighbors to a required point in coordinate space need to be found etc. On the other hand, the regularity of the required grid points may be a very useful ingredient for an on-the-fly scheme. Since DP-DVR is based on a direct-product grid, the spacing of the grid points is well-behaved which would, among others, simplify the creation of possible databases. It may already be sufficient to compute the potential on every ~5th DVR grid point and store the values in a database similar to the one that is used for storing the active basis functions. In contrast, dynamics based on moving Gaussians is more irregular and as such typically also the way how new potential points are evaluated.

One problem of on-the-fly potential calculations in combination with local interpolation schemes is that they lead to time-dependent potentials which can create artifacts, for example negative peaks in spectra.^[404] Another problem are instabilities in the electronic structure calculations. During the dynamics, the wavefunction can visit “problematic” regions in coordinate space, for example, close to conical intersections or other molecular geometries where the electronic configurations change rapidly, e. g., at the Coulson-Fischer point along a bond-dissociation curve, where spin contamination starts in Hartree-Fock.^[30] It is hard to control and repair this during on-the-fly simulations.

Thus, although on-the-fly calculations of the PES are useful for Gaussian-based methods, they may not be the most optimal strategy for DP-DVR. At least, more research needs to be done to automatically select a minimal number of new points for on-the-fly calculations in conjunction with interpolation schemes for *many* used grid points (in contrast to Gaussian-based dynamics). Instead, one might also want to try adaptive global interpolation or fit procedures. That is, several dynamics runs are performed where after each run, new points are added to the PES, based on the density of the wavefunction during the dynamics, for example.^[76,405,406] There are also other procedures that more or less quickly lead to global PES using a minimal number of electronic structure calculations.^[407-411]

III.2.2. Multi-Configuration Time-Dependent Hartree

Whereas pruning the primitive basis is very similar to standard DP-DVR dynamics, pruning the SPF basis is more subtle. So far, the latter has only been tested for the vibronic coupling model of the 24-dimensional pyrazine. More tests and benchmarks are required in order to ensure that DP-MCTDH is as stable and convergent as DP-DVR. As discussed in Section I.2.1.4.2, other than natural orbitals should be tested. As in DP-DVR, better schemes for selecting the active configurations are required. Selection and correction schemes from electronic structure theory could give a considerable improvement;^[71,72] see also Refs. [412, 413].

Another, new idea would be to employ natural orbitals *without* solving an equation of motion (EOM) for the SPFs: For each time step, only the SPF coefficient tensor is propagated and from the propagated coefficients, new natural orbitals are generated. On the one hand, this

simplifies the EOMs and avoids the need to generate the mean-fields for solving the EOMs for the SPFs. On the other hand, probably smaller time steps are required whenever the natural orbitals change quickly.

In DP-MCTDH, the total number of SPFs in each dimension changes. Consequently, new and unoccupied SPFs are added during the whole propagation. Currently, an *ad hoc* scheme is used for defining the form of the new SPFs. How to find the optimal form is known,^[414,415] but the procedure is computationally demanding. One could try to find approximate procedures. This could help to increase the robustness and to decrease the number of required iterations of the differential equation solvers.

The non-Hermiticity introduced by the pruned matrix-vector product in DP-MCTDH is more severe than in DP-DVR. The performance of the used algorithm should be compared to that developed by WODRASZKA AND CARRINGTON,^[236,416] which does not suffer from non-Hermiticity but is more complicated and computationally more involved and requires more memory. A comparison of both algorithms would be illuminating, especially for time-independent problems, where non-Hermiticity leads to more complicated iterative diagonalization algorithms. Currently, WODRASZKA AND CARRINGTON,^[236,416] RAUHUT ET AL.,^[417-419] and MIZUKAMI AND TEW^[420] have tested pruning for solving the TISE with MCTDH (dubbed “improved relaxation” or vibrational multi-configuration self-consistent field). They have not used mode combination. It should be straightforward to use the methodology developed in this thesis for solving the TISE. Mode combination would enable the eigenstate calculation of larger systems. Further, eigenstate calculations with MCTDH are more sensitive to the number of used SPFs.^[153] Typically, more SPFs are required in order to get converged results. DP-MCTDH could leverage improved relaxation calculations by enlarging the used SPF space.

Since DP-MCTDH is still based on a direct-product SPF basis, it is clear that DP-MCTDH cannot defeat ML-MCTDH for model systems and very high dimensions (larger than ~ 50). One could try to improve ML-MCTDH by DP. However, since the size of the coefficient tensors in each layer is smaller than in MCTDH, the gain might not be as large as in standard MCTDH. Further, this would dramatically increase the complexity of the algorithm. Of course, it would be interesting to check the compatibility of DP with other tensor-based methods like tensor trains, density matrix renormalization group, tensor network states and so on; see, e. g., Refs. [53, 421-425].

In general, DP-MCTDH enables faster calculations for larger systems *without* the need to use the more complicated ML-MCTDH. Since higher-dimensional mode combination can be used if the primitive basis is pruned, requirements regarding the SoP form of the PES are reduced. This could enable the computation of larger systems. Interesting systems to study would be larger water clusters. This has already been done for water dimers.^[426,427] Another interesting application would be optimal control calculations, for example, for pyrazine.^[428] Since DP-MCTDH speeds up the computation, many more optimal control iterations are possible. It is planned to include parts of the developed LAGOM package in quantics and/or the Heidelberg MCTDH package. This would allow to make DP-MCTDH accessible to a broader user base.

Another interesting avenue would be to work on variants of DP-MCTDH for Fermions and/or Bosons. This bears some challenges because for those systems, the potential is typically not of SoP form such that the computational bottlenecks are different and new algorithms need to be used and developed in order to enable sparse tensor-transformations for the potential. Further, natural orbital generation for Bosonic systems is computationally more involved but approximate orbitals can probably be used as well.

III.2.3. Electron Dynamics

As stated in Section II.2.4, DP-DVR should be combined with surface flux methods in order to compute observables in ionization dynamics processes. This could also be useful for double ionization dynamics, which is still very challenging.^[429] Besides, the applicability of DP to configuration interaction (CI)-based methods should be investigated and some thoughts regarding this direction have been mentioned in Section II.4.1.4. For applications, more work is required to understand the control of double ionization in helium; see Chapter II.3. Once helium is fully understood, including computations for three-dimensional helium, control of double ionization in diatomic molecules would be very interesting to perform because the nuclear attraction significantly perturbs the preferred direction of ejection of the electrons.^[355]

III.2.4. Molecular Dynamics

In general, solving the electronic structure problem and getting the PES is still computationally demanding, especially when many electronic states are required for nonadiabatic dynamics or when the systems are strongly correlated. Even more progress is required to speed up electronic structure calculations. One new and exciting method is the aforementioned tensor network state algorithm, which is similar to ML-MCTDH.

Besides, quantum dynamics of larger molecular systems is not fully understood and, during the last years, new phenomena like roaming have been studied.^[430-432] Unless the common chemistry rules and intuitions apply, it is not clear how to extrapolate from dynamics of “small” systems with three or four atoms to larger systems. It is also not fully clear when the transition from quantum to classical behavior happens in molecular reactions or when reduced-dimensional approaches work and when they fail.^[433,434] A comparison of (semi-)classical simulations with experiments cannot always give clear answers to these questions because other approximations, for example in the electronic structure, add to the approximation of neglecting quantum effects. Only the study of more and larger systems can help to shed light on the quantum behavior of reactions in molecular systems.

Definitely, to realize all of the ideas mentioned in this Chapter and to answer all of the questions that arose in this thesis is a long-term goal.

Part IV
Appendix

Bibliography

All webpages have been accessed on March 5, 2018.

- [1] A. Lavoisier, *Opuscules physiques et chimiques*, Deterville, 2nd edn., 1801 (cit. on p. 1).
- [2] G. Wedler, *Lehrbuch der Physikalischen Chemie*, Wiley-VCH, 5th edn., 2005 (cit. on pp. 1, 2).
- [3] A. N. Scherer, *Archiv für die theoretische Chemie*, I. G. Voigt, Jena, 1st edn., 1800 (cit. on p. 1).
- [4] K. Jug, *Zweihundert Jahre Entwicklung der Theoretischen Chemie im deutschsprachigen Raum*, Springer Spektrum, 1st edn., 2014 (cit. on pp. 1, 2).
- [5] I. Kant, *Metaphysischen Anfangsgründe der Naturwissenschaft*, J. F. Hartknoch, Riga, 1st edn., 1786 (cit. on p. 1).
- [6] I. Kant, *The Metaphysical Foundations of Natural Science*, <https://en.wikisource.org>, 1786 (cit. on p. 1).
- [7] A. Comte, *Positive Philosophy*, C. Blanchard, New York, 1st edn., 1858 (cit. on p. 1).
- [8] C. Babbage, *The Ninth Bridgewater Treatise: A Fragment*, J. Murray, London, 1st edn., 1838 (cit. on p. 1).
- [9] W. Heisenberg, *Z. Physik*, 1925, **33**, 879-893 (cit. on p. 2).
- [10] M. Born and P. Jordan, *Z. Physik*, 1925, **34**, 858-888 (cit. on p. 2).
- [11] M. Born, W. Heisenberg and P. Jordan, *Z. Physik*, 1926, **35**, 557-615 (cit. on p. 2).
- [12] C. Cohen-Tannoudji, B. Diu and F. Laloe, *Quantum Mechanics, Vol. 1*, Wiley-VCH, 1st edn., 1992 (cit. on p. 2).
- [13] J. J. Sakurai, *Modern Quantum Mechanics*, Pearson Education, 2nd edn., 2013 (cit. on p. 2).
- [14] D. J. Tannor, *Introduction to Quantum Mechanics: A Time-Dependent Perspective*, University Science Books, 1st edn., 2007 (cit. on pp. 2, 3, 14, 113, 118, 183, 184, 189, 262, 263).
- [15] E. Schrödinger, *Ann. Phys.* 1926, **384**, 361-376 (cit. on p. 2).
- [16] E. Schrödinger, *Ann. Phys.* 1926, **384**, 489-527 (cit. on p. 2).
- [17] E. Schrödinger, *Ann. Phys.* 1926, **384**, 734-756 (cit. on p. 2).
- [18] E. Schrödinger, *Ann. Phys.* 1926, **385**, 437-490 (cit. on p. 2).

- [19] E. Schrödinger, *Ann. Phys.* 1926, **386**, 109-139 (cit. on p. 2).
- [20] E. Schrödinger, *Naturwissenschaften*, 1926, **14**, 664-666 (cit. on p. 2).
- [21] E. Schrödinger, *Phys. Rev.* 1926, **28**, 1049-1070 (cit. on p. 2).
- [22] M. Born and R. Oppenheimer, *Ann. Phys.* 1927, **389**, 457-484 (cit. on p. 2).
- [23] W. Heitler and F. London, *Z. Physik*, 1927, **44**, 455-472 (cit. on p. 2).
- [24] H. Eyring and M. Polanyi, *Z. physik. Chem. B*, 1931, **12**, 279-311 (cit. on p. 2).
- [25] H. Hellmann, *Einführung in die Quantenchemie*, Deuticke, Leipzig, 1st edn., 1937 (cit. on p. 2).
- [26] *Hans Hellmann: Einführung in die Quantenchemie*, ed. D. Andrae, Springer, Berlin, Heidelberg, 1st edn., 2015 (cit. on p. 2).
- [27] P. A. M. Dirac, *Proc. Roy. Soc. A*, 1929, **123**, 714-733 (cit. on p. 2).
- [28] P.-O. Löwdin, *Int. J. Quantum Chem.* 1967, **1**, 7-12 (cit. on pp. 2, 3, 5).
- [29] G. E. Moore, *Electronics*, 1965, **38**, 114-118 (cit. on p. 3).
- [30] T. Helgaker, J. Olsen and P. Jørgensen, *Molecular Electronic-Structure Theory*, Wiley, 1st edn., 2013 (cit. on pp. 3, 4, 218, 220, 221, 264).
- [31] C. Riplinger, B. Sandhoefer, A. Hansen and F. Neese, *J. Chem. Phys.* 2013, **139**, 134101 (cit. on pp. 3, 4).
- [32] F. Neese, *WIREs Comput. Mol. Sci.* 2012, **2**, 73-78 (cit. on p. 3).
- [33] H.-J. Werner, P. J. Knowles, G. Knizia, F. R. Manby and M. Schütz, *WIREs Comput. Mol. Sci.* 2012, **2**, 242-253 (cit. on p. 3).
- [34] A. Leach, *Molecular Modelling: Principles and Applications*, Prentice Hall, 2nd edn., 2001 (cit. on p. 3).
- [35] M. Tizniti, S. D. Le Picard, F. Lique, C. Berteloite, A. Canosa, M. H. Alexander and I. R. Sims, *Nat. Chem.* 2014, **6**, 141-145 (cit. on p. 3).
- [36] T. Wu, H.-J. Werner and U. Manthe, *Science*, 2004, **306**, 2227-2229 (cit. on pp. 3, 261).
- [37] Y. Cha, C. Murray and J. Klinman, *Science*, 1989, **243**, 1325-1330 (cit. on p. 3).
- [38] J. P. Layfield and S. Hammes-Schiffer, *Chem. Rev.* 2014, **114**, 3466-3494 (cit. on p. 3).
- [39] S. Kozuch, *Phys. Chem. Chem. Phys.* 2014, **16**, 7718-7727 (cit. on p. 3).
- [40] D. Marx, M. E. Tuckerman, J. Hutter and M. Parrinello, *Nature*, 1999, **397**, 601-604 (cit. on p. 3).
- [41] R. Otto, J. Ma, A. W. Ray, J. S. Daluz, J. Li, H. Guo and R. E. Continetti, *Science*, 2014, **343**, 396-399 (cit. on p. 3).
- [42] T. Westermann, J. B. Kim, M. L. Weichman, C. Hock, T. I. Yacovitch, J. Palma, D. M. Neumark and U. Manthe, *Angew. Chem. Int. Ed.* 2014, **53**, 1122-1126 (cit. on p. 3).

-
- [43] C. Xie, B. K. Kendrick, D. R. Yarkony and H. Guo, *J. Chem. Theory Comput.* 2017, **13**, 1902-1910 (cit. on p. 3).
- [44] C. Brif, R. Chakrabarti and H. Rabitz, *New J. Phys.* 2010, **12**, 075008 (cit. on p. 3).
- [45] J. C. Tully, *J. Chem. Phys.* 1990, **93**, 1061-1071 (cit. on p. 3).
- [46] M. Barbatti, *Wiley Int. Rev.: Comp. Mol. Sci.* 2011, **1**, 620-633 (cit. on p. 3).
- [47] P. R. Schreiner, H. P. Reisenauer, D. Ley, D. Gerbig, C.-H. Wu and W. D. Allen, *Science*, 2011, **332**, 1300-1303 (cit. on p. 3).
- [48] M. H. Beck, A. Jäckle, G. A. Worth and H.-D. Meyer, *Phys. Rep.* 2000, **324**, 1-105 (cit. on pp. 3, 5, 106, 107).
- [49] H. Wang and M. Thoss, *J. Chem. Phys.* 2003, **119**, 1289-1299 (cit. on p. 3).
- [50] U. Manthe, *J. Chem. Phys.* 2008, **128**, 164116 (cit. on pp. 3, 5).
- [51] O. Vendrell and H.-D. Meyer, *J. Chem. Phys.* 2011, **134**, 044135 (cit. on p. 3).
- [52] H. Wang, *J. Phys. Chem. A*, 2015, **119**, 7951-7965 (cit. on p. 3).
- [53] B. N. Khoromskij, *Tensor Numerical Methods for High-dimensional PDEs*, arXiv:1408.4053, 2014 (cit. on pp. 3, 265).
- [54] Y. Xie, J. Zheng and Z. Lan, *J. Chem. Phys.* 2015, **142**, 084706 (cit. on p. 3).
- [55] J. Schulze, M. F. Shibl, M. J. Al-Marri and O. Kühn, *J. Chem. Phys.* 2016, **144**, 185101 (cit. on p. 3).
- [56] R. Welsch and U. Manthe, *J. Phys. Chem. Lett.* 2015, **6**, 338-342 (cit. on p. 3).
- [57] R. Ellerbrock, *private communication*, 2016 (cit. on p. 3).
- [58] S. Grimme and P. R. Schreiner, *Angew. Chem. Int. Ed.* 2017, in press, doi: 10.1002/anie.201709943 (cit. on p. 3).
- [59] *Linear-Scaling Techniques in Computational Chemistry and Physics*, ed. R. Zaleśny, M. G. Papadopoulos, P. G. Mezey and J. Leszczynski, Springer, 1st edn., 2011 (cit. on pp. 4, 263).
- [60] A. L. Fetter and J. D. Walecka, *Quantum Theory of Many-Particle Systems*, Dover, 1st edn., 2003 (cit. on p. 4).
- [61] F. Gatti and C. Iung, *Phys. Rep.* 2009, **484**, 1-69 (cit. on p. 4).
- [62] R. Dawes and S. A. Ndengué, *Int. Rev. Phys. Chem.* 2016, **35**, 441-478 (cit. on p. 4).
- [63] O. Christiansen, *J. Chem. Phys.* 2004, **120**, 2149-2159 (cit. on p. 5).
- [64] R. Welsch and U. Manthe, *J. Chem. Phys.* 2012, **137**, 244106 (cit. on p. 5).
- [65] Q. Meng and H.-D. Meyer, *J. Chem. Phys.* 2014, **141**, 124309 (cit. on p. 5).
- [66] D. Mendive-Tapia, T. Firmino, H.-D. Meyer and F. Gatti, *Chem. Phys.* 2017, **482**, 113-123 (cit. on p. 5).

- [67] D. H. Zhang and J. Z. H. Zhang, *J. Chem. Phys.* 1994, **101**, 1146-1156 (cit. on pp. 5, 11).
- [68] C. F. Bender and E. R. Davidson, *Phys. Rev.* 1969, **183**, 23-30 (cit. on p. 5).
- [69] B. Huron, J. P. Malrieu and P. Rancurel, *J. Chem. Phys.* 1973, **58**, 5745-5759 (cit. on p. 5).
- [70] R. J. Buenker and S. D. Peyerimhoff, *Theor. Chem. Acc.* 1974, **35**, 33-58 (cit. on p. 5).
- [71] J. B. Schriber and F. A. Evangelista, *J. Chem. Phys.* 2016, **144**, 161106 (cit. on pp. 5, 264).
- [72] A. A. Holmes, N. M. Tubman and C. J. Umrigar, *J. Chem. Theory Comput.* 2016, **12**, 3674-3680 (cit. on pp. 5, 264).
- [73] W. Koch, *private communication*, 2016 (cit. on p. 5).
- [74] R. A. Vargas-Hernández, Y. Guan, D. H. Zhang and R. V. Krems, *A Machine-Learning Approach for Determining the Best Potential Surface with the Least Number of ab initio Points and Solving the Inverse Scattering Problem for Quantum Reaction Dynamics*, arXiv:1711.06376, 2017 (cit. on p. 5).
- [75] B. J. Braams and J. M. Bowman, *Int. Rev. Phys. Chem.* 2009, **28**, 577-606 (cit. on p. 5).
- [76] M. A. Collins, *Theor. Chem. Acc.* 2002, **108**, 313-324 (cit. on pp. 5, 264).
- [77] S. Manzhos, R. Dawes and T. Carrington, *Int. J. Quantum Chem.* 2015, **115**, 1012-1020 (cit. on p. 5).
- [78] E. Steffen, *Parallele Implementierung eines Algorithmus zur Wellenpaketpropagation mit adaptiver Basis und Symplektischen Integratoren mittels OpenMP*, Diploma thesis, University of Kiel, 2012 (cit. on pp. 6, 12, 114).
- [79] J. Sielk, *Quantum-Mechanical Reaction Dynamics: Method Development and Applications*, Ph.D. Thesis, University of Kiel, 2010 (cit. on pp. 6, 114).
- [80] A. Shimshovitz, *Phase Space Approach to Solving the Schrödinger Equation*, Ph.D. Thesis, Weizmann Institute of Science, 2015 (cit. on pp. 6, 89, 262, 263).
- [81] R. Abta, Ph.D. Thesis, Weizmann Institute of Science, 2017 (cit. on p. 6).
- [82] N. Takemoto, A. Shimshovitz and D. J. Tannor, *J. Chem. Phys.* 2012, **137**, 011102 (cit. on pp. 6, 12).
- [83] E. Assémat, S. Machnes and D. Tannor, *Double ionization of Helium from a phase space perspective*, arXiv:1502.05165, 2015 (cit. on pp. 6, 12, 114, 182, 192, 199, 214).
- [84] S. Machnes, E. Assémat and D. Tannor, *Quantum Dynamics in Phase space using the Biorthogonal von Neumann bases: Algorithmic Considerations*, arXiv:1603.03963, 2016 (cit. on pp. 6, 114).
- [85] S. Machnes, E. Assémat, H. R. Larsson and D. J. Tannor, *J. Phys. Chem. A*, 2016, **120**, 3296-3308 (cit. on p. 6).

-
- [86] R. Kosloff, in *Numerical Grid Methods and Their Application to Schrödinger's Equation*, ed. C. Cerjan, Nato Science Series C, 1993, vol. 412, ch. The Fourier Method, pp. 175-194 (cit. on p. 11).
- [87] B. Schmidt and U. Lorenz, *Comput. Phys. Commun.* 2017, **213**, 223-234 (cit. on pp. 12, 115).
- [88] B. Hartke, *Quantum-mechanical wavepacket propagation moving beyond a few degrees of freedom*, Talk at the 42nd Symposium for Theoretical Chemistry in Erkner/Berlin, 2006 (cit. on p. 13).
- [89] B. Hartke, *Phys. Chem. Chem. Phys.* 2006, **8**, 3627-3635 (cit. on pp. 12, 114, 263).
- [90] J. Sielk, H. F. von Horsten, F. Krueger, R. Schneider and B. Hartke, *Phys. Chem. Chem. Phys.* 2009, **11**, 463-475 (cit. on pp. 12, 114, 263).
- [91] D. A. McCormack, *J. Chem. Phys.* 2006, **124**, 204101 (cit. on p. 12).
- [92] L. R. Petthey and R. E. Wyatt, *Chem. Phys. Lett.* 2006, **424**, 443-448 (cit. on pp. 12, 262).
- [93] L. R. Petthey and R. E. Wyatt, *Int. J. Quantum Chem.* 2007, **107**, 1566-1573 (cit. on pp. 12, 262).
- [94] J. Z. H. Zhang, *Theory and Application of Quantum Molecular Dynamics*, World Scientific, 1st edn., 1999 (cit. on p. 14).
- [95] R. Schinke, *Photodissociation Dynamics*, Cambridge University Press, 1st edn., 1995 (cit. on p. 14).
- [96] *Multidimensional Quantum Dynamics*, ed. H.-D. Meyer, F. Gatti and G. A. Worth, Wiley-VCH, 1st edn., 2009 (cit. on pp. 14, 113).
- [97] *Tutorials in Molecular Reaction Dynamics*, ed. M. Brouard and C. Vallance, Royal Society of Chemistry, 1st edn., 2011 (cit. on p. 14).
- [98] F. Gatti, B. Lasorne, H.-D. Meyer and A. Nauts, *Applications of Quantum Dynamics in Chemistry*, Springer, 1st edn., 2017 (cit. on p. 14).
- [99] H. R. Larsson, *Laser-Induced Correlated Electron Dynamics in Small Molecules*, Master's thesis, Institute for Theoretical Physics and Astrophysics, University of Kiel, 2014 (cit. on pp. 14, 107, 165, 167, 190, 209, 217-219, 222).
- [100] J. Stohner and M. Quack, in *Handbook of High-resolution Spectroscopy*, John Wiley & Sons, Ltd, 2011, ch. Conventions, Symbols, Quantities, Units and Constants for High-Resolution Molecular Spectroscopy (cit. on p. 14).
- [101] M. J. Davis and E. J. Heller, *J. Chem. Phys.* 1979, **71**, 3383-3395 (cit. on pp. 48, 263).
- [102] A. Shimshovitz and D. J. Tannor, *Phys. Rev. Lett.* 2012, **109**, 070402 (cit. on pp. 48, 51, 263).
- [103] A. Shimshovitz and D. J. Tannor, *J. Chem. Phys.* 2012, **137**, 101103 (cit. on p. 48).
- [104] B. Poirier, *J. Theor. Comput. Chem.* 2003, **2**, 65-72 (cit. on pp. 49, 257).
- [105] B. Poirier and A. Salam, *J. Chem. Phys.* 2004, **121**, 1690-1703 (cit. on pp. 49, 51, 257).

- [106] B. Poirier and A. Salam, *J. Chem. Phys.* 2004, **121**, 1704-1724 (cit. on pp. 49, 257).
- [107] M. J. Bastiaans, *Opt. Eng.* 1981, **20**, 594-598 (cit. on p. 50).
- [108] *Gabor Analysis and Algorithms*, ed. H. G. Feichtinger and T. Strohmer, Birkhäuser, 1st edn., 1998 (cit. on p. 50).
- [109] I. Daubechies and A. J. E. M. Janssen, *IEEE T. Inform. Theory*, 1993, **39**, 3-6 (cit. on p. 50).
- [110] J. Brown and T. Carrington, *Phys. Rev. Lett.* 2015, **114**, 058901 (cit. on p. 51).
- [111] A. Shimshovitz and D. J. Tannor, *Reply to Comment by Brown and Carrington on "Phase-Space Approach to Solving the Time-Independent Schrödinger Equation"*, arXiv:1510.04715, 2015 (cit. on p. 51).
- [112] S. R. White, *Hybrid grid/basis set discretizations of the Schrödinger equation*, arXiv:1709.08059, 2017 (cit. on p. 52).
- [113] Y. Fang, F. Wu and B. Wu, *Quantum phase space with a basis of Wannier functions*, arXiv:1708.06507, 2017 (cit. on p. 52).
- [114] A. P. J. Jansen, *J. Chem. Phys.* 1993, **99**, 4055-4063 (cit. on p. 91).
- [115] U. Manthe, *J. Chem. Phys.* 1994, **101**, 2652-2653 (cit. on p. 91).
- [116] G. A. Worth, *J. Chem. Phys.* 2000, **112**, 8322-8329 (cit. on pp. 92, 115).
- [117] G. A. Worth, M. H. Beck, A. Jäckle and H.-D. Meyer, The MCTDH Package, Version 8.4.10. See <http://mctdh.uni-hd.de>, University of Heidelberg, Germany, 2014 (cit. on pp. 92, 113, 115).
- [118] G. A. Worth, *Presentation of Quantics*, Talk at the International School "Quantum Dynamics with the Multi-Configuration Time-Dependent Hartree (MCTDH) method", 2017 (cit. on p. 105).
- [119] G. A. Worth, K. Giri, G. W. Richings, I. Burghardt, M. H. Beck, A. Jäckle and H.-D. Meyer, The QUANTICS Package, Version 1.1, University of Birmingham, Birmingham, U.K., 2015 (cit. on pp. 105, 115).
- [120] G. A. Worth, M. H. Beck, A. Jäckle, O. Vendrell and H.-D. Meyer, The MCTDH Package, Version 8.5.6.1. See <http://mctdh.uni-hd.de>, University of Heidelberg, Germany, 2016 (cit. on pp. 105, 115).
- [121] P.-O. Löwdin, *Phys. Rev.* 1955, **97**, 1474-1489 (cit. on p. 107).
- [122] A. Szabo and N. S. Ostlund, *Modern Quantum Chemistry*, Dover, 1st edn., 1996 (cit. on pp. 107, 190, 191, 218).
- [123] F. Jensen, *Introduction to Computational Chemistry*, Wiley, 2nd edn., 2006 (cit. on p. 107).
- [124] S. Bauch, L. K. Sørensen and L. B. Madsen, *Phys. Rev. A*, 2014, **90**, 062508 (cit. on pp. 107, 217-219).

-
- [125] A. I. Streltsov, O. E. Alon and L. S. Cederbaum, *Phys. Rev. A*, 2006, **73**, 063626 (cit. on p. 107).
- [126] K. Giesbertz, *Chem. Phys. Lett.* 2014, **591**, 220-226 (cit. on p. 107).
- [127] L. Lain, A. Torre, D. R. Alcoba, O. B. Oña and G. E. Massaccesi, *Theor. Chem. Acc.* 2015, **134**, 85 (cit. on p. 107).
- [128] D. R. Alcoba, A. Torre, L. Lain, G. E. Massaccesi, O. B. Oña, P. W. Ayers, M. V. Raemdonck, P. Bultinck and D. V. Neck, *Theor. Chem. Acc.* 2016, **135**, 153 (cit. on p. 107).
- [129] A. Raab, G. A. Worth, H.-D. Meyer and L. S. Cederbaum, *J. Chem. Phys.* 1999, **110**, 936 (cit. on p. 108).
- [130] H.-D. Meyer, U. Manthe and L. Cederbaum, *Chem. Phys. Lett.* 1990, **165**, 73-78 (cit. on p. 109).
- [131] C. Lubich, *Appl. Math. Res. Express*, 2015, 311-328 (cit. on p. 109).
- [132] B. Kloss, I. Burghardt and C. Lubich, *J. Chem. Phys.* 2017, **146**, 174107 (cit. on p. 109).
- [133] E. F. Valeev, *Libint: A library for the evaluation of molecular integrals of many-body operators over Gaussian functions*, <http://libint.valeev.net/>, version 2.3.1, 2017 (cit. on p. 112).
- [134] Q. Sun, *J. Comput. Chem.* 2015, **36**, 1664-1671 (cit. on p. 112).
- [135] G. Mazur, M. Makowski, R. Łazarski, R. Włodarczyk, E. Czajkowska and M. Glanowski, *Int. J. Quantum Chem.* 2016, **116**, 1370-1381 (cit. on p. 112).
- [136] D. Datta and J. Gauss, *J. Chem. Theory Comput.* 2013, **9**, 2639-2653 (cit. on p. 112).
- [137] M. Krupička, K. Sivalingam, L. Huntington, A. A. Auer and F. Neese, *J. Comput. Chem.* 2017, **38**, 1853-1868 (cit. on p. 112).
- [138] M. K. MacLeod and T. Shiozaki, *J. Chem. Phys.* 2015, **142**, 051103 (cit. on p. 112).
- [139] G. Baumgartner et al., *Proceedings of the IEEE*, 2005, **93**, 276-292 (cit. on p. 112).
- [140] A. Köhn, *J. Chem. Phys.* 2009, **130**, 104104 (cit. on p. 112).
- [141] T. Yanai, Y. Kurashige, M. Saitow, J. Chalupský, R. Lindh and P.-Å. Malmqvist, *Mol. Phys.* 2016, **115**, 2077-2085 (cit. on p. 112).
- [142] T. J. Park and J. C. Light, *J. Chem. Phys.* 1986, **85**, 5870-5876 (cit. on pp. 113, 118, 177).
- [143] M. H. Beck and H.-D. Meyer, *Z. Physik D*, 1997, **42**, 113-129 (cit. on pp. 113, 177, 262).
- [144] E. Jones, T. Oliphant, P. Peterson et al., *SciPy: Open source scientific tools for Python*, 2001 (cit. on pp. 113, 116, 199, 204).
- [145] P. Deuflhard and F. Bornemann, *Numerische Mathematik 2: Gewöhnliche Differentialgleichungen*, de Gruyter, 3rd edn., 2008 (cit. on p. 113).
- [146] J. Stoer and R. Bulirsch, *Numerische Mathematik 2*, Springer, 5th edn., 2005 (cit. on pp. 113, 222).

- [147] S. K. Gray and D. E. Manolopoulos, *J. Chem. Phys.* 1996, **104**, 7099-7112 (cit. on pp. 113, 118).
- [148] D. Lauvergnat, S. Blasco, X. Chapuisat and A. Nauts, *J. Chem. Phys.* 2007, **126**, 204103 (cit. on pp. 113, 118).
- [149] U. Manthe, *Chem. Phys.* 2006, **329**, 168-178 (cit. on p. 113).
- [150] R. Kosloff and H. Tal-Ezer, *Chem. Phys. Lett.* 1986, **127**, 223-230 (cit. on p. 113).
- [151] D. Neuhauser, *J. Chem. Phys.* 1990, **93**, 2611-2616 (cit. on p. 113).
- [152] D. Neuhauser, *J. Chem. Phys.* 1991, **95**, 4927-4932 (cit. on p. 113).
- [153] H.-D. Meyer, F. L. Quéré, C. Léonard and F. Gatti, *Chem. Phys.* 2006, **329**, 179-192 (cit. on pp. 113, 265).
- [154] J. Lill, G. Parker and J. Light, *Chem. Phys. Lett.* 1982, **89**, 483-489 (cit. on p. 113).
- [155] J. C. Light, I. P. Hamilton and J. V. Lill, *J. Chem. Phys.* 1985, **82**, 1400-1409 (cit. on p. 113).
- [156] J. C. Light and T. Carrington, in *Advances in Chemical Physics*, John Wiley & Sons, Inc., 2007, ch. Discrete-Variable Representations and their Utilization, pp. 263-310 (cit. on p. 113).
- [157] C. C. Marston and G. G. Balint-Kurti, *J. Chem. Phys.* 1989, **91**, 3571-3576 (cit. on p. 113).
- [158] D. T. Colbert and W. H. Miller, *J. Chem. Phys.* 1992, **96**, 1982-1991 (cit. on p. 113).
- [159] V. Szalay, *J. Chem. Phys.* 1993, **99**, 1978-1984 (cit. on p. 113).
- [160] D. Baye, *Phys. Rep.* 2015, **565**, 1-107 (cit. on p. 113).
- [161] D. Baye and P. H. Heenen, *J. Phys. A: Math. Gen.* 1986, **19**, 2041 (cit. on p. 113).
- [162] T. Rescigno and C. McCurdy, *Phys. Rev. A*, 2000, **62**, 032706 (cit. on pp. 113, 176).
- [163] K. Balzer, S. Bauch and M. Bonitz, *Phys. Rev. A*, 2010, **81**, 022510 (cit. on pp. 113, 176).
- [164] B. I. Schneider, L. A. Collins and S. X. Hu, *Phys. Rev. E*, 2006, **73**, 036708 (cit. on pp. 113, 176).
- [165] D. E. Manolopoulos and R. E. Wyatt, *Chem. Phys. Lett.* 1988, **152**, 23-32 (cit. on p. 113).
- [166] D. J. Tannor and D. E. Weeks, *J. Chem. Phys.* 1993, **98**, 3884-3893 (cit. on p. 113).
- [167] D. E. Weeks and D. J. Tannor, *Chem. Phys. Lett.* 1993, **207**, 301-308 (cit. on p. 113).
- [168] D. E. Weeks and D. J. Tannor, *Chem. Phys. Lett.* 1994, **224**, 451-458 (cit. on p. 113).
- [169] A. Jäckle and H. Meyer, *J. Chem. Phys.* 1996, **105**, 6778-6786 (cit. on p. 113).
- [170] W. P. Schleich, *Quantum Optics in Phase Space*, Wiley-VCH, 1st edn., 2001 (cit. on pp. 113, 207, 263).
- [171] S. Chelkowski, T. Zuo and A. D. Bandrauk, *Phys. Rev. A*, 1992, **46**, R5342-R5345 (cit. on p. 113).

-
- [172] S. Chelkowski, T. Zuo, O. Atabek and A. D. Bandrauk, *Phys. Rev. A*, 1995, **52**, 2977-2983 (cit. on p. 113).
- [173] F. Großmann, *Theoretical Femtosecond Physics*, Springer, 2nd edn., 2013 (cit. on p. 113).
- [174] H. F. von Horsten, *Quantendynamik größerer Moleküle anhand reduziert-dimensionaler Modelle*, Ph.D. Thesis, University of Kiel, 2009 (cit. on p. 114).
- [175] D. Lauvergnat and A. Nauts, *J. Chem. Phys.* 2002, **116**, 8560 (cit. on p. 114).
- [176] B. Schmidt and C. Hartmann, *WavePacket: A Matlab package for numerical quantum dynamics. II: Open quantum systems, optimal control, and model reduction*, arXiv:1707.06077, 2017 (cit. on p. 115).
- [177] H.-D. Meyer and G. A. Worth, *Theor. Chem. Acc.* 2003, **109**, 251-267 (cit. on p. 115).
- [178] G. A. Worth, M. A. Robb and I. Burghardt, *Faraday Discuss.* 2004, **127**, 307-323 (cit. on pp. 115, 263).
- [179] G. Richings, I. Polyak, K. Spinlove, G. Worth, I. Burghardt and B. Lasorne, *Int. Rev. Phys. Chem.* 2015, **34**, 269-308 (cit. on pp. 115, 262, 263).
- [180] S. K. Gray, *J. Chem. Phys.* 1992, **96**, 6543-6554 (cit. on p. 115).
- [181] S. K. Gray and G. G. Balint-Kurti, *J. Chem. Phys.* 1998, **108**, 950-962 (cit. on p. 115).
- [182] M. Hankel, S. C. Smith, R. J. Allan, S. K. Gray and G. G. Balint-Kurti, *J. Chem. Phys.* 2006, **125**, 164303 (cit. on p. 115).
- [183] U. Manthe, *J. Chem. Phys.* 1996, **105**, 6989-6994 (cit. on p. 115).
- [184] R. van Harrevelt and U. Manthe, *J. Chem. Phys.* 2005, **123**, 064106 (cit. on p. 115).
- [185] U. Manthe, *J. Chem. Phys.* 2009, **130**, 054109 (cit. on p. 115).
- [186] U. Manthe, *J. Phys. Condens. Matter*, 2017, **29**, 253001 (cit. on p. 115).
- [187] U. Manthe, *private communication*, 2017 (cit. on p. 115).
- [188] S. Behnel, R. Bradshaw, C. Citro, L. Dalcin, D. S. Seljebotn and K. Smith, *Comput. Sci. Eng.* 2011, **13**, 31-39 (cit. on p. 115).
- [189] G. van Rossum and J. de Boer, *CWI Q.* 1991, **4**, 283-304 (cit. on p. 116).
- [190] M. Pilgrim, *Dive into Python 3*, Apress, 1st edn., 2009 (cit. on p. 116).
- [191] S. van der Walt, S. C. Colbert and G. Varoquaux, *Comput. Sci. Eng.* 2011, **13**, 22-30 (cit. on pp. 116, 118).
- [192] Q. Sun et al., *WIREs Comput. Mol. Sci.* **8**, 1340 (cit. on p. 116).
- [193] J. M. Turney et al., *WIREs Comput. Mol. Sci.* 2012, **2**, 556-565 (cit. on p. 116).
- [194] J. Enkovaara et al., *J. Phys.: Condens. Matter*, 2010, **22**, 253202 (cit. on p. 116).
- [195] R. P. Muller, PyQuante, <http://pyquante.sourceforge.net/>, 2017 (cit. on p. 116).

- [196] M. F. Herbst and J. E. Avery, molsturm, a modular electronic structure theory code, <https://molsturm.org/>, 2017 (cit. on p. 116).
- [197] T. Verstraelen et al., HORTON 2.1.0b1, <http://theochem.github.com/horton/>, 2015 (cit. on p. 116).
- [198] M. Sibaeve and D. L. Crittenden, *Comput. Phys. Commun.* 2016, **203**, 290-297 (cit. on p. 116).
- [199] S. K. Lam, A. Pitrou and S. Seibert, Proceedings of the Second Workshop on the LLVM Compiler Infrastructure in HPC, ACM, New York, NY, USA, 2015, 7:1-7:6 (cit. on p. 116).
- [200] PyPy 5.9, <https://pypy.org/>, 2017 (cit. on p. 116).
- [201] M. R. B. Kristensen, S. A. F. Lund, T. Blum, K. Skovhede and B. Vinter, 2014 IEEE International Parallel Distributed Processing Symposium Workshops, 2014, pp. 312-321 (cit. on pp. 116, 118).
- [202] K. Hayen, Nuitka 0.5.28, <http://nuitka.net/>, 2017 (cit. on p. 116).
- [203] ISO International Standard ISO/IEC 14882:2014(E) – Programming Language C++, 2016 (cit. on p. 116).
- [204] S. B. Lippman, J. Lajoie and B. E. Moo, *C++ Primer*, Addison-Wesley, 5th edn., 2012 (cit. on pp. 116, 119).
- [205] boost 1.65.1, <http://www.boost.org/>, 2017 (cit. on p. 116).
- [206] M. A. Heroux et al., *ACM Trans. Math. Softw.* 2005, **31**, 397-423 (cit. on p. 116).
- [207] G. Guennebaud, B. Jacob et al., *Eigen v3.3*, <http://eigen.tuxfamily.org>, 2017 (cit. on pp. 116, 118, 123).
- [208] MATLAB, *version 8.5.0 (R2015a)*, Natick, Massachusetts, 2015 (cit. on p. 117).
- [209] J. Bezanson, A. Edelman, S. Karpinski and V. Shah, *SIAM Rev.* 2017, **59**, 65-98 (cit. on p. 117).
- [210] H. Tal-Ezer and R. Kosloff, *J. Chem. Phys.* 1984, **81**, 3967-3971 (cit. on p. 118).
- [211] U. Peskin, R. Kosloff and N. Moiseyev, *J. Chem. Phys.* 1994, **100**, 8849-8855 (cit. on p. 118).
- [212] A. Castro, M. A. L. Marques and A. Rubio, *J. Chem. Phys.* 2004, **121**, 3425-3433 (cit. on p. 118).
- [213] K. Kormann, S. Holmgren and H. O. Karlsson, *J. Chem. Phys.* 2008, **128**, 184101 (cit. on p. 118).
- [214] M. Ndong, H. Tal-Ezer, R. Kosloff and C. P. Koch, *J. Chem. Phys.* 2010, **132**, 064105 (cit. on p. 118).
- [215] V. Ledoux and M. Van Daele, *Comput. Phys. Commun.* 2014, **185**, 1589-1594 (cit. on p. 118).
- [216] J. E. Bækhoj, O. I. Tolstikhin and L. B. Madsen, *J. Phys. B*, 2014, **47**, 075007 (cit. on p. 118).
- [217] I. Schaefer, H. Tal-Ezer and R. Kosloff, *J. Comput. Phys.* 2017, **343**, 368-413 (cit. on p. 118).

-
- [218] M. Caliari, P. Kandolf, A. Ostermann and S. Rainer, *SIAM J. Sci. Comput.* 2016, **38**, A1639-A1661 (cit. on p. 118).
- [219] S. Blanes, F. Casas, J. A. Oteo and J. Ros, *Eur. J. Phys.* 2010, **31**, 907-918 (cit. on p. 118).
- [220] C. Leforestier et al., *J. Comput. Phys.* 1991, **94**, 59-80 (cit. on p. 118).
- [221] R. Kosloff, *Annu. Rev. Phys. Chem.* 1994, **45**, 145-178 (cit. on p. 118).
- [222] L. S. Blackford et al., *Acm. T. Math. Software.* 2001, **28**, 135-151 (cit. on p. 118).
- [223] E. Anderson et al., *LAPACK Users' Guide*, Society for Industrial and Applied Mathematics, Philadelphia, 3rd edn., 1999 (cit. on p. 118).
- [224] E. Solomonik, D. Matthews, J. R. Hammond, J. F. Stanton and J. Demmel, *J. Parallel Distr. Com.* 2014, **74**, 3176-3190 (cit. on p. 118).
- [225] P. Springer and P. Bientinesi, *Design of a high-performance GEMM-like Tensor-Tensor Multiplication*, arXiv:1607.00145, 2016 (cit. on p. 118).
- [226] J. A. Calvin, C. A. Lewis and E. F. Valeev, Proceedings of the 5th Workshop on Irregular Applications: Architectures and Algorithms, ACM, New York, NY, USA, 2015, 4:1-4:8 (cit. on p. 118).
- [227] J. A. Calvin and E. F. Valeev, *Task-Based Algorithm for Matrix Multiplication: A Step Towards Block-Sparse Tensor Computing*, arXiv:1504.05046, 2015 (cit. on p. 118).
- [228] L. International Workshop on Libraries, and Compilers for Array Programming, M. Elsmann, ACM Special Interest Group on Programming Languages, Association for Computing Machinery and ACM SIGPLAN Conference on Programming Language Design and Implementation, *ARRAY'16: proceedings of the 3rd ACM SIGPLAN International Workshop on Libraries, Languages, and Compilers for Array Programming : June 14, 2016, Santa Barbara, CA, USA*, 2016 (cit. on p. 118).
- [229] E. Di Napoli, D. Fabregat-Traver, G. Quintana-Ortí and P. Bientinesi, *Appl. Math. Comput.* 2014, **235**, 454-468 (cit. on p. 118).
- [230] T. Blum, M. R. B. Kristensen and B. Vinter, 2014 IEEE International Parallel Distributed Processing Symposium Workshops, 2014, pp. 1002-1010 (cit. on p. 118).
- [231] P. Peterson, *Int. J. Comput. Sci. Eng.* 2009, **4**, 296-305 (cit. on p. 119).
- [232] pybind11 2.2.1, <https://github.com/pybind/pybind11>, 2017 (cit. on p. 119).
- [233] R. J. Duchovic, Y. L. Volobuev, G. C. Lynch, D. G. Truhlar, T. C. Allison, A. F. Wagner, B. C. Garrett and J. C. Corchado, *Comput. Phys. Commun.* 2002, **144**, 169-187 (cit. on p. 119).
- [234] M. Sibaev and D. L. Crittenden, *J. Comput. Chem.* 2015, **36**, 2200-2207 (cit. on p. 119).
- [235] E. Gamma, R. Helm, R. Johnson and J. Vlissides, *Design Patterns*, Addison-Wesley, 1st edn., 1994 (cit. on pp. 120, 124).
- [236] R. Wodraszka and T. Carrington, *J. Chem. Phys.* 2017, **146**, 194105 (cit. on pp. 121, 258, 265).

- [237] T. H. Group, *Hierarchical Data Format, version 5*, <http://www.hdfgroup.org/HDF5/>, 1997-2017 (cit. on p. 123).
- [238] E. Freeman, B. Bates, K. Sierra and E. Robson, *Head First Design Patterns*, O' Reilly, 1st edn., 2004 (cit. on p. 124).
- [239] T. Darm, *Effective GoF Patterns with C++11 and Boost*, <https://www.infoq.com/presentations/gof-patterns-c-plus-plus-boost> (cit. on p. 124).
- [240] R. Sedgewick and K. Wayne, *Algorithms*, Addison-Wesley, 4th edn., 2011 (cit. on p. 126).
- [241] F. Renth, F. Temps and A. Trölsch, *J. Chem. Phys.* 2003, **118**, 659-668 (cit. on pp. 133, 259).
- [242] B. Bransden and C. Joachain, *Physics of Atoms & Molecules*, Dorling Kindersley, 2nd edn., 2006 (cit. on pp. 165, 166, 169).
- [243] R. Loudon, *The Quantum Theory of Light*, Oxford University Press, 3rd edn., 2000 (cit. on p. 166).
- [244] J. Feist, *Two-photon double ionization of helium*, Ph.D. Thesis, University of Vienna, 2009 (cit. on pp. 166, 216).
- [245] G. C. Schatz and M. A. Ratner, *Quantum Mechanics in Chemistry*, Dover, 1st edn., 2002 (cit. on pp. 166, 171).
- [246] M. Klaiber, K. Hatsagortsyan and C. Keitel, *Phys. Rev. A*, 2005, **71**, 033408 (cit. on p. 166).
- [247] K. J. Meharg, J. S. Parker and K. T. Taylor, *J. Phys. B*, 2005, **38**, 237-254 (cit. on p. 166).
- [248] A. Ludwig, J. Maurer, B. W. Mayer, C. R. Phillips, L. Gallmann and U. Keller, *Phys. Rev. Lett.* 2014, **113**, 243001 (cit. on p. 166).
- [249] Y.-C. Han and L. B. Madsen, *Phys. Rev. A*, 2010, **81**, 063430 (cit. on pp. 167, 200).
- [250] P. B. Corkum and F. Krausz, *Nat. Phys.* 2007, **3**, 381-387 (cit. on pp. 167, 170).
- [251] F. Krausz, *Rev. Mod. Phys.* 2009, **81**, 163-234 (cit. on pp. 167, 170).
- [252] G. Sansone, T. Pfeifer, K. Simeonidis and A. I. Kuleff, *ChemPhysChem*, 2012, **13**, 661-680 (cit. on pp. 167, 170).
- [253] P. H. Bucksbaum, *Science*. 2007, **317**, 766-769 (cit. on p. 167).
- [254] S. Pabst, *Eur. Phys. J. Special Topics*, 2013, **221**, 1-71 (cit. on p. 167).
- [255] T. Brabec and F. Krausz, *Rev. Mod. Phys.* 2000, **72**, 545-591 (cit. on pp. 167, 168).
- [256] T. Popmintchev, M.-C. Chen, P. Arpin, M. M. Murnane and H. C. Kapteyn, *Nature Photon.* 2010, **4**, 822-832 (cit. on pp. 167, 170).
- [257] I. V. Hertel and C.-P. Schulz, *Atome, Moleküle und optische Physik 1*, Springer, 1st edn., 2007 (cit. on pp. 167-170).
- [258] L. V. Keldysh, *Soviet Phys. JETP*, 1965, **20**, 1135-1144 (cit. on p. 168).
- [259] P. B. Corkum, *Phys. Rev. Lett.* 1993, **71**, 1994-1997 (cit. on pp. 170, 171).

-
- [260] V. Mosert and D. Bauer, *Comput. Phys. Commun.* 2016, **207**, 452-463 (cit. on pp. 171, 173).
- [261] J. R. Taylor, *Scattering Theory: The Quantum Theory of Nonrelativistic Collisions*, Dover, 1st edn., 2006 (cit. on p. 171).
- [262] C. J. Joachain, *Quantum Collision Theory*, Elsevier, 1st edn., 1975 (cit. on p. 171).
- [263] L. B. Madsen, L. A. A. Nikolopoulos, T. K. Kjeldsen and J. Fernández, *Phys. Rev. A*, 2007, **76**, 063407 (cit. on pp. 172, 175).
- [264] A. M. Ermolaev, I. V. Puzynin, A. V. Selin and S. I. Vinitzky, *Phys. Rev. A*, 1999, **60**, 4831-4845 (cit. on p. 172).
- [265] A. M. Ermolaev and A. V. Selin, *Phys. Rev. A*, 2000, **62**, 015401 (cit. on p. 172).
- [266] L. Tao and A. Scrinzi, *New J. Phys.* 2012, **14**, 013021 (cit. on p. 172).
- [267] A. Scrinzi, *New J. Phys.* 2012, **14**, 085008 (cit. on p. 172).
- [268] F. Morales, T. Bredtmann and S. Patchkovskii, *J. Phys. B*, 2016, **49**, 245001 (cit. on p. 172).
- [269] C. W. McCurdy, M. Baertschy and T. N. Rescigno, *J. Phys. B*, 2004, **37**, R137-R187 (cit. on p. 172).
- [270] A. Scrinzi, *Phys. Rev. A*, 2010, **81**, 053845 (cit. on p. 172).
- [271] K. J. Schafer and K. C. Kulander, *Phys. Rev. A*, 1990, **42**, 5794-5797 (cit. on p. 172).
- [272] K. J. Schafer, *Comput. Phys. Commun.* 1991, **63**, 427-434 (cit. on p. 172).
- [273] F. Catoire and H. Bachau, *Phys. Rev. A*, 2012, **85**, 023422 (cit. on pp. 172, 173).
- [274] D. Bauer and P. Koval, *Comput. Phys. Commun.* 2006, **174**, 396-421 (cit. on p. 173).
- [275] L.-Y. Peng, E. A. Pronin and A. F. Starace, *New J. Phys.* 2008, **10**, 025030 (cit. on p. 175).
- [276] J. Boersma, *Math. Comp.* 1969, **23**, 51-59 (cit. on p. 175).
- [277] L.-Y. Peng and Q. Gong, *Comput. Phys. Commun.* 2010, **181**, 2098-2101 (cit. on p. 175).
- [278] D. Hochstuhl, C. Hinz and M. Bonitz, *Eur. Phys. J. Special Topics*, 2014, **223**, 177-336 (cit. on pp. 176, 191, 217, 218, 222).
- [279] J. Crank and P. Nicolson, *Adv. Comput. Math*, 1996, **6**, 207-226 (cit. on p. 179).
- [280] H.-R. Schwarz and N. Köckler, *Numerische Mathematik*, Vieweg+Teubner, 1st edn., 2011 (cit. on pp. 179, 185).
- [281] A. Kramida, Yu. Ralchenko, J. Reader and NIST ASD Team, NIST Atomic Spectra Database (ver. 5.5.2), [Online]. Available: <https://physics.nist.gov/asd>. National Institute of Standards and Technology, Gaithersburg, MD. 2018 (cit. on p. 181).
- [282] R. Dörner, T. Weber, M. Weckenbrock, A. Staudte, M. Hattass, H. Schmidt-Böcking, R. Moshhammer and J. Ullrich, in *Advances In Atomic, Molecular, and Optical Physics*, ed. B. Bederson and H. Walther, Academic Press, 2002, vol. 48, ch. Multiple Ionization in Strong Laser Fields, pp. 1-34 (cit. on p. 181).

- [283] W. Becker and H. Rottke, *Contemp. Phys.* 2008, **49**, 199-223 (cit. on p. 181).
- [284] C. F. de Morisson Faria and X. Liu, *J. Mod. Opt.* 2011, **58**, 1076-1131 (cit. on p. 181).
- [285] D. Kosloff and R. Kosloff, *J. Comp. Phys.* 1983, **52**, 35-53 (cit. on pp. 182, 199).
- [286] D. J. Tannor and S. A. Rice, *J. Chem. Phys.* 1985, **83**, 5013-5018 (cit. on p. 183).
- [287] I. Schaefer and R. Kosloff, *Phys. Rev. A*, 2012, **86**, 063417 (cit. on p. 183).
- [288] D. L. Elliott, *Bilinear Control Systems*, Springer, 1st edn., 2009 (cit. on p. 183).
- [289] D. Liberzon, *Calculus of Variations and Optimal Control Theory*, Princeton University Press, 1st edn., 2012 (cit. on pp. 183, 184).
- [290] W. M. Wonham, *Linear Multivariable Control*, Springer, 3rd edn., 1985 (cit. on p. 183).
- [291] V. F. Krotov, *Global Methods in Optimal Control Theory*, Dekker, 1st edn., 1996 (cit. on pp. 183, 184, 187).
- [292] J. E. Bobrow, S. Dubowsky and J. S. Gibson, *Int. J. Robot. Res.* 1985, **4**, 3-17 (cit. on p. 183).
- [293] T. Faulwasser, T. Weber, P. Zometa and R. Findeisen, *IEEE Trans. Control Syst. Technol.* 2017, **25**, 1505-1511 (cit. on p. 183).
- [294] H. Huang and V. K. N. Lau, *IEEE Trans. Signal Process.* 2012, **60**, 2552-2561 (cit. on p. 183).
- [295] R. R. Appino, J. Á. González Ordiano, R. Mikut, T. Faulwasser and V. Hagenmeyer, *Appl. Energy*, 2018, **210**, 1207-1218 (cit. on p. 183).
- [296] J. Andersson, *A General-Purpose Software Framework for Dynamic Optimization*, PhD thesis, Arenberg Doctoral School, KU Leuven, 2013 (cit. on p. 183).
- [297] M. A. Patterson and A. V. Rao, *ACM Trans. Math. Softw.* 2014, **41**, 1-37 (cit. on pp. 183, 188).
- [298] R. Kosloff, S. A. Rice, P. Gaspard, S. Tersigni and D. J. Tannor, *Chem. Phys.* 1989, **139**, 201-220 (cit. on pp. 184, 186, 189).
- [299] G. G. Balint-Kurti, S. Zou and A. Brown, in *Advances in Chemical Physics*, John Wiley & Sons, Inc., 2008, vol. 138, ch. Optimal Control Theory for Manipulating Molecular Processes, pp. 43-94 (cit. on p. 184).
- [300] J. Werschnik and E. K. U. Gross, *J. Phys. B*, 2007, **40**, R175-R211 (cit. on pp. 184, 188, 196).
- [301] R. Eitan, *Optimal Control of Multielectron Systems: Four New Methodology Developments*, Ph.D. Thesis, Weizmann Institute of Science, 2012 (cit. on p. 184).
- [302] R. Eitan, M. Mundt and D. J. Tannor, *Phys. Rev. A*, 2011, **83**, 053426 (cit. on pp. 184, 185, 187, 188).
- [303] C. Lubich, *From Quantum to Classical Molecular Dynamics: Reduced Models and Numerical Analysis*, European Mathematical Society, 1st edn., 2008 (cit. on p. 185).
- [304] J. Nocedal and S. J. Wright, *Numerical Optimization*, Springer, 2nd edn., 2006 (cit. on p. 186).

-
- [305] P. E. Gill, W. Murray and M. H. Wright, *Practical Optimization*, Academic Press, 1st edn., 1997 (cit. on p. 186).
- [306] J. Somló, V. A. Kazakov and D. J. Tannor, *Chem. Phys.* 1993, **172**, 85-98 (cit. on p. 187).
- [307] D. J. Tannor, V. Kazakov and V. Orlov, in *Time-Dependent Quantum Molecular Dynamics*, ed. J. Broeckhove and L. Lathouwers, Springer, 1992, ch. Control of photochemical branching: Novel procedures for finding optimal pulses and global upper bounds, pp. 347-360 (cit. on p. 187).
- [308] W. Zhu, J. Botina and H. Rabitz, *J. Chem. Phys.* 1998, **108**, 1953-1963 (cit. on p. 188).
- [309] Y. Maday and G. Turinici, *J. Chem. Phys.* 2003, **118**, 8191-8196 (cit. on p. 188).
- [310] S. E. Sklarz and D. J. Tannor, *Phys. Rev. A*, 2002, **66**, 053619 (cit. on p. 188).
- [311] D. M. Reich, M. Ndong and C. P. Koch, *J. Chem. Phys.* 2012, **136**, 104103 (cit. on pp. 188, 197).
- [312] I. Degani, A. Zanna, L. SÆlen and R. Nepstad, *SIAM J. Sci. Comput.* 2009, **31**, 3566-3594 (cit. on p. 188).
- [313] I. Degani and A. Zanna, *SIAM J. Sci. Comput.* 2012, **34**, A1488-A1521 (cit. on p. 188).
- [314] T. Hornung, M. Motzkus and R. de Vivie-Riedle, *J. Chem. Phys.* 2001, **115**, 3105-3111 (cit. on p. 188).
- [315] C. Gollub, M. Kowalewski and R. de Vivie-Riedle, *Phys. Rev. Lett.* 2008, **101**, 073002 (cit. on p. 188).
- [316] M. Schröder and A. Brown, *New J. Phys.* 2009, **11**, 105031 (cit. on pp. 188, 203).
- [317] J. P. Palao, D. M. Reich and C. P. Koch, *Phys. Rev. A*, 2013, **88**, 053409 (cit. on p. 188).
- [318] D. M. Reich, J. P. Palao and C. P. Koch, *J. Mod. Optic.* 2014, **61**, 822-827 (cit. on p. 188).
- [319] A. R. Conn, K. Scheinberg and L. N. Vicente, *Introduction to Derivative-Free Optimization*, SIAM, 1st edn., 2009 (cit. on p. 188).
- [320] M. J. D. Powell, *Cambridge NA Report NA200906*, 2009 (cit. on pp. 188, 204).
- [321] N. Rach, M. M. Müller, T. Calarco and S. Montangero, *Phys. Rev. A*, 2015, **92**, 062343 (cit. on p. 188).
- [322] T. Caneva, T. Calarco and S. Montangero, *Phys. Rev. A*, 2011, **84**, 022326 (cit. on p. 188).
- [323] P. Doria, T. Calarco and S. Montangero, *Phys. Rev. Lett.* 2011, **106**, 190501 (cit. on p. 188).
- [324] M. H. Goerz, K. B. Whaley and C. P. Koch, *EPJ Quantum Technol.* 2015, **2**, 21 (cit. on p. 189).
- [325] D. E. Goldberg, *Genetic Algorithms in Search, Optimization, and Machine Learning*, Addison-Wesley, 1st edn., 1989 (cit. on p. 189).
- [326] I. Gerdes, F. Klawonn and R. Kruse, *Evolutionäre Algorithmen*, Vieweg+Teubner, 1st edn., 2004 (cit. on p. 189).

- [327] T. Weise, *Global Optimization Algorithms*, www.it-weise.de, 3rd edn., 2011 (cit. on pp. 189, 204).
- [328] S. Talukder, P. Chaudhury and S. Adhikari, *Mol. Phys.* 2017, 1-11 (cit. on p. 189).
- [329] S. Machnes, D. J. Tannor, F. K. Wilhelm and E. Assémat, *Gradient Optimization of Analytic Controls: The Route to High Accuracy Quantum Optimal Control*, arXiv:1507.04261, 2015 (cit. on p. 189).
- [330] S. J. Glaser, U. Boscain, T. Calarco, C. P. Koch, W. Köckenberger, R. Kosloff, I. Kuprov, B. Luy, S. Schirmer, T. Schulte-Herbrüggen et al., *Eur. Phys. J. D*, 2015, **69**, 279 (cit. on p. 189).
- [331] V. Engel, C. Meier and D. J. Tannor, in *Advances in Chemical Physics*, John Wiley & Sons, Inc., 2009, vol. 141, ch. Local Control Theory: Recent Applications to Energy and Particle Transfer Processes in Molecules, pp. 29-101 (cit. on p. 189).
- [332] Y. Ohtsuki, Y. Yahata, H. Kono and Y. Fujimura, *Chem. Phys. Lett.* 1998, **287**, 627-631 (cit. on p. 189).
- [333] Y. Ohtsuki, H. Kono and Y. Fujimura, *J. Chem. Phys.* 1998, **109**, 9318-9331 (cit. on p. 189).
- [334] M. Sugawara and Y. Fujimura, *J. Chem. Phys.* 1994, **100**, 5646-5655 (cit. on p. 189).
- [335] J. Salomon and G. Turinici, *J. Chem. Phys.* 2006, **124**, 074102 (cit. on p. 189).
- [336] D. J. Tannor, R. Kosloff and A. Bartana, *Faraday Discuss.* 1999, **113**, 365-383 (cit. on p. 189).
- [337] D. J. Tannor and A. Bartana, *J. Phys. Chem. A*, 1999, **103**, 10359-10363 (cit. on p. 189).
- [338] D. P. Tew, W. Klopper and T. Helgaker, *J. Comput. Chem.* 2007, **28**, 1307-1320 (cit. on p. 190).
- [339] P. W. Atkins and R. S. Friedman, *Molecular Quantum Mechanics*, Oxford University Press, 5th edn., 2010 (cit. on p. 191).
- [340] C. Yu and L. B. Madsen, *Phys. Rev. A*, 2016, **94**, 053424 (cit. on p. 192).
- [341] A. Bande, K. Gokhberg and L. S. Cederbaum, *J. Chem. Phys.* 2011, **135**, 144112 (cit. on p. 192).
- [342] M. Brehm, *Analyzing Trajectories from Molecular Simulation*, Ph.D. Thesis, University of Leipzig, 2013 (cit. on p. 197).
- [343] W. H. Press, S. A. Teukolsky, W. T. Vetterling and B. P. Flannery, *Numerical Recipes*, Cambridge University Press, 3rd edn., 2007 (cit. on p. 199).
- [344] H.-D. Meyer and H. Wang, *On regularizing the MCTDH equations of motion*, preprint, 2018 (cit. on p. 200).
- [345] L. B. Madsen, *Phys. Rev. A*, 2002, **65**, 053417 (cit. on p. 200).
- [346] D. Sugny, S. Vranckx, M. Ndong, N. Vaeck, O. Atabek and M. Desouter-Lecomte, *Phys. Rev. A*, 2014, **90**, 053404 (cit. on p. 201).

-
- [347] I. R. Sola, J. Santamaria and D. J. Tannor, *J. Phys. Chem. A*, 1998, **102**, 4301-4309 (cit. on p. 204).
- [348] H. R. Larsson and B. Hartke, *Comput. Meth. Mater. Sci.* 2013, **13**, 120-126 (cit. on p. 204).
- [349] H. R. Larsson, A. C. T. van Duin and B. Hartke, *J. Comput. Chem.* 2013, **34**, 2178-2189 (cit. on p. 204).
- [350] H. R. Larsson, *Globale Parameteroptimierung des reaktiven Kraftfeldes ReaxFF mit Hilfe von evolutionären Algorithmen*, Bachelor's thesis, Institute for Physical Chemistry, University of Kiel, 2012 (cit. on p. 204).
- [351] S. Ruetzel, C. Stolzenberger, S. Fechner, F. Dimler, T. Brixner and D. J. Tannor, *J. Chem. Phys.* 2010, **133**, 164510 (cit. on p. 204).
- [352] M. J. D. Powell, *Acta Numer.* 1998, **7**, 287-336 (cit. on p. 204).
- [353] S. G. Johnson, *The NLOpt nonlinear-optimization package*, <http://ab-initio.mit.edu/nlopt>, 2018 (cit. on p. 204).
- [354] S. Fechner, F. Dimler, T. Brixner, G. Gerber and D. J. Tannor, *Opt. Express*, 2007, **15**, 15387-15401 (cit. on p. 207).
- [355] H. R. Larsson, S. Bauch, L. K. Sørensen and M. Bonitz, *Phys. Rev. A*, 2016, **93**, 013426 (cit. on pp. 209, 217, 218, 253, 266).
- [356] D. Hochstuhl and M. Bonitz, *Phys. Rev. A*, 2012, **86**, 053424 (cit. on p. 217).
- [357] S. Bauch, *The TD-GAS-CI approach to the time-resolved photoionization of molecules*, Talk at Kiel University, 2014 (cit. on p. 219).
- [358] J. A. Pople, J. S. Binkley and R. Seeger, *Int. J. Quantum. Chem.* 1976, **10**, 1-19 (cit. on p. 220).
- [359] R. J. Bartlett, *Annu. Rev. Phys. Chem.* 1981, **32**, 359-401 (cit. on p. 220).
- [360] J. Olsen, *private communication*, 2014 (cit. on pp. 220, 221).
- [361] J. Olsen, B. O. Roos, P. Jørgensen and H. J. A. Jensen, *J. Chem. Phys.* 1988, **89**, 2185-2192 (cit. on p. 221).
- [362] P. G. Szalay, T. Müller, G. Gidofalvi, H. Lischka and R. Shepard, *Chem. Rev.* 2012, **112**, 108-181 (cit. on p. 221).
- [363] T. Fleig, J. Olsen and C. M. Marian, *J. Chem. Phys.* 2001, **114**, 4775 (cit. on p. 221).
- [364] J. Ivanic, *J. Chem. Phys.* 2003, **119**, 9364 (cit. on p. 221).
- [365] J. Ivanic, *J. Chem. Phys.* 2003, **119**, 9377 (cit. on p. 221).
- [366] T. Sato and K. L. Ishikawa, *Time-dependent multiconfiguration self-consistent-field method based on occupation restricted multiple active space model for multielectron dynamics in intense laser fields*, arXiv:1411.3077, 2014 (cit. on pp. 221, 223).

- [367] L. K. Sørensen, S. Bauch and L. B. Madsen, *The Integral Screened Configuration Interaction Method*, arXiv:1609.07757, 2016 (cit. on pp. 221, 224).
- [368] T. Kato and H. Kono, *Chem. Phys. Lett.* 2004, **392**, 533-540 (cit. on p. 222).
- [369] J. Zanghellini, M. Kitzler, C. Fabian, T. Brabec and A. Scrinzi, *Laser Phys.* 2003, **13**, 1064-1068 (cit. on p. 222).
- [370] M. Nest, T. Klamroth and P. Saalfrank, *J. Chem. Phys.* 2005, **122**, 124102 (cit. on p. 222).
- [371] O. Koch and C. Lubich, *Ima. J. Numer. Anal.* 2011, **31**, 379-395 (cit. on p. 222).
- [372] O. Koch, W. Kreuzer and A. Scrinzi, *Appl. Math. Comput.* 2006, **173**, 960-976 (cit. on p. 222).
- [373] H. Miyagi and L. B. Madsen, *J. Chem. Phys.* 2014, **140**, 164309 (cit. on p. 223).
- [374] H. Miyagi and L. B. Madsen, *Phys. Rev. A*, 2014, **89**, 063416 (cit. on p. 223).
- [375] H. Miyagi and L. B. Madsen, *Phys. Rev. A*, 2013, **87**, 062511 (cit. on p. 223).
- [376] D. J. Haxton and C. W. McCurdy, *Phys. Rev. A*, 2015, **91**, 012509 (cit. on p. 223).
- [377] A. Troellsch and F. Temps, *Z. Phys. Chem.* 2001, **215**, 207-232 (cit. on p. 259).
- [378] L. Chen, K. Shao, J. Chen, M. Yang and D. H. Zhang, *J. Chem. Phys.* 2016, **144**, 194309 (cit. on p. 261).
- [379] H. Song, J. Li, M. Yang, Y. Lu and H. Guo, *Phys. Chem. Chem. Phys.* 2014, **16**, 17770-17776 (cit. on p. 261).
- [380] G. G. Balint-Kurti and A. Palov, *Theory of Molecular Collisions*, Royal Society of Chemistry, 1st edn., 2015 (cit. on p. 262).
- [381] A. Simoni, A. Viel and J.-M. Launay, *J. Chem. Phys.* 2017, **146**, 244106 (cit. on p. 262).
- [382] E. J. Heller, *J. Chem. Phys.* 1975, **62**, 1544-1555 (cit. on pp. 262, 263).
- [383] A. P. Harrison and D. Joseph, *High Performance Rearrangement and Multiplication Routines for Sparse Tensor Arithmetic*, arXiv:1802.02619, 2018 (cit. on p. 262).
- [384] S. Bittens, R. Zhang and M. A. Iwen, *A Deterministic Sparse FFT for Functions with Structured Fourier Sparsity*, arXiv:1705.05256, 2017 (cit. on p. 262).
- [385] R. R. Khorasani and R. S. Dumont, *J. Chem. Phys.* 2007, **127**, 184107 (cit. on p. 262).
- [386] V. Gradinaru, *Computing*, 2007, **80**, 1-22 (cit. on p. 262).
- [387] A. B. Atanasov and E. Schnetter, *Sparse Grid Discretizations based on a Discontinuous Galerkin Method*, arXiv:1710.09356, 2017 (cit. on p. 262).
- [388] H.-J. Bungartz and M. Griebel, *Acta Numer.* 2004, **13**, 147-269 (cit. on p. 262).
- [389] G. Avila and T. Carrington, *J. Chem. Phys.* 2009, **131**, 174103 (cit. on p. 262).
- [390] D. Lauvergnat and A. Nauts, *Spectrochim. Acta A*. 2014, **119**, 18-25 (cit. on p. 262).
- [391] I. Degani, J. Schiff and D. J. Tannor, *Numer. Math.* 2005, **101**, 479-500 (cit. on p. 262).

-
- [392] I. Degani and D. J. Tannor, *J. Phys. Chem. A*, 2006, **110**, 5395-5410 (cit. on p. 262).
- [393] N. Takemoto and D. J. Tannor, unpublished, 2017 (cit. on p. 263).
- [394] W. H. Miller, *J. Chem. Phys.* 2006, **125**, 132305 (cit. on p. 263).
- [395] B. Poirier, *Found. Phys.* 2000, **30**, 1191-1226 (cit. on p. 263).
- [396] J. B. Anderson, *J. Chem. Phys.* 1975, **63**, 1499-1503 (cit. on p. 263).
- [397] G. H. Booth, A. J. W. Thom and A. Alavi, *J. Chem. Phys.* 2009, **131**, 054106 (cit. on p. 263).
- [398] T. J. Frankcombe, M. A. Collins and G. A. Worth, *Chem. Phys. Lett.* 2010, **489**, 242-247 (cit. on p. 263).
- [399] M. Ben-Nun, J. Quenneville and T. J. Martínez, *J. Phys. Chem. A*, 2000, **104**, 5161-5175 (cit. on p. 263).
- [400] M. Wehrle, M. Šulc and J. Vaníček, *J. Chem. Phys.* 2014, **140**, 244114 (cit. on p. 263).
- [401] H.-J. Werner, C. Bauer, P. Rosmus, H.-M. Keller, M. Stumpf and R. Schinke, *J. Chem. Phys.* 1995, **102**, 3593-3611 (cit. on p. 263).
- [402] J. Jakowski, I. Sumner and S. S. Iyengar, *J. Chem. Theory Comput.* 2006, **2**, 1203-1219 (cit. on p. 263).
- [403] J. Li, X. Li and S. S. Iyengar, *J. Chem. Theory Comput.* 2014, **10**, 2265-2280 (cit. on p. 263).
- [404] M. Wehrle, S. Oberli and J. Vaníček, *J. Phys. Chem. A*, 2015, **119**, 5685-5690 (cit. on p. 264).
- [405] O. Godsi, M. A. Collins and U. Peskin, *J. Chem. Phys.* 2010, **132**, 124106 (cit. on p. 264).
- [406] W. Koch and D. H. Zhang, *J. Chem. Phys.* 2014, **141**, 021101 (cit. on p. 264).
- [407] R. Dawes, D. L. Thompson, Y. Guo, A. F. Wagner and M. Minkoff, *J. Chem. Phys.* 2007, **126**, 184108 (cit. on p. 264).
- [408] M. Majumder, S. A. Ndengue and R. Dawes, *Mol. Phys.* 2016, **114**, 1-18 (cit. on p. 264).
- [409] N. DeGregorio and S. S. Iyengar, *J. Chem. Theory Comput.* 2018, **14**, 30-47 (cit. on p. 264).
- [410] C. König and O. Christiansen, *J. Chem. Phys.* 2016, **145**, 064105 (cit. on p. 264).
- [411] E. L. Klinting, B. Thomsen, I. H. Godtliebsen and O. Christiansen, *J. Chem. Phys.* 2018, **148**, 064113 (cit. on p. 264).
- [412] G. Rauhut, *J. Chem. Phys.* 2007, **127**, 184109 (cit. on p. 264).
- [413] M. Odunlami, V. Le Bris, D. Bégué, I. Baraille and O. Coulaud, *J. Chem. Phys.* 2017, **146**, 214108 (cit. on p. 264).
- [414] K.-S. Lee and U. R. Fischer, *Int. J. Mod. Phys. B*, 2014, **28**, 1550021 (cit. on p. 265).
- [415] U. Manthe, *J. Chem. Phys.* 2015, **142**, 244109 (cit. on p. 265).
- [416] R. Wodraszka and T. Carrington, *J. Chem. Phys.* 2016, **145**, 044110 (cit. on p. 265).
- [417] S. Heislbeitz, F. Pfeiffer and G. Rauhut, *J. Chem. Phys.* 2011, **134**, 204108 (cit. on p. 265).

- [418] F. Pfeiffer and G. Rauhut, *J. Chem. Phys.* 2014, **140**, 064110 (cit. on p. 265).
- [419] P. Meier, D. Oschetzki, F. Pfeiffer and G. Rauhut, *J. Chem. Phys.* 2015, **143**, 244111 (cit. on p. 265).
- [420] W. Mizukami and D. P. Tew, *J. Chem. Phys.* 2013, **139**, 194108 (cit. on p. 265).
- [421] M. Rakhuba and I. Oseledets, *J. Chem. Phys.* 2016, **145**, 124101 (cit. on p. 265).
- [422] A. Baiardi, C. J. Stein, V. Barone and M. Reiher, *J. Chem. Theory Comput.* 2017, **13**, 3764-3777 (cit. on p. 265).
- [423] R. Orús, *Ann. Phys.* 2014, **349**, 117-158 (cit. on p. 265).
- [424] A. Leclerc and T. Carrington, *J. Chem. Phys.* 2014, **140**, 174111 (cit. on p. 265).
- [425] P. S. Thomas and T. Carrington, *J. Chem. Phys.* 2017, **146**, 204110 (cit. on p. 265).
- [426] O. Vendrell, F. Gatti and H.-D. Meyer, *J. Chem. Phys.* 2007, **127**, 184303 (cit. on p. 265).
- [427] D. Peláez and H.-D. Meyer, *Chem. Phys.* 2017, **482**, 100-105 (cit. on p. 265).
- [428] L. Wang, H.-D. Meyer and V. May, *J. Chem. Phys.* 2006, **125**, 014102 (cit. on p. 265).
- [429] A. Scrinzi, *New J. Phys.* 2012, **14**, 085008 (cit. on p. 266).
- [430] D. H. Zhang and H. Guo, *Annu. Rev. Phys. Chem.* 2016, **67**, 135-158 (cit. on p. 266).
- [431] J. M. Bowman and P. L. Houston, *Chem. Soc. Rev.* 2017, **46**, 7615-7624 (cit. on p. 266).
- [432] X. Ma and W. L. Hase, *Phil. Trans. R. Soc. A*, 2017, **375**, 20160204 (cit. on p. 266).
- [433] F. Huarte-Larrañaga and U. Manthe, *J. Phys. Chem. A*, 2001, **105**, 2522-2529 (cit. on p. 266).
- [434] A. Vikár, T. Nagy and G. Lendvay, *J. Phys. Chem. A*, 2016, **120**, 5083-5093 (cit. on p. 266).

Declaration

I hereby declare that the work presented in this thesis was done by me, under the supervision of Prof. Dr. Bernd Hartke and Prof. Dr. David Tannor, with no other help than the referenced sources in the text.

This is my first dissertation and the work has never been used in any other dissertation attempts. I have never been deprived of an academic title.

The dissertation complies to the good scientific practice rules as proposed by the German Research Foundation (DFG).

Kiel, March 2018

Henrik R. Larsson

Academic Curriculum Vitae

	Henrik R. Larsson
Date of birth	11.02.1990
Birth place	Hamburg, Germany
Nationality	German
Address	Düppelstr. 85, 24105 Kiel
ORCID	https://orcid.org/0000-0002-9417-1518
	Education
since Dec. 2014	Doctoral candidate at University of Kiel Supervisors: Prof. Dr. B. Hartke and Prof. Dr. D. J. Tannor (Weizmann Institute of Science, Rehovot, Israel)
2014	Master's Thesis in Theoretical Physics: <i>Laser-Induced Correlated Electron Dynamics in Small Molecules</i> Supervisors: Prof. Dr. M. Bonitz and Dr. S. Bauch
2013	Guest Student Program at Jülich Supercomputing Center <i>Molecular Orbital Generation Sequences</i> Supervisor: Dr. Thomas Müller
2013–2014	Master of Science (Chemistry) at University of Kiel, Germany (3 semesters)
2012–2013	Visiting student (Master of Science) at Lund University, Sweden (1 semester)
2012	Bachelor's Thesis in Theoretical Chemistry: <i>Global Optimization of Parameters for the Reactive Force Field ReaxFF</i> Supervisor: Prof. Dr. B. Hartke
2009–2012	Bachelor of Science (Chemistry) at University of Kiel, Germany (6 semesters)
2004–2009	Secondary school at "Domschule Schleswig"
2000–2004	Secondary school at "Coppernicus-Gymnasium Norderstedt"
	Awards and scholarships
2018	Travel grant by the German Academic Exchange Service (DAAD)
2017	Best poster award at the 11th Congress of the World Association of Theoretical and Computational Chemists (WATOC)

- 2017 Paul Barbara Scholarship for visiting a conference at the Telluride Science Research Center
- since 2014 PhD Scholarship by the German Academic Scholarship Foundation (“Studienstiftung”)
- 2014–2017 PhD Scholarship by the Fund of the Chemical Industry (FCI)
- 2015 Scholarship for studying abroad by the German Academic Exchange Service (DAAD)
- 2009–2014 Scholarship by the German Academic Scholarship Foundation
- 2014 Otto-Diels-Prize for the best Master’s thesis by the Chemistry Department at University of Kiel
- 2014 Annual prize by the Association for the Support of the Faculty of Mathematics and Natural Sciences at University of Kiel
- 2014 Award for studies and social commitment by the “Iuventus Academia Holsatorium”
- 2013 Admission to the Lindau Nobel Laureate Meeting, supported by the Fund of the Chemical Industry (FCI)
- 2012 Prize for the Bachelor’s thesis by the Chemistry Department at University of Kiel
- 2009 Award for the best school-leaving examination in Chemistry by the German Chemical Society (GDCh)
- Talks and presentations**
- Jan. 2018 Talk in the group of Prof. G. Chan, Pasadena, USA.
- Jan. 2018 Talk in the group of Prof. A. I. Krylov, Los Angeles, USA.
- Jan. 2018 Talk in the group of Prof. E. Neuscamman, Berkeley, USA.
- Nov. 2017 Invited talk at the Theoretical Chemistry Seminar at Heidelberg University, Germany.
- Oct. 2017 Two invited talks at the school “Quantum Dynamics with the Multi-Configuration Time-Dependent Hartree (MCTDH) method: future and perspectives”, Saint-Aubin, France.
- Aug. 2017 Poster at the WATOC conference, Munich, Germany.
- Jul. 2017 Invited talk at the workshop “Spectroscopy and Dynamics of Coupled Anharmonic Vibrations of Floppy Molecular Systems”, Telluride, USA.
- Apr. 2017 Invited talk (stand-in for D. J. Tannor) at the Annual Meeting of the American Chemical Society, San Francisco, USA.
- Jan. 2017 Two posters at the workshop “From Ultrafast to Ultraslow Dynamics in Molecules and Clusters”, Rehovot, Israel.
- Oct. 2016 Poster at the summer school “Modern Wavefunction Methods in Electronic Structure Theory”, Gelsenkirchen, Germany.
- Sep. 2016 Poster at the conference “Quantum Dynamics”, Greifswald, Germany.

Aug. 2016	Talk at the workshop “High Dimensional Quantum Dynamics”, Rostock, Germany.
Apr. 2016	Invited talk in the group of Prof. U. Manthe, Bielefeld, Germany.
Mar. 2016	Invited talk in the group of Prof. I. Burghardt, Frankfurt, Germany.
Dec. 2015	Invited talk at the Christmas Colloquium, Chemistry Department, Univ. of Kiel, Germany.
Dec. 2015	Talk at the FCI PhD scholar meeting, Braunschweig, Germany.
Apr. 2015	Talk at the PhD scholar meeting of the German Academic Scholarship Foundation, Berlin, Germany.
Oct. 2015	Talk at the “Advanced Study Group 2015: Semiclassical Methods: Insight and Practice in ‘Many’ Dimensions”, Dresden, Germany.
Sep. 2015	Poster at the Symposium on Theoretical Chemistry, Potsdam, Germany.
Jun. 2015	Poster at the CECAM workshop “Molecular Quantum Dynamics Methods”, Lausanne, Switzerland.
Dec. 2014	Poster at the workshop “Coherence and Control in the Quantum World”, Rehovot, Israel.
Sep. 2014	Poster at the Symposium on Theoretical Chemistry, Vienna, Austria.
Jul. 2014	Poster at the Sostrup Summer School: Quantum Chemistry and Molecular Properties, Vesterled, Denmark.
	Teaching experience
2016	Lecturer for a 16-day course “Quantum Chemistry” at the “Deutsche Schüler-Akademie” for 15 talented pupils.
2015/2016	Lecturer for “Numerical Mathematics for Chemists” (2 hours lecture & 2 hours exercises per week), including a full revision and extension of the lecture notes and exercises.
2013, 2014	Half-day lectures about Analytical Chemistry for pupils participating in the selection rounds of the International Chemistry Olympiad (IChO).
2010, 2011	Preparatory class for first year Chemistry students.
	Activities
2016	Lecturer for a 16-day course “Quantum Chemistry” at the “Deutsche Schüler-Akademie” for 15 talented pupils.
2010–2014	Student representative for Chemistry at University of Kiel.
2010–2012	“MINTor” for the Foundation of German Business encouraging pupils to study a discipline in Science, Engineering, Mathematics or Computer Science.
since 2009	Work for the Friends of the Chemistry Olympiad (FChO), among others organizing Chemistry contests for pupils.

Publications related to the thesis

- [1] J. Svensmark, Y. Wang, D. Ursrey, H. R. Larsson, D. J. Tannor, N. Douguet, K. Bartschat, A. N. Grum-Grzhimailo, B. Schulz, A. Saenz, A. Scrinzi, F. Morales, T. Bredtmann, H. G. Muller, S. Patchkovskii, X. Wang, F. Robicieux, V. Mosert, D. Bauer, X. M. Tong and B. D. Esry, *Comparing the performance of time-dependent-Schrödinger-equation solvers for the 800-nm, one-electron-atom, strong-field problem*, in preparation, 2018.
- [2] H. R. Larsson, J. Riedel, J. Wei, F. Temps and B. Hartke, *J. Chem. Phys.*, 2018, **148**, in press, arXiv:1802.07050.
- [3] D. J. Tannor, S. Machnes, E. Assémat and H. R. Larsson, in *Advances in Chemical Physics*, John Wiley & Sons, Inc., 2018, vol. 163, pp. 273-323.
- [4] D. Azoury, M. Krüger, G. Orenstein, H. R. Larsson, S. Bauch, B. D. Bruner and N. Dudovich, *Nat. Commun.* 2017, **8**, 1453.
- [5] H. R. Larsson and D. J. Tannor, *J. Chem. Phys.* 2017, **147**, 044103.
- [6] H. R. Larsson, B. Hartke and D. J. Tannor, *J. Chem. Phys.* 2016, **145**, 204108.
- [7] S. Machnes, E. Assémat, H. R. Larsson and D. J. Tannor, *J. Phys. Chem. A*, 2016, **120**, 3296-3308.

Publications unrelated to the thesis

- [1] H. R. Larsson, S. Bauch, L. K. Sørensen and M. Bonitz, *Phys. Rev. A*, 2016, **93**, 013426.
- [2] S. Bauch, H. R. Larsson, C. Hinz and M. Bonitz, *J. Phys. Conf. Ser.* 2016, **696**, 012008.
- [3] H. R. Larsson, A. C. T. van Duin and B. Hartke, *J. Comput. Chem.* 2013, **34**, 2178-2189.
- [4] H. R. Larsson and B. Hartke, *Comput. Meth. Mater. Sci.* 2013, **13**, 120-126.

Acknowledgments

” *It is only with the heart that one can see rightly;
What is essential is invisible to the eye.*

— **Antoine de Saint-Exupéry**
The Little Prince

First and foremost, I thank my supervisors Prof. Bernd Hartke and Prof. David Tannor for so much support, many helpful guidance, advice, enlightening discussions, and allowing me for having so much scientific freedom, including this unusual, coherent superposition of two advisors. I really enjoyed it!

I thank Prof. Nirit Dudovich, Prof. Friedrich Temps and their groups for nice and fruitful collaborations. Further, I am deeply grateful for *many* stimulating discussions and helpful advice about the topics presented in thesis to (given in random order determined by a Python script) Mark Dittner, Michael Herbst, Dr. Daniel Reich, Prof. Bill Poirier, Dr. Shai Machnes, Prof. Irene Burghardt, Dr. Sven Krönke, Dr. Ralph Welsch, Prof. Karl Worthmann, Dr. Rafael Abta, Prof. Hans-Dieter Meyer, Prof. Ove Christiansen, Dr. Elie Assémat, Prof. Armin Scrinzi, Prof. Tucker Carrington, Prof. Eli Pollak, Dr. Norio Takemoto, Dr. Timm Faulwasser, Dr. Werner Koch, Prof. Uwe Manthe, Dr. Michael Krüger and to all I forgot to mention (I hope I did not). Thank you!

I thank (again, in random order) Prof. Bernd Hartke, Mark Dittner, Tim Raeker, Dr. Sebastian Bauch, Michael Herbst and Dr. Daniel Reich for careful proofreadings of earlier versions of this thesis and comments on it.

I thank the Studienstiftung des deutschen Volkes, Fonds der Chemischen Industrie, Deutscher Akademischer Austauschdienst, Telluride Science Research Center, University of Kiel and the Weizmann Institute of Science for financial and scientific support. I thank the Studienstiftung des deutschen Volkes for so many wonderful events and summer schools.

The past and present members of the Hartke and Tannor groups I thank for nice discussions and the nice time, in general.

I thank Dr. Simone Knief, Dr. Karsten Balzer, Dr. Mark Vilensky, Sascha ‘Sushi’ Frick, Christopher Witt and Dr. Werner Koch for help with the computing facilities at CAU Kiel, Weizmann Institute and in the Hartke and Tannor groups. I am also very thankful to Terry Debesh, Tanja Stojšić and Sonja Ehmke for helping me with the bureaucracy.

I am deeply grateful to Mark Dittner for countless discussions on various topics and for the friendship in general. There is no better colleague and companion for operas, orchestras, movies or for discussing 'fremde Gedanken'. The same holds true for Michael Herbst. Thank you for lecturing with me a course at the DSA. Without you, I would not have done it and I am looking forward to the next one.

Further, I thank Dr. Shai Machnes and Dr. Elie Assémat for helping me when I arrived in Israel. I never felt lost or alone. I thank Dr. Shai Machnes, Amit Cohen and Prof. David Tannor for introducing me to the Jewish culture and language! חורה רבה In general, I thank Dr. Noa Zamstein, Dr. Werner Koch, Dr. Shai Machnes, Dr. Elie Assémat, Dr. Rafael Abta, Dr. Norio Takemoto, Dr. Jerry Fereiro, Maren Lück and all the others at Weizmann for the wonderful time. Thanks to Ariel and Stephen from Finjan and all the other hiking companions for many inspiring and unique days and nights in the desert. Thanks to my other friends from Germany, Switzerland, Sweden, Israel and elsewhere. Thanks to the nice people I have met at CAU, on conferences, summer schools or during activities of the FChO, CdE or the DSA, including the Schrödinger's cat fan club. The list would, unfortunately, be too long to mention all of them. Thanks to Sascha 'Ragazzo' for never-ending nights. Thanks to Miriam Schehr for her help.

Finally, I thank my parents, Knut Larsson and Sigrid Larsson, for their continuous support.

Writing this thesis was only possible with the massive consumption of bananas, apples, green tea and Swedish coffee.